THE MECHANICAL PROPERTIES OF GLASS-CERAMICS IN THE SYSTEM CaO - MgO - Al_2O_3 - SiO_2

by

Clive Brian Ponton, B.Sc.(Eng), A.R.S.M.

Thesis submitted
for the degree of Doctor of Philosophy
of the University of London
and
for the Diploma of Membership
of the Imperial College of Science and Technology.

March 1987

Department of Materials, Royal School of Mines,
Imperial College of Science and Technology,
London SW7 2BP.

ABSTRACT

The mechanical properties of four glass-ceramics in the system CaO - MgO - Al_2O_3 - SiO_2 were measured and related to both microstructure and other physical property data. They are novel materials, known as 'Silcerams', and are produced by a patented process. In the patented Silceram process, controlled crystallization of the parent-glass is achieved by cooling the worked glass directly from its working temperature to a holding temperature at which nucleation and crystal growth occur simultaneously, the former more rapidly than the latter. The glass-ceramics studied were a laboratory produced reference material (SCF5) and three other materials produced at a pilot-plant (SCR25.76, SCR19.34, and SCR19.13). Their microstructures purposely ranged from the highly crystalline SCF5 to the glassy SCR19.13 material. One of the two properly crystallized pilot-plant materials was made from iron blast-furnace slag and colliery shale (SCR25.76); the other materials were made using pure components.

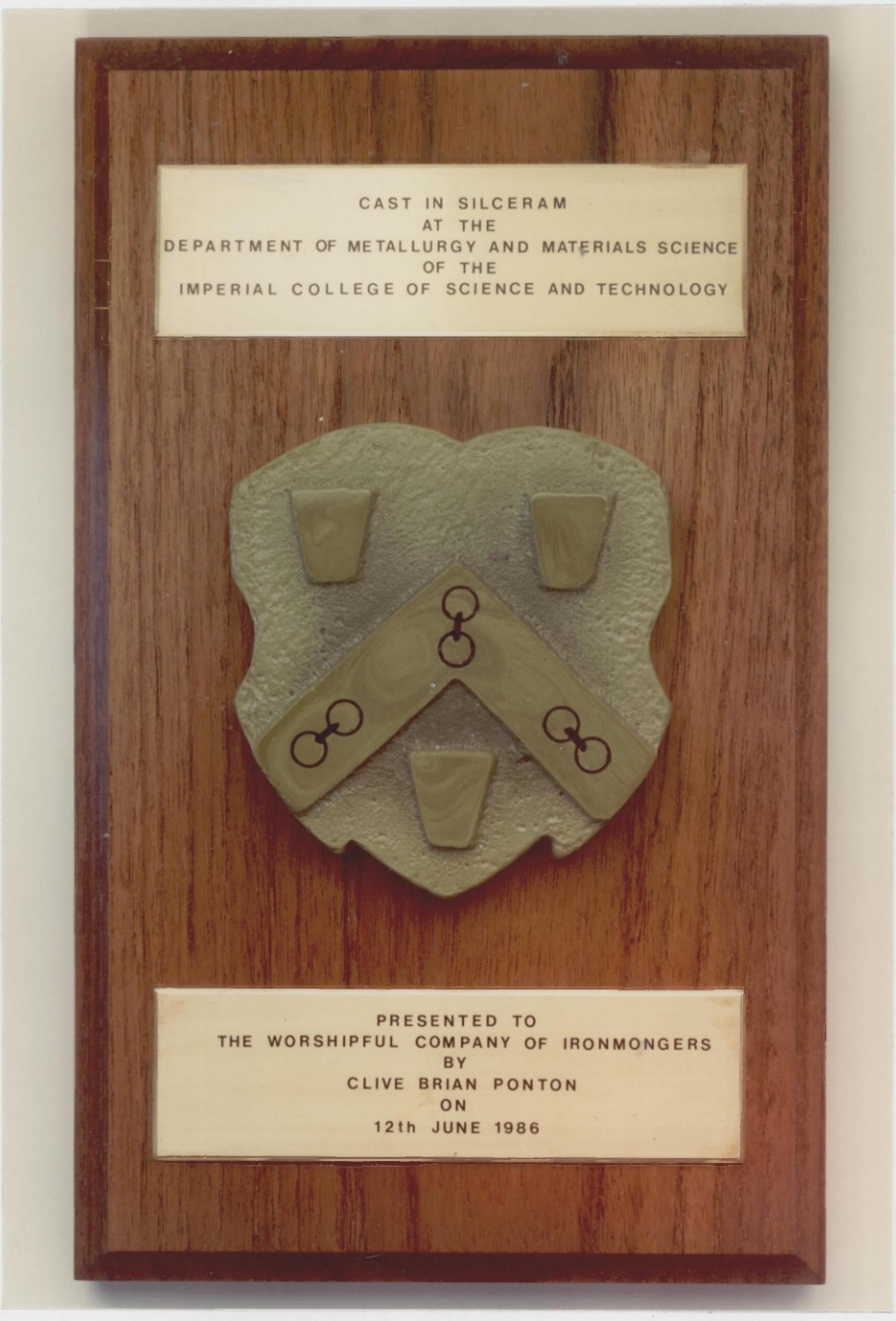
The following room temperature data were obtained, (a) the Vickers hardness and indent fracture toughness (16 indent fracture toughness formulae in the literature were reviewed, used and compared), (b) the three-point flexural strength and SENB fracture toughness, and (c) the Young's modulus (using a dynamic resonance method). The 3-point bending technique was critically reviewed and the effect of fracture away from the mid-span position (on the tensile face) and wedging on the calculated flexural strength considered. In addition, the temperature dependence of the flexural strength, SENB fracture toughness, Young's modulus, and internal friction were determined for the crystalline materials. The Weibull moduli of SCR25.76 and SCR19.34 were calculated using 4 survival probability estimators and the results compared; SPT diagrams were also drawn using flexural strength data at different strain rates. Other mechanical property data were obtained, e.g., the stress dependence of the compression secondary creep rates of SCR25.76 and SCR19.34 at 709°C.

To my parents
with thanks for their support and consideration
over the past five months
while I was writing up.

IF

If you think you are beaten, you are
If you think you dare not, you do not
If you would like to win, but think you cannot
It is almost certain you will not
If you think you will lose, you have lost
For out of the world we find
Success begins with a fellow's will -
It is all in the state of mind
If you think you are outclassed, you are
You have got to think high to rise
You have got to be sure of yourself before
You can ever win a prize
Life's battles do not always go
To the stronger or faster man
But sooner or later the man who wins
Is the one who Thinks he can.

Anonymous


CAST IN SILCERAM
AT THE
DEPARTMENT OF METALLURGY AND MATERIALS SCIENCE
OF THE
IMPERIAL COLLEGE OF SCIENCE AND TECHNOLOGY
PRESENTED TO
THE WORSHIPFUL COMPANY OF IRONMONGERS
BY
CLIVE BRIAN PONTON
ON
12th JUNE 1986

ACKNOWLEDGEMENTS

I wish to thank my supervisors, Dr. R.D. Rawlings and Dr. P.S. Rogers for their friendship, support and guidance, and Dr. S. Carter for (a) the interesting discussions on the correlation between the mechanical properties and the microstructure, chemical composition and residual glass viscosities, and (b) for her generous assistance in the preparation of the micrographs and equipment photographs. I thank Hitesh Patel for the use of his dynamic resonance rig, Darren Evans for performing the serial polishing, and Miss M. Campbell and Dr. J.F. Bell for producing the laboratory and pilot-plant materials respectively.

The provision of laboratory facilities by Professor D.W. Pashley F.R.S., the award of a three year Research Studentship by the SERC, and the financial support of The Worshipful Company of Ironmongers through a bursary for the last two years of my Ph.D. studentship are all gratefully acknowledged. The Ironmongers' crest cast in Silceram (see page 5) was presented to The Worshipful Company of Ironmongers by the author in gratitude.

I thank all the technical, photographic, and administrative staff who have provided practical advice and support, and in particular, those who were involved in the construction of my experimental equipment (i.e., all the Materials Workshop staff !):

High Temperature Furnace:

R.Baxter, K. Hortin, D.W. Tickner, A.J. Tipple, J.M. Sullivan, and J. Wright.

Dynamic Resonance Rig:

R. Baxter, K. Hortin, W.I. Hutton, D. Raj, and J. Wright.

Compression Creep Rig:

R. Baxter, K. Hortin, W.I. Hutton.

Last, but not least, I wish to thank my fellow students (past and present) and friends (the two are synonymous) in Dr. Rawling's research group for their friendship, support, and interest in my work: Shabbar Atiq, "Stef" Carter, David Miller, Clive Orrock, Aba Persiano, Ahmet Selcuk, "Muj" Shahrooz, and Ian Thompson.

CONTENTS

CHAPTER 1 : SCIENCE AND TECHNOLOGY OF GLASS-CERAMICS 15

1.1 Introduction 15

1.2 Controlled Crystallization 16

1.3 Working and Heat Treatment Procedures 19

1.3.1 Working techniques 19

1.3.2 Heat treatment regime 20

CHAPTER 2 : GLASS-CERAMICS IN THE SYSTEM

$CaO - MgO - Al_2O_3 - SiO_2$ 24

2.1 Introduction 24

2.2 Controlled Crystallization of Silceram Glass-Ceramics 25

2.3 Production of Silceram SCF5, SCR25.76, SCR19.34 and SCR19.13 Glass-Ceramics 27

2.3.1 Production of SCF5 27

2.3.2 Production of the pilot-plant glass-ceramics, SCR25.76, SCR19.34 and SCR19.13 28

2.4 Microstructure of SCR25.76, SCR19.34, SCR19.13 and SCF5, and Volume Fraction of Residual Glass 30

2.5 Chemical Composition Analyses of SCF5, SCR25.76, SCR19.34 and SCR19.13 Glass-Ceramics 32

CHAPTER 3 : ELASTIC PROPERTIES AND INTERNAL FRICTION . 37

3.1 Introduction 37

3.2 Isotropic Elastic Constants 40

3.3 Fundamental Significance of Isotropic Elastic Moduli 43

3.4 Factors Influencing Elastic Properties 44

3.4.1 Effect of temperature 44

3.4.2 Effect of porosity 46

3.4.3 Effect of multiple phases in a material 46

3.5 Internal Friction 49

3.5.1 Determination of internal friction by forced vibration 50

3.5.2 Determination of internal friction by free decay and the attenuation of a travelling elastic wave 52

3.6 Experimental Determination of Elastic Moduli and Internal Friction 53

3.6.1 Static methods of measuring elastic moduli 53

3.6.2 Dynamic methods of measuring elastic moduli ... 54

3.6.3 Experimental measurement of internal friction . 55

3.6.4 Advantages of dynamic techniques 56

3.6.5 Elastic moduli and the thermoelastic effect ... 56

3.7 Experimental Determination of the Elastic Moduli and Internal Friction of Glass-Ceramics in the System $CaO - MgO - Al_2O_3 - SiO_2$ 59

3.7.1 Experimental methods employed 59

(1) Main method (horizontal suspension technique) . 61

(1.1) Description of the electronic instrumentation 61

(1.2) Description of the high temperature furnace ... 64

(1.3) Description of the vacuum system 66

(1.4) Determining the resonant frequency 68

(1.5) Room temperature measurements 70

(1.6) High temperature measurements 72

(2) Subsidiary method (horizontal clamping technique) 73

(3) Specimen requirements and preparation 77

(4) Calculation of elastic moduli using resonant frequency data 78

3.7.2 Experimental results and their analysis 81

(1) Preliminary data obtained using Förster's method 81

(2) Primary data obtained using Förster's method and the horizontal clamping method 84

(2.1) Effect of suspension position in Förster's method 84

(2.2) Determination of the shear modulus of specimens SCR25.76 D and SCR19.34 D at room temperature 98

(2.3) Determination of the Young's modulus of SCR25.76, SCR19.34, SCF5 and SCR19.13 glass-ceramics at room temperature 100

(2.4) Estimation of the bulk modulus, longitudinal modulus, longitudinal and shear stress wave velocities of SCR25.76 and SCR19.34 104

(2.5) Summary of the room temperature elastic properties of CaO - MgO - Al_2O_3 - SiO_2 glass-ceramics and comparison with the equivalent properties of some other ceramic materials 105

(2.6) Young's modulus and internal friction of SCR25.76, SCR19.34 and SCF5 as functions of temperature 107

3.8 Temperature Dependence of the Internal Friction of Other Ceramic Materials 113

CHAPTER 4 : NON-DUCTILE BEHAVIOUR AND STRENGTH 116

4.1 Introduction 116

4.2 Non-Ductile Behaviour of Glass-Ceramics 117

4.3 Strength of a Non-Ductile Material 119

4.3.1 Griffith criterion for non-ductile fracture ... 120

4.4 Uniaxial Tensile Strength Measurement Techniques for Non-Ductile Materials 125

4.4.1 Bend testing using three or four-point loading 127

4.4.2 Sources of error in three-point bending tests 131

4.5 Uniaxial Compressive Strength Measurement Techniques for Non-Ductile Materials 144

4.6 Statistical Characterization of the Tensile Strength of Non-Ductile Materials 145

4.7 Long-Term Strength and Service-Life Prediction 150

4.7.1 Time to failure under a constant load 153

4.7.2 Sub-critical crack growth at a constant strain-rate 156

4.8 Strength-Probability-Time (SPT) Diagram 158

4.9 Experimental Determination of the Fracture Strength Properties of Glass-Ceramics in the System CaO - MgO - Al_2O_3 - SiO_2 162

4.9.1 Experimental apparatus used to determine the flexural and compressive strength 163

(1) Room temperature bending test rig 163

(2) High temperature bending test rig 163

(3) Room temperature compression test rig 173

4.9.2 Preparation procedure for strength test specimens 173

(1) Flexural strength specimens 173

(2) Compressive strength specimens 174

4.9.3 Experimental flexural and compressive strength results at room temperature 175

(1) Effect of the equation used to calculate fracture stress on the calculated mean flexural strength 176

(2) Effect of strain-rate on the mean flexural strength of SCR25.76 and SCR19.34 178

(3) Comparison of the mean flexural strengths of SCR25.76, SCR19.34, SCF5 and SCR19.13 measured at a strain-rate of $\approx 7.5 \times 10^{-4}\ s^{-1}$ and calculated taking account of wedging and fracture origin 178

(4) Crack propagation and branching patterns of SCR25.76, SCR19.34, SCF5 and SCR19.13 and the representative fracture surfaces of flexural strength test specimens SCR19.34 MB401 and SCR25.76 MA401 179

(5) Mean compressive strength data for SCR25.76 and SCR19.34 181

4.9.4 Room temperature Weibull modulus data assuming a threshold stress of zero 185

4.9.5 Effect of stressed volume on the fracture stress 195

4.9.6 Comparison of the nominal room temperature flexural strength of SCR25.76, SCR19.34, SCF5 and SCR19.13 glass-ceramics with those of other typical ceramic materials 196

4.9.7 Comparison of the nominal room temperature Weibull modulus values of SCR25.76, SCR19.34, SCF5 and SCR19.13 with those of other typical ceramic materials 197

4.9.8 Strength-probability-time (SPT) diagrams for SCR25.76 and SCR19.34 at room temperature 198

4.9.9 Estimation of Weibull parameters using the graphical approach of Leon and Kittl 203

4.9.10 Experimental flexural strength results at elevated temperatures 208

CHAPTER 5 : FRACTURE TOUGHNESS AND HARDNESS 218

5.1 Introduction to Conventional Toughness 218

5.2 Introduction to Hardness 224

5.3 Introduction to Indentation Fracture Toughness 227

5.3.1 Summary of indentation fracture toughness equations 252

5.4 Experimental Determination of Plane Strain Fracture Toughness, K_{Ic}, Using Single-Edge Notched Bend (SENB) Specimens in Three-Point Bending 253

5.5 Experimental Determination of the Fracture Toughness and Hardness of Glass-Ceramics in the System CaO - MgO - Al_2O_3 - SiO_2 262

5.5.1 Experimental determination of SENB K_{Ic} 263

(1) Specimen preparation and testing 263

(2) Room temperature experimental results 264

(3) High temperature experimental results 266

5.5.2 Experimental determination of SENB G_{Ic} 272

(1) Introduction 272

(2) Specimen preparation and experimental procedure 273

(2.1) Determination of the room temperature Young's modulus in flexure of ICI 'Perspex' acrylic sheet 274

(2.2) Room temperature compliance measurement 275

5.5.3 Experimental determination of Vickers hardness and indentation fracture toughness, K_c 278

(1) Specimen preparation and experimental procedure 278

(2) Experimental macro-hardness and fracture toughness results 279

(2.1) Relationship between indenter load and surface radial crack length 282

(2.2) Indentation fracture toughness results 284

(2.3) Determination of the Young's modulus-to--hardness ratio (E/H) of SCF5 from the recovered Knoop indent dimensions for different indenter loads 290

CHAPTER 6 : STRESS DEPENDENCE OF SECONDARY COMPRESSION CREEP OF SCR25.76 AND SCR19.34 AT 709°C 292

6.1 Introduction 292

6.2 Compression Creep Testing 296

6.3 Compression Creep Rig and Specimen Preparation 301

6.4 Determination of Secondary Creep Rates at 709°C 305

6.5 Experimental Data at 709°C and Data Analysis .. 309

CHAPTER 7 : DISCUSSION OF RESULTS, CONCLUSIONS AND SUGGESTIONS FOR FURTHER WORK 322

7.1 Discussion of Results 322

7.2 Conclusions 327

7.3 Suggestions for Further Work 328

APPENDICES : CHAPTER 3

Appendix 3A 330

Appendix 3B 331

Appendix 3C 334

Appendix 3D 335

Appendix 3E 336

APPENDICES : CHAPTER 4

Appendix 4A 343

Appendix 4B 345

Appendix 4C 347

Appendix 4D 350

Appendix 4E 351

Appendix 4F 355

Appendix 4G 358

APPENDICES : CHAPTER 5

Appendix 5A 362

Appendix 5B 365

Appendix 5C 366

Appendix 5D 370

Appendix 5E 371

Appendix 5F 373

Appendix 5G 375

APPENDICES : CHAPTER 6

Appendix 6A 377

Appendix 6B 378

REFERENCES 380

ERRATA :

Page 52, Paragraph 2, Line 5 should read "reflections at the material boundaries. In the wave attenuation method the"

Page 324, Paragraph 1, Line 8 should read "Furthermore, the flexural strength data for SCR25.76 and SCR19.34 are the 20 S4 data"

CHAPTER 1

SCIENCE AND TECHNOLOGY OF GLASS-CERAMICS

1.1 Introduction

Glass-ceramics are polycrystalline materials formed when glasses of suitable composition are subjected to a carefully controlled heat treatment regime and thereby undergo controlled crystallization. As they are formed from conventional glasses and have a microstructure not unlike that of a conventional ceramic, it is appropriate to briefly define what a conventional glass and ceramic are; a conventional glass is usually the product of fusion of inorganic oxides which has cooled to a rigid condition without crystallizing as per the A.S.T.M. definition, while in the context of the present work, a conventional ceramic is a polycrystalline material consisting of one or more crystalline phases bonded together by an intergranular glass phase, and produced by heating a mixture of inorganic polycrystalline raw materials to a temperature at which a viscous liquid phase forms.

A glass-ceramic is distinct from a glass in that typically at least 50 % and as much as 98 % of the volume is crystalline, with the remaining volume being an intergranular residual glass phase whose composition is generally different from that of the glass used to make the glass-ceramic, i.e., the parent-glass, due to depletion of the components necessary for crystallization. Glass-ceramics are distinct from ceramics in general because the crystalline phase or phases are formed from a homogeneous vitreous parent phase, rather than being originally present as the raw materials. The most notable feature of a typical glass-ceramic is its polycrystalline microstructure, which can be described as near ideal, consisting of small, uniformly sized, randomly oriented, frequently interlocking crystals whose sizes range from fractions of a micron to a few microns, with essentially zero porosity and a small amount of intergranular glass.

1.2 Controlled Crystallization

The crystallization process in any glass involves two distinct, temperature dependent sub-processes, (i) the nucleation of crystal nuclei and (ii) the growth of the crystal nuclei or the growth of one or more crystalline phases on the nuclei. In order to produce the desirable microstructure described above a very large number of crystal nuclei must be formed and be uniformly distributed throughout the glass, and their subsequent growth or crystal growth upon them should occur in a controlled and uniform manner. The present-day ability to produce glass-ceramics with the microstructure described above and the desired physical and chemical properties, both economically and reproducibly, is due to efficient bulk crystal nucleation, which is made possible by the use of what are known as 'nucleating agents', prior to controlled, uniform crystal growth.

Nucleating agents are materials which are added to and are completely soluble in the parent-glass at the melting and working temperatures, but which initiate efficient bulk nucleated crystallization during the carefully controlled heat treatment of the worked parent-glass. The discovery and use of a wide variety of nucleating agents, which are matched to one or more parent-glass systems, began with the work of S.D. Stookey on photosensitively opacified glasses leading to the production of the first true glass-ceramic by the Corning Glass Works (U.S.A.) in 1957 (Stookey, S.D. and Maurer, R.D., 1962). Nucleating agents may initiate nucleated crystallization in one or more of the following ways:

(a) By precipitating out in the glass and forming crystal nuclei upon which epitaxial growth of the main crystalline phase occurs as a consequence of their crystallographic similarity.

(b) By precipitating out in the glass and forming heterogeneous nucleation sites on which embryos of the major crystalline phase or phases can readily nucleate and subsequently grow.

(c) By acting as a surface active agent, i.e., a surfactant, and reducing the critical size of an embryo required to form a stable nucleus by reducing the interfacial surface energy between the crystal embryo and the glass, and thereby increasing the nucleation density.
(d) By inducing amorphous or glass-in-glass phase separation either on cooling or re-heating of the worked parent-glass, and becoming concentrated in the dispersed, separating phase, hence forming heterogeneous nucleation sites or metastable crystal nuclei; nucleation and growth of the main crystalline phase or phases thus occurs in the dispersed phase during heat treatment.

The actual mechanisms by which nucleating agents nucleate bulk crystallization are in general not fully understood due to their complexity; a possible exception is the formation of metallic crystal nuclei in certain glasses of the Li_2O - Al_2O_3 - SiO_2 system on which lithium metasilicate ($Li_2O.SiO_2$) crystals form and grow (Stookey, S.D. and Maurer, R.D., 1962). Various materials added in small amounts are successfully used as nucleating agents, for example, precious metals (e.g., Ag, Pt, Au) usually added as the chloride, oxides (e.g., TiO_2, ZrO_2, P_2O_5, Fe_2O_3, Cr_2O_3, V_2O_5), fluorides (LiF, MgF_2), and sulphides (FeS, MnS); however most nucleating agents are specific to certain parent-glass systems or composition ranges. The number of glass compositions from which glass-ceramics can be produced is in the high thousands (by the 1970's there were over 5000 suitable glasses (Berezhnoi, A.I., 1970)); the more important parent-glass and nucleating agent systems from the scientific, technological and commercial viewpoints are summarized in Table 1.1. As it is not the purpose of this chapter to review the subject of glass-ceramics in great detail, the reader is referred to the following references, especially McMillan's monograph: Stookey, S.D. and Maurer, R.D. (1962); Berezhnoi, A.I. (1970); Stewart, D.R. (1972), (1985); McMillan, P.W. (1979); Beall, G.H. and Duke, D.A. (1983); Hlaváč, J. (1983); the symposium proceedings edited by Hench, L.L. and Freiman, S.W. (1971), and Simmons, J.H. et al. (1982).

Table 1.1 Important Commercial Glass-Ceramic Systems:

Parent-Glass System	Nucleating Agent
$Li_2O - Al_2O_3 - SiO_2$ (< 10 mass % Al_2O_3)	Ag, Au, Pt, Cu, P_2O_5

This system forms the basis of photochemically nucleated glass-ceramics (UV light or X-rays) when Ag, Au, Pt or Cu are used as the nucleants; the major crystalline phase, $Li_2O.SiO_2$, is much more soluble in hydrofluoric acid than the parent glass enabling it to be preferentially etched away, i.e., the material can be "chemically" machined to whatever photochemical pattern has been imprinted by the crystal nuclei; e.g., Corning 'Fotoceram' 8063.

$Li_2O - Al_2O_3 - SiO_2$ (> 10 mass % Al_2O_3)	TiO_2, $TiO_2 + ZrO_2$, P_2O_5, $TiO_2 + P_2O_5 + ZrO_2$

The glass-ceramics in this system are the most important commercially because they can be produced with linear thermal expansivities ranging from negative values through zero to low positive values, endowing them with excellent thermal shock resistance; e.g., Corning 'Pyroceram' 9608.

$MgO - Al_2O_3 - SiO_2$	TiO_2, $TiO_2 + ZrO_2$, ZrO_2, P_2O_5

Glass-ceramics in this system, when free of alkali metal cations, have low dielectric loss at high frequencies (e.g., ≥ 1 MHz) and temperatures (e.g., 500°C); hence their use as radomes; e.g., Corning 'Pyroceram' 9606.

$K_2O - MgO - Al_2O_3 - B_2O_3 - SiO_2$	F

The main crystalline phase in the glass-ceramics of this system is a flourine mica, which like natural mica (which has hydroxyl instead of fluorine anions) has a sheet-like structure which cleaves readily parallel to the atomic layers because of the weak inter-layer bonding, but because of the strong intra-layer bonding resists fracture across the atomic layers; this enables the glass-ceramics to be machined with conventional cutting tools because the material "flakes" easily, i.e., crystals break away singly or in small clusters; e.g., Corning 'Macor' 9658.

$CaO - MgO - Al_2O_3 - SiO_2$	Fe_2O_3, Cr_2O_3, FeS

Glass-ceramics in this system are discussed in Chapter 2.

1.3 Working and Heat Treatment Procedures

Both crystal nucleation and crystal growth are temperature dependent processes because they involve the diffusion of atoms which is a thermally activated process, i.e., it depends on thermal energy; thus the parent-glasses have to be heat treated to bring about bulk crystallization.

1.3.1 Working techniques

The raw materials for the parent-glass together with the appropriate nucleating agent (or agents) are fused and the melt homogenized and refined in the manner of conventional glass melts. The homogeneous parent-glass is then cooled to its working temperature; depending on the glass-ceramic in question, one or more of the following techniques can be used to form and shape the parent-glass (McMillan, P.W., 1979); (Doyle, P.J., 1979):

(a) Conventional glass working methods such as blowing, pressing, rolling and drawing, with the process economy associated with high speed, high volume continuous manufacturing.

(b) Powder-forming techniques used in the conventional and special ceramics industries, such as slip-casting, dry pressing, hot pressing and so on.

(c) Techniques used in the metals fabrication industry, in particular gravity casting, centrifugal (i.e., spin-casting), investment casting (i.e., the "lost wax" process), hot extrusion, hot drawing.

The above techniques may require modification to allow their use with some compositions, as glass-ceramics usually have higher working temperatures ($\geq$ 900°C) and different rheological characteristics compared to those of conventional glasses, ceramics and metals. Note that when using powder-forming techniques, i.e., using the powdered parent-glass, a nucleating agent is not always essential because the large surface area of the powder, and the particle surface damage and trace contaminants due to the milling process ensure adequate bulk crystallization.

1.3.2 Heat treatment regime

A typical standard heat treatment regime involves re-heating the worked parent-glass to its nucleation temperature, that is the temperature at which the nucleation rate is a maximum and usually corresponds a temperature at which the viscosity of the glass is ≈ 10^{10} to 10^{11} Pa.s. To a first approximation this temperature lies between the dilatometric softening temperature (at which the viscosity is ≈ 10^{10} to 10^{11} Pa.s) and a temperature 50°C higher, and is generally in the range ≈ 500 to 900°C depending on the glass-ceramic. In some cases the worked glass is cooled below its working temperature to its annealing temperature (i.e., a temperature at which the viscosity is in the range $10^{12.4}$ to $10^{13.6}$ Pa.s, the former being the annealing point and the latter the strain point), or even to room temperature for inspection or storage prior to heat treatment.

The glass is held at the nucleation temperature for about 1 to 2 hours before the temperature is slowly increased at a rate usually not exceeding 300°C per hour to the crystallization temperature. The crystallization temperature is chosen so that (i) the rate of crystal growth is as fast as possible while still allowing viscous flow to relieve the streses in the glass and the growing crystals arising from the volume change due to crystallization (typically a change of 1 to 5 volume %, and either an increase or a decrease in volume), and (ii) coarsening processes, which would inhibit the formation of a fine-grained microstructure, are not initiated. Furthermore, the temperature must be lower than the liquidus temperature of the predominant phase or the least refractory phase or the residual glass to prevent distortion of the glass components, e.g., slumping. The glass is usually held at the crystallization temperature for at least an hour until the desired degree of crystallinity (usually maximum crystallinity) is achieved before being cooled slowly to room temperature. A schematic idealised temperature versus time schedule for

this two stage re-heat heat treatment is shown in Figure 1.1; in practice, however, the heat treatment schedule depends on the parent-glass/nucleating agent system, the degree of crystallinity required, and the size of the articles being heat treated; in many cases the enthalpy of fusion liberated, i.e., heat of crystallization, can be high, with temperature gradients of as much as 100°C between the interior and the surface of an article; the thicker the cross-section of an article, the higher the probability of a high temperature gradient and hence differential crystal growth rates within the section resulting in a non-uniform structure and even cracking. So practical heat treatment regimes may be more complex than that shown in Figure 1.1 (Berezhnoi, A.I., 1970); (Beall, G.H. and Duke, D.A., 1983).

The typical two-stage heat treatment discussed here is employed when the nucleation and crystal growth rate curves of a given glass-ceramic are well separated as shown schematically in Figure 1.2, i.e., the curves only overlap slightly; thus in order to obtain appreciable and convenient nucleation and crystal growth rates a different heat treatment temperature is required for each process. If, however, there is a significant overlap of the nucleation and crystal growth rate curves as shown schematically in Figure 1.3, then a single stage, i.e., an isothermal heat treatment can be used; depending on the parent-glass/nucleating agent system, the isothermal treatment may involve (i) heating the worked parent-glass from room temperature or from the annealing temperature up to a holding temperature at which crystal nucleation and growth occur simultaneously, the latter at a much slower rate than the former (Stewart, D.R., 1972, 1985), or (ii) direct or controlled cooling of the worked parent-glass from its working temperature to a holding temperature at which crystal nucleation and growth occur simultaneously, the latter at a much slower rate than the former (as used for the glass-ceramics in the present work; see Chapter 2). A schematic temperature-time diagram of these two isothermal heat treatments is shown in Figure 1.4.

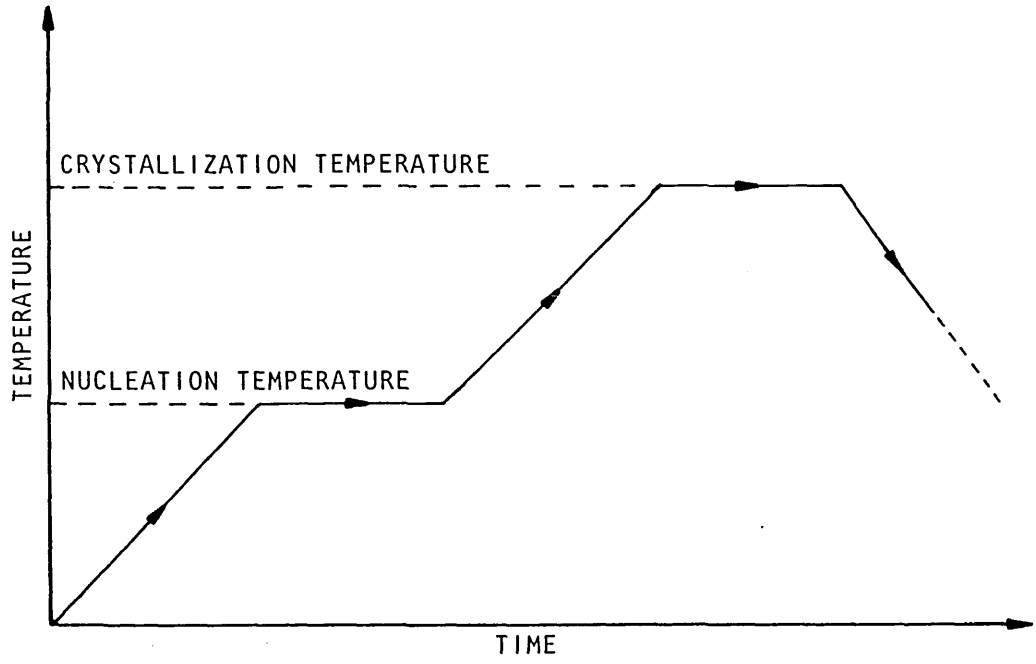


Figure 1.1 Schematic Temperature - Time Schedule for a Typical Conventional Two-Stage Re-Heat Treatment Regime.

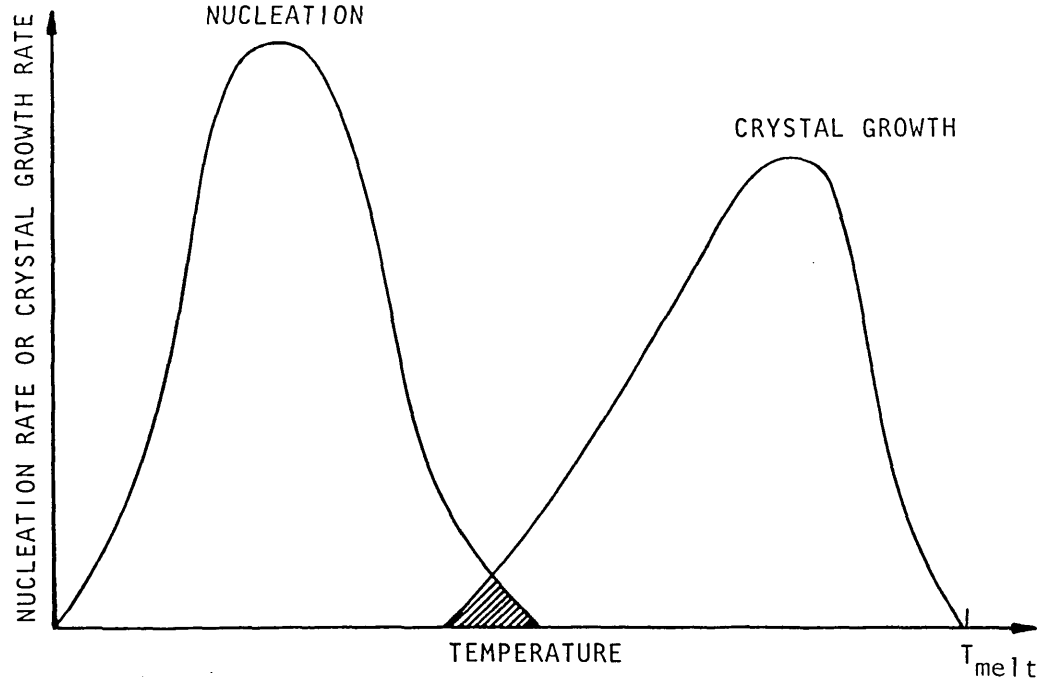


Figure 1.2 Schematic Tammann Curves With Only a Small Overlap of the Nucleation Rate and Crystal Growth Rate Curves.

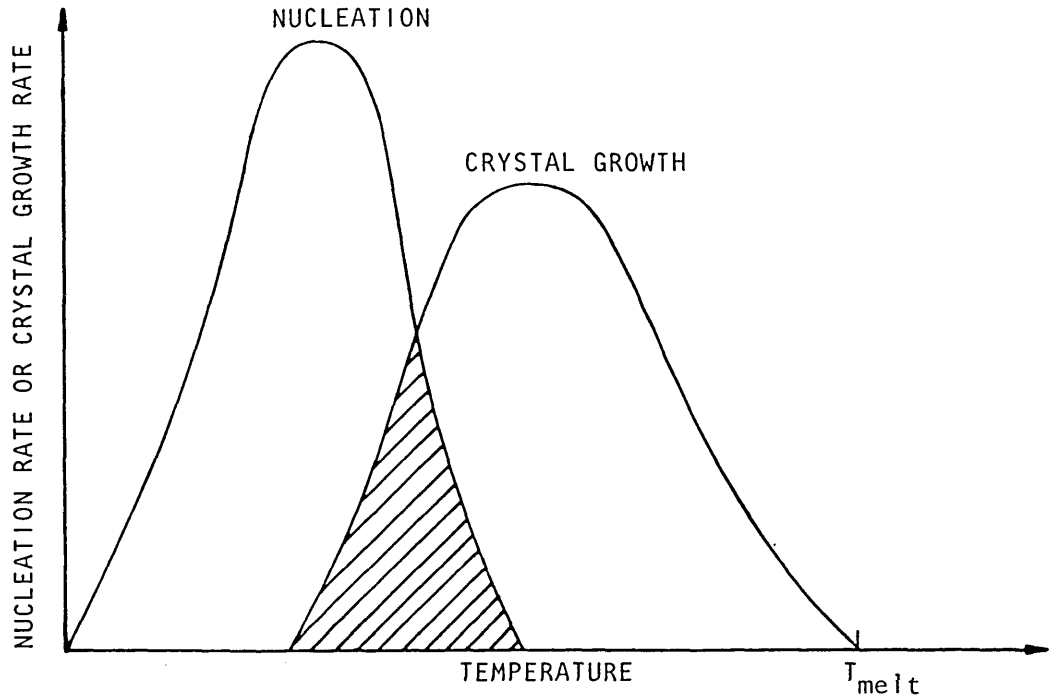


Figure 1.3 Schematic Tammann Curves With a Significant Overlap of the Nucleation Rate and Crystal Growth Rate Curves.

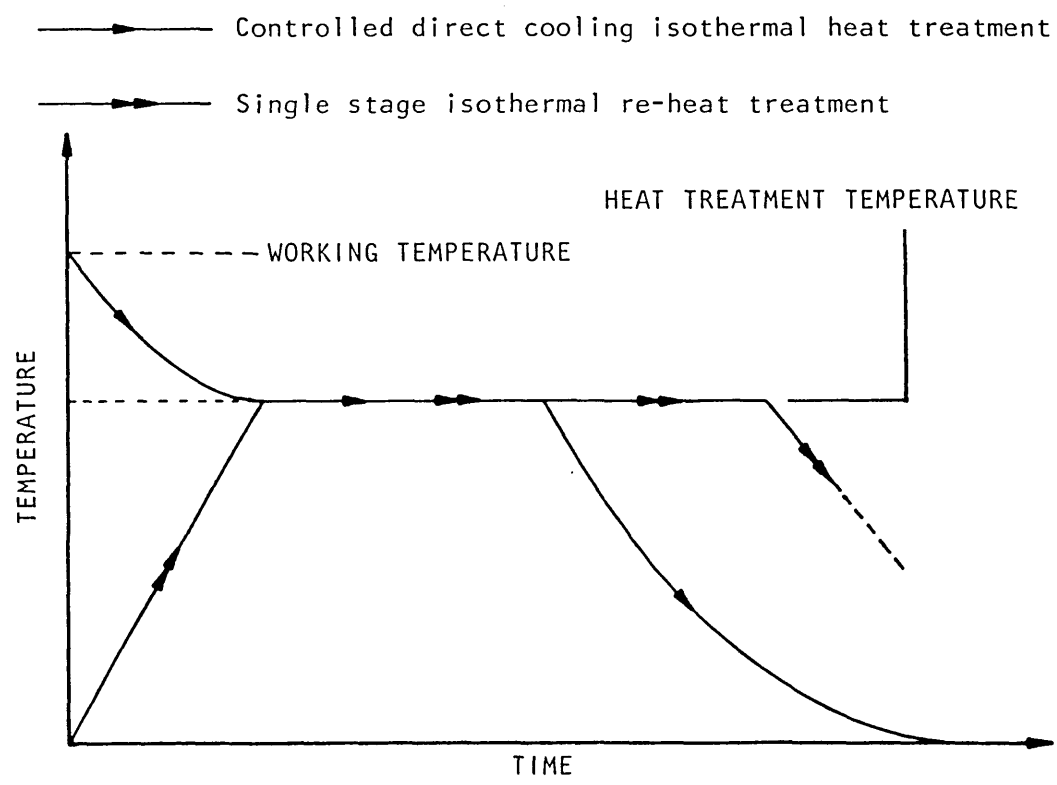


Figure 1.4 Schematic Temperature - Time Schedule for Controlled Direct Cooling, or Single Stage Re-Heat Treatment Regimes.

CHAPTER 2

GLASS-CERAMICS IN THE SYSTEM CaO - MgO - Al_2O_3 - SiO_2

2.1 Introduction

The four glass-ceramics whose mechanical properties were the subject of investigation in the present work were produced by the controlled crystallization of parent-glass compositions in the system CaO - MgO - Al_2O_3 - SiO_2. These compositions lie within the composition range specified in the patents taken out by P.S. Rogers et al. (1974, 1975), as given here:

Component	Mass %
CaO	0 - 30
MgO	0 - 30
Al_2O_3	5 - 35
SiO_2	35 - 75

Additives to the parent-glass are (i) a nucleating agent and (ii) fluxing and refining agents; the nucleating agent specified is a 'mixed' nucleating agent consisting of chromium oxide (Cr_2O_3) and iron oxide (Fe_2O_3) which can be added as 0.5 to 3 parts by mass and 0.5 to 10 parts by mass of the parent-glass respectively. Depending on the parent-glass composition it is stated that it may be beneficial to add further transition metal oxides; to aid refining and homogenization of the glass melt and reduce the liquidus temperature, Na_2O may also be added.

The parent-glass batch compositions can be made up of any of the following materials: (a) pure oxides, e.g., Al_2O_3, SiO_2, and carbonates, e.g., dolomite (a solid solution, $CaCO_3.MgCO_3$), limestone (calcite, i.e., $CaCO_3$ and possibly some dolomite), or (b) iron blast-furnace slags (consisting of CaO, SiO_2, Al_2O_3, MgO in decreasing amounts as the major components, together with, for example, MnO, Fe_2O_3 and sulphur as minor components), colliery shale (mainly SiO_2 and Al_2O_3, with SiO_2 as the

major component and MgO, CaO, Fe_2O_3 as minor components, the CaO content being in the order of 1 to 3 mass % ; certain shales contain sufficient combined iron oxide so that the addition of pure iron oxide may not be necessary), minestone (mainly SiO_2, with Al_2O_3 and Fe_2O_3 in decreasing amounts), the residues from coal-fired power stations and coal gasification plants, with pure oxides and carbonates added where necessary to supplement the components already present in the raw materials. The nucleating agents can be added as the oxides or as suitable precursor compounds of iron and chromium, both chemically bound to oxygen; they are usually added as ferric oxide (Fe_2O_3) and as sodium chromate (Na_2CrO_4) or sodium dichromate ($Na_2Cr_2O_7$) respectively (Bell, J.F., 1982); (Rogers, P.S., et al., 1986). All the glass--ceramics produced from parent-glass compositions within the patent have been given the generic name of 'Silceram'.

2.2 Controlled Crystallization of Silceram Glass-Ceramics

The patented Silceram process for producing glass-ceramics by controlled or nucleated crystallization employs a single-stage isothermal heat treatment regime which involves direct controlled cooling from the melt without any re-heating of the worked parent glass; this is possible because the nucleating agents, Fe_2O_3 and Cr_2O_3, acting in conjunction nucleate and control the crystallization of the parent-glass by promoting the formation, i.e., nucleation, of very small spinel crystals (typically $< 1\mu m$ in size) in large numbers over a relatively low and wide temperature range, which significantly overlaps the temperature range for crystal growth of the primary crystalline phase in Silceram glass-ceramics, which is a pyroxene. The spinel nuclei are formed without any prior amorphous phase separation and act as heterogeneous nucleation sites for the subsequent nucleation and growth of the pyroxene crystals. The crystalline phases in a number of laboratory and

pilot-plant Silceram glass-ceramics have been identified by X-ray diffraction (Rogers, P.S., et al., 1986); in all materials, the major crystalline phase was a pyroxene, specifically a diopside solid solution: $CaMgSi_2O_6$ with some substitution of Ca by Na or K, Mg by Fe^{2+}, Al^{3+}, or Mn, and Si by Al or Fe^{3+}. Lattice parameter data showed the nuclei to be slightly substituted magnesio-chromite spinels, i.e., not pure $MgCr_2O_4$ spinels.

When Cr_2O_3 is used on its own, the spinel nuclei are formed to all intents and purposes at a single temperature (1350°C); however, when Fe_2O_3 and Cr_2O_3 are used together, i.e., as a 'mixed' nucleating agent (with > 0.4 mass % Fe_2O_3), spinel nuclei are formed both at 1350°C and at temperatures below 1350°C. The former nuclei nucleated by the Cr_2O_3 acting in isolation are termed 'primary' nuclei, while the latter nuclei nucleated by the Cr_2O_3 and Fe_2O_3 acting in conjunction are referred to as 'secondary' nuclei. The secondary spinel nuclei are formed over a temperature range between approximately 850 and 1150°C with a maximum nucleation rate at ≈ 950°C, while crystal growth of the diopside solid solution occurs over a temperature range between about 800 and 1300°C with a maximum crystal growth rate at ≈ 1150°C (after unpublished work by P.E. Johnson as cited by J.F. Bell, 1982).

Measurements of the number of nuclei per unit volume suggest that the secondary nuclei outnumber the primary nuclei by approximately three orders of magnitude, and indicate that the number of secondary nuclei formed in excess of the number of primary nuclei reaches a maximum at a temperature slightly below 950°C, with no excess formed below 800°C or above 1100°C. The measurements also showed that the number of secondary nuclei formed above ≈ 1000°C was less than the number of primary nuclei formed at 1350°C, dropping to a minimum at a temperature a little below 1050°C; this has been attributed to the preferential growth of large nuclei at the expense of small nuclei, i.e., Ostwald ripening (after unpublished work by P.E. Johnson and cited by J.F. Bell, 1982). It has been found that at temperatures ≥ 960°C there is increasing evidence

of distortion of the cast shapes due to viscous flow and non-uniform crystallization (Bell, J.F., 1982). The data of Johnson demonstrate the synergistic effect of the 'mixed' Cr_2O_3 + Fe_2O_3 nucleating agent; the enhancement of nucleation has also been observed with some other mixed nucleating agents (McMillan, P.W., 1979).

As a result of these findings, a single-stage isothermal heat treatment in which the worked parent-glass is directly cooled from its working temperature to a temperature in the range ≈ 900 to 950°C and held there for three hours to ensure that the bulk nucleation and growth of the diopside solid solution goes to completion before being furnace cooled to room temperature, was adopted as specified in the patents; this heat treatment is much more economical than conventional two- or single-stage re-heat treatments (Rogers, P.S., et al., 1984, 1986).

2.3 Production of Silceram SCF5, SCR25.76, SCR19.34 and SCR19.13 Glass-Ceramics

The four glass-ceramics whose mechanical properties were investigated in the present work were produced to give a range of microstructures rather than the optimum microstructure, in order to study the influence of microstructure on mechanical properties. The SCF5 material was a laboratory produced material while the other materials were produced at a pilot-plant facility; the production processes of the glass-ceramics are described below.

2.3.1 Production of SCF5

The SCF5 parent-glass was prepared from pure oxides and carbonates (after Bell, J.F., 1982) using:

Component	Mass %
CaO	20
MgO	14
Al_2O_3	10
SiO_2	56

The nucleating agents Cr_2O_3 and Fe_2O_3 were specified in amounts of 0.8 parts by mass and 3 parts by mass per 100 parts by mass of the parent-glass respectively. They were added as Fe_2O_3 and as $Na_2Cr_2O_7$ in 1.38 parts by mass, providing 0.8 parts Cr_2O_3 and 0.33 parts Na_2O or as Na_2CrO_4 in 1.7 parts by mass, providing 0.8 parts Cr_2O_3 and 0.65 parts Na_2O. The calcium oxide was added as calcium carbonate which liberated carbon dioxide within the melt, helping to homogenize and refine the melt by its "foaming" action, while the other base components were added as the pure oxide. The raw materials were melted in a small fireclay crucible with a maximum batch capacity of ≈ 250 g at 1450 ± 20°C for three hours to ensure a homogeneous melt; the melt was then cast into a pre-heated steel mould, and the cast quickly transferred to the heat treatment furnace (pre-heated to 950°C) and heat treated at 950°C for three hours. The furnace was then switched off, and the cast furnace-cooled to room temperature over a 12 to 18 hour period (Bell, J.F., 1982).

2.3.2 Production of the pilot-plant glass-ceramics, SCR25.76, SCR19.34 and SCR19.13

These materials were produced at a pilot-plant facility employing a 50 kg batch process using an oil-fired, tilting tank furnace, operated under the direction of J.F. Bell; details of the pilot-plant operation and the 220 batches of 30 different experimental glass-ceramic compositions produced at the plant are given elsewhere (Rogers, P.S., et al., 1984, 1986). The SCR19.13 and SCR19.34 glass-ceramics were made from pure oxides and carbonates using the following nominal batch composition (SCR19):

Component	Parts by Mass
CaO	27
MgO	7
Al_2O_3	15
SiO_2	51

The Fe_2O_3 was added directly, while the Cr_2O_3 was added as sodium dichromate, with the amount of combined nucleating agent (i.e., Fe_2O_3 + Cr_2O_3) being equal to 5.5 parts by mass per 100 parts by mass of parent-glass composition. The melting temperature used was in the range 1480 to 1520°C, with a three hour melting stage, followed by heat treatment of the worked parent-glass for three hours at a temperature in the range 890 to 930°C.

The SCR25.76 glass-ceramic was produced from a nominal base composition based on an iron blast-furnace slag and red colliery shale mixture (SCR25):

Component	Parts by Mass
Slag	65
Shale	35
CaO	--
MgO	1 *
Al_2O_3	0.5 *
SiO_2	--

* pure components added to supplement the components already present in the slag and shale; Fe_2O_3 was also added as a supplement, while the Cr_2O_3 was again added as sodium dichromate. All the constituents in addition to the slag and shale amount to 7 parts by mass per 100 parts by mass of the parent-glass composition. The furnace charge was melted at a temperature in the range 1490 to 1520°C for 2 to 3 hours, while the worked parent-glass was heat treated at a temperature in the range 880 to 930°C for 3 to 3.5 hours.

All the pilot-plant material tested in the present work was sourced from flat tiles produced by gravity casting the melts via a ladle into open steel moulds and then heat treating the cast tiles in electric kilns before cooling them to room temperature inside the kilns. The amount of SCF5 and SCR19.13 glass-ceramic available for the determination of mechanical properties was very limited, so only the SCR25.76 and SCR19.34 glass-ceramics could be subjected to detailed mechanical property tests, both at room and elevated temperatures.

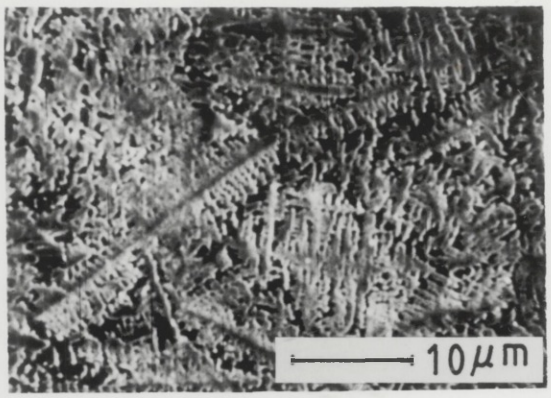
2.4 Microstructure of SCR25.76, SCR19.34, SCR19.13 and SCF5, and Volume Fraction of Residual Glass

The microstructures of the SCR19.34, SCR19.13, SCF5 and SCR25.76 glass-ceramics were studied using samples which were polished on a 1μm diamond lap, etched in 2% HF(aq) etchant, vacuum-coated with gold and then examined in a JEOL T-200 scanning electron microscope (SEM). All the materials have the same general microstructure, namely pyroxene crystals dispersed in a residual glass matrix; however, the volume fraction of residual glass and the pyroxene crystal morphology differed in each material. The amount of residual glass in the materials was determined either directly from SEM micrographs or filled-in tracings of the micrographs or both, using a Bausch & Lomb Omnicon-TM 3000 computer-based image analyser (Carter, S., 1986); the estimated volume fractions (normalized to 100 % and given with the sample standard deviations, the number of estimates averaged and the coefficients of variation) are given below:

Material		Vitreous Phase (Volume %)		Crystalline Phase (Volume %)	
SCF5	(22 data)	18 ± 5	28 %	82 ± 5	6 %
SCR25.76	(11 data)	29 ± 3	10 %	71 ± 3	4 %
SCR19.34	(7 data)	42 ± 2	5 %	58 ± 2	3 %
SCR19.13	(8 data)	70 ± 8	11 %	30 ± 4	13 %

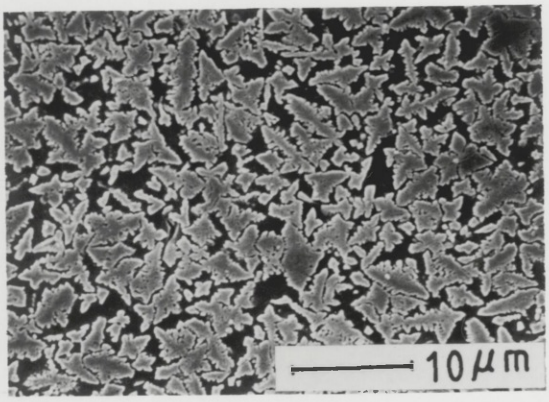
These results give an indication of the morphology span of the glass-ceramics produced for investigation in the present work. SEM micrographs of the representative microstructures of the four glass-ceramics are shown in Figure 2.1.

Comparing the micrographs shows that SCF5 has a very dendritic microstructure which is highly interlocked, i.e., intermeshed, because although the dendritic pyroxene crystals may have a "backbone" length of up to ≈ 30μm, the dendrite arm lengths are of the order of 3 to 10μm and have widths of the order of 0.5 to 1μm. The three-dimensional intermeshing crystal network appears to



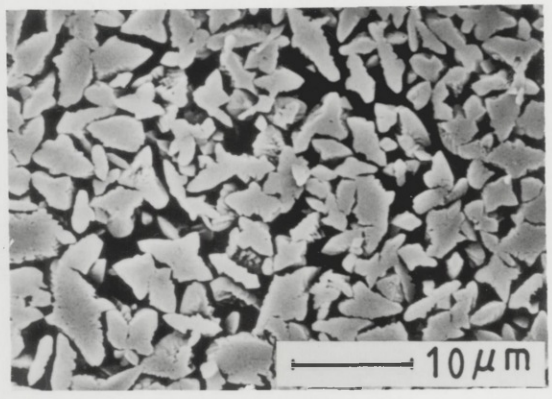
'Silceram' SCF5

A material produced in the laboratory using pure oxides and carbonates to give an acceptable reference microstructure.



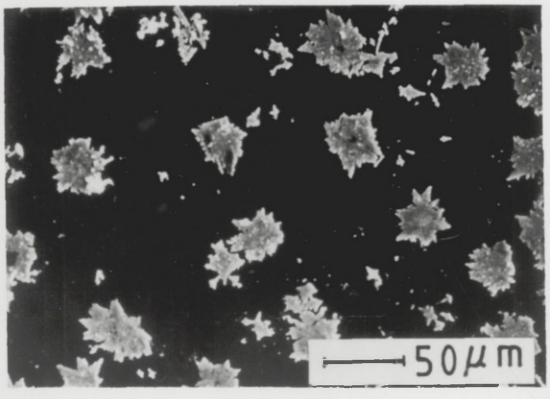
'Silceram' SCR19.34

A material produced at the pilot-plant facility using pure oxides and carbonates to give a barely acceptable microstructure.



'Silceram' SCR25.76

A material produced at the pilot-plant facility using iron blast-furnace slag and colliery shale, together with supplemental pure components to give a barely acceptable microstructure.



'Silceram' SCR19.13

A material produced at the pilot-plant facility using pure oxides and carbonates to give an unacceptable microstructure.

Figure 2.1 Scanning Electron Microscope (JEOL T-200) Micrographs of Etched (~2% HF(aq)) 'Silceram' Specimens With Representative Microstructures of SCF5, SCR19.34, SCR25.76 and SCR19.13.

be effectively continuous due to the nature and the degree of interlocking. In SCR19.34 the pyroxene crystals are much smaller with a mean "backbone" length of ≈ 5μm and are not as markedly dendritic as the crystals in SCF5 because (i) the "backbone" thickness is of the same order as the dendrite arm lengths and (ii) the dendrite arm widths are comparable with their length. As a result the crystals have a relatively equiaxial appearance in contrast to the dendritic SCF5 crystals, and hence are effectively discrete crystals even though they are in physical contact. The pyroxene crystals in SCR25.76 are more consolidated in nature and ≈ 3 to 10μm in size, and only betray their dendritic origin at the extremities; hence the crystals form an even more discrete distribution in the glass matrix than those in SCR19.34. The microstructure of SCR19.13 consists of a relatively small number of widely separated, roughly equiaxial pyroxene crystals with a typical size of ≈ 20 to 50μm, in the glass matrix.

2.5 Chemical Composition Analyses of SCF5, SCR25.76, SCR19.34 and SCR19.13 Glass-Ceramics

Both bulk chemical composition analyses and chemical composition analyses of the residual glass phase and the pyroxene primary crystalline phase have been conducted on samples of the SCR25.76, SCR19.34, and SCF5 glass-ceramics (Carter, S., 1986); in the case of the poorly crystallized SCR19.13, chemical compostion analyses were conducted on the pyroxene crystalline phase, and on the residual glass both near to and far from the crystal - glass interface.

The bulk chemical composition analyses were carried out on samples polished on a 1μm diamond lap, carbon coated, and examined using a JEOL JSM-35 SEM equipped with computer linked EDAX (Energy Dispersive Analysis of X-Rays) facilities. The chemical composition analyses of the residual glass and pyroxene phases were conducted on thin specimens prepared by ion-beam thinning and examined using a JEOL TEMSCAN scanning transmission electron

microscope (STEM) fitted with EDAX facilities, using the transmission electron microscope (TEM) mode. The analysed bulk chemical compositions of SCR25.76, SCR19.34, and SCF5 and the analysed chemical compositions of the residual glass (G) and pyroxene (P) phases are given in Table 2.1 and Table 2.2 respectively; the chemical composition analysis data for SCR19.13 are presented in Table 2.3. Note that the EDAX facilities cannot distinguish between different oxidation states, so although the iron content has been prescribed as Fe_2O_3, some or all of the iron may be FeO, rather than Fe_2O_3.

Examination of the pyroxene and residual glass compositons in Table 2.2 indicates that the residual glass in SCR25.76, SCR19.34 and SCF5 is very low in magnesium and iron, whereas the pyroxene phase is very high in magnesium and iron. The data for SCR19.13 given in Table 2.3 shows that concentration gradients exist in the residual glass as a function of distance away from the crystal - glass interface; within experimental error, the calcium, magnesium, and iron content of the residual glass increases with increasing distance from the interface. In contrast, the silicon content of the residual glass decreases with increasing distance from the interface.

During isothermal heat treatment of the Silceram parent glasses, the more siliceous nature and the relative paucity of the modifying elements (Mg, Fe, and Ca), which are necessary for the formation of the crystalline phase (pyroxene), in the residual glass near the crystal - glass interface affect the resulting crystal morphology. The higher viscosity of the residual glass near the interface (due to the higher Si content, and the scarcity of network modifying elements due to crystallization) reduces the diffusion rate, while the lower magnesium, calcium and iron concentrations increase the stability of the residual glass with respect to crystallization; as a consequence, the crystal growth rate will be faster ahead of the general crystal growth front. So any protuberance on the growth front will rapidly grow away from the bulk of the crystal; the tendency for the enhanced growth of

Table 2.1 Bulk Chemical Compositions of SCF5, SCR19.34, and SCR25.76 as Analysed By SEM/EDAX [After S. Carter (1986)]:

Component	SCF5 mass %	SCR19.34 mass %	SCR25.76 mass %
CaO	16.3	20.1	24.7
MgO	9.7	5.9	5.7
Al_2O_3	13.2	12.5	13.3
SiO_2	56.6	52.8	48.3
Fe_2O_3	2.8	4.6	4.0
Cr_2O_3	0.7	0.8	0.8
TiO_2	0.2	0.3	0.6
MnO	---	0.1	0.4
Na_2O	0.4	2.8	1.2
K_2O	0.4	0.1	1.1

Table 2.2 Chemical Compositions of the Residual Glass (G) and Pyroxene (P) Phases in SCF5, SCR19.34, and SCR25.76 as Analysed By STEM/EDAX [After S. Carter (1986)]:

Component	SCF5 mass %		SCR19.34 mass %		SCR25.76 mass %	
	P	G	P	G	P	G
CaO	19.3	10.0	24.4	19.1	25.5	25.3
MgO	12.9	1.3	10.0	1.3	7.7	0.1
Al_2O_3	9.6	17.9	8.3	15.0	10.7	16.5
SiO_2	52.1	65.9	47.0	57.5	45.8	52.8
Fe_2O_3	4.0	1.1	8.7	2.5	6.3	1.1
Cr_2O_3	0.7	1.0	1.0	0.2	1.7	0.1
TiO_2	0.4	0.4	0.2	1.1	1.0	0.5
MnO	0.1	0.1	0.1	0.1	0.7	0.3
Na_2O	0.5	1.1	0.4	2.6	0.7	0.3
K_2O	0.2	0.9	<0.1	0.3	0.3	2.2

Table 2.3 Chemical Compositions of the Pyroxene (P) Phase, and the Residual Glass (G) Phase as a Function of Distance Away From the Crystal - Glass Interface, in SCR19.13 as Analysed By STEM/EDAX [After S. Carter (1986)]:

Component	P mass %	G1 mass %	G2 mass %	G3 mass %
CaO	25.8	12.8	16.2	24.8
MgO	10.2	1.7	4.2	4.0
Al_2O_3	7.7	15.8	15.7	12.2
SiO_2	47.4	62.0	57.0	51.4
Fe_2O_3	8.1	1.7	1.4	4.9
Cr_2O_3	0.7	0.6	0.9	0.8
TiO_2	0.1	1.2	0.8	0.9
MnO	---	---	---	0.2
Na_2O	---	3.1	3.9	0.9
K_2O	0.1	1.2	0.2	0.1

Key: G1 denotes the residual glass region adjacent to the crystal - glass interface,
G2 denotes a residual glass region further away from the interface than region G1, and
G3 denotes the residual glass region furthest away from any crystal - glass interface.

such protuberances, leading to a more dendritic crystal morphology, increases with increasing viscosity and concentration gradients ahead of the general crystal growth front. The observed pyroxene crystal morphologies in SCR25.76, SCR19.34 and SCF5 support the above hypothesis. The greatest viscosity and concentration gradients would be established in the parent-glasses for which the bulk composition of the glass-ceramic differed most from the composition of the residual glass. A comparison of the data in Tables 2.1 and 2.2 shows that the greatest viscosity and concentration gradients would have arisen in the SCF5 material, while the smallest gradients will have occurred in the SCR25.76 material, with the SCR19.34 material having viscosity and concentration gradients intermediate between those in SCF5 and SCR25.76; the viscosity and concentration gradient differences are reflected in the pyroxene crystal morphologies, as shown in Figure 2.1. The pyroxene crystals in SCF5 are highly dendritic, while those in SCR25.76 are subhedral, tending towards a euhedral morphology, with relatively planar crystal - glass interfaces; the SCR19.34 crystals were more dendritic than those in SCR25.76, but less so than those in SCF5 (Carter, S., and Rogers, P.S., 1986).

CHAPTER 3

ELASTIC PROPERTIES AND INTERNAL FRICTION

3.1 Introduction

When a solid material is stressed its constituent atoms are displaced from their equilibrium positions and the mean interatomic separation changes; hence the solid is in a state of strain. On a macroscopic scale this is manifested as a relative change in the characteristic dimensions of the solid, e.g., length, volume, angular orientation, etc. The elastic properties of a material are important in any consideration of its mechanical behaviour, i.e. its response to imposed stresses, because any non-elastic response to an imposed stress is invariably preceded by a component of elastic behaviour, however small. The response of a homogeneous solid to an imposed stress is said to be perfectly elastic if the following conditions obtain:

(i) the strain due to an imposed stress has a value unique to that stress (and vice versa) and is such that the imposed force and the interatomic restoring force are in equilibrium,

(ii) the attainment of this unique equilibrium value is independent of time and the prior stress-strain state of the solid, and

(iii) the strain resulting from the imposed stress is small enough for the imposed stress to be considered unchanged despite the change in the characteristic dimensions of the solid due to the imposed stress.

The first condition implies completely reversible behaviour and is responsible for the most characteristic feature of ideal elastic behaviour, namely the complete recovery of the strain on the removal of the imposed stress *without any hysteresis or energy loss*. Note that for a bulk solid as opposed to an infinitely small solid, the unique strain (or stress) value is not reached

instantaneously due to the finite velocity of elastic stress waves through a solid. Nevertheless, when a bulk solid behaves in an elastic manner the equilibrium response is to all intents and purposes instantaneous, and the mathematical description of the response does not include time as a variable. Furthermore, an elastic solid is said to be linear elastic if when the imposed stress is doubled the resultant strain is also doubled, i.e., stress and strain are linearly related.

Real materials, however, do not exhibit perfect elastic behaviour even when subject to an oscillating "elastic" stress below that required to initiate plastic or non-recoverable strain because the elastic stress waves propagating through the material always lose energy by various mechanisms and at any instant the strain lags behind the stress, i.e., there is hysteresis. All of the energy loss mechanisms ultimately dissipate the energy as heat and the general phenomenon is known as "internal friction". In spite of this phenomenon, the behaviour of many materials can usually be regarded as "perfectly" elastic up to their experimental elastic limit.

The empirical law expressed by Robert Hooke (1678) regarding the frequently observed linear relationship between stress and strain in many materials for small strains (i.e., up to $\approx$ 0.5 % depending on the material), and the principle of superposition form the basis of the theory of linear elasticity. The principle of superposition states that if an imposed stress σ_1 causes a strain ϵ_1, and an imposed stress σ_2 causes a strain ϵ_2, then the simultaneous application of σ_1 and σ_2 will cause a strain equivalent to $\epsilon_1 + \epsilon_2$. The scalar form of Hooke's law states that the stress and strain in a homogeneous, linear elastic solid are directly proportional,

$$\sigma = M\epsilon \qquad [3.1]$$

or

$$\epsilon = C\sigma \qquad [3.2]$$

where σ is the imposed stress, ϵ the resultant strain, and $C = 1/M$; the constant M is an elastic modulus, while its reciprocal C is an elastic compliance.

Solid materials can be isotropic, quasi-isotropic, or anisotropic as regards their elastic properties; it all depends on their structure, i.e., whether they are amorphous or crystalline, mono- or poly-crystalline, etc. The general three-dimensional form of Hooke's law for a homogeneous, anisotropic, linear elastic solid with no spatial or structural symmetry states that in the absence of body torques there are six independent stress components and six independent strain components, and that each stress component is linearly related to each strain component via a proportionality constant and vice versa. Thus there are 36 independent elastic modulii and 36 independent elastic compliances respectively; however, consideration of the elastic energy stored when a solid is elastically strained reduces the number of independent elastic constants to 21 (Nye, J.F., 1969).

Crystalline materials are generally elastically anisotropic because the equilibrium interatomic spacing, (and in some materials the interatomic bond strength, e.g., covalent crystals) depends on the crystallographic direction; however, depending on the crystal symmetry, certain directions are equivalent as regards elastic behaviour, imposing restrictions on the number of independent elastic constants. The higher the degree of crystal symmetry, the fewer the number of independent elastic constants. Amorphous materials, however, are elastically isotropic, i.e., the elastic properties are independent of direction, and therefore only have two independent elastic constants (Nye, J.F., 1969).

If the individual crystals in a polycrystalline material are sufficiently small, randomly oriented and randomly distributed, so that in any direction there are sufficient grains to provide all possible orientations, then on a macroscopic scale the average elastic properties will be the same in any direction, i.e., the elastic behaviour of the bulk material will be quasi-isotropic. The term quasi-isotropic is used to distinguish such materials from materials which are elastically isotropic in the true sense, e.g., glass. Polycrystalline materials

prepared by sintering compacted powders, e.g., ceramics are usually quasi-isotropic, but production methods which induce a preferred grain orientation, i.e., texture, such as rolling, drawing, forging, extrusion, chemical vapour deposition (CVD), and so on, will make the materials anisotropic. Some examples of anisotropic polycrystalline ceramic materials are pyrolytic (CVD) graphite, hot-pressed and especially pyrolytic (CVD) boron nitride; these materials have graphitic, i.e., hexagonal-layer crystal structures.

3.2 Isotropic Elastic Constants

Glass-ceramics in the CaO - MgO - Al_2O_3 - SiO_2 system in common with most non-ductile materials, e.g., other glass-ceramics, glass, ceramics, etc. exhibit linear elastic behaviour at room temperature at all stresses up to their fracture stress. Furthermore, like other glass--ceramics, they are usually elastically quasi-isotropic for the following reasons:

(i) the parent-glasses are isotropic and homogeneous, and the glass-ceramic components are fabricated while still in the form of parent-glasses; thus no microstructural orientation is produced during forming, and

(ii) the high density of small crystals formed during the process of controlled crystallization are randomly oriented and distributed, so their anisotropic properties are negated in the bulk material.

So being quasi-isotropic, linear elastic materials, only the elastic properties of homogeneous, isotropic, linear elastic solids will be considered. Six elastic constants exist or are defined for such solids:

(1) Bulk or volume modulus, K (or B) is the hydrostatic or spherical stress required to produce unit volumetric strain or dilatation,

$$K \equiv \sigma_{hyd} / (\Delta V / V_o) \qquad [3.3]$$

where σ_{hyd} is the hydrostatic tensile or compressive

stress, ΔV the volume expansion or contraction of a body of original volume V_o.

(2) Shear or rigidity modulus, G (or μ) is the shear stress acting on the opposite faces of a body required to produce unit shear strain (equivalent to unit angular rotation of the normal to the shear plane),

$$G \equiv \tau/\phi = \rho(v_s)^2 \qquad [3.4]$$

where τ is the shear stress and ϕ is the angular rotation in measured in radians, and ρ is the density and v_s the shear elastic stress wave propagation velocity.

(3) Young's modulus, E is the uniaxial stress required to produce unit strain in the same direction as the imposed stress in the absence of any orthogonal contraints,

$$E \equiv \sigma/\epsilon \qquad [3.5]$$

where σ is the stress and ϵ the resultant strain.

(4) Poisson's ratio, ν is the ratio of the strain ϵ_o experienced in the directions orthogonal to the direction of the strain ϵ caused by an imposed stress σ acting in the same direction (in the absence of any orthogonal constraints),

$$\nu \equiv -(\epsilon_o/\epsilon) \qquad [3.6]$$

If the imposed strain is tensile, the orthogonal strain is compressive and vice versa, thus Poisson's ratio is positive for normal materials. There is a theoretical upper limit of 0.5 for the Poisson's ratio of normal materials (see Appendix 3A). Poisson's ratio for an isotropic material was calculated to be 0.25 by Poisson himself; experimental values show a wide variation; they range from almost zero for cork to about 0.5 for rubber, with a mean value close to 0.3. Glass which is isotropic has values in the range $\approx$ 0.2 to 0.27, while the majority of the technological materials such as polycrystalline metals and ceramics, and most plastics, which are quasi-isotropic if no microstructural directionality is imparted during fabrication, have values in the range 0.2 to 0.4. For concrete $\nu \approx 0.1 - 0.2$.

(5) Longitudinal modulus, L is related to the velocity of propagation of longitudinal elastic stress waves through a solid. Longitudinal waves propagate as acoustic, i.e.,

sound waves through a medium, regardless of the nature of the medium and are called longitudinal because the medium through which it propagates is perturbed in the direction of propagation. In physical terms a longitudinal elastic stress wave is a propagating dilatation or volumetric strain that subjects the material through which it travels to both compressive and shear stresses. This is because during the passage of the wave the volume of an element changes due to the change in the element's dimensions parallel to the direction of propagation, while the cross-sectional area (of the element) normal to the direction of propagation remains unchanged, and hence the element undergoes a change in shape and volume. So the longitudinal wave velocity depends on both the shear and bulk modulus, as well as the density of the solid,

$$L = K + 4G/3 = \rho(v_L)^2 \qquad [3.7]$$

where ρ is the density and v_L the longitudinal velocity (Kolsky, H., 1963); (Schreiber, E., et al., 1973).

(6) Lamé constant, λ is an elastic constant with no direct physical interpretation, but it and the shear modulus G form the two independent elastic constants of a homogeneous, isotropic solid as follows; $c_{11} = \lambda + 2G$ and $c_{12} = \lambda$, hence $(c_{11} - c_{12})/2 = G$ where c_{11} and c_{12} are the two independent elastic moduli in matrix notation (Nye, J. F., 1969); (Pollard, H.F., 1977). Together they completely define its elastic behaviour, since all the other elastic constants defined above can be written in terms of λ and G as summarised below:

(i) Longitudinal modulus, $L = \lambda + 2G$

(ii) Young's modulus, $E = G(3\lambda + 2G)/(\lambda + G)$

(iii) Bulk modulus, $K = \lambda + 2G/3$

(iv) Poisson's ratio, $\nu = \lambda/[2(\lambda + G)]$

Furthermore, regarding the physically significant elastic constants, i.e., E, G, K, L, ν, any two are sufficient to completely describe the elastic behaviour of an isotropic solid since any of them can be written in terms of any two of the other constants (see Schreiber, E., et al., 1973). The three basic elastic moduli, i.e., those directly relating stress to strain, namely the bulk, shear, and

Young's moduli, and Poisson's ratio are related as follows,

$$E = 3K(1 - 2\nu) = 2G(1 + \nu) \qquad [3.8]$$

3.3 Fundamental Significance of Isotropic Elastic Moduli

The bulk modulus (K) of a material is a measure of its resistance to elastic volumetric strain when subject to a hydrostatic stress, and is a fundamental parameter because it relates pressure to volume at a given temperature, and since pressure, volume and temperature are thermodynamic variables it relates elasticity to thermodynamics. The shear modulus (G) of a material is measure of its resistance to elastic shearing when subject to a shear stress, and like K is a fundamental parameter because for a high modulus solid G and K are both high, but when it melts G becomes zero, but the melt is effectively incompressible like all liquids, i.e., K remains high; so G and K are related to the nature of atomic bonding in a material. In fact both K and G can be related explicitly to the curvature of the atomic potential (P) versus interatomic separation (s) curve of a material, i.e., the second derivative, d^2P/ds^2 (= dF/ds, where F is the net interatomic force); see for example, Wyatt, O.H. and Dew-Hughes, D., (1974).

The Young's modulus (E) of a material is a measure of its resistance to a change in length when loaded in uniaxial tension or compression, and for many structural materials has the same magnitude in tension and compression. Since engineering structures are designed so that the in-service uniaxial stresses they experience do not strain them beyond their elastic limit, E is a very important design parameter. Both E and Poisson's ratio frequently appear as constants in many equations dealing with, for example, (i) the mechanics of elastically deformed bodies, (ii) the fracture mechanics of linear elastic materials, and so on. Furthermore, E also depends

on the second derivative of P versus s, i.e., d^2P/ds^2, as F and $s - S_E$ represent, on a macroscopic scale, stress and strain respectively, but on an atomic scale $F = dP/ds$ and $F \approx (s - s_E)\&F/\&s$ where s_E is the equilibrium interatomic spacing; thus $F \approx (s - s_E)dF/ds = (s - s_E)d^2P/ds^2$. So the elastic moduli are functions of d^2P/ds^2, and materials with very low potential energy minima (i.e., high bond energies) and hence high second derivatives such as most covalently and ionically bonded solids, e.g., ceramics, and some high sublimation temperature metals, e.g., tungsten, have high elastic moduli.

3.4 Factors Influencing Elastic Properties

The elastic moduli of some pure, single phase, fully dense (i.e. zero porosity) polycrystalline ceramics, e.g., MgO, Al_2O_3 are reported to be similar to the corresponding single crystal values showing that the elastic properties are effectively independent of grain size (Bailey, J.E. and Hill, N.A., 1970) just as they are in metals. In both instances this is due to the dependence of elastic properties on atomic bonding forces and atomic structure. The elastic properties of ceramics are, however, affected by temperature, porosity and the presence of more than one phase; the effect of each of these factors will be briefly discussed in turn.

3.4.1 Effect of temperature

The interatomic potential energy, and hence the mean interatomic separation of the atoms in a solid increase with increasing temperature. As a result the slope (dF/ds) of the interatomic force versus separation curve at F = 0 decreases with increasing temperature; the curve, however, still retains the shape it has at absolute zero at s = 0 and s = ∞ (see Eisenstadt, M.M., 1971). So the elastic moduli of a solid would be expected to decrease as well. Although there are exceptions, most materials show the expected decrease in elastic moduli with increasing

temperature. For example, the Young's modulus of a number of steels was found to decrease by about 25 % between room temperature and 600°C in a roughly linear manner (Roberts, M.H. and Nortcliffe, J., 1947), while the Young's modulus of a number of refractory single (e.g., Al_2O_3) and polycrystal ceramic materials was found to decrease in a linear manner with increasing temperature (Wachtman, J.B. and Lam, J.R., 1959). Wachtman and Lam reported that in the case of polycrystalline Al_2O_3, MgO, ThO_2, and mullite, the Young's moduli decreased linearly up to a temperature that was characteristic of the material, after which the decrease was rapid and non-linear; furthermore, the decrease in Young's modulus for polycrystalline spinel and stabilized zirconia was non-linear at lower temperatures, but also fell rapidly at high temperatures. Other ceramic materials showing "normal" behaviour are nickel-bonded titanium carbides (Spinner, S., 1961), polycrystalline Y_2O_3 up to 1100°C (Marlowe, M.O. and Wilder, D.R., 1965), silicon nitride and partially stabilized zirconia (Masahiko Shimada, et al., 1984), dental porcelain (Käse, H.R., et al., 1985).

Most glasses behave as expected, but vitreous SiO_2 and high-silica glasses exhibit anomalous behaviour, e.g., the Young's and shear modulus of Pyrex No. 7740 glass ($\approx$ 80 % SiO_2) and Vycor glass (96 % SiO_2) was found to increase with increasing temperature, imitating the behaviour of vitreous silica (Spinner, S., 1956). A later study found that the Young's modulus of vitreous silica reached a maximum at 1175°C, and that the temperature dependence of the Young's modulus of vitreous GeO_2 follows a similar pattern to that of vitreous SiO_2; the similar elastic behaviour has been attributed to the similarity in atomic structure (Spinner, S. and Cleek, G.W., 1960). It has been reported that the Young's modulus of glasses and glass-ceramics in the $0.98Li_2O - Al_2O_3 - nSiO_2$ system with n = 8,10,12 and n = 6,8,10 respectively increased linearly up to 550°C (Field, M.B. and Tucker, R.W., 1971).

3.4.2 Effect of porosity

Porosity has a deleterious effect on the elastic moduli of materials because it is equivalent to the presence of a phase with effectively zero bulk modulus, i.e., infinite compressibility. Porosity is particularly important in conventional sintered ceramic materials because incomplete densification during production will, and often does, result in a significant void content. There are a number of equations in the literature relating the volume fraction of porosity to the effective elastic modulus; they all take the form $M = S.M_o$ where M is the effective elastic modulus, M_o the zero-porosity elastic modulus, and $S = f(P)$ where S is a function of the volume fraction of porosity P which takes into account the nature of the material and the porosity via constants to varying degrees depending on the equation, i.e., S is a porosity dependent scaling factor less than unity (see for example, Bailey, J.E. and Hill, N.A., 1970).

Porosity is seldom a problem in glass-ceramics as the parent-glasses are normally refined and homogenized; however, some porosity may be introduced when the glass is worked, e.g., during gravity casting. The glass-ceramics investigated in this work were to all intents and purposes pore-free.

3.4.3 Effect of multiple phases in a material

In a multiple phase material each phase will make a contribution to the effective elastic moduli of the material. The contribution each phase makes will depend on its intrinsic elastic properties, volume fraction, and physical form and distribution in the material with regard to the direction of applied stresses and the resultant strains, i.e., the elastic anisotropy of each phase must be considered. So calculating the effective elastic moduli of a real multi-phase material using the elastic moduli of its constituent phases is not possible unless the material possesses a well defined phase geometry and distribution.

For a simple two-phase material in which one of the phases has higher elastic moduli, the material elastic moduli will have values between those of the two constituent phases. If the two-phase material is assumed to consist of alternate layers of a phase 1 with Young's modulus E_1 and volume fraction V_1 and a phase 2 with Young's modulus E_2 and volume fraction V_2, which can be uniaxially stressed in two ways, i.e, parallel or perpendicular to the layers, the following approximations of the Young's modulus of the material can be made (see Appendix 3B):

(i) if the material is stressed perpendicular to the layers each layer will be subject to the same stress, but the phase 1 layers and the phase 2 layers will be strained different amounts (Reuss model),

$$E = E_1 E_2 / (E_1 V_2 + E_2 V_1) \qquad [3.9]$$

(ii) if the material is stressed parallel to the layers each layer will be strained by the same amount, but the phase 1 layers and the phase 2 layers will experience different stresses (Voigt model),

$$E = E_1 V_1 + E_2 V_2 \qquad [3.10]$$

The Voigt model and the Reuss model give the maximum and minimum limits respectively for the Young's modulus of a two-phase material. Since the Young's moduli of real two-phase materials as opposed to artificial two-phase materials lie between these extreme estimates, the average of the two estimates should be used. A rough estimate for multi-phase materials can be obtained by summing the weighted Young's modulus values of the constituent phases,

$$E = E_1 V_1 + E_2 V_2 + \ldots + E_j V_j + \ldots + E_n V_n \qquad [3.11]$$

where E_j and V_j are the Young's modulus and volume fraction respectively of the jth phase.

Many ceramics are two phase systems consisting of a high volume fraction crystalline phase and a low volume fraction, intergranular amorphous or glassy phase. The intergranular phase usually has lower elastic moduli than the crystalline phase it bonds together, and the effective elastic moduli of the ceramic will decrease rapidly as the volume fraction of glass increases. For example, the Young's modulus of $Li_2O.2SiO_2$ glass-ceramics (parent glass

$Li_2O.SiO_2$) is strongly dependent on the volume fraction of $Li_2O.2SiO_2$ crystals in an additive fashion; the Young's modulus of a glass-ceramic with about 0.9 volume fraction of crystals was about 70 % higher than that of the parent glass (Freiman, S.W. and Hench, L.L., 1972).

Another aspect concerning the elastic moduli of polyphase ceramics is the effect of differential expansion and contraction during thermal cycling on their temperature dependence. An early study of the temperature dependence of the Young's modulus of a number of refractory materials using a resonance technique involving the aural matching of resonant frequencies within ± 1 % (Ault, N.N. and Ueltz, H.F.G., 1953) found that the Young's modulus of sintered magnesia-magnesia aluminate spinel bars (a two-phase material of equal mass % components, both with cubic structures) first decreased and then increased with increasing temperature between room temperature and 800°C, before slowly flattening out up to 900°C. They also found that on cooling the Young's modulus at 600°C was higher than the highest value obtained on heating (at 900°C) and that although the modulus decreased on cooling it remained higher than that measured on heating but gave roughly the same room temperature value. The component materials themselves, however, behave normally, i.e., their Young's moduli decrease with increasing temperature.

The anomalous behaviour of the two-phase material during heating was attributed to the internal stresses generated by differential thermal expansion; the linear thermal expansivity of magnesia is ≈ 1.5 times higher than that of the spinel between 25 and 900°C (Whittemore, O.J. and Ault, N.N., 1956). No explanation was offered for the hysteresis observed on cooling; it is interesting, however, that on cooling their Young's modulus versus temperature curve for spinel was also shifted to slightly higher values than the heating curve.

3.5 Internal Friction

If a perfectly elastic material specimen - vibrating system is operated in complete isolation from its surroundings so that no energy is lost by the system, the following situations would occur. In the case of an oscillating pendulum system the pendulum would keep oscillating indefinitely at constant amplitude with no further energy input beyond that required to initiate oscillation, while a forced vibration system subject to an externally applied alternating stress of constant amplitude such that it vibrated at its natural resonant frequency, would continuously increase its vibrational amplitude to infinity.

If, however, the specimen was a real material the vibrational amplitude of the pendulum system would decrease with time if there were no further input of energy, while the vibrational amplitude of the forced vibration system would have a constant finite value. The loss of vibrational amplitude by real materials is indicative of the elastic stress waves losing energy as they travel within the material due to energy dissipation mechanisms collectively known as internal friction. This dissipation of vibrational elastic strain energy, ultimately in the form of thermal energy, occurs because the elastic strain response to an imposed elastic stress has two components, (i) a component directly coupled to the stress and (ii) a component indirectly coupled to the stress via time-dependent material parameters which cause the strain response to lag behind the stress, i.e., when the stress is imposed the resultant strain which follows is time dependent, likewise when the stress is removed the strain recovery is time dependent. Note there is no definition of the time scale for the attainment of equilibrium, it may be seconds, microseconds or less; the important point is that the time-dependence of strain, i.e., its lagging behind the stress, is responsible for real materials not being perfectly elastic and for internal friction.

The internal friction of a material is measured by a dimensionless number which represents the phase angle by which the strain lags behind the stress; the larger the number the higher the internal friction. In general it is much smaller than unity for most linear elastic materials, in which case it can be measured indirectly in a number of ways: (i) from the forced vibrations of a material, (ii) from the exponential decay of the amplitude of the free vibrations of a material, and (iii) from the attenuation of a propagating elastic stress wave pulse in a material.

3.5.1 Determination of internal friction by forced vibration

In the present work the internal friction was measured by a forced vibration technique, so only this technique will be considered in any detail. In forced vibration both the stress and strain are periodic functions of time and may be represented by (Nowick, A.S. and Berry, B.S., 1972)

$$\sigma = \sigma_o \exp(iwt) \qquad [3.12]$$

$$\epsilon = \epsilon_o \exp(i[wt - \phi]) \qquad [3.13]$$

where w is the angular frequency (= $2\pi f$), $i = (-1)^{1/2}$, σ_o the stress amplitude, ϵ_o the strain amplitude, and ϕ the phase angle by which the strain lags behind the stress. Defining C^* as a complex elastic compliance so that

$$C^* = \epsilon/\sigma = |C^*|\exp(-i\phi) \qquad [3.14]$$

In equation [3.14] $|C^*|$ is the absolute value of C^* and is equal to ϵ_o/σ_o, and $C^* \equiv C_R + iC_I$ by definition. Since $\exp(-i\phi) = \cos\phi - i\sin\phi$, it follows from the Argand diagram of C^* that $C_R = |C^*|\cos\phi$ and is the real part of C^*, i.e., the part in phase with σ, while $C_I = |C^*|\sin\phi$ and is the imaginary part of C^*, i.e., the part out of phase with σ. Furthermore, $|C^*|^2 = (C_R)^2 + (C_I)^2$ and $\tan\phi = C_I/C_R$. Now ϵ can be written as $(\epsilon_R - i\epsilon_I)\exp(iwt)$, i.e., $\epsilon_o = \epsilon_R - i\epsilon_I$, and hence $\epsilon_R \equiv C_R\sigma_o$ and $\epsilon_I \equiv C_I\sigma_o$; this gives the result that $\tan\phi = \epsilon_I/\epsilon_R$. Furthermore, the energy dissipated in a full cycle, ΔW is given by

$$\Delta W = \pi C_I (\sigma_o)^2 \qquad [3.15]$$

while the maximum energy stored in the cycle, W is

$$W = (\sigma_o)^2 C_R/2 \qquad [3.16]$$

(both per unit volume) which gives $\Delta W/W = 2\pi\tan\phi$ (see Appendix 3C). So $\tan\phi$ can be regarded as the ratio of the strain component out of phase with the stress to the strain component in phase with the stress and except for a constant, is equivalent to the fractional energy loss per full cycle per unit volume due to internal friction; thus $\tan\phi$ is a measure of internal friction. Note that, for a given frequency, the internal friction of a homogeneous material is independent of the nature of the vibrating system used to determine it (Nowick, A.S. and Berry, B.S., 1972).

Under forced vibration the vibrational amplitude varies with the driving frequency. It is a maximum when the driving frequency and the natural resonant frequency of the material are equal, but decreases symmetrically about the resonant frequency to essentially zero when the driving frequency is higher or lower than the resonant frequency. If f_r is the resonant frequency, and f_U and f_L are the driven frequencies above and below f_r respectively at which the vibrational amplitude is half its maximum, then an indirect measure of $\tan\phi$ is given by (Zener, C., 1948); (Kolsky, H., 1963)

$$Q^{-1} \equiv 3^{-1/2}(f_U - f_L)/f_r = \phi \qquad [3.17]$$

where $\phi \ll 1$ so that $\tan\phi \approx \phi$ and Q^{-1} is called the internal friction. An alternative form of equation [3.17] is

$$Q^{-1} \equiv (f_U - f_L)/f_r = \phi \qquad [3.18]$$

where f_U and f_L are the driven frequencies at which the square of the amplitude has fallen to half its maximum value or at which the amplitude has fallen to $2^{-1/2}$ of its maximum value at the resonant frequency f_r (Nowick, A.S. and Berry, B.S., 1972), but equation [3.17] is used more frequently in the literature and was therefore used in the present work. Both equations assume that the internal friction is independent of the stress amplitude.

3.5.2 Determination of internal friction by free decay and the attenuation of a travelling elastic wave

In the case of free vibration the vibrational amplitude, A decays exponetially with time t after the initiating stress is removed,

$$A = A_o \exp(-Bt) \qquad [3.19]$$

where A_o is the maximum amplitude, i.e., the amplitude at $t = 0$ and B is a constant which determines the rate of decay. If τ is the period of oscillation ($= 1/f$) then at a time $n\tau$, $A_n = A_o \exp(-Bn\tau)$ and at a time $(n + m)\tau$, i.e., m periods later, $A_{n+m} = A_o \exp(-B(n + m)\tau)$ where by definition $A_{n+m} < A_n$. Thus $A_n/A_{n+m} = \exp(mB\tau)$; for $m = 1$, $A_n/A_{n+1} = \exp(B\tau)$. The logarithmic decrement is defined as $\ln(A_n/A_{n+1}) = B\tau \equiv \delta$. So for m successive periods it follows that $\ln(A_n/A_{n+m}) = mB\tau = m\delta$, which is used to obtain a more precise experimental δ value, i.e., m, A_n and A_{n+m} are experimental parameters. It can be shown (Nowick, A.S and Berry, B.S., 1972) that for $\phi \ll 1$,

$$\phi = \delta/\pi \qquad [3.20]$$

The methods of forced vibration and free decay are standing wave phenomena; the standing waves are generated by the interference of continuous elastic stress waves travelling in opposite directions due to successive reflections at the material boundaries. In this method the elastic stress wave is a pulsed wave that travels in one direction only at any instant of time and whose reflections at the material boundaries do not, therefore, interfere with each other. The attenuation of the pulse is determined from the decrease in its amplitude after successive reflections at the material boundaries. It can be shown that for $\phi \ll 1$, $\phi = \alpha\lambda/\pi$, where λ is the wavelength (set equal to v/f where v and f are the wave velocity and frequency respectively) and the attenuation α has dimensions of $[\text{length}]^{-1}$ (Nowick, A.S. and Berry, B.S., 1972). To summarise then, the internal friction parameters obtained from forced vibration, free decay and wave attenuation techniques are related for $\phi \ll 1$ (in practice $\phi < 0.1$) as follows, $\phi = Q^{-1} = \delta/\pi = \alpha\lambda/\pi$.

3.6 Experimental Determination of Elastic Moduli and Internal Friction

Experimental techniques for determining the elastic moduli of a material can be classified as being either static or dynamic; in general the static methods pre-date the dynamic methods.

3.6.1 Static methods of measuring elastic moduli

The most common static method for determining the Young's modulus of a material is uniaxial tension or compression in which the specimen strain is measured by means of strain gauges attached to the test specimen. Poisson's ratio can also be measured by placing strain gauges circumferentially and longitudinally. For non-ductile materials, however, the experimental problems associated with tensile tests in particular (Marschall, C.W. and Rudnick, A., 1974) have lead to the use of the flexure test, i.e., 3- or 4-point bending of bar specimens in which the actual centre-deflection of the specimen is measured using linear displacement transducer(s). The Young's modulus may also be calculated from the load versus cross-head displacement plots if the machine compliance has been determined using a specimen with an accurately known Young's modulus, but direct displacement measurement is recommended.

The shear modulus is measured by applying a known torque to a rod specimen, i.e., the specimen is loaded in torsion and the angular rotation determined by strain guages or by an optical lever system. The torque may be applied mechanically via a rotating grip or by a torque wheel and dead-weight balance system. For further details of static methods see J.T. Richards (1952) and F. Garofalo (1952).

3.6.2 Dynamic methods of measuring elastic moduli

The dynamic techniques may be divided into three groups depending on the frequency range of the specimen-apparatus system. The technique categories are (i) low frequency, (ii) medium frequency and (iii) high frequency methods. The purpose of this section is only to place the forced vibration technique used in the present work, which was a standard dynamic resonance method (see Section 3.7), in perspective as regards dynamic techniques in general. So no consideration beyond a brief description is given to low and high frequency dynamic techniques.

The categories are briefly described below:

(a) Low-frequency techniques ($\approx$ 0.2 - < 1000 Hz)

The techniques in this group are free or natural vibration methods based on a standing wave phenomenon and employ auxiliary inertia members to induce pendulum motion of the specimen, e.g., the torsional pendulum which is used to measure G.

(b) Medium-frequency techniques ($\approx$ 100 Hz - $\approx$ 5 MHz)

These techniques, known as dynamic resonance methods, normally rely on the forced vibration at constant stress amplitude but variable frequency of a specimen and are based on a standing wave phenomenon. The standard dynamic resonance techniques involve the excitation of longitudinal, flexural or torsional vibration modes (usually the fundamental mode but also the overtones) in a uniform bar specimen which is either suspended or supported with free ends, or is fixed at one or both ends. The longitudinal and the flexural modes relate to the Young's modulus while the torsional mode relates to the shear modulus.

There are a number of ways in which the vibrations of the specimen can be excited and detected: (1) direct coupling via mechanical contact, (2) indirect acoustic coupling via a vibrating air column, (3) indirect electromagnetic coupling, (4) indirect electrostatic coupling, and (5) directly by using a composite piezo--electric transducer(s) and specimen oscillator system.

(c) High-frequency (≈ 1 MHz - ≈ 1 GHz)

These techniques involve the determination of the velocity of propagation of pulsed elastic stress waves. They can be placed in one of three groups, (i) those that measure the time taken by a wave pulse to travel the length of the specimen, i.e., transit-time determination; they are pulse-transmission methods, (ii) those that measure the time delay or transit time between successive wave pulse echoes arising from reflections between the specimen ends; they are called pulse-echo methods, and (iii) those based on wave pulse interference; they are called acoustic interferometry techniques.

The generalised dynamic moduli, M as determined directly by low and normal medium frequency techniques (i.e., E and G) are proportional to the square of the resonant frequency, while those determined by high frequency techniques (i.e., L and G) are proportional to the square of the wave velocity. For more information on the use of dynamic techniques to measure elastic moduli see M.E. Fine (1952); J.T. Richards (1952); W.R. Davis (1968); E. Schreiber, et al. (1973); H.F. Pollard (1977).

3.6.3 Experimental measurement of internal friction

If the internal friction of a material is small ($\phi \ll 1$) and independent of the vibrational amplitude (i.e., the strain amplitude) and the material is vibrating under conditions of non-uniform stress amplitude (and hence non-uniform strain amplitude), e.g., in standard dynamic resonance techniques where bar specimens are subject to forced vibration, then for a given frequency, the internal friction is independent of the nature of the vibration. It can be measured (i) from the logarithmic decrement of free decay using low or medium frequency techniques, (ii) from the resonance peak of forced vibration using medium frequency techniques, and (iii) from the attenuation of a propagating elastic stress wave using high frequency techniques. See C. Zener (1948); A.S. Nowick (1953); H. Kolsky (1963); A.S. Nowick and B.S. Berry (1972).

3.6.4 Advantages of dynamic techniques

Dynamic techniques have a number of advantages over static methods apart from usually greater accuracy and precision:
(a) The stress and strain amplitudes produced by standard dynamic resonance methods are very small which makes them very good methods for measuring the elastic moduli of non-ductile materials; for example, the alternating stresses are invariably lower than 0.1 MPa (Förster, F. and Köster, W., 1938), while the strain amplitudes associated with dynamic tests are of the order of 10^{-5} or less (Nowick, A.S., 1953); (Nowick, A.S. and Berry, B.S., 1972). So there is no risk of plastic deformation in ductile materials when using dynamic techniques,
(b) Dynamic methods enable the measurement of the amplitude independent internal friction; usually it can be measured simultaneously with the elastic moduli,
(c) Many dynamic methods can be conveniently adapted to make high temperature measurements (some up to $\approx$ 1700°C) or low temperature measurements (i.e., below 0°C), and
(d) In general, the specimens required are smaller and particularly small specimens can be used with the high frequency techniques.

3.6.5 Elastic moduli and the thermoelastic effect

There is a difference between the elastic moduli as measured by dynamic methods and as measured by static methods due to the thermoelastic effect which relates the stress and strain to the temperature and entropy in a material when it is behaving elastically. When a material with a positive thermal expansivity, i.e., nearly all materials, undergoes an increase in temperature at constant pressure its volume increases and vice versa. Conversely, if the same material is in an adiabatic system (in which all changes occur at constant entropy, i.e., the changes are isentropic) and undergoes a uniform volume increase its temperature will decrease and vice versa.

Consider now a homogeneous, isotropic material which is subject to a uniform cyclic stress; if the stress cycling rate is such that the thermal energy transfer rate can maintain the specimen in thermal equilibrium with its environment during a strain cycle, then the specimen temperature remains constant and the straining process is said to be isothermal and the entropy changes. If, however, it is such that the thermal energy transfer rate cannot maintain the specimen in thermal equilibrium with its environment, then the specimen temperature changes and the straining process is said to be adiabatic and the entropy of the system remains constant (Nowick, A.S., 1953); (Schreiber, E., et al., 1972).

In the adiabatic process the periodic stress-induced strain and the specimen temperature are in phase, but the frequency is so high the thermal energy of the specimen is effectively in stasis and there is no conversion of strain energy to thermal energy, i.e., no loss of strain energy. As a result (i) there is no internal friction and (ii) there is a temperature-induced volumetric strain which is always in opposition to the stress-induced strain, i.e., a tensile stress will cause a volume increase but the concomitant decrease in temperature will cause a volume decrease, and vice versa.

In the isothermal process the periodic stress-induced strain has such a low frequency that the thermal energy transfer between the specimen and its environment is in phase with the strain and hence the specimen is always in thermal equilibrium with its environment. As a result (i) there is no net energy change per cycle and therefore no net conversion of strain energy to thermal energy, i.e., no internal friction and (ii) there is no volumetric strain in opposition to the stress-induced strain. So under perfectly adiabatic or isothermal conditions there is no thermoelastic internal friction and the adiabatic elastic modulus is higher than the isothermal elastic modulus. At some frequency the thermoelastic internal friction will be a maximum, i.e., when the conditions are neither adiabatic nor isothermal.

When the stress and hence the strain amplitude within a material are not uniform, the volume changes and the concomitant temperature changes will be non-uniform; thus thermal gradients will arise and thermal energy will flow in order for thermal equilibrium to obtain. The attainment of thermal equilibrium will take time and hence there will be a strain component indirectly coupled to the stress via time-dependent temperature and hence volume changes causing thermoelastic internal friction. This situation can arise in flexural vibration at intermediate frequencies, i.e., when conditions are neither isothermal nor adiabatic. Thermoelastic internal friction may arise even if the periodic stress is homogeneous, for example, in polycrystalline materials. The elastic anisotropy of individual crystals will result in the crystals being subject to different stresses and hence strains; thus the temperature of individual crystals will differ and again thermal energy will flow in an effort to establish internal thermal equilibrium, resulting in thermoelastic internal friction (Nowick, A.S., 1953);(Kolsky, H., 1963).

If experiments, however, are carried out under isothermal or adiabatic conditions, thermoelastic internal friction can be prevented. Furthermore, since static techniques are effectively isothermal and dynamic techniques effectively adiabatic, the dynamic value of any elastic modulus (and compliance) associated with a volume change, e.g., Young's modulus, bulk modulus, will usually be higher than the static value. The dynamic and isothermal shear modulus are, however, equal (likewise the compliances) since shear strains only involve a change of shape at constant volume. The difference is normally of the order of 0.1 % (Fine, M.E., 1952) and is usually less than the experimental error; it is thus of no concern in the present work.

3.7 Experimental Determination of the Elastic Moduli and Internal Friction of Glass-Ceramics in the System CaO - MgO - Al_2O_3 - SiO_2

To iterate, the mechanical properties of four glass--ceramics in this system have been investigated; they are referred to as SCF5, SCR25.76, SCR19.34 and SCR19.13 (see Chapter 2). Regarding their elastic moduli and apparent internal friction the following data have been obtained:

(1) Room temperature Young's modulus and apparent internal friction; the former for all materials and the latter for all materials except SCR19.13.
(2) Room temperature shear modulus for SCR25.76 and SCR19.34.
(3) Room temperature bulk modulus, longitudinal modulus, shear and longitudinal sound wave velocities, and Poisson's ratio for SCR25.76 and SCR19.34.
(4) Young's modulus and internal friction as functions of elevated temperature relative to the room temperature values for all materials except SCR19.13.

Data concerned with the experimental methods used as regards accuracy, reproducibility, etc. of the elastic moduli and internal friction data have also been obtained.

3.7.1 Experimental methods employed

Two dynamic resonance techniques were used; a main method used for the room and elevated temperature measurements and a subsidiary method to provide a check on the room temperature data obtained using the main method. Both methods involved the forced vibration of bar specimens of uniform rectangular cross-section and both ends free, i.e., so-called "free-free" vibration. The vibration shapes of the fundamental flexural vibration mode and the fundamental torsional vibration mode excited by these methods are shown schematically in Figure 3.1 (a) and (b) respectively. The distance of the two nodes from one end of the bar for the fundamental mode in flexure as a fraction of the bar length are 0.224 and 0.776, while for

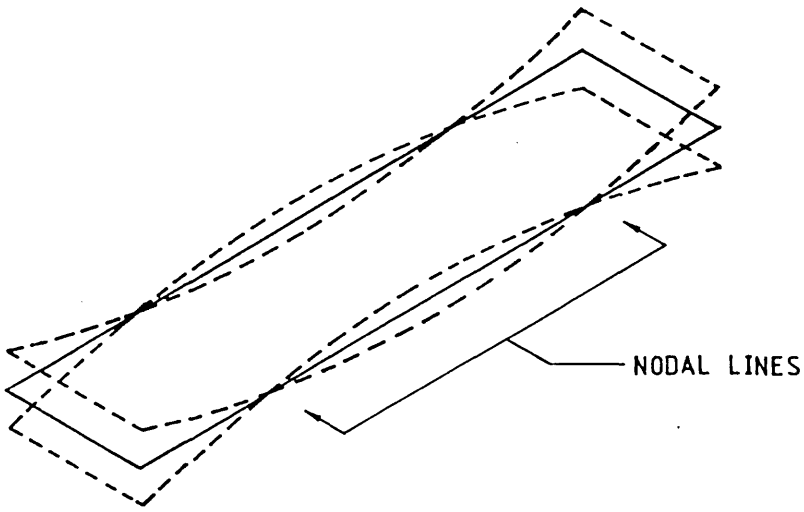


Figure 3.1 (a) Schematic Vibration Shape for a Free-Free Bar Vibrating in the Fundamental Flexural Mode.

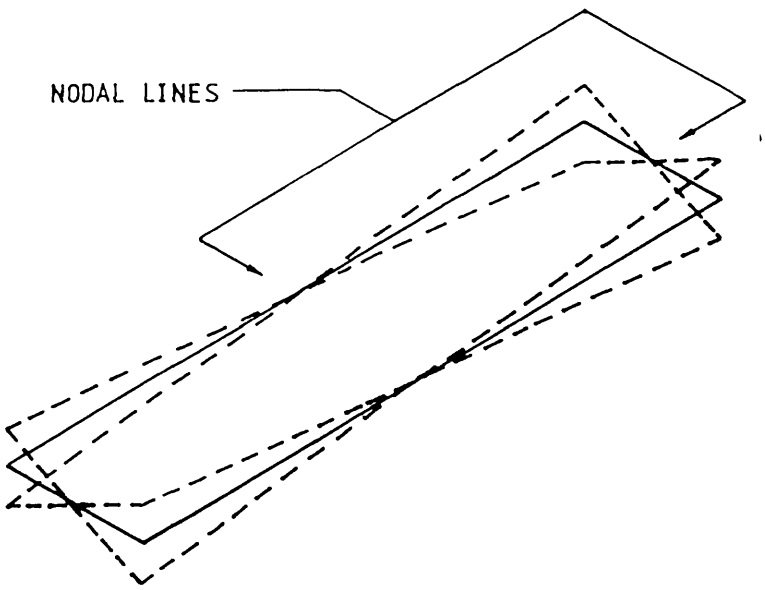


Figure 3.1 (b) Schematic Vibration Shape for a Free-Free Bar Vibrating in the Fundamental Torsional Mode.

the fundamental mode in torsion the single node is situated at 0.5 of the bar length.

(1) Main method (horizontal suspension technique):

This dynamic resonance method is due to F. Förster (1937) and has been, and is widely used because of its simplicity and applicability to high temperature studies of elastic moduli and internal friction. In this method a uniform bar specimen, with preferably a rectangular cross-section, is suspended horizontally by two flexible wires or non-metallic threads as shown schematically in Figure 3.2 (a) and (b)., and as the diagrams indicate, the suspension wires or threads are used both as specimen supports and as direct mechanical couplings to the exciting and detecting transducers. A schematic block diagram of the instrumentation set up and used in the implementation of this method is shown in Figure 3.3.

(1.1) Description of the electronic instrumentation:

With reference to Figure 3.3 the electrical equipment used was as follows:
(a) A Levell Meteor 100 digital frequency counter fitted with a 10MHz temperature compensated crystal oscillator which provided a very accurate, highly stable and temperature insensitive frequency reference. It had a resolution of ± 0.1Hz for a 10 second gate time (i.e., measurement period) over the frequency range 5Hz to 10MHz.
(b) A Farnell LFM3 RC Wien-bridge sine wave oscillator with an output continuously variable in both frequency and amplitude and with a frequency response of 100Hz to 1MHz ± 0.2dB, a frequency and amplitude stability of ± 0.2 % over this frequency range, a sine wave distortion of < 0.05 % over the frequency range 100Hz to 20kHz at the output voltage used in this work, and very good temperature stability.
(c) A Levell TM3B switchable pass-band A.C. microvoltmeter which was mean-sensing with a sine wave calibrated r.m.s.

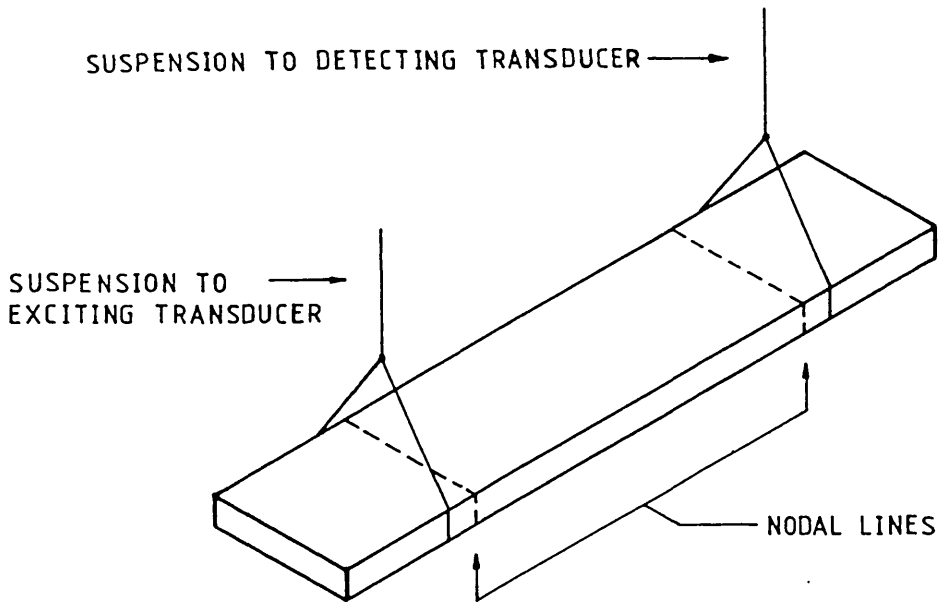


Figure 3.2 (a) Schematic Specimen Suspension Layout for Determining the Flexural Resonant Frequency.

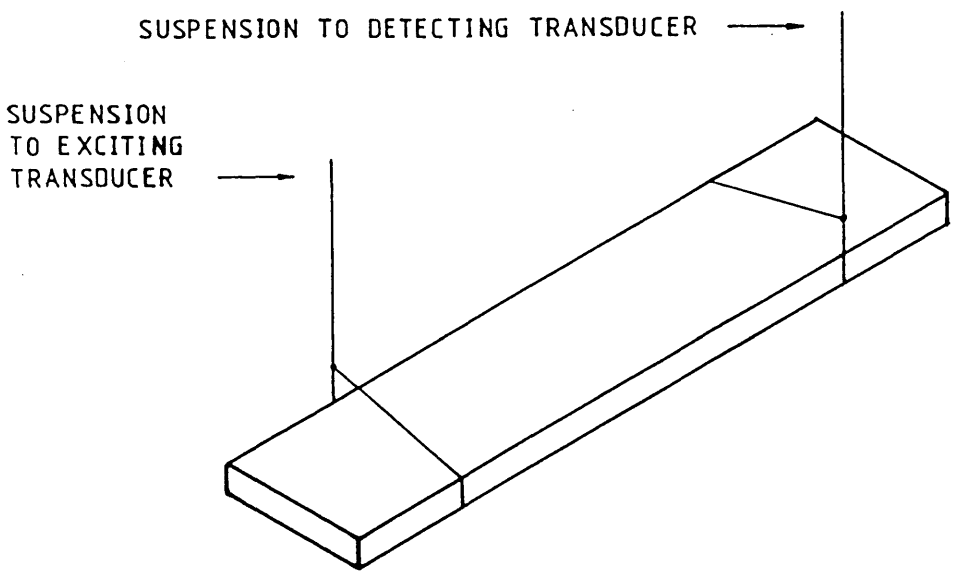


Figure 3.2 (b) Schematic Specimen Suspension Layout for Determining the Flexural and Torsional Resonant Frequencies Simultaneously.

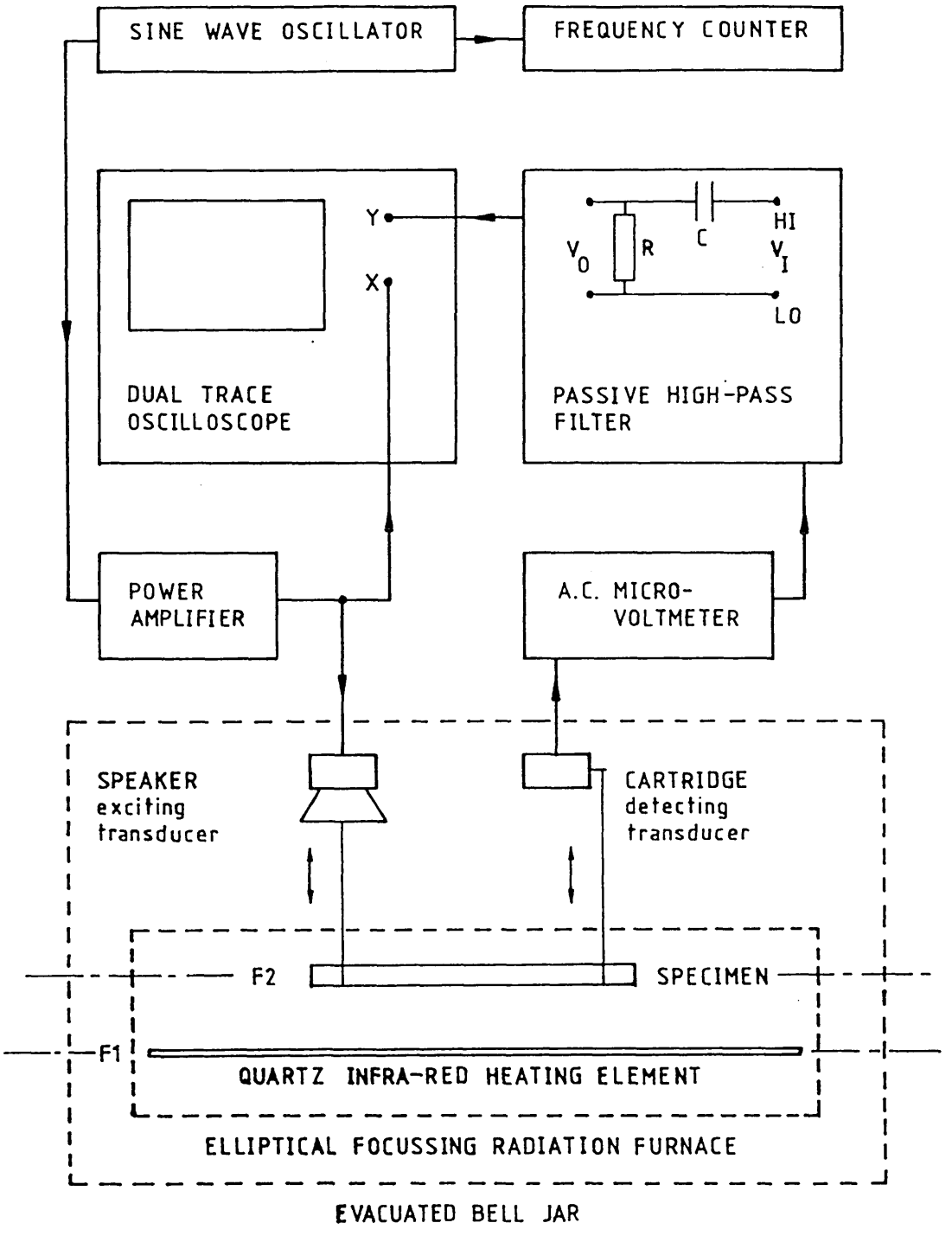


Figure 3.3 Schematic Block Diagram of the Apparatus Used for Förster's Dynamic Resonance Technique.

voltage, no-parallax mirror scale meter accurate to ± 2 % f.s.d. at 1.5 mV f.s.d. at 1kHz. The frequency response was 4Hz to 1MHz ± 0.3dB and the output voltage had a fixed sensitiviy of 150mV f.s.d. enabling its use as a low noise oscilloscope preamplifier.

(d) A Hitachi V-222 dual trace oscilloscope with a bandwidth of D.C. to 20MHz and a sensitivity of 1mV/div. accurate to ± 5 %, and X (channel 1)-Y (channel 2) operation from D.C. to 500kHz to display Lissajous figures.

(e) A commercial 20W r.m.s. 8Ω "hi-fi" audio amplifier.

(f) A passive high-pass filter with a -3dB cut-off at ≈ 1000Hz, i.e., a time constant (≡ RC) of 1.59×10^{-4} ΩF.

(g) An Altai 8Ω 40W mid-range speaker (500Hz to 8000Hz range) used as the exciting transducer, i.e., driver.

(h) A BSR X5M monophonic piezoelectric record-deck cartridge (40Hz to 10kHz range) used as the detecting transducer, i.e., pickup.

A small hook was attached to the speaker-coil dust cover using a cyanoacrylate adhesive ("superglue") and the driver suspension thread tied to it, while the pickup suspension thread was tied to the stylus of the cartridge which was positioned on its side so that when a specimen underwent forced vibration the stylus moved in the vertical plane and the maximum voltage output achieved. All signal leads, whenever feasible, except those to the speaker, were "low noise" coaxial screened cables terminated in 50Ω BNC connectors to minimise electrical interference, particularly on the pickup side.

(1.2) Description of the high temperature furnace:

The elliptical focussing radiation furnace was based on the design used by J.L. Lytton, et al. (1964) and apparently constructed by B.A. Parker (1967). It was modified and re-commissioned for the present work, and a schematic section along the long axis of the furnace is shown in Figure 3.4. The furnace consisted of an elliptically contoured thin stainless steel tube whose inner

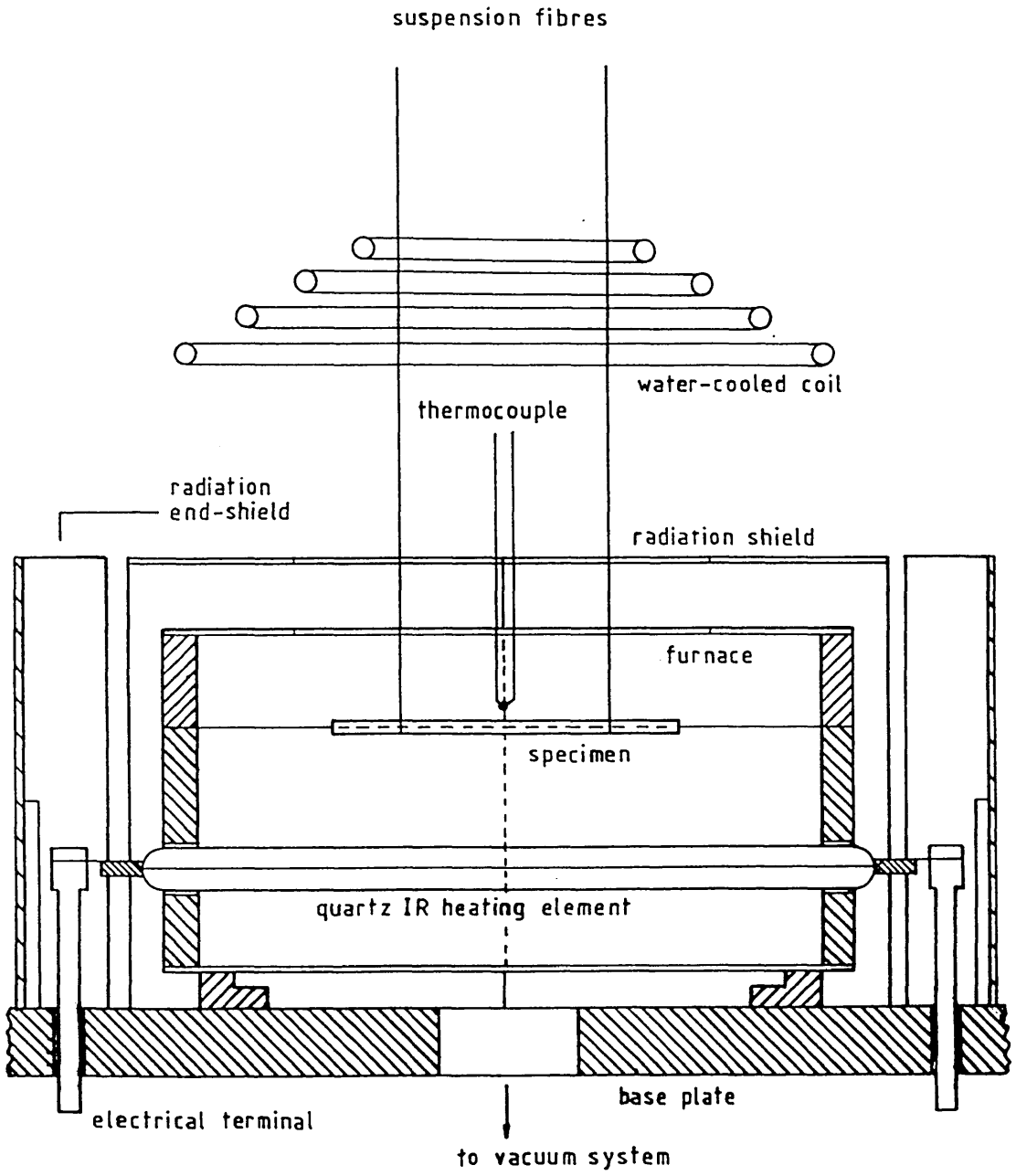


Figure 3.4 Schematic Sectioned Front Elevation of the High Temperature Elliptical Focussing Radiation Furnace.

surface was polished to a highly reflective mirror finish using a 1μm diamond polish together with elliptical steel end-plates. It separated into two sections along the horizontal plane containing the top focal axis (F2) to allow a specimen to be placed in the suspension loops; the top section had a central slot cut out in line with the vertical plane through the two foci large enough to allow the suspension wires through. The bottom section had a polished thin stainless steel elliptical plate fronting each steel end-plate; these acted as positioning guides for the top section when placing it on the bottom section.

A Philips IRK 13168X quartz tube infra-red heating element (2000W, 220-250V, 8A) situated horizontally along the bottom focal axis (F1) provided the line heat source and was powered via a 250V 8A variable voltage transformer ("VARIAC"). It was positioned at the focus by two alumina tubes resting in the end plates and connected to the VARIAC by sliding brass terminals to allow for thermal expansion. The specimen was positioned centrally along F2 so that the thermal energy radiating from the element was focussed on it; when run at about 130V the temperature recorded by the type K thermocouple positioned centrally within 1mm of the top face of the specimen was ≈ 790°C. At any given voltage the temperature was sufficiently stable after about 20 minutes for measurements to be taken, so no additional temperature control was required, but measurements were taken at 30 minute intervals to allow the specimen temperature to stabilize.

(1.3) Description of the vacuum system:

A vacuum system was required for two reasons, (i) all the measurements were done under vacuum to prevent the specimen vibrations being damped by the air, and (ii) to prevent any oxidation at elevated temperatures of (a) the wire specimen suspensions used for the high temperature measurements and (b) the polished surfaces which would have effectively reduced their reflectivity and hence efficiency to zero. The "vacuum chamber" was a bell jar

just large enough to hold the furnace and resonance apparatus, with an L-section rubber gasket fitted along its bottom edge. It rested on a steel base plate and was covered with a removable wire safety cage when evacuated.

A number of steps were taken to reduce radiant and conductive heating of the base plate, the bell jar (particularly the rubber gasket), the speaker and the cartridge, their support stands, the thermocouple holder and the electrical signal wiring within the bell jar; there was (i) a water-cooled copper coil within the bell jar just below the driver and pickup, "straddling" the furnace to act as a cold sink and which, with the aid of removable hooks, also acted as a support for the top section of the furnace to allow single-handed suspension of a specimen, (ii) a two-section inverted-U shaped radiation shield made from thin sheet brass which was bright tin plated on the inner surface, each section having a matching half-slot at one end on the top to allow the specimen suspension wires through when it was placed over the furnace from each end and giving a clearance of 25 mm between the shield and the furnace, (iii) a thin curved stainless steel radiation shield was placed across each furnace end between the bell jar wall and the furnace element terminals (an alumina plate was used to insulate each terminal from the adjacent shield), and (iv) the water cooled baffle valve of the vacuum system was coupled to the vacuum chamber via a circular water-cooled flange attached to the base plate directly beneath the furnace. A thermocouple placed at the top of the copper coil between the cartridge and speaker recorded a temperature of 32°C when the furnace thermocouple was at 793°C.

A water-cooled vapour diffusion pump (an Edwards F203) was fixed to the bottom of the baffle valve and backed by a single-stage rotary pump (an Edwards ES200). The pressure in the vacuum chamber could only be measured down to a pressure of 0.1 Pa (i.e., 7.5×10^{-4} mmHg) as only an Edwards "Vacustat 2" McLeod gauge was available. Use of the vacuum chamber air-admittance valve, the roughing valve, and the baffle valve allowed continuous

operation of the vacuum system; the bell jar was initially evacuated to a pressure of about 13 Pa in ≈ 20 minutes using only the rotary pump via the roughing line which entered the chamber via the baffle valve just above the baffle, while the diffusion pump was isolated by means of the closed baffle and backing valves. The roughing valve was then closed and these valves opened; a pressure of 0.1 Pa was attained about 30 minutes later.

(1.4) Determining the resonant frequency:

As will be shown later the resonant frequency of a specimen depends on its dimensions, mass and elastic modulus and, in general, a correction factor; a rough estimate of the resonant frequency can be made using approximate values for these data. This was done in this instance by assuming a value of E = 100 GPa for a typical glass-ceramic, and that since Poisson's ratio for normal materials is between 0 and 0.5, G is in the range E/3 to E/2 from equation [3.8], with the aim of preparing usable specimens with a resonant frequency in the range of 2000Hz to 7000Hz as there were a number of strong system resonances below 2000Hz.

The natural resonant frequency of a specimen was then found by scanning this frequency range very slowly in both directions using the oscillator which simultaneously input a variable frequency A.C. sinusoidal signal to both the amplifier and the frequency counter. Note that the lowest possible driving amplitude was used to avoid exciting spurious system resonances within this frequency range and for other reasons discussed later, and that both the power amplifier and the oscillator were set to fixed output voltages such that the voltage across the speaker coil was constant at 850mV r.m.s. (i.e., ≈ 0.1W into 8Ω) for all measurements; this voltage signal was input to the horizontal channel (X-axis) of the oscilloscope. The amplified signal input to the specimen and the flexural or torsional vibrations thereby excited in the specimen were detected by the pickup and input to the A.C.

microvoltmeter. This signal was then separated into two signals, (i) a full wave rectified signal input to the meter and (ii) an amplified signal input to the vertical channel (Y-axis) of the oscilloscope. The microvoltmeter output worked in a manner such that the filter appeared to attenuate any spurious low frequency vibrations of the specimen and electrical "noise" below ≈ 1kHz in the signals to the oscilloscope *and* the microvoltmeter meter.

As the driving frequency approached the resonant frequency of the specimen from either above or below the amplitude of the output signal from the pickup approached the maximum amplitude which obtained when the driving frequency and the resonant frequency were identical. The resonant frequency was detected by observing what oscillator frequency produced a maximum voltage reading on the voltmeter as well as observing either the peak-to-peak amplitude of the pickup signal or the nature of the Lissajous figure on the oscilloscope screen; both the peak-to-peak amplitude and the inclination of the Lissajous figure were very sensitive to the resonant position, e.g., at resonance the Lissajous figure was a very narrow ellipse inclined either left or right at an angle to the horizontal, but away from resonance the Lissajous figure was effectively a horizontal line. Once the approximate resonant frequency was located the frequency was slightly adjusted to give a maximum reading on the voltmeter. The resonant frequency was then measured to ± 0.1 Hz using the frequency counter.

When driving a specimen in flexural vibration the position of the suspension threads was a compromise between (i) suspending the specimen at the nodes, (in practice, positions of minimum rather than zero displacement from equilibrium) where the contribution by the suspension to the measured internal friction is a minimum but the driving and pickup amplitudes are effectively zero, and (ii) suspending the specimen at or close to the ends where the driving and pickup amplitudes are at or approaching a maximum but so too is the damping due to the suspension. The chosen position was that

closest to the nodes (and in this work, outside the nodes) which gave an acceptable pickup signal-to-noise ratio, i.e., signal amplitude but kept the suspension damping to a minimum; the driver and pickup suspensions were placed symmetrically with respect to the nodes. When driving a specimen in torsional vibration, however, the same suspension positions were used as no internal friction measurements were made using this vibrational mode.

(1.5) Room temperature measurements:

For the room temperature measurements ordinary cotton sewing thread was used to suspend the specimens; when using flexural vibration the specimen was supported in loops as shown in Figure 3.2 (a) but when using torsional vibration the specimen was supported by gluing a single cotton thread to each side of the specimen at the flexural nodes (which were convenient reference points) using a very small amount of a cyanoacrylate adhesive as shown in Figure 3.5 as opposed to the normal loop arrangement shown in Figure 3.2 (b). This was found to maintain the specimen in a more stable and horizontal position with regard to the driver and pickup for the specimens used in this investigation.

Although the resonance peak-width was obtained by noting the frequency above and below the resonant frequency at which the pickup amplitude fell to half its maximum value at resonance, the amplitude was also recorded as a function of frequency either side of the resonant frequency under vacuum in order examine the behaviour of the resonance curve. Measurements were done in air and under a vacuum pressure of $\leq$ 0.1 Pa in order to obtain (i) data on the effect of air damping on the measured values of internal friction and Young's modulus as compared to the values measured under vacuum, and (ii) data on the effect of suspension position with respect to the nodes on the measured internal friction and Young's modulus values under both conditions. With regard to air damping it is reported that its effect is only eliminated

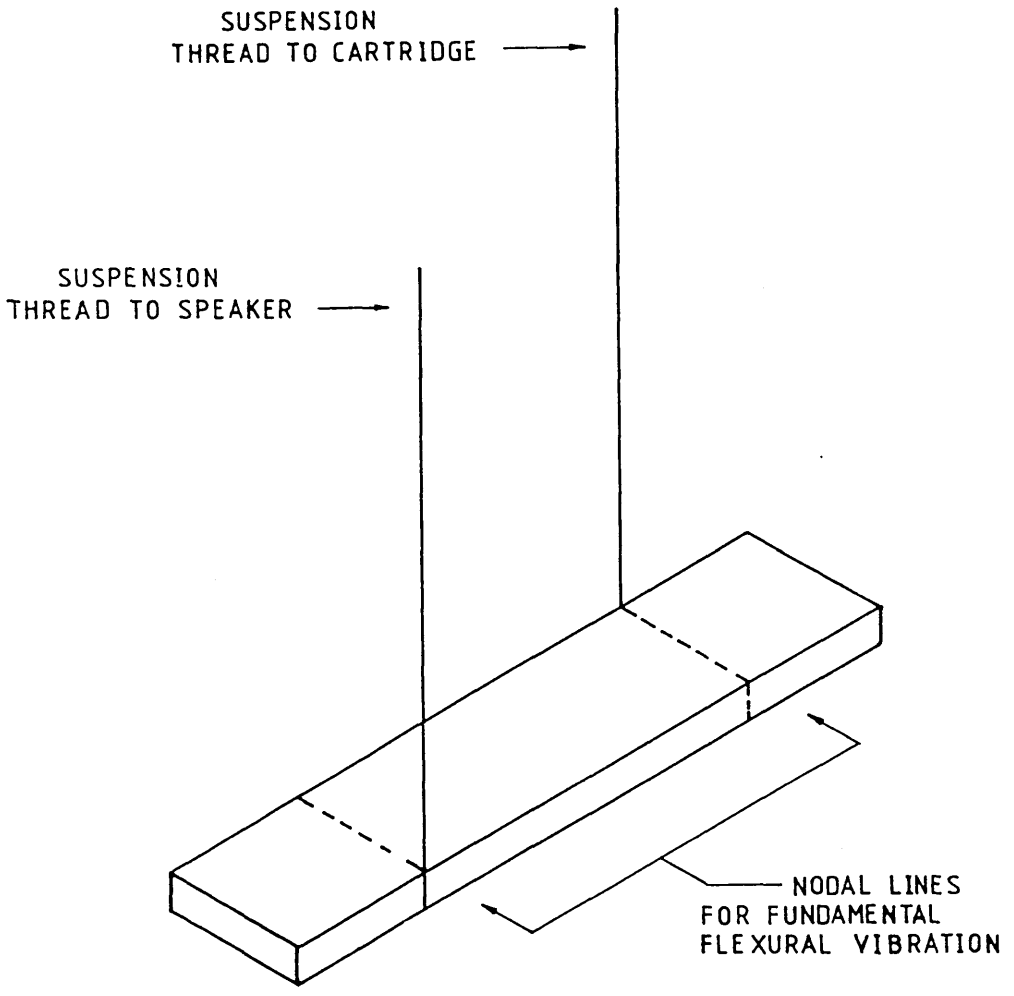


Figure 3.5 Schematic Specimen Suspension Arrangement Used to Determine the Fundamental Torsional Resonant Frequency.

at vacuum pressures of less than 0.0013 Pa and that such measurements were made at a pressure of ≈ 0.00004 Pa (Wachtman, J.B. and Tefft, W.E., 1958), or lower, e.g., < 6.7 x 10^{-6} Pa (Marlowe, M.O. and Wilder, D.R., 1965). So the results obtained in vacuo in this work, although self-consistent were possibly still affected by air damping.

(1.6) High temperature measurements:

When performing the high temperature measurements the specimens were suspended by composite cotton thread-iron wire suspensions as this combination gave more efficient coupling than the all metal wire suspensions; the cotton thread was used to couple the 0.05 mm diameter iron suspension wires supporting the specimen within the furnace to the driver and the pickup. It was found that the most efficient coupling was obtained when (i) the iron wires were as short as possible, i.e., ending just below the water cooled copper coil (see Figure 3.4), (ii) the cotton thread was joined to the iron wire by tying the cotton thread through a very small loop at the top of the wire, and (iii) the wire loops supporting the specimen were moulded to conform to the shape of the specimen, i.e., lying flat against the bottom face and the thin sides of the specimen. The high temperature values of the Young's modulus and internal friction were measured under a vacuum pressure of ≤ 0.1 Pa in ≈ 30 to 60°C steps to within ± 2°C over the time it took to record the required data.

It was found that the Young's modulus could be determined to significantly higher temperatures (i.e., ≈ 200°C higher on average) than the internal friction; this was either because (i) while the resonant frequency could be detected the amplitude at resonance was barely above the background, e.g., ≈ 0.5mV as compared to ≈ 0.3mV and the amplitude could not be reduced to half the maximum or (ii) the half-amplitude frequencies were very asymmetric, e.g., 15Hz below the resonant frequency and 120Hz above. The asymmetry was thought to be due to an adjacent system resonance peak as sometimes a faint "whistling" was

audible or a very small momentary peak was detected in the pickup amplitude on moving away from the specimen resonance. Specimen overtones were not really suspected as flexural vibration frequencies increase very nearly as 3^2, 5^2, 7^2, 9^2,..... (Nowick, A.S and Berry, B.S., 1972). As regards the problem of a very low amplitude at resonance, it was found that inceasing the driving amplitude did not help as it appeared that the background and the resonance amplitudes increased in roughly the same proportion. In most cases the maximum temperature at which the internal friction could be measured was limited by the very low amplitude at resonance rather than overlapping adjacent resonance curves. Specimen sagging was not a concern because the room temperature Young's modulus after testing at the highest temperature for any specimen was always within $\pm \leq 0.9$ % of its original room temperature value.

(2) Subsidiary method (horizontal clamping technique):

This method involved clamping the specimen at the nodes or node using two pairs or one pair of opposing steel knife-edges respectively and exciting and detecting resonance using rigid driver and pickup probes in direct contact with the appropriate parts of the specimen (Patel, H., 1985); other than this the two methods were identical as regards detecting resonance. Apart from a different oscillator, amplifier, driver and pickup, and the absence of a high pass filter and A.C. microvoltmeter, the equipment was the same as for the main method. The latter two items were not necessary as there were no spurious low frequency vibrations and only flexural and torsional resonant frequencies were measured. The driver was an electromagnetic vibration generator and the pickup a piezoelectric cartridge; both were coupled directly to the specimen by rigid wire probes lightly touching the specimen surface. A schematic diagram of the specimen, driver and pickup arrangement for the fundamental flexural mode is shown in Figure 3.6 (a); for the fundamental torsional mode the specimen was clamped at its single node,

and the driver and pickup placed as in Figure 3.6 (b). Although it was unlikely that any higher harmonics or overtones were excited when using the main method given the fundamental resonant frequencies of the specimens and the frequency ranges of the driver and pickup, this method was used in air to determine the room temperature Young's and shear moduli because the fundamental flexural and torsional vibration modes could be more easily identified than in the main method. When a specimen is vibrating at a characteristic resonant frequency both the vibrational mode, e.g., flexural, and order, e.g., fundamental, can be determined by placing the pickup or a second pickup in contact with different parts of the specimen and observing the resultant changes in the orientation and shape of the Lissajous figure on the oscilloscope. The shape and orientation of a Lissajous figure depends on the phase relationship between the electrical signals of the X and Y inputs, and in this instance reflects the exact phase relationship between the mechanical vibration of the specimen at the driver's position and at the pickup position during resonance (Spinner, S. and Tefft, W.E., 1961); (Davis, W.R., 1968). The Lissajous figures corresponding to the different pickup positions during fundamental flexural and torsional resonance are shown schematically in Figure 3.7 (a) and (b) respectively; note the two alternative, equally valid Lissajous figure arrangements which may be found experimentally for the flexural and the torsional modes.

This method was found to be less reliable and less precise than the suspension method due to the problems associated with the clamping arrangement and with the wire probes of the driver and pickup; it was difficult to clamp the specimens exactly at the nodes with the same pressure and evenly across their width, and to achieve the same probe pressures in repeated tests on the same specimen. It was also easier to excite spurious system resonances.

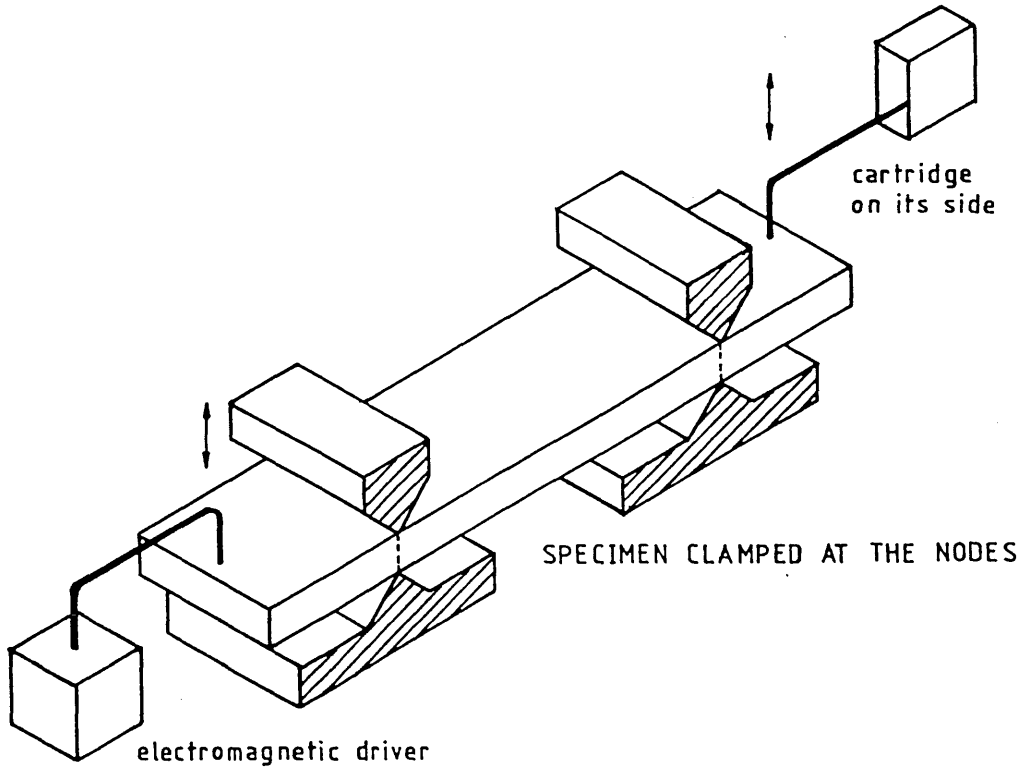


Figure 3.6 (a) Schematic Arrangement of the Specimen, Driver and Pickup for Determining the Fundamental Flexural Resonant Frequency.

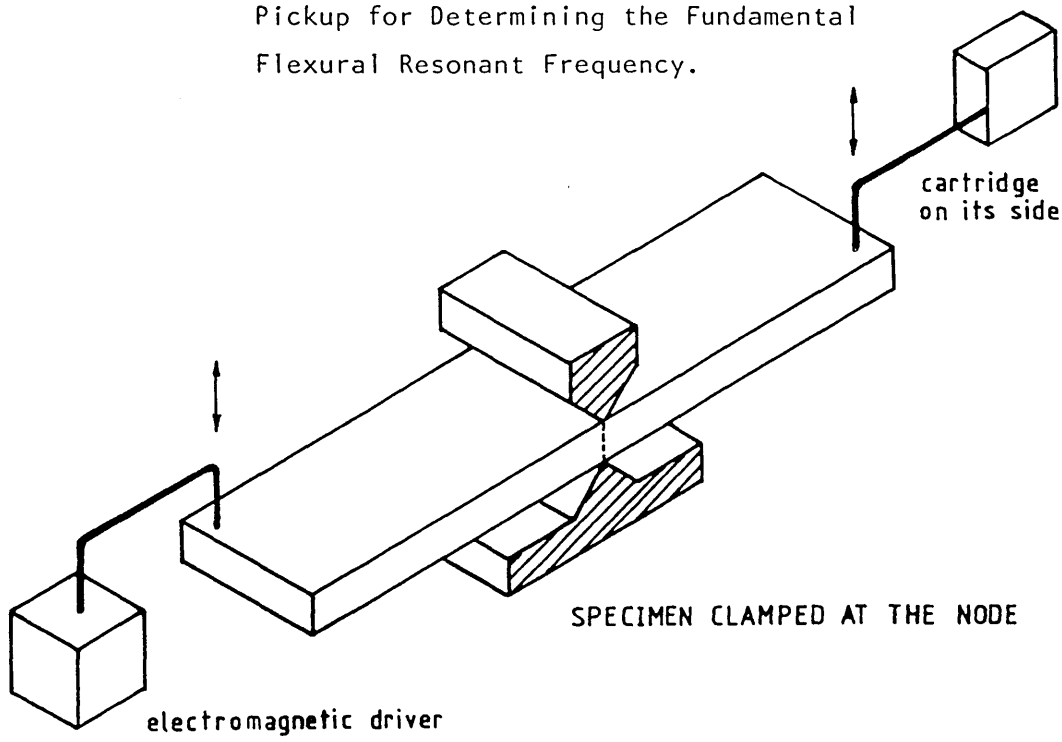


Figure 3.6 (b) Schematic Arrangement of the Specimen, Driver and Pickup for Determining the Fundamental Torsional Resonant Frequency.

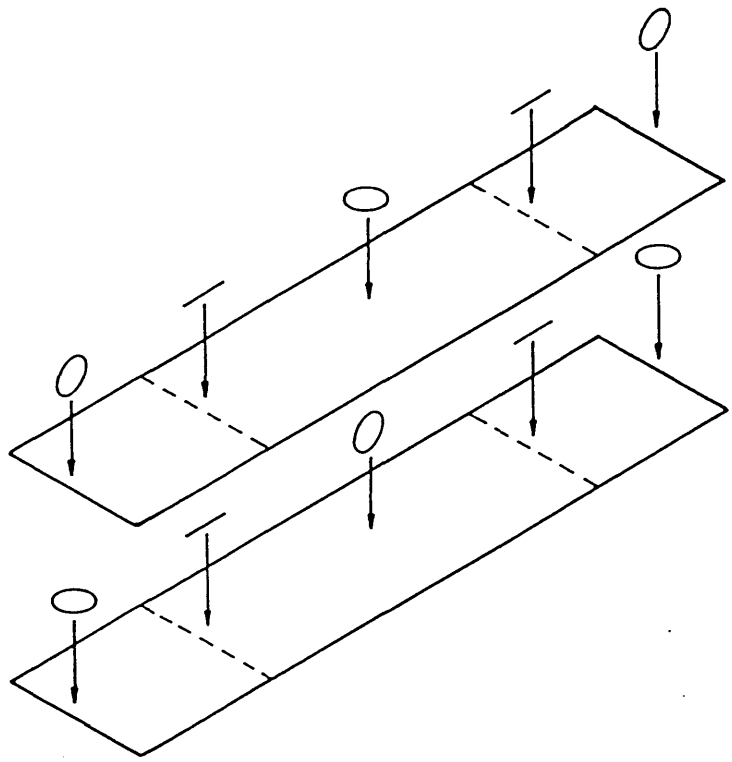


Figure 3.7 (a) Schematic Diagram of the Appearance of the Lissajous Figures at Different Pickup Positions for the Fundamental Flexural Vibration Mode.

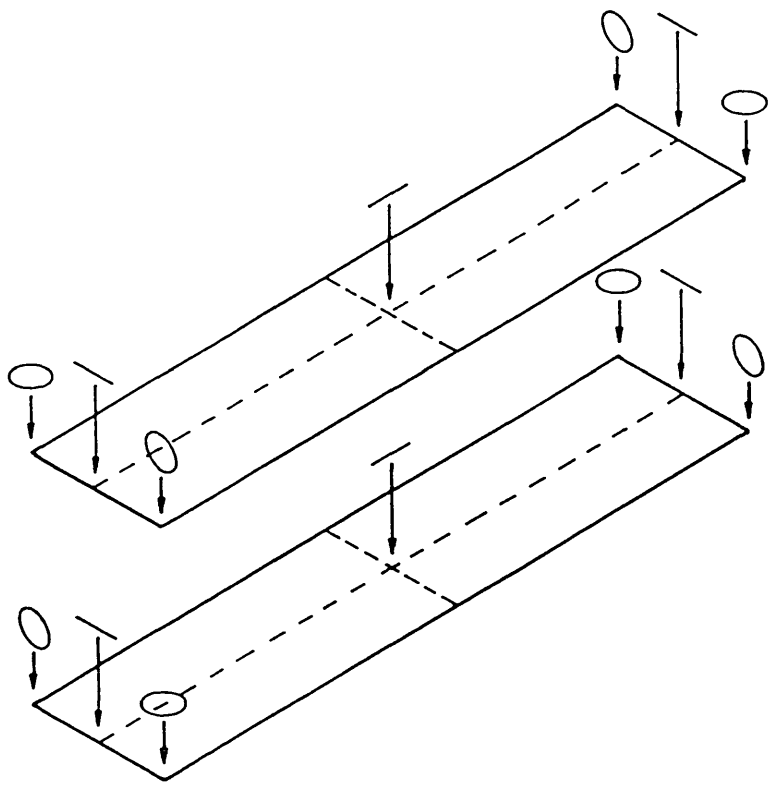


Figure 3.7 (b) Schematic Diagram of the Appearance of the Lissajous Figures at Different Pickup Positions for the Fundamental Torsional Vibration Mode.

(3) Specimen requirements and preparation:

The specimen requirements for the suspension method were more stringent than for the clamping method; as the weight of a specimen was supported by a stylus mounted in a rubber bush and the paper diaphragm of a speaker only specimens with a mass of $\approx \leq 12$ g were used. According to the ASTM Standards C848-78 and C623-71(1977), specimens must have a minimum mass of 5 g to avoid coupling problems, although specimens with a mass of $\approx$ 3 g were tested successfully with the present equipment using cotton thread suspensions. There were no mass limitations when using the clamping technique. It is also suggested that the ratio of length to both width and thickness should exceed 3:1 for rectangular specimens (Spinner, S. and Tefft, W.E., 1961); for most specimens tested in this work the ratio was $\approx$ 7:1 and never less than $\approx$ 5:1.

The ASTM standards also state that the specimen surfaces should flat and ground to 400-grit or finer and that opposite faces be parallel to ± 0.02 mm. Furthermore, the specimen dimensions should be measured to ± 0.01 mm and weighed to ± 0.01 g; the specimens tested in this work had their widths and thicknesses measured to ± 0.01 mm and their mass measured to ± 0.0001 g, but their lengths could only be measured to ± 0.02 mm. The SCR25.76 and SCR19.34 specimen dimensions were parallel to within 0.04 mm, while the SCF5 and SCR19.13 specimens could only be ground and cut parallel to within 0.2 mm due to the precision of the diamond grinding and cutting equipment available at the time of their preparation. The ground faces of the specimens were ground on a flat glass plate with a water based slurry of 1000-grit SiC abrasive powder to remove any machining damage; care was taken not to bevel the specimens or grind away their parallelism. The SCR19.34 and SCR25.76 specimens were ground to their widths (using a medium-grit diamond grinding wheel) and cut to their thicknesses (using a fine-grit diamond slitting wheel) on a Jones and Shipman 540P surface grinding machine; the as-cut surfaces were fine enough not to require grinding.

(4) Calculation of elastic moduli using resonant frequency data:

The equation used to calculate the Young's modulus from the fundamental flexural resonant frequency of rectangular bar specimens was (Spinner, S. and Tefft, W.E., 1961)

$$E = 0.94642(L/t)^3(M/b)f^2T \qquad [3.21]$$

where E is the Young's modulus (Pa), L the specimen length (m), t the specimen thickness (m) in the direction of vibration, b the specimen breadth (m), M the specimen mass (kg), f the fundamental flexural resonant frequency of the specimen (Hz) and T a correction factor which is a function of Poisson's ratio, ν and the thickness-to-length ratio t/L. It is given approximately by

$$T = 1 + 6.585(1 + 0.0752\nu + 0.8109\nu^2)D^2 - 0.868D^4 - \frac{[8.340(1 + 0.2023\nu + 2.173\nu^2)D^4]}{[1 + 6.338(1 + 0.14081\nu + 1.536\nu^2)D^2]} \qquad [3.22]$$

where D = t/L.

The equation used to calculate the shear modulus from the fundamental torsional resonant frequency of rectangular bar specimens was (ASTM Standard C623-71 [1977]); (ASTM Standard C848-78); (Spinner, S. and Valore, R.C., 1958):

$$G_{mat.} = G_{theor.}/(1 + C) \qquad [3.23]$$

where $G_{mat.}$ is the shear modulus of the material (Pa), C an empirical correction factor dependent on the width-to-thickness ratio, b/t, and $G_{theor.}$ the shear modulus (Pa) given by the theoretical approximation (Pickett, G., 1945)

$$G_{theor.} = SMf^2 \qquad [3.24]$$

where M and f are defined as for equation [3.21] and S is a shape factor given by

$$S = 4LR/bt \qquad [3.25]$$

where R is given approximately by

$$R = \frac{(t/b) + (b/t)}{4(t/b) - 2.52(t/b)^2 + 0.21(t/b)^6} \qquad [3.26]$$

where b > t. In [3.25] and [3.26] L, b and t are defined as for equation [3.21]. The correction factor C is the fractional difference between the theoretical and

empirical values of Sbt/L obtained by S. Spinner and R.C. Valore (1958), i.e., $C = [(Sbt/L)_{theor.}/(Sbt/L)_{expt.}] - 1$. The graph of C against b/t given by them and reproduced in the ASTM Standards C623-71(1977) and C848-78 was used to obtain the appropriate C values for the specimens tested; it is shown in Figure 3.8 with the notation used here. Equations [3.21] and [3.23] were used because they are effectively those given in the ASTM standards but in S.I. units and with T in [3.21] calculated directly from equation [3.22].

Poisson's ratio, ν and the bulk modulus, K were calculated from the E and G data using equations obtained by manipulation of equation [3.8], namely

$$\nu = (E/2G) - 1 \qquad [3.27]$$

$$K = EG/[3(3G - E)] \qquad [3.28]$$

By combining equations [3.7] and [3.28] the following equation for the longitudinal modulus, L was obtained

$$L = G[(4G - E)/(3G - E)] \qquad [3.29]$$

Since $G = \rho(v_s)^2$ and $L = \rho(v_L)^2$ where ρ is the density, and v_s and v_L are the shear and longitudinal elastic stress wave propagation velocities respectively (see equations [3.4] and [3.7]), these sound wave velocities could be calculated. Note that since the correction factor T in equation [3.21] is a function of ν, an iterative procedure was used to obtain both E and ν for a given specimen using the value determined for G. Initially ν was assumed to be 0.3 and an initial value of E calculated; this E value was then used to calculate a new value for ν, which produced a new value for E and so on. This iteration was done using a computer and continued until the E value and the ν value had each converged; the values converged after four iterations.

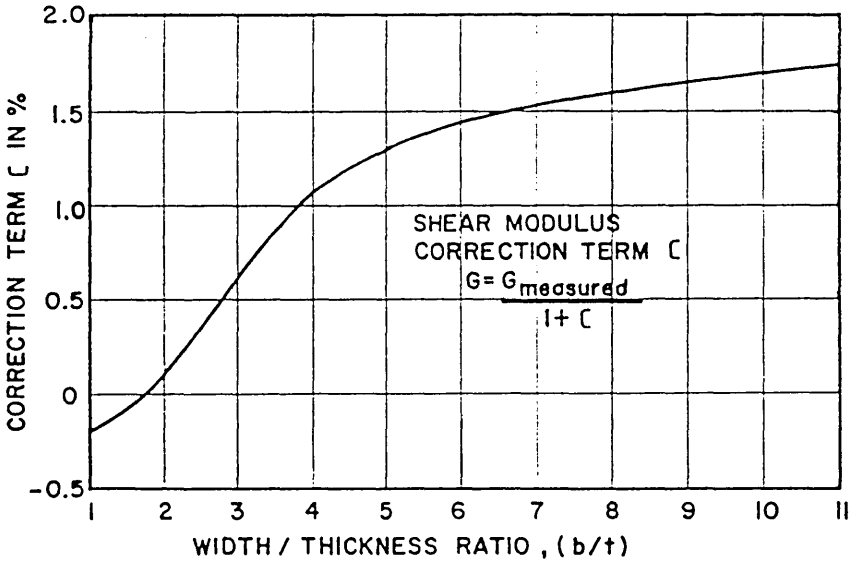


Figure 3.8 Shear Modulus Correction Factor, C as a Function of the Width to Thickness Ratio, b/t (after S. Spinner and R.C. Valore, 1958).

3.7.2 Experimental results and their analysis

(i) Preliminary data obtained using Förster's method:

The following preliminary results have been obtained using the rig modified and re-commissioned for the present work:
(a) In order to ascertain the reproducibility and accuracy of the data obtained using this method and the equipment specified, the room temperature Young's modulus of some different purity alumina materials was measured in air and compared with data typically reported in the literature for these materials. The measured values and the literature values are given in Table 3.1; they agree to within 10 % for all the materials which is good given that materials of the same nominal purity can have varying degrees of residual porosity and their Young's moduli may have been measured by different techniques.
(b) The effect of increasing driving amplitude on the fundamental flexural resonant frequency and internal friction of specimen SCR19.34 B when suspended 2 mm outside the nodes on cotton thread in air has been investigated (Evans, D., 1986) using equation [3.18]; the results are presented in Table 3.2. In the present work, however, equation [3.17] was used; in order to compare the Q^{-1} values given by [3.18] and [3.17] in the absence of the data required to calculate Q^{-1} directly using [3.17] it is necessary to digress a little. If the resonance curve is assumed to be essentially symmetric about the resonant frequency at half the maximum amplitude, i.e., the average of the frequencies at these points equals the resonant frequency $\approx \leq$ 0.1Hz, then by similar triangles,

$$Q^{-1}_{(0.707A_{max})} \approx 1.0146 Q^{-1}_{(0.5A_{max})} \qquad [3.30]$$

to a first approximation. For example, using the data for specimen SCR19.34 A, whose resonance curve satisfied the given symmetry criterion, gave $Q^{-1}_{(0.5A_{max})} = 5.10 \times 10^{-4}$ and $Q^{-1}_{(0.707A_{max})} = 5.23 \times 10^{-4}$ from the curve; using [3.30] gave $Q^{-1}_{(0.707A_{max})} = 5.17 \times 10^{-4}$, i.e., an error of just over 1 % (See the resonance curve for specimen SCR19.34 A in Figure 3.9).

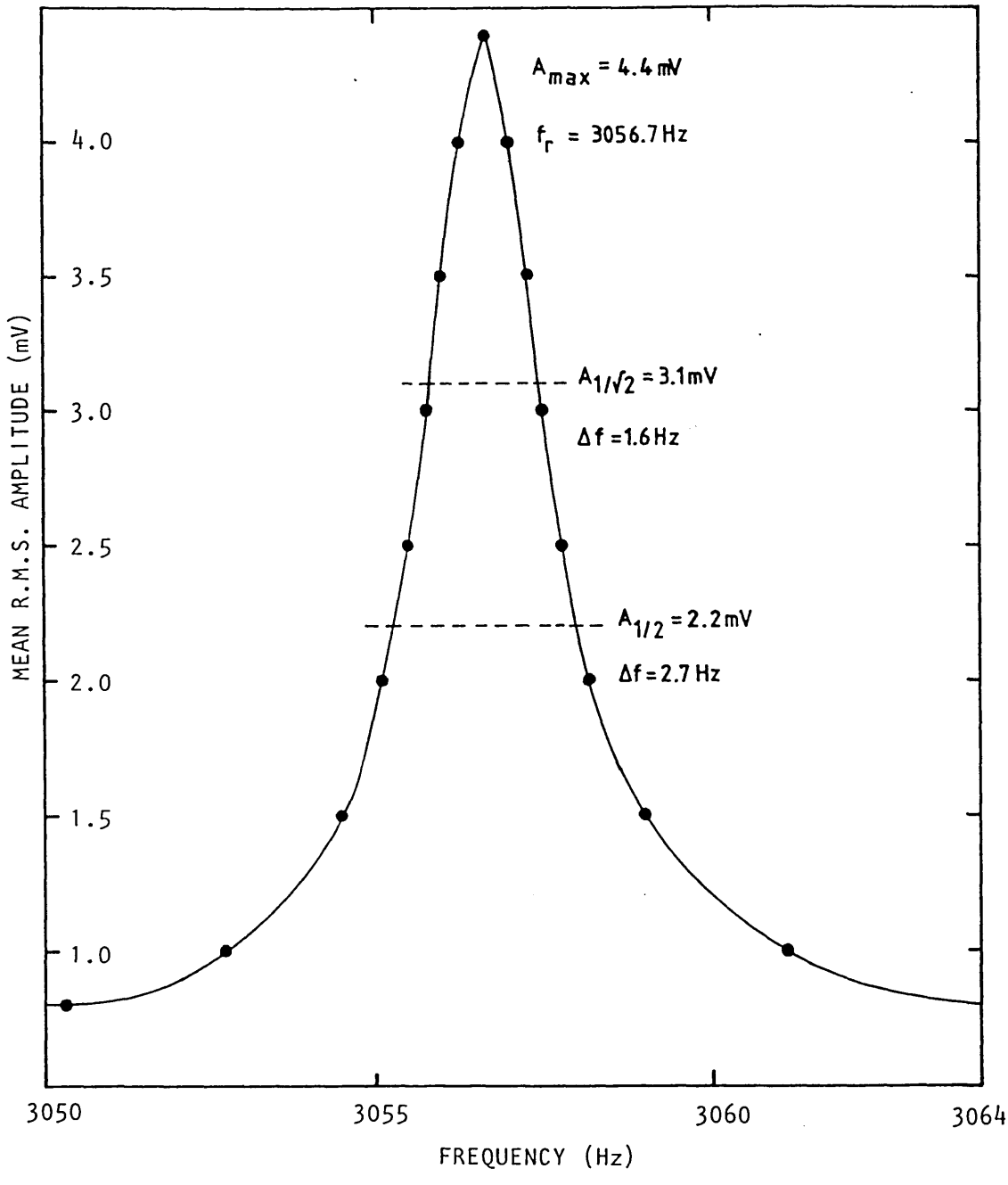


Figure 3.9 Resonance Peak for Specimen SCR19.34 A at 20°C Under Vacuum (Suspended 4 mm Outside the Nodes) When Vibrating in the Fundamental Flexural Mode.

Table 3.1 Comparison of Room Temperature Young's Modulus Data for Some Alumina Materials:

Alumina Grade % Al_2O_3	E (GPa) Measured Values	E (GPa) Literature Values
85	225 ± 2 (2) 1%	220
88	228 ± 6 (2) 3%	250
95	292 ± 9 (3) 3%	320
97.5	341 (1)	338

The measured E values are given with the sample standard deviation and the percentage coefficient of variation; the number of specimens tested are in parentheses.

Table 3.2 Effect of Driving Amplitude on the Fundamental Flexural Resonant Frequency and Internal Friction of Specimen SCR19.34 B Suspended 2 mm Outside the Nodes in Air:

Driving Amplitude (V r.m.s.)	Resonant Frequency (Hz)	Internal Friction Q^{-1} ($x10^{-4}$)
1.7	3067.1	3.9125
4.8	3067.2	3.9124
14.5	3067.0	3.5866

In this instance the internal friction values were calculated using equation [3.18] rather than [3.17] which was used to calculate all the other internal friction values presented in the present work.

Regarding Table 3.2 and remembering that the primary results were obtained using a driving amplitude of 0.85V r.m.s., the resonant frequency and the internal friction were amplitude independent up to 14.5V r.m.s. and 4.8V r.m.s. respectively.

(2) Primary data obtained using Förster's method and the horizontal clamping method:

The dimensions and masses of the specimens tested are tabulated in Appendix 3D. The room temperature elastic moduli and internal friction data will be presented first.

(2.1) Effect of suspension position in Förster's method:

The effect of suspension position with respect to the nodes on the measured Young's modulus and internal friction values, both in air and in vacuum, will be considered first. The Young's modulus (E) and the internal friction (Q^{-1}) of specimens SCR25.76 C and SCR19.34 C were measured in air (i.e., the bell jar was at atmospheric pressure) and in vacuum ($\leq$ 0.1 Pa) with the suspensions placed symmetrically at a number of positions, both outside and inside the nodes at 21°C; the data are tabulated in Table 3.3 and Table 3.4 respectively. The Young's modulus data were considered regardless of the suspension position; the mean Young's modulus regardless of suspension position in air and under vacuum is given in Table 3.5 along with the sample standard deviation and the coefficient of variation. Table 3.5 also gives the range of the Young's modulus values in air and under vacuum, both in GPa and in terms of the number of sample standard deviations (s.d.) away from the mean Young's modulus.

Comparing the mean values in air and under vacuum shows that the mean Young's modulus in air is 0.1 % lower than that under vacuum for both SCR25.76 C and SCR19.34 C. The mean value of all 24 Young's modulus data for SCR25.76 C was 119.71 GPa with a sample standard deviation of 0.11 GPa and a coefficient of variation of 0.09 %,

Table 3.3 Frequency, Internal Friction and Young's Modulus Data for SCR25.76 C in Air and Under Vacuum at Different Suspension Positions Relative to the Nodes (-ve ≡ outside nodes; +ve ≡ inside nodes):

Data Measured in Air (21°C)

Position ($\times 10^{-3}$ m)	f_r (Hz)	f_u (Hz)	f_L (Hz)	Q^{-1} ($\times 10^{-4}$)	E (GPa)
-14	3003.0	3007.9	2999.7	15.77	119.42
-10	3004.9	3007.5	3003.2	8.26	119.57
- 8	3005.4	3007.0	3004.0	5.76	119.61
- 6	3006.0	3007.0	3004.7	4.42	119.66
- 4	3006.2	3007.1	3005.2	3.65	119.68
- 2	3006.5	3007.3	3005.6	3.26	119.70
+ 2	3006.6	3007.4	3005.9	2.88	119.71
+ 4	3006.3	3007.3	3005.5	3.46	119.68
+ 6	3006.3	3007.3	3005.3	3.84	119.68
+ 8	3006.1	3007.2	3004.8	4.61	119.67
+10	3005.4	3006.9	3004.0	5.57	119.61
+14	3005.1	3006.6	3003.2	6.53	119.59

Data Measured in Vacuum (21°C)

Position ($\times 10^{-3}$ m)	f_r (Hz)	f_u (Hz)	f_L (Hz)	Q^{-1} ($\times 10^{-4}$)	E (GPa)
-14	3004.9	3009.2	2998.3	20.94	119.57
-10	3006.8	3008.5	3004.7	7.30	119.72
- 8	3007.0	3008.6	3005.1	6.72	119.74
- 6	3007.9	3008.9	3007.0	3.65	119.81
- 4	3008.3	3008.9	3007.4	2.88	119.84
- 2	3008.7	3009.2	3007.6	3.07	119.88
+ 2	3008.6	3009.2	3007.3	3.65	119.87
+ 4	3008.1	3008.7	3007.2	2.88	119.83
+ 6	3008.3	3009.0	3007.3	3.26	119.84
+ 8	3008.0	3009.0	3006.8	4.22	119.82
+10	3007.4	3008.7	3005.8	5.57	119.77
+14	3007.0	3008.5	3005.4	5.95	119.74

Table 3.4 Frequency, Internal Friction and Young's Modulus Data for SCR19.34 C in Air and Under Vacuum at Different Suspension Positions Relative to the Nodes (-ve ≡ outside nodes; +ve ≡ inside nodes):

Data Measured in Air (21°C)

Position ($\times 10^{-3}$ m)	f_r (Hz)	f_u (Hz)	f_L (Hz)	Q^{-1} ($\times 10^{-4}$)	E (GPa)
-14	2998.8	3001.6	2995.0	12.71	114.49
-10	3001.0	3003.3	2998.9	8.46	114.66
- 8	3001.6	3002.9	2999.3	6.92	114.71
- 6	3001.8	3002.9	2999.3	6.92	114.72
- 4	3002.5	3004.1	3001.5	5.00	114.78
- 2	3002.2	3003.3	3000.8	4.81	114.75
+ 2	3002.3	3003.8	3001.6	4.23	114.76
+ 4	3002.5	3004.1	3001.5	5.00	114.78
+ 6	3002.1	3003.7	3000.7	5.77	114.75
+ 8	3001.8	3003.2	3000.2	5.77	114.72
+10	3001.6	3003.0	2999.9	5.96	114.71
+14	3000.9	3003.1	2998.6	8.66	114.65

Data Measured in Vacuum (21°C)

Position ($\times 10^{-3}$ m)	f_r (Hz)	f_u (Hz)	f_L (Hz)	Q^{-1} ($\times 10^{-4}$)	E (GPa)
-14	3001.6	3004.8	2997.7	13.66	114.71
-10	3002.8	3004.8	3000.1	9.04	114.80
- 8	3003.4	3005.0	3001.7	6.34	114.85
- 6	3004.2	3005.4	3002.8	5.00	114.91
- 4	3004.5	3005.4	3002.9	4.80	114.93
- 2	3004.2	3005.1	3000.9	----	114.91
+ 2	3004.3	3005.5	------	----	114.91
+ 4	3004.4	3005.5	3002.8	5.19	114.92
+ 6	3004.2	3005.3	3002.9	4.61	114.91
+ 8	3003.7	3005.0	3002.3	5.19	114.87
+10	3003.7	3005.0	3002.0	5.77	114.87
+14	3003.0	3004.9	3000.8	7.88	114.81

Table 3.5 Room Temperature Young's Modulus (E) Data for Specimens SCR25.76 C and SCR19.34 C Regardless of Suspension Position in Air and Under Vacuum:

Mean E Data Regardless of Suspension Position

Specimen	Mean E (GPa)	Stand. Dev. (GPa)	Coeff. of Var. (%)
SCR25.76 C = 0.20	12 data		
Air	119.63	0.08	0.07
Vacuum	119.79	0.09	0.08
SCR19.34 C = 0.20	12 data		
Air	114.71	0.08	0.07
Vacuum	114.87	0.07	0.06

Range of E Data Regardless of Suspension Position

Specimen	Minimum E (GPa)	Mean E (GPa)	Maximum E (GPa)
SCR25.76 C			
Air	119.42	119.63	119.71
ΔE	-2.6 s.d.		+1.0 s.d.
Vacuum	119.57	119.79	119.88
ΔE	-2.4 s.d.		+1.0 s.d.
SCR19.34 C			
Air	114.49	114.71	114.78
ΔE	-2.8 s.d.		+0.9 s.d.
Vacuum	114.71	114.87	114.93
ΔE	-2.3 s.d.		+0.9 s.d.

Note: ΔE denotes the minima and maxima relative to the mean E value in terms of the sample standard deviation, s.d.

while for SCR19.34 C the mean value was 114.79 GPa with a sample standard deviation of 0.11 GPa and a coefficient of variation of 0.1 %. So for most intents and purposes it appears that it does not matter at what position a specimen is suspended nor if the measurements were made in air rather than under vacuum when using Förster's method to determine the Young's modulus; it is also reasonable to assume that the same is therefore true when determining the shear modulus.

The pickup amplitudes for both SCR25.76 C and SCR19.34 C are tabulated against suspension position in Table 3.6, and plotted against suspension position in Figure 3.10 (a) and (b) respectively, both in air and under vacuum. The plots show that outside the nodes the pickup amplitudes in air and under vacuum are of similar magnitude, but inside the nodes the amplitude in air is noticeably higher than that under vacuum; the difference gets larger the further the distance from the nodes.

The resonant frequency (f_r) and the internal friction data for SCR25.76 C (see Table 3.3) are plotted against suspension position in Figure 3.11 (a) and (b) respectively, both in air and under vacuum; likewise for the SCR19.34 C data (see Table 3.4) in Figure 3.12 (a) and (b). The features to note from Figures 3.11 and 3.12 are (i) that at the nodes the resonant frequency is a maximum and the internal friction a minimum, (ii) in general the resonant frequency is higher at suspension positions inside the nodes than at the corresponding suspension positions outside the nodes, while the reverse is true for the Q^{-1} values, and (iii) although the Q^{-1} values in air and under vacuum are close together (suggesting that air damping was still occurring under vacuum as suspected due to the vacuum pressure) and subject to scatter the internal friction under vacuum, appears, on balance, to be lower than that in air. Note that the scatter in the Q^{-1} data is lower than in the pickup amplitude data, and the higher pickup amplitudes in air compared to under vacuum do not correlate with higher attenuation, i.e., higher Q^{-1} values in air as compared to under vacuum.

Table 3.6 Pickup Amplitude Data in Air and Under Vacuum at Different Suspension Positions Relative to the Nodes (-ve ≡ outside nodes; +ve ≡ inside nodes) at 21°C:

Data for SCR25.76 C

Position ($\times 10^{-3}$ m)	Pickup Amplitude in Air (mV r.m.s.)	Pickup Amplitude in Vacuum (mV r.m.s.)
-14	6.0	7.4
-10	7.6	10.5
- 8	6.6	8.0
- 6	5.8	7.2
- 4	6.0	4.4
- 2	3.1	1.7
+ 2	6.0	1.5
+ 4	7.8	4.2
+ 6	12.2	6.2
+ 8	16.2	7.0
+10	15.5	9.0
+14	16.5	10.8

Data for SCR19.34 C

Position ($\times 10^{-3}$ m)	Pickup Amplitude in Air (mV r.m.s.)	Pickup Amplitude in Vacuum (mV r.m.s.)
-14	9.7	8.6
-10	9.2	7.6
- 8	5.1	6.5
- 6	2.5	4.2
- 4	2.9	2.4
- 2	1.7	1.2
+ 2	5.0	1.0
+ 4	5.7	2.0
+ 6	7.7	4.0
+ 8	15.2	5.5
+10	21.0	6.4
+14	16.4	8.4

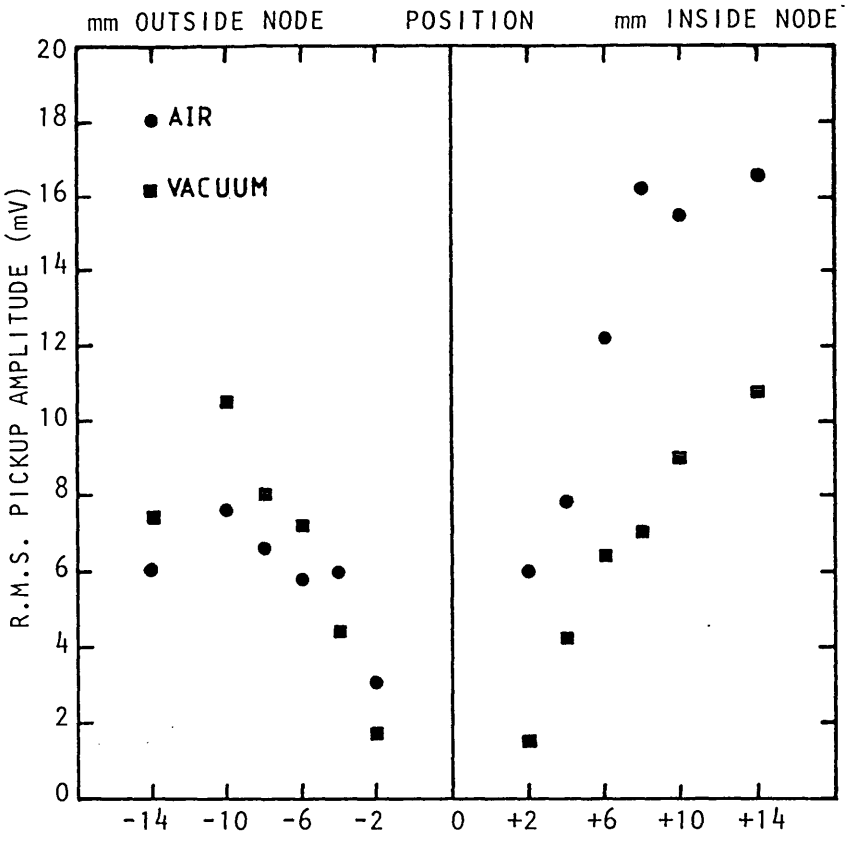


Figure 3.10 (a) Pickup Amplitude for SCR25.76 C as a Function of Suspension Position in Air and Under Vacuum.

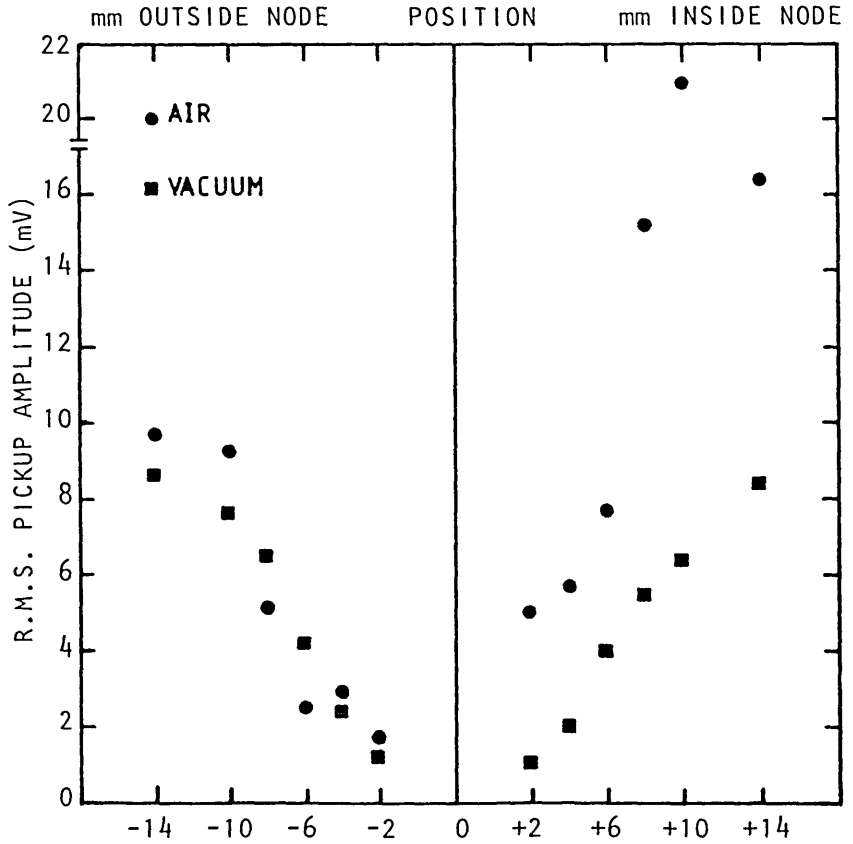


Figure 3.10 (b) Pickup Amplitude for SCR19.34 C as a Function of Suspension Position in Air and Under Vacuum.

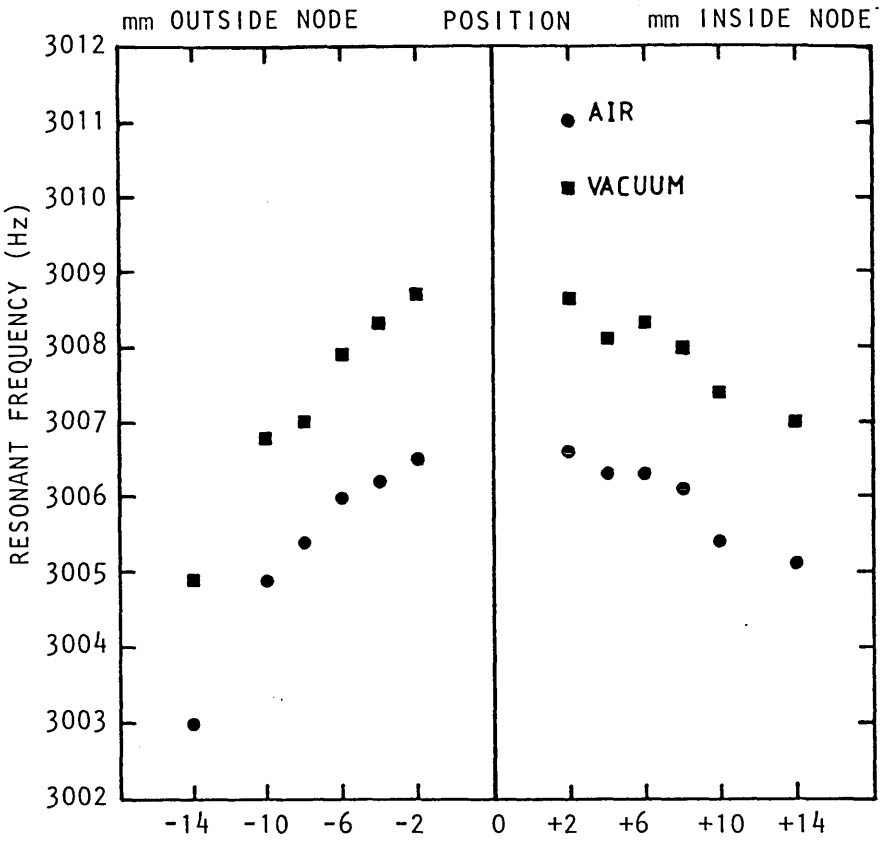


Figure 3.11 (a) Fundamental Flexural Resonant Frequency of SCR25.76 C Versus Suspension Position in Air and Under Vacuum.

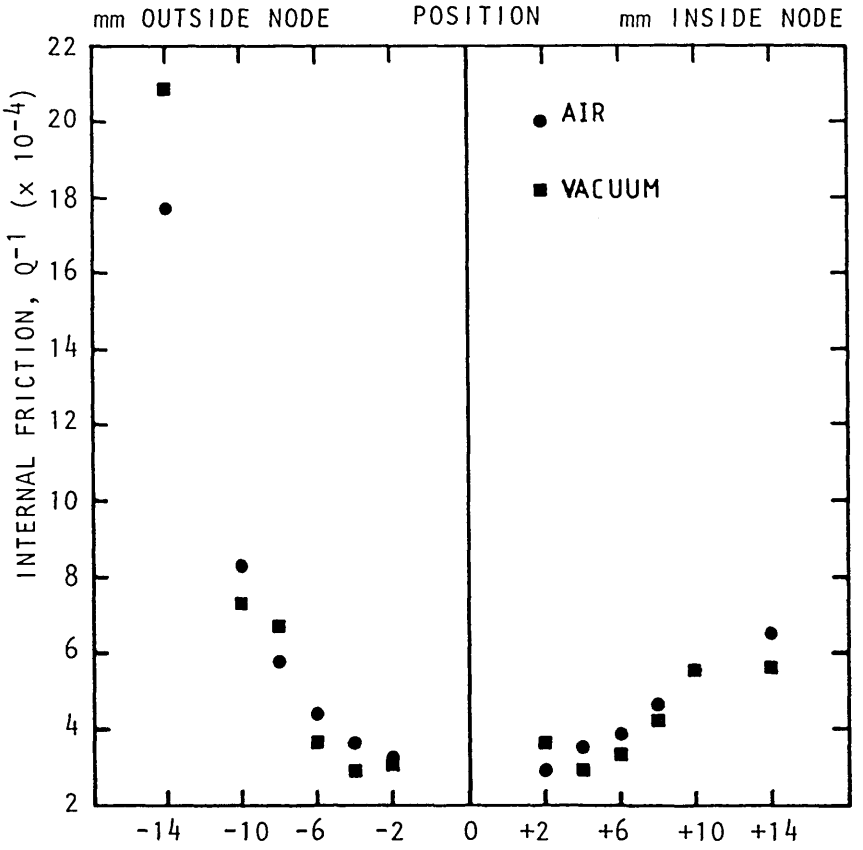


Figure 3.11 (b) Internal Friction of SCR25.76 C as a Function of Suspension Position in Air and Under Vacuum.

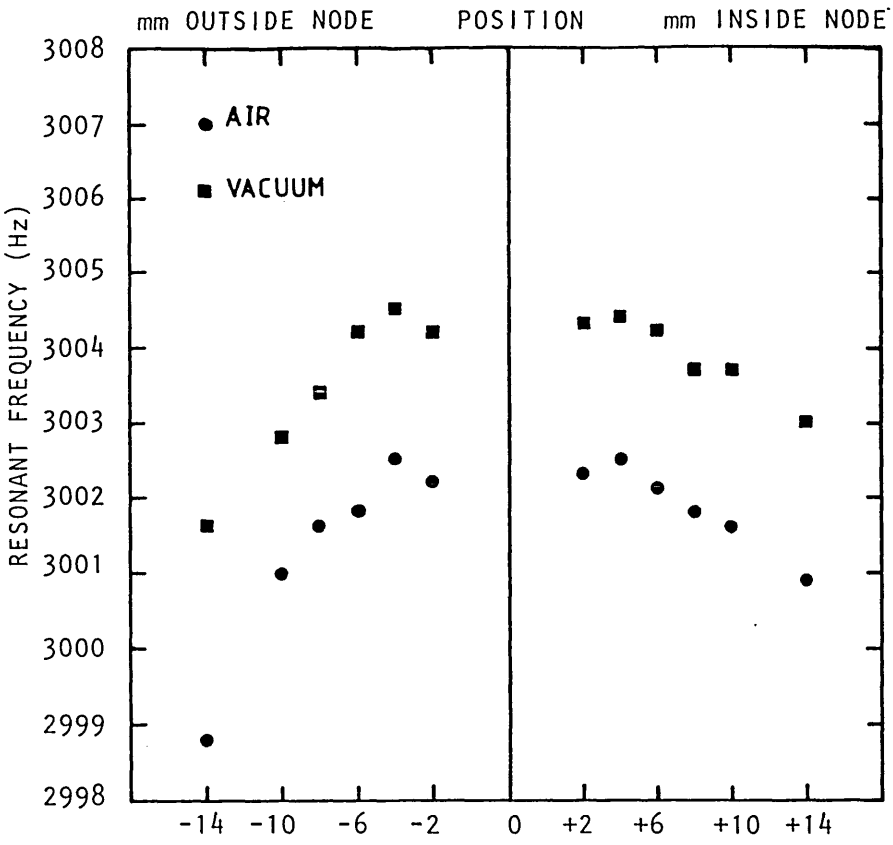


Figure 3.12 (a) Fundamental Flexural Resonant Frequency of SCR19.34 C Versus Suspension Position in Air and Under Vacuum.

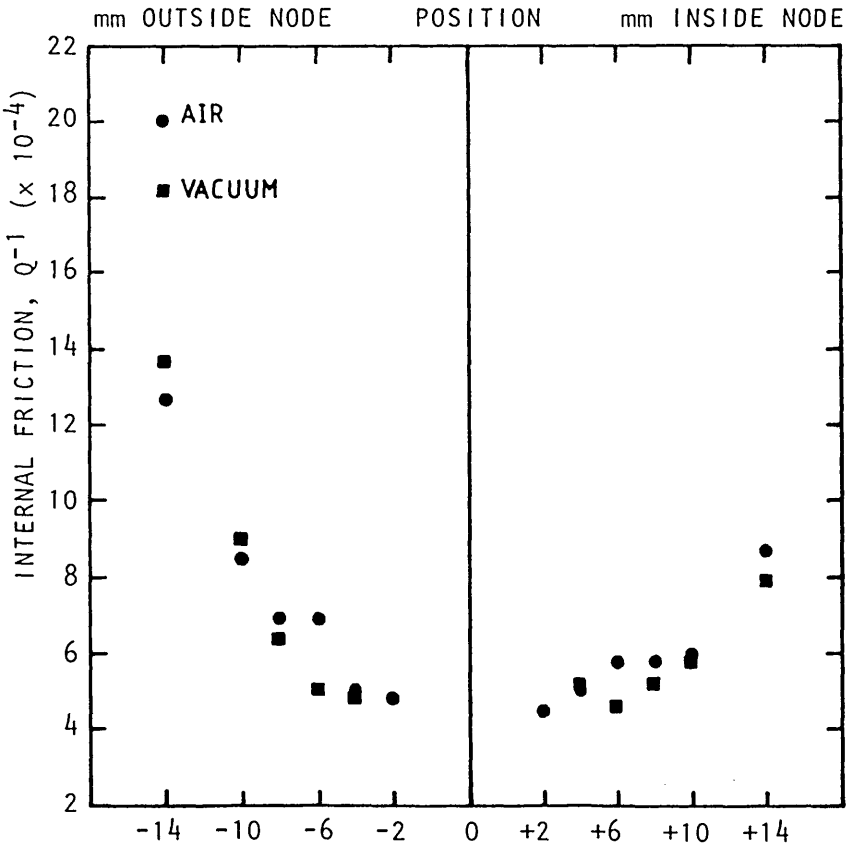


Figure 3.12 (b) Internal Friction of SCR19.34 C as a Function of Suspension Position in Air and Under Vacuum.

The effect of suspension position on the values of internal friction measured using horizontal suspension was analysed quantitatively using the theory developed by J.B. Wachtman and W.E. Tefft (1958) and which is summarised here. They considered the vibrational energy and the damping capacity of the system, i.e., specimen and apparatus, as a whole and the individual vibrational energies and damping capacities of the specimen and the apparatus; from such considerations they derived the following equation

$$Q^{-1}_m = \frac{Q^{-1}_s + kQ^{-1}_A (y/y_o)^2}{1 + k(y/y_o)^2} \qquad [3.31]$$

where Q^{-1}_m is the experimentally measured internal friction, Q^{-1}_s the internal friction of the specimen in air or under vacuum, k the ratio of the apparatus energy to the specimen energy when the specimen is suspended at the ends, Q^{-1}_A the damping capacity of the apparatus (i.e. the suspension, driver and the pickup), and y/y_o is the ratio of the vertical displacement of the point of suspension from equilibrium, y to the displacement of the end of the specimen from equilibrium, y_o assuming the driver and pickup suspensions are placed symmetrically. The ratio y/y_o is expressed in terms of the distance of the points of suspension from the ends of the specimen, x and for the fundamental mode of flexural vibration is given by

$$(y/y_o) = (1.018[\cosh(4.730x/L) + \cos(4.730x/L)] - [\sinh(4.730x/L) + \sin(4.730x/L)])/2.036 \qquad [3.32]$$

where L is the specimen length.

The internal friction data for SCR25.76 C and SCR19.34 C was analysed as follows:

(a) values of x/L corresponding to the twelve suspension positions used were calculated and substituted in equation [3.32] to obtain the corresponding $(y/y_o)^2$ values,

(b) equation [3.31] was re-written in the following form

$$1Q^{-1}_s + (y/y_o)^2 kQ^{-1}_A - Q^{-1}_m (y/y_o)^2 k = Q^{-1}_m \qquad [3.33]$$

where the variables, i.e., "unknowns", are Q^{-1}_s, kQ^{-1}_A and k and the coefficients are 1, $(y/y_o)^2$ and $Q^{-1}_m (y/y_o)^2$ respectively, and the equation equals the constant Q^{-1}_m,

(c) solving this general linear equation required the solution of three such equations simultaneously; the number of possible combinations, and hence solutions of three equations from twelve data is 220. The physics of the situation require that all the unknown parameters are positive quantities, thus not all 220, and possibly none of the solutions obtained using experimental data will be valid. It would have taken an inordinately long time to solve all 220 sets of equations, so sets were chosen at random and solved with the result that a solution was obtained for SCR19.34 C in air and under vacuum after 4 and 6 attempts respectively; a solution was obtained for SCR25.76 C in air after 8 attempts but no solution was obtained for vacuum conditions after 12 attempts and no more were attempted due to lack of time.

The solutions obtained for SCR19.34 C were (i) in air, $Q^{-1}_{s} = 2.97 \times 10^{-4}$, $kQ^{-1}_{A} = 3.428 \times 10^{-3}$ and $k = 1.842648$, and (ii) under vacuum, $Q^{-1}_{s} = 1.66 \times 10^{-4}$, $kQ^{-1}_{A} = 2.736 \times 10^{-4}$ and $k = 0.532415$. The solution obtained for SCR25.76 C in air was $Q^{-1}_{s} = 2.66 \times 10^{-4}$, $kQ^{-1}_{A} = 2.968 \times 10^{-3}$ and $k = 1.842248$. These solutions were used to calculate corrected values of Q^{-1}_{m} in air and under vacuum where possible; these theoretical values, denoted by Q^{-1}_{c}, are tabulated against suspension position in Table 3.7 together with the experimentally measured Q^{-1}_{m} values, the x/L values and the $(y/y_{o})^{2}$ values. According to Wachtman and Tefft fitting experimental data to equation [3.31] provides accurate Q^{-1}_{s} values but not Q^{-1}_{A} and k values because of the nature of the equation. These solutions show that the internal friction of a specimen is lower under vacuum than in air like Figures 3.11 (b) and 3.12 (b) suggest. The theoretical curves of measured internal friction versus suspension position in air for SCR25.76 C and SCR19.34 C, together with the experimental data, are shown in Figure 3.13 (a) and (b) respectively. The theoretical curve for SCR19.34 C in vacuum is shown in Figure 3.14, again with the experimental data. The data for SCR25.76 C in air fitted the theoretical curve quite closely except the value for 14 mm outside the nodes, and

Table 3.7 Internal Friction As Measured and As Calculated to Correct for Suspension Damping in Air and Under Vacuum at 21°C at Different Suspension Positions (as per Tables 3.4 to 3.6)

Data for SCR25.76 C

Position ($\times 10^{-3}$ m)	x/L	$(y/y_o)^2$	Air		Vacuum	
			Q^{-1}_a	Q^{-1}_c	Q^{-1}_a	Q^{-1}_c
			($\times 10^{-4}$)		($\times 10^{-4}$)	
-14	0.0488	0.5979	15.77	9.71	20.94	----
-10	0.0989	0.2942	8.26	7.39	7.30	----
- 8	0.1239	0.1838	5.76	6.06	6.72	----
- 6	0.1489	0.1004	4.42	4.76	3.65	----
- 4	0.1739	0.0432	3.65	3.65	2.88	----
- 2	0.1990	0.0104	3.26	2.91	3.07	----
+ 2	0.2490	0.0091	2.88	2.88	3.65	----
+ 4	0.2741	0.0344	3.46	3.46	2.88	----
+ 6	0.2991	0.0722	3.84	4.24	3.26	----
+ 8	0.3241	0.1186	4.61	5.07	4.22	----
+10	0.3491	0.1695	5.57	5.86	5.57	----
+14	0.3992	0.2688	6.53	7.11	5.95	----

Data for SCR19.34 C

Position ($\times 10^{-3}$ m)	x/L	$(y/y_o)^2$	Air		Vacuum	
			Q^{-1}_a	Q^{-1}_c	Q^{-1}_a	Q^{-1}_c
			($\times 10^{-4}$)		($\times 10^{-4}$)	
-14	0.0489	0.5976	12.71	11.16	13.66	13.66
-10	0.0989	0.2940	8.46	8.46	9.04	8.39
- 8	0.1239	0.1837	6.92	6.92	6.34	6.09
- 6	0.1489	0.1004	6.92	5.41	5.00	4.18
- 4	0.1740	0.0431	5.00	4.12	4.80	2.78
- 2	0.1990	0.0104	4.81	3.26	----	1.93
+ 2	0.2490	0.0091	4.23	3.23	----	1.90
+ 4	0.2740	0.0344	5.00	3.90	5.19	2.55
+ 6	0.2991	0.0722	5.77	4.81	4.61	3.50
+ 8	0.3241	0.1186	5.77	5.77	5.19	4.61
+10	0.3491	0.1694	5.96	6.69	5.77	5.77
+14	0.3991	0.2687	8.66	8.15	7.88	7.88

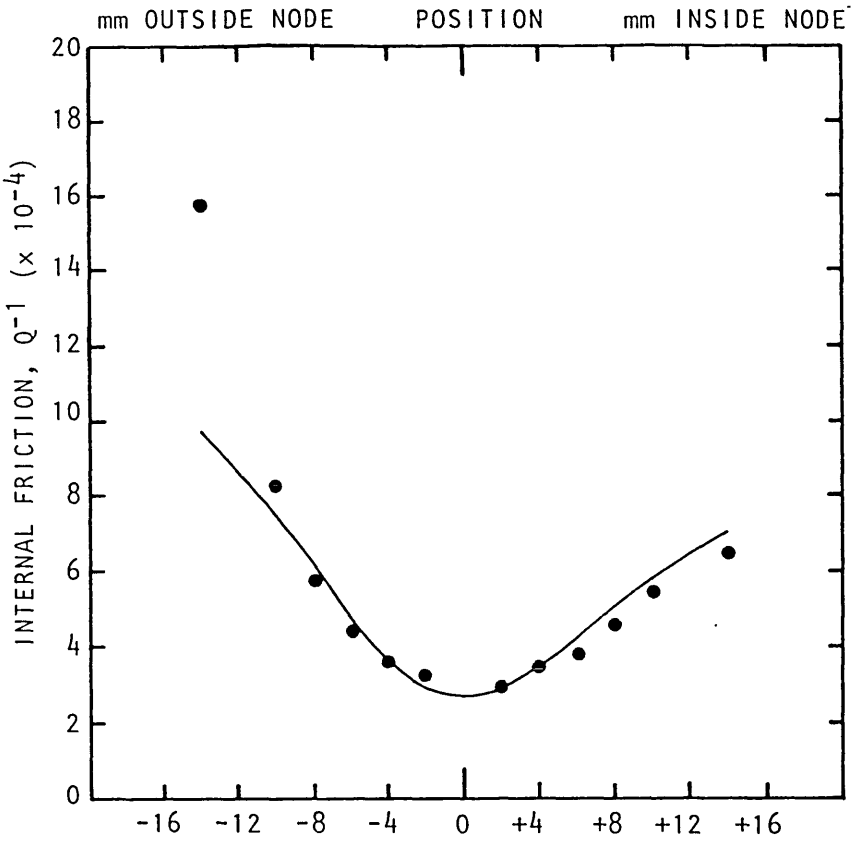


Figure 3.13 (a) Internal Friction Data for SCR25.76 C in Air Superposed on Fitted Theoretical Curve.

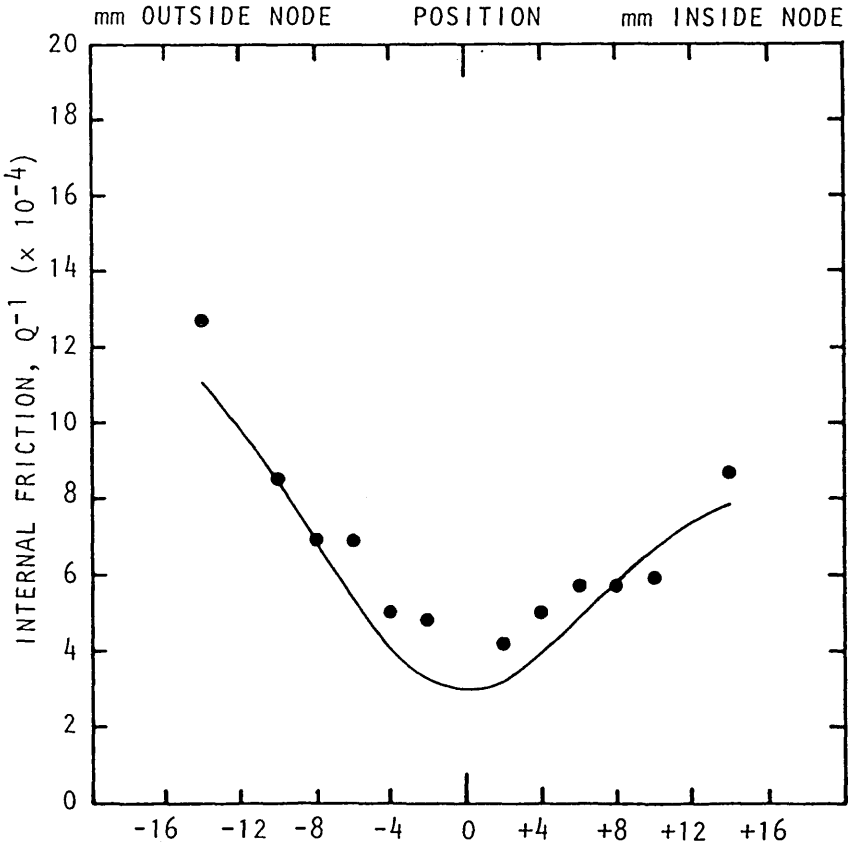


Figure 3.13 (b) Internal Friction Data for SCR19.34 C in Air Superposed on Fitted Theoretical Curve.

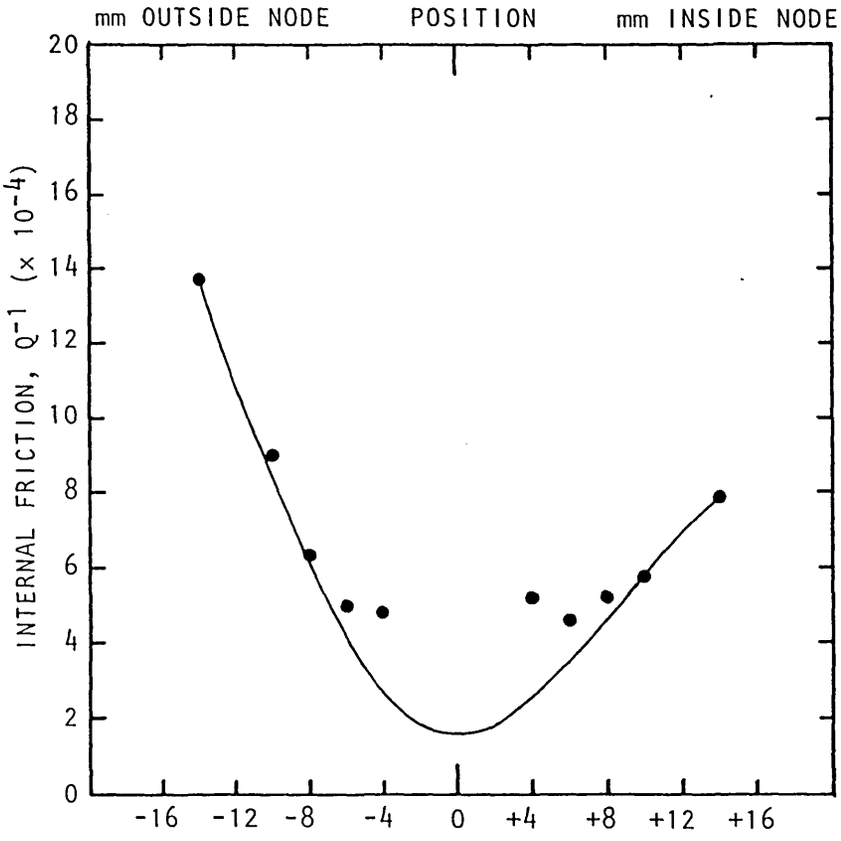


Figure 3.14 Internal Friction Data for SCR19.34 C in Vacuum Superposed on Fitted Theoretical Curve.

although the theoretical curves for SCR19.34 C were fitted at three points, the experimental data errs on the high side close to the nodes, especially under vacuum. This was probably due to system resonances since the internal friction could not be measured at 2 mm either side of the nodes under vacuum (see Table 3.4). To summarise, assuming the results obtained under vacuum were not affected by air damping, the internal friction of SCR19.34 C under vacuum of 1.66×10^{-4} is (i) a factor of ≈ 8 smaller than that measured 14mm outside the nodes under vacuum and (ii) a factor of ≈ 1.8 smaller than the calculated theoretical value in air (note, however, that residual air damping may be responsible for such a small difference). Thus errors of an order of magnitude can occur if the effects of air and suspension damping are not negated.

(2.2) Determination of the shear modulus of specimens SCR25.76 D and SCR19.34 D at room temperature:

The shear modulus was measured in air and under vacuum. The measurements under vacuum were obtained using Förster's method while the horizontal clamping method was used for the measurements in air. The results are presented in Table 3.8; the values measured using the former method were used to calculate the convergent Young's modulus and Poisson's ratio values in view of the better overall reproducibility of this method. The mean value obtained in air for specimen SCR25.76 D was 49.3 GPa with a sample standard deviation of 0.3 GPa and a coefficient of variation of 0.6 % ; the difference between the value in vacuum and that in air was 0.9 % for SCR25.76 D and 0.3 % for SCR19.34 D. Thus in this particular instance the agreement between the data obtained from the two methods is very good.

Table 3.8 Room Temperature Shear Modulus Data for Specimens SCR25.76 D and SCR19.34 D Obtained at 24°C in Air and Under Vacuum:

Specimen	Test Conditions	f_r (Hz)	G (GPa)
SCR25.76 D	Suspended at flexural nodes in vacuum	5702.8	49.74
SCR25.76 D	Clamped at torsional node in air	5683	49.4
		5687	49.5
		5657	48.9
		5669	49.2
SCR19.34 D	Suspended at flexural nodes in vacuum	5674.2	47.68
SCR19.34 D	Clamped at torsional node in air	5678	47.8

Table 3.9 Room Temperature Young's Modulus Data for SCR25.76 and SCR19.34 Glass-Ceramics Obtained Using the Horizontal Clamping Method in Air:

Specimen		f_r (Hz)	Young's Modulus, E (GPa)
SCR25.76	A	2996	131.9
	A	2893	123.0
	B	2897	112.0
	B	2906	112.7
	C	2928	113.5
	C	2903	111.6
SCR19.34	A	2890	103.0
	A	2916	104.9
	B	2926	104.8
	B	2927	104.9
	C	2997	114.4
	C	2922	108.7

(2.3) Determination of the Young's modulus of SCR25.76, SCR19.34, SCF5 and SCR19.13 glass-ceramics at room temperature:

The Poisson's ratio values used to calculate the Young's moduli for the SCR25.76 and SCR19.34 specimens were calculated using equation [3.27] and the respective shear modulus values, while a value of 0.25 was assumed for the other glass-ceramic specimens. Using 0.25 rather than the actual values had little effect on the calculated Young's modulus values because equation [3.22] for the correction factor T depends on quadratic equations in ν, e.g., T ranges from ≈ 1.01 to 1.03 as t/L ranges from 0.037 to 0.073 for any Poisson's ratio between 0.15 and 0.3, i.e., ν has a negligible effect on T compared to t/L.

The resonant frequency and Young's modulus data obtained for SCR25.76 and SCR19.34, using the horizontal clamping method in air, are tabulated in Table 3.9, while the corresponding data for SCF5 are tabulated in Table 3.10. The mean E values together with the sample standard deviations (s.d.), the coefficients of variation (CV) and the number of data averaged (n) are given below:

Material	Mean E (GPa)	s.d. (GPa)	CV (%)	n
SCR25.76	117.5	8.3	7	6
SCR19.34	106.8	4.2	4	6
SCF5	120.6	6.8	6	16

The Young's moduli of the glass-ceramic specimens were also measured by the horizontal suspension method in vacuum, except for the only available specimen of SCR19.13 whose Young's modulus was measured in air by this method. The Young's modulus data so obtained are presented in Table 3.11, along with the Poisson's ratio values calculated by iteration and the internal friction of the specimens if it was measurable.

Table 3.10 Room Temperature Young's Modulus Data for SCF5 Glass-Ceramic Obtained Using the Horizontal Clamping Method in Air:

Specimen		f_r (Hz)	Young's Modulus, E (GPa)
SCF5 A			
Test Run	1	5871	127.7
	2	5863	127.3
	3	5696	120.2
	4	5760	122.9
SCF5 B			
Test Run	1	5643	123.3
	2	5627	122.6
	3	5703	126.0
	4	5603	121.6
SCF5 C			
Test Run	1	6517	124.5
	2	6525	124.8
	3	6541	125.4
	4	6522	124.7
SCF5 D			
Test Run	1	6441	107.5
	2	6598	112.8
	3	6505	109.6
	4	6492	109.2

Table 3.11 Room Temperature Young's Modulus and Internal Friction Data for SCR25.76, SCR19.34, SCF5 and SCR19.13 Glass-Ceramics Obtained by Förster's Method (suspensions outside the nodes):

Specimen	Test Conditions	f_r (Hz)	f_u (Hz)	f_L (Hz)	Q^{-1} ($\times 10^{-4}$)	E (GPa)
SCR25.76	Vacuum					
0.24 A	4mm C 24	2895.1	2895.7	2894.4	2.59	123.18
0.24 A	6mm W 24	2895.1	2896.2	2893.9	4.59	123.18
0.23 B	4mm C 20	3023.7	3024.4	3022.9	2.86	122.06
0.23 B	10mm W 24	3023.5	3025.4	3021.7	7.07	122.04
0.20 C	4mm C 22	3007.8	3008.6	3007.0	3.07	119.81
SCR19.34	Vacuum					
0.21 A	4mm C 20	3056.7	3058.4	3055.2	6.04	115.22
0.21 A	6mm W 28	3055.7	3056.8	3053.8	5.67	115.14
0.21 B	4mm C 23	3064.6	3065.9	3062.9	5.65	114.98
0.21 B	10mm W 24	3068.2	3074.7	3061.6	24.65	115.25
0.20 C	4mm C 21	3003.4	3004.2	3002.2	3.84	114.85
SCR19.13	Air					
A	2mm C 20	5057	----	----	-----	100.6
SCF5	Vacuum					
A	8mm C 24	5694.6	5697.0	5687.1	-----	120.1
B	8mm C 24	5585.3	5587.8	5580.5	-----	120.8
B'	4mm C 22	2293.0	2294.2	2291.9	5.79	121.7
B'	6mm W 23	2290.0	2293.9	2289.6	-----	121.4
C	8mm C 24	6399.8	----	----	-----	120.1
D	8mm C 24	6789.6	----	----	-----	119.4

Note that (i) Poisson's ratio was assumed to be 0.25 for SCF5 and SCR19.13, but was calculated for each SCR25.76 and SCR19.34 specimen (as given in the first column), and (ii) the second column gives from left to right the suspension position, the type of suspension, i.e., C ≡ cotton and W ≡ cotton/wire, and the test temperature (°C).

The mean Young's modulus values for SCR25.76, SCR19.34 (including the mean values obtained for the C specimens in vacuum, given in Section 3.7.2 sub-section (2.1)) and SCF5 regardless of suspension position and type of suspension are tabulated below, together with the sample standard deviations (s.d.) and the coefficients of variation (CV) and the number of data averaged (n):

Material	Mean E (GPa)	s.d. (GPa)	CV (%)	n
SCR25.76	121.7	1.5	1.2	6
SCR19.34	115.0	0.2	0.2	6
SCF5	120.6	0.9	0.7	6

Comparing the data obtained in air with these data shows that the horizontal suspension method gives the same (for SCF5) or a higher mean Young's modulus value (SCR25.76 and SCR19.34) with a significantly lower coefficient of variation. For the latter two materials the mean values obtained by the two methods agreed to within 4 % and 8 % respectively which is good, although Förster's method is apparently more precise and the results therefore more reproducible and probably more accurate; hence the original E and G data were given to two decimal places.

The possible percentage error in the Young's modulus values measured by Förster's method were estimated for SCR25.76 and SCR19.34; the error in the frequency and mass measurements was estimated as 0.004 % and 0.003 % respectively. Using the nominal dimensions L = 79.93 mm, t = 2.98 mm accurate to ± 0.04 mm, b = 11.88 mm accurate to ± 0.02 mm and ν = 0.22, the error in T was 0.03 % and the error in E, i.e., the error in $(L/t)^3(M/b)f^2T$ was given by $[(3 \times 0.05)^2 + (3 \times 1.3)^2 + (0.003)^2 + (0.2)^2 + (2 \times 0.004)^2 + (0.03)^2]^{1/2} \approx 4$ %. For SCF5, it was assumed that L = 74.65 mm, t = 4.50 mm, b = 9.41 mm to ± 0.2 mm and ν = 0.25, with the same error in the frequency and the mass. So the error in T was 0.5 % and the error in E was given by $[(3 \times 0.3)^2 + (3 \times 4.4)^2 + (0.003)^2 + (2.1)^2 + (2 \times 0.004)^2 + (0.5)^2]^{1/2} \approx 13$ %. For the C specimens t was

accurate to 0.02 mm, so the error in G was estimated as ≈ 5 % with 3 % due to R. The precision of the method, however, was ≈ 0.1 % or better. The ASTM standards state that the precision and accuracy of the horizontal suspension method are of the order of 1 % if the specified frequency, dimensional and mass measurement tolerances are observed. The errors in the E values from the clamping method were higher due to the higher uncertainty in the resonant frequencies (thus they were recorded to ± 1Hz) and a lower reproducibility for a given specimen. The Poisson's ratio values for the SCR25.76 and SCR19.34 specimens were averaged as per the E values to give a mean value for the glass-ceramics of 0.23 ± 0.02 (9 %) and 0.21 ± 0.004 (2 %) respectively with an estimated possible error of ≈ 48 %.

The mean values of the internal friction data obtained at 4 mm outside the nodes for the SCR25.76 and SCR19.34 specimens were 2.84 x 10^{-4} (with a sample standard deviation of 0.24 x 10^{-4} and a coefficient of variation of 8 %) and 5.18 x 10^{-4} (with a sample standard deviation of 1.17 x 10^{-4} and a coefficient of variation of 23 %) respectively. The single corresponding value for SCF5 was 5.79 x 10^{-4}. These values, however, should not be taken as absolute (Section 3.7.2 sub-section (2.1)).

(2.4) Estimation of the bulk modulus, longitudinal modulus, longitudinal and shear stress wave velocities of SCR25.76 and SCR19.34:

The bulk modulus, K and longitudinal modulus, L of SCR25.76 and SCR19.34 were estimated using the shear modulus and mean Young's modulus values obtained by Förster's method under vacuum (see Section 3.7.1 sub-section (4)); the results were:

(a) SCR25.76 : K = 73 GPa and L = 140 GPa

(b) SCR19.34 : K = 65 GPa and L = 129 GPa

The shear wave velocity, v_s and the longitudinal wave velocity, v_L were estimated using the density value for SCF5 of 2900 kgm^{-3} (Rogers, P.S., et al., 1984) as:

(a) SCR25.76 : $v_s \approx 4100\ ms^{-1}$ and $v_L \approx 6900\ ms^{-1}$

(b) SCR19.34 : $v_s \approx 4000\ ms^{-1}$ and $v_L \approx 6600\ ms^{-1}$

(2.5) Summary of the room temperature elastic properties of CaO - MgO - Al_2O_3 - SiO_2 glass-ceramics and comparison with the equivalent properties of some other ceramic materials:

The elastic properties data obtained by Förster's method for all the glass-ceramics studied are tabulated in Table 3.12, together with corresponding typical data for a number of other ceramic materials where available. When comparing the data it must be remembered that the SCR19.13 glass-ceramic is a very glassy, i.e., poorly crystallized material produced at the pilot-plant for comparison purposes, while SCR25.76 and SCR19.34 were also pilot-plant materials produced to give barely acceptable microstructures from iron blast-furnace slag, colliery shale, supplemental pure components and pure components respectively. The SCF5 glass-ceramic was a material produced in the laboratory from pure components to give a fine, interlocking dendritic microstructure to act as a reference. The data given in Chapter 2 for the estimated volume fraction of vitreous phase and crystalline phase in representative samples of these materials (Carter, S., 1986) are repeated here for convenience (normalised to 100 % and given with the sample standard deviations, the coefficients of variation and the number of estimates):

Material		Vitreous Phase (Volume %)		Crystalline Phase (Volume %)	
SCF5	(22 data)	18 ± 5	28 %	82 ± 5	6 %
SCR25.76	(11 data)	29 ± 3	10 %	71 ± 3	4 %
SCR19.34	(7 data)	42 ± 2	5 %	58 ± 2	3 %
SCR19.13	(8 data)	70 ± 8	11 %	30 ± 4	13 %

Comparison of the elastic moduli of these glass-ceramics with the commercial glass-ceramics given in Table 3.12 indicates that their elastic moduli are high for glass-ceramics, especially in view of the volume fraction of residual glass present in both SCR25.76 and SCR19.34.

Table 3.12 Room Temperature Elastic Properties of the $CaO - MgO - Al_2O_3 - SiO_2$ Glass-Ceramics Investigated and Some Other Ceramic Materials:

Ceramic Material	E (GPa)	G (GPa)	K (GPa)	ν
Glass-Ceramics:				
SCR25.76	122	50	c 73	0.23
SCR19.34	115	48	c 65	0.21
SCF5	121	---	---	-----
SCR19.13	101	---	---	-----
Pyroceram C9606 *	120	---	---	0.24
Pyroceram C9608 *	88	---	---	0.25
EE 1087 *	92	37	---	0.245
Zerodur *	84	---	---	-----
Glasses:				
Vitreous Silica	74	---	---	0.16
Soda Lime, Float	73	30	---	0.22
Oxide Ceramics:				
Alumina:				
> 99 % Al_2O_3	380	160	230	0.22
95 % Al_2O_3	320	130	180	0.22
90 % Al_2O_3	260	105	160	0.22
85 % Al_2O_3	220	90	140	0.22
Dense Spinel	260	100	---	0.29
Dense Magnesia	300	124	---	0.21

c ≡ calculated values; * ≡ commercial trade-names.
All the comparative data are typical room temperature values after R. Morrell (1985).

(2.6) Young's modulus and internal friction of SCR25.76, SCR19.34 and SCF5 as functions of temperature:

The Young's moduli and internal friction were determined as functions of temperature using the suspension technique with specimens suspended at 6, 8 and 10 mm outside the nodes. The resonant frequency and Young's modulus data for the SCR25.76, SCR19.34 and SCF5 specimens tested are tabulated against temperature in Appendix 3E in Tables 3E.1, 3E.2 and 3E.3 respectively. The Young's modulus values at temperatures above room temperature for a given specimen were calculated using the following equation (Spinner, S., 1956):

$$M_T = M_R (f_T / f_R)^2 (1/[1 + \alpha\Delta T]) \qquad [3.34]$$

where M_T is the elastic modulus at temperature T, M_R the elastic modulus at room temperature, f_T the resonant frequency at temperature T, f_R the resonant frequency at room temperature, α the average linear thermal expansivity of the material from room temperature to the test temperature, and ΔT the differential temperature (i.e., test - room temperature). The average linear thermal expansivity of SCF5 between room temperature and 800°C is $7.5 \times 10^{-6}\ K^{-1}$ (Rogers, P.S., et al., 1984); this value was used for all materials because corresponding values for SCR25.76 and SCR19.34 were not available. The factor $1/(1 + \alpha\Delta T)$, however, is equal to 0.9944 for the maximum temperature differential of 745 K and for a 50 % variation in the α value the error in the factor is $\approx$ 0.3 %; thus a highly accurate value for α is not required to determine sufficiently accurate high temperature elastic modulus values.

The Young's modulus and the internal friction data obtained in a given high temperature test run at a given suspension position were normalized with respect to the respective intial room temperature values determined prior to the test run in order to obtain a master curve for the temperature dependence of these parameters; this procedure was especially necessary for the internal friction data as the magnitude of this parameter varied significantly with

suspension position. In view of the overall trends observed in the measured internal friction data the following procedure was adopted to take account of the observed asymmetry of some of the resonance peaks at higher temperatures:

(a) The degree of asymmetry at the half-maximum amplitude positions was measured by the absolute magnitude of $f_u + f_L - 2f_r$, that is, the absolute difference between $f_u - f_r$ and $f_r - f_L$ where f_r is the resonant frequency, f_u and f_L are the driven frequencies above and below f_r respectively at which the pickup amplitude had fallen to half its maximum (see equation [3.17]).

(b) If the degree of asymmetry was $\leq$ 12Hz. the internal friction was calculated using $f_u - f_L$ and the smaller of $2(f_u - f_r)$ and $2(f_r - f_L)$.

(c) The test temperatures covering a ten degree span and their corresponding normalized Young's modulus and internal friction values were averaged to give mean values and tabulated with the remaining singular test temperature data regardless of the suspension position; if the mean normalized room temperature values were nearly equal to unity all the data were re-normalized to room temperature. It was found that the use of the smaller of $2(f_u - f_r)$ and $2(f_r - f_L)$ as opposed to the average calculated as per (b) whenever the asymmetry was $\geq$ 1Hz produced internal friction values which when normalized and treated as per (c) resulted in much greater scatter in the data; the increased scatter masked the general trend of increasing internal friction with increasing temperature shown by the original internal friction data at each suspension position position. So the procedures in (b) and (c) were used to produce the normalized temperature dependent internal friction data for SCR25.76, SCR19.34 and SCF5 which are tabulated in Appendix 3E in Tables 3E.4, 3E.5 and 3E.6 respectively.

The normalized Young's modulus and internal friction data for the three glass-ceramics are plotted against temperature in Figure 3.15 to illustrate the relative behaviour of the materials. Although the scatter

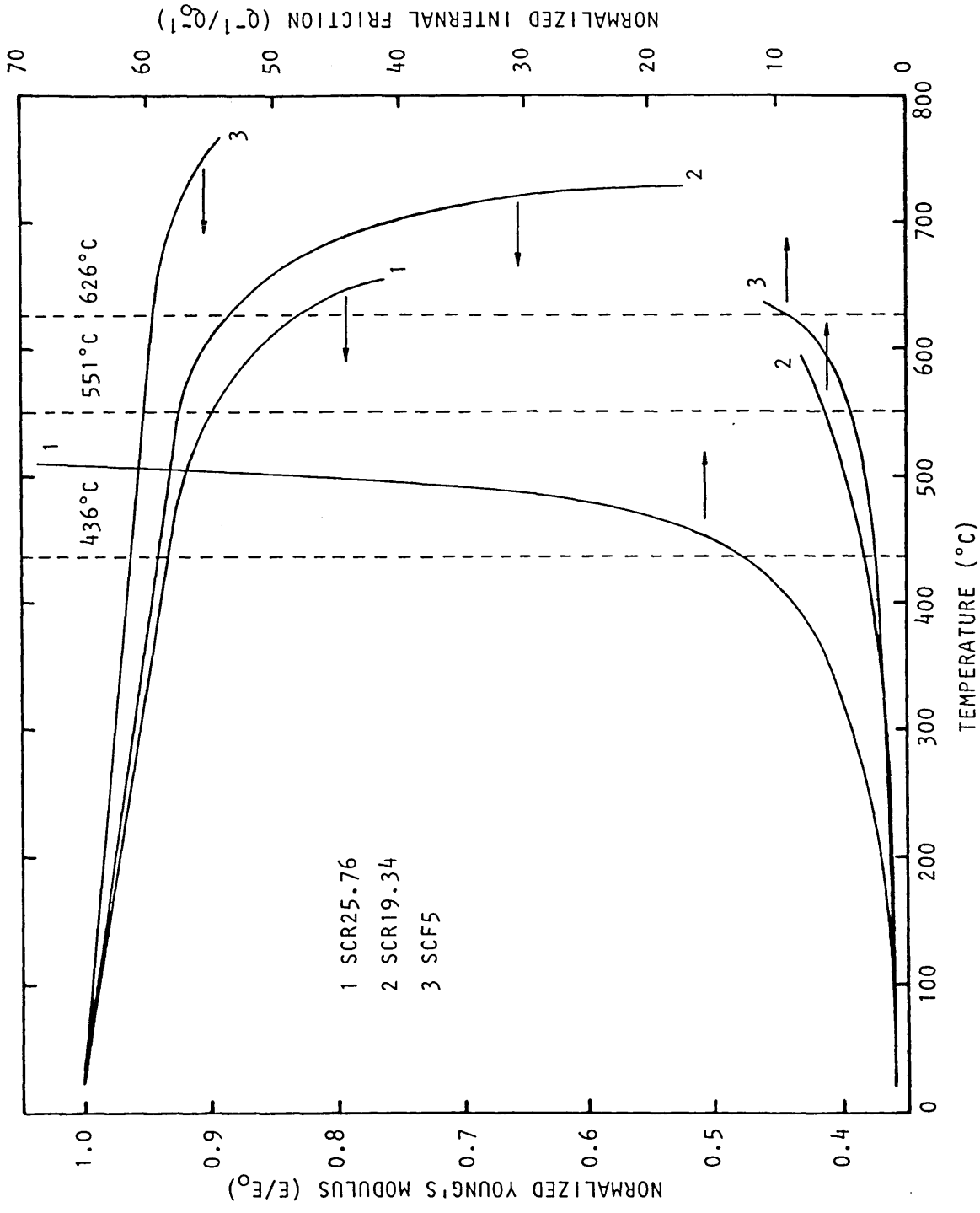


Figure 3.15 Normalized Young's Modulus (E/E_o) and Normalized Internal Friction (Q^{-1}/Q_o^{-1}) of SCR25.76, SCR19.34 and SCF5 as a Function of Temperature.

in the internal friction data was not insignificant the general trends are apparent, particularly the rapid increase at lower temperatures in the internal friction of the SCR25.76 glass-ceramic compared to the other two materials. These results implied that at high temperatures the viscosity of the residual glass may be more important than the volume fraction of residual glass. As Figure 3.15 shows, the Young's modulus of the three materials is a linear function of temperature up to a temperature characteristic of the material. In order to determine the characteristic temperature for each material a customised "least-squares" linear regression computer programme was written; the programme sorted the temperature data and the corresponding Young's modulus data given in Tables 3D.1 to 3D.3 in Appendix 3D into an array of increasing temperature versus Young's modulus data and then performed an automatic iterative linear regression analysis in which the number of data pairs analysed was decreased by one starting at the maximum temperature until only the first three data pairs were analysed. The slope, the coefficient of determination and the root-mean-square percentage difference between the measured and the calculated Young's modulus values were calculated for each iteration.

The characteristic temperature and the parameters of the linear equation $E = a + bT$ giving the best fit were obtained from the iteration which produced the coefficient of determination nearest to unity (in this case -1) and secondly used most of the data. The characteristic temperature was that corresponding to the highest temperature used in the analysis. The data so obtained for the three materials are tabulated in Table 3.13. The characteristic temperatures are 436°C, 551°C and 626°C for SCR25.76, SCR19.34 and SCF5 respectively. Preliminary estimates of the temperature dependence of the viscosity of the residual glass in the three materials have been obtained by calculation from a knowledge of the composition using the model of G. Urbain (Carter, S., 1986) indicate that the viscosities at any given temperature increase in the order SCR25.76, SCR19.34, SCF5

Table 3.13 Linear Regression Data for the Temperature Dependence of the Young's Modulus of the SCR25.76, SCR19.34 and SCF5 Glass-Ceramics:

Regression Parameters	Glass-Ceramic		
	SCR25.76	SCR19.34	SCF5
No. of Data Logged :	62	80	37
No. of Data Analysed :	54	66	30
Slope b of E=a+bT :	-1.90×10^7	-1.53×10^7	-1.06×10^7
Stand. Dev. of b :	0.05×10^7	0.04×10^7	0.03×10^7
Intercept a of E=a+bT :	122.8×10^9	114.7×10^9	121.3×10^9
Stand. Dev. of a :	0.1×10^9	0.1×10^9	0.1×10^9
Coeff. of Determ. :	0.9671	0.9584	0.9822
R.M.S. % Difference:	0.4	0.5	0.2
Temperature Validity Range (°C):	21 to 436	22 to 551	22 to 626

The coefficient of determination = (correlation coeff.)^2. All the correlation coefficients are significant at the 0.5 % level, i.e., the probability of rejecting the hypothesis that the true correlation coefficient is zero when in fact the hypothesis is true is 0.005. So the probability of mistakenly accepting a correlation is 0.5 %

with the viscosity of the SCF5 residual glass significantly higher than that of SCR25.76 and SCR19.34. Furthermore, the incipient softening point at which the viscosity is ≈ 10^{10} to 10^{11} Pa.s corresponds approximately to the temperature range 440 to 480°C for SCR25.76, 480 to 520°C for SCR19.34 and 630 to 680°C for SCF5.

To summarise, the characteristic temperatures which indicate the empirical upper limit of the linear temperature dependence of the Young's modulus of SCR25.76, SCR19.34 and SCF5 are within ≈ 20°C, 50°C and 30°C of the mid-band incipient softening temperatures which are 460°C, 500°C and 655°C respectively. Unfortunately, however, the scatter in the internal friction data precluded any quantitative estimate of the change in the slopes of the internal friction curves at the characteristic temperatures; in qualitative terms, however, the internal friction appeared to increase more rapidly above the characteristic temperatures, particularly in the case of SCR25.76. Note the incipient softening point is also referred to as the dilatometric softening point (McMillan, P.W., 1979).

So the viscosity of the residual glass of the SCR19.34 glass-ceramic appears to dominate the effect of the volume fraction of residual glass on the temperature dependence of the Young's modulus because although it has a higher volume fraction of residual glass (≈ 9 % higher) than the SCR25.76 material and a lower room temperature Young's modulus the relative decrease in the Young's modulus with increasing temperature is lower (see Figure 3.15 and Table 3.13) and the linear dependence is maintained to a higher temperature (110°C higher); this is attributed to the higher viscosity of its residual glass compared to that of SCR25.76 at any given temperature.

3.8 Temperature Dependence of the Internal Friction of Other Ceramic Materials

As far as the author is aware, few studies have been conducted on the temperature dependence of internal friction of mono- and poly-crystalline ceramics. An early study of the temperature dependence of the Young's modulus and internal friction of single and polycrystalline alumina, as well as other refractory ceramics (Wachtman, J.B. and Lam, D.G., 1959) using Förster's technique found that within experimental limits, the internal friction of single crystal alumina (i.e., sapphire [99.9 % Al_2O_3] and ruby [99.25 % Al_2O_3 + 0.75 % Cr_2O_3]) was essentially independent of temperature up the highest temperature of measurement (1400°C and 1700°C for sapphire and ruby respectively). It was also found that the internal friction of polycrystalline alumina varied little between room temperature and 800°C, but increased rapidly above 800°C; the scatter in the data from successive tests was such that no curve of internal friction versus temperature above 800°C could be plotted and the drastic reduction in the vibrational amplitude at resonance due to the increase in internal friction established the maximum temperature at which the resonant frequency and hence the internal friction could be reliably measured. Furthermore, Wachtman and Lam found that the rapid increase in internal friction at high temperatures was accompanied by a rapid non-linear decrease in the Young's modulus for all the polycrystal ceramics studied; this behaviour was attributed to grain boundary sliding.

The temperature dependence of the Young's modulus and internal friction of polycrystalline yttrium oxide (Y_2O_3) has been investigated by M.O. Marlowe and D.R. Wilder (1965). They found that the Young's modulus decreased rapidly, in a non-linear manner, with increasing temperature between 1350 and 1658°C, and was accompanied by a rapid increase in the internal friction. Furthermore, the internal friction did not decrease with increasing temperature to its former level; Marlowe and Wilder

concluded that the temperature at which the internal friction reached a maximum was higher than 1658°C. This rapid decrease in E and the concomitant rapid increase in internal friction at high temperatures was analogous to the general behaviour of the polycrystalline ceramics investigated by Wachtman and Lam, e.g., for alumina between 800 and 1200°C.

A recent study of the temperature dependence (to 650°C or 800°C) of the Young's modulus and internal friction of partially stabilized zirconia (3 mol% Y_2O_3 + ZrO_2), alumina, and silicon nitride (Masahiko Shimada, et al., 1984) found that the internal friction of alumina was relatively constant up to the maximum test temperature of 650°C (supporting the results of Wachtman and Lam), while that of silicon nitride increased between 750 and 800°C (the maximum test temperature) which was attributed to the softening of the vitreous grain boundary phase deriving from the additive (3 wt% MgO) used to promote pressureless sintering. The internal friction of the partially stabilized zirconia increased rapidly with temperature up to a maximum at 200°C and then decreased rapidly with increasing temperature up to 400°C, and was thereafter similar to the room temperature value. The peak in the internal friction at 200°C coincided with an inflection in the Young's modulus versus temperature curve which decreased non-linearly with temperature up to 400°C, but then decreased linearly up to 650°C. The internal friction peak was suggested as possibly being due to twin motion in monoclinic ZrO_2 or the bowing of dislocations.

In summary, the bulk of the data on the temperature dependence (above room temperature) of the internal friction in various conventional polycrystalline ceramics (i.e., not yttria stabilized zirconia) such as alumina, magnesia, silicon nitride and so on, indicate that the rapid, non-linear decrease in the Young's modulus which usually occurs at elevated temperatures is accompanied by a rapid increase in the internal friction, which has been generally attributed to grain boundary sliding.

The reasons for attributing the generally observed rapid increase in the internal friction at elevated temperatures and the concomitant rapid non-linear decrease in the Young's modulus to a grain boundary energy-dissipation mechanism are:

(a) Wachtman and Lam found that no change occurred in the temperature dependence of the Young's modulus of the single crystal alumina (from linear to non-linear) at ≈ 950°C as observed for polycrystalline alumina,

(b) Furthermore, the internal friction of the single crystal alumina was essentially independent of temperature both above and below 950°C, unlike that of polycrystalline alumina which increased extremely rapidly with temperature above 950°C.

In the present work, the rapid non-linear decrease in the Young's modulus and the rapid increase in the internal friction (starting at a lower temperature than the characteristic temperature at which the temperature dependence of the Young's modulus became non-linear) correlated reasonably well with the calculated estimates of the incipient or dilatometric softening-temperature bands of the intergranular residual glass. Under the imposed periodic flexural stress, shear stresses are presumed to arise at the residual glass - crystal and crystal - crystal interfaces and the reduced viscosity of the residual glass at elevated temperatures facilitates both the relative movement of crystals within the anelastically deforming residual glass matrix and the sliding of adjacent, impinging crystal boundaries with consequent elastic deformation of the neighbouring crystals; the recovery of the elastic strain in the adjacent crystals will be time-dependent since the relative movement of the crystals is controlled by the anelastic response of the residual glass to the imposed periodic flexural stress.

CHAPTER 4

NON-DUCTILE BEHAVIOUR AND STRENGTH

4.1 Introduction

The "strength" of a material is usually defined as the maximum stress the material can be subjected to without it "failing"; the most common usage of the term strength is in the context of an imposed tensile stress. The point of engineering failure of a material depends on the nature of its response to any imposed stresses; the term engineering failure is used in preference to the term failure because there are strength parameters in use which do not refer to the ultimate failure or fracture of a material, i.e., the catastrophic rupture of the interatomic bonds in the region of maximum stress. One example is the tensile strength (formerly the ultimate tensile strength) of a metal, another is the yield strength.

When a material is subject to an imposed stress its behaviour can be classified as non-ductile, ductile, anelastic or linear viscoelastic according to its post-elastic strain response, i.e., its response when the imposed stress has produced the maximum elastic strain and exceeds the elastic stress limit, as described below:

(a) It can fail catastrophically, i.e., fracture, in which case its behaviour is said to be non-ductile.

(b) It can be strained further before fracture, but the additional strain is not recoverable on the removal of the imposed stress prior to fracture, i.e., it is a permanent or plastic strain, in which case its behaviour is said to be ductile. Plastic strain occurs because the constituent atoms of the material in the region undergoing deformation move to new equilibrium positions by inhomogeneous slip.

(c) It can be strained further before fracture, but the additional strain is either completely or partially recoverable as a function of time on the removal of the imposed stress prior to fracture, i.e., its behaviour is anelastic or linear viscoelastic respectively.

4.2 Non-Ductile Behaviour of Glass-Ceramics

The normal non-ductile, linear-elastic fracture behaviour of glass-ceramics at room temperature can be understood by considering the non-ductile fracture behaviour typical of glasses and the majority of mono- or poly-crystalline ceramics at room temperature when they are subject to stresses above their elastic stress limit. The amorphous structure of glass, i.e., the absence of any long range order in the atomic structure, precludes the existence of dislocations and thus it behaves in a non-ductile manner until fracture.

Mono- and poly-crystalline ceramics, like other crystalline materials, invariably contain dislocations, but their movement and interaction are, however, restricted in comparison to those occurring in pure and alloyed metals, and in most ceramic materials the number of operative slip systems (i.e., the combination of a slip plane and a slip direction in the plane) is limited; some of the reasons for the limited number of slip systems, the restricted movement of dislocations, and hence the typical non-ductile behaviour of most ceramic materials are briefly described here:

(a) The interatomic bonding in ceramic materials ranges from essentially ionic, e.g., MgO to essentially covalent, e.g, SiC; in ionic and covalent crystals the number of operative slip systems is usually low because ions with the same electrostatic charge cannot become nearest neighbours as a result of the formation or the movement of dislocations. In covalent crystals the highly directional bonding (i.e., between particular atoms) means that there is high resistance to the misalignment of atoms as regards bond angles resulting in a very small dislocation width, thus the Peierls-Nabarro stress (i.e., the stress required to move a dislocation through an otherwise perfect crystal) which is proportional to exp(-dislocation width), is high, making dislocation movement very difficult.

(b) In ceramics more than one atom is usually associated with each lattice point, the atoms being of different

species, i.e., the crystal structures are complex. As a consequence the length of the Burgers vector, which is the distance between identical atoms or ions, is greater than unit interatomic spacing and hence the dislocation energies are high (since the elastic strain energy associated with a dislocation is proportional to the square of the magnitude of the Burgers vector) and their concomitant strain (and stress) fields are complex in nature; so it is more difficult for dislocations to form and to move.

(c) The small number of operative slip systems and the relatively restricted dislocation motion in many mono- and poly-crystalline ceramics can result in the formation of microcracks within a crystal by the coalescence of edge dislocations on intersecting slip planes or bands (which act as mutual barriers to dislocation movement); the stress concentrations arising from the inability of a crystal to undergo sufficient plastic deformation when subject to an externally imposed stress are responsible for the dislocations coalescing.

Polycrystalline materials are also subject to the constraint that during plastic deformation adjacent grains must deform in the same way to prevent the formation of voids or cracks at the grain boundaries which would result in premature failure. R. Von Mises showed in 1928 (as cited by Davidge, R.W., 1979 for example) that this requirement of homogeneous plastic deformation can only be satisfied by the operation of five independent slip systems (i.e., slip systems whose individual operation produce shape changes that cannot be brought about by the simultaneous operation of one or more of the other four independent slip systems) within the individual grains which enables an arbitrary change in their shape.

The lack of five independent slip systems in the grains of many polycrystalline ceramics can lead to the pile-up of dislocations at grain boundaries; the resulting stress concentrations ahead of the pile-ups can thus cause the dislocations in the pile-ups to coalesce and nucleate microcracks at the grain boundaries (Davidge, R.W., 1979).

In summary, (i) the applied stress may be sufficient to propagate any inherent cracks but not high enough to move any dislocations, i.e., cause plastic deformation which would blunt the cracks and thereby delay fracture, or (ii) the lack of five independent slip systems may result in the formation of microcracks due to insufficient plastic deformation for strain accommodation, causing premature fracture of the polycrystalline ceramic material.

4.3 Strength of a Non-Ductile Material

As implied above, the engineering failure at room temperature of non-ductile materials such as glasses, ceramics and glass-ceramics usually occurs through linear-elastic fracture caused by the catastrophic propagation of pre-existing cracks or flaws; magnesia ceramics are unusual in that the cracks or flaws causing fracture may be pre-existing or formed under stress by limited and inadequate plastic deformation. So as surmised by A.A. Griffith in 1920 the strength of "real" non-ductile materials is essentially controlled by the structural flaws invariably present in the material rather than by the interatomic bonding forces as in the case of a non-ductile material free of any structural defects.

The stress required to propagate such cracks and flaws will be considered using his energy-balance approach (Griffith, A.A., 1920). The underlying basis of this approach can be stated in the contemporary form, "a crack is unstable with respect to extension if the stored elastic strain energy released upon crack extension or fracture is greater than the sum total of the energy required to create the new fracture surfaces and the energy dissipated prior to or during the creation of the new fracture surfaces". The stored elastic strain energy consists of two energy terms, the elastic strain energy stored by virtue of the presence of the crack and the elastic strain energy stored by virtue of the imposed stress acting as if the crack were absent, while the energy required to create the new surfaces is the

thermodynamic surface free energy and the dissipative energy term is due to generally unquantifiable energy dissipation mechanisms operative immediately prior to and during fracture. The sum total energy required to create the new surfaces can be usefully thought of as the effective fracture surface energy. The above statement of the Griffith energy-balance concept allows for limited microplastic deformation at the crack tip just prior to crack extension and other energy losses during fracture.

4.3.1 Griffith criterion for non-ductile fracture

When a through-thickness crack of length 2c in a infinite plate of unit thickness, subject to a uniform biaxial tensile stress σ imposed at infinity, is at equilibrium with respect to extension the total potential energy of the applied load-crack-plate system is given by

$$U = U_E + U_C + U_S + U_W \qquad [4.1]$$

where U is the total energy, U_E the elastic strain energy stored by virtue of the imposed stress perpendicular to the crack acting as if the crack were absent, U_C the elastic strain energy stored by virtue of the presence of the crack, U_S the effective surface energy required to create the new fracture surfaces and U_W the negative potential energy of the load which does work on the plate because the plate's compliance increases due to the crack. Now $U_E = \sigma^2/2E$ per unit volume where E is the Young's modulus, while $U_W = -2U_C$ during crack extension under constant load (Orowan, E., 1955), and $U_W = 0$ during crack extension under zero displacement conditions (thus U_C is negative, i.e., U_C decreases). Furthermore, $U_S = 2(2c)\gamma_E$ per unit thickness of plate where γ_E is the effective fracture surface energy per unit area and $U_C = (\beta\pi c^2\sigma^2)/E$ where β is 1 for plane stress conditions and $(1 - \nu^2)$ for plane strain conditions where ν is Poisson's ratio. So equation [4.1] can be written as

$$U = \sigma^2/2E - (\beta\pi c^2\sigma^2)/E + 4c\gamma_E \qquad [4.2]$$

A schematic plot of equation [4.2] is shown in Figure 4.1. Note that during a crack extenstion δc there is an

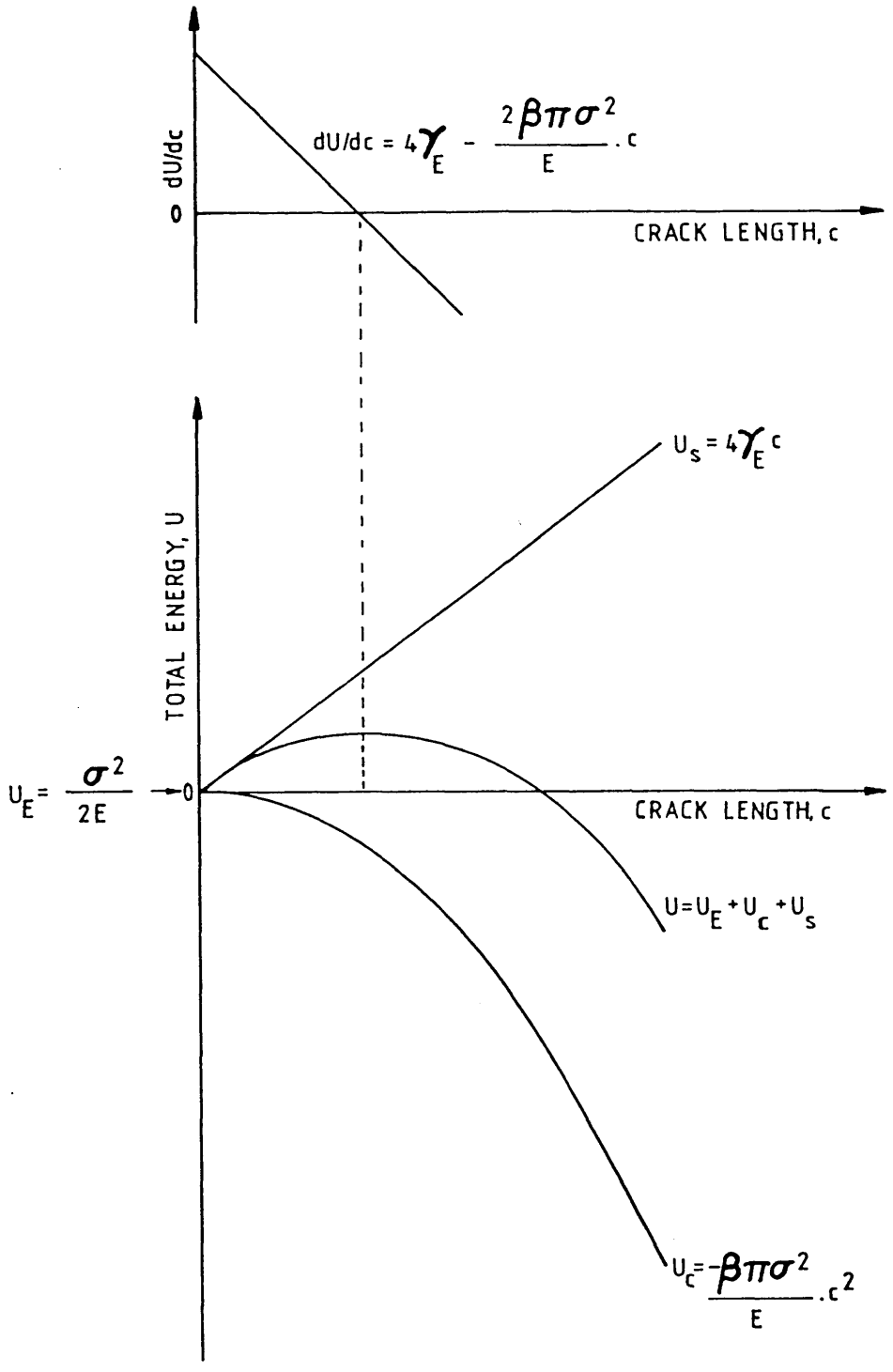


Figure 4.1 Schematic Diagrams of (a) the Energy Components in the Griffith Energy Balance Equation, $U = U_E + U_C + U_S$ and (b) the Derivative, dU/dc as Functions of the Crack Length c.

increase in U_c and a decrease in U_c under constant load and constant displacement loading conditions respectively, but the stored energy released is the same in both cases (See Appendix 5A). The Griffith criteria are (i) $dU/dc < 0$ for unstable cracks, (ii) $dU/dc = 0$ for cracks at equilibrium and (iii) $dU/dc > 0$ for stable cracks. The necessary and critical condition for crack extension is thus given by $dU/dc = 0$ and hence the imposed stress at equilibrium must be given by

$$\sigma = (2E\gamma_E/[\beta\pi c])^{1/2} \qquad [4.3]$$

Since non-ductile fracture occurs by the rupture of the interatomic bonds the maximum stress at the crack tip at fracture must equal the theoretical cleavage or tensile strength of the material. The theoretical tensile strength of a material at any temperature depends on the nature of its Condon-Morse curve of interatomic force versus atomic separation (a) at that temperature; the interatomic stress (i.e., force per unit area) versus atomic separation curve is similar in form except for a scaling factor (i.e., the area over which the force acts). The curve can be approximated by a sinusoidal function (Orowan, E., 1948-9)

$$\sigma = \sigma_{theor.}\sin(2\pi x/\lambda) \qquad [4.4]$$

where λ is the wavelength of the sine wave and x is the displacement from the equilibrium atomic separation a_o. The work done per unit area in separating the atoms a distance $x = \lambda/2$ such that the interatomic force is essentially zero, is the integral of σ with respect to x between the limits 0 and $\lambda/2$, which is $\lambda\sigma_{theor.}/\pi$. The work done is the source of the energy required to create the two new fracture surfaces which is 2γ per unit area; thus

$$\sigma_{theor.} = 2\pi\gamma/\lambda \qquad [4.5]$$

For small displacements δx from a_o, the small stress increment $\delta\sigma$ is given by $\delta\sigma = (E/a_o)\delta x$ for isotropic materials, thus in the limit $\delta x = 0$ (i.e., $x = 0$), $d\sigma/dx = E/a_o$. Now $d\sigma/dx$ is also equal to $(2\pi/\lambda)\sigma_{theor.}$; hence

$$\sigma_{theor.} = E\lambda/(2\pi a_o) \qquad [4.6]$$

Re-arranging, $\lambda = \sigma_{theor.}(2\pi a_o/E)$ and substituting in

[4.5] gives

$$\sigma_{theor.} = (E\gamma/a_o)^{1/2} \qquad [4.7]$$

The well documented result [after C.E. Inglis (1913)] that the maximum stress at the tip of a narrow crack as modelled by a very narrow ellipse is given by

$$\sigma_{max.} = 2\sigma(c/\rho)^{1/2} \qquad [4.8]$$

where c is the semi-crack length of an internal crack or the crack length of a surface crack and ρ the radius of curvature, in plane stress (see for example, Lawn, B.R., and Wilshaw, T.R., 1975). Equating [4.7] and [4.8] gives

$$\sigma = (E\gamma\rho/[4ca_o])^{1/2} \qquad [4.9]$$

The crack-tip radius in a real material is finite because a cleavage crack is situated between two neighbouring atomic planes and the reasonable assumption is $\rho = a_o/2$. Substituting for ρ in equation [4.9] and using γ_E instead of the thermodynamic surface free energy γ gives as a second necessary condition to be fulfilled by the imposed stress,

$$\sigma = (E\gamma_E/[8c])^{1/2} \qquad [4.10]$$

Note that this equation is only approximate because of the approximate nature of equation [4.4], which is sometimes integrated between 0 and $\lambda/4$ giving equation [4.7] as $\sigma_{theor.} = (2E\gamma/a_o)1/2$ and hence 4 instead of 8 in [4.10]. Comparing [4.10] with equation [4.3] shows that the Griffith stress criterion requires a stress about 5 times greater than that required by equation [4.10] for $\rho = a_o/2$; the two criteria are equivalent at $\rho \approx 3a_o$. So as a reasonable approximation, for crack-radius values up to approximately 3 times the equilibrium interatomic spacing, the Griffith fracture stress criterion is both necessary and sufficient for the fracture of non-ductile materials.

The above analysis was based on a two-dimensional model for mathematical convenience; Griffith's theory was extended to three dimensions by assuming the crack to be an oblate spheroid and considering (i) the action of a uniform tensile stress on the outer surfaces (Sack, R.A., 1946) and (ii) the action of a uniform pressure on the inner surfaces (Sneddon, N.I., 1946). Both of these approaches gave the critical tensile stress when the crack

is at equilibrium with respect to extension as

$$\sigma = (\pi E / [2c(1 - \nu^2)])^{1/2} \qquad [4.11]$$

where c is the circular radius of the oblate spheroid, i.e., of the circular plane perpendicular to the critical tensile stress. So Griffith's criterion may be written in the general form

$$\sigma = \alpha(E\gamma_E / c)^{1/2} \qquad [4.12]$$

where α is a numerical constant which depending on the boundary conditions, e.g, crack geometry, body dimensions, stress configuration, etc. may vary with Poisson's ratio. For the differing boundary conditions considered here α ranges between $(2/\pi)^{1/2}$ and $(2\pi/3)^{1/2}$.

There is no general agreement as to whether or not under biaxial stress conditions the stress applied parallel to the crack plane has any effect on the fracture stress measured normal to the crack plane (Davidge, R.W., 1979). Griffith, however, concluded from his experimental data that the parallel stress had no detectable effect on crack stability. According to Sack the tensile strength in one direction will not be affected by the presence of smaller tensile stresses or within limits, compressive stresses, at right angles to it.

Experimental work by Griffith and later workers confirms that the tensile strength data for non-ductile materials obeys the general form of equation [4.12], i.e., the dependence of strength on $c^{-1/2}$ where c is a characteristic crack length, Young's modulus, E and the effective fracture surface energy, γ_E. The following general conclusions can therefore be drawn: (i) the observed difference between the experimentally measured fracture strengths of non-ductile materials ($\sigma_{expt.} \approx 0.001E$) and the estimated theoretical strengths ($\sigma_{theor.} \approx 0.1E$) is due to the invariable presence of structural defects or flaws in the material, (ii) whatever the true nature of the individual flaws, they act as stress concentrators increasing the stress in their immediate vicinity significantly above the level of the measured, remotely imposed stress and behave as if they are microcracks whose sizes are quantified by a characteristic

length c, and (iii) the measured fracture stress σ in equation [4.9] depends on this effective critical crack "size" since the crack-tip radius, ρ which effectively characterizes the flaw "shape" and the maximum possible stress at the crack tip, $\sigma_{theor.}$ are essentially predetermined by the atomic structure.

4.4 Uniaxial Tensile Strength Measurement Techniques for Non-Ductile Materials

The dependence of the tensile fracture strength of glass, glass-ceramic, ceramic and other non-ductile materials on the presence of flaws (due to their stress concentration effect) has influenced the choice of methods used to measure the strength. The measured average tensile strength of a material should be representative of the true tensile strength of the bulk material which would be the case for a homogeneous, isotropic material. The random distribution of flaw locations, flaw sizes, flaw shapes, and flaw orientations with respect to the applied stress typical of bulk glass, glass-ceramics and ceramics makes them statistically homogeneous and isotropic in the bulk as regards stress distribution, but on a localised, microstructural scale they are inhomogeneous; so ideally the largest possible volume should be uniformly stressed.

The ideal uniaxial method from a theoretical viewpoint is the standard uniaxial direct tension test as used for ductile materials because the entire gauge length volume is subject to a uniform tensile stress assuming the material is perfectly homogeneous and isotropic and the specimen is loaded uniformly across the end surfaces. This is essentially the situation under true axial loading (i.e., when the resultant force acts through the centroid of every transverse plane) because the stress distribution is effectively uniform on any transverse plane within the gauge length. The reasons for this are (a) the stress concentrations, which occur in the region of load application (e.g., at the specimen screw threads, pin holes or shoulders in contact with the collet grips,

depending on the specimen fixing arrangement) decrease with increasing distance away from the regions of load application and (b) the non-uniform stress distributions in the regions where the specimen cross-section changes from the larger cross-section of the specimen ends (required to maintain the stress in the specimen ends at a safe level well below that necessary to raise the stress concentrations to critical levels) to the smaller cross-section of the gauge length, approach uniformity with increasing distance away from the points of greatest change in the cross-section.

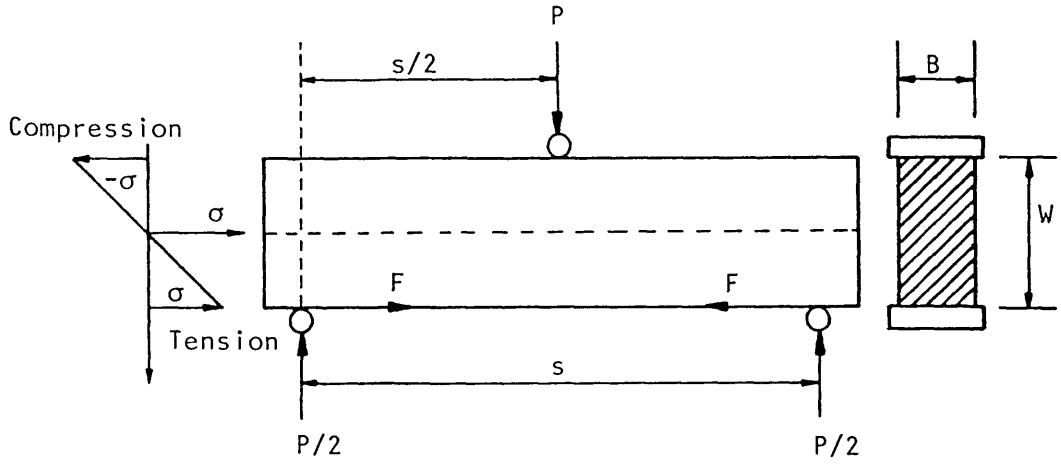
Experimentally, however, it is difficult to ensure true axial loading and hence bending moments or possibly even torques may act on the specimen with resultant non-uniform pure bending or torsional stresses being superposed on the tensile stress distribution of any given transverse plane. The causes of non-axial loading are (i) grip heads offset in the same direction, (ii) grip heads offset in opposite directions, (iii) bending moments or torques at the grip heads or elsewhere in the load-train and (iv) eccentric specimen geometry which is especially troublesome (Marschall, C.W. and Rudnick, A., 1974). When conducting direct uniaxial tensile tests on ductile materials the additive parasitic tensile stresses may be reduced to an acceptable level by accommodation of axial misalignment by microplastic pre-strain which also reduces the stress concentrations with the result that premature failure at or near the grips is unlikely to occur and the stress within the gauge length volume will be acceptably uniform. As previously discussed, plastic strain is not generally possible in non-ductile materials at room temperature so the non-uniform parasitic stresses may be significant and the much greater sensitivity of non-ductile materials to surface flaws may lead to premature fracture at the regions of stress concentration or at least erroneously low fracture stress values based on the assumption of a uniform stress distribution. Even if non-axial loading is not a problem, gripping the specimen is likely to be a problem because of the sensitivity to

stress concentrations, and the machining of ceramic specimens is comparatively time consuming and expensive. There are uniform, uniaxial indirect tensile stress tests, e.g., the pressurised ring, the theta specimen test, etc. (Marschall, C.W. and Rudnick, A., 1974), but the most commonly used test is the non-uniform, uniaxial tensile bend-stress test.

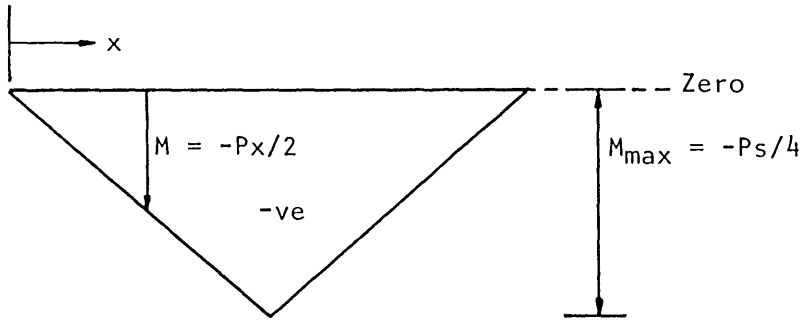
4.4.1 Bend testing using three or four-point loading

The bend test involves loading a beam specimen using three or four-point simple loading; the theoretical bending moment and shearing force diagrams for three and four-point loading are shown in Figure 4.2 and Figure 4.3 respectively. Both figures show a beam with a rectangular cross-section for which the tensile stress on the bottom surface acts over an area as opposed to a line as is the case for a specimen of circular cross-section.

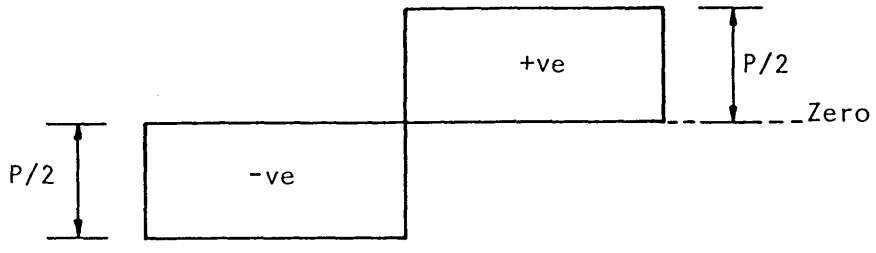
As Figure 4.2 illustrates, the bending moment for three-point loading varies linearly from zero at the supports to a maximum at the mid-span position, i.e., at the loading line; hence the tensile bending stress is a maximum at mid-span. The non-uniform bending moment induces a shear stress in the beam perpendicular to the neutral axis and hence a complementary shear stress parallel to the neutral surface which varies parabolically from zero at the top of the beam to zero at the bottom of the beam and is a maximum at the neutral surface. Cross-sections normal to the neutral axis cannot remain plane after bending because the resulting shear strain must also vary parabolically in the same way, with zero shear strain at the top and bottom surfaces and maximum shear strain at the neutral surface. Note that since the shear force magnitude is constant along the beam either side of the mid-span the deformation of all cross-sections is identical; thus the bending moment and the distribution of bending stress either side of the mid-span are unaffected by the shear strains.



(a) Schematic Diagram of a Beam Subject to Three-Point Loading.



(b) Bending Moment Diagram: M = f(x).



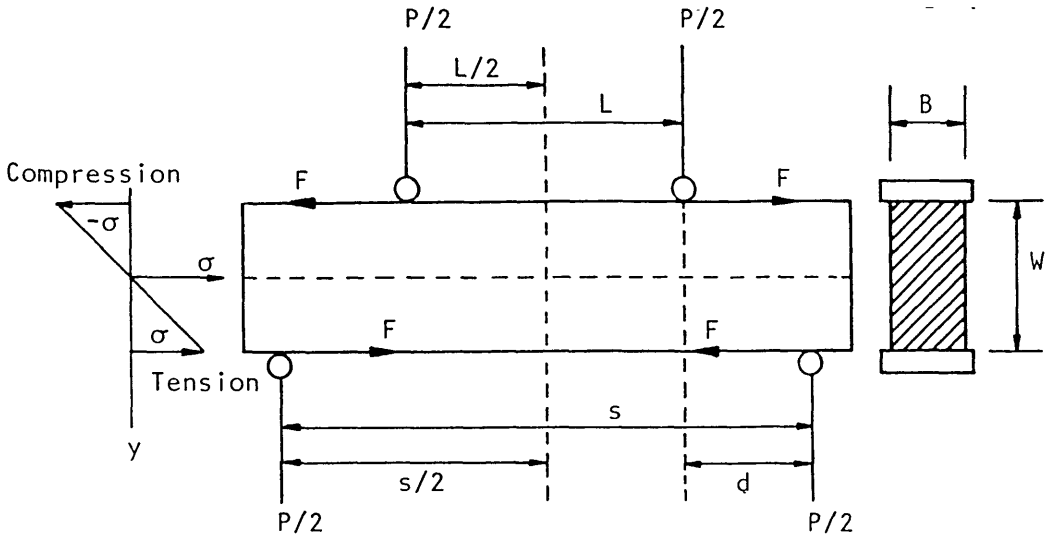
(c) Shearing Force Diagram: S = f(x) = dM/dx.

Figure 4.2 Schematic Bending Moment and Shearing Force Diagrams for a Simply Supported Beam Subject to Three-Point Loading Assuming the Friction Force (F) = 0.

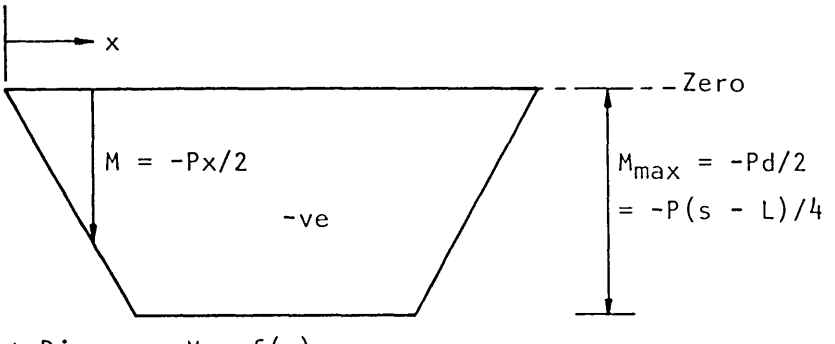
As shown in Figure 4.3, the bending moment for four-point loading varies linearly from zero at the supports to a maximum at the loading lines and remains constant between them; so there is no shear force and hence no shear stress between the loading lines, i.e., the bending within the inner span is pure. Between the supports and the loading lines the bending moment is non-uniform and hence shear stresses exist in these regions of the beam. In four-point bending of a rectangular cross-section beam the area of the bottom face directly beneath and between the loading lines is subject to the maximum bending stress, whereas in three-point bending the maximum stress only acts along a line on the bottom face directly beneath the loading line.

For both loading configurations the tensile bending stress is assumed to be constant across the breadth of the beam, but it decreases with depth into the beam away from the bottom face to zero at the neutral surface, i.e., the volume of the material between the supports is subject to a non-uniform stress; nevertheless four-point loading is preferable because on any plane parallel to the neutral surface the stress is constant within the inner span. Three-point bending, however, was used in the present work because (a) it had been used to obtain room temperature flexural strength data for other glass-ceramics in the system CaO - MgO - Al_2O_3 - SiO_2 (Rogers, P.S., et al., 1984), and (b) it was easier to design and build a three-point bending test rig for use at room and high temperatures.

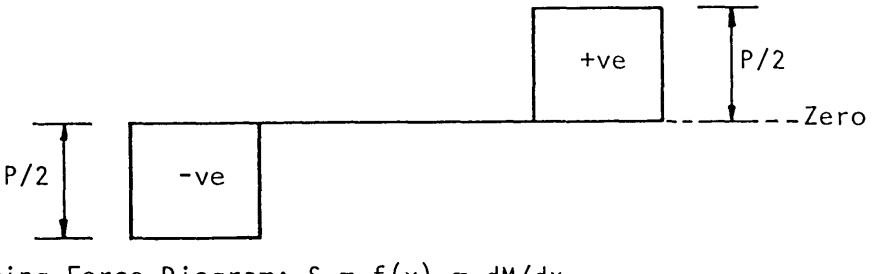
The nominal test specimen cross-section dimensions were such that W = 2B, while the nominal span-to-width ratio (s/W) was 4 (see Figure 4.2). The shear stress in a rectangular cross-section beam is zero at $y = \pm W/2$ and a maximum at the neutral axis ($y = 0$) and is given by $\tau_{xy} = (S/2I)(W^2/4 - y^2)$, i.e., a parabolic function of y; the maximum shear stress, $\tau_{MAX.} = SW^2/8I = 3S/(2BW) = 3P/4BW$ as $S = dM/dx$ (Gere, J.M., and Timoshenko, S.P., 1984) and the maximum bending stress, $\sigma_{MAX.} = 3Ps/2BW^2$ ($\sigma = My/I$; $M = Ps/4$; $y = W/2$; $I = BW^3/12$); $\tau_{MAX.}$ is accurate for $W/B \geq 2$ and $\sigma_{MAX.}$ is 4.4 % too large (for s/W = 4; see later).



(a) Schematic Diagram of a Beam Subject to Four-Point Loading.



(b) Bending Moment Diagram: M = f(x).



(c) Shearing Force Diagram: S = f(x) = dM/dx.

Figure 4.3 Schematic Bending Moment and Shearing Force Diagrams for a Simply Supported Beam Subject to Four-Point Loading Assuming the Friction Force (F) = 0.

The ratio of the maximum shearing stress to the maximum bending stress is thus given by $\tau_{MAX.}/\sigma_{MAX.} = W/2s$, which for $s/W = 4$ equals 1/8. Assuming a bending stress of 200 MPa and a shear modulus of 50 GPa and using $\phi = \tau_{MAX.}/G$ gives the maximum shear strain as 5×10^{-4}, i.e., 0.05 %; thus the shear strains are unlikely to have any significant affect on the tensile strains some distance away from the neutral axis and warping of the planes normal to the neutral axis is insufficient to seriously violate the assumption that they remain plane after bending, i.e., the bending is pure, which is used in the derivation of the elementary bending stress formula $\sigma = My/I$.

4.4.2 Sources of error in three-point bending tests

A number of sources of error arise in the practical implementation of the three-point bending technique whose cumulative effect can result in experimental flexural strength data totally unrepresentative of the true flexural strength. They will be considered with reference to specimens of rectangular or square cross-section; the fracture stress in three-point bending is invariably calculated using the elementary bending stress formula

$$\sigma = 3Ps/2BW^2 \qquad [4.13]$$

where σ is the maximum tensile bending stress at fracture, P is the load at fracture, s the support span, B the specimen breadth and W the specimen width. The use of this equation embodies a number of assumptions:

(1) The theory of pure bending is applicable to both the specimen and the material; this assumption was considered in relation to shear stresses in Section 4.4.1 for $W = 2B$ and $s/W = 4$.

(2) The stress distribution is uniform across the breadth of the specimen.

(3) The specimen cross-section is perfectly rectangular or square and is uniform along the specimen length.

(4) The specimen is perfectly straight over its length.

(5) There are no frictional forces at the knife-edge or

roller supports nor at the loading line, i.e., at the loading knife-edge or roller.

(6) The long side of the specimen is at right angles to the supports and the loading line until fracture (which implies that the supports and the loading line are mutually parallel).

(7) The loading line is exactly at the mid-span position,

(8) There are no stress-field perturbations at the supports and the loading line nor anywhere else in the specimen due to stress concentrations.

(9) Fracture initiates on the bottom face, i.e., on the tensile face of the specimen, at the mid-span position directly opposite the loading line.

Serious violation of one or more of these assumptions is responsible for the error in the apparent fracture stress. The sources of error are discussed below with reference to Figures 4.2 and 4.3:

(i) The longitudinal frictional forces generated at the specimen supports and the specimen loading line; frictional forces at the supports induce bending moments in opposition to the applied bending moment and hence erroneously increase the apparent fracture strength. The bending moment due to the frictional force (F) is - FW/2 = - μPW/4 where μ is the coefficient of friction, while that due to the applied load is Ps/4; thus the effective bending moment is (Ps - μPW)/4 and the resultant maximum bending stress is $3P(s - \mu W)/2BW^2$ giving

$$\sigma_2/\sigma_1 = 1 - \mu W/s \qquad [4.14]$$

where σ_1 is the apparent maximum tensile bending stress and σ_2 is the actual maximum tensile bending stress when there are frictional forces. So the error due to friction at the supports increases with increasing μ and W/s; for W/s = 1/4 and μ = 0.2, the error is + 5 %. In four-point bending, equation [4.14] becomes $\sigma_2/\sigma_1 = 1 - \mu W/d$ (see Hoagland, R.G., Marschall, C.W., and Duckworth, W.H., 1976 for example).

It is appropriate to digress a little and consider the possible effects of lateral friction. The theory of pure bending assumes that there are no contraints on the

deformation of the beam orthogonal to the neutral axis, i.e., there are no lateral friction forces at the supports nor at the loading line and that the beam is in a state of plane stress during deformation; however, the deformation may be constrained due to (i) lateral friction, or (ii) the excessive breadth of the beam, or both. In practice, lateral friction is negligible and breadth constraint will not occur if (Newnham, R.C., 1975)

$$B/W \ll (2E/\nu\sigma_F)^{1/2} \qquad [4.15]$$

where σ_F is the fracture stress, E is Young's modulus and ν is Poisson's ratio. So for σ_F = 100 MPa, E = 100 GPa and ν = 0.25, B/W must be $\ll \approx 89$. So in practice, beam specimens with sensible dimensions, e.g., B/W in the range $1/2 \leq B/W \leq 2$, will always be in a state of plane stress during deformation.

(ii) The existence of a non-uniform stress distribution across the breadth of the specimen due to twisting of the specimen caused by improper loading of the specimen or by specimens with poor dimensional uniformity or both, i.e., the support and loading rollers or knife-edges do not make complete contact with the specimen surface resulting in uneven loading and hence a twisting moment. In practice, it is not possible to determine the magnitude of the twisting moment; however, R.G. Hoagland, et al. (1976) considered the maximum error due to twisting under four-point loading by assuming a torsional moment of PB/2 and derived the following equation

$$\sigma_2/\sigma_1 = 1/2 + (1/6k_2)([B/d]^2 + 9(k_2)^2)^{1/2} \qquad [4.16]$$

where σ_1 is the appparent maximum tensile bending stress, calculated using the 4-point elementary bending equation ($\sigma = 6Pd/2BW^2$), σ_2 is the actual maximum tensile bending stress when there is specimen twisting, and k_2 is a function of B/W (Timoshenko, S.P. and Goodier, J.N., 1970), i.e., a constant which for B/W = 0.5 equals 0.154.

In the limit d = s/2, i.e., in three-point bending, equation [4.16] reduces to

$$\sigma_2/\sigma_1 = 1/2 + (1/6k_2)(4[B/s]^2 + 9(k_2)^2)^{1/2} \qquad [4.17]$$

where σ_1 and σ_2 now refer to three-point bending. So for B/W = 0.5 and s/W = 4 and three-point bending σ_2/σ_1 =

1.07; this compares with σ_2/σ_1 = 1.24 for quarter-point four-point bending, i.e., d = s/4 , when B/W = 0.5 and s/W = 4. So for the given specimen dimensions and span parameters the error is ≈ - 7 % under three-point loading compared to ≈ - 24 % under quarter-point four-point loading; thus for a given moment-arm (i.e., s or d) and support span, and given specimen dimensions, the possible twisting error is greater under four-point loading than under three-point loading, as might be expected given the greater alignment difficulties of a four-point bending test rig. Note that the error due to twisting decreases with decreasing B/W and decreasing B/d (or B/s in the case of three-point bending). So the apparently greater risk of obtaining incorrect strength data from four-point bending tests further justified the use of three-point bending.

(iii) The occurrence of a lateral displacement in the loading line relative to the mid-span position results in a small error; If the lateral displacement is δ, the reactions at the two supports are $P(1/2 + \delta/s)$ and $P(1/2 - \delta/s)$ which gives a maximum bending moment of $Ps(1/2 + \delta/s)(1/2 - \delta/s)$ which equals $Ps[1/4 - (\delta/s)^2]$; the maximum bending moment for δ = 0 is Ps/4. Thus

$$\sigma_2/\sigma_1 = 1 - 4(\delta/s)^2 \qquad [4.18]$$

where σ_1 is the apparent maximum tensile bending stress for δ = 0 and σ_2 is the actual maximum tensile bending stress when there is a lateral displacement δ. For δ/s = 2/32, the error is + 1.6 % .

A similar analysis for the common case of quarter-point four-point bending, in which it is assumed that both the loading lines are displaced by the same amount in the same direction relative to the quarter-point positions, gives the reactions at the two supports as $(1 + 2\delta/s)P/2$ and $(1 - 2\delta/s)P/2$, which gives the maximum bending moment of $(s/4 + \delta)(1 - 2\delta/s)P/2 \approx Ps(1/8 + \delta/4s)$ and the minimum bending moment of $(s/4 - \delta)(1 + 2\delta/s)P/2 \approx Ps(1/8 - \delta/4s)$, since $(\delta/s)^2 \ll \delta/s$. The maximum bending moment for δ = 0 is Ps/8. Using the same notation as above, $\sigma_2/\sigma_1 = 1 \pm 2\delta/s$; thus for δ/s = 2/32, the error is ± 12.5 %. Note that for the same lateral displacement, the

percentage error is ≈ 8 % greater illustrating the sensitivity of four-point bending to misalignment; this problem of unequal moments in four-point bending also occurs when the loads applied via the two loading knife-edges or rollers are not equal.

(iv) Longitudinal curvature of a beam specimen can be a source of error; the maximum error would arise if the beam were positioned on the supports so that the applied bending moment tended to reduce the initial curvature of the beam. The pure bending of a longitudinally curved beam loaded in the plane of curvature, e.g., in the manner described above, has been analysed (Timoshenko, S.P., 1955); hence for r/W = 10 where r is the radius of curvature of the centre-line (through every cross-section centroid), the error in using equation [4.13] is 3.2 %. So, for r/W > 20 say, [4.13] can be used with sufficient accuracy.

(v) Frequently the longitudinal edges of the tensile face-to-be of the specimen are rounded off to remove edge flaws produced during the fabrication process which may cause premature failure of the specimens and would result in a skewed, unrepresentative average flexural strength and sample strength distribution for the material. This was done for all the flexural strength specimens tested for the present work; the procedure, however, changes the moment of inertia (I) of the cross-section and hence the true maximum tensile bending stress will be higher than the nominal maximum tensile bending stress calculated using equation [4.13].

The correct moment of inertia with respect to the "centroidal" axis at W/2 parallel to the breadth (B) of the specimen for this particular cross-section was derived by applying the "parallel-axis" theorem of the strength of materials theory to a composite area (See Appendix 4A); the correct moment of inertia is

$$I = Bh^3/12 + Bhr^2/4 + (B - 2r)(r^3/12 + rh^2/4) \quad [4.19]$$
$$+ 2([9\pi^2 - 64]r^4/(144\pi) + [\pi r^2/4][(h - r)/2 + 4r/(3\pi)]^2)$$

where r is the radius of both the bottom corners of the cross-section and h = W - r. Using equation [4.19] shows

that the reduction in the moment of inertia is < 1 % for r/W < 0.06 and W/B = 2; the percentage reduction increases with increasing r/W and W/B. The error in practice will depend on the actual profile of the "rounded" edges which may range from a quarter-circle at one extreme to a bevel at the other. The two edge profiles may also be slightly different or have different radii; nevertheless the error incurred by rounding off the bottom edges is likely to be less than that due to premature fracture at an edge flaw.

(vi) In the region of contact between a knife-edge or roller and the specimen surface, the contact area is a very narrow strip and hence the stress in the contact area is extremely high; this stress concentration perturbs or distorts the general stress field in its immediate vicinity. This stress perturbation effect is known as "wedging" and in three-point bending is most severe under the loading knife-edge or roller; it will be considered using the results of T. von Kármán and F. Seewald (1927).

Their results are summarised by S.P. Timoshenko and J.N. Goodier (1970), and show that when a concentrated load is acting on a beam the resultant tensile bending stress, σ_x has two components, (a) one calculated using the elementary bending stress formula, σ = My/I and (b) another which is due to the stress-field perturbation in the vicinity of the concentrated load. Component (a) is represented by σ_x', while component (b) is represented in the form $\sigma_x'' = \beta(2P/BW)$ where β is a function of x/W for any given value of y, which is the distance from the neutral axis and is positive in the direction of load application. Thus the resultant bending stress is

$$\sigma_x = \sigma_x' + \sigma_x'' = \sigma_x' + \beta(2P/BW) \qquad [4.20]$$

where x is the distance along the beam parallel to the neutral axis with its origin at the mid-span position (i.e., x and y are orthogonal axes). Again it is assumed (i) the beam is in a state of plane stress, i.e., the stress component (σ_z) orthogonal to both the tensile stress (σ_x) and the compressive stress (σ_y) is zero and (ii) the stress distribution across the breadth (B) of the beam is uniform. Values of β and corresponding values for

x/W are tabulated in Table 4.1 for a number of y values, while Figure 4.4 shows, schematically, the corresponding curves of $\beta = f(x/W)$.

As the tabulated data and the curves indicate, the local stresses as represented by β decay rapidly with distance away from the region of application of the concentrated load to essentially zero at a distance W away from the mid-span position. Furthermore, the tensile bending stress does not reach a maximum at the mid-span position at the tensile face as predicted by the elementary bending theory for three-point bending due to the "wedging" effect; the tabulated data and the curves show that as the distance from the neutral axis increases, β approaches a maximum value of + 0.0868 at $x = W/4$ on both sides of the mid-span at the tensile face. Thus for a specimen width of 8 mm, the maximum stress arises on both sides of the mid-span position at a distance of $x = 2$ mm and is higher than that predicted by the elementary equation.

(vii) It has so far been assumed that fracture always occurs on the tensile face of the specimen at the mid-span position; this assumption is not valid because the flaws in a typical ceramic or glass-ceramic are randomly distributed throughout the material and the fracture initiating flaw is not necessarily the largest flaw in the region of the specimen subject to the highest tensile stress, i.e., on the surface at the mid-span (the reasons for this will be considered in Chapter 5 with reference to the stress intensity factor, K). On the valid assumption that (i) fracture will only initiate within the tensile stress-field volume of the beam and (ii) the fracture initiating flaw may be situated anywhere within the stress-field volume, a generalised tensile bending stress equation can be derived using the pure bending stress equation $\sigma = My/I$ as shown in Appendix 4B. The resultant generalised tensile bending stress is

$$\sigma = (3Ps/2BW^2)(1 - 2x/s)(1 - 2v/W) \qquad [4.21]$$

where with reference to Figure 4B.1 in Appendix 4B, v is the axis with its origin at the mid-span position on the

Table 4.1 β Factors for Wedging Correction for Tensile Stress σ_x as a Function of x/W and y:

x/W	Distance from the Neutral Axis, y				
	-W/2	-W/4	Zero	+W/4	+W/2
	β Values				
+ 1.500	+0.0011	-0.00166	-0.00039	+0.00042	+0.00074
+ 1.250	------	------	------	------	------
+ 1.000	+0.014	-0.0025	-0.0098	+0.0017	+0.0095
+ 0.750	+0.048	-0.0180	-0.0264	+0.0047	+0.0220
+ 0.500	+0.159	-0.0490	-0.0378	+0.0210	+0.0421
+ 0.375	+0.214	-0.0810	-0.0263	+0.0204	+0.0640
+ 0.250	+0.311	-0.1402	+0.021	-0.0048	+0.0868
+ 0.125	+0.447	-0.149	+0.089	-0.084	+0.0137
<+ 0.125	+0.616	------	------	------	------
0	- ∞	+0.428	+ 0.121	-0.136	-0.1332
>- 0.125	+0.616	------	------	------	------
- 0.125	+0.447	-0.149	+0.089	-0.084	+0.0137
- 0.250	+0.311	-0.1402	+0.021	-0.0048	+0.0868
- 0.375	+0.214	-0.0810	-0.0263	+0.0204	+0.0640
- 0.500	+0.159	-0.0490	-0.0378	+0.0210	+0.0421
- 0.750	+0.048	-0.0180	-0.0264	+0.0047	+0.0220
- 1.000	+0.014	-0.0025	-0.0098	+0.0017	+0.0095
- 1.250	------	------	------	------	------
- 1.500	+0.0011	-0.00166	-0.00039	+0.00042	+0.00074

Data after S.P. Timoshenko and J.N. Goodier (1970).
The concentrated load acts in the mid-span plane.
Distance away from the mid-span plane, parallel to the neutral axis, is denoted by x.
The specimen width is denoted by W.

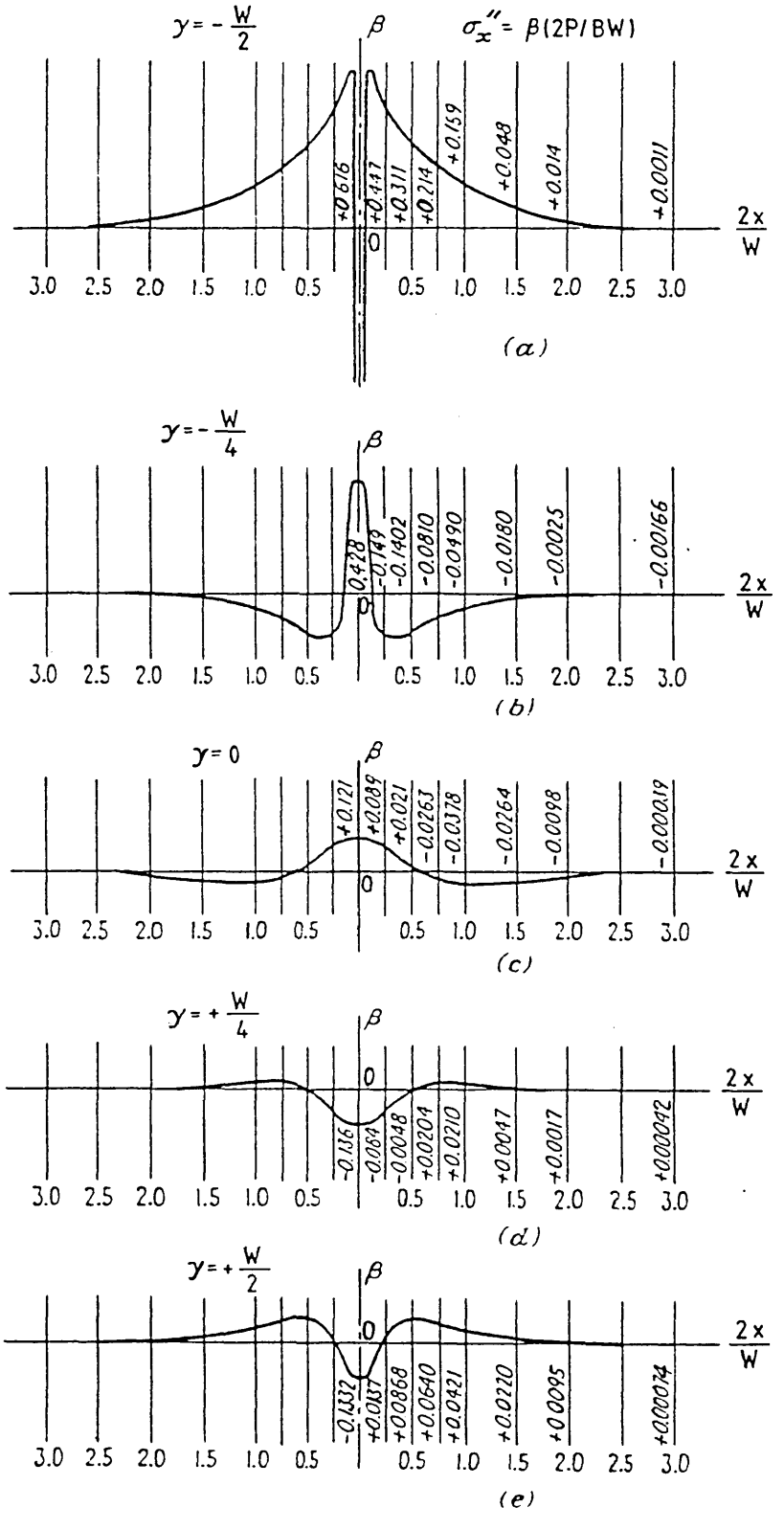


Figure 4.4 Diagrams of the Variation of β as a Function of x/W in the Form $\beta = f(2x/W)$ for Different Values of y for the Stress Component $\sigma_x'' = \beta(2P/BW)$ [after S.P. Timoshenko and J.N. Goodier (1970)].

tensile face of the beam, perpendicular to x and positive in the -y direction; this equation has been given without derivation by R.W. Davidge (1979). According to [4.21], $\sigma/(3Ps/2BW^2)(1 - 2v/W)$ and $\sigma/(3Ps/2BW^2)(1 - 2x/s)$ decrease linearly with increasing x (at constant v with slope = $- 2/s$) from 0 to s/2 and increasing v (at constant x with slope = $- 2/W$) from 0 to W/2 respectively.

Time and expense usually preclude a complete fractographic investigation of the two fracture faces of an individual specimen to locate, if possible, the fracture initiating flaw on the fracture surface; so it is assumed that failure occurs at the tensile surface, which is frequently the case, particularly in flexural strength tests for obvious reasons. This assumption is the accepted practice when calculating fracture stress values, so equation [4.21] can be simplified by assuming v = 0. Setting v = 0 in equation [4.21] and re-arranging it into a convenient form for calculation and comparison with the elementary equation [4.13] gives

$$\sigma = (3P/2BW^2)(s - 2x) \qquad [4.22]$$

The various forms of the tensile bending stress equation, based on the assumption that (a) $\sigma = My/I$ is applicable and (b) fracture initiation occurs at the tensile face, which may be used to calculate the flexural strength or fracture stress in three-point bending are presented together for reference:

(1) The standard elementary equation which assumes (a) there is no "wedging" effect and (b) that fracture occurs at the mid-span position,

$$\sigma_1 = 3Ps/2BW^2 \qquad [4.23]$$

(2) An equation which corrects for "wedging" but still assumes that fracture occurs at the mid-span position,

$$\sigma_2 = 3Ps/2BW^2 + 2\beta P/BW = \sigma_1(1 - 0.1776W/s) \qquad [4.24]$$

(3) An equation which assumes there is no "wedging" effect but corrects for fracture at a position x units away from the mid-span position,

$$\sigma_3 = (3P/2BW^2)(s - 2x) \qquad [4.25]$$

(4) An equation which corrects for both "wedging" and fracture at a position x units away from the mid-span position,

$$\sigma_4 = (3P/2BW^2)(s - 2x) + 2\beta P/BW$$
$$= \sigma_1(1 - [6x - 4\beta W]/3s) \qquad [4.26]$$

If fracture occurs away from the mid-span position (on either side of it) as is invariably the case and due in part to there being a point of equal maximum stress on both sides of the mid-span position, then the equations are listed in order of increasing accuracy. The accuracy of equations [4.25] and [4.26] depends strongly on the accuracy to which x can be measured. It was found in the present work that x could be measured to within ± 0.5 mm, so x values below 0.5 mm were taken as zero, and as only the tabulated β values were available, the β value used in equation [4.26] when calculating the fracture stress for any given experimental x/W value was the one corresponding to the tabulated x/W value closest to the experimental x/W value.

In summary, the sources of error in the three-point bending technique, with reference to Figure 4.2, are:

1. Frictional forces at the supports oppose the applied bending moment and so reduce the effective bending moment for a given load, thereby lowering the tensile stress in the specimen; thus the fracture load and hence the apparent flexural strength are increased, giving a positive error which increases with increasing coefficient of friction and decreasing span to width ratio (s/W).

2. Twisting of the specimen due to a non-uniform stress distribution across the breadth of the specimen induces a torsional moment whose tensile component increases the total tensile stress in the specimen; thus for a given load the tensile stress is higher than it would be in the absence of twisting. So the fracture load and hence the apparent flexural strength are decreased; this negative error increases with increasing breadth to width ratio (B/W) and increasing breadth to span ratio (B/s).

3. Lateral displacement of the loading knife-edge or roller relative to the mid-span position reduces the bending moment, which for a given load results in a lower tensile stress than there would be with no lateral shift. So the fracture load, and hence the apparent flexural strength are increased; this positive error increases with increasing displacement to span ratio (δ/s); for $\delta/s < 0.05$ the error is $< + 1$ %.

4. Loading of longitudinally curved specimens in their plane of curvature so that the applied bending moment decreases the initial curvature, which is the worst possible way of loading a curved specimen in bending, can be disregarded as a source of error for $r/W \geq 20$ where r is the radius of curvature of the centre-line through every transverse-plane centroid. Curved bars, even with $r/W > 20$, should not be loaded in bending outside their initial plane of curvature as torsional stresses are induced in addition to the bending stresses.

5. Rounding of the longitudinal edges of the tensile face of the specimen reduces the moment of inertia of the cross-section which increases the tensile stress in the specimen at a given load. So the fracture load and hence the apparent flexural strength are reduced. This negative error increases with increasing radius to width ratio (r/W) and increasing width to breadth ratio (W/B). Assuming the corner radii are equal, the error is $< - 2$ % for $r/W < 0.1$ and $W/B = 2$. Not rounding chipped edges may, however, result in even less representative flexural strength data due to premature fracture at edge flaws.

6. "Wedging" under the loading knife-edge or roller produces, at the tensile face, a maximum compressive stress component at the mid-span line, a lower, tensile stress component at a distance of W/4 and an essentially zero tensile stress component at a distance of W, both measured away from the mid-span line. So at the mid-span position the tensile stress is lower at a given load due to "wedging"; thus the fracture load and the apparent flexural strength are increased. this positive error increases with decreasing s/W and is $\approx + 4$ % for $s/W = 4$.

7. Calculating the flexural strength as if fracture had occurred at the mid-span line on the tensile face when it actually occurred (i) at the tensile face but away from the mid-span line or (ii) within the tensile stress-field volume of the specimen results in erroneously high apparent flexural strength data because the bending moment at the fracture origin is lower than the maximum moment at the mid-span position at the tensile face. This positive error increases with increasing distance between the fracture origin and the mid-span line at the tensile face. The error when fracture actually occurs within the tensile stress-field volume cannot be quantified without a knowledge of the fracture origin in relation to the mid-span line at the tensile face which requires a thorough fractographic analysis; this possibility is therefore usually neglected and it is assumed that fracture occurs at the tensile face, which fortunately is a common occurrence. The error when fracture actually occurs at the tensile face away from the mid-span line is easily quantified; it increases with increasing distance along the tensile face from the mid-span line and can be corrected for by using equation [4.26] to calculate the flexural strength of a specimen; this equation also corrects for the effects of "wedging".

The errors due to friction, specimen twisting and lateral deflection of the loading knife-edge or roller can be minimised by (i) careful design of the three-point bending test rig, (ii) using specimens with appropriate dimensions in relation to the support span and each other, a uniform cross-section and a polished tensile face, and (iii) correctly positioning the specimen with respect to the supports and the loading edge before testing it. The error due to rounding the specimen edges can be reduced by rounding them to a quarter circle profile with a radius of $< 0.1W$ for a given W/B ratio. The most serious errors are (i) not correcting for fracture at the tensile face away from the mid-span, (ii) not correcting for the effect of "wedging", (iii) friction at the supports and (iv) twisting of the specimen during bending. Errors due to

lateral deflection of the loading edge and rounding off the specimen edges are potentially serious.

As a final word on the comparative merits of four and three-point bending, four-point bending has the advantages of (i) subjecting a large area of the tensile face to a nominally uniform, maximum tensile stress and (ii) doing so in the absence of shear stresses, whereas three-point bending has the disadvantages of (i) subjecting only two transverse lines on the tensile face to a nominally uniform, maximum tensile stress, while the rest of the tensile face is subject to a linearly non-uniform tensile stress and (ii) doing so in the presence of shear stresses. On the otherhand, the errors due to friction, specimen twisting, and lateral displacement of the loading edges are significantly larger in four-point bending under identical conditions. So unless special care is taken, four-point bending will give less accurate results.

4.5 Uniaxial Compressive Strength Measurement Techniques for Non-Ductile Materials

The term compressive strength is mis-leading because it implies failure due to a uniaxial, purely compressive stress; in practice the compressive failure of glass, most glass-ceramics and ceramics is actually caused by induced tensile stresses at the tips of microcracks whose lengths are at an angle θ to the direction of the imposed compressive load such that $90° > \theta \geq 0°$. In the case of materials with a plate-like crystal structure, e.g., graphite, machinable glass-ceramics, failure is caused by induced shear stresses which cleave the plate-like crystals, while very porous materials fail through structural collapse. When the compressive strength of a non-ductile material is determined by the uniaxial compressive loading of cubic, rectangular or preferably right-cylindrical specimens due to the less complex stress distribution in the latter, a number of experimental factors generally prevent ideal uniaxial compression:

(a) Barrelling of the specimen caused by the constraint on lateral Poisson expansion of the specimen ends due to friction between the specimen ends and the loading platens which induces biaxial compressive stresses at the ends, (b) Buckling of the specimen caused by the imposition of bending stresses or shear stresses of unknown magnitude and distribution by platen misalignment or specimens with non-parallel end-faces for example, which leads to flexural failure or shear failure respectively. The possibility of barrelling and buckling occurring can be minimised by using a specimen height to diameter (or thickness) ratio, h/d in the range $1 < h/d < 2$ (See Chapter 6, Section 6.2).

Since failure in compression is invariably due to an induced tensile or shear stress rather than a purely compressive stress, the compressive strength of a material is not a suitable parameter for characterizing the strength of a material; although it is of general interest being typically ≈ 8 times the nominal tensile strength. For further details see Jayatilaka, Ayal de S., (1979).

4.6 Statistical Characterization of the Tensile Strength of Non-Ductile Materials

The literature provides ample and continuing evidence that the tensile strength data obtained from strength tests conducted on nominally identical specimens of a given non-ductle material, e.g., ceramic, glass-ceramic, etc., under nominally constant test conditions exhibits a generally random and frequently wide distribution in comparison to the tensile strength data for metals. This random distribution of tensile strengths is due to the random distribution of flaw locations, flaw sizes, and flaw orientations with respect to the applied stress. The flaws may be classified as (i) non-stress induced flaws due to the ceramic fabrication process, e.g., pores or voids, inclusions, etc., or (ii) stress induced flaws, e.g., surface cracks due to machining or rough handling, microcracks due to large residual stresses within the

material generated by thermal expansion-contraction anisotropy and mismatch, martensitic transformation, etc. The severity of a given flaw as regards the initiation of catastrophic non-ductile fracture depends not only on its size and shape, but also on its position and orientation with respect to the applied stress field; thus the most dangerous or critical flaw may not be the largest flaw nor be situated in the region of highest applied stress, but it will be subject to the highest stress intensity factor (as will be discussed in Chapter 5).

In order to completely characterize the strength of a non-ductile material the assumed random distribution of fracture stresses (and hence by implication the random distribution of flaw location, size, shape and orientation) must be described by an appropriate statistical distribution function. Obviously the exact distribution function is difficult to determine exactly since it would require a knowledge of the range of flaw locations, sizes, shapes and orientations in a representative volume of the given material. So it is assumed, depending on the theoretical model in question and any supporting experimental evidence of the flaw size distribution in the given material, that the flaw sizes, locations, orientations, etc., are distributed according to an approximate distribution function (Jayatilaka, Ayal de S. and Trustrum, K., 1977). In fact, the most widely applicable and hence most commonly used distribution function is not one obtained in the above manner, but an empirical cumulative distribution function due to Waloddi Weibull (Weibull, W., 1951), based on the "weakest-link" theory. The theory states that "a chain is only as strong as the strength of its weakest link", i.e., if one link breaks, then the whole chain breaks"; thus the survival probability of the chain must equal the probability of the simultaneous survival of all the links in the chain and the probability of the simultaneous survival of all the links is sensibly seen to decrease as the number of links increase because the probability of a "rogue" link being used increases as the chain length increases.

This concept can be applied to the flaws in a homogeneous, isotropic, non-ductile material subject to a uniform, uniaxial tensile stress, since the survival probability of the material is determined by the survival probability of the most serious, i.e., the critical flaw in the material and the probability of a critical flaw for the given applied stress being present in the material increases as the volume of material stressed increases. So denoting the probability of survival of a volume element δV by S and given that its survival probability is independent of that of any other volume element and is only a function of the applied stress, the probability of the simultaneous survival of n such volume elements is $(S)^n$. Now $S = 1 - F$ where F is the probability of failure, so $(S)^n = (1 - F)^n$; using the result that the limit of $(1 - x/n)^n$ as n tends to infinity is equivalent to $\exp(-x)$, gives

$$(S)^n = (1 - nF/n)^n \approx \exp(-nF) \qquad [4.27]$$

where nF is known as the "risk of rupture". Since δV is the elemental volume, the volume of n such elements, V is equal to $n\delta V$, thus $n = V/\delta V$. If δV is defined as the unit volume V_o, $(S)^n$ is denoted by P_s, and F is denoted by $g(\sigma)$, equation [4.27] becomes

$$P_s = \exp[-(V/V_o)g(\sigma)] \qquad [4.28]$$

The function $g(\sigma)$ has to be a positive, non-decreasing function which vanishes at a value σ_L, which is not necessarily equal to zero. Weibull chose the following empirical function on the basis that it is the least mathematically complex function satisfying the above condition,

$$g(\sigma) = ([\sigma - \sigma_L]/\sigma_o)^m \qquad [4.29]$$

So the Weibull cumulative distribution function for a uniform, uniaxial tensile stress-field situation is

$$P_s = \exp[-(V/V_o)([\sigma - \sigma_L]/\sigma_o)^m] \qquad [4.30]$$

where P_s is the survival probability of the stressed volume of material (V), V_o is the unit volume, σ the applied stress (when analysing the strength distribution it is the fracture stress), σ_L is the limiting or threshold stress below which the failure probability is zero, i.e., $P_s = 1$, σ_o is a normalising or scaling

parameter (i.e., a constant), and m is the Weibull modulus, which characterises the spread or width of the fracture stress distribution for a given value of σ_o; the higher m the narrower the distribution, i.e., the lower the variability of the fracture stress.

This function can be generalised by denoting the risk of rupture by R so that $R = (V/V_o)g(\sigma)$; thus

$$dR = (1/V_o)g(\sigma)dV \qquad [4.31]$$

where dR is the risk of rupture of an infinitesimal volume element dV. Therefore, the survival probability of an arbitrary volume V is given by

$$P_s = \exp\left\{ -(1/V_o) \int_V g(\sigma)dV \right\} \qquad [4.32]$$

where $g(\sigma) = ([\sigma - \sigma_L]/\sigma_o)^m$. This general form is known as the "three parameter Weibull function" and applies when the stress within the material varies with position, i.e., is uniaxial but not uniform; the integral is taken over all the volume elements. For a stressed area, unit area (A_o) and area element (dA) are substituted for V_o and dV. In practice, however, it is assumed, in the absence of any experimental evidence of a maximum flaw size in the material, that σ_L is zero, i.e., the only safe stress is a compressive stress; this is to prevent the safety factor (i.e., the ratio of the mean strength to the strength at a given survival probability) being too low, as it decreases as σ_L increases and σ_L may depend on the volume stressed (Jayatilaka, Ayal de S. and Trustrum, K., 1979). Equation [4.30] then becomes

$$P_s = \exp[-(V/V_o)(\sigma/\sigma_o)^m] \qquad [4.33]$$

and is known as the "two parameter Weibull function". This equation can be "linearized" to give the following form

$$\ln\ln(1/P_s) = m\ln\sigma + \ln(V/[V_o(\sigma_o)^m]) \qquad [4.34]$$

Thus a plot of $\ln\ln(1/P_s)$ against $\ln\sigma$ should be a straight line of slope m and intercept $\ln(V/[V_o(\sigma_o)^m])$, assuming there is only one flaw size distribution in the material and that the Weibull distribution is applicable. To provide a visual link with a plot of P_s against σ, it is common practice to plot $-\ln\ln(1/P_s)$ against $\ln\sigma$ to obtain a line of slope -m.

It should be noted that so long as evaluation of the intercept is not required, equation [4.34] can be used to determine the Weibull modulus for a given material using fracture stress data obtained under non-uniform, uniaxial stress conditions, e.g., three-point bending. This is because only the parameter σ_o changes according to the form the risk of rupture (R) takes; in three-point bending with $\sigma_L = 0$, R equals $(V/V_o)(\sigma/\sigma_o)^m(1/[2(m + 1)^2])$ (Weil, N.A. and Daniel, I.M., 1964) which gives an intercept of $\ln(V/[2(m + 1)^2 V_o(\sigma_o)^m])$. So even if V is the same, σ_o is different.

There are a number of methods for estimating the Weibull modulus, e.g., maximum likelihood method, direct non-linear "least-squares" method, etc., but the most frequently used method is the standard "least-squares" linear regression analysis applied to equation [4.34], due to its computational simplicity. For a reliable estimate of m at least 20 fracture stress values should be used, providing a reasonable number of both low and high stress values. The data for $\ln\sigma$ are the fracture stress values obtained experimentally, but the corresponding expected values for P_s and hence $\ln\ln(1/P_s)$ are far from obvious and their estimation involves complex statistical arguments starting with the requirement that the experimentally determined fracture stress values be ranked in order of ascending magnitude, i.e., $\sigma_1 \leq \sigma_2 \leq \sigma_3 \leq \ldots\ldots\ldots\leq \sigma_j \leq \ldots\ldots\leq \sigma_n$. The fracture stress of each ranked specimen sets an upper limit on the range of stresses at which the preceding ranked specimen could have fractured whilst maintaining its rank position within the set of specimens tested. Given that if a large number of sets of n specimens (n being constant) were tested to fracture under identical conditions, the upper limiting stress of each equivalent rank in each set tested would be different, a fracture stress distribution must exist for each rank.

The cumulative distribution function, $P_F = 1 - P_s$ gives the probability that the random variable σ is less than or equal to a specified value of σ, σ_j. Since σ_j is

different for each set tested, the P_F values associated with each rank comprise a random distribution; thus a representative estimate of P_F (and hence P_S) is required for each rank. Furthermore, as the estimate of P_F appropriate to each rank must be the same for the equivalent rank in every set of n specimens tested, the appropriate estimate of P_F must be judged from its rank order and not the fracture stress value assigned to each rank for any given set of n specimens tested. Other than noting the various survival probability estimators (P_S) established by statistical theory, further consideration of the method of estimating values for P_F and hence P_S was not appropriate in the present work.

There are a number of different estimates for P_F in use (Kapur, K.C., and Lamberson, L.R., 1977): [4.35]

(1) $P_F = j/(n + 1)$ which is known as the mean rank value,

(2) $P_F = (j - 0.3)/(n + 0.4)$ which is an approximation to the median rank value,

(3) $P_F = (j - 0.5)/n$, and

(4) $P_F = (j - 3/8)/(n + 1/4)$.

4.7 Long-Term Strength and Service-Life Prediction

The flexural strength of non-ductile materials considered previously was their short-term strength, i.e., their strength when subject to an increasing stress to the point of fracture; the typical time under stress ranges from a few seconds to a few hundreds of seconds depending on the loading rate. In this section the long-term strength which is time dependent due to the phenomenon of delayed fracture caused by sub-critical crack growth and the prediction of service-life are considered.

It has been found that for many "ceramic" materials, e.g., glass, ceramics and glass-ceramics, etc., slow or sub-critical crack growth occurs prior to rapid catastrophic propagation of the crack under constant or variable loading at stresses well below the critical stress for fracture. The slow crack growth is in general due to either (a) a stress enhanced thermally activated

growth mechanism, (b) a stress enhanced chemical reaction or adsorption activated growth mechanism or (c) a stress independent chemical diffusion activated growth mechanism at the crack tip. Regardless of which of the above mechanisms is operative, sub-critical crack growth increases with increasing temperature. Slow crack growth occurs in oxide glasses and ceramics at ambient temperature in environments containing hydroxyl ions (OH^-) such as water, while it is significant in non-oxide materials at elevated temperatures (Evans, A.G. and Langdon, T.G., 1976) and has been observed for some glasses in vacuo (Wiederhorn, S.M., 1974).

A schematic diagram of crack growth velocity (v) against stress intensity factor (K_I) is shown in Figure 4.5 in the form of log(v) versus log(K_I). The data for such a diagram are frequently obtained from double torsion tests (Wiederhorn, S.M., 1974). Note (i) the crack growth velocity data are independent of crack length, test geometry and so on, and (ii) the diagram is a composite diagram in that not every material exhibits all three regions of slow crack growth behaviour prior to fracture. Region 1 behaviour begins at K_{I_0} which either represents the minimum stress intensity required for the commencement of sub-critical crack growth or a lower limit ($\approx < 0.1K_I$) below which the crack velocity ($< 10^{-10}$ ms^{-1}) is too slow to be accurately measured at present. In region 1, K_I increases as v increases such that v is proportional to $\exp(\alpha K_I)$ where α is a constant; however, the experimental data are generally better fitted by

$$v = A(K_I)^n \qquad [4.36]$$

where the subscript 1 of K_I denotes that the crack surfaces are displaced in a manner which widens or opens the crack in the plane of the applied tensile stress (see Chapter 5), and A and n are constants characteristic of the material and its environment; for ceramics and glasses $n \approx \geq 10$. In this region the crack growth velocity is controlled by the stress enhanced adsorption or reaction rate of the corrosive species (in the environment) at the crack tip. In region 2 the crack growth velocity is

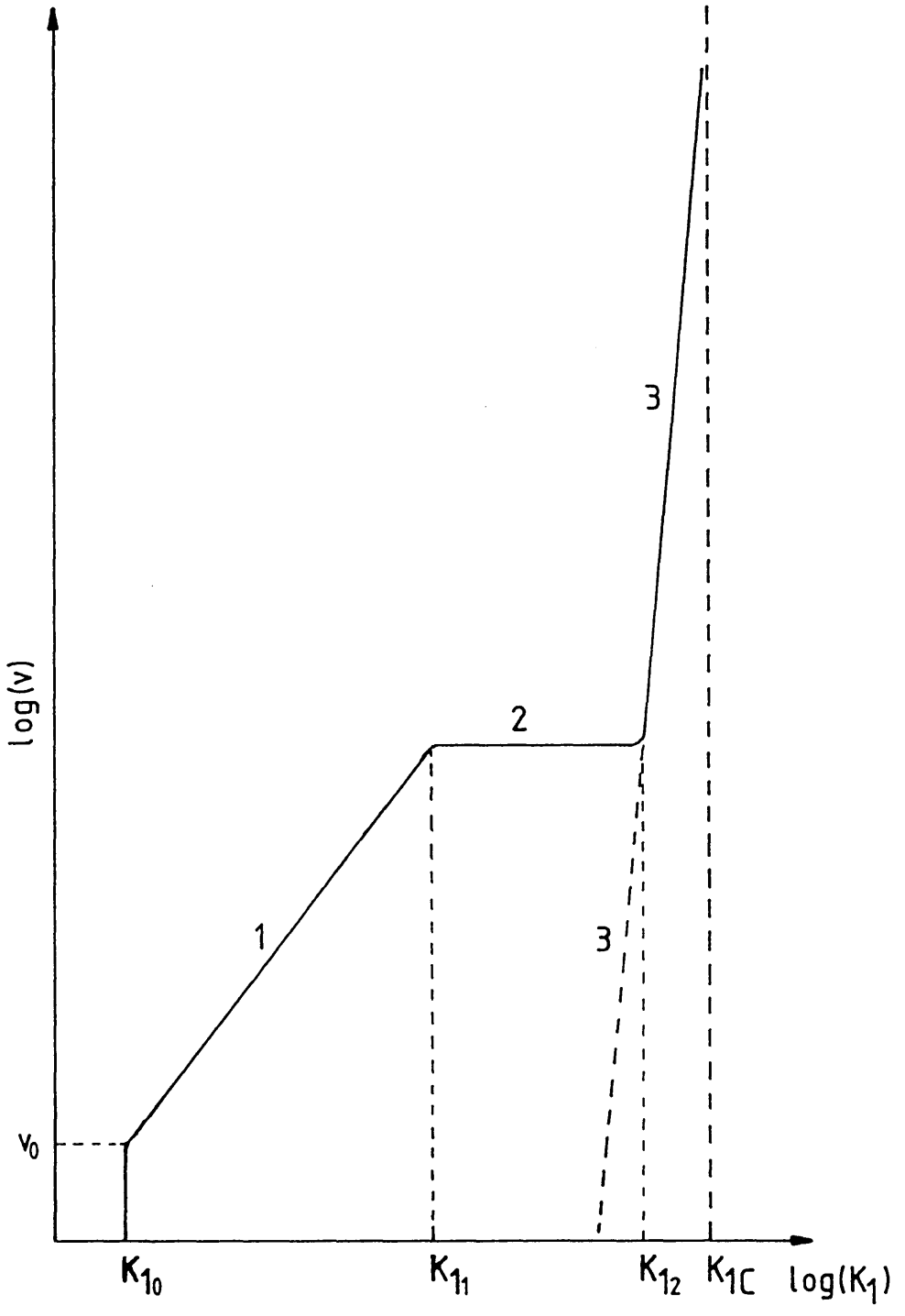


Figure 4.5 Idealized Composite Diagram of Crack Growth Velocity (v) Versus the Mode 1 Stress Intensity Factor (K_1).

effectively constant and it and K_I are not inter-dependent and mutually enhancing as in region 1; thus the crack growth velocity is stress independent. The constancy and magnitude of the velocity are, however, strongly affected by the environment and the velocity is dependent on the diffusion rate of the corrosive species to the crack tip.

In region 3 the crack growth velocity and K_I are again strongly inter-dependent, but compared with region 1 the rate of increase of velocity with respect to stress intensity (dv/dK_I) is much higher; also the magnitude of K_I is similar to that of K_{Ic} which is the critical stress intensity factor for catastrophic crack propagation without prior sub-critical crack growth (see Chapter 5). Region 3 behaviour has been observed in vacuo for some glasses which suggests that it is due to a stress enhanced, possibly thermally activated growth mechanism which unlike the mechanisms in regions 2 and 3 is independent of environment. Some materials exhibit tri-region behavior, while others are relatively unaffected by the environment and show only region 3 behaviour. Experimentally others may show only region 1 behaviour.

4.7.1 Time to failure under a constant load

As will be discussed in Chapter 5, the stress intensity K_I is related to the applied stress σ and the effective crack length c as follows

$$K_I = D\sigma c^{1/2} \qquad [4.37]$$

where D is a dimensionless, composite constant equal to Y/Z where Y is the compliance factor and Z is the flaw shape factor; at fracture $\sigma \equiv \sigma_F$ and $K_I \equiv K_{Ic}$. So the stress intensity factor is a function of both crack growth velocity and crack length, and although K_{Ic} may be considered as a material constant when measured in an inert environment at a given temperature, e.g., in vacuo at ambient temperature, it is, perhaps, better thought of under normal conditions as just the stress intensity factor at fracture and a point on the v versus K_I plot.

The reason for this is that unless K_I reaches K_{Ic} instantly when the material is stressed there may, depending on the environmental conditions, be some slow crack growth prior to fracture, giving rise to a loading or strain rate dependence of K_{Ic}.

The crack growth velocity v is by definition equal to dc/dt, so from equation [4.36]

$$dc/dt = A(K_I)^n \qquad [4.38]$$

while from [4.37], under a constant applied stress

$$dK_I/dc = (D\sigma/2)c^{-1/2} \qquad [4.39]$$

Therefore since $dK_I/dt = (dK_I/dc)(dc/dt)$ and $c^{1/2} = K_I/D\sigma$

$$dK_I/dt = (A/2)D^2\sigma^2(K_I)^{n-1} \qquad [4.40]$$

Now the time taken for the stress intensity factor at the most severe flaw in the body to increase from some initial value K_{Ii} to K_{If} can be obtained as follows. Separating the variables in equation [4.40]

$$2/(AD^2\sigma^2(K_I)^{n-1})\, dK_I = dt \qquad [4.41]$$

gives the following integral equivalence

$$(2/AD^2\sigma^2)\int_{K_{Ii}}^{K_{If}} (K_I)^{1-n}\, dK_I = \int_0^{t_f} dt = t_f \qquad [4.42]$$

This form of integral can be written for each crack growth region as shown below (note for region 2, $v = A_2$), and the time to failure, t_F is obtained by summing the stress intensity integrals of the respective regions, i.e.,

$t_F =$ [4.43]

$$H\left[(1/A)\int_{K_{Ii}}^{K_{I1}} (K_I)^{1-n}\, dK_I + (1/A_2)\int_{K_{I1}}^{K_{I2}} K_I\, dK_I + (1/A_3)\int_{K_{I3}}^{K_{Ic}} (K_I)^{1-p}\, dK_I\right]$$

where $H = 2/D^2\sigma^2$ and $n = p$ (for region 3, $v = A_3(K_I)^p$).

In general, however, both the crack growth velocity and the stress intensity in region 3 are high enough to assume that at the end of region 2 fracture is essentially instantaneous with $K_{I2} = K_{Ic}$. Furthermore, when ceramic materials exhibit region 2 behaviour the crack growth velocity is usually high enough for the time to failure to almost wholly dependent on the crack growth behaviour of region 1. So to a good approximation sub-critical crack growth occurs for stress intensities in the range K_{Io} to

K_{I1} where K_{I1} is the stress intensity at the end of region 1 behaviour; hence the latter two integrals can be neglected without serious error to give on integration

$$t_F \approx t_1 = [2/AD^2\sigma^2(n-2)][(K_{Ij})^{2-n} - (K_{I1})^{2-n}] \quad [4.44]$$

A further simplification can be made on the basis that as n is > 10 and $K_{I1} > K_{Ij}$, $(K_{Ij})^{2-n} \gg (K_{I1})^{2-n}$; thus

$$t_F \approx [2(K_{Ij})^{2-n}]/[AD^2\sigma^2(n-2)] \quad [4.45]$$

As discussed above, the K_{Ic} value measured in an inert environment can be considered to be a material constant; thus the mean fracture strength measured in the same inert environment, σ_o defines the nominal intial flaw size. This is because K_{Ic} obtains instantaneously, i.e., fracture occurs without any sub-critical crack growth, and hence the nominal critical flaw size, c_o given by

$$c_o = (K_{Ic}/D\sigma_o)^2 \quad [4.46]$$

is effectively the nominal initial flaw size. Therefore, since $K_{Ij} = D\sigma(c_j)^{1/2}$ and $c_o \equiv c_j$, the initial stress intensity factor can be related to K_{Ic} and σ_o as follows

$$K_{Ij} = (\sigma/\sigma_o)K_{Ic} \quad [4.47]$$

Substituting [4.47] in equation [4.45] gives

$$t_F \approx B(\sigma_o/\sigma)^n(1/[\sigma_o]^2) \quad [4.48]$$

where $B = 2/(AD^2[n-2](K_{Ic})^{n-2})$ and is a constant for a given material, environment and temperature. From equation [4.48] it can be seen that since $\sigma_o/\sigma > 1$, the magnitude of $(\sigma_o/\sigma)^n$ far outweighs the effect of $1/[n-2]$; thus the higher n, the longer t_F. Furthermore, for a given n value t_F increases with decreasing σ, since t_F is proportional to $1/\sigma^n$.

Expressing equation [4.36] in the normalized form,

$$v = \alpha(K_I/K_{Ic})^n \quad [4.49]$$

where α and n are constants characteristic of the material and its environment, and comparing it with [4.36] shows that A in [4.36] is dependent on n,

$$A = \alpha/(K_{Ic})^n \quad [4.50]$$

Thus the normalized power function is more rigorous as α does not depend on n. Using equation [4.49] to derive the time to failure, t_F in the manner described above gives

$$t_F \approx \beta(\sigma_o/\sigma)^n(1/[\sigma_o]^2) \quad [4.51]$$

where $\beta = 2(K_{Ic})^2/(\alpha D^2[n-2])$. Comparing equations [4.48]

and [4.51] shows that $B \equiv \beta$; furthermore, it can be seen from [4.50] that for given α and n, A decreases rapidly as $(K_{Ic})^n$, i.e., K_{Ic} increases. So in [4.48] the decrease in A outweighs the increase in $(K_{Ic})^{n-2}$; hence B increases as K_{Ic} increases. To summarise then, t_F increases with increasing K_{Ic}, σ_a and n, and decreasing α and σ.

Consider two groups of N specimens of a given material which are tested to failure under different constant stress levels, σ_A and σ_B. Assume that the two fracture strength distributions at the two different constant stress levels are identical, i.e., equivalent rank specimens have the same inert fracture strength as well as the same survival probability (i.e., the same initial flaw size). If the failure times of any two equivalent rank specimens are t_A and t_B respectively, then it follows from equation [4.48] that $t_A(\sigma_A)^n \equiv t_B(\sigma_B)^n$; hence

$$(\sigma_A/\sigma_B)^n \equiv t_B/t_A \qquad [4.52]$$

This equation allows the fracture stress corresponding to a specified failure time to be calculated using a different fracture stress and its corresponding failure time.

4.7.2 Sub-critical crack growth at a constant strain-rate

A three-point bending test is an example of constant strain-rate loading since the cross-head of the testing machine moves at a constant speed when loading the specimen. The maximum stress at fracture is found in a manner after A.G. Evans, (1974a); in general the stress (σ) and strain (ϵ) in a cracked body are related via

$$\sigma = E\epsilon f(c) \qquad [4.53]$$

where f(c) decreases with increasing c and E is the Young's modulus. For small cracks such that the compliance factor $Y \approx \pi^{1/2}$, i.e., $c/W < 0.1$ where W is the specimen width (see Figure 4.2), f(c) = 1 and [4.52] reduces to

$$\sigma = E\epsilon \qquad [4.54]$$

Now to relate the stress to the crack length,

$$d\sigma/dc = (d\sigma/dt)(dt/dc) = (d\sigma/dt)(1/v) \qquad [4.55]$$

But from equation [4.54]

$$d\sigma/dt = E(d\epsilon/dt) = E\dot{\epsilon} \qquad [4.56]$$

And since $v = A(K_I)^n$ and $K_I = D\sigma c^{1/2}$

$$d\sigma/dc = E\dot{\epsilon}/[A(K_I)^n] = E\dot{\epsilon}/[A(D\sigma c^{1/2})^n \qquad [4.57]$$

Separating the variables

$$\sigma^n \, d\sigma = (E\dot{\epsilon}/AD^n)c^{-n/2} \, dc \qquad [4.58]$$

gives the integral equivalence

$$\int_0^{\sigma_F} \sigma^n \, d\sigma = (E\dot{\epsilon}/AD^n)\int_{c_i}^{c_F} c^{-n/2} \, dc \qquad [4.59]$$

where σ_F is the fracture stress (i.e., the stress when $K_I = K_{Ic}$, c_i the initial size of the most serious flaw in the body and c_F the size reached by this flaw when $K_I = K_{Ic}$. Integrating [4.59] gives

$$(\sigma_F)^{n+1} = \qquad [4.60]$$

$$(2E\dot{\epsilon}[n + 1]/AD^n[n - 2])(c_i/(c_i)^{n/2} - c_F/(c_F)^{n/2})$$

The term in c of [4.60] can be written in the more symmetrical form

$$[c_i/(c_F)^{n/2}][(c_F/c_i)^{n/2} - (c_F/c_i)] \qquad [4.61]$$

Furthermore, since n is typically > 10 and $c_F > c_i$ (hence $c_F/c_i > 1$), $(c_F/c_i) \ll (c_F/c_i)^{n/2}$. So (c_F/c_i) in [4.60] can be disregarded, reducing equation [4.60] to

$$(\sigma_F)^{n+1} = (2E\dot{\epsilon}[n + 1]/AD^n[n-2])([c_i]^{(2 - n)/2}) \qquad [4.62]$$

But $c_i = (K_{Ic}/D\sigma_o)^2$ from equation [4.46]; thus

$$(\sigma_F)^{n+1} = (2E\dot{\epsilon}[n + 1]/AD^2[n - 2])(K_{Ic}/\sigma_o)^{2-n} \qquad [4.63]$$

which can be written (for a reason; see [4.48])

$$(\sigma_F)^{n+1} = [2E\dot{\epsilon}(n + 1)(\sigma_o)^{n-2}]/[AD^2(n - 2)(K_{Ic})^{n-2}] \qquad [4.64]$$

This can be rearranged to give

$$(\sigma_F)^{n+1} = B(n + 1)E\dot{\epsilon}(\sigma_o)^{n-2} \qquad [4.65]$$

where $B = 2/(AD^2[n - 2](K_{Ic})^{n-2})$, i.e., the constant in equation [4.48].

Using a similar argument to that giving equation [4.52], by assuming that the two fracture strength distributions at the two strain-rates $\dot{\epsilon}_A$ and $\dot{\epsilon}_B$ are identical, i.e., equivalent rank specimens have the same inert fracture strength and survival probability (i.e., the same initial flaw size), produces from [4.65]

$$(\sigma_A/\sigma_B)^{n+1} = \dot{\epsilon}_A/\dot{\epsilon}_B \qquad [4.66]$$

where σ_A and σ_B are the respective fracture stresses.

4.8 Strength-Probability-Time (SPT) Diagram

The strength-probability-time diagram was proposed by R.W. Davidge and relates the survival probability of a component to its projected life-time under a given stress (Davidge, R.W., McLaren, J.R., and Tappin, G, 1973). An SPT diagram can be constructed for a given material if its sub-critical crack growth exponent (n) is known (defined in equation [4.36]); the n-value is most conveniently obtained from the flexural strength testing of batches of specimens at different constant strain-rates. Data at three or more strain-rates (which differ by at least an order of magnitude) are required for a reliable n-value.

Equation [4.66] can be used in two ways to estimate n; (i) the mean flexural strength values can be used by direct substitution or (ii) the equation can be "linearized" as follows

$$\ln\sigma_A = \ln\sigma_B + (1/[n+1])\ln(\dot{\epsilon}_A/\dot{\epsilon}_B) \qquad [4.67]$$

The equivalent rank fracture stresses σ_A and σ_B are then used in this equation and n calculated from the intercept. Note that if the assumption of identical fracture strength distributions is not valid the data will produce a slope significantly different from 1. This approach requires an equal number of strength data at each strain-rate, whereas the former does not. In both cases the two mean strain-rate magnitudes are required; for the three-point bending test the maximum strain of the tensile face (ϵ_{MAX}) is given by (Hollenberg, G.W., et al., 1971)

$$\epsilon_{MAX} = (6W/s^2)\delta_c \qquad [4.68]$$

where W and s are as shown in Figure 4.2 and δ_c is the specimen mid-span deflection. Note that as with the beam equations given previously, it is assumed that the strain-rate is directly proportional to σ^N where N = 1 (i.e., Newtonian viscous creep obtains) and that the elastic deflections are small. The strain-rate ($\dot{\epsilon}$) is the derivative of [4.68] with respect to time; thus

$$\dot{\epsilon} = 6WV/s^2 \qquad [4.69]$$

where V is the testing machine cross-head speed and is equivalent to $d\delta_c/dt$.

The value of n estimated in the above manner may be different from that obtained directly from a K_I-v curve because the former value derives from the propagation of microscopic inherent flaws in the material, whereas the latter value is obtained from the propagation velocity and stress intensity data for an artificial macroscopic crack, e.g., in a double-torsion specimen. The strain-rate method for determining n has the advantage that it does not require the assumption of equivalent propagation behaviour for macroscopic cracks and microscopic flaws.

In addition to a value for n, data on the failure times under a range of constant stress levels are required to construct the SPT diagram. The data may be obtained experimentally by conducting delayed fracture tests at different static loads or indirectly by converting constant strain-rate failure time data to equivalent failure times under a constant stress equal to the constant strain-rate fracture stresses. For the same stress level σ_F, the time to failure at a constant strain-rate $t_{\dot{\epsilon}}$ is longer than that under constant stress t_c because until the stress level is near the fracture stress σ_F there is little slow crack growth.

Rearranging equation [4.48] gives

$$t_F = C/\sigma^n \qquad [4.70]$$

where C is a constant for a given specimen ($= B(\sigma_o)^{n-2}$). When the stress is increasing, the stress σ is constant for only an infinitesimal time dt of the specimen life-time $t_{\dot{\epsilon}}$; this time is only a fraction of what it would have been if σ were constant, i.e., dt/t_F. Using [4.70] gives (Davidge, R.W., 1979)

$$dt/t_F = dt(\sigma^n/C) \qquad [4.71]$$

Now as $\dot{\sigma} = E\dot{\epsilon}$ and $\dot{\epsilon}$ is constant, $\dot{\sigma} \equiv d\sigma/dt = \sigma_F/t_{\dot{\epsilon}}$ and $dt = (t_{\dot{\epsilon}}/\sigma_F)d\sigma$. So equation [4.71] becomes

$$dt/t_F = (\sigma^n/C)(t_{\dot{\epsilon}}/\sigma_F)d\sigma \qquad [4.72]$$

When the constant stress is σ_F then the time to failure (t_c) is given by $C/(\sigma_F)^n$ according to equation [4.70], so equation [4.72] becomes

$$dt/t_F = [\sigma^n/(\sigma_F)^{n+1}][t_{\dot{\epsilon}}/t_c]\, d\sigma \qquad [4.73]$$

The following integral equivalence can thus be formed

$$(1/t_F)\int_0^{t_F} dt = (t_{\dot\epsilon}/t_c)\int_0^{\sigma_F} \sigma^n/(\sigma_F)^{n+1}\, d\sigma \qquad [4.74]$$

which gives $1 = (t_{\dot\epsilon}/t_c)(1/[n+1])$. Therefore

$$t_c = t_{\dot\epsilon}/(n+1) \qquad [4.75]$$

The relationship between $t_{\dot\epsilon}$ and t_c can also be derived in the following manner using the following equations:

$$\sigma_o = (K_{Ic}/D)(c_o)^{-1/2} \qquad [4.76]$$

$$c_o = (K_{Ic}/D\sigma_o)^2 \qquad [4.77]$$

$$dc/dt = A(K_I)^n \qquad [4.78]$$

$$K_I = (\sigma/\sigma_o)K_{Ic} \qquad [4.79]$$

$$B = 2/(AD^2[n-2](K_{Ic})^{n-2}) \qquad [4.80]$$

$$t_c = (B(\sigma_o)^{n-2})(\sigma_F)^{-n} \qquad [4.81]$$

$$\dot\sigma \equiv d\sigma/dt = E\dot\epsilon = (\sigma_F/t_{\dot\epsilon}) \qquad [4.82]$$

Differentiating [4.76] with respect to time using $dy/dx = (dy/dw)(dw/dx)$ gives

$$d\sigma_o/dt = [-(K_{Ic}/2D)(c_o)^{-3/2}][\,dc/dt] \qquad [4.83]$$

Substituting [4.77] for c_o in [4.83] gives

$$d\sigma_o/dt = [-D^2(\sigma_o)^3/2(K_{Ic})^2][dc/dt] \qquad [4.84]$$

Now substituting [4.79] for K_I in [4.78] gives $dc/dt = A\sigma^n(K_{Ic})^n/(\sigma_o)^n$ which on substitution for dc/dt in [4.84] gives

$$d\sigma_o/dt = -AD^2(K_{Ic})^{n-2}\sigma^n/(2(\sigma_o)^{n-3}) \qquad [4.85]$$

Separating the variables in [4.85] gives

$$(\sigma_o)^{n-3}\, d\sigma_o = -(AD^2(K_{Ic})^{n-2}/2)\sigma^n\, dt \qquad [4.86]$$

Thus the following integral equivalence can be written

$$\int_{\sigma_o}^{\sigma_T} (\sigma_o)^{n-3}\, d\sigma_o = -(AD^2(K_{Ic})^{n-2})/2\int_0^T \sigma^n\, dt \qquad [4.87]$$

where σ_T is the fracture strength at some time T such that $\sigma_T < \sigma_o$, the inert fracture strength. This gives

$$(\sigma_T)^{n-2} = (\sigma_o)^{n-2} - (AD^2[n-2](K_{Ic})^{n-2})/2\int_0^T \sigma^n\, dt \qquad [4.88]$$

Comparing [4.80] and the coefficient of the integral shows

$$(\sigma_T)^{n-2} = (\sigma_o)^{n-2} - (1/B)\int_0^T \sigma^n\, dt \qquad [4.89]$$

From equation [4.82] it can be seen that when $\dot{\epsilon}$ and hence $\dot{\sigma}$ are constant, the stress σ at any time t is equal to $(\sigma_F/t_{\dot{\epsilon}})t$. So when $T = t_{\dot{\epsilon}}$, equation [4.89] can be written

$$(\sigma_T)^{n-2} = (\sigma_o)^{n-2} - [(\sigma_F/t_{\dot{\epsilon}})^n/B]\int_0^{t_{\dot{\epsilon}}} t^n \, dt \qquad [4.90]$$

Integrating [4.90], and dividing the integration result through by $(\sigma_o)^{n-2}$ produces

$$(\sigma_T/\sigma_o)^{n-2} = 1 - [(\sigma_F)^n/(B(\sigma_o)^{n-2})][t_{\dot{\epsilon}}/(n+1)] \qquad [4.91]$$

Now $t_c = (B(\sigma_o)^{n-2})(\sigma_F)^{-n}$, so [4.91] can be written

$$(\sigma_T/\sigma_o)^{n-2} = 1 - t_{\dot{\epsilon}}/[(n+1)t_c] \qquad [4.92]$$

As $n > 10$ and σ_T/σ_o is < 1, equation [4.92] becomes

$$1 - t_{\dot{\epsilon}}/[(n+1)t_c = 0 \qquad [4.93]$$

to a very good approximation; therefore,

$$t_c = t_{\dot{\epsilon}}/(n+1) \qquad [4.94]$$

So using [4.94] the actual failure time $t_{\dot{\epsilon}}$ recorded in a constant strain-rate $\dot{\epsilon}$ test up to the fracture stress σ_F can be converted to an equivalent failure time t_c under a constant stress of σ_F. Using equation [4.52] the constant stress σ_F corresponding to the failure time t_c can be converted to the constant stress corresponding to a reference failure time of, say 1 second, σ_1. That is

$$\sigma_1 = \sigma_F(t_c)^{1/n} \qquad [4.95]$$

Substituting [4.94] in [4.95] then gives for a reference life-time of 1 second

$$\sigma_1 = \sigma_F(t_{\dot{\epsilon}}/[n+1])^{1/n} \qquad [4.96]$$

where σ_F and $t_{\dot{\epsilon}}$ are experimental data and n is calculated.

The reference 1 second life-time line is plotted "Weibull fashion" by plotting the σ_1 data calculated using [4.96] against the appropriate P_s data (which are the same since the rank order is not changed on converting from σ_F to σ_1, but the Weibull modulus will be different) on axes of $-\log\ln(1/P_s)$ and $\log\sigma_1$. These axes are chosen for convenience in generating a series of parallel lines for life-times a decade apart on both sides of the 1-second line; a life-time ratio of 10^x in [4.52] gives the horizontal shift of the reference datum point (R) at a given survival probability for x decades time-shift as

$$\log\sigma_x = \log\sigma_R - (x/n) \qquad [4.97]$$

4.9 Experimental Determination of the Fracture Strength Properties of Glass-Ceramics in the System $CaO - MgO - Al_2O_3 - SiO_2$

The elastic properties and internal friction of four glass-ceramics in the $CaO - MgO - Al_2O_3 - SiO_2$ system have been detailed in Chapter 3, Section 3.7. The fracture strength properties of the same glass-ceramics, namely SCR25.76, SCR19.34, SCF5 and SCR19.13 are described in this section. The following fracture strength data have been obtained:

(1) The mean room temperature flexural strengths of all four materials for a given strain-rate.

(2) The mean room temperature flexural strengths of SCR25.76 and SCR19.34 for three strain-rates.

(3) The Weibull modulus for a zero threshold stress at room temperature for SCR25.76 and SCR19.34 at three strain-rates.

(4) The sub-critical crack growth exponent (n) at room temperature for SCR25.76 and SCR19.34, as determined from strain-rate strength data.

(5) Room temperature strength-probability-time diagrams for SCR25.76 and SCR19.34.

(6) The mean flexural strength of SCR25.76 and SCR19.34 as a function of temperature.

(7) The mean uniaxial compressive strength of SCR25.76 and SCR19.34 at room temperature for a given strain-rate. Note the flexural strength data refer to uniaxial tensile fracture strength under three-point bending.

In addition, data have been obtained concerning the methods of analysing fracture strength data; for example, (a) the variation in the Weibull modulus with the survival probability estimator used, (b) the effect of "wedging" and fracture away from the mid-span position on the calculated flexural strengths, and (c) the practical application of a new graphical method (Leon, M. and Kittl, P., 1985) for determining all three parameters of the "three parameter" Weibull function.

4.9.1 Experimental apparatus used to determine the flexural and compressive strength

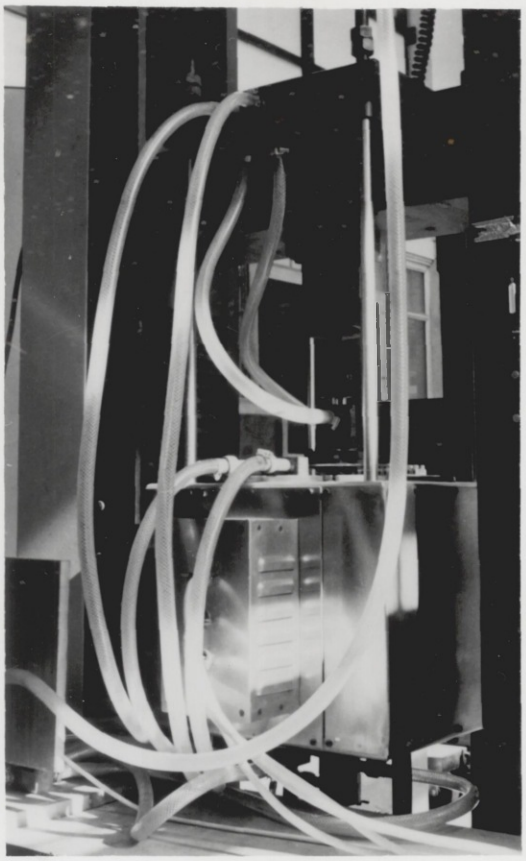
(1) Room temperature bending test rig:

The primary room temperature flexural strength data, i.e., the data used to estimate the Weibull moduli, slow crack growth exponents, and so on, were obtained using an Instron 1185 testing machine with a 2518-200 series 1 kN static load cell operating in tension. The three-point bending test rig was a stainless steel inter-penetrating cage design with the loading cage fixed underneath the machine cross-head and the support span cage attached to the load cell. The rig had generous clearance fittings for the 3mm diameter tungsten carbide support and loading rollers and the loading roller support was free to rotate about an axis parallel to the long side of the specimens. The load - time responses were recorded on the high performance chart recorder of the Instron.

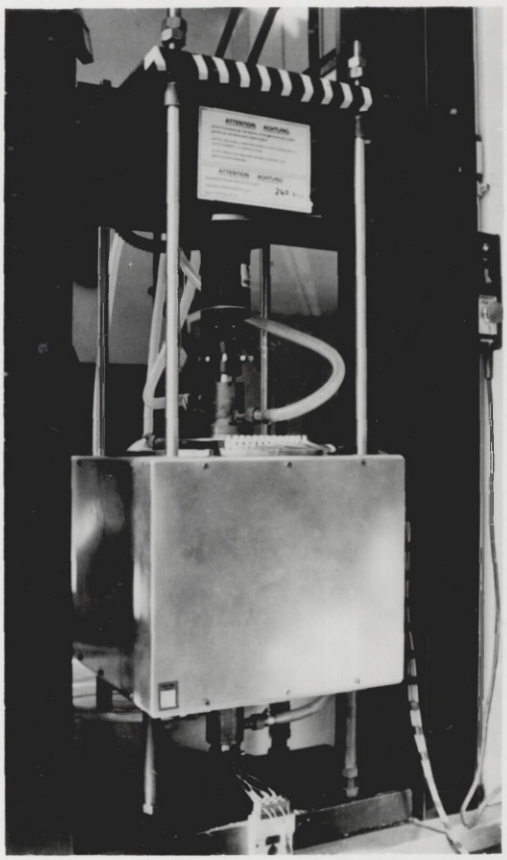
(2) High temperature bending test rig:

The elevated temperature flexural strength data were obtained using a high temperature three-point bending test system designed by the author (a) expressly for the present project and (b) to be used with an Instron 1185 machine and 2518-200 series 1kN and 10 kN load cells. The system consisted of three components, (i) the load-train assembly, (ii) the vertical tube-furnace assembly, and (iii) the temperature control system, as shown in the photographs in Figure 4.6. The complete system had a number of interesting design and operational features:

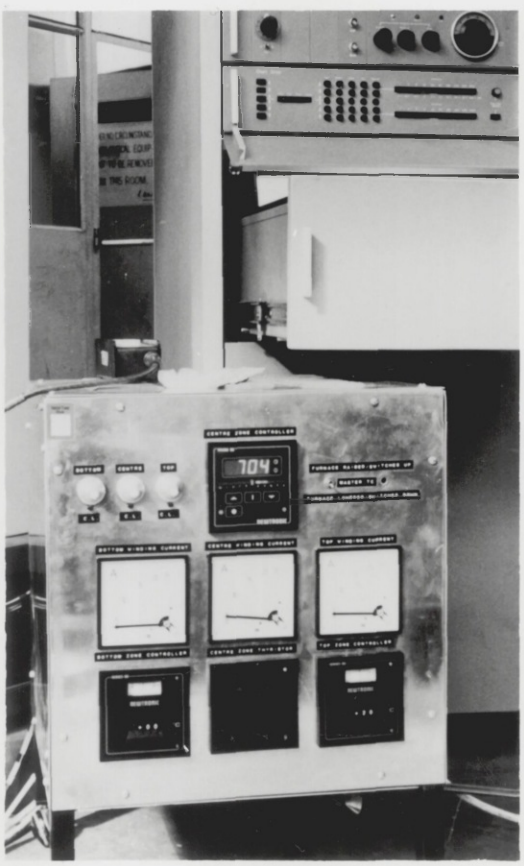
(a) The furnace was attached to the cross-head via four BS321 stainless steel rods which were permanently fixed to it through the corners of the furnace end-plates and went in brass guide-sleeves in the 25 mm thick mild steel plate screwed on the top of the cross-head of the Instron. Double-nut sets were screwed onto the rod tops which enabled the furnace to be raised and lowered at a set



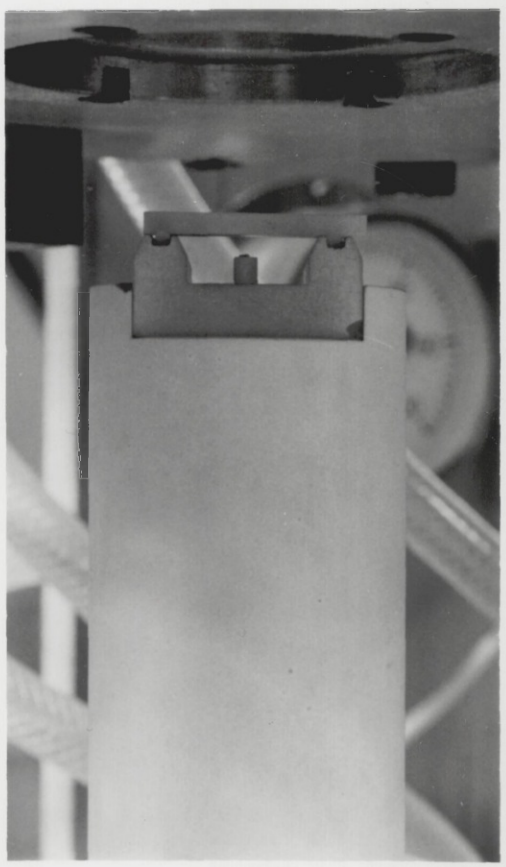
Furnace - Rear View.



Furnace - Front View.



Temperature Control System.



Lower Silicon Nitride Ram.

Figure 4.6 Photographs of the High Temperature Three-Point Bending Test Apparatus Designed for the Present Work.

speed by moving the cross-head up or down respectively.
(b) The load-train consisted of an upper loading ram attached to the load cell, which was screwed to the underneath of the cross-head and a separate, lower support ram which sat on a hardened steel spacer in a mild steel collar screwed to the 50 mm thick mild steel compression beam fixed to the base of the Instron. The two rams were accurately aligned by moving the cross-head down so that a sliding-precision guide-mandrel, which fitted onto the end of the load cell, could be moved down into the recess in the collar (whose fixing screws have been loosened) such that it was a sliding fit, enabling the mandrel to be rotated freely about the axis of the load cell. When this was achieved, the fixing screws of the collar were tightened again. The furnace lifting plate was centred with respect to the load cell fixing diameter, so that once the rams had been aligned, the furnace tube was concentric with the load-train and never made physical contact with the load-train at any point along its length.
(c) Both the (cylindrical cross-section) rams consisted of two sections, (i) a BS321 stainless steel section, with a brass water cooled jacket, situated outside the furnace tube and (ii) a "Nitrasil" reaction-bonded Si_3N_4 section located inside the furnace tube. The reinforced PVC hoses carrying water to and from the jacket of the upper ram were connected to a brass coupling block permanently attached to the back of the furnace lifting plate; another pair of PVC hoses, one from the water supply and another to the drain, were connected to the coupling block. This arrangement prevented the PVC hoses imposing a "dragging" load on the load cell when the cross-head moved up or down. Furthermore, the furnace end-plates were also water cooled; all three inlet hoses (i.e., one to the furnace and one to each ram) connected to a single water supply hose via a 3-way brass coupling block to which was fitted a Bourden-type pressure gauge. The corresponding three outlet hoses connected to a single drainage hose via a another 3-way brass coupling block; a pressure switch was fitted to the block, which switched off the furnace if the

water pressure dropped below a certain level.

(d) The two square (395 mm side), 22 mm thick HS30 aluminium alloy end-plates of the furnace had annular channels machined in them for the passage of cooling water (see the schematic section of the furnace and the load-train in Figure 4.7); an HS30 aluminium alloy dam was fixed (with nylon screws to avoid problems with galvanic corrosion) in the annular channel of each end-plate, between the inlet and outlet ports in the respective HS30 aluminium alloy 8 mm thick cover plate. The face of the brass coupling block (for the PVC hoses) in contact with the respective cover plate was coated with an acrylic laquer and then a thin layer of silicon grease again to avoid problems with galvanic corrosion. Another point to note is that all water tight seals were achieved through the use of rubber "O"-ring seals which facilitated easy construction and easy maintainence compared to welded-on or permanently sealed water jackets; this included the custom-made brass screw connectors for the PVC hoses, which consequently only required hand tightening to obtain a watertight seal and so were more convenient to use than standard "Jubilee" clips.

The furnace tube was a 320 mm x ≈ 76 mm I.D. x ≈ 90 mm O.D. "Triangle" 55E sillimanite refractory tube with three separate "Fecralloy A" resistance wire (1.2 mm diameter and ≈ 1.15 Ω/m) windings; a 100 mm long centre winding (11.8 Ω) forming the "hot-zone" and two 80 mm long end windings (≈ 8.6 Ω each). The bulk furnace insulation was standard duty "Triton" loose kaowool. In addition, to reduce the thermal losses at the end-plates, a 25 mm thick "Micropore H.T. Microtherm" ultra-high efficiency, thermal insulating annular disc was placed adjacent to the inner face of each end-plate. The furnace had a double casing, (i) a 1.5 mm thick, 340 mm diameter BS321 stainless steel inner case and (ii) a 1.5 mm thick HS30 aluminium alloy outer case fixed to the square end-plates; both casings were polished on their inner surface. With a total current input of ≤ 15A a.c., a hot-zone temperature in the tube centre of 1100°C was maintained with the inner case at ≈

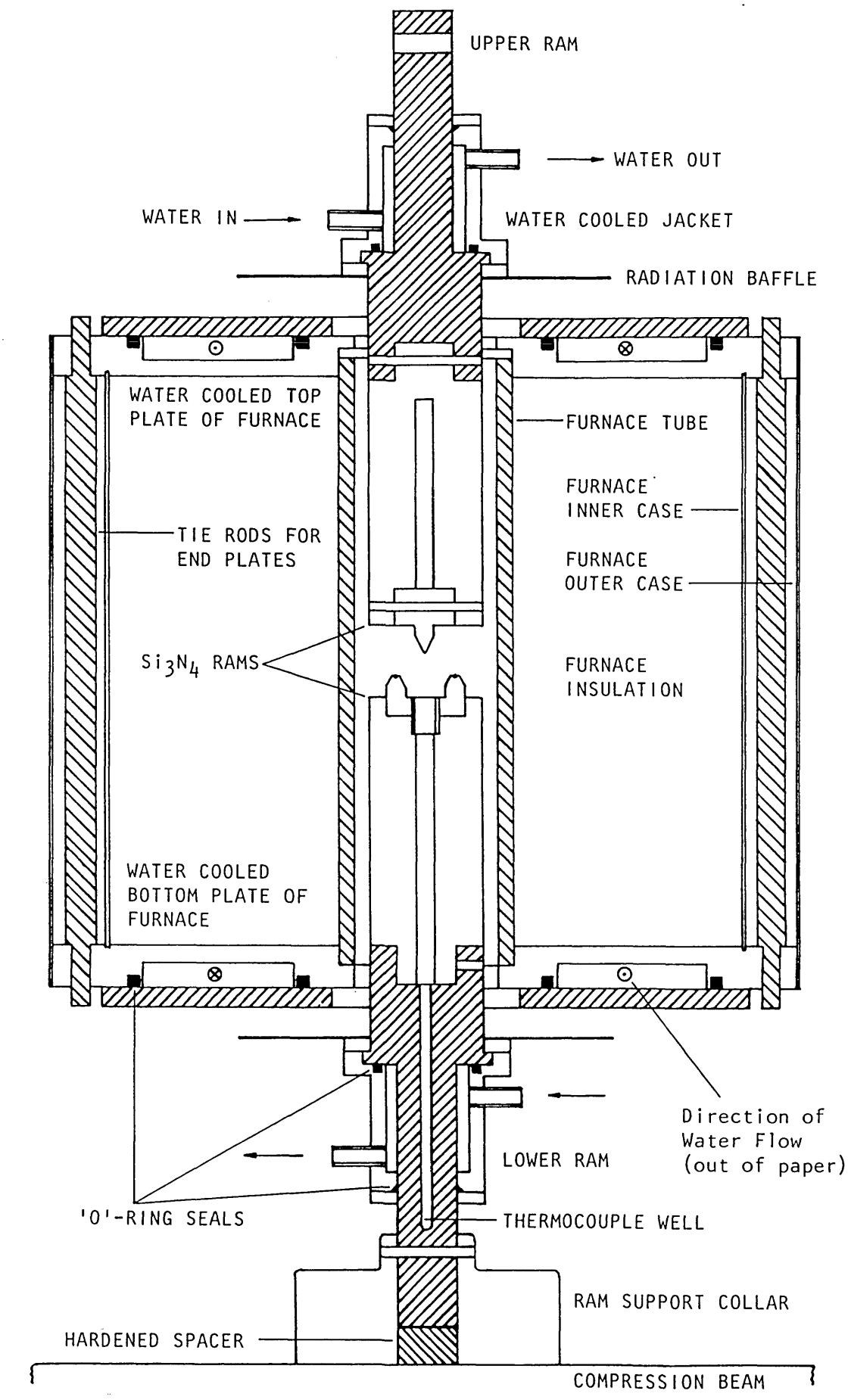


Figure 4.7 Schematic Cross-Section Elevation of the Furnace and Load-Train Assembly.

110°C and the outer case at room temperature,

(e) The temperature control system consisted of three temperature controllers; a master controller with a 15A external thyristor and a digital temperature display (Newtronic Micro 96T) to control the hot-zone temperature, and a differential slave controller, with an internal 15A thyristor, a digital setpoint and an analogue setpoint error display (Newtronic Series 96), for each end-zone. All three controllers were phase angle, 3 term P+I+D units with a user variable current limit and operated with type R, i.e., Pt/13%Rh-Pt thermocouples. The master controller had a temperature range of 0 to 1700°C with automatic cold junction compensation and gave a continuous display of the thermocouple temperature and the setpoint error; the slave controllers had a range of ± 99°C and being differential controllers, required no cold junction compensation.

The slave controllers were set to maintain a + 20°C temperature differential between the reference thermocouple temperature and the slave thermocouple temperatures at all times. Five thermocouples were used to control the temperature as discussed below:

(i) Two thermocouples were placed together about 1 to 2 mm below the tensile face of the specimen in the central thermocouple well of the bottom ram; one was the master thermocouple connected to the master controller and the other was the reference thermocouple for the slave controllers.

(ii) Another thermocouple pair was situated in the horizontal plane of the specimen, adjacent to the inner wall of the furnace tube; one thermocouple of this pair was switched in circuit (via a gold-plated contact, D.P.D.T make-before-break toggle switch) when the furnace was lifted clear of the bottom ram to act as the master thermocouple. The other thermocouple was a spare. When the furnace enclosed the bottom ram prior to a test run the master thermocouple in the bottom ram was switched in; the purpose of switching the master thermocouples was to prevent the centre winding overheating without having to reduce the setpoint temperature or the current limit of

the master controller; the centre winding would overheat if the master thermocouple in the bottom ram was in circuit when the furnace tube was clear of the bottom ram. Another related point concerning the furnace tube winding, is that practical considerations made it necessary for the top and the centre windings to have a common neutral and hence the same single phase power supply was required for all the controllers and thyristors on both safety and electrical grounds.

(iii) A slave thermocouple was placed adjacent to the inner wall of the furnace tube level with each end of the hot-zone winding. Furthermore, thermocouple compensating cable was used for the thermocouple circuit connections wherever feasible; the thermocouple circuit diagram is shown in Figure 4.8.

Both rams had a reflective 3 mm thick, circular (200 mm diameter) HS30 aluminium alloy radiation baffle screwed to their respective water jackets; the purpose of the baffle on the upper ram was to reduce the amount of radiant heat impinging on the load cell and keep it at ambient temperature. An annular disc of "Triton" kaowool blanket rested on the bottom baffle; the geometry of the furnace and the bottom ram had been designed so that when the furnace was standing on the compression beam under its own weight (i.e., free standing) the horizontal centre of the hot-zone was coplanar with the specimen, and the kaowool blanket disc compressed sufficiently to seal the bottom of the furnace tube, essentially stopping the thermal convection currents which would have prevented the attainment of thermal equilibrium at the set temperature. No kaowool packing was used at the top end of the furnace tube because it was found that it produced a frictional force of about 2 to 4 N on the upper ram. The absence of convection currents enabled the displayed temperature of the master thermocouple to remain constant to within ± 1°C for at least the duration of a test, i.e., a few minutes and to within ± 2°C over longer periods; it was estimated from temperature measurements in the specimen plane at the ram diameter (= 60 mm; cf. ≈76 mm tube I.D.) that the

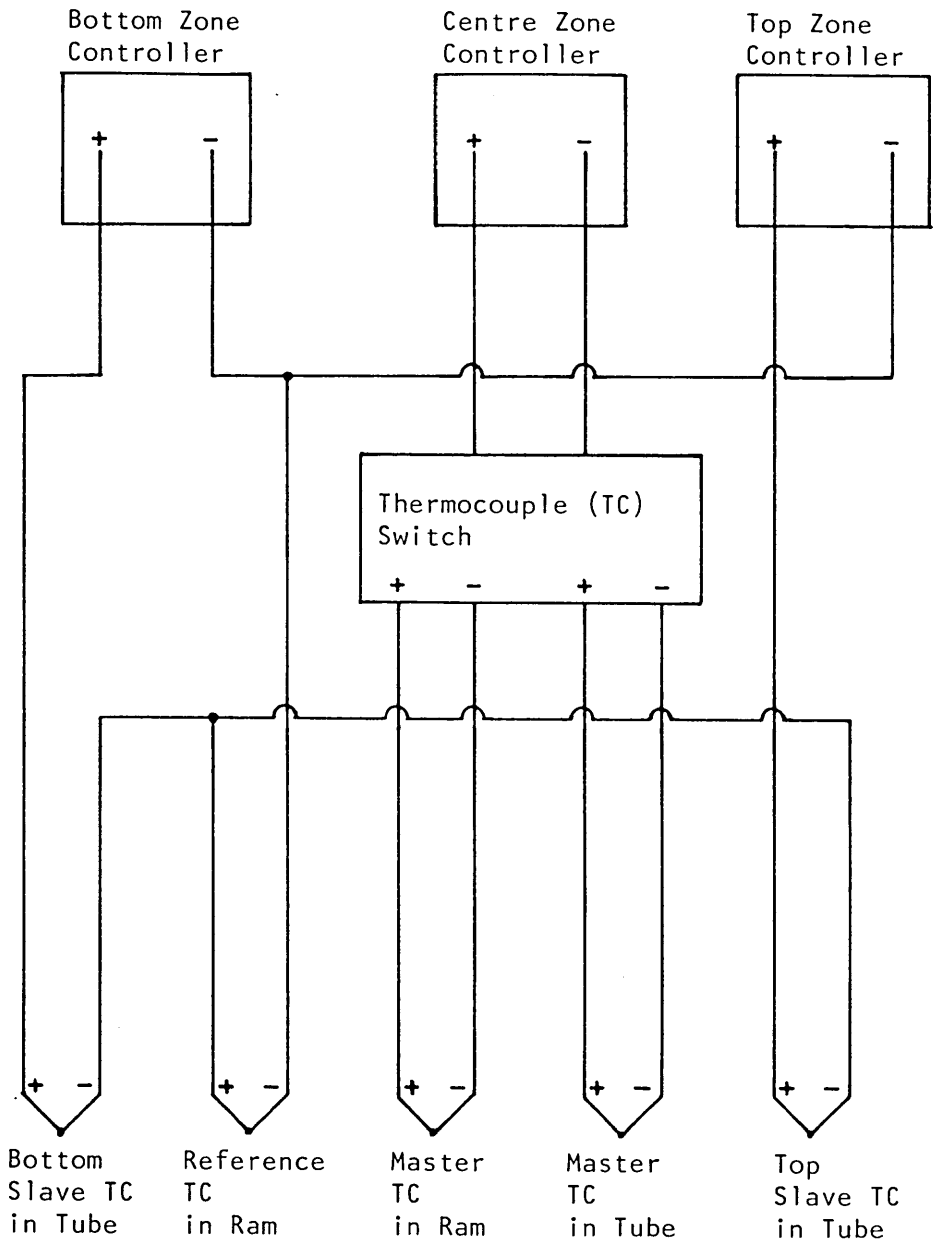


Figure 4.8 Schematic Thermocouple Circuit Design (after G.A. Cotton of Newtronic Controls, private communication, 1984).

temperature difference between the centre and diametral edge of the ram was < 7°C after the setpoint was reached,

(f) The pressure switch was connected in series with the power supply to the temperature controllers (as opposed to that to the furnace via the thyristors) giving the furnace a number of operational modes:

1. If there was no cooling water the pressure switch cut out and the furnace could not be operated.
2. The switch diaphram spring was briefly heated to red heat to increase its ductility and give the pressure switch a sufficiently wide switching hysteresis; in practice a water supply pressure of ≈ 0.07 MPa was required to make the circuit while a pressure of < ≈ 0.02 MPa broke the circuit. So initially a water pressure of > 0.07 MPa (i.e., > 10 p.s.i.) was used to make the circuit and then the pressure was reduced to just > 0.02 MPa (i.e., ≈ 3 p.s.i.) by partially closing the water supply stopcock. Thus the pressure switch operated in a failsafe manner when the water pressure dropped below ≈ 0.02 MPa.
3. A further safeguard was provided by the master controller which was configured so that in the event of a power failure, it could only be switched on again via a manual reset switch, and although the slave controllers operated automatically on power recovery, they were controlled by the hot-zone temperature and hence essentially by the master controller.

(g) The specimen was loaded by a silicon nitride knife-edge block attached to the ceramic section of the upper ram by a silicon nitride locking pin; this block could swivel slightly about the pin axis which was parallel to the long edge of the specimen. The knife-edge itself has a rounded edge profile which was polished on a 6μm diamond lap to reduce frictional effects. The specimen was supported on a silicon nitride support span block located on the top of the ceramic section of the bottom ram by a silicon nitride annular locking pin which slotted into the thermocouple well (see Figure 4.7). There were two such blocks; one block had knife-edges like that of the loading block and the other had two U-shaped channels

in place of the knife-edges which accommodated 2.5 mm diameter alumina rollers with a generous clearance fit.

The alumina roller block was used after one of the the knife-edges of the other block was damaged; the mean room temperature fracture strength obtained using it was different to that obtained using the other block. Both produced mean values at room temperature which were different to those obtained using the tungsten carbide roller room temperature rig. The differences were not unexpected, for a number of reasons; (i) only 8 tests were conducted at room temperature using the alumina roller block and only 2 using the silicon nitride knife-edge block, compared to 20 at the same cross-head speed on the tungsten carbide roller rig, (ii) the friction, wedging and twisting force magnitudes were probably different for each rig configuration, and (iii) the two load-trains will have had different stiffnesses; this may have affected the effective specimen loading time at a given cross-head speed. These factors would result in a different scatter of fracture stress data for each system, and only a large number of tests, e.g., 50 to 100, would give a reliable indication of any significant difference in the fracture strength distributions obtained from each rig.

(h) The dimension of both support blocks parallel to the compressive face of the specimen was 32 mm, which equalled the chosen nominal support span; this facilitated the parallel alignment of the loading knife-edge and the specimen supports, prior to attaching the furnace to its lifting plate. The ceramic section of the bottom ram was free to rotate in the recess in the steel section of the ram and enabled its accurate alignment with the upper ram; when the support block was properly aligned with the loading knife-edge, location marks were made at the junction of the steel and ceramic ram sections. After the furnace was attached to the lifting plate, the lower ceramic section was relocated in the lower steel section and the location marks matched-up; the ceramic section was then fixed in position by screwing in the ball-bearing tipped grub screw situated in the recess wall of the steel

section until the ball just touched the stub locating the ceramic section in the recess (See Figure 4.7).

(3) Room temperature compression test rig

The rig used for the room temperature flexural strength tests was also used to determine the compressive strength of the right cylindrical SCR25.76 and SCR19.34 glass-ceramic specimens; the three-point loading and support rig were replaced by polished, hardened steel compression platens and the rig placed on another Instron with a 5000 kgf tensile load cell.

4.9.2 Preparation procedure for strength test specimens

(1) Flexural strength specimens:

Tablets of nominal size 80 mm x 50 mm were cut from gravity cast tiles of the four glass-ceramics to produce test specimens; the tablets had a varying thickness (≈ 10 to 15 mm) along the long side. The tablets of SCR25.76 and SCR19.34 were ground parallel to within ≈ ± 0.025 mm and to a nominal thickness of 8 mm using a Jones and Shipman 540P surface grinding machine with a medium grit peripheral diamond abrasive wheel; each tablet was ground by mounting it on a 200 x 130 x 12 mm^3 precision-ground mild steel plate with "Lakeside" temporary cement and then mounting the plate on the magnetic chuck of the machine. The SCF5 and SCR19.13 tablets had been ground and cut into specimens on inferior equipment prior to having access to the Jones and Shipman machine and hence the dimensional uniformity of the SCR19.13 specimens was within ≈ ± 0.1 mm while that of the SCF5 specimens was within ≈ ± 0.3 mm; thus the procedure described below for the tablets of SCR25.76 and SCR19.34 was applied to the individual specimens.

The ground faces of the SCR25.76 and SCR19.34 tablets were then abraded using a water based slurry of 1000-grit SiC abrasive powder on a flat glass plate, to

remove any machining damage. The grinding was done carefully to prevent the parallelism of the faces being destroyed. One face, which was to be the tensile face of the individual specimens, was then polished for about 1 to 2 hours using a 14μm diamond polishing compound on a rotary polishing wheel. The tablets were then cut into individual specimens with nominal dimensions of 40 x 8 x 4 mm^3, using a fine grit diamond slitting disc on the Jones and Shipman machine; prior to cutting the tablets were mounted, using "Lakeside" temporary cement, on a 6 mm thick float glass plate which was mounted on a similar steel plate to that used for the grinding with "Lakeside" thermoplastic cement to prevent the slitting disc cutting into the metal plate. The longitudinal edges of the specimens were then carefully given a rounded profile by manual grinding on 800-grit and then 1000-grit SiC abrasive paper on a rotary pre-grinder. The tensile face and the rounded edges were then manually polished on a 6μm diamond lap on a rotary polishing machine. The specimens were given a final sonic cleaning in an ultrasonic bath and carefully stored prior to being tested.

(2) Compressive strength specimens:

The right cylindrical specimens of SCR25.76 and SCR19.34 used for the compressive strength tests were cut from similar size tablets to those described above which were ground parallel to within ± 0.025 mm and to a nominal thickness of 10 mm using the Jones and Shipman machine; the machining damage was removed in the manner described above using 1000-grit SiC abrasive powder. Thin glass sheets were then glued to the ground faces using "Lakeside" temporary cement to reduce the occurrence of "oyster shell chipping" around the edge of the end-faces. The specimens were the drill cores produced by an 8 mm internal diameter electroplated diamond core drill, and had nominal dimensions of 10 mm high by 7 mm diameter.

4.9.3 Experimental flexural and compressive strength results at room temperature

The room temperature three-point bending flexural strength data for SCR25.76 and SCR19.34 will be considered first; all the relevant data for all the test specimens of these two materials are tabulated in Appendix 4C. The key to the table headings is given below:

(a) TEST #. refers to the identification code of the test specimen,

(b) B and W are the specimen breadth and width respectively in mm; the values quoted are the mean of three measurements accurate to ± 0.001 mm made along its length at the mid-span and support positions (± s/2),

(c) P is the load required to fracture the specimen in newtons rounded to the nearest newton, and x is the distance, measured to the nearest 0.5 mm, between the fracture line on the tensile face and that on the compressive face of the specimen which defines the position of the central load, i.e., the mid-span position,

(d) t is the time to failure in seconds, measured to the nearest second from the load - displacement record,

(e) the β-value is that used to account for the effect of "wedging" as determined from the x/W value (See Section 4.4.2, part (vi)),

(f) S1 is the flexural strength calculated using the standard equation [4.23] which takes no account of "wedging" nor fracture away from the mid-span,

(g) S2 is the flexural strength calculated using equation [4.24] which accounts for "wedging" but not fracture away from the mid-span,

(h) S3 is the flexural strength calculated using equation [4.25] which accounts for fracture away from the mid-span, but not "wedging", and

(i) S4 is the flexural strength calculated using equation [4.26] which accounts for both "wedging" and fracture away from the mid-span.

All strength values were rounded to the nearest 0.1 MPa and measured at 20 ± 4°C in air at normal humidity.

Table 4C.2 in Appendix 4C lists the data obtained on the high temperature rig; these data will not be considered here, but in the section on the temperature dependence of the flexural strength.

(1) Effect of the equation used to calculate fracture stress on the calculated mean flexural strength:

The mean flexural strength, the sample standard deviation and the coefficient of variation, which is defined as the quotient of the sample standard deviation and the sample mean, are tabulated in Tables 4.2, 4.3 and 4.4 for SCR25.76 and SCR19.34. The data show that the standard equation [4.23] overestimates the mean strength of SCR25.76 by between ≈ 5 and 9 % compared to equation [4.26], depending on the strain-rate. Similarly, the mean strength of SCR19.34 is overestimated by between ≈ 6 and and 10 %. It is interesting to note that the mean position of fracture for SCR25.76 was a distance of 2 mm from the mid-span to the nearest mm, compared with 1 mm for SCR19.34.

The maximum possible error due to wedging arises when fracture occurs at the mid-span, in which case it is a negative error, i.e., neglecting its effect results in the flexural strength being overestimated by just over 4 % for s/W = 4; the error increases as s/W decreases. When fracture occurs away from the mid-span, the maximum error due to wedging occurs at a distance of W/4 from the mid-span and is positive; thus for s/W = 4 the flexural strength may be underestimated by up to ≈ 3 %. If fracture occurs at this position and the standard equation is used, the flexural strength for s/W = 4 will be overestimated by ≈ 10 %. So the greatest error arises in assuming that fracture occurs at the mid-span which is generally not the case. Since it is easy to take account of both wedging and fracture at the tensile face away from the mid-span by using equation [4.26] it is difficult to justify the continued use of the standard bending stress equation as it invariably overestimates the flexural strength.

Table 4.2 Summary of Room Temperature Flexural Strength Data for SCR25.76 and SCR19.34 from 20 Data at a Mean Strain-Rate of 7.45 x 10^{-4} s^{-1}:

Strength Parameter	Mean Value (MPa)	Stand. Dev. (MPa)	Coeff. Var. (%)
	Data for SCR25.76		
S1	117.6	10.4	9
S2	112.6	10.0	9
S3	105.5	11.4	11
S4	107.9	11.3	10
	Data for SCR19.34		
S1	120.7	9.2	8
S2	115.5	8.8	8
S3	114.0	9.6	8
S4	114.2	9.0	8

Table 4.3 Summary of Room Temperature Flexural Strength Data for SCR25.76 and SCR19.34 from 10 Data at a Mean Strain-Rate of 7.45 x 10^{-3} s^{-1}:

Strength Parameter	Mean Value (MPa)	Stand. Dev. (MPa)	Coeff. Var. (%)
	Data for SCR25.76		
S1	140.8	7.0	5
S2	134.8	6.8	5
S3	129.8	8.5	7
S4	132.0	7.8	6
	Data for SCR19.34		
S1	137.2	11.6	8
S2	131.4	11.2	9
S3	124.1	12.6	10
S4	124.6	11.9	10

Table 4.4 Summary of Room Temperature Flexural Strength Data for SCR25.76 and SCR19.34 from 10 Data at a Mean Strain-Rate of 7.45 x 10^{-5} s^{-1}:

Strength Parameter	Mean Value (MPa)	Stand. Dev. (MPa)	Coeff. Var. (%)
	Data for SCR25.76		
S1	110.6	9.4	8
S2	106.0	9.0	8
S3	104.6	6.9	7
S4	105.2	8.2	8
	Data for SCR19.34		
S1	110.8	7.3	7
S2	106.1	7.0	7
S3	101.1	9.1	9
S4	102.7	8.8	9

(2) Effect of strain-rate on the mean flexural strength of SCR25.76 and SCR19.34:

The flexural strength data in Tables 4.2, 4.3 and 4.4 demonstrates that the measured flexural strength of a specimen as represented by the mean flexural strength increases with increasing strain-rate. The mean flexural strength of SCR25.76 and SCR19.34 increased by approximately 20 % for a two orders of magnitude increase in strain-rate; note that the increase was non-linear. The lower the strain-rate, the slower the increase in the stress intensity factor of the critical flaw in a specimen as a function of increasing stress; hence the greater the degree of environmentally determined slow growth of the flaw prior to catastrophic fracture. As a consequence the stress required to cause fracture from the flaw decreases as the strain-rate decreases.

(3) Comparison of the mean flexural strengths of SCR25.76, SCR19.34, SCF5 and SCR19.13 measured at a strain-rate of $\approx 7.5 \times 10^{-4}\ s^{-1}$ and calculated taking account of wedging and fracture origin:

It is instructive to compare the mean flexural strengths of the four materials, but the comparison is in no sense absolute because (i) the strength values calculated using a given fracture stress equation depend on the actual surface finish of the specimens, the fracture load which is influenced by the frictional and twisting forces which are characteristics of the test rig used, and the environment at the time of testing for specimens of a similar nominal size and surface finish tested by the same technique at a given strain-rate, and (ii) the mean strength of a given material depends on the number of specimens tested, becoming more representative of the true strength as characterised by the given method as the number tested increases. So even greater care should be taken when comparing the three-point bending flexural strengths of materials from different literature sources.

The mean values are summarized below:

Material	Flexural Strength (MPa)	Residual Glass (Av. Volume %)
SCF5 *	185	18
SCR19.34	114	42
SCR25.76	108	29
SCR19.13 *	80	71

(* see Appendix 4D and Table 4.5)

The fact that the mean strengths do not correlate with the average volume fractions of residual glass, except at the extremes when the effect of the amount of glass is either dominant or insignificant, emphasises the importance of microstructure in determining the mechanical properties of a material. A comparison of the SEM micrographs of the typical microstructures of the four materials shown in Figure 2.1 of Chapter 2 and the corresponding micro-structural descriptions given in the text shows that the increasingly discrete nature of the pyroxene crystal morphology, from the essentially continuous, highly dendritic crystal skeleton of the highly crystallized SCF5 glass-ceramic to the barely crystalline SCR19.13 "glass-ceramic" via the SCR19.34 and SCR25.76 materials correlates with the apparent decrease in their mean flexural strengths.

(4) Crack propagation and branching patterns of SCR25.76, SCR19.34, SCF5 and SCR19.13 and the representative fracture surfaces of flexural strength test specimens SCR19.34 MB401 and SCR25.76 MA401:

The generalized crack propagation patterns observed in the strength test specimens at both room and elevated temperatures are shown schematically in Figure 4.9, where the specimens are shown in elevation with the tensile face at the bottom and the dotted line denotes the vertical mid-span plane. The most frequently observed pattern was (a), which was typically observed in the weaker specimens. Patterns (c) and (d) were usually seen in the specimens

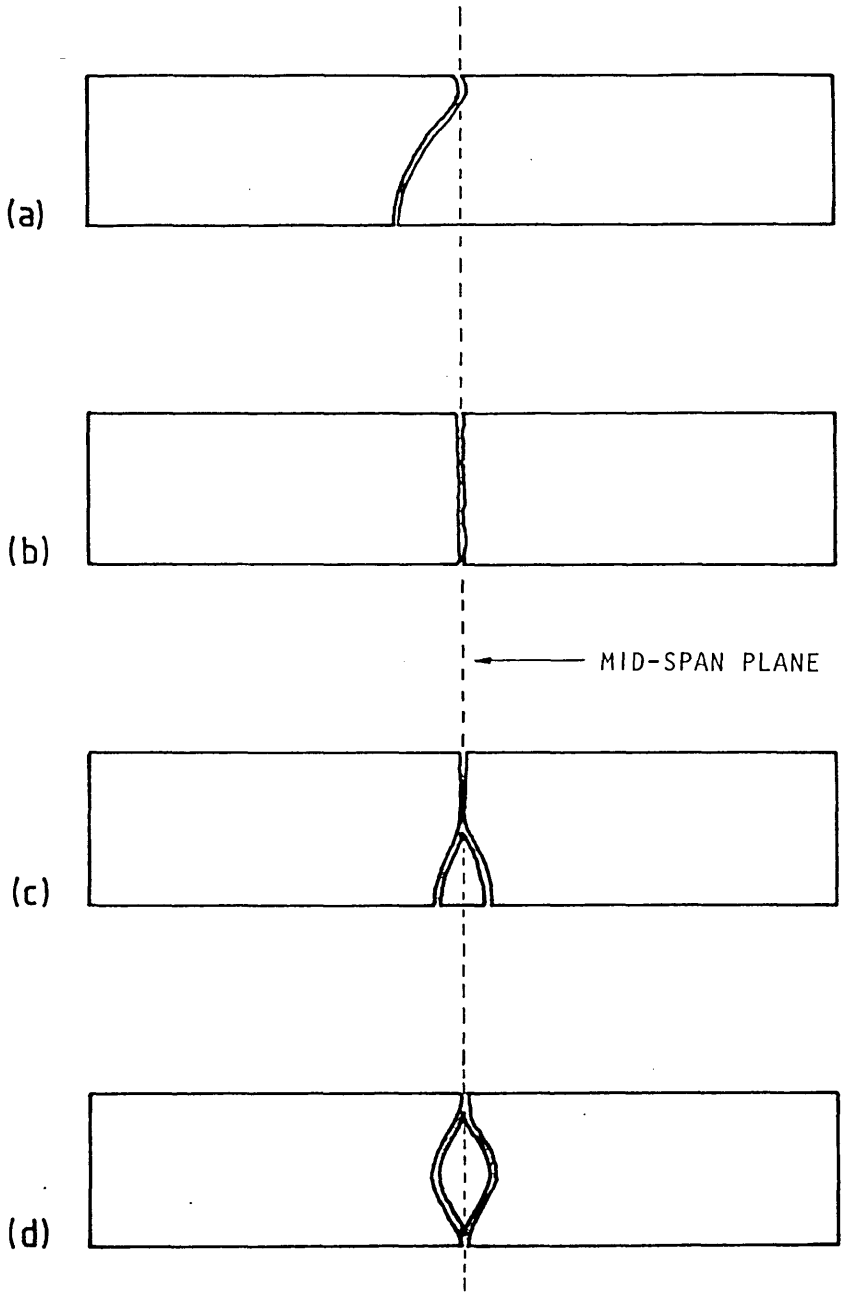


Figure 4.9 Schematic Elevations of Flexural Strength Test Specimens With Their Tensile Faces at the Bottom, Showing the Various Crack Propagation Patterns Observed.

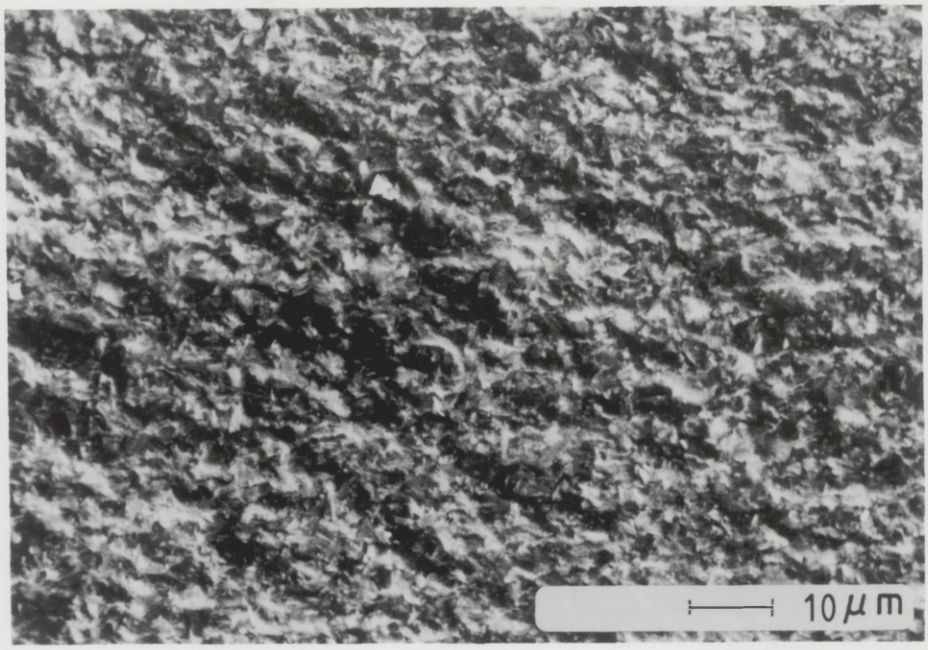
with the highest overall fracture stresses, particularly the SCR19.34 and SCF5 specimens.

It was observed that the macroscopic "visual roughness" of the fracture surfaces of the specimens appeared to increase as their fracture stresses increased. Figure 4.10 (a) shows two SEM micrographs of the typical nature of the fracture surface of SCR19.34 specimen MB401, while Figure 4.10 (b) shows two SEM micrographs of the typical nature of the fracture surface of SCR25.76 specimen MA401. Both specimens were tested to fracture at room temperature using a cross-head speed of 1 mm/minute (See Appendix 4C, Table 4C.2); the micrographs were taken on a JEOL JSM-35 SEM.

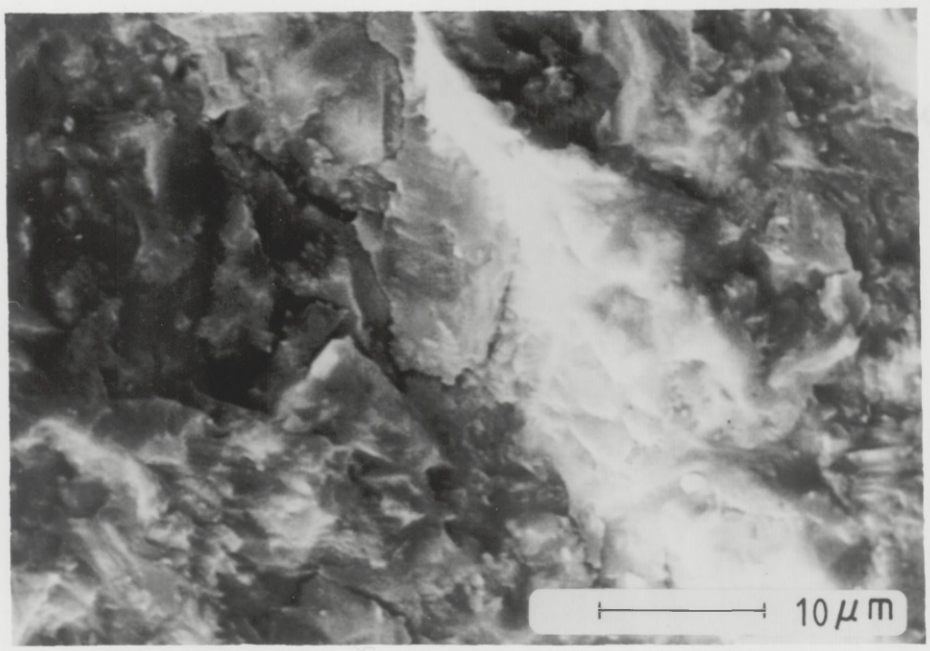
The micrographs show that the fracture is inter-granular; those at x500 magnification illustrate the some-what finer microstructure of the SCR19.34 material in comparison to the SCR25.76 material. The micrograph of MB401 at x2000 shows some evidence of the dendritic nature of the pyroxene crystals and intergranular cracking, while the micrograph of MA401 at x3600 shows the pyroxene crystals in SCR25.76 to be more rounded, i.e., less angular than those in SCR19.34.

(5) Mean compressive strength data for SCR25.76 and SCR19.34:

The compressive strength specimen dimensions, fracture loads and fracture stresses are tabulated in Table 4.6, while the mean compressive strength, the sample standard deviation and the coefficient of variation are tabulated in Table 4.7. The mean compressive strengths are about 5 to 10 times greater than the flexural strengths, while the mean strength of SCR19.34 is noticeably lower than that of SCR25.76, the greater scatter of data notwithstanding. The difference is tentatively attributed to the greater volume of residual glass in, and, in anticipation of the data in Chapter 5, the lower fracture toughness of SCR19.34. The specimens fractured explosively into needle-like fragments, leaving some fine powder between the platens.

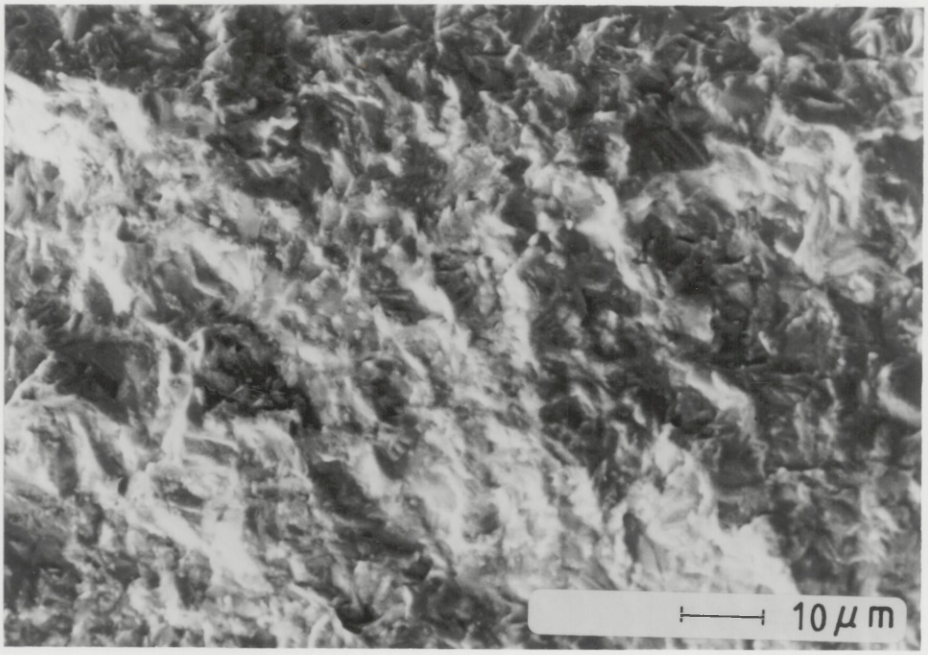


20 kV x500

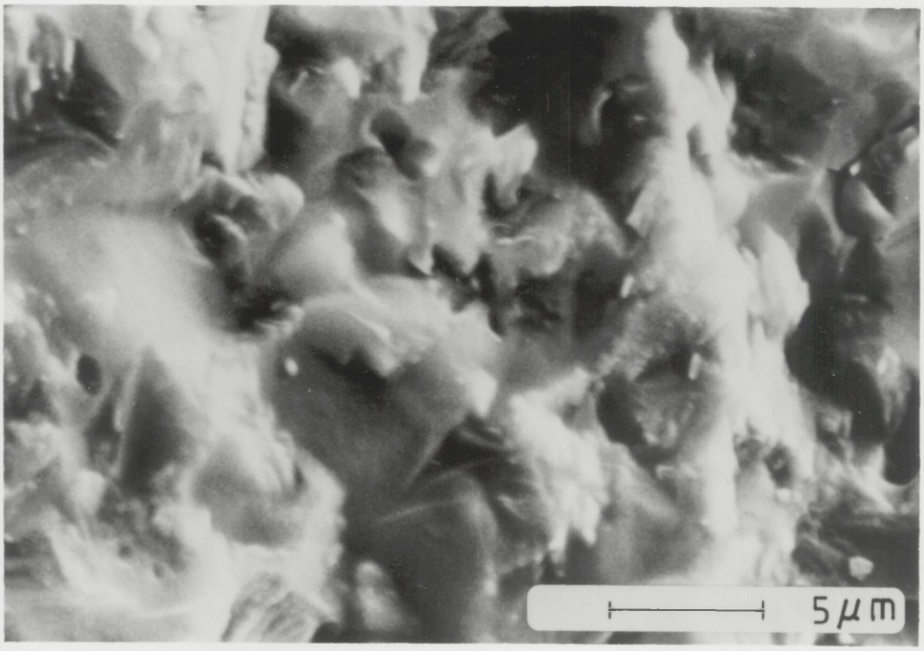


20 kV x2000

Figure 4.10 (a) Scanning Electron Microscope (JEOL JSM-35) Micrographs of the Fracture Surface of SCR19.34 Room Temperature Flexural Strength Test Specimen MB401.



20 kV x500



20 kV x3600

Figure 4.10 (b) Scanning Electron Microscope (JEOL JSM-35) Micrographs of the Fracture Surface of SCR25.76 Room Temperature Flexural Strength Test Specimen MA401.

Table 4.5 Summary of Room Temperature Flexural Strength Data for SCF5 and SCR19.13 at a Mean Strain-Rate of 7.55 x 10^{-4} s^{-1}:

Strength Parameter	Mean Value (MPa)	Stand. Dev. (MPa)	Coeff. Var. (%)
	Data for SCF5 from 4 data		
S1	205.1	37.4	18
S2	196.3	35.4	18
S3	179.3	44.5	25
S4	184.5	46.7	25
	Data for SCR19.13 from 5 data		
S1	88.9	5.2	6
S2	85.0	5.0	6
S3	79.7	5.8	7
S4	79.7	3.7	5

The SCF5 data were determined using the high temperature three-point bending rig with the alumina roller supports. The SCR19.13 data was determined using the room temperature three-point bending rig.

Table 4.6 Uniaxial Compressive Strength Test Data for SCR25.76 and SCR19.34 at Room Temperature:

Specimen Number	Height (mm)	Diameter (mm)	Fracture Load (N)	Fracture Stress (MPa)
	Data for SCR25.76			
1	10.008	6.815	38793	1063
2	10.004	6.794	40215	1109
3	10.012	6.819	40723	1115
4	10.010	6.812	37778	1037
5	10.002	6.787	33411	924
	Data for SCR19.34			
1	10.023	6.809	19904	547
2	10.030	6.820	44886	1229
3	10.006	6.795	20615	568
4	10.003	6.796	18787	518
5	10.027	6.817	28029	768

The above data were determined at a cross-head speed of 1.66. x 10^{-5} ms^{-1} without any packing or lubrication between the specimen ends and the compression platens. The diameter is the mean of the top, centre and bottom diameters measured to ± 0.001 mm.

Table 4.7 Summary of Uniaxial Compressive Strength Data for SCR25.76 and SCR19.34:

Material	Mean Value (MPa)	Stand. Dev. (MPa)	Coeff. Var. (%)
SCR25.76	1050	77	7
SCR19.34	726	298	41

4.9.4 Room temperature Weibull modulus data assuming a threshold stress of zero

The room temperature Weibull modulus was determined for the SCR25.76 and SCR19.34 glass-ceramics by conducting "least-squares" linear regression analyses of the "linearized" survival probability and fracture stress data obtained from the tests performed at the three strain-rates. The Weibull moduli for the 20 data obtained for each material at a cross-head speed of 1 mm/minute (corresponding to a strain-rate of 7.45×10^{-4} s^{-1}) were estimated using the survival probabilities estimated from the four common survival probability functions (See Section 4.6) and fracture stresses calculated from equations [4.23], [4.24], [4.25] and [4.26], which are denoted by S1, S2, S3 and S4 respectively. The regression data generated are tabulated in Appendix 4E in Table 4E.1. For the samples of 10 data obtained at the other strain-rates, only the S1 and S4 fracture stress data were used with the four survival probability estimators; the regression data are tabulated in Tables 4E.2 and 4E.3 of Appendix 4E. For each material, the Weibull modulus (m), the standard deviation of m, the Pearson correlation coefficient (r), the more meaningful coefficient of determination (r^2), the intercept I, the standard deviation of I, and the standard error of m are tabulated against a given fracture stress parameter (S) and survival probability estimator (P_s).

The linear regression model assumes that the distribution of y values for a given x value is normal and that the variance of the y distribution for any x value is constant, i.e., is independent of x. Hence the variances of the parameters A and B of the estimated regression line $Y = A + Bx$, V(A) and V(B) are (Chatfield, C., 1983)

$$V(A) = R\Sigma x^2/(n\Sigma x^2 - (\Sigma x)^2) \qquad [4.98]$$

$$V(B) = Rn/(n\Sigma x^2 - (\Sigma x)^2) \qquad [4.99]$$

where n is the number of data and R is the estimate of the residual variance and given by $[\Sigma(y - [A + Bx])^2]/[n - 2]$. The standard deviations are thus $[V(A)]^{1/2}$ and $[V(B)]^{1/2}$.

The standard deviations of A and B are thus $[V(A)]^{1/2}$ and $[V(B)]^{1/2}$ respectively. The standard deviations of m and the intercept I were obtained by substituting $\ln\sigma$ for x and $\ln\ln(1/P_s)$ for y in the above equations. The coefficient of determination is the ratio of the explainable variation, i.e., the variation in $\ln\ln(1/P_s)$ explained by the estimated regression equation, to the total variation in $\ln\ln(1/P_s)$ and for linear regression equals the square of the Pearson correlation coefficient. The standard error of m is defined as $m/(2n)^{1/2}$ assuming m is normally distributed (Fessler, H., et al., 1983).

The results in Appendix 4E are interesting in a number of ways:

(a) For a given flexural strength parameter, e.g., S1, the estimated Weibull modulus increases in the following order with the survival probability estimator used,

1. $P_s = 1 - j/(n + 1)$; mean rank estimator
2. $P_s = 1 - (j - 0.3)/(n + 0.4)$; median rank estimator
3. $P_s = 1 - (j - 3/8)/(n + 1/4)$
4. $P_s = 1 - (j - 0.5)/n$.

(b) Considering the results in Table 4E.1 for 20 fracture stress data (the minimum recommended number for a reliable Weibull modulus value) indicates that using the S4 data (which are corrected for wedging and fracture away from the mid-span) for the SCR25.76 specimens, which on average fractured at a distance of ≈ 2 mm from the mid-span, as opposed to the standard S1 data reduced the Weibull modulus by a nominal 15 % for all the probability estimators, and reduced its standard deviation in the order of the probability estimators given above, by ≈ 37 %, 42 %, 43 % and 47 % respectively. In contrast, the use of S4 instead of S1 for the SCR19.34 specimens, which fractured at ≈ 1 mm from the mid-span on average, reduced the Weibull modulus by only ≈ 5 % for all the probability estimators and had no effect on its standard deviation for any of the estimators.

(c) Correcting only for the effect of wedging (for both glass-ceramics) had no effect on the estimated Weibull moduli nor on their standard deviations.

The room temperature Weibull modulus values obtained from the test data determined at the three strain-rates are tabulated against the four flexural strength parameters and the four survival probability estimators in Table 4.8; the mean Weibull modulus is given for each strength parameter. Note that while the mean Weibull modulus for S4 is lower than for S1 for both materials at the two higher strain-rates and for SCR19.34 at the lowest strain-rate, the opposite is true for SCR25.76 at the lowest strain-rate. Furthermore, the standard deviations of m for S4 are higher than the corresponding deviations for S1 in the order of the probability estimators given in (b) above, at ≈ 41 %, 31 %, 29 % and 25 % respectively.

Bergman has published some very interesting work on the estimation of the Weibull modulus in a series of recent papers. He used a computer to generate random fracture stresses and sample sets of the fracture stresses selected at random and then analysed the sample data using the standard "least-squares" linear regression technique for different sample sizes below 50 in order to compare the statistical properties of the four survival probability estimators used in the present work (Bergman, B., 1984). Bergman states that only one prescribed Weibull modulus value, m is required to evaluate the bias and standard deviation of the linear "least-squares" estimate of m for all m values and for an unbiased estimate of m, the mean value of the M/m values should be close to unity. $M = (\Sigma m_0)/k$ where k is the number of samples and m_0 is the m value of sample '0' for a given sample size; as the sample size increases the bias in m due to a given survival probability estimator will decrease. His results for sample sizes of 10 and 20 are presented in Table 4.9.

As the experimentally estimated Weibull modulus values may be expected to correspond reasonably well to the statistical mean values of the computer generated random m data, the experimental values can be divided by the appropriate M/m values to produce a corrected m value which is expected to be close to the true m value, i.e., the experimental value can be corrected for the bias

Table 4.8 Room Temperature Weibull Modulus (m) for Zero Threshold Stress as a Function of the Flexural Strength Distribution (represented by the mean strength, S_M) and the Survival Probability Estimator (P_s) for SCR25.76 and SCR25.34:

S_M (MPa)	$P_s(1)$ m	$P_s(2)$ m	$P_s(3)$ m	$P_s(4)$ m	Av. m
		Data for SCR25.76			
S1 = 117.6	11.75	13.43	12.65	12.92	12.69
S2 = 112.6	11.75	13.42	12.64	12.91	12.68
S3 = 105.5	9.66	11.06	10.41	10.63	10.44
S4 = 107.9	9.96	11.40	10.72	10.96	10.76
		Data for SCR19.34			
S1 = 120.7	13.96	15.75	14.92	15.21	14.96
S2 = 115.5	13.96	15.76	14.93	15.22	14.97
S3 = 114.0	12.25	13.90	13.14	13.40	13.17
S4 = 114.2	13.28	15.01	14.22	14.49	14.25

The above data are for the 20 specimens tested at a mean strain-rate of 7.45×10^{-4} s^{-1} (see Table 4.2)

S_M (MPa)	$P_s(1)$ m	$P_s(2)$ m	$P_s(3)$ m	$P_s(4)$ m	Av. m
		Data for SCR25.76			
S1 = 140.8	19.05	23.30	21.27	21.96	21.40
S4 = 132.0	16.51	19.98	18.34	18.90	18.43
		Data for SCR19.34			
S1 = 137.2	11.44	13.77	12.67	13.05	12.73
S4 = 124.6	10.22	12.32	11.33	11.67	11.39

The above data are for the 10 specimens tested at a mean strain-rate of 7.45×10^{-3} s^{-1} (see Table 4.3).

S_M (MPa)	$P_s(1)$ m	$P_s(2)$ m	$P_s(3)$ m	$P_s(4)$ m	Av. m
		Data for SCR25.76			
S1 = 110.6	11.60	13.99	12.86	13.24	12.92
S4 = 105.2	12.47	15.05	13.83	14.25	13.90
		Data for SCR19.34			
S1 = 110.8	14.46	17.75	16.18	16.71	16.28
S4 = 102.7	10.73	13.08	11.96	12.34	12.03

The above data are for the 10 specimens tested at a mean strain-rate of 7.45×10^{-5} s^{-1} (See Table 4.4).
The survival probability esimators used above were:
(1) $P_s = 1 - j/(n + 1)$
(2) $P_s = 1 - (j - 0.5)/n$
(3) $P_s = 1 - (j - 0.3)/(n + 0.4)$
(4) $P_s = 1 - (j - 3/8)/(n + 1/4)$
See Section 4.6.
The Weibull modulus values were determined by the standard "least-squares" linear regression method; the regression parameters are tabulated in Appendix 4E.

Table 4.9 Statistically Estimated Means and Sample Standard Deviations of m for Sample Sizes of 10 and 20 (after B. Bergman, 1984)

Survival Probability Estimator (P_s)	n = 10		n = 20	
	M/m	s/M	M/m	s/M
1-j/(n+1)	0.869	0.333	0.890	0.240
1-(j-0.5)/n	1.062	0.330	1.011	0.230
1-(j-0.3)/(n+0.4)	0.978	0.328	0.963	0.226
1-(j-3/8)/(n+1/4)	1.010	0.332	0.986	0.228

M is the mean and s the sample standard deviation of m_0. The theoretical coefficient of variation of m is $1/(n)^{1/2}$; it is 0.316 for n = 10 and 0.224 for n = 20.

Table 4.10 Experimental (m_E) and Corrected (m_C) Weibull Moduli of SCR25.76 and SCR19.34 S1 and S4 Data

The data below are for the 20 tests at $\dot{\epsilon}$ = 7.45 x 10^{-4} s^{-1}

S_M (MPa)	P_s(1)		P_s(2)		P_s(3)		P_s(4)	
	m_E	m_C	m_E	m_C	m_E	m_C	m_E	m_C
				Data for SCR25.76				
S1=117.6	11.75	13.20	13.43	13.28	12.65	13.14	12.92	13.10
S4=107.9	9.96	11.19	11.40	11.28	10.72	11.13	10.96	11.12
				Data for SCR19.34				
S1=120.7	13.96	15.69	15.75	15.58	14.92	15.49	15.21	15.43
S4=114.2	13.28	14.92	15.01	14.85	14.22	14.77	14.49	14.70

The data below are for the 20 tests at $\dot{\epsilon}$ = 7.45 x 10^{-3} s^{-1}

S_M (MPa)	P_s(1)		P_s(2)		P_s(3)		P_s(4)	
	m_E	m_C	m_E	m_C	m_E	m_C	m_E	m_C
				Data for SCR25.76				
S1=140.8	19.05	21.92	23.30	21.94	21.27	21.75	21.96	21.74
S4=132.0	16.51	19.00	19.98	18.81	18.34	18.75	18.90	18.71
				Data for SCR19.34				
S1=137.2	11.44	13.16	13.77	12.97	12.67	12.96	13.05	12.92
S4=124.6	10.22	11.76	12.32	11.60	11.33	15.58	11.67	11.55

The above data are for the 20 tests at $\dot{\epsilon}$ = 7.45 x 10^{-5} s^{-1}

S_M (MPa)	P_s(1)		P_s(2)		P_s(3)		P_s(4)	
	m_E	m_C	m_E	m_C	m_E	m_C	m_E	m_C
				Data for SCR25.76				
S1=110.6	11.60	13.35	13.99	13.17	12.86	13.15	13.24	13.11
S4=105.2	12.47	14.35	15.05	14.17	13.83	14.14	14.25	14.11
				Data for SCR19.34				
S1=110.8	14.46	16.64	17.75	16.71	16.18	16.54	16.71	16.54
S4=102.7	10.73	12.35	13.08	12.32	11.96	12.23	12.34	12.22

arising from a particular survival probability estimator. The Weibull modulus values for S1 and S4 of SCR25.76 and SCR19.34 given in Table 4.8 were corrected for bias using Bergman's results in Table 4.9; they are tabulated with the corrected values in Table 4.10; the key to $P_s(1)$, etc. is given in Table 4.8. Bergman's simulated data showed that for sample sizes ≥ 20 the bias of the m estimate decreases with the survival probability estimator used in the following order:

1. $P_s = 1 - j/(n + 1)$
2. $P_s = 1 - (j - 0.3)/(n + 0.4)$
3. $P_s = 1 - (j - 3/8)/(n + 1/4)$
4. $P_s = 1 - (j - 0.5)/n$

For smaller sample sizes, e.g., 10, the order of decreasing bias becomes:

1. $P_s = 1 - j/(n + 1)$
2. $P_s = 1 - (j - 0.5)/n$
3. $P_s = 1 - (j - 0.3)/(n + 0.4)$
4. $P_s = 1 - (j - 3/8)/(n + 1/4)$

The differences between the experimental Weibull modulus values (m_E) and corrected Weibull modlus values (m_C) given in Table 4.10 are tabulated for S1 and S4 of SCR25.76 and SCR19.34 in Table 4.11; the key to $P_s(\ )$ is given in Table 4.8 and the difference is denoted by Δm. The differences reflect the relative bias of the different estimators.

So the preferred estimator for sample sizes of ≥ 20 is $P_s = 1 - (j - 0.5)/n$, while for sample sizes of < 20 $P_s = 1 - (j - 3/8)/(n + 1/4)$ is preferred. The mean rank value estimator $P_s = 1 - j/(n + 1)$ is presently the most popular, but it produces the most biased m values. It may still, however, be preferable for engineering survival prediction since it gives the lowest survival probability at low stresses, i.e., a conservative probability.

In response to the computer simulations of Bergman, the biasing properties of these four survival probability estimators have been investigated using real experimental data (Sullivan, J.D., and Lauzon, P.H., 1986a). Rather than prescribing the m and σ_o values, these parameters were estimated for the fracture stress population of 2

Table 4.11 Difference (Δm) Between the Experimental (m_E) and Corrected (m_C) Weibull Moduli of SCR25.76 and SCR19.34 S1 and S4 Data

The data below are for the 20 tests at $\dot{\epsilon}$ = 7.45 x 10^{-4} s^{-1}

S_M (MPa)	$P_s(1)$ Δm	$P_s(2)$ Δm	$P_s(3)$ Δm	$P_s(4)$ Δm
	Data for SCR25.76			
S1 = 117.6	1.45	0.15	0.49	0.18
S4 = 107.9	1.23	0.12	0.41	0.16
	Data for SCR19.34			
S1 = 120.7	1.73	0.17	0.57	0.22
S4 = 114.2	1.64	0.16	0.55	0.21

The data below are for the 10 tests at $\dot{\epsilon}$ = 7.45 x 10^{-3} s^{-1}

S_M (MPa)	$P_s(1)$ Δm	$P_s(2)$ Δm	$P_s(3)$ Δm	$P_s(4)$ Δm
	Data for SCR25.76			
S1 = 140.8	2.87	1.36	0.48	0.22
S4 = 132.0	2.49	1.17	0.47	0.19
	Data for SCR19.34			
S1 = 137.2	1.72	0.80	0.29	0.13
S4 = 124.6	1.54	0.72	0.27	0.12

The data below are for the 20 tests at $\dot{\epsilon}$ = 7.45 x 10^{-5} s^{-1}

S_M (MPa)	$P_s(1)$ Δm	$P_s(2)$ Δm	$P_s(3)$ Δm	$P_s(4)$ Δm
	Data for SCR25.76			
S1 = 110.6	1.75	0.82	0.29	0.13
S4 = 105.2	1.88	0.88	0.31	0.14
	Data for SCR19.34			
S1 = 110.8	2.18	1.04	0.36	0.17
S4 = 102.7	1.62	0.76	0.27	0.12

mol% yttria fully tetragonal zirconia specimens by testing a set of 100 specimens to fracture at room temperature under four-point bending. Subsets, i.e., samples, were selected randomly from this population by repeatedly assigning a computer-generated random number to each member of the population, sorting the data according to the assigned numbers and choosing the first 10, 20, etc. sorted data. The total number of subsets (t) generated for each prescribed sample size was such that the standard error of m (i.e., standard deviation of $m/(t)^{1/2}$) was less than 0.1; the Weibull modulus m was determined by "least-squares" linear regression.

They obtained the following results:

(a) The standard deviation of m decreases as the sample size increases, as expected.

(b) Bias correction of the data using computer-generated bias correction factors predicted m = 9.5.

(c) Only the estimator, $P_s = 1 - (j - 0.5)/n$ approached an asymptotic m value, of 9.58 ± 0.04, for sample sizes of 20 and greater, with m = 9.59 for n = 100.

The Weibull moduli for sample sizes of 10, 20, 30, 50, and 100 as a function of estimator are given below:

P_s	n = 10	20	30	50	100
$1 - (j - 0.5)/n$	9.74	9.52	9.55	9.58	9.59
$1 - (j - 3/8)/(n + 1/4)$	9.20	9.18	9.28	9.38	9.47
$1 - (j - 0.3)/(n + 0.4)$	8.92	8.99	9.14	9.28	9.41
$1 - j/(n + 1)$	8.02	8.38	8.65	8.91	9.17

These results of Sullivan and Lauzon confirm Bergman's conclusions regarding the choice of estimator, with $P_s = 1 - (j - 0.5)/n$ being the least biased estimator for $n \geq 20$, except that the use of $P_s = 1 - (j - 3/8)/(n + 1/4)$ for $n < 20$ is not to be preferred as suggested by Bergman, since no estimator predicts a reasonable m value for $n < 20$. The conclusion to be drawn is that a large sample size does not compensate for a poor choice of estimator; given that the least biased estimator is used, the accuracy of the estimated Weibull modulus is strongly dependent on the sample size, for example, the coefficient of variation of m was 17 % for n = 20, 7 % for n = 50, ≈ 4 % for n = 80.

The sample size effect on the apparent Weibull modulus of commercial alumina has been investigated (Glandus, J.C., and Boch, P., 1984); they found that for a commercial alumina the mean flexural strength in three-point bending of 98 strength data could be estimated to within ≈ 5 % by random sampling of the 98 data through sets of 10 random data. The estimated Weibull modulus from random sets of 10 samples was, however, only within ≈ 40 % of the estimate from all the 98 data; for sets of 20 samples the estimate was within ≈ 20 % of the 98 sample estimate of m = 12; and even for sets of 40 samples the estimate was only accurate to within ≈ 10 %.

Considering that Sullivan and Lauzon found that for a sample size of 100, the maximum error in the estimated m value (compared to the statistically predicted m value of 9.5) due to estimator bias was ≈ - 1 to - 3 %, the results of Glandus and Boch, and Sullivan and Lauzon concerning the sample size effect on m suggest that concern over which survival probability estimator gives the least biased Weibull modulus estimate verges on the pedantic. This is not the case, however, when estimating the Weibull modulus by "least-squares" linear regression as discussed below.

Any set of specimens of a given material tested to fracture represents a random sample of the true universal fracture stress distribution of the material, and the fracture stress distribution of this random sample will in general be roughly "bell shaped"; i.e.,the majority of the data will cluster around a median, modal or mean value with only a minority of data very much higher and lower than it. When using the linear regression method the survival probability is constant for a given estimator and rank order, i.e., sample size; thus for a given sample the scatter in the data is due to the independent variable, $\ln\sigma$ and not the dependent variable, $\ln\ln(1/P_s)$. These relatively few extreme $\ln\sigma$ values, which are not really representative of the fracture stress distribution, influence the value of the slope and the intercept of the estimated regression line to a degree which far outweighs

their frequency of occurrence. This suggests that a more reliable estimate of the slope and intercept would be obtained if the data were multiplied by an "influence or weight factor" indicative of its relation to the median, modal or mean value. The least complex weighting function is the step function for which the weight factor is equal to either one or zero, i.e., a particular datum is either used or omitted; thus a specified fraction of the extreme data at each tail may be omitted, e.g., 2 to 4 % (Kamiya, N. and Kamigaito, O., 1984).

An appropriate weight function for the linear regression analysis of the Weibull function has been derived analytically using the theory of propagation of errors and critically tested using computer simulations (Bergman, B., 1986). It was shown that the implicit assumption in the standard "least-squares" analysis of a constant or random uncertainty in $\ln\ln(1/P_s)$, i.e., the uncertainty in the value of $\ln\ln(1/P_s)$ is independent of its value, overemphasises the influence of fracture stress data at high survival probabilities. Use of the variable weight function reduces the bias of $P_s = 1 - j/(n + 1)$ to some degree, e.g., for n = 20, M/m increased from 0.890 (See Table 4.9) to 0.9171; an increase of 3 %. However, the bias of $P_s = 1 - (j - 0.5)/n$ is not significantly reduced by using the variable weight function instead of a constant weight function of unity, e.g., for n = 20, M/m changed from 1.011 (See Table 4.9) to 0.9895; thus M/n is within 1.06 % of 1 using the variable weight function and within 1.1 % of 1 using the constant weight function.

So the standard "least-squares" linear regression method can be used to estimate the Weibull modulus without further biasing the Weibull modulus estimate if the survival probabilities are estimated by $P_s = 1 - (j - 0.5)$ which has been shown to give the least biased estimate of the Weibull modulus for sample sizes $\geq$ 20 (Bergman, B., 1984); (Sullivan, J.D., and Lauzon, P.H., 1986). Thus given the effect of the sample size on the estimated Weibull modulus it is obvious that the minimum sample size should be 20 and that the above estimator should be used

if the Weibull modulus is estimated by linear regression analysis, assuming a zero threshold stress as invariably recommended.

4.9.5 Effect of stressed volume on the fracture stress

The effect of the volume of a specimen stressed during a fracture test using a given loading configuration on the fracture stress of the specimen will be considered. From section 4.6 it is apparent that greater the specimen or component volume stressed the lower the fracture stress. It can be shown that (Jayatilaka, Ayal de S., 1979)

$$\sigma_M = \sigma_L + [\sigma_o/(V)^{1/m}][\Gamma(1 + 1/m)]f(m) \quad [4.100]$$

where σ_M is the mean fracture stress, V the total volume stressed, σ_o the scaling parameter, σ_L the threshold stress, $\Gamma(1 + 1/m)$ the 'gamma function' whose values can be found in most standard texts of mathematical tables, and f(m) is a function of m only and depends on the given loading configuration. If two groups of specimens (with nominal specimen volumes of V_1 and V_2) are taken from a material of Weibull modulus m and tested in the same manner under identical conditions and produce mean fracture stresses of σ_{M1} and σ_{M2}, then assuming a zero threshold stress gives

$$\sigma_{M1} = [\sigma_o/(V_1)^{1/m}][\Gamma(1 + 1/m)]f(m)_1$$

and

$$\sigma_{M2} = [\sigma_o/(V_2)^{1/m}][\Gamma(1 + 1/m)]f(m)_2$$

with $f(m)_1 \equiv f(m)_2$. Hence

$$\sigma_{M1}/\sigma_{M2} = (V_2/V_1)^{1/m} \quad [4.101]$$

This equation shows that for a given volume ratio the mean fracture stress ratio decreases with increasing m to unity for $m = \infty$, and that if $V_2 > V_1$ then $\sigma_{M2} < \sigma_{M1}$ as expected.

For equal volumes stressed under different loading configurations $f(m)_1$ and $f(m)_2$ the ratio of the mean fracture stresses is given by

$$\sigma_{M1}/\sigma_{M2} = f(m)_1/f(m)_2 \quad [4.102]$$

Some f(m) functions for stressed volumes are given below:

direct tension	$f(m) = 1$
3-point bending (d = s/2)	$f(m) = [2(m + 1)^2]^{1/m}$
4-point bending (d = s/4)	$f(m) = [4(m + 1)^2/(m + 2)]^{1/m}$

Note d is the moment arm and s is the support span. So for equal volumes and a given Weibull modulus, the strength order is tensile < 4-point bending < 3-point bending. If surface flaws are dominant the stressed volume term is replaced by a stressed area term; for 3-point bending, $f(m) = [4(m + 1)^2/(m + 2)]^{1/m}$ for B/W = 1 and for B/W = 1/2, $f(m) = [6(m + 1)^2/(m + 3)]^{1/m}$. For four-point bending (d = s/4), $f(m) = [8(m+1)^2/(m+2)^2]^{1/m}$ for B/W = 1 and for B/W = 1/2, $f(m) = [12(m+1)^2/([m+3][m+2])]^{1/m}$. These functions and those for other bending moment-arm values are given by N.A. Weil and I.M. Daniel, (1964).

4.9.6 Comparison of the nominal room temperature flexural strength of SCR25.76, SCR19.34, SCF5 and SCR19.13 glass-ceramics with those of other typical ceramic materials

The values quoted are intended for qualitative not quantitative comparison for the reasons discussed previously, e.g., the dependence on size, surface finish and so on. The comparative data for the other materials are after W.E.C. Creyke (1979) as cited by A. Bennett (1986). The mean S1 flexural strengths are quoted for the CaO - MgO - Al_2O_3 - SiO_2 system glass-ceramics since they are the mean values of the S1 data calculated using the standard 3-point bending flexural strength equation.

Material	Flexural Strength (MPa)
SCR25.76 (20 data)	118
SCR19.34 (20 data)	121
SCF5 (4 data)	205
SCR19.13 (5 data)	89
Soda lime glass	45
Borosilicate glass	50
Vitreous silica	60
Low-expansion glass-ceramic	130
Cast iron	300

Material	Flexural Strength (MPa)
Sintered alumina	250
Typical hot-pressed silicon nitride	600
Metal bonded tungsten carbide	1500
High density graphite	30
Self-bonded SiC	525

The comparative data show that the acceptably crystalline glass-ceramics, SCR25.76 (71 vol.%), SCF5 (82 vol.%) and SCR19.34 (58 vol.%) have flexural strengths typical of glass-ceramics, while the poorly crystallized glass--ceramic SCR19.13 (30 vol.%) has a higher strength than the typical glasses but lower than typical glass-ceramics.

4.9.7 Comparison of the nominal room temperature Weibull modulus values of SCR25.76, SCR19.34, SCF5 and SCR19.13 with those of other typical ceramic materials

The values quoted for the $CaO - MgO - Al_2O_3 - SiO_2$ glass--ceramics SCR25.76 and SCR19.34 are the mean integer values obtained using $P_s = 1 - j/(n + 1)$ and the 20 S1 data. The values for SCF5 and SCR19.13 were estimated using

$$m \approx 1.2/(C_v) \qquad [4.103]$$

where C_v is the coefficient of variation of the flexural strength (Fessler, H., et al., 1983); for comparison, the Weibull moduli of SCR25.76 and SCR19.34 were estimated using [4.103]. The estimates are given in parentheses. The comparative data for the other materials are after W.E.C. Creyke (1979) as cited by A. Bennett (1986):

Material		Weibull Modulus (m)
SCR25.76		12 (14)
SCR19.34		14 (16)
SCF5	(4 data)	≈ 7
SCR19.13	(5 data)	≈ 21

Material	Weibull Modulus (m)
Soda lime glass	6
Borosilicate glass	6
Vitreous silica	6
Low-expansion glass-ceramic	12
Cast iron	25
Sintered alumina	12
Typical hot-pressed silicon nitride	10
Metal bonded tungsten carbide	25
High density graphite	12
Self-bonded SiC	12

The estimated m values for SCF5 and SCR19.13 should be regarded with extreme caution given the small sample size. The Weibull modulus values for SCR25.76 and SCR19.34 are typical of most modern engineering ceramic materials.

4.9.8 Strength-probability-time (SPT) diagrams for SCR25.76 and SCR19.34 at room temperature

The strain-rates given in Table 4.2 were calculated using equation [4.69] and the estimates of the sub-critical crack growth exponents were calculated using equation [4.66] in the form

$$n = [\ln(\dot{\epsilon}_A/\dot{\epsilon}_B)]/[\ln(\sigma_A/\sigma_B)] - 1 \qquad [4.104]$$

and the median flexural strengths of the S4 data. The rank order for a survival probability of 0.5 is $j = (n + 1)/2$, which for n = 20 and n = 10 is effectively 10 or 11 and 5 or 6 respectively; thus the median value (which is the arithmetic mean of the two middle data in even size samples or the middle datum in odd size samples) is a sensible value to use, which avoids the necessity of using equivalent rank fracture stress data, i.e., having equal size data samples. The median values are given below together with the mean values for each of the three strain rates ($\dot{\epsilon}$) used in the present work:

Material & $\dot{\epsilon}$	Median (MPa)	Mean (MPa)
$\dot{\epsilon}_1 = 7.45 \times 10^{-5}\ s^{-1}$		
SCR25.76	106.7	105.2
SCR19.34	106.4	102.7
$\dot{\epsilon}_2 = 7.45 \times 10^{-4}\ s^{-1}$		
SCR25.76	109.5	107.9
SCR19.34	116.1	114.2
$\dot{\epsilon}_3 = 7.45 \times 10^{-3}\ s^{-1}$		
SCR25.76	132.9	132.0
SCR19.34	125.3	124.6

The n values estimated using the above data, the $\dot{\epsilon}$-ratio, and the median stress ratio are given below:

Material & $\dot{\epsilon}$-ratio	Median stress ratio	n
$\dot{\epsilon}_2/\dot{\epsilon}_1 = 10$		
SCR25.76	1.026	89.7
SCR19.34	1.091	26.4
$\dot{\epsilon}_3/\dot{\epsilon}_2 = 10$		
SCR25.76	1.214	11.9
SCR19.34	1.079	30.2
$\dot{\epsilon}_3/\dot{\epsilon}_1 = 100$		
SCR25.76	1.246	20.9
SCR19.34	1.174	28.7

Note the extremely wide scatter in the n values for SCR25.76 compared to SCR19.34; the mean values are 28.4 ±

1.9 for SCR19.34 and 40.8 ± 42.6 for SCR25.76. The fracture stresses recorded at strain-rate $\dot{\epsilon}_2$ for SCR25.76 and SCR19.34 were down-rated to the equivalent values corresponding to a failure time of 1 second under constant stress using equation [4.96], n values of 28 and 41 for SCR19.34 and SCR25.76 respectively, and the constant strain-rate fracture stress and failure time data tabulated in Appendix 4C. The equivalent fracture stresses (rounded to the nearest MPa) are tabulated in Table 4.12.

The survival probabilities corresponding to the data in Table 4.12 were estimated by $P_s = 1 - (j - 0.5)/n$; a standard "least-squares" linear regression analysis of $\log\ln(1/P_s) = m\log\sigma + \log(V/[V_o(\sigma_o)^m])$ was carried out and the results are presented in Table 4.13. The $-\log\ln(1/P_s)$ data are the values calculated using the respective regression equations and not the original P_s values and together with the corrected $\log(\sigma)$ values enable the construction of an SPT diagram for SCR25.76 and SCR19.34 as shown in Figure 4.11 and Figure 4.12 respectively. Note the Weibull modulus values for the SPT data and the original S4 data are: m (Original) = 11.4 and m (SPT) = 11.2 for SCR25.76, and m (Original) = 15.0 and m (SPT) = 15.0 for SCR19.34.

The effect the choice of strength parameter on the estimated n values is of interest; using the mean strength values for comparison gives mean n values of: 22.1 ± 12.8 (S1) and 40.2 ± 42.6 (S4) for SCR25.76, and 21.8 ± 5.0 (S1) and 23.0 ± 2.4 (S4) for SCR19.34. These results raise two points of contention; (i) although the S1 values are more consistent and less variable, they imply that SCR25.76 and SCR19.34 exhibit similar slow crack growth behaviour, (ii) whereas although the S4 value for SCR25.76 is very variable and the S4 value for SCR19.34 is consistent with the S1 value, the two S4 values imply a possibly significant difference in the slow crack behaviour of SCR25.76 and SCR19.34, the former material being less prone to slow crack growth. Only real delayed fracture data superposed on the SPT plots will indicate which n values, i.e., S1 or S4 are the most reliable.

Table 4.12 Room Temperature Constant Flexural Stresses Corresponding to a Failure Time of 1 Second for SCR25.76 and SCR19.34

Rank Order	SCR25.76 Data (MPa)	SCR19.34 Data (MPa)
1	79	96
2	85	97
3	93	98
4	97	101
5	97	102
6	100	106
7	102	110
8	104	112
9	105	112
10	106	113
11	107	114
12	108	114
13	108	116
14	108	117
15	111	118
16	112	119
17	114	118
18	117	119
19	121	124
20	124	125

Table 4.13 SPT Diagram Data for SCR25.76 and SCR19.34

	Data for SCR25.76		Data for SCR19.34		
j	$\log(\sigma)$	$-\log\ln(1/P_s)$	$\log(\sigma)$	$-\log\ln(1/P_s)$	P_s
1	1.898	+1.594	1.982	+1.202	0.975
2	1.929	+1.239	1.987	+1.135	0.925
3	1.968	+0.802	1.991	+1.068	0.875
4	1.987	+0.597	2.004	+0.872	0.825
5	1.987	+0.597	2.009	+0.807	0.775
6	2.000	+0.450	2.025	+0.557	0.725
7	2.009	+0.353	2.041	+0.316	0.675
8	2.017	+0.259	2.049	+0.199	0.625
9	2.021	+0.213	2.049	+0.199	0.757
10	2.025	+0.167	2.053	+0.141	0.525
11	2.029	+0.121	2.057	+0.083	0.475
12	2.033	+0.076	2.057	+0.083	0.425
13	2.033	+0.076	2.064	-0.030	0.375
14	2.033	+0.076	2.068	-0.086	0.325
15	2.045	-0.057	2.072	-0.141	0.275
16	2.049	-0.101	2.072	-0.141	0.225
17	2.057	-0.187	2.076	-0.196	0.175
18	2.068	-0.313	2.076	-0.196	0.125
19	2.083	-0.476	2.093	-0.464	0.075
20	2.093	-0.595	2.097	-0.516	0.025

The $-\log\ln(1/P_s)$ data were calculated from $-(m\log(\sigma) + I)$.
Regression Data for SCR25.76: m = 11.18 ± 0.33 r = 0.9923
Coeff. of Det. = 0.9847 Intercept, I = -22.81 ± 0.66
Regression Data for SCR19.34: m = 14.99 ± 0.89 r = 0.9700
Coeff. of Det. = 0.9409 Intercept, I = -30.91 ± 1.8

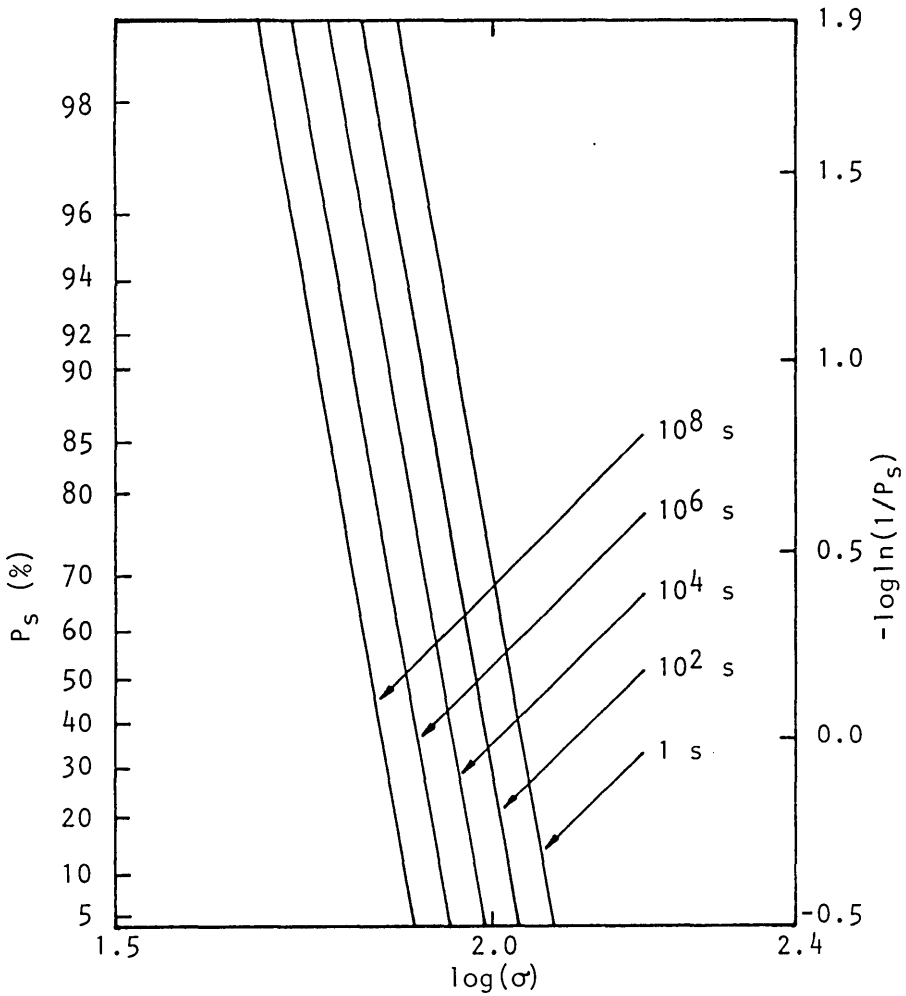


Figure 4.11 SPT Diagram for SCR25.76 (n = 41).

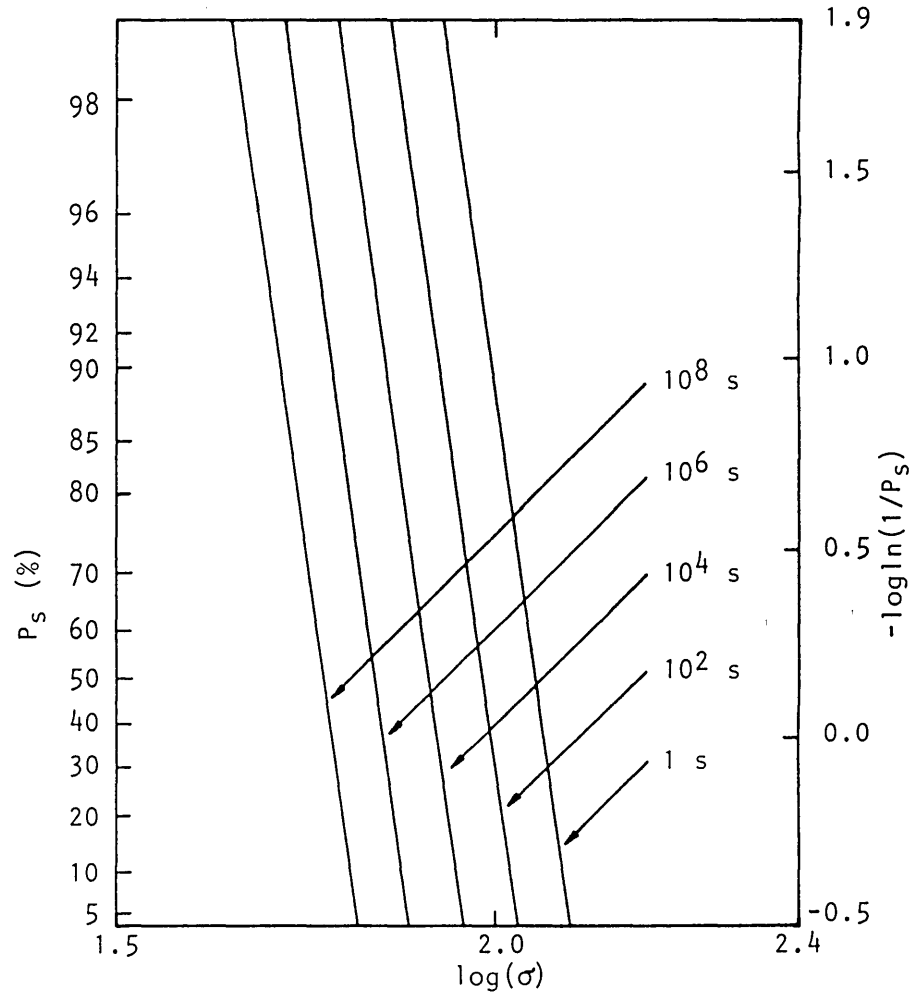


Figure 4.12 SPT Diagram for SCR19.34 (n = 28).

4.9.9 Estimation of Weibull parameters using the graphical approach of Leon and Kittl

An exact expression for the cumulative probability of failure of a rectangular bar subject to three-point bending (i.e., a variable tensile stress field) has been derived (Kittl, P., 1980) and for the cumulative survival probability P_s is

$$P_s = \exp\left[- \frac{BWs}{2(m+1)V_o} \left(\frac{\sigma_L}{\sigma_o} \right)^m \cdot \frac{1}{(\sigma/\sigma_L)} \int_1^{\sigma/\sigma_L} \frac{(\phi - 1)^{m+1}}{\phi} \, d\phi \right] \quad [4.105]$$

where B is the specimen breadth, W the specimen width, s the support span and σ is the maximum bending stress in the bar. In the present analysis only the effect of "wedging" was accounted for; thus

$$\sigma = (3Ps)(1 - 0.1776W/s)/(2BW^2) \quad [4.106]$$

that is the S2 strength parameter. σ_L is the threshold stress, σ_o the scaling parameter, V_o the unit volume, m the Weibull modulus and ϕ an auxiliary variable under the integral. This equation is not easily solved to find the values of m, σ_o and σ_L, but they can be estimated by a graphical technique which involves comparing the standard "linearized" Weibull plot with a non-dimensional Weibull function nomogram (after Leon, M. and Kittl, P., 1985); taking logarithms of equation [4.105] gives

$$\Phi(\sigma) = \ln(1/P_s) = \frac{BWs}{2(m+1)V_o} \left(\frac{\sigma_L}{\sigma_o} \right)^m \cdot \frac{1}{(\sigma/\sigma_L)} \int_1^{\sigma/\sigma_L} \frac{(\phi - 1)^{m+1}}{\phi} \, d\phi$$

Thus

$$\Phi(\sigma) = \ln(1/P_s) = \frac{BWs}{2(m+1)^2 V_o} \cdot (m+1) \cdot (\sigma_L/\sigma_o)^m \cdot (\sigma/\sigma_L)^m \times \frac{1}{(\sigma/\sigma_L)^{m+1}} \int_1^{\sigma/\sigma_L} \frac{(\phi - 1)^{m+1}}{\phi} \, d\phi$$

This gives the following non-dimensional form

$$\bar{\Phi}(\sigma) = \ln(1/P_s) = \frac{BWs}{2(m+1)^2 V_o}\left(\frac{\sigma_L}{\sigma_o}\right)^m \cdot \left(\frac{\sigma}{\sigma_L}\right)^m \cdot \frac{m+1}{(\sigma/\sigma_L)^{m+1}} \times \int_1^{\sigma/\sigma_L} \frac{(\phi - 1)^{m+1}}{\phi}\, d\phi$$

Hence equation [4.106] is

$$\ln\bar{\Phi}(\sigma) = \ln\ln(1/P_s) = \ln\left[\frac{BWs}{2(m+1)^2 V_o}\left(\frac{\sigma_L}{\sigma_o}\right)^m\right] + m\ln(\sigma/\sigma_L) + \ln\frac{m+1}{(\sigma/\sigma_L)^{m+1}}\int_1^{\sigma/\sigma_L}\frac{(\phi - 1)^{m+1}}{\phi}\, d\phi$$

Now if the function $\ln\bar{\Phi}^*$ is plotted against $\ln(\sigma/\sigma_L)$ for different m values the nomogram for 3-point bending is obtained, where the function $\ln\bar{\Phi}^*$ is given by

$$\ln\bar{\Phi}^* = m\ln(\sigma/\sigma_L) + \ln\left[\frac{m+1}{(\sigma/\sigma_L)^{m+1}}\int_1^{\sigma/\sigma_L}\frac{(\phi - 1)^{m+1}}{\phi}\, d\phi\right] \qquad [4.107]$$

The standard Weibull plot of $\ln\bar{\Phi}(\sigma) \equiv \ln\ln(1/P_s)$ against $\ln\sigma$ is drawn on tracing paper and placed over the nomogram. Estimates of m, σ_o and σ_L are obtained by moving the Weibull plot, keeping the $\ln\sigma$ axis parallel to the $\ln(\sigma/\sigma_L)$ axis, so that the experimental data are positioned over the nomogram m-curve which gives the best visual fit to the data; this gives the m estimate. As $\ln\bar{\Phi}(\sigma)$ has been positioned on the $\ln\bar{\Phi}^*$ axis as a function of $\ln\sigma$ and hence at $\ln(\sigma/\sigma_L) = 0$, $\ln\sigma_L \equiv \ln\sigma$ and the intercept $C \equiv \ln\bar{\Phi}^*$ where the $\ln\sigma$ axis intersects the $\ln\bar{\Phi}^*$ axis, i.e., at $\ln\bar{\Phi}(\sigma) = 0$. The intercept C is given by

$$C = \ln\left[\frac{BWs}{2(m+1)^2 V_o}\left(\frac{\sigma_L}{\sigma_o}\right)^m\right] \qquad [4.108]$$

In order to evaluate the definite integral

$$\int_{1}^{\sigma/\sigma_L} \frac{(\phi - 1)^{m+1}}{\phi} \, d\phi \qquad [4.109]$$

requires a reduction formula for the integral which was not given by Leon and Kittl; the reduction formula was derived for the present analysis using integration by parts and is given in Appendix 4F along with a BASIC computer programme, written around the algorithm for determining the magnitiude of the integral for different m values, which was used to evaluate equation [4.107].

This graphical approach was used to estimate m, σ_o and σ_L for SCR25.76 using the 20 S2 data obtained at a strain-rate of 7.45 x 10^{-4} s^{-1}. A Weibull plot using P_s = 1 - j/(n + 1), because it is presently the most popular estimator and gives a conservative estimate, was drawn on tracing paper and superposed on the nomogram constructed for m = 2,5,6,7, and 12 as shown in Figure 4.13. The standard regression parameters obtained using $\ln\sigma$ in MPa and $\ln\ln(1/P_s)$ data rounded to 3 decimal places were:

m = 11.74

Standard deviation of m = 0.53

Correlation coefficient, r = 0.9824

Coefficient of determination = 0.9652

Intercept I = - 55.95

Standard deviation of I = 2.48

Initial comparison with the nomogram suggested a Weibull modulus of 6, and gave $\ln\sigma_L$ as 3.73 and C = 2.5; hence σ_L = 41.7 MPa. Using the mean SCR25.76 specimen dimensions of B = 4.005 mm, W = 7.633 mm and the nominal span of 32 mm and an arbitrary unit volume of V_o = 1 mm^3 in equation [4.108] gave $\ln(9.98[41.7/\sigma_o]^6)$ = 2.5; thus σ_o = 40.3 MPa. The graphical estimate of m was checked retrospectively by subtracting the σ_L value from the original S2 data and then conducting a second linear regression analysis on the Weibull plot data.

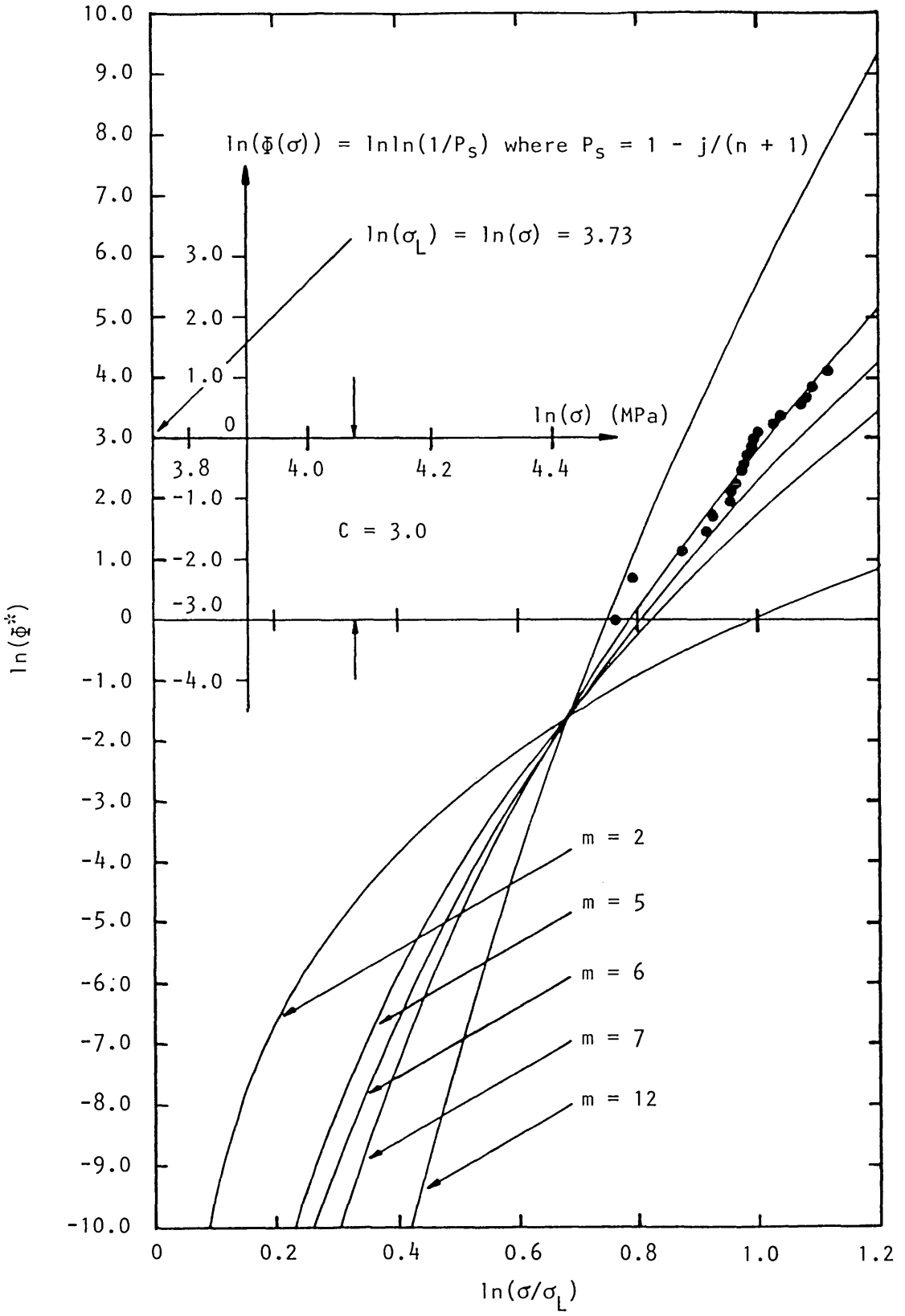


Figure 4.13 Standard Weibull Data ($\ln\ln(1/P_s)$ vs. $\ln(\sigma)$) Superposed on the Weibull Function Nomogram for Three-Point Flexure Constructed After M. Leon and P. Kittl (1985) for SCR25.76 Using $P_s = 1 - j/(n + 1)$ and the S2 Strength Data.

The "linearized" Weibull function employed was the standard one given for three-point bending,

$$\ln\ln(1/P_s) = m\ln(\sigma-\sigma_L) + \ln(V/[2(m+1)^2 V_o(\sigma_o)^m]) \quad [4.110]$$

The results of the analysis for $\ln\sigma$ in MPa were:

m = 7.18

Standard deviation of m = 0.34

Correlation coefficient, r = 0.981 to 3 decimal places

Coefficient of determination = 0.962 to 3 decimal places

Intercept I = - 31.05

Standard deviation of I = 1.43

Using the mean specimen dimensions and span given above produces the equation

$$[9.98/(\sigma_o)^{7.18}] = 3.27 \times 10^{-14}$$

which gives σ_o = 104.1 MPa.

The graphical estimate of 6 is 2.9 standard deviations from the "least-squares" estimate of 7.18 and the standard error of m is 1.11; the Weibull plot was placed on the nomogram such that $\ln\sigma_L$ = 3.73 as before, but shifted vertically to position it over the m = 7 nomogram curve. As can be seen from Figure 4.10, the experimental data does fit the curve quite well except at the two lowest fracture stresses (in fact much better than it did the m = 6 nomogram curve). The new estimate for C was 3.0; hence

$$\ln(9.98[41.7/\sigma_o]^{7.18}) = 3.0$$

which gives σ_o = 49.3 MPa. Comparing this estimate with that given by the standard Weibull function for three--point bending, i.e., equation [4.110] shows that the error in using [4.110] with a non-zero threshold stress is ≈ 100 %; this has already been pointed out by P. Kittl and O. Günther (1979).

Although this graphical method produces less accurate estimates of the Weibull parameters m, σ_o and σ_L than the sophisticated methods requiring the use of a powerful computer, e.g., the maximum-likelihood method, it is the quickest and least expensive way to estimate all three Weibull parameters. Furthermore, equation [4.110] can be used to check the estimated m value and provide a revised estimate for σ_o for a fixed σ_L value.

4.9.10 Experimental flexural strength results at elevated tempertures

All the high temperature flexural strength measurements on SCR25.76, SCR19.34 and SCF5 were conducted on the high temperature three-point bending rig previously described in Section 4.9.1; the dimensions of the specimens tested, the fracture loads, and so on are tabulated in Appendix 4G for a given temperature under the same headings as the room temperature data tabulated in Appendix 4C. Note that the room temperature specimen dimensions were used to calculate the flexural strength data; the effect of neglecting thermal expansion was considered by assuming that the linear thermal expansivity of SCR25.76 and SCR19.34 is the same as that of SCF5, namely 7.5×10^{-6} K^{-1} between room temperature and 800°C and using a nominal linear thermal expansivity of 3×10^{-6} K^{-1} between room temperature and 1000°C for silicon nitride. Thus using the data for SCR25.76 specimen MA63 tested at 700°C as an example (See Table 4G.4 in Appendix 4G), the flexural strength (S2 strength parameter) calculated using the room temperature dimensions was 107.4 MPa compared to 106.0 MPa if thermal expansion was accounted for, i.e., an error of 1 % which is negligible compared to the nominal coefficient of variation in the flexural strength of 20 %.

The dependence on temperature of the flexural strength of SCR25.76 and SCR19.34 will be considered first; data were obtained at 20, 250, 500, 600, 700, 750 and 800°C and the data at 20°C are tabulated in Table 4C.2 of Appendix 4C. The mean value of all the S4 strength parameter data, the sample standard deviation, the coefficient of variation and the number of test data (N) at each test temperature are tabulated in Table 4.14 for SCR25.76 and SCR19.34. The test specimens deformed plastically at 750 and 800°C (see Table 4G.5); assuming that the cross-head displacement at these temperatures was due entirely to the specimen displacement, the load and displacement at the limit of the linear load-displacement response was used to estimate the stress and strain at the

Table 4.14 Elevated Flexural Strength Data for SCR25.76 and SCR19.34:

Temperature (°C)	Mean S4 (MPa)	Stand. Dev. (MPa)	Coeff. Var. (%)	N
	Data for SCR25.76			
20	136.7	24.3	18	10
250	108.8	20.6	19	8
500	122.2	21.2	17	8
600	131.3	31.5	24	8
700	110.2	18.4	17	8
	Data for SCR19.34			
20	194.0	51.5	27	10
250	153.4	18.0	12	8
500	159.1	42.6	27	8
600	159.9	27.4	17	8
700	157.2	40.4	26	8

Stand. Dev. is the sample standard deviation
Coeff. Var. is the coefficient of variation

Table 4.15 Approximate Stress and Strain Data at the Linear Load-Displacement Response Limit for SCR25.76 and SCR19.34:

Temperature (°C)	Maximum Stress (MPa)	Maximum Strain
	Data for SCR25.76	
750	51	0.020
800	34	0.015
800	28	0.014
	Data for SCR19.34	
750	48	0.020
800	33	0.017
800	34	0.017

limit using equations [4.24] and [4.68] respectively. The results are presented in Table 4.15.

The mean flexural strength values for both SCR25.76 and SCR19.34 are plotted against temperature from 20 to 700°C in Figure 4.14, together with the maximum stress at the respective linear response limits at 750 and 800°C and the mean flexural strengths obtained at 20°C on the room temperature test rig. The sample standard deviation bars and the percentage coefficient of variation for the high temperature rig data are also shown. The most intriguing feature is the marked separation of the mean strengths of the two materials at room temperature as determined from the fewer and more scattered data obtained using the high temperature rig compared to the essentially equal room temperature values obtained from the room temperature rig.

There are a number of possible explanations for the separation of the mean room temperature strengths:

(a) The silicon nitride and alumina rollers produced greater frictional forces than the tungsten carbide rollers, giving erroneously high fracture stresses.

(b) The indirect room temperature rig may induce greater twisting stresses in the specimens than the direct high temperature rig, giving lower apparent fracture stresses.

(c) The small number of specimens tested on the high temperature rig (10) would in general be expected to give a mean value less representative of the true mean strength than the mean value of 20 test specimens and may by chance represent the higher end of the strength distribution.

(d) The specimens tested on the room temperature rig had a different strength distribution, either due to a different surface flaw distribution due to a difference in the polishing conditions or to a different volume flaw distribution as a consequence of material inhomogeneity.

The sample variances (SV) of the two data sets were markedly dissimilar for both the SCR25.76 and the SCR19.34 data; for SCR25.76, SV(HT rig)/SV(RT rig) = 4.6 while for SCR19.34, SV(HT Rig)/SV(RT Rig) = 32.7. Thus a comparison of the sample means using the t-test would appear to be invalid as the test is based on the assumption that the

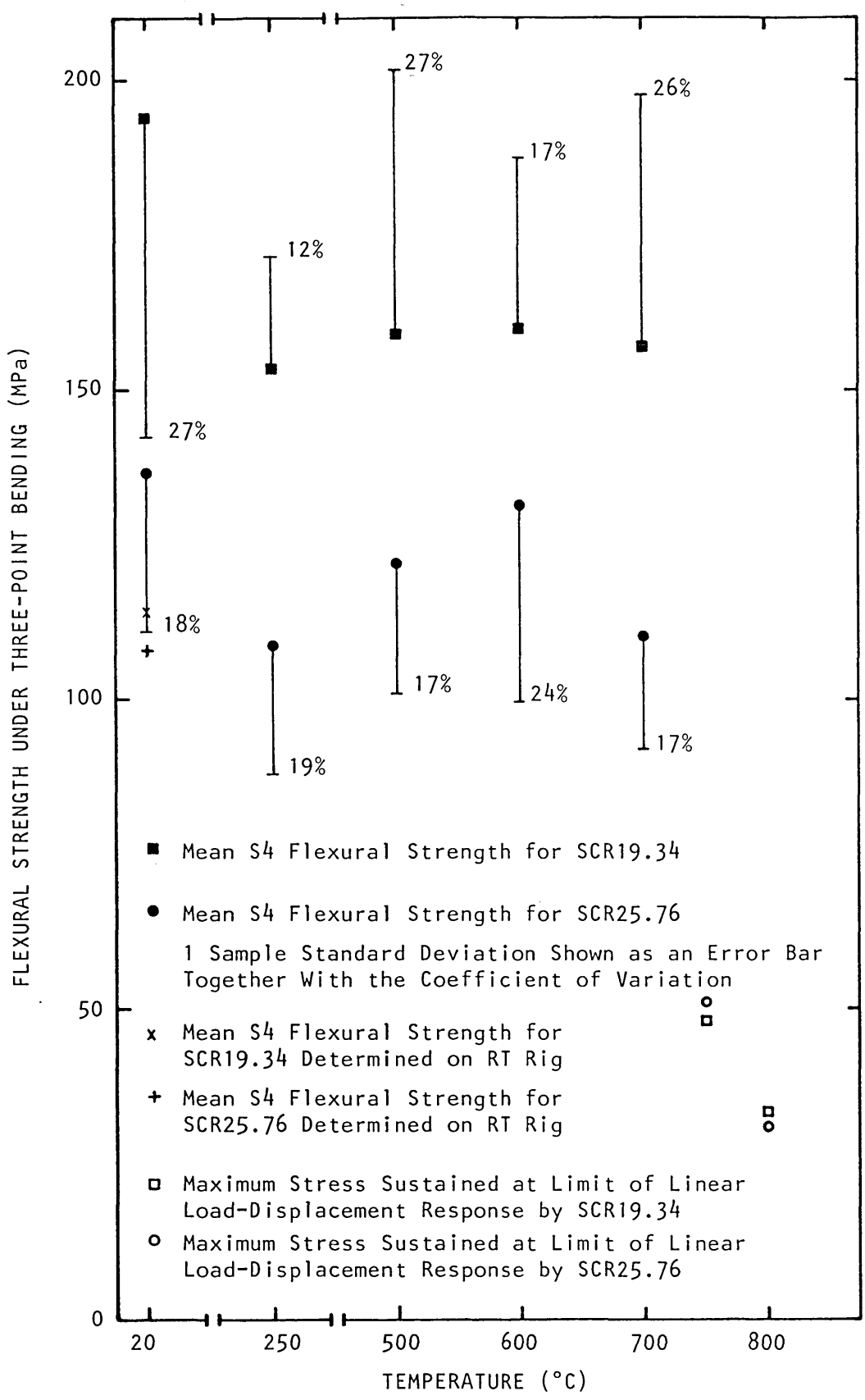


Figure 4.14 Mean Flexural Strength (S4 Data) of SCR25.76 and SCR19.34 as a Function of Temperature.

two parent populations have the same variance (in addition to the assumptions that the samples are independent and normally distributed), which means that $SV(1)/SV(2) \approx 1$ for reasonably large samples. An F-test [$F = SV(1)/SV(2)$ where $SV(1) > SV(2)$] of the null hypothesis that the samples have the same population variance with the alternative hypothesis that the samples have different population variances, i.e., a two-tailed test, (Chatfield, C., 1983) was conducted. The F-tests were significant at the 1 % level, i.e., the probability of obtaining an F-value as or more contradictory to the null hypothesis than the present value is only 1 %; in otherwords, the null hypothesis that the population variances are identical is almost certainly untrue.

So doing a t-test using the data would not really be valid; however, nothwithstanding the F-test results, a two-tailed t-test was conducted on the null hypothesis that the population means were equal. The t-test value for the SCR25.76 data was significant at the 0.02 % level, while that for the SCR19.34 data was significant at the 0.00005 % level. Thus in both cases the population means of the samples tested on the room temperature and the high temperature rigs were different; however, it is not possible on the basis of these results alone, to attribute the strength difference to any particular one of the four reasons (a, b, c, and d) given previously.

For both SCR25.76 and SCR19.34, four of the eight specimens tested at each of the temperatures, 500, 600 and 700°C and two of the ten specimens tested at 20°C on the high temperature rig were cut from the same tablets as all the specimens tested on the room temperature rig; all the other specimens tested on the high temperature rig were cut from the other tablets cut from the same parent tile. Table 4.16 presents the mean strengths (S4 parameter) obtained on the high temperature rig and which correspond to the two batches of tablets cut from the same parent tile (Batch A and Batch B) tabulated against temperature, together with the sample standard deviations and the percentage coefficient of variation. Taking the A batch

Table 4.16 Mean Flexural Strength Data for SCR25.76 and SCR19.34 Classified According to Specimen Batch and Test Temperature:

Data for SCR25.76 (MPa)

θ (°C)	Batch A			Batch B		
	Mean & s.d.	N	C_v %	Mean & s.d.	N	C_v %
20	134.5 ± 8.5	2	6	137.3 ± 27.3	8	20
250	----------	-	--	108.8 ± 20.6	8	19
500	117.6 ± 17.3	4	15	126.8 ± 26.4	4	21
600	141.7 ± 29.8	4	21	121.0 ± 33.7	4	28
700	96.2 ± 8.4	4	9	124.3 ± 14.1	4	11

Data for SCR19.34 (MPa)

θ (°C)	Batch A			Batch B		
	Mean & s.d.	N	C_v %	Mean & s.d.	N	C_v %
20	126.5 ± 12.0	2	9	210.8 ± 42.0	8	20
250	----------	-	--	153.4 ± 18.0	8	12
500	124.7 ± 21.8	4	17	193.6 ± 24.2	4	13
600	149.1 ± 32.8	4	22	170.8 ± 18.9	4	11
700	149.8 ± 34.4	4	23	164.5 ± 49.8	4	30

(a) N is the number of data, s.d. the sample standard deviation and C_v the coefficient of variation.
(b) Batch A refers to the specimens taken from the same tablets as the specimens tested on the room temperature rig, while batch B refers to the specimens cut from other tablets cut from the single parent tile.
(c) All batch A specimens were tested on silicon nitride knife-edges, while all batch B specimens tested at 20°C, 250°C, 600°C and 700°C were tested on alumina roller supports. Of the B batch specimens tested at 500°C, 2 specimens of SCR19.34 B and 3 specimens of SCR25.76 B were tested on silicon nitride knife-edges (See Appendix 4G, Table 4G.2).

values as reference data, the mean values of the batches differ as a function of temperature as follows:

Temperature (°C)	SCR25.76	SCR19.34
20	- 2 %	-67 %
500	- 8 %	-55 %
600	+15 %	-15 %
700	-30 %	-10 %

The root-mean-square difference between the batch means regardless of temperature is 17 % for SCR25.76 and 44 % for SCR19.34; the root-mean-square coefficient of variation regardless of batch classification is 18 % and 19 % for SCR25.76 and SCR19.34 respectively. The root-mean-square coefficient of variation for the two batches A and B are 14 % and 19 % respectively for SCR25.76, and 19 % and 20 % respectively for SCR19.34. These results tend to suggest that there is no significant difference in the mean values of the batches of SCR25.76 specimens, but that there may be a significant difference in the strength distribution of the two batches of SCR19.34 specimens.

Given that the specimens in batch A and batch B were polished under nominally identical conditions, i.e., on the same 14μm and 6μm laps for roughly the same period of time under the same load, and that the results at 20°C for batches A and B of SCR25.76 imply that the frictional forces at the silicon nitride knife-edges and the alumina rollers may be similar in magnitude (no comment can be made regarding the frictional forces at the tungsten carbide rollers due to the lack of comparative data), the most probable explanation for the difference in the mean strengths obtained on the room and high temperature rigs at room temperature and the difference between the A and B batches of SCR19.34, at 20°C in particular, is that there are microstructural differences between the specimens from batch A and batch B, i.e., from the different tablets sourced from the same parent tile.

The mean flexural strength at room temperature of all the 22 A batch data for both materials is given below with the sample standard deviation and percentage coefficient of variation:

SCR25.76 : 110.3 ± 13.4 MPa (12 %)

SCR19.34 : 115.3 ± 9.6 MPa (8 %)

This compares with the results from the 20 A batch data obtained on the room temperature test rig:

SCR25.76 : 107.9 ± 11.3 MPa (10 %)

SCR19.34 : 114.2 ± 9.0 MPa (8 %)

The equivalent mean flexural strength data for the 8 B batch data are:

SCR25.76 : 137.3 ± 27.3 MPa (20 %)

SCR19.34 : 210.8 ± 42.0 MPa (20 %)

These results again suggest that there are microstructural differences between the batch A and batch B specimens, especially of SCR 19.34; the results also suggest that the microstructural differences may vary gradually within the parent tile since the scatter in data for the specimens from a given tablet is not excessively high. Only a thorough SEM microstructural and fractographic study of the specimens in batches A and B will provide further information regarding the apparent differences in strength; unfortunately, time did not allow for such a study during the present project.

Despite the differences in the apparent flexural strength data from both batches, both the A and B batch data in Table 4.16 and the mean strength data (of the combined A and B batch data) plotted in Figure 4.14 show roughly similar behaviour as a function of increasing temperature. At all temperatures the SCR19.34 material exhibited a higher flexural strength than the SCR25.76 glass-ceramic; for both materials the mean flexural strength (of the combined A and B data) increased with increasing temperature from 250°C up to a maximum at 600°C and then fell continuously. The behaviour was still effectively linear elastic at 700°C, but specimens of both materials deformed plastically at 750 and 800°C; the approximate maximum stress endured before plastic

deformation commenced was ≈ 50 MPa at 700°C and ≈ 30 MPa at 800°C. None of the specimens tested above 700°C were deformed to failure as the tests were stopped well before failure.

The peak in the flexural strength of SCR25.76 and SCR19.34 (nominally at 600°C) is attributed to the softening of the intergranular residual glass which blunts the flaws in the glass which then require an increased crack-tip stress to continue propagating, increasing the stress required for fracture. However, as the temperature increases the glass softens to such an extent that the material can no longer sustain an applied load and deforms plastically.

At 600°C the Young's modulus of SCR19.34 is ≈ 10 % lower than the nominal room temperature value of 115 GPa, while that of SCR25.76 is ≈ 14 % lower than the nominal room temperature value of 122 GPa; this was discussed in Chapter 3, Section 3.7.2, sub-section (2.6), and was explained by the fact that although SCR19.34 has a higher volume fraction of residual glass than SCR25.76 (i.e., ≈ 0.4 for SCR19.34 compared to ≈ 0.3 for SCR25.76), the viscosity of the SCR19.34 residual glass is higher than that of SCR25.76. The difference in the residual glass viscosities was illustrated by the temperature range corresponding to the incipient softening or dilatometric viscosity of ≈ 10^{10} to 10^{11} Pa.s; the incipient softening point of the SCR19.34 residual glass corresponds to the temperature range ≈ 480°C to 520°C, while that of the SCR25.76 residual glass corresponds to a temperature range of ≈ 440°C to 480°C. So at 600°C, the effective Young's modulus of SCR19.34 is ≈ 104 GPa, while that of SCR25.76 is ≈ 105 GPa; thus the room temperature flexural strength differential between SCR19.34 and SCR25.76 is maintained up to 700°C.

Two specimens of the SCF5 glass-ceramic were tested at elevated temperatures of 600°C, 800°C, and 850°C, and one specimen at both 745°C and 900°C; the data are tabulated in Appendix 4G, Table 4G.6. The fracture behaviour was linearly elastic up to 800°C, while one of

the two specimens tested at 850°C deformed plastically and the specimen tested at 900°C deformed plastically almost immediately. The better high temperature behaviour of SCF5 compared to SCR25.76 and SCR19.34 can explained by a number of factors, (i) the volume fraction of residual glass is ≈ 0.2, (ii) the Young's modulus at 600°C is only ≈ 5 % lower than the nominal room temperature value of 121 GPa, i.e., ≈ 115 GPa, (iii) the incipient softening point corresponds to a temperature range of ≈ 630 to 680°C, and (iv) the essentially continuous interlocking crystal network. The mean flexural strength at 800° was 185 MPa, i.e., the same as the room temperature strength.

CHAPTER 5

FRACTURE TOUGHNESS AND HARDNESS

5.1 Introduction to Conventional Fracture Toughness

The fracture toughness of a material is defined as its resistance to the catastrophic, rapid propagation under stress of a pre-existing flaw in the material. The stress required to cause catastrophic fracture from a flaw in a non-ductile material depends on the flaw size according to the Griffith criterion for fracture

$$\sigma = \alpha(E\gamma_E/c)^{1/2} \qquad [5.1]$$

where σ is the tensile stress acting on the material body, E is the Young's modulus, γ_E is the effective fracture surface energy, c is the characteristic crack length and α is a numerical constant of the order of one (see Chapter 4). Thus the stress which can be endured by the body without rapid and fatal propagation of the crack decreases as the initial size of the flaw increases, and as the crack propagates the stress required for further propagation decreases; for a given flaw size the critical stress for rapid crack propagation depends on E and γ_E. Hence the effective fracture surface energy of a material, γ_E, is a fracture toughness parameter, i.e., it describes the resistance to crack propagation.

From Chapter 4, a crack is at equilibrium with respect to propagation when dU/dc = 0, that is

$$\frac{dU}{dc} = \frac{d}{dc}(U_C + U_W) + \frac{dU_S}{dc} = 0 \qquad [5.2]$$

where U is the total potential energy of the applied load-crack-plate system, U_C the elastic strain energy stored by virtue of the presence of the crack, U_W the negative potential energy of the load and U_S the effective surface energy required to create the new fracture surfaces. Equation [5.2] refers to a through-thickness crack in an infinite plate of unit thickness; in practice a plate whose length and breadth are very much larger than those of the crack itself.

The strain energy release rate with respect to the crack length per unit thickness, G, is defined by

$$G = - \frac{d}{dc}(U_w + U_c) \qquad [5.3]$$

The crack propagation resistance, R, per unit thickness is defined by

$$R = \frac{dU_s}{dc} \qquad [5.4]$$

G represents the rate of change of energy available for crack propagation with respect to crack length per unit thickness, while R represents the rate of change of energy required to create new fracture surfaces with respect to crack length per unit thickness; note that the definitions of G and R are in fact the rates of change with respect to crack area. An equation for G can be derived analytically for a body of thickness B with an edge-crack of length c, which is loaded in uniaxial tension perpendicular to the crack plane by a load P; the derivation after Irwin is given in Appendix 5A and the result repeated here

$$G = (P^2/2B)(d\bar{\varsigma}/dc) \qquad [5.5]$$

where $\bar{\varsigma}$ is the compliance of the body (defined as the load application-surface displacement/applied load with units of mN^{-1}, i.e., the reciprocal of stiffness) and G is independent of the loading configuration and has units of Nm^{-1}, i.e., Jm^{-2}.

The crack propagation resistance, R, is a constant for a given non-ductile material at a given temperature and under plane strain conditions (i.e., when a non-zero stress is induced parallel to the crack front and there is no strain parallel to the crack); so for the crack to be unstable with respect to propagation such that it propagates with accelerating velocity until fracture occurs, G must exceed a critical, constant value equal in magnitude to R. This critical value of G is denoted by $G_{crit.}$ and is a material property; so the necessary condition for fracture is

$$G \geq G_{crit.} \qquad [5.6]$$

$G_{crit.}$ is thus another fracture toughness parameter, i.e., a measure of the resistance to crack propagation.

In Chapter 4 it was stated that the presence of a crack in a body raises the stress in the immediate vicinity of the crack-tip above that of the remotely applied stress; the stress intensity factor is a measure of the degree to which the localised stress field near a crack is intensified by the presence of the crack compared to the general stress field. The stress intensity factor describes the intensity, but not the distribution of the local stress field at a crack tip, and depends only on the crack-body geometry and the applied loading configuration.

There is a stress intensity factor for each of the three independent ways of stressing a crack; the three modes are shown in Figure 5.1 (a) and are:

(i) The tensile opening mode or mode 1

(ii) The sliding mode or mode 2

(iii) The tearing mode or mode 3

The crack propagation modes describe the relative motions of the two crack surfaces as the crack propagates; either singly or in combination they describe all the possible modes of crack propagation in an elastic material. Modes 2 and 3 involve shearing displacements, whereas mode 1 involves cleaving displacements. Mode 1 is the predominant mode for many materials, particularly non-ductile materials, and thus mode 1 behaviour will be assumed from here on.

The evaluation of stress intensity factors is based on the principles of Linear Elastic Fracture Mechanics (LEFM) which assumes the material is perfectly linear elastic and isotropic in behaviour and generally is mathematically very complex; it involves assuming plane deformation, i.e., plane stress or plane strain conditions and then finding a 'stress function', ϕ which satisfies the 'biharmonic' equation of linear elasticity

$$\frac{\partial^4 \phi}{\partial x^4} + \frac{2\partial^4 \phi}{\partial x^2 \partial y^2} + \frac{\partial^4 \phi}{\partial y^4} = 0 \qquad [5.7]$$

derived from the equilibrium equations of stress and the compatibility equations of strain and whose stress solutions satisfy the boundary conditions of the given crack problem (Parker, A.P., 1981).

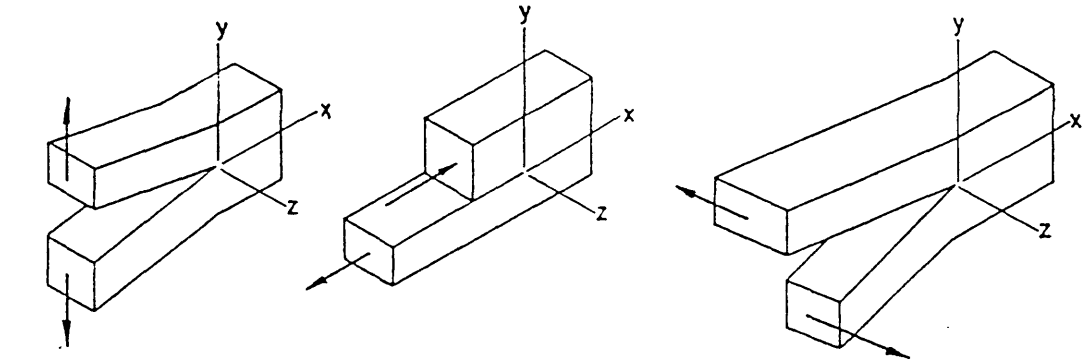


Figure 5.1 (a) Schematic Diagram Showing the Three Independent Crack Propagation Modes.

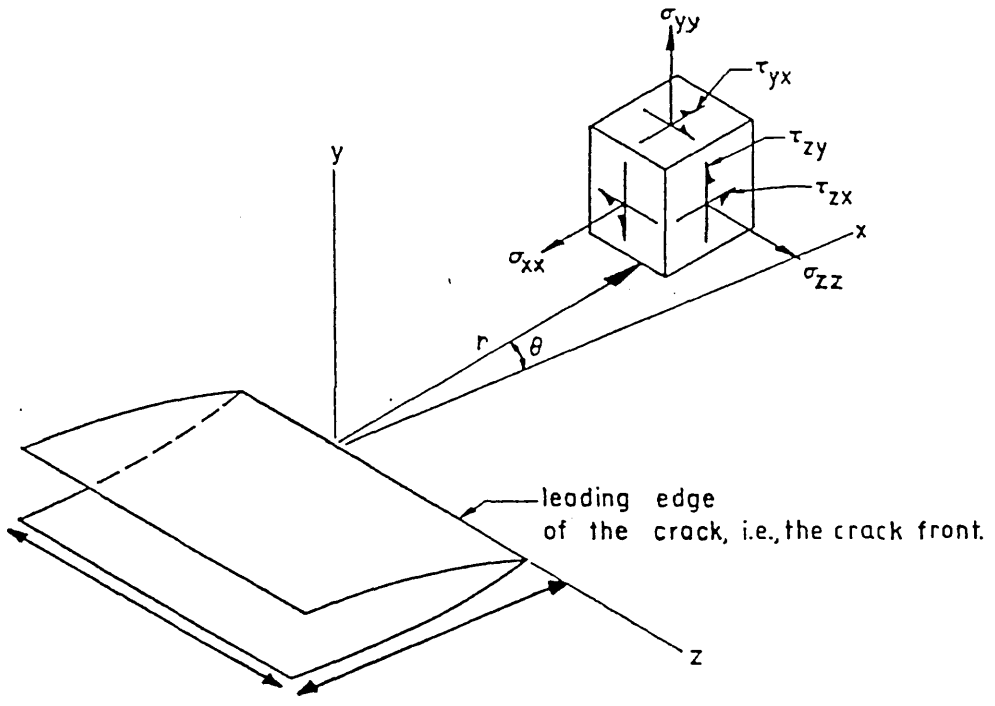


Figure 5.1 (b) Coordinate System With Respect to the Crack Front for the Stress Components in the Crack Tip Stress Field.

The general form of the stress components describing the elastic stress field in the vicinity of a plane crack tip, whose tip is assumed to be infinitely sharp, is

$$\sigma_{ij} = K_N(2\pi r)^{-1/2}[f(\theta)]_{ij} + O(r) \qquad [5.8]$$

where σ_{ij} is the stress component in the direction j in the plane normal to the direction i, K_N the stress intensity factor where N = 1,2,3 (i.e., the crack propagation modes), r the radial distance from the crack tip to the infinitesimal continuum body element which is at an angle θ to the crack plane, and $f(\theta)_{ij}$ is a function of θ (See Figure 5.1 (b)). Note that O(r) denotes an infinite series of higher-order terms in r which, being negligible for $0 < r \ll c$ where c is the crack length, are neglected without significant loss of accuracy for $0 < r \ll c$. This equation shows that the stress intensity factor is a stress scaling factor independent of the stress spatial distribution variables r and θ. Dimensional analyses of equations of the form of equation [5.8] (Paris, P.C. and Sih, G.C., 1965) show that in general the mode 1 stress intensity factor (K_1) is a function of the applied stress (σ) and the characteristic crack length (c)

$$K_1 = D\sigma c^{1/2} \qquad [5.9]$$

where D is a dimensionless constant which is specific to a given loading geometry and body-crack configuration through the compliance factor Y and a given flaw shape via the flaw shape parameter Z since D = Y/Z. There are some exceptions to equation [5.9]; most notably the double torsion test specimen stress intensity factor which is not a function of crack length.

For an internal through-thickness crack of length 2c with a linear crack front in a infinite plate, $Y = \pi^{1/2}$ and Z = 1, i.e., $D = \pi^{1/2}$; hence $K_1 = \sigma(\pi c)^{1/2}$. From Appendix 5A equation [5A.2] gives $G = (\beta\pi\sigma^2 c)/E$, and for the crack length 2c, $G = (\beta\pi\sigma^2 c)/E$. Since $\sigma^2 = (K_1)^2/(\pi c)$,

$$G_1 = \beta(K_1)^2/E \qquad [5.10]$$

where as per [5A.2], $\beta = 1$ and $(1 - \nu^2)$ for plane stress and plane strain conditions respectively. This equivalence between G and K has been demonstrated analytically (Irwin, G.R., 1957), and is valid for all loading configurations

and crack-body geometries. Considering equations [5.6] and [5.10] indicates that the following equation can be written

$$G_{crit.} = \beta(K_{1crit.})^2/E \qquad [5.11]$$

where K_{1crit} is constant under plane strain conditions and a material property like $G_{crit.}$ and likewise it forms the basis of a fracture criterion; for fracture to occur, the mode 1 stress intensity factor, K_1, must satisfy the condition

$$K_1 \geq K_{1crit.} \qquad [5.12]$$

As both $G \geq G_{crit.}$ and $K_1 \geq K_{1crit.}$ are fracture criteria for mode 1 crack propagation, the criteria are normally written as

$$G_1 \geq G_{1c} \qquad [5.13]$$

and

$$K_1 \geq K_{1c} \qquad [5.14]$$

where G_{1c} is known as the critical plane strain elastic strain energy release rate (i.e., the critical rate at which energy is made available for crack propagation under plane strain conditions) and where K_{1c} is the critical plane strain stress intensity factor, but normally called the plane strain fracture toughness. Although K_{1c} is regarded as a material property at a given temperature if the material behaviour is elastic, the apparent value is affected by strain rate and the environment for the reasons discussed in Chapter 4, Section 4.7.1.

The three fracture toughness parameters, γ_E, G_{1c} and K_{1c} are related to each other via the following equations which refer to a crack length of c at fracture

(a) $G_{1c} = 2\gamma_E$ (see equations [4.2] and [5.4]),

(b) $\sigma = (2E\gamma_E/[\beta\pi c])^{1/2}$ (see equation [4.3]), and

(c) $K_{1c} = D\sigma c^{1/2}$ (see equation [5.9]); hence

$$K_{1c} = D(2E\gamma_E/[\beta\pi])^{1/2} = D(EG_{1c}/[\beta\pi])^{1/2} \qquad [5.15]$$

Since $D = \pi^{1/2}$ for an infinite body or in practice, $D \approx \pi^{1/2}$ for a body wherein $c \ll L$, L being the smallest linear dimension of the body, equation [5.15] becomes

$$K_{1c} = (2E\gamma_E/\beta)^{1/2} = (EG_{1c}/\beta)^{1/2} \qquad [5.16]$$

where $\beta = 1$ and $(1 - \nu^2)$ for plane stress and plane strain conditions respectively.

5.2 Introduction to Hardness

The hardness of a material is not a uniquely defined material property as there are a number of test techniques which claim to measure it. The term hardness is taken to mean the deformation resistance of a material, but each test method only defines a self-consistent resistance to deformation, and a comparison of hardness values from one test method with those from another for a given material is to be avoided. Hardness measurements can be classified into three generic groups:

(i) Scratch hardness which measures the resistance to to scratching, e.g., the Mohs' scale of hardness which is only a measure of relative scratch resistance.

(ii) Indentation hardness which measures the resistance to plastic, i.e., permanent, deformation under an essentially static load, e.g., Vickers, Knoop, Brinell, and Rockwell static indentation hardness tests.

(iii) Dynamic or rebound hardness which measures the resistance to elastic-plastic deformation under impact, i.e., dynamic or kinematic loading, e.g., the Shore Scleroscope method which involves measuring the rebound height of a small anvil dropped from a height of 0.25 m. See D. Tabor (1951) for a full treatment of hardness.

The most frequently used hardness tests for ceramics are the Vickers, Knoop and Rockwell-Superficial (N scale) tests. Due to the high hardness of most ceramics, these tests employ diamond-tipped indenters; the Vickers test employs a square-based pyramidal indenter, the Knoop test a rhombohedral-based pyramidal indenter, and the Rockwell test a hemispherical-tipped cone. In these methods the hardness is calculated from (1) a specified dimension of the indent made in the material by the indenter and (2) the load applied to it, via an equation which accounts for the indenter geometry; the Vickers and Knoop tests use the indent diagonal width, and the Rockwell test the indent depth. Schematic diagrams of the Vickers and Knoop indenter geometries are shown in Figure 5.2 (a) and (b) respectively.

The Vickers and Knoop hardness tests were used in the present work and are therefore discussed below. The Vickers test gives the hardness in terms of the Diamond Pyramid Number (DPN) or Vickers Pyramid Number (VPN) or HV. These numbers are all defined as the applied load in kgf divided by the actual surface area of the indent in mm^2; thus according to Figure 5.2 (a) the base diagonal length is DE and the area of a face equals AB x AO. So the total facial area, A_F equals 4.AB.OA. The square-base area of the pyramid equals the projected area of the indenter faces, $A_P = d^2/2$. Now $AB = d/(2.2^{1/2}) = AC$ and $AO = AC/\sin(136°/2)$, so $A_F = 4.AB.AB/\sin(68°) = (d^2/2)/\sin(68°) = A_P/\sin(68°) = A_P/0.9272$. By definition, $HV = P/A_I$ where P is the applied indenter load and A_I the actual indent surface area, and $A_I \equiv A_F = A_P/0.9272 = d^2/1.8544$. Hence

$$HV = 1.8544P/d^2 \qquad [5.17]$$

where P is the applied indenter load in kgf and d is the mean of the two diagonals in mm; the result is usually quoted as, e.g., 700 HV10 for a load of 10 kgf.

The Knoop hardness test gives the hardness number in terms of the Knoop Hardness Number (KHN) or HK. These numbers are defined as the applied load in kgf divided by the projected area of the unrecovered indent in mm^2; from Figure 5.2 (b) the length of the long projected diagonal is AB = a and the length of the short projected diagonal is DE = b. Now it can be seen from the inset diagram that (1) $\tan(65°) = b/2.OC$ and (2) $\tan(86.25°) = a/2.OC$; hence dividing (2) by (1) gives $\tan(86.25°)/\tan(65°) = a/b$, i.e., $a = 7.1145b$ where a and b are the lengths of the long and short projected diagonals respectively. Now the projected indent area equals $ab/2 = a^2/14.229$; thus

$$HK = 14.229P/a^2 \qquad [5.18]$$

where P is the applied load in kgf and a is in mm; the result is quoted as, e.g., 1000 HK0.1 for a 0.1 kgf load. In the ceramics literature, however, Vickers and Knoop hardness values are quoted in S.I. units of Pa (= Nm^{-2}). As 1 kgf ≡ 9.80665 N, equations [5.17] and [5.18] become $HV = 18.1855P/d^2$ Pa and $HK = 139.5388/a^2$ Pa respectively, where P is the indenter load in kgf, and d and a are in m.

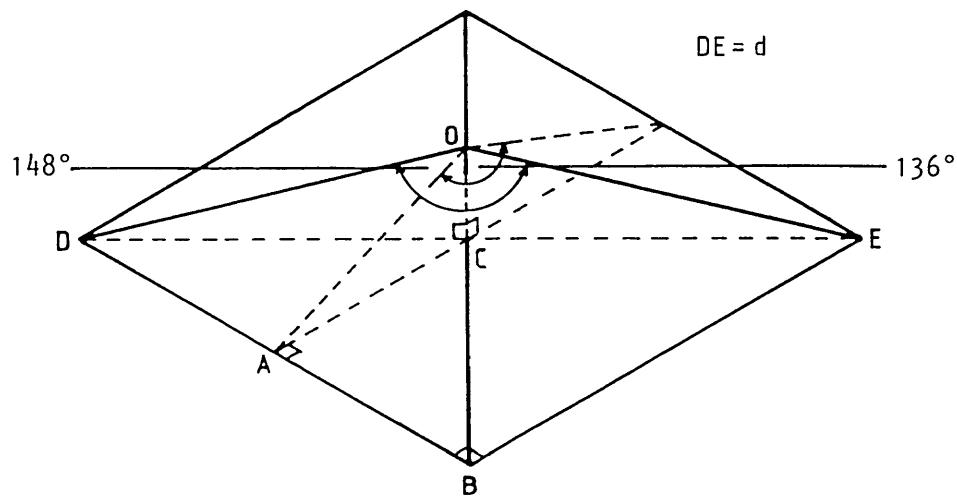


Figure 5.2 (a) Schematic Diagram of the Vickers Indenter Geometry.

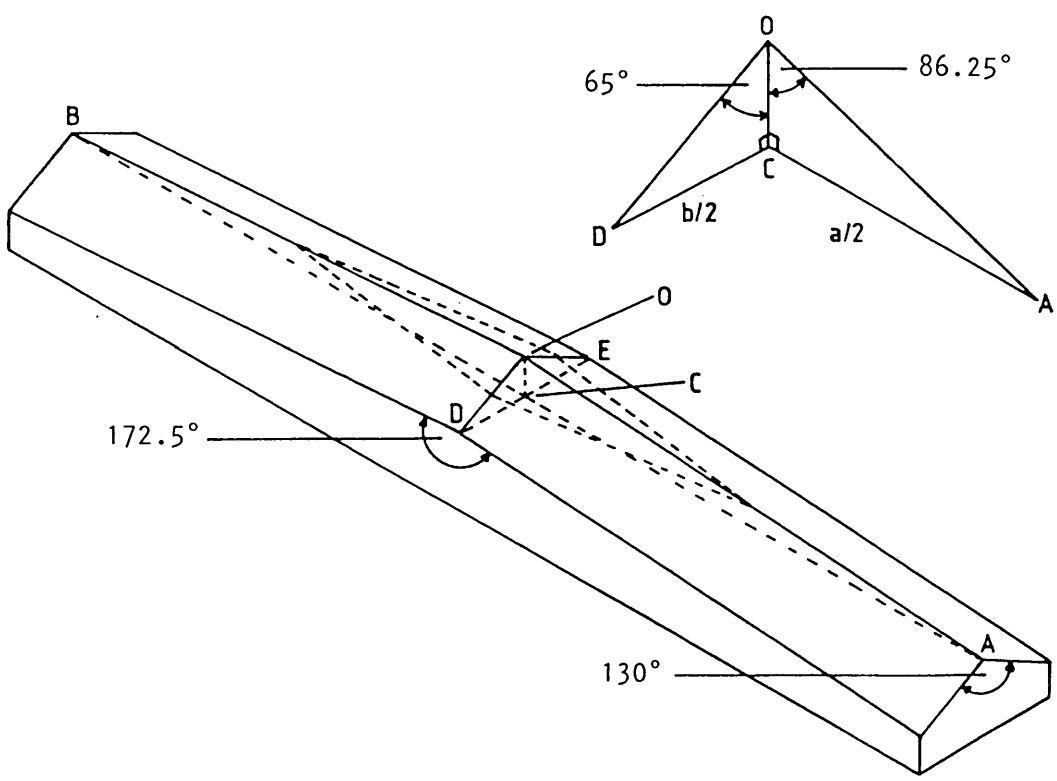


Figure 5.2 (b) Schematic Diagram of the Knoop Indenter Geometry.

5.3 Introduction to Indentation Fracture Toughness

The determination of the fracture toughness of a non-ductile material by direct measurement of the lengths of the cracks which invariably emanate from the corners of the indent produced by a sharp-pointed indenter such as a Vickers or Knoop indenter is a relatively recent technique; the recognition that the extent of the concomitant cracking of a hardness indent in a non-ductile material must be indicative of the fracture toughness of the material is attributed to S. Palmqvist (See A.G. Evans (1979) for example). A comparison of the cracks formed around the indents produced in soda-lime glass by various sharp-pointed indenters, including Vickers and Knoop indenters has been conducted (Marion, R.H., 1979); the study demonstrated that the cracks produced by a Vickers indenter were the easiest to measure for length and that the measured crack lengths had the least scatter, and concluded that the Vickers indenter is the most suitable indenter for determining indentation fracture toughness.

There are two approaches to the determination of indentation fracture toughness depending on what indentation crack geometry is assumed to exist or exists beneath the Vickers indent in a given material; one approach assumes a fully developed 'half-penny' radial/median crack system, while the other assumes a Palmqvist (radial) crack system as shown schematically around a Vickers indent in Figure 5.3 (a) and (b) respectively. Both figures also show the crack front of sub-surface lateral fractures which generally form around an indent, and the characteristic dimensions of the indent-crack systems; the indent half-diagonal length, a, the Vickers radial crack length, c, and the Palmqvist radial crack length, l. Note the typical idealised conception of the median crack as a 'half-penny' shape of radius c. A brief survey of the various relationships between the fracture toughness and the applied indenter load and the characteristic crack length, i.e., either c or l, to be found in the literature is presented below.

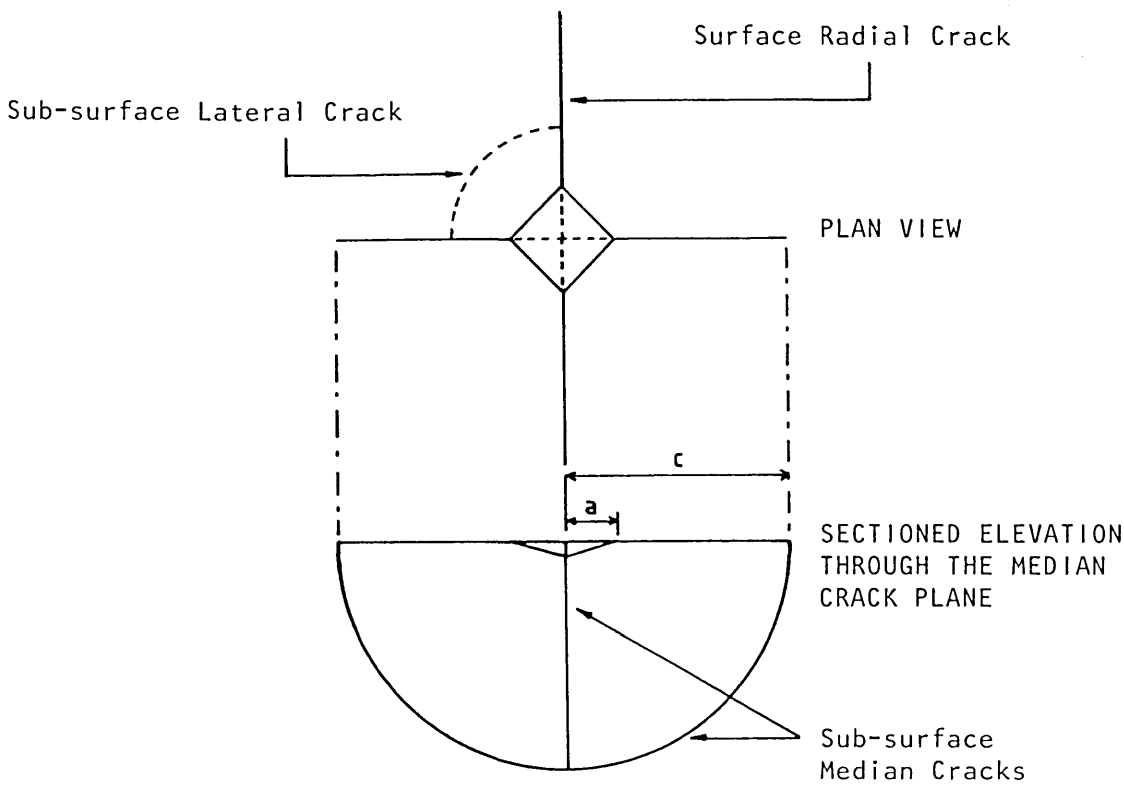


Figure 5.3 (a) Schematic Idealized Plan and Elevation of a Vickers Radial-Median 'Half-Penny' Crack System.

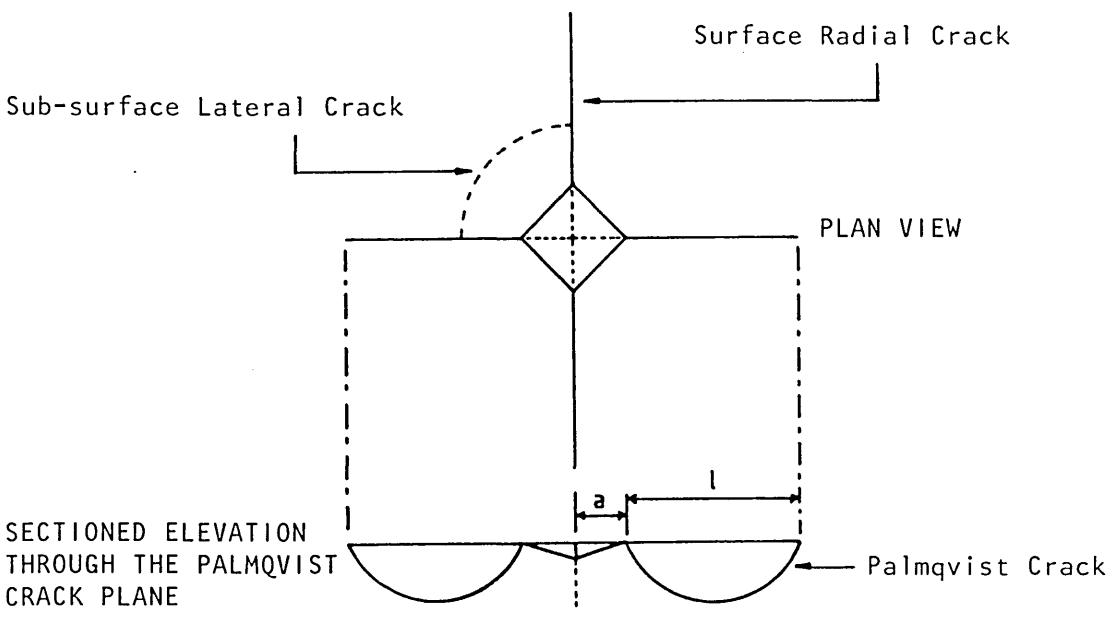


Figure 5.3 (b) Schematic Idealized Plan and Elevation of a Vickers Palmqvist Crack System.

Fracture toughness relationships assuming the crack system to be radial/median will be described first. R.H. Marion (1979) has reviewed the use of the elastic fracture mechanics analyses of Lawn, B.R., and Swain, M.V., (1975) and Lawn, B.R., and Fuller, E.R., (1975); both these analyses considered the fully developed 'half-penny' shaped median crack which generally forms beneath the indent caused by a sharp-pointed indenter, typified by the Vickers indenter. The Lawn and Swain two dimensional elastic fracture mechanics analysis yielded an equation of the form

$$K_c = \text{constant}.(P/D)^{1/2} \qquad [5.19]$$

where K_c is the indentation fracture toughness (a critical stress intensity value for indentation fracture), P is the indenter load, D is the major median crack depth. The constant is a function of (i) Poisson's ratio, (ii) dimensionless constants determined by the indenter geometry and the deformation zone geometry, and (iii) and the mean contact or indentation pressure exerted by the indenter, p_M (= P/A_P and is independent of the applied indenter load for non-spherical indenters which form geometrically similar indents in a homogeneous material regardless of the applied load[Tabor, D., (1951)], e.g., HK = p_M and HV = $0.9272p_M$). The Lawn and Fuller dimensional analysis (only strictly valid for cone indenters) gave

$$K_c = (1/[\pi^{3/2}\tan\Xi])(P/D^{3/2}) \qquad [5.20]$$

where $\Xi = \Theta \pm \arctan(\mu)$ in which Θ is the indenter cone half-angle (in the case of the Vickers indenter, Θ was taken as the angle between opposite edges (74°) by Lawn and Fuller and the angle between opposite faces (68°) by Marion) and μ is the sliding coefficient of friction between the indenter and material; also it does not involve the hardness, i.e., p_M. Equations [5.19] and [5.20] predict that a plot of P against D and $D^{3/2}$ respectively should be a straight line for a given material, i.e., for a given fracture toughness. Marion found that $c \approx D$ for the Vickers indents in soda-lime glass in agreement with Lawn and Fuller, and concluded that both equations were equally good for qualitatively

ranking the fracture toughness of ceramic materials when using a Vickers indenter at high loads, although [5.20] is less complex.

An important development was the recognition by A.G. Evans and T.R. Wilshaw (1976) that the indentation stress field due to a sharp indenter is essentially elastic-plastic in nature; a dimensional analysis of indentation fracture showed that the indentation radial crack length, c should be related to the indent half-diagonal length, a by

$$K_c\phi/(Ha^{1/2}) = F_1(c/a)F_2(\nu,\mu,r_p/a) \qquad [5.21]$$

where K_c is the fracture toughness, H the hardness, ϕ the constraint factor (= H/σ_Y where σ_Y is the uniaxial yield stress (tensile or compressive) and taken as ≈ 3), r_p the plastic zone radius, and F_1 and F_2 are empirically determined functions. The validity of this functional relationship was investigated (Evans, A.G. and Charles, E.A., 1976) using conventional fracture toughness (DT K_{Ic}) data measured in a dry N_2 environment in place of K_c, i.e., assuming $K_c \equiv K_{Ic}$; no valid correlation between c/a and $K_c\phi/(Ha^{1/2})$ was found for the Knoop indent data, regardless of which diagonal was used to obtain a. A correlation was, however, observed in the Vickers indent data, but an additional dependence of c/a on hardness at a given $K_c\phi/Ha^{1/2}$ value was also observed; the trend being that c/a decreased with increasing hardness. They presumed that the known effect of r_p/a decreasing with increasing hardness was the primary source of the hardness dependence of F2, and their analysis based on this presumption implied that F2 is a power function of $E\phi/H$; this was confirmed by data fitting, giving $F2 = (E\phi/H)^{2/5}$.

The slope of $\log([K_c\phi/(Ha^{1/2})][H/E\phi]^{2/5})$ versus $\log(c/a)$ for the large c/a polycrystal data was effectively -3/2, which is the same slope given by $K = P/(\pi c)^{3/2}$ which is the elastic solution for a penny-shaped crack wedged at the centre by a load P. Using the Vickers hardness, $H = 0.47P/a^2$ (cf. $HV = 1.8544P/(4a^2) = 0.46P/a^2$), Evans and Charles obtained by analogy

$$K_c\phi/(Ha^{1/2}) = 0.15k(c/a)^{-3/2} \qquad [5.22]$$

where k is a correction factor to $K = P/(\pi c)^{3/2}$ required by the presence of the free surface and equal to 3.2. Substituting $1.8544P/(4a^2)$ for H, equation [5.22] can be rearranged to give K_c in $Pa.m^{1/2}$ ($= Nm^{-3/2}$)

$$K_c = 0.16Ha^2/c^{3/2} = 0.074176P/c^{3/2} \qquad [5.23]$$

where P is the indenter load in N and c is in m.

In a review of the elastic-plastic stress field approach to indentation fracture (Evans, A.G., 1979), it was shown that the use of either a generalised stress analysis in conjunction with linear elastic fracture mechanics concepts or a dimensional analysis procedure could be used to obtain the following crack extension relationship

$$K_c/(Ha^{1/2}) = g_1(c/a)g_2(E/H) \qquad [5.24]$$

where g_1 and g_2 are independent dimensionless functions if stresses within the plastic deformation zone do not exert a significant influence on the crack extension. By regarding the indenter as a wedge and applying the solution for a penny crack wedged by a force Q at the centre, i.e., $K = Q/(\pi c)^{3/2}$, an analogous crack extension relationship was obtained

$$K_c/(Ha^{1/2}) = k(H/E)(c/a)^{-3/2} \qquad [5.25]$$

where k is a function and $g_1 \equiv (c/a)^{-3/2}$. It was found from data analysis that an appropriate function for g_2 was $g_2 = (E/H)^{2/3}$ and a covenient polynomial fit to the data plot of log(A) versus log(c/a) was log(A) = F where $F = -1.59 - 0.34B - 2.02B^2 + 11.23B^3 - 24.97B^4 + 16.32B^5$ and B = log(c/a), and $A = ([K_c/(Ha^{1/2})][H/E]^{2/3})$. Note that log denotes $\log_{10}$. An equation for K_c can be written by noting that as log(A) = F, $A = 10^F$; this gives

$$K_c = Ha^{1/2}(E/H)^{2/3}.10^F = 0.6305E^{0.4}P^{0.4}.10^F a^{-0.7} \qquad [5.26]$$

where $H = 1.8544P/(4a^2)$, P is the indenter load in N, and a and c are in m, giving K_c in $Pa.m^{1/2}$. Note the data analysed above to give equation [5.26] were the polycrystal data of Evans and Charles, and that the constraint factor, ϕ was not considered in the analysis; also it has been reported that (a) there was an error in the choice of the constraint factor used by Evans and Charles, and (b) the above polynomial fitted curve gives

an equally good data fit albeit with a slope of -1.32 and not -1.5 as obtained by Evans and Charles (Marshall, D.B., and Evans, A.G., 1981). Evans attempted to correlate the data in terms of g_1 alone as if the plastic zone size and residual stresses were not significant factors and found it to be inadequate, suggesting that their effects via $g_2(E/H)$ may be significant; he also attempted to correlate the data with the prediction of the Lawn and Fuller equation [5.20], namely that P is proportional to $c^{3/2}$; he found that at large c/a ratios, the prediction is a reasonable approximation, because at large c/a the influence of the local elastic-plastic stress field around the indent is negligible. This helps to explain Marion's favourable verdict regarding the Lawn and Fuller equation.

At this point it is appropriate to briefly discuss some of the experimental evidence in the literature for the existence of a residual tensile stress component in the elastic-plastic stress field of an indent produced by a sharp indenter. A systematic study of the microcracking associated with the indents produced in non-ductile solids by various pointed diamond indenters, including Vickers and Knoop indenters (Lawn, B.R., and Swain, M.V., 1975) showed that in general median cracks form during indenter loading and propagate downward beneath the indent on planes of symmetry, while lateral cracks form during indenter unloading and propagate sideways, away from the indent and roughly parallel to the specimen surface. Furthermore, the lateral cracks continue to extend after complete unloading, arcing towards the specimen surface, and they may even intersect the specimen surface, thereby causing chipping. It was also observed that during the latter stages of indenting at high loads, e.g., 500 N in soda-lime glass, the primary median cracks intersect the specimen surface forming the commonly observed radial surface cracks.

A study of indentation cracking in non-ductile materials was conducted on single crystal NaCl, spinel and sapphire, polycrytalline ZnSe (CVD), ZnS (CVD), silicon nitride (HP), and glass using spherical tungsten carbide

indenters and a rigidly mounted Vickers indenter (Evans, A.G., and Wilshaw, T.R., 1976). Direct *in situ* observation and acoustic emission monitoring during indentation using a spherical indenter showed (for all materials, except ZnSe, NaCl and glass) that surface radial cracks of the Palmqvist type formed initially during loading, followed by the formation of sub-surface "penny shaped", i.e., circular, median cracks beneath the indent on planes of symmetry about the load axis. On loading up to the peak load, coplanar radial surface cracks and median cracks combined, while non-coplanar radial surface cracks and median cracks continued to develop independently. Furthermore, sub-surface lateral cracks formed and propagated between the radial/median cracks, roughly parallel to the specimen surface.

Upon unloading, it was noted that all three crack species, i.e., radial, median, and lateral, continued to extend, with the merged radial/median cracks taking on an approximate "half-penny" configuration. Occasionally additional cracks were formed on unloading; however, the degree of extension on unloading decreased with increasing peak load and time at the peak load. Other significant observations were that (a) the incidence of chipping increased with increasing peak load, (b) the radial cracks terminated at or near the indent perimeter with a large, permanent crack-mouth displacement which indicated the existence of a substantial residual strain (and hence stress) field, (c) the existence of more than one lateral crack stratum, (d) the extensive microcracked zone directly beneath the indent, and (e) the negligible "pile-up" of material at the indent perimeter, which indicated that plastic deformation, i.e., strain, beneath the indenter was accommodated by the elastic matrix surrounding the plastic zone.

In the case of ZnSe, it was observed that while the radial and median cracks formed in the above sequence, the radial crack extension was both more intermittent and variable in magnitude, and that lateral cracks did not form around isolated indents, but did form when the

indents were juxtaposed. On indenting NaCl it was observed that shallow radial cracks formed between slip bands on {110} planes rather than on the normal {100} cleavage planes; this behaviour was attributed to the deformation anisotropy of the material. When the glass was indented, only median cracks were observed to form during loading, but on unloading the median cracks propagated towards the specimen surface, intersecting it and forming surface radial cracks, and lateral cracks developed and propagated prior to complete unloading. This behaviour was similar to that observed in soda-lime glass by Lawn and Swain (1975). A comparison of the cracking produced by spherical indenters (as summarized above) with that produced by a Vickers indenter (for all the materials) showed that the lateral crack extensions were almost identical, but the radial crack extensions were markedly greater for the Vickers indenter.

Further *in situ* observation of median crack development in soda-lime glass subject to a Vickers indentation loading and unloading cycle (Marshall, D.B., and Lawn, B.R., 1979) at peak loads in the range $\approx$ 20 to 150 N showed that during loading "penny shaped" sub-surface median cracks formed beneath the indent on essentially orthogonal planes coincident with the indent diagonals. As the load increased up to the peak load, the "penny" median cracks propagated outwards and downwards with respect to the indent; on unloading, however, the penny cracks did not continue to extend downwards beneath the indent, but extended outwards and upwards, breaking through the specimen surface and forming radial surface cracks, i.e., a "half-penny" radial/median crack. At full unloading, c was roughly 1.8 times greater than at maximum loading, in the example given. At zero loading lateral cracking was also apparent.

At higher peak loads ($> \approx$ 150 N) the median cracks intersected the specimen surface prior to unloading as per the observations of Lawn and Swain (1975), while at lower peak loads ($<$ 20 N) cracks were not initiated until unloading commenced, and the half-penny configuration

developed without the formation of the intermediate sub--surface penny crack. Nevertheless, the final crack configuration attained was always similar to an idealised half-penny crack regardless of the peak indenter load.

A recent *in situ* investigation of the acoustic emission associated with cracking behaviour of soda-lime glass during Vickers indentation at different peak loads (Lee, S.H., and Kim, H.C., 1984) concluded that only crack initiation and propagation were accompanied by acoustic emission, since no acoustic emission was detected during an indenter loading - unloading cycle without an apparent crack at indenter loads $\leq$ 0.1 kgf. The level of acoustic emission for a given indenter load increased significantly during loading and unloading but was essentially constant during the peak load holding time for peak loads $\leq$ 5 kgf. There was an incubation time from the intial contact between the indenter and the specimen to the commencement of acoustic emission; the incubation time decreased with increasing peak load.

At peak loads $\geq$ 5 kgf, acoustic emission began almost immediately on loading; furthermore, a sudden large increase in the acoustic emission level was observed during the peak load holding period. In contrast, at loads $\leq$ 0.3 kgf, the level of acoustic emission during loading was negligible, but it increased with increasing indenter load. The increase in the acoustic emission during the peak load holding time was attributed to the median cracks intersecting the specimen surface, forming radial surface cracks. The acoustic emission after complete unloading, when the lateral cracks formed just prior to complete unloading are extending, was negligible in comparison to that emitted during loading and unloading, hence it was concluded that the median crack development was the major source of acoustic emission; although it was not stated explicitly by Lee and Kim, the acoustic emission during unloading would appear to be due to the extension of the median cracks into effectively a half-penny configuration.

In summary, the above data are evidence of the existence of a residual tensile stress component which

remains after complete unloading, and depending on the material it provides a sufficient tensile driving force (i) for both the initiation and the propagation of sub-surface lateral cracks upon unloading, or (ii) for the continued extension of the radial, median, and lateral cracks during on unloading, or (iii) for the initiation and propagation of both the radial surface and the lateral cracks upon unloading; however, according to the above data, this behaviour was only observed in soda-lime glass. For all the materials investigated, median cracks were initiated and primarily propagated during the loading cycle, and regardless of the actual cracking sequence all developed an essentially half-penny configuration on unloading.

The elastic-plastic model of "sharp" indenter indentation fracture was extended (Lawn, B.R., Evans, A.G. and Marshall, D.B., 1980) by explicitly resolving the complex elastic-plastic stress field beneath the indent into an elastic stress component, which is reversible, and a residual stress component, which is irreversible. This enhanced quantitative analysis of the radial/median crack system is based on fully-developed cracks, i.e., $c \gg a$ and the requirement that the indent geometries are similar regardless of the applied indenter load, e.g., as for Vickers indents, such that the relationship, $P/c^{3/2}$ = constant, is satisfied; this model is only concerned with far-field crack propagation in the radial/median single plane fracture system.

The elastic stress field component is taken to operate outside the plastic deformation zone, i.e, away from the indent, in the region where cracking occurs. Its operation is reversible in that it enhances sub-surface (median) crack propagation but suppresses surface (radial) crack propagation during the loading half-cycle, and then completely reverses its operation during the unloading half-cycle; thus the maximum median crack growth is attained during the load half-cycle and during unloading the constraint on radial crack extension is removed. The residual stress field component which provides the driving

force for continued radial and median (and lateral) crack extension during the unloading half-cycle, enabling the radial/median crack system to attain its near-half-penny equilibrium configuration upon complete unloading, results from the stresses induced by the strain mismatch between the surrounding elastic matrix and the plastic zone beneath the indent.

As a consequence of the reversibility of the elastic stress field component, its contribution to crack propagation is negligible in comparison with that of the irreversible residual stress field component. In accordance with the approximation that $c \gg a$, the residual stress component can be regarded as being concentrated at a point located at the crack centre at the elastic-plastic interface; so the plastically deformed zone is the source of a resultant residual crack-mouth opening point-force, and hence the stress intensity, K_r, due to the residual far-field force can be shown to be proportional to $P/c^{3/2}$. The point-force approximation has been shown to be valid for $c/a > \approx 2$ for Vickers indents (Marshall, D.B., 1983) and microscopic observation of radial cracks shows that they do not extend back into the plastically deformed zone (Evans, A.G., and Wilshaw, T.R., 1976). Furthermore, although the resultant residual force is a maximum under under the peak indenter load, it persists during unloading because it is due to a strain mismatch.

The crack extenstion relationship derived from the analysis of this model is

$$c = (\Xi_r (\cot\theta)^{2/3}[(E/H)^{1/2}/K_c])^{2/3} P^{2/3} \qquad [5.27]$$

where c is the surface (radial) equilibrium crack length after unloading, Ξ_r a dimensionless constant independent of the indenter/specimen system, θ the characteristic indenter half-angle (= 74° for the Vickers indenter), E the Young's modulus, H the hardness defined in terms of the projected indent area (= $P/2a^2$; i.e., not the actual indent surface area as defined for the Vickers hardness), K_c the indentation fracture toughness and P the applied indenter load. Note the indentation fracture toughness is now uniquely characterized from measurements of the

surface (i.e., radial) crack length alone, without any reference to the sub-surface (i.e., median) crack length; an advantage for opaque ceramics. Equation [5.27] can be rearranged to give

$$K_c = \Xi_r (\cot\theta)^{2/3} (E/H)^{1/2} P/c^{3/2} \qquad [5.28]$$

where Ξ_r was evaluated as 0.032 ± 0.002 using $\theta = 74°$ and the E/H ratio for soda-lime glass, to "calibrate" [5.28]. Using $H = P/2a^2$, equation [5.28] can be re-written as

$$[K_c/(Ha^{1/2})][H/E]^{1/2} = 0.028(c/a)^{-3/2} \qquad [5.29]$$

Comparing [5.29] with the equation of Evans and Charles (without considering the constraint factor)

$$[K_c/(Ha^{1/2})][H/E]^{2/5} = (c/a)^{-3/2} \qquad [5.30]$$

shows that for $c \gg a$, the two equations have the same form except for the exponent of H/E. In the above analysis Poisson's ratio was neglected on the empirical basis that curve fits to the indentation toughness data for different materials when plotted on a 'universal' curve are insensitive to the relatively small variations in Poisson's ratio for different ceramics. As a final note, the Lawn and Fuller equation (i.e., [5.20]), assuming $\mu = 0$ and $c \approx D$, can be re-written as

$$K_c = \pi^{-3/2} \cot\theta P/c^{3/2} \qquad [5.31]$$

Comparing this equation with [5.28] shows that the quantity E/H appears naturally as a consequence of considering the elastic-plastic nature of the indentation stress field and the residual stress field component.

Experimental optical observation of the evolution of the radial/median crack system in soda-lime glass subject to Vickers indentation showed that the median cracks developed during the loading half-cycle, while the surface radial cracks developed only during the unloading half-cycle as the indenter loads used (50, 90, and 130 N) were not high enough to force the sub-surface median cracks to intersect the specimen surface during loading. Similar observations of the Vickers indentation of zinc sulphide showed that as with soda-lime glass the median cracks developed during loading, but the radial crack extension during the loading half-cycle was significantly greater than in the soda-lime glass. This observation was

consistent with the model analysis; during loading the elastic stress field component suppresses surface radial crack growth and is effectively constant over the indenter load range employed in practical indentation testing, while the residual stress field component is scaled by the approximate factor $(E/H)^{1/2}$. Thus as the Young's modulus to hardness ratio increases the residual component becomes even more dominant relative to the elastic component and thereby more influential during the loading half-cycle as regards crack evolution; comparing the E/H ratios for zinc sulphide and soda-lime glass, 53.7 and 12.7 respectively shows why radial crack extension during loading was enhanced in zinc sulphide relative to soda-lime glass.

Furthermore, examination of the unloading data for radial crack evolution in zinc sulphide and in soda-lime glass given by Lawn, Evans and Marshall (1980) shows that the radial crack extension during unloading was lower for zinc sulphide; the change in the normalized crack size $(c^{3/2}K_c/P)$ on unloading from the peak load (P) to zero load was $\approx$ 0.05 for soda-lime glass compared to $\approx$ 0.02 for zinc sulphide. A recent study of the Vickers hardness of different alumina ceramics (95 to 99.7 % purity) in air and a simulated body environment (Rawlings, R.D., 1983) in which the acoustic emission during indenter loading and unloading was monitored, found that the sum total of acoustic emission ringdown, or event, counts during an indenting cycle increased with increasing indenter peak load over the range 25 to 200 N. During the unloading half-cycle, however, the number of counts detected was effectively constant, i.e., independent of load, and only a small fraction of the counts detected on loading; furthermore, the events were of low energy. It was thus concluded that for the alumina materials studied the amount of radial, median, and lateral crack extension on unloading was negligible compared with the extension during loading. The E/H ratio for 95 to 99.7 % Al_2O_3 is of the order of $\approx$ 20; this compares with $\approx$ 13 for soda-lime glass and $\approx$ 54 for zinc sulphide. So the results of Rawlings appear to be consistent with the above model.

A critical evaluation of the determination of fracture toughness from measurements of the lengths of the surface (i.e., radial) cracks emanating from Vickers indents in a wide range of technologically important ceramic materials has been conducted (Antis, G.R., et al., 1981) using equation [5.28] in the form

$$K_c = \Omega_r (E/H)^{1/2} (P/c^{3/2}) \qquad [5.32]$$

where Ω_r is a material-independent constant for Vickers-produced surface (radial) cracks; it replaces the quantity $\Xi_r (\cot\theta)^{2/3}$ in [5.28]. In order to evaluate the constant Ω_r, certain ceramic materials, i.e., glasses, a glass-ceramic, and ceramic polycrystals, were chosen as "reference" materials and tested (or literature values taken) to determine the hardness, Young's modulus and the double-cantilever-beam (DCB) K_{Ic} value of each. Each material was also tested to determine K_c, with care being taken to minimise non-equilibrium effects, e.g., environmentally-assisted post-indentation slow crack growth. As in [5.28], the hardness is taken as the mean contact or indentation pressure, i.e., $H = P/2a^2 = p_H$. According to equation [5.32], the parameter $P/c^{3/2}$ is constant, i.e., independent of P; this was found to be so for each material within experimental scatter by plotting $P/c^{3/2}$ against P. Thus substituting K_{Ic} for K_c and using the mean value of $P/c^{3/2}$, the hardness and Young's modulus for each chosen "reference" material in the following equation (rearranging [5.32])

$$\Omega_r = K_{Ic}/[(E/H)^{1/2}(P/c^{3/2})] \qquad [5.33]$$

gave a Ω_r value for each reference material and enabled the evaluation of a mean "calibration" constant, $\Omega_r = 0.016 \pm 0.004$. So equation [5.32] becomes

$$K_c = 0.016(E/H)^{1/2}(P/c^{3/2}) \qquad [5.34]$$

A correlation plot of K_c values obtained using this equation against conventional K_{Ic} values demonstrated the validity of this equation. It was concluded that an accuracy of better than 30 to 40 % should be obtainable if

(a) The indentation response of the material to be tested is such that a well defined radial/median crack system is formed,

(b) There are no pre-existing residual stresses in the material (which would result in a systematic variation in $P/c^{3/2}$),

(c) The indentation loads used produce radial cracking which satisfies the criterion $c \geq 2a$, but little or no chipping due to the sub-surface lateral cracks "breaking" the surface,

(d) The indented surface should be optically reflective to enable accurate surface (radial) crack length measurements (which are the major source of error), and

(e) The crack lengths, both radial and median should not exceed 0.1 of the specimen thickness in order to avoid free-surface/crack system interactions.

Furthermore, the accuracy will depend on (i) the susceptibility of the material to non-equilibrium mechanical effects, particularly post-indentation slow crack growth, and (ii) the minimization of these effects via testing procedures, e.g., testing in an inert environment. This level of accuracy is acceptable for the comparative fracture toughness determinations of similar materials. The analysis of Lawn, Evans and Marshall (1980) led to the expression $K \approx f(\phi)(\cot\theta)^{2/3}(E/H)^{1/2}P/c^{3/2}$ where $f(\phi)$ is an angular function introduced to take account of the free surface. Note the double tilde ($\approx$) is to be read as "varies as" and in equation [5.28] $f(\phi)$ is replaced by Ω_r. An equation of this form in which the exponent of E/H is different has been derived analytically (Laugier, M.T., 1985), i.e., $K \approx f(\phi)(\cot\theta)^{2/3}(E/H)^{2/3}P/c^{3/2}$. Laugier evaluated "calibration" constants using an equation of the form, $k = K_{Ic}/[(E/H)^n(P/c^{3/2})]$ with n = 2/5 for the Evans and Charles relationship [EC] (neglecting the constraint factor), n = 2/3 for the Laugier equation [L], and n = 1/2 for the Antis et al. equation [A]. The data used to determine the constants were those of Antis et al; these data along with the individual constants and the subsequently predicted toughness data are tabulated in Appendix 5B, Table 5B.1, where the constants and toughness values are denoted by k_{EC}, k_L, k_A and K_cEC, K_cL, K_cA respectively. Laugier obtained the mean constants and

hence toughness in two ways; by (i) using all the data, and (ii) using all except the WC-Co data, which did not develop a well defined radial/median crack system.

The author used Laugier's and Antis et al.'s data in Table 5B.1 to evaluate the mean constants for (i) all the data, (ii) all except the WC-Co data (as Laugier did), but also only for the well-behaved, "reference" materials used by Antis et al. to determine their original calibration constant of 0.0016 ± 0.004, in order to make a fairer comparison. The results obtained are tabulated in Appendix 5B, Table 5B.2; the results in Appendix 5B show that all three fracture toughness relationships provide essentially similar correlations using all the data, but that when (a) WC-Co is excluded or (b) only the reference data are used, the correlations improve in the order Evans and Charles < Antis et al. < Laugier equation. The Laugier constant is 0.010 ± 0.002 for (a) and (b), while the Antis et al. constants are 0.017 ± 0.004 and 0.016 ± 0.004 respectively. So for glasses, glass-ceramics and ceramics

$$K_c = 0.010(E/H)^{2/3}P/c^{3/2} \qquad [5.35]$$

At this point it is appropriate to consider the scatter in the $\log[K_c\phi/(Ha^{1/2})]$ versus $\log(c/a)$ plot of Evans and Charles (1976) as shown in Figure 5.4 (a); the data for WC-12%Co, ZnS and ZnSe polycrystals are displaced to higher $K_c/(Ha^{1/2})$ values relative to the other data and have c/a values $\leq \approx 3$, while the other data have c/a values $\geq \approx 3$. Their plot of $\log([K_c\phi/(Ha^{1/2})][H/E\phi]^{0.4})$ versus $\log(c/a)$ shows that their equation gives a good fit to the data at $c/a \geq \approx 3$; see Figure 5.4 (b). The Lawn, Evans & Marshall (1980) plot of $\log([K_c/(Ha^{1/2})][H/E]^{1/2})$ versus $\log(c/a)$, using the Evans and Charles data, given in Figure 5.5, however, shows a marked deviation between the calibrated line predicted by equation [5.29] and the data at $c/a \geq \approx 3$, notably SiC and B_4C.

The apparent discrepancy between the fit of Evans and Charles' equation [5.22] and that of Lawn, Evans and Marshall [5.29] to the Evans and Charles data has been commented on (Bhat, D.G., 1981); Bhat used both equations to measure the fracture toughness of SiC and Si_3N_4

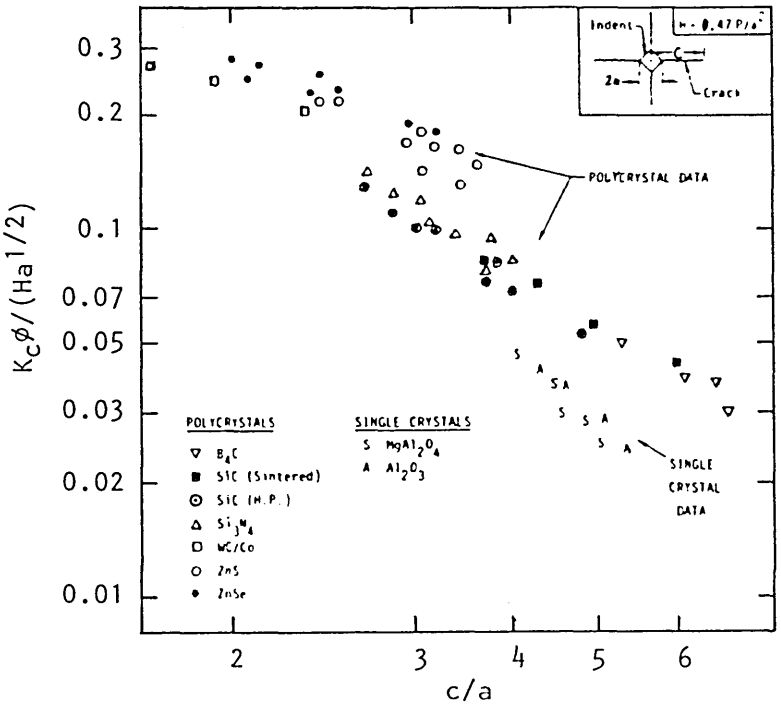


Figure 5.4 (a) $K_c \phi/(Ha^{1/2})$ as a Function of c/a
[after A.G. Evans and E.A. Charles (1976)].

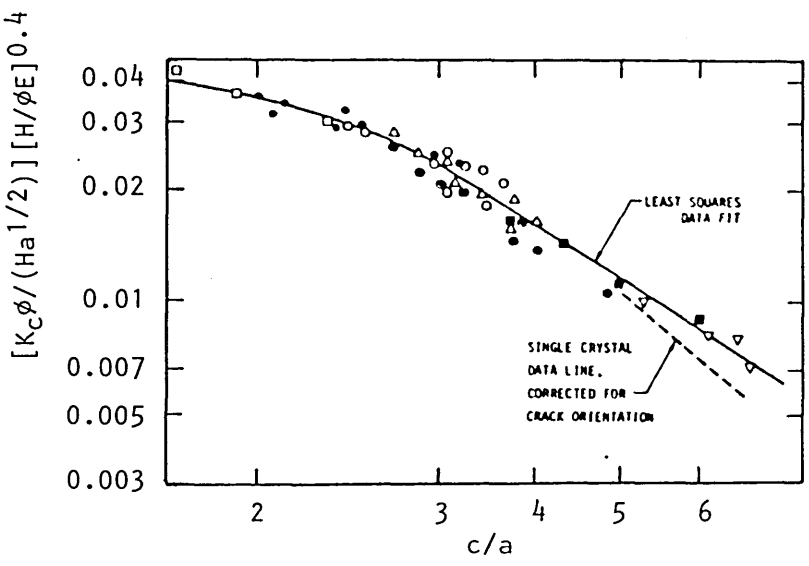


Figure 5.4 (b) $[K_c \phi/(Ha^{1/2})][H/\phi E]^{0.4}$ as a Function of c/a
[after A.G. Evans and E.A. Charles (1976)].

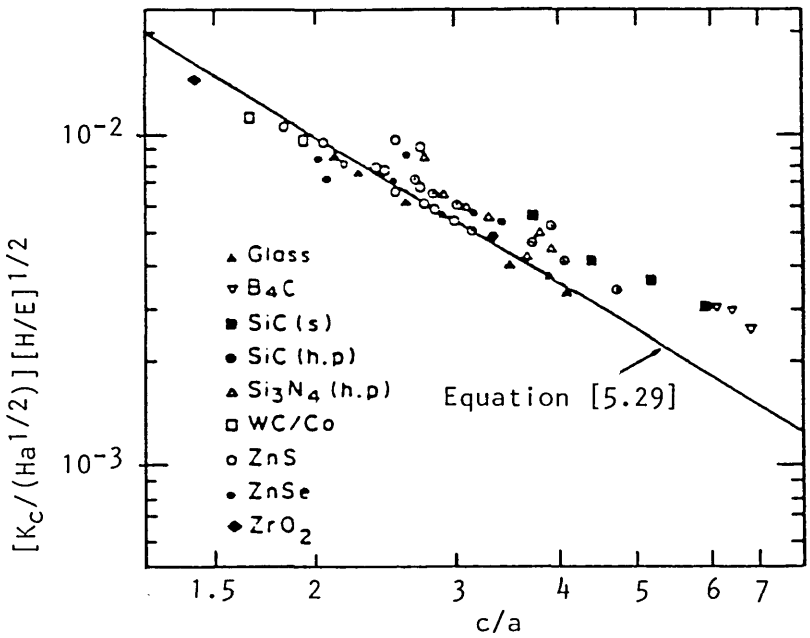


Figure 5.5 $[K_c/(Ha^{1/2})][H/E]^{1/2}$ as a Function of c/a [after B.R. Lawn, A.G. Evans and D.B. Marshall (1980)].

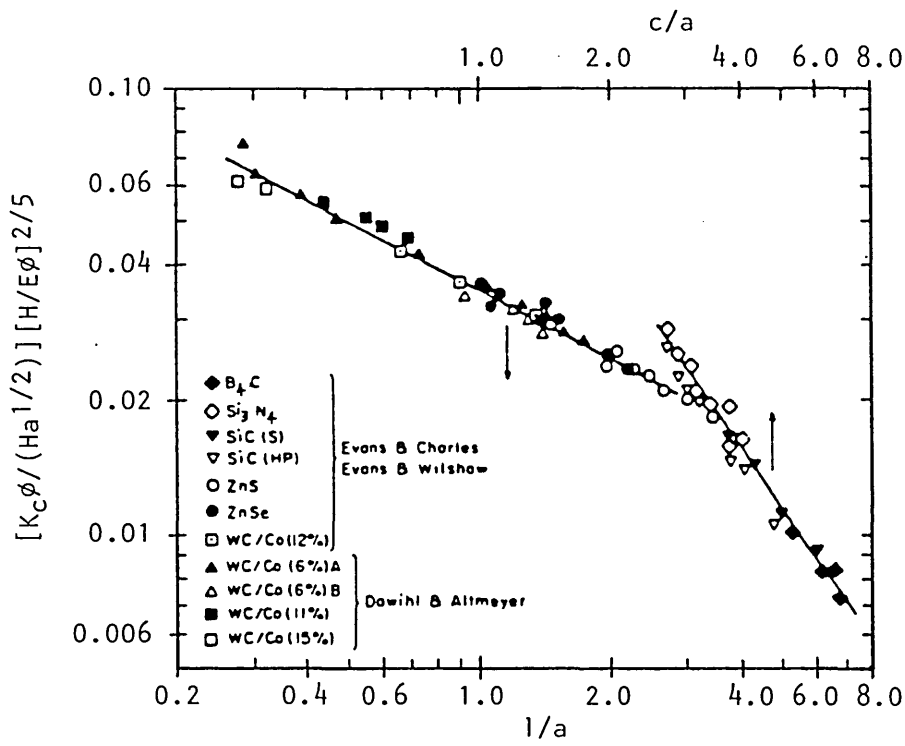


Figure 5.6 $[K_c\phi/(Ha^{1/2})][H/E\phi]^{2/5}$ as a Function of c/a or 1/a [after Niihara et al. (1982)].

materials produced by chemical vapour deposition and found significant differences in the calculated toughness values. He found that the "best-fit" line to his data with $c/a < 3.0$ using the Evans and Charles plotting axes had a slope of -0.36 rather than -1.5. He was thus able to write $[K_c\phi/(Ha^{1/2})][H/E\phi]^{0.4} = 0.05(c/a)^{-0.36}$ as an equation for K_c at $c/a < 3$; however, the discrepancy between the data obtained from this equation and that of Lawn, Evans and Marshall was still significant. His results suggested that the deviation of indentation data from the Evans and Charles model at $c/a < \approx 3$ and from the Lawn, Evans and Marshall model at $c/a > \approx 3$ may be a function of c/a. In reply to Bhat, Marshall and Evans (1981), however, suggest that the deviations are due to material variations rather than the c/a ratio since (i) the data for individual materials follow curves of slope -3/2 quite closely in line with the assumption that $c \gg a$ and (ii) the predicted dependence was followed by glass to $c/a = 2$. So Marshall and Evans attach no special significance to the ratio $c/a = 3$; a conclusion supported by the results of Antis et al. (1981). As regards the systematic deviation from the predicted line of Lawn et al., Evans and Marshall considered that it may be due to the fact that neither Poisson's ratio nor the indenter-material interface sliding friction coefficient were explicitly incorporated into their analysis. It appears, however, that the inclusion of a Poisson's ratio term results in a further deviation of the data from the predicted line; it therefore seems unlikely that Poisson's ratio effects are responsible for the discrepancy. They thus concluded that until the interface frictional effects are quantified, the discrepancy cannot be resolved.

The removal of successive surface layers of cobalt bonded tungsten carbide materials after Vickers indentation have confirmed that in general WC-Co "cermet" alloy materials with $\geq \approx 5$ volume % cobalt content develop four Palmqvist surface radial cracks which go deeper than the indent itself and extend radially from the corners of the indent (Francois, J-P., and McLaren, J.R., 1982);

(Shetty, D.K., Wright, I.G., et al., 1985); see Figure 5.3 (b). Noting that both the WC-Co indentation data of Evans and Charles and other WC-Co data in the literature, for which c/a was < 3, deviated from the behaviour predicted by the Evans and Charles relationship, i.e., $P/c^{3/2}$ = constant and that it was based on the assumption the indentation crack system was a fully developed radial/median crack system, K. Niihara et al. (1982) proposed that the deviation in the data for $c/a \leq \approx 3$ is due to a transition from a Palmqvist crack sytem for $c/a < \approx 3$ to a radial/median crack system for $c/a > \approx 3$.

Figure 5.6 shows the data plotted by Niihara et al. (1982) on axes of $\log([K_c\phi/(Ha^{1/2})][H/E\phi]^{2/5})$ versus $\log(c/a)$ or $\log(l/a)$ where $l/a = c/a - 1$. Note that the data essentially fall into three groups depending on the c/a ratio; all the WC-Co data have c/a ratios < 2 while all the Si_3N_4, SiC and B_4C data have c/a ratios > 2. The ZnS and ZnSe data c/a ratios are seen to fall within the range $1 < c/a < 4$, and thus overlap the other two groups. Correlation analyses split the data into two distinct groups, each with very good linearity. For data with c/a ratios in the range $1.25 \leq c/a \leq 3.5$, i.e., l/a ratios in the range $0.25 \leq l/a \leq 2.5$, the best fit equation was

$$[K_c\phi/(Ha^{1/2})][H/E\phi]^{2/5} = 0.035(l/a)^{-1/2} \qquad [5.36]$$

while for data with $c/a \geq 2.5$, the best fit equation was

$$[K_c\phi/(Ha^{1/2})][H/E\phi]^{2/5} = 0.129(c/a)^{-3/2} \qquad [5.37]$$

These equations are the result of a data fitting exercise and if the fracture toughness of a material is determined using either equation only on the basis of the measured c/a or l/a ratios, then the answers have no rigorous physical interpretation. This has also been been noted in the literature (Lankford, J., 1982); he noted that Niihara et al. had re-plotted Evans and Charles data on ZnS and ZnSe in terms of l/a rather c/a without offering any evidence that they develop Palmqvist cracks when indented. Lankford re-plotted these data in their original form (i.e., in terms of c/a), together with the other Evans and Charles data in c/a and Niihara et al.'s data in terms of l/a, and found that all the Evans and Charles data are

adequately described by equation [5.37] without recourse to [5.36] for ZnS and ZnSe.

Lankford also obtained indentation data on four other materials which develop Palmqvist cracks at low indentation loads and well developed radial/median cracks at high loads (as previously demonstrated by him). He correlated the $[K_c\phi/(Ha^{1/2})][H/E\phi]^{2/5}$ data for these materials and the WC-Co data of Niihara et al. with l/a. When representing the l/a dependence of each material type by $(l/a)^{-m}$, m ranged from 0.5 to 1.05 with the various lines diverging at low l/a ratios where equation [5.36] should be most appropriate. On the otherhand, re-plotting all the data in terms of c/a, the line for Niihara et al.'s WC-Co data and all Lankford's material data lines clustered about the "universal" line of Evans and Charles in a roughly parallel manner; representing the c/a dependence by $(c/a)^{-n}$, n ranged from n = 1.45 for the WC-Co data to 1.66 for Lankford's sintered SiC data. These slopes agree well with Evans and Charles' average of 1.5. Furthermore, he states that equation [5.37] lies sufficiently close to the centroid of the data band, that its use for materials on the band periphery would involve an error of no more than ≈ 35 % in K_c. He reduced the error by data fitting both his data and the original data of Evans and Charles, giving

$$[K_c\phi/(Ha^{1/2})][H/E\phi]^{2/5} = 0.142(c/a)^{-1.54} \qquad [5.38]$$

He concluded that the basic Evans and Charles relationship in terms of c/a is valid for non-ductile materials over the entire indentation fracture morphology spectrum, from Palmqvist to radial/median morphology and capable of giving K_c to an accuracy of better than 35 %, given adequately accurate E and H data.

Further investigation of the validity of equation [5.36] and [5.37] has been reported (Niihara et al., 1983) using data for hot-pressed Si_3N_4 and soda-lime-silica glass. They addressed the question of differentiating between Palmqvist and radial/median indentation crack systems, prior to selecting either of their proposed equations, i.e., equation [5.36] or [5.37], in two ways;

(i) they gave criteria for determining whether the observed surface radial cracks are the trace of Palmqvist or median cracks which do not require a knowledge of the sub-surface crack profile. They show that if the hardness is load-independent, then the indenter load is proportional to l for Palmqvist cracks, which contrasts with the load being proportional to $c^{3/2}$ for median cracks (see Lawn et al., 1980 and Evans, 1979), and
(ii) they calculated the fracture toughness of the soda-lime-silica glass using (a) l/a and [5.36] and (b) c/a and [5.37], irrespective of the actual crack system morphology, and analysed the K_c data as a function of l/a + 1 or c/a, and compared the results with the literature fracture toughness values determined using the double-cantilever-beam (DCB) method. They found that for c/a < 3, only the data obtained using l/a (i.e., assuming Palmqvist cracks) was in agreement with the DCB data; for c/a > 3, only the data obtained using c/a (i.e., assuming median cracks) agreed with the DCB data.

They then calculated the indentation fracture toughness of the glass using the following equation which was cited (Niihara et al., 1982) as having been fitted to the data of Evans and Charles by J.E. Blendell (1979)

$$[K_c\phi/(Ha^{1/2})][H/E\phi]^{2/5} = 0.055\log(8.4a/c) \qquad [5.39]$$

and compared the data with that obtained using equations [5.36] and [5.37] and with the DCB data; they found that the Evans and Charles equation as expressed by Blendell gave results that were in good agreement with the DCB data and the data evaluated by their method at intermediate values of c/a of the order of $2 \leq c/a < 3$, but deviated outside this range.

Niihara et al. quote a DCB K_{Ic} value of 0.75 MPa.$m^{1/2}$ for the glass; their indentation values spanned the range 0.70 to 0.78 MPa.$m^{1/2}$, while the values obtained from Blendell's equation ranged from 0.58 to 0.84 MPa.$m^{1/2}$, i.e., from the DCB value - 23 % to the DCB value + 12 %. It is interesting to note that the minimum indentation toughness values of 0.7 MPa.$m^{1/2}$ (Niihara) and 0.58 MPa.$m^{1/2}$ (Blendell) corresponded to c/a = 1.5, which

is effectively violating the assumption upon which the radial/median crack system analyses of Evans and Charles, and Lawn et al. are based, i.e., $c \gg a$, which leads to the result $P/(c/a)^{3/2}$ = constant; furthermore the plastic zone radius is ≈ 1.1 to 1.3a (Evans, A.G., 1979). It should be noted that Antis et al. only suggest an accuracy of better than 30 to 40 % for "well-behaved" materials, i.e., those developing a radial/median crack system with $c \gg a$, while Lankford claims an accuracy of better than 35 % for his equation [5.38] over the whole indentation fracture morphology spectrum and an error of no more than ≈ 35 % for Niihara et al.'s equation for $c/a \geq 2.5$, i.e.,[5.37]; thus an error of - 23 % using Blendell's fit to Evans and Charles data is not serious, especially for c/a = 1.5.

Lankford's claim that equation [5.36] which is in terms of l/a gives errors relative to K_{Ic} for SiC and Al_2O_3 (at l/a = 0.5, i.e., c/a = 1.5) of the order of 100 % must be seen in context; The bulk of the data used to "calibrate" equation [5.36] were data for WC-Co cermets with 6 to 15 volume % Co, i.e., two-phase composite materials consisting of small non-ductile tungsten carbide particles (WC) in a ductile cobalt metal (Co) "matrix". It is therefore not surprising that indentation fracture toughness relationships calibrated using WC-Co data give inaccurate results when applied to archetypal non-ductile ceramic materials (and vice versa; see J-P. Francois and J.R. McLaren (1982)). Interestingly, a model has been formulated for Palmqvist cracks using fundamental theoretical fracture mechanics principles (Niihara, K., 1983); the Palmqvist crack was modelled by a semi-elliptical surface crack and the following relationship derived

$$[K_c\phi/(Ha^{1/2})][H/E\phi]^{2/5} = k_2(l/a)^{-1/2} \qquad [5.40]$$

where k_2 is a constant (= $0.085k_ok_1$), and k_o is the free-surface correction factor (≈ 1.12) and k_1 the crack-depth factor which is assumed to be independent of the crack size (= 1/2). So k_2 = 0.048; note that in the derivation of [5.40] it was assumed that typically $1 \leq l/a \leq 2.5$. Thus, assuming ϕ = 3, equation [5.40] can

be written as

$$K_c = 0.025(E/H)^{2/5}Ha/l^{1/2} \qquad [5.41]$$

An elastic-plastic analysis was used to derive [5.40] as Palmqvist cracks are predominantly nucleated and propagated on unloading by residual stresses, hence the natural appearance of E/H as a manifestation of the elastic-plastic nature of the indentation stress field and the residual stress field component. The present author has assumed H = 1.8544P/(4a2) for [5.41], as per equations [5.36], [5.37], [5.38] as they involve ϕ.

Recently an analytical expression which takes account of Poisson's ratio has been derived on the basis of the elastic-plastic solution for a spherical cavity subject to an internal pressure and a modification due to the creation of the free surface (Miranzo, P. and Moya, J.S., 1984); the model used for the derivation is valid for all c/a ratios > 1.3 (note $r_p/a \approx 1.3$, so $c/a \leq 1.3$ implies $c = r_p$, the plastic zone radius, i.e., the crack is within the plastically deformed zone). The expression derived was a continuous function of c/a for c/a > 1.3, and thus is claimed to be unique; however it is analytically complex and not in a readily useful form, but Miranzo and Moya state, however, that the experimental data of Evans and Charles were in good agreement with the derived expression for c/a > 1.3; this enabled them to re-write the expression in the following useful decomposed form

$$[K_c/(Ha^{1/2})][f(E/H)]^{-1} = 0.05(c/a)^{-0.5} \qquad [5.42]$$

for $c/a \leq 2.8$, and

$$[K_c/(Ha^{1/2})][f(E/H)]^{-1} = 0.09(c/a)^{-1.09} \qquad [5.43]$$

for $c/a \geq 2.8$. The equations can be rearranged as

$$K_c = 0.05[f(E/H)]Ha/c^{0.5} \qquad [5.44]$$

for $c/a \leq 2.8$, and

$$K_c = 0.09[f(E/H)]Ha^{1.59}/c^{1.09} \qquad [5.45]$$

for $c/a \geq 2.8$. It was assumed here that $H = 1.8544P/(4a^2)$. The function f(E/H) equals $(1 - \nu)^{-1}([\beta^2/\delta] - 1.5)$ where β equals $(E/[H(1 - \nu)])^{1/3}$ and $\delta = [2/3][1 + 3\ln(\beta)]$. As a result of their being able to decompose their derived expression about a "pivot-point" of c/a = 2.8, they

concluded that the discrepancy at c/a ≈ 3 pointed out by Bhat depends only on the value of c/a and not because there is a transition from a Palmqvist crack system to a radial/median crack system as suggested by Niihara et al.

As previously noted, the length of a surface radial Palmqvist crack (l) is proportional to the indenter load (P); a toughness parameter has been defined for Palmqvist cracks by H.E. Exner (1969) as cited by Shetty, D.K., Wright, I.G., et al. (1985) based on the linear relationship between the indenter load and the mean Palmqvist crack length

$$W = P/4l \qquad [5.46]$$

where W is known as the Palmqvist crack resistance. Thus using [5.46] and $H = 1.8544P/(4a^2)$ in equation [5.41] gives

$$K_c = \beta(HW)^{1/2} \qquad [5.47]$$

where $\beta = 0.034(E/H)^{2/5}$. Shetty et al. (1985) represented each collinear pair of Palmqvist cracks by a through thickness crack which is loaded at the centre by a rigid wedge and is in equilibrium with the wedge. The wedge thickness was assumed to equal the depth of the plastic deformation zone below the indent. They used this two--dimensional crack model of three-dimensional surface cracks to derive the following equation

$$K_c = [1/[3(1-\nu^2)(2^{1/2}\pi^{5/2}\tan\theta)^{1/3}]][HP/(4l)]^{1/2} \qquad [5.48]$$

where θ is the indenter cone half-angle; Shetty et al. take θ = 68°, whereas most authors, including this author, take θ = 74°. This equation can be re-written in the form using [5.46]

$$K_c = \beta(HW)^{1/2} \qquad [5.49]$$

where $\beta = 1/[3(1-\nu^2)(2^{1/2}\pi^{5/2}\tan\theta)^{1/3}]$; Note that in the original paper by Shetty et al. (1985) the exponent of π was accidently omitted in their equation (12); it was also omitted in two subsequent papers (Shetty, D.K., Rosenfield, A.R., and Duckworth, W.H., 1985); (Shetty, D.K. and Wright, I.G., 1986). In the above analysis H was defined as $P/(2a^2)$. For $\nu = 0.22$ and θ = 68°, $\beta = 0.089$, while for $\nu = 0.22$ and θ = 74°, $\beta = 0.079$.

5.3.1 Summary of indentation fracture toughness equations

The following indentation fracture toughness equations are all based on the assumption that the cracks which develop as a result of Vickers indentation are well-developed radial/median, "half-penny" shaped cracks:

1. $K_c = 0.0515P/c^{3/2}$
   assuming c = D and $\mu = 0$, [Lawn and Fuller (1975)]
2. $K_c = 0.16Ha^2/c^{3/2} = 0.074176P/c^{3/2}$
   where $H = 1.8544P/(4a^2)$, [Evans and Charles (1976)]
3. $K_c = Ha^{1/2}(E/H)^{2/5}.10^F = 0.6305E^{0.4}P^{0.6}.10^F.a^{-0.7}$
   where $F = -1.59 - 0.34B - 2.02B^2 + 11.23B^3 - 24.97B^4 + 16.32B^5$, $B = \log(c/a)$ and $H = 1.8544P/(4a^2)$, [B.I. Davis]; see Evans (1979)
4. $K_c = 0.014(E/H)^{1/2}P/c^{3/2}$
   where $H = P/(2a^2)$, [Lawn et al. (1980)]
5. $K_c = 0.016(E/H)^{1/2}P/c^{3/2}$
   where $H = P/(2a^2)$, [Antis et al. (1981)]
6. $K_c = 0.010(E/H)^{2/3}P/c^{3/2}$
   where $H = P/(2a^2)$, [Laugier (1985)]
7. $K_c = 0.022(E/H)^{2/5}P/c^{3/2}$
   where $H = 1.8544P/(4a^2)$, [Laugier (1985)]
8. $K_c = 0.067(E/H)^{2/5}(Ha^2)/c^{3/2}$ for $c/a \geq 2.5$
   where $H = 1.8544P/(4a^2)$, [Niihara et al. (1982)]
9. $K_c = 0.073(E/H)^{2/5}(Ha^{1/2})(c/a)^{-1.56}$
   where $H = 1.8544P/(4a^2)$, [Lankford (1982)]
10. $K_c = 0.028(E/H)^{2/5}(Ha^{1/2})\log(8.4a/c)$
    where $H = 1.8544P/(4a^2)$,
    [J.E. Blendell (1979)]; see Niihara et al. (1982)
11. $K_c = 0.09[f(E/H)]Ha^{1.58}/c^{1.08}$ for $c/a \geq 2.8$ and
12. $K_c = 0.05[f(E/H)]Ha/c^{0.5}$ for $c/a \leq 2.8$
    where $f(E/H) = (1 - \nu)^{-1}([\beta^2/\xi] - 1.5)$,
    $\beta = (E/[H(1 - \nu)])^{1/3}$, $\xi = [2/3][1 + 3\ln(\beta)]$,
    and $H = 1.8544P/(4a^2)$, [Miranzo and Moya (1984)].

The following indentation fracture toughness equations, in contrast, are based on the assumption that the cracks which develop as a result of Vickers indentation are radial Palmqvist cracks:

13. $K_c = 0.018(E/H)^{2/5}Ha/l^{1/2}$ for $0.25 \leq l/a \leq 2.5$
    where $H = 1.8544P/(4a^2)$, [Niihara et al. (1982)]
14. $K_c = 0.025(E/H)^{2/5}Ha/l^{1/2}$ for $1 \leq l/a \leq 2.5$
    where $H = 1.8544P/(4a^2)$, [Niihara (1983)]
15. $K_c = 0.034(HW)^{1/2}$
    where $H = 1.8544P/(4a^2)$ and $W = P/4l$
    [Shetty et al. (1985)]
16. $K_c = \beta(HW)^{1/2}$ where $W = P/4l$, $H = P/2a^2$,
    and $\beta = 1/[3(1 - \nu^2)(2^{1/2}\pi^{5/2}\tan\theta)^{1/3}]$, and θ is the indenter cone half-angle [Shetty et al. (1985)]; θ is generally taken as 74°, although Shetty et al. used θ = 68°, the former being the angle between opposite edges and the latter the angle between opposite faces of a standard Vickers indenter. Note that for WC cermets with $< \approx$ 10 % binder, $W = P/4l$, while for WC cermets with $> \approx$ 10 % binder, $W = (P - P_o)/4l$ where P_o is a threshold indenter load for crack initiation.

A word of caution is appropriate; the most suitable equation to use with a given set of data for any given material is the one which gives a toughness value close to a reliable K_{Ic} value and whose underlying assumptions most closely model the indentation fracture behaviour. Also note that most of the equations are calibrated using reliable, conventionally determined K_{Ic} values for ceramic materials with reliably documented properties and thus do not give truly independent estimates of the fracture toughness; hence they are best suited to determining relative fracture toughness data.

5.4 Experimental Determination of Plane Strain Fracture Toughness, K_{Ic}, Using Single-Edge Notched Bend (SENB) Specimens in Three-Point Bending

Ceramic materials invariably contain inherent flaws, which in general can be assumed to be randomly distributed as regards shape, size and orientation with respect to an applied stress, e.g., a uniaxial tensile stress. There will be a stress intensity factor associated with each flaw, the magnitude of which can considered in terms of

the stress intensity components for each of the three basic modes of crack propagation when a multiaxial stress field is operative. For the most common case of a uniaxial stress field, the stress intensity associated with any flaw is given by equation [5.9] in its most explicit form, i.e., $K_I = (Y/Z)\sigma c^{1/2}$. The flaw shape factor (Z) characterizes the flaw shape, the compliance factor (Y) characterizes the geometrical relationship between the flaw, the remote boundary of the body and the remotely imposed load, i.e., the loading configuration, and the effective crack length (c) characterizes the flaw size. So the stress intensity associated with any flaw depends on Y, Z, σ and c; thus neither the largest flaw (i.e., largest c) nor the flaw subject to the highest imposed stress (i.e., highest σ) is necessarily the critical flaw at any given applied load, P. Rather, it is the flaw for which the magnitudes of Y, Z, σ and c are such that the concomitant stress intensity factor is the highest for the given load. The reason for distinguishing between the applied load, P and the general stress field, σ, is to emphasize the importance of the stress distribution, which may be uniform or variable depending on the loading configuration, in determining (in conjunction with Y, Z and c) which flaw becomes a critical flaw at a given load P. Thus the flaw with the highest concomitant stress intensity factor, K_I, is the strength controlling flaw, such that at fracture $K_I \geq K_{Ic}$; K_{Ic} being the critical stress intensity for fracture and a "material" property as opposed to a stress-field intensity parameter like K_I.

The fracture toughness of a material cannot be determined from a standard fracture strength test because it is usually impossible to categorically and repeatedly ascertain which inherent flaw propagated catastrophically when $K_I \geq K_{Ic}$ and hence assign values for Y, Z, c and σ, in order to calculate a reliable K_{Ic} value. In order to determine K_{Ic} in practice, it is therefore necessary to introduce an artificial critical crack, i.e., flaw, for which Y and Z are known theoretically or empirically, and for which c, and σ at fracture can be experimentally

measured. Since fracture in ceramics invariably originates at atomically sharp cracks and the LEFM approach assumes an infinitely sharp crack, the artificial crack tip radius should also be atomically sharp in theory.

The plane strain fracture toughness (K_{Ic}) of non-ductile materials is usually determined by testing specimens with an artificial crack in bending rather than in direct tension for the reasons discussed in Chapter 4 concerning strength tests. There is no standardized plane strain fracture toughness test for ceramics; there are various test techniques, which can be classified into two groups depending on whether or not measurement of the initial crack length is required, and each technique has advantages and disadvantages. Examples of test techniques and specimens utilizing a crack of known length are the single-edge notched bend (SENB) specimen loaded in three- or four-point bending, the double-cantilever-beam (DCB) specimen; the most popular test technique not requiring a crack of known length is the double-torsion (DT) test. The various techniques and their advantages and disadvantages have been reviewed in detail elsewhere (Evans, A.G., 1974b); (Freiman, S.W., 1983). The three-point bending SENB technique was employed in the present work due to its simplicity of preparation, economical use of material and suitability for high temperature tests; furthermore, in a study of the fracture toughness of commercial sintered aluminas using the DCB, DT and SENB test methods, the SENB test (using a specimen with a sharp crack) gave the most reliable K_{Ic} data (Dalgleish, B.J., et al., 1980).

A schematic diagram of a SENB test specimen loaded in three-point bending is shown in Figure 5.7 (a); the fracture stress is subject to error due to friction at the supports, twisting of the specimen and wedging (as in the flexural strength tests). The effect of wedging was neglected when calculating the fracture stress in the present work as is the common practice, while the effects of friction and twisting are not readily quantifiable, and were therefore assumed not to be a problem. As regards introducing a sharp crack of known length, it is usually

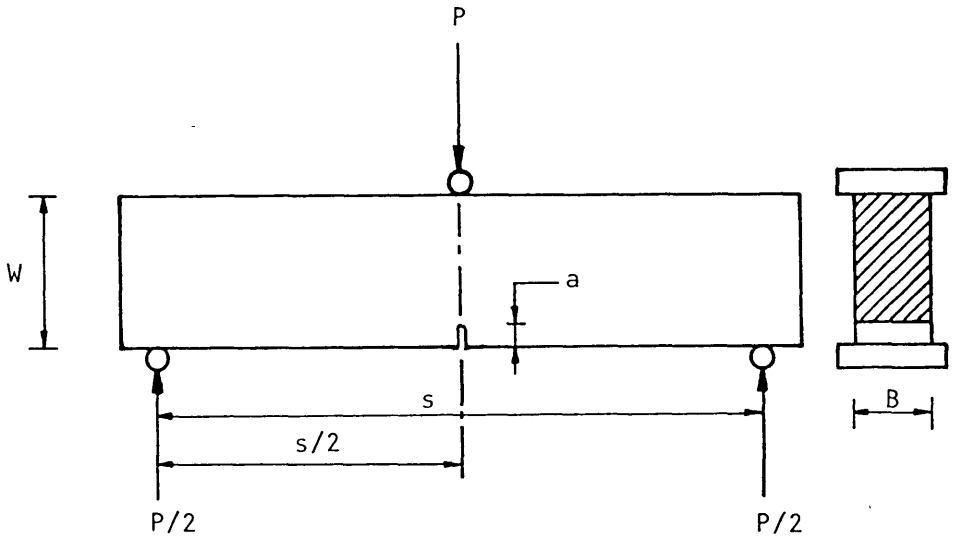


Figure 5.7 (a) Schematic Diagram of a Single-Edge Notched Bend (SENB) Specimen Loaded in Three-Point Bending.

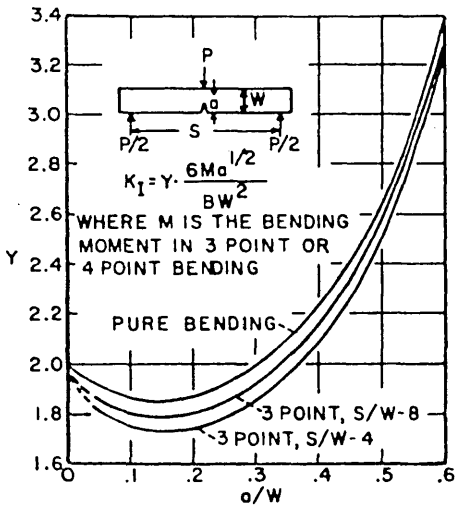


Figure 5.7 (b) Compliance Factor Y as a Function of a/W According to Equation [5.50] - A Fourth Order Polynomial Function [after W.F. Brown and J.E. Srawley (1966)].

very difficult to introduce a single sharp crack of a nominal, prescribed length with a known flaw shape factor without the specimen fracturing before the test; even if a sharp crack can be produced in the material, it is not easy to accurately measure the length of a sharp crack in opaque ceramics and the use of a dye-penetrant to facilitate location of the crack-tip will affect the measured fracture toughness by enhancing sub-critical crack growth and thus increasing the effective crack length prior to fracture.

Since Z = 1 for a through-thickness crack with a linear crack front, e.g., a notch (Bansal, G.K., 1976), it is common practice to machine a finite width notch in the SENB specimen using a diamond abrasive slitting wheel to simulate a crack. The measurement of K_{Ic} for ceramic materials, particularly alumina, using SENB specimens notched using a diamond saw has been considered (Pabst, R.F., 1974); (Pabst, R.F., et al., 1982); no significant correlation was found between K_{Ic} and the relative notch depth (a/W). The measured K_{Ic} values were independent of the specimen volume, support span (s), width-to-breadth ratio (W/B), and loading configuration (i.e., three- or four-point loading), but were affected by the notch-root width, profile and roughness when the notch-root radius, r was above a critical value, r_c. It was found that for many ceramics the critical notch-root width ($2r_c$) ≈ 0.1 mm, and that there was no significant difference between the K_{Ic} values obtained from a notch of $r < r_c$ and those obtained from a sharp, short (≈ 300μm) pre-crack at the notch-root.

A compliance factor Y has been determined analytically for both three- and four-point bending of SENB specimens (Brown, W.F.and Srawley, J.E., 1966); the expression for Y is a fourth-order polynomial function of a/W and the loading configuration, and has the form

$$Y = A_0 + A_1(a/W) + A_2(a/W)^2 + A_3(a/W)^3 + A_4(a/W)^4 \quad [5.50]$$

where the coefficients have the values:

Loading Geometry	A_0	A_1	A_2	A_3	A_4
4-point bending: (pure bending)	+1.99	-2.47	+12.97	-23.17	+24.80

Loading Geometry	A_0	A_1	A_2	A_3	A_4
3-point bending:					
s/W = 8	+1.96	-2.75	+13.66	-23.98	+25.22
s/W = 4	+1.93	-3.07	+14.53	-25.11	+25.80

The Y expression for three-point bending with s/W = 4 used to form the basis of ASTM standard for the plane strain fracture toughness testing of metals, E399, and was only valid within the narrow terms of the standard in the range $0.45 < a/W < 0.55$; however, equation [5.50] describes the K_I calibration for SENB specimens to within 0.2 % for all a/W values up to 0.6; see Figure 5.7 (b).

This expression was superseded in 1981 by a new compliance factor expression for the three-point bending SENB specimen with s/W = 4 (Srawley, J.E., 1976) [5.51]

$$Y = \frac{1.99 - (a/W)[1 - (a/W)][2.15 - 3.93(a/W) + 2.7(a/W)^2]}{[1 + 2(a/W)][1 - (a/W)]^{3/2}}$$

which is valid for $0 \leq a/W \leq 1$, and has a minimum value of 1.7466 at a/W = 0.1734. Note that for a = 0, Y = 1.99; this compares with $Y = 1.12\pi^{1/2} = 1.98515$ for a single edge crack in a semi-infinite plate, i.e., $a \ll W$ (Lawn, B.R., and Wilshaw, T.R., 1975). The variation of Y with a/W according to [5.51] is very similar to that according to [5.50] for three-point bending (s/W = 4) between a/W = 0 and 0.6, which has a minimum value of 1.7246 at a/W = 0.1543.

Examination of the ceramics literature shows that it is still customary for SENB specimens to be notched to a relative depth (a/W) of 0.5 in keeping with the old ASTM standard for metals. However, there were, and still are good reasons for not using a/W = 0.5 when testing ceramic materials, particularly opaque ceramics, which apply equally to both the old and the new compliance factor expressions for three-point SENB specimens, as discussed below. For a/W nominally equal to 0.5, Y = 2.51, while for a/W equal to 0.4 and 0.6, Y = 2.09 and 3.25 respectively; thus for a change of 0.1 in a/W there is a maximum change of 0.74 in Y, i.e., a 20 % change in a/W produces a change of up to 29 % in Y. In comparison, for a/W nominally equal to 0.17, Y = 1.75, while for a/W = 0.07 and 0.27, Y = 1.83

and 1.81 respectively; hence for a change of 0.1 in a/W there is a maximum change of 0.08 in Y, i.e., a 59 % change in a/W results in a change in Y of at most 5 %. Therefore, given the difficulty in accurately measuring the true effective crack length as opposed to the notch depth in either notched or notched and pre-cracked specimens, it is obvious that a/W should be ≈ 0.17 and not 0.5 as the error in the calculated toughness due to the error in Y will be much reduced; the percentage error in the notch depth or notch plus precrack length is halved because the square root is taken.

The stress intensity approach is based on linear elastic fracture mechanics (LEFM) which predicts that the stresses and hence strains adjacent to the the crack-tip are infinite in an ideally linear elastic solid (Lawn, B.R. and Wilshaw, T.R., 1975); however, real materials cannot sustain an infinite stress and on a macroscopic scale they either fracture catastrophically (non-ductile behaviour) or they deform plastically until they ultimately rupture (ductile behaviour). At a crack-tip in non-ductile materials as the stress attains the level required for bond rupture, the response to the stress in a microscopic region surrounding the crack tip becomes non-linear; in semi-ductile materials (which are macroscopically linear elastic to fracture) this region of non-linear behaviour is regarded as a plastically deformed zone in which localized plastic yielding occurs at a local yield stress, σ_Y^*, which may equal or exceed the macroscopic uniaxial yield stress in tension or compression σ_Y. The magnitude of this local crack-tip yield stress is determined by the general stress state in the material surrounding the crack, which depends on the width of the crack front, i.e., the specimen thickness.

A state of plane stress exists when there is a biaxial stress state such that $\sigma_{yy} > \sigma_{xx} > 0$ and $\sigma_{zz} = 0$, while a state of plane strain exists when there is a triaxial stress state such that $\sigma_{yy} > \sigma_{zz} = \nu(\sigma_{xx} + \sigma_{yy}) > \sigma_{xx} > 0$. So given that the stress normal to a free surface is zero (a condition of equilibrium, i.e., a free surface

does not move), a state of plane stress must always exist at the free surface of a body; thus the surfaces of the crack are stress-free boundaries of the specimen.

As plastic deformation occurs at constant volume (ν = 0.5), there is no effective constraint on the plastic zone contracting in the z direction (and thus expanding in the x and y directions, noting that σ_{xx} = 0 at the crack-tip surface, but non-zero away from it) when the specimen is very thin because the specimen is essentially two adjacent free surfaces, i.e., plane stress exists across the thickness. When the specimen is very thick the free surfaces are essentially at infinity; this allows an effective stress to develop in the z direction along the interface between the plastic zone and the surrounding elastic envelope due to the elastic material not being able to contract to the same degree as the plastic zone (i.e., ϵ_{zz} is effectively zero), i.e., plane strain exists across the thickness. As a result, expansion of the plastic zone in the x and y directions is constrained.

For specimens of intermediate thickness there will be a transition from plane stress at the free surfaces to plane strain at the mid-thickness region, with σ_{zz} a maximum at the centre; thus the size of the plastic zone varying across the thickness, being smaller in the region of plane strain. For plane stress conditions, $\sigma_Y^* = \sigma_Y$, while for plane strain conditions, $\sigma_Y^* \approx 3\sigma_Y$ (Lawn, B.R. and Wilshaw, T.R., 1975); thus the distance to which the plastic zone extends ahead of the crack-tip is $(1/2\pi)(K_I/\sigma_Y)^2$ for plane stress conditions and approximately $(1/6\pi)(K_I/\sigma_Y)^2$ for plane strain conditions (Broek, D., 1983). So, the greater the specimen thickness, the greater the region in which a state of plane strain exists, and hence the smaller the plastic zone.

As the size of the plastic zone decreases, so does the critical stress intensity for fracture; thus when the specimen thickness is such that a state of plane strain exists across the thickness, the plastic zone will be subject to the maximum constraint and the critical stress intensity factor for fracture, $K_{crit.}$, attains a lower

limit, namely K_{Ic}, which is independent of the specimen thickness and hence is a material property as a critical fracture criterion should be. An investigation of the plane strain fracture toughness of high strength steels (Brown, W.F., and Srawley, J.E., 1966) has given rise to certain empirical indications of the validity of an experimentally determined critical stress intensity factor (i.e., when $K_{Icrit.} = K_{Ic}$) which relate to the specimen dimensions; see Figure 5.7 (a)

$$B, a, \text{ and } W - a \geq 2.5(K_{Ic}/\sigma_Y)^2 \qquad [5.52]$$

Since the plastic zone size, r_Y, for plane strain conditions is $(1/6\pi)(K_{Ic}/\sigma_Y)^2$ at fracture, [5.52] becomes

$$B, a, \text{ and } W - a \geq 15\pi r_Y \approx 50 r_Y \qquad [5.53]$$

For the purposes of illustration assume that this approach can be applied to non-ductile materials, i.e., a localized plastic zone surrounds the crack-tip. For ceramic materials, the yield stress is inferred from the hardness, i.e., $\sigma_Y \approx H/3$ (Tabor, D., 1951); so for H = 12 GPa, $\sigma_Y \approx$ 4 GPa, and $K_{Ic} \approx 4$ MPa.$m^{1/2}$, $r_Y \approx 0.05\mu m$, and a, and W - a $\geq \approx 3\mu m$. So for ceramic materials the plastic zone size is negligible and the dimensional constraints for obtaining valid experimental K_{Ic} results are invariably satisfied, except when plasticity effects become significant at elevated temperatures.

The final point to consider when choosing the SENB specimen dimensions, is the scale of the microstructure of the bulk material. The cross-sectional area of the ligament should be much greater than the cross-sectional areas of the microstructural features which characterize the bulk material fracture behaviour; the cross-section required will thus be predominantly determined by the average grain size. For all but the most coarse microstructures, this requirement is not a problem.

5.5 Experimental Determination of the Fracture Toughness and Hardness of Glass-Ceramics in the System CaO - MgO - Al_2O_3 - SiO_2

The following experimental data have been obtained for the specified glass-ceramics:

(1) The three-point bending SENB plane strain fracture toughness (K_{Ic}) of SCR25.76 and SCR19.34 as a function of temperature in air, together with the following data at room temperature in air,

(2) The three-point bending SENB plane strain fracture toughness (K_{Ic}) of SCR25.76, SCR19.34, SCF5 and SCR19.13,

(3) The Vickers indentation fracture toughness of SCR25.76, SCR19.34, SCF5 and SCR19.13 as calculated using the fracture toughness equations found in the ceramics and materials science literature,

(4) The Vickers hardness of SCR25.76, SCR19.34, SCF5 and SCR19.13; with the hardness of SCF5 as a function of indenter load,

(5) The Knoop hardness and the Young's modulus to hardness ratio for SCF5, using the Knoop indentation data, as a function of indenter load,

In addition, the Young's modulus in flexure of ICI 'Perspex' acrylic sheet was determined, along with the compliance of 'Perspex' SENB specimens as a function of notch depth, in order to evalulate the compliance of the glass-ceramic SENB specimens and thereby experimentally determine the critical strain energy release rate (G_{Ic}) in air at room temperature for SCR25.76, SCR19.34, SCF5 and SCR19.13 and compare the data with that calculated using the K_{Ic} data.

The morphology of the crack system developed beneath Vickers indentations in SCR25.76, SCR19.34, SCF5 and SCR19.13 was investigated by the removal of successive surface layers by diamond abrasive polishing; schematic crack profiles were drawn from the crack length data obtained as a function of depth below the specimen surface.

5.5.1 Experimental determination of SENB K_{Ic}

(1) Specimen preparation and testing:

Glass-ceramic tablets were machined to a nominal thickness of 8 mm in the manner described for the flexural strength specimens in Chapter 4; after the machining damage had been removed from the tablet faces and one face polished on a 14μm diamond lap, the tablets were cut into individual specimens with nominal dimensions of 40 x 8 x 4 mm^3. Unlike the strength specimens, however, the intended tensile faces were not polished on a 6μm diamond lap nor were the longitudinal edges of the intended tensile faces rounded. A notch with a nominal width of 0.15 mm and depth of 1.2 mm was then machined in the tensile face of each specimen at the mid-length position, using a 0.15 mm thick 'Loadpoint' resin-bonded 320-grit diamond slitting disc on a Jones and Shipman 540P surface grinding machine.

The notches were cleared of debris using strips of thin, stiff tracing paper before their depths were measured using an optical microscope with a graduated and calibrated eyepiece; the notch depth was measured from each side of the specimen to an accuracy of ± 0.0254 mm and the average taken. So, say for example, that W = 7.894 ± 0.01 mm and the notch depth (a) = 1.200 mm, the possible percentage error in a is 2 %, while that in a/W is given by $[(0.254/1.200)^2 + (0.01/7.894)^2]^{1/2}$ = 2 %. As for the flexural strength specimens, the dimensions of the SENB specimens were measured at the ends and at the centre, to within 0.001 mm using a screw micrometer, and the average of the three readings taken. The faces of the tablets were parallel to within ≈ 0.025 mm (see Chapter 4). The average notch width was 0.152 mm along the entire notch depth and the notch-root profile was U-shaped. All the tests were conducted in air at a cross-head speed of 1 mm/minute; the five SCR19.13 specimens were tested on the WC roller room temperature testing rig, whereas the other specimens were tested on the high temperature three-point bending test rig with either Si_3N_4 knife-edges or alumina rollers.

(2) Room temperature experimental results:

The specimen breadth (B), width (W) and notch depth (a), the relative notch depth (a/W), the fracture load (P), the failure time (t_F), the compliance factor (Y) and the plane strain fracture toughness (K_{Ic}) are tabulated for each specimen tested, together with the support span and the test temperature in Appendix 5C; the room temperature data are tabulated in Table 5C.1 of the appendix. The plane strain fracture toughness (K_{Ic}) was calculated in units of $Pa.m^{1/2}$ using

$$K_{Ic} = Y(3Ps/2BW^2)a^{1/2} \qquad [5.54]$$

where Y is the compliance factor given by equation [5.51], P the fracture load, s the three-point bending support span, B and W the specimen breadth and width respectively, and a the notch depth. The mean K_{Ic} values are given in Table 5.1 for each material, together with the sample standard deviation (s.d), the number of data obtained in parenthesis and the coefficient of variation (C_v).

The mean K_{Ic} values were compared with the volume fraction of residual glass and the room temperature Young's modulus; the data are presented in Table 5.2. The data show that K_{Ic} increased with increasing Young's modulus as may be expected for the reasons given below. Fracture at room temperature in non-ductile materials occurs by the rupture of successive atomic bonds at the tips of propagating cracks; thus their resistance to fracture is dependent on the interatomic bond strengths, i.e., bond energies; this is especially true for glass, and single phase mono- and polycrystalline ceramics. Since the elastic moduli are proportional to $dF/ds = d^2P/ds^2$, where F is the interatomic force, P the interatomic potential energy and s the interatomic separation and d^2P/ds^2 increases with increasing bond energy, the higher the bond energy the higher the elastic moduli. For an infinite body $K_{Ic} = (2E\gamma_E/\beta)^{1/2} = (EG_{Ic}/\beta)^{1/2}$ (equation [5.16]). Note that $K_{Ic} = 1.06\ MPa.m^{1/2}$ for SCR19.13 (30 % crystalline), compared to $\geq 1.83\ MPa.m^{1/2}$ for the other materials, which are $\geq$ 58 % crystalline.

Table 5.1 Room Temperature SENB Plane Strain Fracture Toughness Data for SCR25.76, SCR19.34, SCF5 and SCR19.13:

Material	K_{Ic} (MPa.m$^{1/2}$)	s.d. (MPa.m$^{1/2}$)	C_v (%)
SCR25.76	2.29	0.21 (7)	9
SCR19.34	1.83	0.06 (7)	3
SCF5	2.02	0.11 (4)	5
SCR19.13	1.06	0.11 (5)	11

Table 5.2 Room Temperature Fracture Toughness and Young's Modulus Data, and Percentage of Residual Glass for SCR25.76, SCR19.34, SCF5 and SCR19.13:

Material	Residual Glass (vol. %)	K_{Ic} (MPa.m$^{1/2}$)	E (GPa)
SCR25.76	29	2.29	121.7
SCF5	18	2.02	120.6
SCR19.34	42	1.83	115.0
SCR19.13	70	1.06	100.6

Table 5.3 SENB Plane Strain Fracture Toughness of SCF5, SCR25.76 and SCR19.34 as a Function of Temperature:

Temp. (°C)	SCR25.76 K_{Ic} (MPa.m$^{1/2}$)	SCR19.34 K_{Ic} (MPa.m$^{1/2}$)	SCF5 K_{Ic} (MPa.m$^{1/2}$)
20	2.29 ± 0.21 9%	1.83 ± 0.06 3%	2.02 ± 0.11 5%
250	1.46 ± 0.10 7%	1.35 ± 0.04 3%	----------
500	1.58 ± 0.24 15%	1.50 ± 0.20 13%	----------
600	1.83 ± 0.28 15%	1.59 ± 0.09 6%	1.42 ± 0.01 1%
700	1.62 ± 0.27 17%	1.34 ± 0.10 8%	----------
750	1.80 ± 0.17 9%	2.86 ± 0.71 25%	----------
775	2.09 ± 0.31 15%	4.20 ± 1.23 29%	----------
800	----------	----------	1.95 ± 0.25 13%
850	----------	----------	2.77 ± 0.55 20%

(3) High temperature experimental results:

The elevated temperature K_{Ic} data obtained for SCR25.76, SCR19.34 and SCF5 are tabulated in Tables 5C.2 to 5C.9 of Appendix 5C. Five data were obtained for SCR25.76 and for SCR19.34 at 250, 500, 600, 700, 750 and 775°C, and a single datum at 792°C. Both the SCR25.76 and SCR19.34 specimens deformed plastically at 792°C after an initial linear load versus cross-head displacement response. Two data were obtained for SCF5 at 600, 800, 850 and 900°C; at 900°C every specimen underwent marked plastic deformation almost immediately on being loaded with no initial linear load versus cross-head displacement response.

The mean K_{Ic} values obtained for the three materials are tabulated against temperature in Table 5.3, together with the sample standard deviation and the percentage coefficient of variation. The mean K_{Ic} values for these materials are plotted against temperature in Figure 5.8. The Young's moduli of SCR25.76, SCR19.34 and SCF5 were found to be decreasing linear functions of temperature (T) up to a temperature characteristic of the material (see Chapter 3); the empirical functions are:

(1) SCR25.76 $E = 122.8 - 0.0190T$ GPa up to 436°C

(2) SCR19.34 $E = 114.7 - 0.0153T$ GPa up to 551°C

(3) SCF5 $E = 121.3 - 0.0106T$ GPa up to 626°C

The Young's moduli were calculated, if possible at 250, 500 and 600°C, using these functions; if the Young's modulus could not be calculated from them, the value for the nearest experimental temperature was estimated from the normalised experimental Young's modulus (E/E_o) data (see Chapter 3). The Young's moduli, Poisson's ratio, K_{Ic} and Y data were used then to estimate the effective fracture surface energy (γ_E) using the equation $\gamma_E = [\pi(1 - \nu^2)/2E][K_{Ic}/Y]^2$ which was derived from equation [5.15] for plane strain conditions and $Z = 1$; the effective fracture surface energy data are tabulated against temperature in Table 5.4, with the sample standard deviation and percentage coefficient of variation.

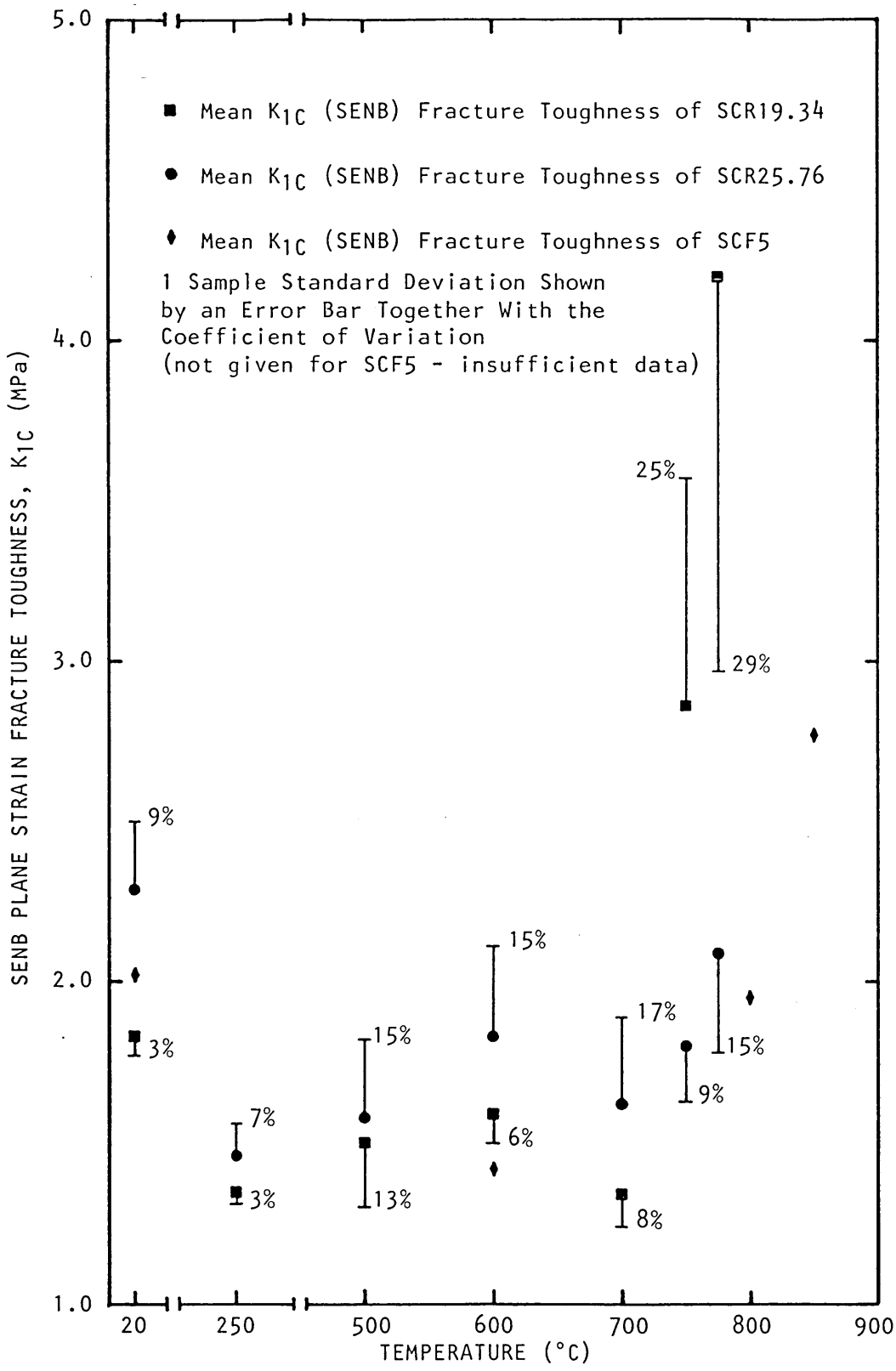


Figure 5.8 SENB Plane Strain Fracture Toughness (K_{1C}) as a Function of Temperature for SCR25.76, SCR19.34 and SCF5.

Table 5.4 Effective Fracture Surface Energy (γ_E) as a Function of Temperature:

Temp. (°C)	SCR25.76 γ_E (Jm^{-2})	SCR19.34 γ_E (Jm^{-2})	SCF5 γ_E (Jm^{-2})
20	21.12 ± 3.56 17%	14.36 ± 0.87 6%	16.38 ± 1.74 11%
250	8.84 ± 1.20 14%	7.54 ± 0.49 7%	----------
500	10.94 ± 3.02 30%	10.39 ± 2.70 26%	----------
600	15.45 ± 4.65 30%	11.95 ± 1.32 11%	8.45 ± 0.16 2%
700	----------	10.52 ± 1.58 15%	----------

Note: The Young's modulus data for the temperatures nearest to the following temperatures were used:

(1) SCR25.76

500°C : used E at 493°C

600°C : used E at 585°C

(2) SCR19.34

600°C : used E at 596°C

Table 5.5 Plane Strain Fracture Toughness, Young's Modulus and Effective Fracture Surface Energy as a Function of Temperature:

Temp. (°C)	SCR25.76			SCR19.34			SCF5		
	E	K_{Ic}	γ_E	E	K_{Ic}	γ_E	E	K_{Ic}	γ_E
20	122	2.29	21	115	1.83	14	121	2.02	16
250	118	1.46	9	111	1.35	8	----------		
500	113	1.58	11	107	1.50	10	----------		
600	107	1.83	15	104	1.59	12	115	1.42	8
700	----------			84	1.34	11	----------		

Note: (i) The Young's modulus (E) data are in GPa, the effective fracture surface energy (γ_E) data in Jm^{-2} and the plane strain fracture toughness (K_{Ic}) in $MPa.m^{1/2}$.

(ii) The Young's modulus and fracture surface energy data have been rounded to the nearest integer because apart from the room temperature Young's modulus values, the data are only estimates.

The effective fracture surface energy of the SCR19.13 glass-ceramic was 5.35 ± 1.19 (coefficient of variation of 22 %) at room temperature; less than half that of SCR25.76, SCR19.34 and SCF5 at room temperature. In order to illustrate the variation with temperature of the Young's modulus, fracture toughness and effective fracture surface energy of SCR25.76, SCR19.34 and SCF5, the data are tabulated simultaneously as a function of temperature in Table 5.5; the data show that the variation in fracture toughness with temperature is essentially equivalent to the variation in the effective fracture surface energy with temperature. For example the Young's modulus of SCR25.76 at 600°C is 12 % lower than the room temperature value, whereas K_{Ic} is 20 % lower and γ_E is 29 % lower. In the case of SCR19.34, the Young's modulus is 10 % lower, while K_{Ic} is 27 % lower and γ_E is 21 % lower. So while the Young's modulus plays a role in the fracture toughness of a non-ductile material through its relationship to bond energy, the toughness is strongly dependent on the microstructure of the material in terms of its effect on the energy required for fracture, e.g., as measured by the effective fracture surface energy. Thus the toughness may be increased by microstructures which cause crack deflection, crack branching, induce residual stresses which pin propagating cracks, and so on.

The fracture toughness (as measured by the mean K_{Ic} data) of both SCR25.76 and SCR19.34 shows an upward trend from 250 to 775°C, with the toughness of SCR25.76 being slightly higher than that of SCR19.34 at all temperatures up to 700°C; however, at 750°C and 775°C the toughness of SCR19.34 is much greater than that of SCR25.76, although the scatter about the mean is of the order of 25 to 30 % for SCR19.34 compared to ≈ 10 to 15 % for SCR25.76. The increasing trend in toughness is primarily due to the decrease in viscosity of the intergranular residual glass with increasing temperature; the dilatometric softening point (≈ 10^{10} to 10^{11} Pa.s) of the residual glass corresponds to a temperature range of ≈ 440 to 480°C and ≈ 480 to 520°C for SCR25.76 and SCR19.34 respectively.

The cross-over in the fracture toughness is considered to be due to the greater volume fraction of residual glass in SCR19.34 compared to SCR25.76 (i.e., ≈ 0.4 compared to ≈ 0.3) outweighing its higher viscosity compared to that of the residual glass in SCR25.76 because (a) the presence of the notch reduces the effective cross-sectional area of the specimen to just the ligament area, and (b) there is a higher statistical probability of there being a larger area fraction of residual glass in the ligament area of the SCR19.34 specimens compared with the SCR25.76; thus a higher fraction of the apparent fracture toughness of SCR19.34 (compared to SCR25.76) at temperatures ≥ 750°C was due to the plasticity of the residual glass, i.e., the fracture behaviour of SCR19.34 was more ductile than that of SCR25.76.

Two experimental observations suggested this to be the case, (i) while both materials deformed plastically at 792°C, it was observed that at a cross-head displacement of 0.455 mm (which was within the linear load versus cross-head displacement response region of both materials) the SCR25.76 specimen sustained a load of 263 N while the SCR19.34 specimen sustained a load of 181 N, and (ii) on matching up the fractured halves of the SCR19.34 specimens tested at 775°C, so that the fracture-face edges on the compressive face were in contact, it was observed that the plane of the tensile face of each specimen was slightly convex, i.e., a small amount of plastic deformation had occurred, notwithstanding the fact that the recorded load versus cross-head displacement curves were to most intents and purposes linear-elastic until fracture.

In contrast, the mean flexural strength of SCR25.76 was lower than that of SCR19.34 at all temperatures up to 700°C; this was explained by the higher viscosity of the residual glass in SCR19.34 outweighing its higher volume fraction in comparison to the lower volume fraction of lower viscosity residual glass in SCR25.76. At 750°C, however, SCR25.76 specimen MA701 supported a load of ≈ 255 N, while SCR19.34 specimen MB701 supported a load of ≈ 243 N at the same cross-head displacement of ≈ 0.43 mm.

The small amount of high temperature fracture toughness data for SCF5 (see Appendix 5C) tend to indicate that the room temperature fracture toughness may be maintained to ≈ 800°C at least, with plastic deformation occurring at 900°C. The reasons for the better high temperature toughness of SCF5 compared to SCR25.76 and SCR19.34 are the same as those given for its better high temperature strength; (a) a low volume fraction of residual glass (≈ 0.2), (b) the dilatometric softening point corresponds to a temperature of ≈ 630 to 680°C, (c) the Young's modulus at 600°C is only ≈ 5 % down on the room temperature value of 121 GPa, and (d) the highly "interlocking", essentially continuous crystal network.

An anomaly was observed in the temperature dependence of both the flexural strength and the fracture toughness of the SCR25.76 and SCR19.34 glass-ceramics; a distinct decrease in the flexural strength (data obtained using the high temperature three-point bending test rig) and fracture toughness occurred at 250°C (see Chapter 4 and Table 5.5 in this chapter) relative to the room temperature strength and toughness. Both the strength and toughness increased with temperature above 250°C. The small decrease in Young's modulus of ≈ 3 % cannot explain this anomaly, and neither dislocation movement nor viscosity effects are expected at such a relatively low temperature. If thermal expansion mismatch induced residual stresses are responsible for the anomaly, then their effect would be expected to become more significant with increasing temperature. Given the limited amount of data available, no firm conclusions regarding this anomaly may be drawn at present; further tests on the same rig and a different rig at room temperature and at temperatures of 250°C and higher would serve to distinguish between a material behaviour anomaly and a test rig/testing technique characteristic.

Finally, it should be noted that the apparent increase in strength and toughness at elevated temperatures of ≈ 600°C and higher due to softening of the intergranular residual glass (or in general, any other

intergranular phase which softens at high temperature) is essentially a feature of the testing technique itself, in particular the strain rate. Flaws and microcracks in the residual glass are healed and blunted at high temperatures by viscous flow of the glass, a process which is time dependent; therefore if the chosen cross-head speed is very much higher than the rate of viscous flow, there will be insufficient time for any crack-tip healing or blunting to occur before catastrophic fracture takes place. So at some strain rate at which the crack-tip propagation and blunting rates are in equilibrium, the fracture toughness will be a maximum; at high strain rates the toughness may be effectively independent of the test temperature.

5.5.2 Experimental determination of SENB G_{Ic}

(1) Introduction:

The critical strain energy release rate under plane strain conditions, G_{Ic}, of a cracked body can be determined experimentally using equation [5.5]. In the present work, G_{Ic} was determined experimentally using the fracture load and specimen thickness data for the SENB specimens used to determine K_{Ic} at room temperature in air, and equation [5.5] which was re-written as

$$G_{Ic} = (P_F^2/2B)(d\bar{\Omega}/da) \qquad [5.55]$$

where P_F is the fracture load, B the specimen thickness, and $d\bar{\Omega}/da$ the rate of change of compliance ($\bar{\Omega}$) with notch depth (a). In three-point bending,

$$\bar{\Omega} = d_c/P \qquad [5.56]$$

where d_c is the centre deflection of the SENB specimen and P the applied load. Experimentally $d\bar{\Omega}/da$ could be obtained using the material for which G_{Ic} is to be determined by recording the load - centre deflection curves of SENB specimens with different notch depths, the slopes of which are P/d_c, and then plotting $1/(P/d_c)$ against a, i.e., $\bar{\Omega}$ as a function of a. Thus for a given notch depth, a_j, the slope of $\bar{\Omega}$ versus a at a_j gives the appropriate $d\bar{\Omega}/da$ value. In practice, however, the compliance measurements

are conducted using SENB specimens made from a material of lower Young's modulus as the centre diplacements at a given load are larger and hence can be measured more accurately. This experimental approach to evaluating $d\bar{\Omega}/da$ is inherently inaccurate because $d\bar{\Omega}/da$ is obtained by graphically measuring two gradients; as the plot of $\bar{\Omega}$ versus a is a positive, non-decreasing curve a large number of $(\bar{\Omega},a)$ data are required for good accuracy.

The elastic centre deflection of an un-notched beam of given dimensions, resting on a given support span, is proportional to the applied load and the proportionality constant is inversely proportional to the Young's modulus of the beam. Hence the beam compliance is also inversely proportional to E and for two identical beams which are loaded in the same manner, $\bar{\Omega}_1 = k/E_1$ and $\bar{\Omega}_2 = k/E_2$ where k is a constant and E_1 and E_2 are the Young's moduli of beams 1 and 2 respectively. Now consider two SENB specimens with the same nominal length, breadth, width, notch-depth, notch-width and notch-root profile, but with different Young's modulus, which are subject to the same loading configuration; it follows from above that

$$\bar{\Omega}_2 = \bar{\Omega}_1 (E_1/E_2) \qquad [5.57]$$

where $\bar{\Omega}_1$, E_1 and $\bar{\Omega}_2$, E_2 are the compliance and Young's modulus of SENB specimens 1 and 2 respectively. Thus the compliance of the G_{Ic} test material can be calculated for the prescribed notch depths from a knowledge of the Young's modulus of both the compliance and the G_{Ic} test materials and the compliance data obtained experimentally for the different notch depths. The calculated compliance data are then plotted against the corresponding notch depths to produce a compliance curve from which $d\bar{\Omega}/da$ can be evaluated for a given notch depth and used in equation [5.55] to determine G_{Ic}.

(2) Specimen preparation and experimental procedure:

In the present work specimens of nominal dimensions of 40 x 8 x 4 mm^3 were machined from ICI 'Perspex' acrylic sheet; two specimens were used to determine the Young's

modulus in flexure from load versus centre-deflection data, while other specimens were notched at the mid-length position using the same 0.15 mm thick diamond slitting disc which was used to notch the SENB K_{Ic} specimens. Most of the specimens were notched to depths in the range ≈ 1 to 1.5 mm because the nominal notch depth of the K_{Ic} specimens was 1.2 mm, and one to a depth of ≈ 2.4 mm to check for the markedly higher compliance expected at greater notch depths. The specimen dimensions and notch depths were measured as per the SENB K_{Ic} specimens. The notch depths were measured directly after machining and again about two weeks later, and it was found that the apparent depth had decreased by ≈ 4 %; this was presumably due to anelastic strain recovery.

(2.1) Determination of the room temperature Young's modulus in flexure of ICI 'Perspex' acrylic sheet:

The two specimens were loaded in three-point bending on a span of 30 mm, using a JJ T20K tensile testing machine with a 1000 N load cell loaded in compression; a cross-head speed of 1 mm/minute was used. The centre-deflections of the specimens were measured by means of a Schlumberger 'Sangamo' a.c. linear voltage displacement transducer (model AG with a ± 5.0 mm stroke, 0.3 % linearity and a C31 signal conditioner); the transducer body was rigidly attached the support span base of the test rig while the probe-tip was in contact with the tensile face of the specimen at the mid-span position. This arrangement ensured that only the deflection of the specimen was measured.

The centre deflection of a beam in three-point loading, d_c, is (Ryder, G.H., 1969)

$$d_c = Ps^3/48EI \qquad [5.58]$$

where P is the applied load, s the support span, E the Young's modulus and I the moment of inertia of the beam cross-section. For a rectangular beam of breadth B and width W, $I = BW^3/12$. So substituting for I in [5.58] and re-arranging gives

$$E = (\Delta P/\Delta d_c)(1/4B)(s/W)^3 \qquad [5.59]$$

where $\Delta P/\Delta d_c$ is the graphically determined slope of the load versus centre-defection curve for each specimen. The experimental data are given below:

Specimen #.	B (mm)	W (mm)	ΔP (N)	Δd_c (mm)	E (GPa)
1	4.010	8.103	120	0.123	3.02
2	4.019	8.084	125	0.134	2.90

The mean Young's modulus was 2.97 ± 0.08 GPa; this compares extremely well with the manufacturer's quoted data for the Young's modulus in flexure at 20°C of 2.9 ± 0.1 GPa (ICI Technical Service Note PX127 3rd ed., 1981). So no further Young's modulus measurements were conducted and the ICI value used in the compliance calculations.

(2.2) Room temperature compliance measurement:

The compliance measurements were conducted using the high temperature three-point bending rig designed for the present work; the rig was used with a 1000 N static load cell operating in compression and silicon nitride knife-edges with a span of 31.53 mm. A cross-head speed of 0.1 mm/minute was used and it was assumed that the cross-head displacement equalled the centre-deflection of the specimen; this assumption was made because it was not possible to use a displacement transducer in contact with the tensile face of the specimens. It should be noted that (i) the maximum load applied to all the specimens was 98 N, (ii) the axial compliance of the Instron 1185 machine is specified by the manufacturer as 300 $kNmm^{-1}$.

Nine load, cross-head displacement data pairs were extracted from the load (P) versus cross-head displacement (y) curve of each specimen tested; these data are tabulated in Table 5D.1 of Appendix 5D, along with the specimen dimensions and notch depths. The load and corresponding cross-head displacement data for each specimen were analysed using "least-squares" linear regression analysis on the equation $y = \Phi P + i$ where i is

the intercept; the compliance ($\bar{\mathcal{C}}$) data obtained are tabulated in Table 5D.2 of Appendix 5D. A "least-squares" regression analysis of the ($\bar{\mathcal{C}}$,a) data assuming $\bar{\mathcal{C}} = A + Ba$ where $B \equiv d\bar{\mathcal{C}}/da$ and A is the intercept at a = 0 was found to give the best fit to the data for tests 1 to 7 (See Table 5D.2); the analysis gave $d\bar{\mathcal{C}}/da$ as 3.21×10^{-4} N^{-1} for $0.978 \leq a \leq 1.448$ mm. From equation [5.57] it follows that $d\bar{\mathcal{C}}_2/da = (E_1/E_2)(d\bar{\mathcal{C}}_1/da)$; in the present work E_1 = 2.9 GPa and $d\bar{\mathcal{C}}_1/da = 3.21 \times 10^{-4}$ N^{-1}, while E_2 is the room temperature Young's modulus of the glass-ceramic in question. Using the $d\bar{\mathcal{C}}_2/da$ values so obtained, together with the load and specimen breadth data for SCR25.76, SCR19.34, SCF5 and SCR19.13 (See Appendix 5C, Table 5C.1) in equation [5.55], G_{Ic} data were calculated for each glass-ceramic (for room temperature in air) The mean G_{Ic} values are presented in Table 5.6.

The SENB plane strain critical strain energy release rate can also be calculated using the following equation derived from equation [5.15] for plane strain conditions and Z = 1

$$G_{Ic} = [\pi(1 - \nu^2)/E][K_{Ic}/Y]^2 = 2\gamma_E \qquad [5.60]$$

The room temperature Young's modulus, Poisson's ratio, K_{Ic} and Y data for SCR25.76, SCR19.34, SCF5 and SCR19.13 (see Chapter 3 and Appendix 5C, Table 5C.1) were thus used to calculate the corresponding mean G_{Ic} data. Note that as before (See Section 5.5.1 (2)) the Poisson's ratio of SCF5 and SCR19.13 was assumed to be 0.25; ν appears in the form $1 - \nu^2$ and the the resulting errors are small because ν is $\approx$ 0.20 to 0.30. The calculated G_{Ic} data are given in Table 5.7, along with the sample standard deviation (s.d.), the number of data in parenthesis ( ) and the percentage coefficient of variation as per Table 5.6.

Both the experimentally determined mean G_{Ic} values (G_{Ic}^E) and the mean G_{Ic} values calculated using the K_{Ic} data (G_{Ic}^C) are tabulated in Table 5.8 for SCR25.76, SCR19.34, SCF5 and SCR19.13 (at room temperature in air) for comparison. The data show that the calculated G_{Ic} values are higher than the experimentally determined G_{Ic} values, except in the case of SCR19.13, and that the

Table 5.6 Experimental Room Temperature SENB Plane Strain Critical Strain Energy Release Rate Data for SCR25.76, SCR19.34, SCF5 and SCR19.13:

Material	G_{Ic} (Jm^{-2})	s.d. (Jm^{-2})	C_v (%)
SCR25.76	37.70	6.48 (7)	17
SCR19.34	24.38	1.45 (7)	6
SCF5	26.62	4.53 (4)	17
SCR19.13	10.95	2.18 (5)	20

Note: s.d. is the sample standard deviation, C_v the percentage coefficient of variation, and the number of data tested is given in ( ).

Table 5.7 Calculated Room Temperature SENB Plane Strain Critical Strain Energy Release Rate Data for SCR25.76, SCR19.34, SCF5 and SCR19.13:

Material	G_{Ic} (Jm^{-2})	s.d. (Jm^{-2})	C_v (%)
SCR25.76	42.24	7.13 (7)	17
SCR19.34	28.71	1.75 (7)	6
SCF5	32.75	3.47 (4)	11
SCR19.13	10.70	2.38 (5)	22

Table 5.8 Mean Experimentally Determined SENB G_{Ic} Data (G_{Ic}^E) and Mean Calculated SENB G_{Ic} Data (G_{Ic}^C) for SCR25.76, SCR19.34, SCF5 and SCR19.13:

Material	Mean G_{Ic}^E (Jm^{-2})	Mean G_{Ic}^C (Jm^{-2})	%-Diff.
SCR25.76	37.70	42.24	+ 11
SCR19.34	24.38	28.71	+ 15
SCF5	26.62	32.75	+ 19
SCR19.13	10.95	10.70	- 2

Note: The %-Diff. = $100(G_{Ic}^C - G_{Ic}^E)/G_{Ic}^C$.

values agree to within 19 % or better; the two values for SCR19.13 agree to within 2 % which is remarkable considering that (i) the K_{Ic} data were determined using the room temperature three-point bending test rig with the tungsten-carbide roller supports and loading edge on another model of Instron testing machine and (ii) the specimens were notched using a diamond slitting disc which produced a nominal notch-width of 0.27 mm instead of 0.15 mm as for the other specimens. The fact that the two sets of data agree to within 19 % or better suggests that the the errors caused by (a) not correcting for the machine and load-train compliances and (b) the assumption that the cross-head displacement equalled centre-deflection of the specimen were not too serious. The range of the room temperature values of the effective fracture surface energy, γ_E (= $G_{Ic}/2$) is typical of most glass-ceramics.

5.5.3 Experimental determination of Vickers hardness and indentation fracture toughness, K_c

(1) Specimen preparation and experimental procedure:

The specimens used for the indentation measurements were either broken bend test specimens as in the case of SCF5 or unbroken bend test specimens whose dimensional non-uniformity precluded their use in bend tests. All the specimens were polished on their wide face using a rotary diamond abrasive polishing wheel; they were polished for about 20 - 30 minutes on successive diamond grades, going in order of increasing fineness, 14μm, 6μm, 3μm, 1μm and finally 0.25μm. The resulting surface finish fulfilled two requirements,

(i) the residual stresses due to the surface damage caused by the diamond abrasive machining were removed or at least reduced and (ii) provided a flat, reflective surface, which when coated with a vacuum deposited layer of gold (≈ 20 to 40 nm thick) was very reflective; this enabled the measurement of the indent and crack dimensions using an optical microscope with a calibrated, graduated eyepiece.

Indentations were made on SCF5 using both a macro-Vickers indenter and a macro-Knoop indenter attached to an Instron testing machine, while the macro-Vickers indents in the SCR19.13 specimen were made on a JJ testing machine; in both cases a cross-head speed of 0.5 mm/minute was used with a nominal time under the peak indenter load of 15 seconds. Due to machine failure, the tests on SCR25.76 and SCR19.34 were carried out using a Vickers macro-hardness testing machine with a load of 5 kgf (equivalent to 49 N). Six Vickers indents were made on the SCR19.13 specimen using the Vickers machine with a 5 kgf load, and six with a load of 2.5 kgf; at the 5 kgf load the Vickers hardness was 6.8 ± 0.3 GPa, while at the 2.5 kgf load the hardness was 5.9 ± 0.3 GPa. The mean hardness value obtained at 5 kgf was only ≈ 3 % down on the value measured using the JJ testing machine, but the value obtained at 2.5 kg was ≈ 16 % down on the JJ value.

(2) Experimental macro-hardness and fracture toughness results:

The peak Vickers indenter load (P), the mean half--diagonal length (a), the mean surface radial crack length (c), the mean surface radial Palmqvist crack length (l), and the Vickers hardness data for SCR25.76, SCR19.34, SCF5 and SCR19.13 are tabulated in Appendix 5E, together with the peak Knoop indenter load (P), major indent diagonal length (a*), minor indent diagonal length (b*), the b*/a* ratio, and Knoop hardness data for SCF5. The c/a and l/a ratios for these four materials are tabulated in Appendix 5F, along with the $P/c^{3/2}$ and P/l data. The Vickers indentation fracture toughness of the four materials was calculated using the data in Appendix 5E in each of the sixteen fracture toughness equations listed in Section 5.3.1; the values obtained from the sixteen equations are tabulated in Appendix 5G.

The mean Knoop hardness values of two SCF5 specimens under nominal peak indenter loads of 50, 100 and 150 N are given in Table 5.9; the data show that the

measured hardness decreases slightly with increasing indenter load. The mean of all the data for SCF5, regardless of load, was 6.0 ± 0.2 GPa; i.e., a coefficient of variation of ≈ 3 %. The mean Vickers hardness values of three SCF5 specimens under the same nominal loads are tabulated in Table 5.10; again the apparent hardness decreases with increasing indenter load. The mean Vickers hardness of SCF5 regardless of load is 7.0 ± 0.2 GPa, i.e., a coefficient of variation of ≈ 3 %. The apparently general decrease in measured hardness with increasing load is presumably related to the increasing size of the plastic deformation zone and degree of concomitant cracking around the indent, which reduce the constraining influence of the surrounding elastic matrix on the plastic deformation zone beneath the indenter, enabling deeper penetration of the indenter. Note that the mean Knoop hardness is ≈ 14 % lower than the mean Vickers hardness, but the coefficient of variation is similar.

The Vickers hardness of SCR19.13 was measured under a nominal load of 57 N, while that of SCR25.76 and SCR19.34 was measured at a nominal load of 49 N. The mean hardness values for these glass-ceramics are given in Table 5.11, along with that of SCF5. Table 5.12 lists the Young's modulus values and the percentage volumes of residual glass of the materials; there is no apparent correlation between residual glass content or Young's modulus and the hardness. Furthermore, the hardness is apparently insensitive to the microstructural differences between the materials. Additional hardness tests on the materials under exactly the same conditions, i.e., using the same load and testing machine, may either indicate that the hardness of the materials is essentially the same or show up some differences; as it is, taking the average of the mean hardness values of the materials gives a hardness value of 7.2 ± 0.3 GPa, i.e., a coefficient of variation of only ≈ 4 %.

Table 5.9 Room Temperature Knoop Hardness for SCF5:

Sp.#.	Indenter Peak Load (N)	Knoop Hardness (GPa)	Specimen Knoop Hardness (GPa)
1	147 ± 2 (3)	5.8 ± 0.1 (3)	
1	97 ± 1 (3)	6.0 ± 0.1 (3)	
1	48 ± 1 (3)	6.1 ± 0.0 (3)	6.0 ± 0.1 (9)
2	149 ± 1 (4)	5.7 ± 0.1 (4)	
2	100 ± 1 (3)	6.1 ± 0.2 (3)	
2	50 ± 1 (3)	6.3 ± 0.2 (3)	6.0 ± 0.3 (10)

Note: Sp.#. denotes the specimen number, and ( ) the number of data.
The mean Knoop hardness of SCF5 regardless of indenter load is 6.0 ± 0.2 GPa (19).

Table 5.10 Room Temperature Vickers Hardness for SCF5:

Sp.#.	Indenter Peak Load (N)	Vickers Hardness (GPa)	Specimen Vickers Hardness (GPa)
1	148 ± 1 (3)	6.8 ± 0.2 (3)	
1	97 ± 1 (3)	7.0 ± 0.1 (3)	
1	49 ± 2 (3)	7.1 ± 0.1 (3)	7.0 ± 0.2 (9)
2	148 ± 3 (3)	6.8 ± 0.1 (3)	
2	100 ± 3 (3)	7.1 ± 0.2 (3)	
2	51 ± 2 (3)	7.1 ± 0.3 (3)	7.0 ± 0.2 (9)
3	150 ± 2 (3)	6.9 ± 0.2 (3)	
3	101 ± 2 (3)	7.0 ± 0.2 (3)	
3	49 ± 2 (3)	7.3 ± 0.3 (3)	7.1 ± 0.3 (9)

Note: Sp.#. denotes the specimen number, and ( ) the number of data.

Table 5.11 Room Temperature Vickers Hardness for SCR25.76, SCR19.34, SCF5, and SCR19.13:

Material	Indenter Peak Load (N)	Vickers Hardness (GPa)
SCR25.76	49	7.5 ± 0.1 (9)
SCR19.34	49	7.4 ± 0.1 (9)
SCR19.13	57 ± 7 (9)	7.0 ± 0.3 (9)
SCF5	149, 99, 50	7.0 ± 0.2 (27)

Table 5.12 Room Temperature Vickers Hardness, Young's Modulus and Percentage of Residual Glass for SCR25.76, SCR19.34, SCF5 and SCR19.13:

Material	Residual Glass (vol. %)	E (GPa)	Vickers Hardness (GPa)
SCR25.76	29	121.7	7.5
SCF5	18	120.6	7.0
SCR19.34	42	115.0	7.4
SCR19.13	70	100.6	7.0

(2.1) Relationship between indenter load and surface radial crack length:

The assumption of a fully developed radial/median "half-penny" crack system leads to the result that if the assumption is valid, then $P/c^{3/2}$ should be constant. On the otherhand, if the cracks formed are Palmqvist cracks, then assuming the hardness to be load independent (which is for most intents and purposes a reasonable assumption, notwithstanding the general decrease in hardness with increasing indenter load), P/l should be constant. The $P/c^{3/2}$ and P/l data for SCF5 and SCR19.13 are given in Table 5.13; without taking the results seriously, it is interesting to note that for SCF5, which is highly crystalline, the coefficient of variation of $P/c^{3/2}$ is 11 %, whereas that of P/l is 18 %. For SCR19.13, which is very vitreous, the coefficient of variation of $P/c^{3/2}$ is 36 %, while that of P/l is 12 %. Furthermore, it can be seen that for SCF5, P/l increases with increasing indenter load, while $P/c^{3/2}$ is effectively independent of load.

Some indentation fracture toughness equations are only "calibrated" for certain ranges of c/a values (and l/a values since $l/a + 1 = c/a$); of the equations listed in ection 5.3.1, equation 8 is valid for $c/a > 2.5$, while equations 11 and 12 are valid for $c/a \geq 2.8$ and $c/a \leq 2.8$ respectively. Equations 13 and 14 are only valid between $0.25 - 1 \leq l/a \leq 2.5$, i.e., $1.25 - 2 \leq c/a \leq 3.5$; these equations assume that Palmqvist cracks are formed. The maximum, minimum and mean c/a values observed for SCF5, SCR25.76, SCR19.34, and SCR19.13 are listed in Table 5.14; the minimum c/a value is 2.85. So equation 12 was not expected to give values in reasonable agreement with the SENB values. Note that $c/a < 4$ for SCF5, SCR25.76 and SCR19.34, but > 4 for SCR19.13; this was expected given the greater ease of crack propagation in glass with SCR19.13 being 70 % glass by volume.

Table 5.13 $P/c^{3/2}$ and P/l Data for SCF5 and SCR19.13 in Relation to Indenter Load:

Material	Indenter Load (N)	$P/c^{3/2}$ (x 10^7 MPa.$m^{1/2}$)	P/l (x 10^5 Nm^{-1})
SCF5 a	149 ± 2 1%	2.03 ± 0.19 9%	5.37 ± 0.44 8%
SCF5 b	99 ± 2 3%	1.88 ± 0.09 5%	4.48 ± 0.17 4%
SCF5 c	50 ± 2 4%	1.90 ± 0.27 14%	3.74 ± 0.52 14%
SCF5	95 ± 42 44%	1.93 ± 0.21 11%	4.46 ± 0.80 18%
SCR19.13	57 ± 7 12%	1.02 ± 0.37 36%	2.43 ± 0.28 12%

Note: SCF5 a, b, c refer to the data for SCF5 at a mean indenter load of 149 N, 99 N, 50 N respectively, while SCF5 refers to all 23 data regardless of indenter load.

Table 5.14 c/a Data for SCR25.76, SCR19.34, SCF5 and SCR19.13:

Parameter	SCR25.76	SCR19.34	SCF5	SCR19.13
Max. c/a	3.94	3.71	3.97	5.58
Min. c/a	3.61	3.46	2.85	4.43
Av. c/a	3.79	3.58	3.61	4.86
s.d	0.10	0.10	0.28	0.44
C_v (%)	3	3	8	9

Table 5.15 Mean Room Temperature K_c Data for SCF5 as a Function of Fracture Toughness Equation and Indenter Load:

Eq.#	149 ± 2 N	99 ± 2 N	50 ± 2 N
	K_c (MPa.$m^{1/2}$)	K_c (MPa.$m^{1/2}$)	K_c (MPa.$m^{1/2}$)
1	1.04 ± 0.10	0.97 ± 0.05	0.98 ± 0.14
2	1.51 ± 0.14	1.40 ± 0.07	1.41 ± 0.20
3	2.05 ± 0.18	1.89 ± 0.09	1.87 ± 0.25
4	1.15 ± 0.09	1.06 ± 0.04	1.05 ± 0.15
5	1.31 ± 0.11	1.20 ± 0.05	1.20 ± 0.17
6	1.30 ± 0.10	1.19 ± 0.05	1.19 ± 0.17
7	1.41 ± 0.12	1.30 ± 0.06	1.29 ± 0.18
8	1.98 ± 0.17	1.83 ± 0.08	1.82 ± 0.26
9	2.00 ± 0.17	1.84 ± 0.08	1.85 ± 0.28
10	2.11 ± 0.15	1.94 ± 0.07	1.85 ± 0.19
11	2.87 ± 0.16	2.61 ± 0.07	2.46 ± 0.26
12	3.44 ± 0.09	3.11 ± 0.03	2.76 ± 0.13
13	2.34 ± 0.10	2.14 ± 0.04	1.96 ± 0.13
14	3.25 ± 0.14	2.97 ± 0.06	2.72 ± 0.18
15	1.03 ± 0.05	0.95 ± 0.03	0.88 ± 0.06
16	2.54 ± 0.13	2.34 ± 0.03	2.16 ± 0.14

See Section 5.3.1 for key to equation numbers, Eq.#.

(2.2) Indentation fracture toughness results:

Using the Vickers indentation data for SCF5, the mean values of fracture toughness calculated using each of the sixteen equations given in Section 5.3.1 are tabulated against indenter load in Table 5.15; as in previous tables the sample standard deviations are also given. In general the mean fracture toughness at 149 N is noticeably higher than at 99 and 50 N, for which the values are similar. The SENB fracture toughness is 2.02 MPa.$m^{1/2}$ and the data show that of the equations based on $P/c^{3/2}$ = constant, the best are 3, 8, 9, and 10, regardless of indenter load. They all gave values within 10 % or better of the SENB value. A surprising result is that equations 13 and 16 which assume that the cracks are Palmqvist in nature gave values accurate to within 16 % and 26 %; this is surprising since the data in Table 5.13 suggest that the cracks are radial-median in nature. It is interesting that all these equations were calibrated using the data of Evans and Charles (1976); Evans and Charles equation (#3) gave values accurate to within ≈ 30 %. The equation of Antis et al. (1981), i.e., #5 was accurate to within ≈ 35 to 40 %.

The mean indentation fracture toughness values for the three SCF5 specimens are tabulated as a function of fracture toughness equation in Table 5.16. Equations 3, 8, 9, and 10 were again the best of the radial-median equations; they gave values accurate to 12 % or better, regardless of the SCF5 specimen. Also as before, equations 13 and 16 gave good results, accurate to within 18 % or better. The mean indentation fracture toughness data for SCF5 regardless of load or specimen, together with the corresponding data for SCR25.76, SCR19.34 and SCR19.13 are tabulated as a function of fracture toughness equation in Table 5.17; again the best equations for the SCF5 data are 3, 8, 9, and 10, with 13 and 16 giving good results as before. The situation for SCR25.76 is different however, as the best equations are 11, 12, 14, and 16; they gave values accurate to 12 % or better. Note that equations 12 and 14 have restricted validity ranges for c/a which were

Table 5.16 Mean Room Temperature K_c Data for SCF5 as a Function of Fracture Toughness Equation and Specimen:

Eq.#	SCF5 Spec. 1 K_c (MPa.m$^{1/2}$)	SCF5 Spec. 2 K_c (MPa.m$^{1/2}$)	SCF5 Spec. 3 K_c (MPa.m$^{1/2}$)
1	0.94 ± 0.07	1.01 ± 0.09	1.04 ± 0.13
2	1.35 ± 0.09	1.45 ± 0.13	1.50 ± 0.19
3	1.83 ± 0.13	1.95 ± 0.16	2.02 ± 0.25
4	1.02 ± 0.08	1.09 ± 0.09	1.13 ± 0.15
5	1.17 ± 0.09	1.24 ± 0.10	1.30 ± 0.17
6	1.16 ± 0.09	1.23 ± 0.10	1.28 ± 0.17
7	1.26 ± 0.09	1.34 ± 0.11	1.39 ± 0.18
8	1.77 ± 0.13	1.89 ± 0.16	1.96 ± 0.25
9	1.78 ± 0.13	1.91 ± 0.17	1.99 ± 0.27
10	1.88 ± 0.15	1.96 ± 0.13	2.03 ± 0.22
11	2.54 ± 0.24	2.62 ± 0.17	2.73 ± 0.31
12	3.04 ± 0.34	3.03 ± 0.24	3.14 ± 0.35
13	2.08 ± 0.20	2.12 ± 0.14	2.19 ± 0.22
14	2.89 ± 0.28	2.94 ± 0.20	3.04 ± 0.30
15	0.92 ± 0.08	0.94 ± 0.07	0.97 ± 0.09
16	2.27 ± 0.20	2.32 ± 0.17	2.39 ± 0.22

See Section 5.3.1 for key to equation numbers, Eq.#.

Table 5.17 Mean Room Temperature K_c Data for SCR25.76, SCF5, SCR19.34, and SCR19.13 as a Function of Fracture Toughness Equation:

Eq.#	SCR25.76 K_c (MPa.m$^{1/2}$)	SCF5 K_c (MPa.m$^{1/2}$)	SCR19.34 K_c (MPa.m$^{1/2}$)	SCR19.13 K_c (MPa.m$^{1/2}$)
1	0.84 ± 0.04	1.00 ± 0.11	0.90 ± 0.04	0.57 ± 0.07
2	1.20 ± 0.05	1.43 ± 0.15	1.30 ± 0.05	0.83 ± 0.10
3	1.59 ± 0.07	1.95 ± 0.25	1.69 ± 0.07	1.03 ± 0.11
4	0.88 ± 0.04	1.08 ± 0.11	0.93 ± 0.04	0.57 ± 0.07
5	1.01 ± 0.04	1.24 ± 0.13	1.07 ± 0.04	0.65 ± 0.08
6	0.99 ± 0.04	1.22 ± 0.13	1.04 ± 0.04	0.63 ± 0.08
7	1.09 ± 0.05	1.33 ± 0.14	1.16 ± 0.05	0.71 ± 0.09
8	1.54 ± 0.06	1.87 ± 0.20	1.63 ± 0.07	1.01 ± 0.12
9	1.55 ± 0.07	1.89 ± 0.21	1.65 ± 0.07	1.00 ± 0.13
10	1.64 ± 0.05	1.96 ± 0.18	1.71 ± 0.05	1.06 ± 0.17
11	2.05 ± 0.06	2.63 ± 0.25	1.98 ± 0.06	1.47 ± 0.15
12	2.46 ± 0.03	2.07 ± 0.31	2.30 ± 0.03	2.03 ± 0.11
13	1.83 ± 0.04	2.13 ± 0.19	1.85 ± 0.03	1.47 ± 0.09
14	2.54 ± 0.05	2.96 ± 0.26	2.57 ± 0.05	2.04 ± 0.12
15	0.83 ± 0.02	0.95 ± 0.08	0.85 ± 0.02	0.70 ± 0.05
16	2.02 ± 0.05	2.33 ± 0.20	2.05 ± 0.04	1.71 ± 0.11

not met by SCR25.76 (see Appendix 5F, Table 5F.3) and yet they gave the most accurate values (i.e., assuming as before that the SENB value is the correct one). The best equations for the SCR19.34 data were 3, 8, 9, 10, and 11, together with 13 and 16; they gave values accurate to 12 % or better. The best equations for SCR19.13 were 3, 8, 9, and 10; they were accurate to within 6 % or better.

It appears from the above data that some equations give answers which are in very good agreement with the SENB value, but whose assumptions are violated, e.g., equations 12 and 14 in the case of SCR25.76, i.e., their answers are fortuitous; equation 13 is on the borderline of being invalid for the SCF5 and SCR19.34 data. To summarise, the most accurate of the valid equations for SCF5, SCR19.34 and SCR19.13 were numbers 3, 8, 9, and 10; these equations assume a radial-median crack develops. Equation 13 and 16, which assume a Palmqvist crack is produced, also give good results for SCF5 and SCR19.34. The odd result is that only equations 11 and 16 were valid for SCR25.76; they were accurate to ≈ 10 to 12 %, while equation 12 gave an answer fortuitously accurate to ≈ 7 %.

The profile of the indentation cracks formed beneath a Vickers indent was investigated by serial polishing of indented specimens of SCR25.76, SCR19.34, SCR19.13 and SCF5; the lengths of the surface radial cracks were measured as a function of depth below the original surface by polishing away successive layers of material. The thickness of material removed was determined from the change in diagonal dimensions of secondary Vickers indentations as successive layers were removed. The profiles of the indent cracks as determined by the serial polishing could not be predicted on the basis of the typical c/a ratios; as shown schematically in Figure 5.9, the cracks formed on a median plane in SCR19.34 by a nominal indenter load of ≈ 25 N (to preclude or minimise lateral cracking and attendant "chipping") are Palmqvist in nature, but unlike typical Palmqvist cracks for which the ratio (crack depth)/l is less than 1, the (crack depth)/l ratio was ≈ 1.8. It therefore appears that the

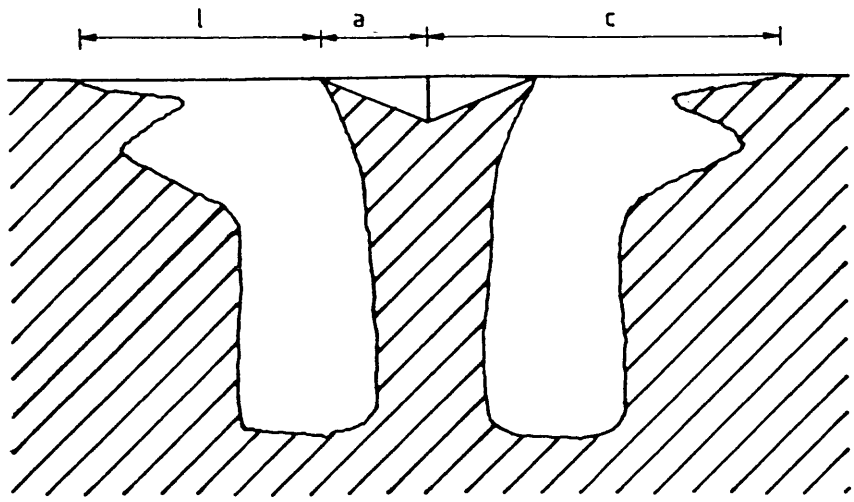


Figure 5.9 Schematic Sectioned Elevation Through the Surface Radial Crack Plane Showing the General Form of the Cracks Formed by a Vickers Indenter at a Nominal Load of 25N in SCR19.34 (as Determined by Serial Polishing).

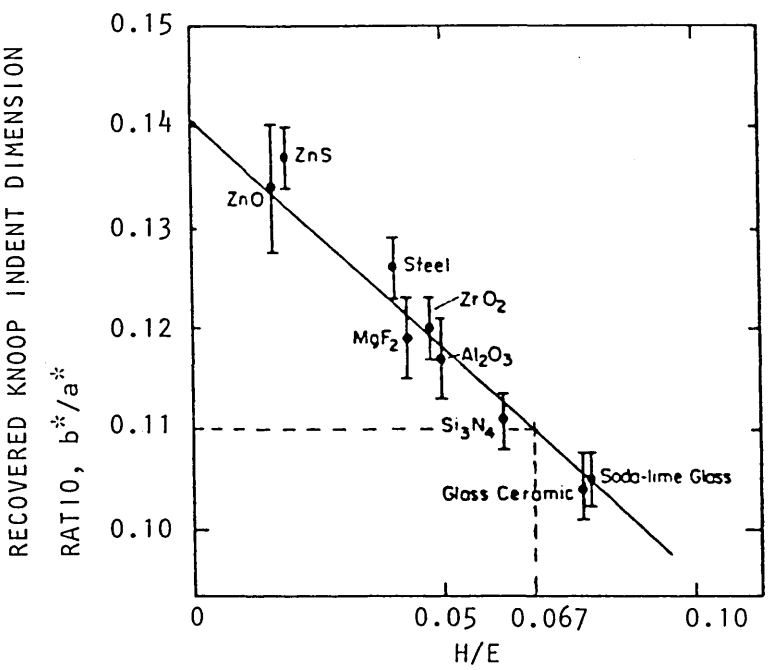


Figure 5.10 Recovered Knoop Indent Dimension Ratio (b^*/a^*) as a Function of the Hardness-to-Young's Modulus Ratio (H/E) (at Indenter Loads Between 10 and 100N) [after D.B. Marshall, Tatsuo Noma and A.G. Evans (1982)].

cracks, although Palmqvist in form, effectively behave as "half-penny" cracks by virtue of the crack depth exceeding the Palmqvist crack length; hence the good results given by equations 3, 8, 9 and 10. Material was removed from the SCR25.76 specimen such that the ratio (crack depth)/l was $\approx$ 0.7, while material was removed from the SCR19.13 and SCF5 specimens to the depth of the indent. As with SCR19.34, the cracks are Palmqvist in nature, but no comment could be made regarding the relationship between the crack depth and the Palmqvist crack length, and hence the most suitable fracture toughness equation.

A more thorough investigation of indenter flaw geometry has been conducted on 'Pyroceram 9606' glass-ceramic (Shetty, D.K., Rosenfield, A.R. and Duckworth, W.H., 1985); it was found that the cracks formed beneath Vickers indentations were of the Palmqvist type, even under indents produced with a 200 N load. The ratio of crack depth to surface crack length (l) in the Pyroceram 9606 material was found to be of the order of one. They also investigated the load dependence of the crack length c in terms of $c = kP^{2/3}$ and $c = a + l = (P/2H)^{1/2} + (P/4W)$ and found that it was not possible to distinguish between the "half-penny" and Palmqvist crack models on the basis of the apparent load dependence of the surface crack lengths. In addition, they found that the indentation fracture toughness values calculated using equations derived on the assumption of well developed "half-penny" cracks were in closer agreement with the conventional double-torsion and chevron-notch bend values than those which assume the cracks to be Palmqvist in nature, which in fact they were.

Although the Vickers indentation cracks in both 'Pyroceram 9606' glass-ceramic and the glass-ceramics investigated in the present work are Palmqvist in nature, with (crack depth)/l ratios of the order of $\approx$ 1 to 2, there is no basis at present for assuming that in general the Vickers indentation cracks in glass-ceramics are of the Palmqvist type with (crack depth)/l ratios $\geq \approx$ 1 and thus behave as well developed "half-penny" cracks.

As regards the shape profiles of the cracks formed under a Vickers indent in other materials, a study of the crack profile as a function of varying c/a ratio has been made by indenting materials with differing fracture toughnesses with a constant peak load of 294 N. The indents were dyed with suitable penetrant dyes (different dyes being suited to different materials) and the c and a values measured. The specimens were broken in three-point bending with the indented face being stressed in tension (presumably the indent was situated at the mid-span position), and the depth of the crack front (d) measured using optical microscopy (Sullivan, J.D., and Lauzon, P.H., 1986b). The materials examined included one type of alumina (A-16 SG, ALCOA) and two types of zirconia (1. ZYP 4.4 mol% Y_2O_3, Zircar Products Inc., and 2. TZ-2Y, Toyo Soda Mfg. Co. Ltd.).

The measured crack shape parameters were:

Material	a (μm)	c (μm)	d (μm)	c/a	d/c
Alumina	90	392	390	4.4	1.0
ZYP	142	289	165	2.0	0.6
TZ-2Y	109	145	48	1.3	0.3

Note that for the ideal half-penny crack d/c = 1, while for a typical Palmqvist crack, d/c < 1. A number of specimens of each material were examined; in the case of TZ-2Y, more than ten were examined and each specimen exhibited similar, very shallow Palmqvist cracks. The crack profile in the alumina specimens was a "half-penny", while that in the ZYP zirconia displayed Palmqvist crack profiles, but they were deeper than those in the TZ-2Y material.

Sullivan and Lauzon suggested that these results support the hypothesis that there is a transition in the crack profile formed beneath a Vickers indent at $c/a \approx 3$, from a half-penny profile for $c/a \approx \geq 3$, to a Palmqvist profile for $c/a \approx \leq 3$ (Niihara, K., et al., 1982), and that a more thorough study of the effect of indenter load on the crack profile in a given material is warranted.

(2.3) Determination of the Young's modulus-to-hardness ratio (E/H) of SCF5 from the recovered Knoop indent dimensions for different indenter loads:

A simple method for determining E/H to a claimed accuracy of better than 10 % for materials with H/E $\approx >$ 0.03, from measurements of the in-surface dimensions of elastically recovered Knoop indents has been developed (Marshall, D.B., Noma, T., and Evans, A.G., 1982) and is summarized here. When a Knoop indent is in contact with the indenter, i.e., under load, the diagonal dimensions of the indent are in the ratio 1 : 7.11 because the geometry of the Knoop indenter is such that a/b = 7.11 (See Section 5.2 and Figure 5.2 (b)). On unloading, however, both the depth and the short diagonal length (b) of the indent are reduced by elastic recovery of the indent, while the long diagonal length (a) remains relatively constant.

Marshall et al. showed that the 'recovered' Knoop indent dimensions as characterized by the recovered long diagonal length (a^*) and the short diagonal length (b^*), are related to E/H as follows

$$b^*/a^* \approx b^*/a = b/a - \alpha H/E \qquad [5.61]$$

where α is a gradient and $a \approx a^*$. A plot of b^*/a^* against H/E should be linear with an intercept of $b^*/a^* \approx b/a = 1/7.11$, and a slope of α. This was verified experimentally by Marshall et al. for different materials covering a wide range of H/E values, as shown in Figure 5.10. The slope α was obtained by fitting the best straight line with an intercept of 1/7.11 to the data, and was found to be 0.45 which is much smaller than the theoretical value of 1.5 predicted by the two-dimensional elliptical indentation model used to derive equation [5.61]; it was presumed that the discrepancy was due to the lesser elastic recovery of the more constrained three-dimensional Knoop indent.

The experimental measurements showed that b^*/a^* is independent of the indenter load and insensitive to the incidence of concomitant cracking for all the materials tested. Figure 5.10 shows that materials with a high H/E ratio (i.e., highly elastic or with a low stiffness)

exhibit the greatest elastic recovery (i.e., low b^*/a^*, but since $b^*/a^* \approx b^*/a$, the smallest b^* value) while materials with a low H/E ratio (i.e., highly plastic or with high stiffness) exhibit little or no recovery, i.e., in the limit of H/E = 0, $b^*/a^* = b/a = 1/7.11$.

The relevant Knoop indentation data are tabulated in Appendix 5E, Table 5E.1. The average b^*/a^* ratio of all the data in Table 5E.1 is 0.1104 ± 0.0042. Plotting $b^*/a^* = 0.11$ on Figure 5.10 gives a corresponding H/E value of 0.067. Using the mean hardness value for SCF5 of 7.0 GPa, gives a Young's modulus estimate of 104.5 GPa; this compares with a value of 120.6 GPa determined by dynamic resonance methods (See Chapter 3, Section 3.7.2 (2.3)), i.e., the estimate derived from the Knoop indentation data is 13 % lower than the reference value of 120.6 GPa. Given that (i) most indentation fracture toughness equations do not give independent fracture toughness estimates, and (ii) the claimed accuracy of most indentation fracture toughness equations is of the order 30 to 40 % or better, estimating the E/H ratio by the above method for use in the equations is sensible in the absence of readily available literature values for E in particular, since H is easily measurable.

CHAPTER 6

STRESS DEPENDENCE OF SECONDARY COMPRESSION CREEP OF SCR25.76 AND SCR19.34 AT 709°C

6.1 Introduction

The phenomenon of creep deformation has been observed in many solid materials, both metallic and non-metallic, and depending on the material in question can occur at all temperatures above absolute zero because the process of creep is dependent on the thermal energy of the atoms in the material, i.e., it is a thermally activated process. Creep deformation or more commonly creep is the continuous, i.e., time-dependent strain which occurs when a material is subject to a constant stress. For a given material the amount of creep strain observed over a given time period is a function of both the applied stress and the material temperature. The creep strain may consist of a combination of elastic, anelastic and plastic strain components.

The important temperature parameter in the study of creep is the homologous temperature, T_H which is the ratio of the material temperature, T to the melting or liquidus temperature, T_H (both expressed in kelvins). Creep in pure metals and alloys usually becomes significant at homologous temperatures above approximately $0.3T_H$ and $0.4T_H$ respectively; creep occurs in most ceramic materials at homologous temperatures above $\approx 0.5T_H$. A further point to note is that in general, at a given temperature, particularly at an elevated temperature, creep occurs at a stress level below that of the tensile yield or fracture stress at that temperature. A study of the high temperature creep of Li_2O - ZnO - SiO_2 glass-ceramics (Morrell, R., and Ashbee, K.H.G., 1973) showed that the stress required to maintain a given creep rate is very much higher for compression creep than for tensile creep. Note the room temperature compressive strengths of SCR25.76 and SCR19.34 were much higher than the flexural strengths.

In general, a typical creep curve (i.e., creep strain versus time curve) for most materials has the form shown in Figure 6.1; as shown the creep behaviour which occurs after the initial "instantaneous" strain (which has both elastic and plastic components), ϵ_o, can be classified into three stages. The intial stage (1) is known as transient or primary creep, during which the strain rate continuously decreases, while during the second stage (2) the strain rate is to most intents and purposes constant and the creep is said to be secondary or steady-state. During the final stage (3) of tertiary creep the strain rate increases continuously until fracture occurs. The exist nce, nature and extent of each creep stage depends on the material and the experimental conditions, e.g., the nature and magnitude of applied stress, the temperature and so on (Cannon, W.R. and Langdon, T.G., 1983); for example, a tertiary stage is not always observed in compression creep of ceramics.

The observed creep strain of a material is a function of the applied stress, σ, the temperature, T and the structure as characterized by a generic structure parameter, S, which involves all the microstructural features which influence creep behaviour such as porosity, grain size, dislocation density, phase distributions, and so on. A generalized function for the creep strain rate, $\dot{\epsilon}$ can be written (Garofalo, F., 1965) as follows

$$\dot{\epsilon} = \Sigma\, Z(T, S, \nu)\sigma(T, S)\exp[-Q(T, S)/RT] \qquad [6.1]$$

where σ is a stress function, R the universal gas constant, ν a vibrational frequency term for the thermally activated deformation process, Q the true molar activation energy for the deformation process, and Σ denotes the summation of the strain contributions of each operative creep deformation mechanism. Normally, however, it is assumed that there is a single dominant and hence rate-controlling deformation mechanism; thus equation [6.1] can be written as

$$\dot{\epsilon} = Z(T, S, \nu)\sigma(T, S)\exp[-Q(T, S)/RT] \qquad [6.2]$$

The existence of an essentially constant strain rate stage at a given temperature and stress is said to imply

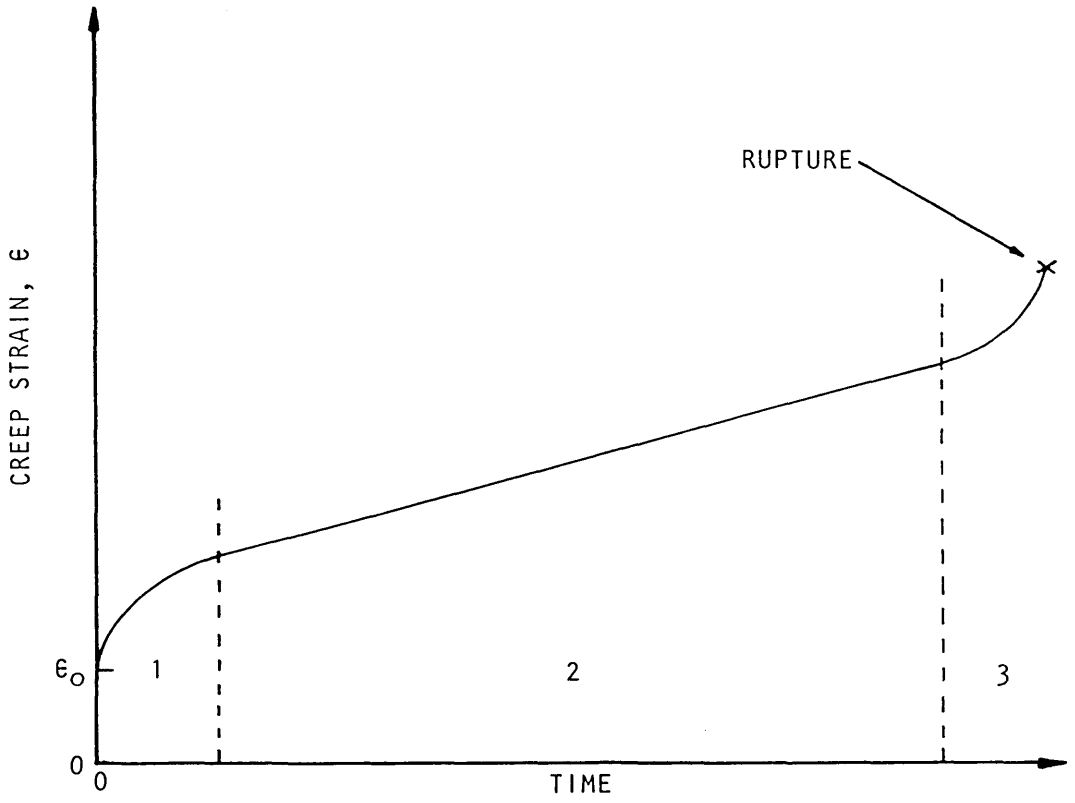


Figure 6.1 A Schematic Creep Curve Showing the Three Stages of Creep Observed in Many Materials.

that the structure parameter attains an equilibrium state, i.e., all the microstructural features which affect creep behaviour do not change during secondary creep; thus the strain rate during secondary creep is given by

$$\dot{\epsilon} = Z(T, \mathcal{V})\sigma(T)\exp[-Q(T)/RT] \qquad [6.3]$$

As these equations indicate, the generalized creep function is very complex and unless the exact form of the pre-exponential term is known, Q cannot be determined explicitly; in practice an apparent activation energy, Q_A which may involve terms other than Q, is determined. For the high temperature secondary creep of many materials it is found experimentally that (i) Q_A is essentially independent of the applied stress and a function of temperature only, and (ii) the pre-exponential term $Z(T, \mathcal{V})\sigma(T)$ is independent of temperature and a power function of the applied stress. Thus the secondary creep rate function takes the customary empirical form

$$\dot{\epsilon} = C\sigma^n \exp(-Q_A/RT) \qquad [6.4]$$

where C and n are constants independent of the applied stress, σ. At constant stress, equation [6.4] takes the form of an empirical Arrhenius rate equation

$$\dot{\epsilon} = A\exp(-Q_A/RT) \qquad [6.5]$$

where A is a constant, while at constant temperature, equation [6.4] has the empirical form

$$\dot{\epsilon} = B\sigma^n \qquad [6.6]$$

where B and n are constants independent of the applied stress over a limited range of stress and temperature.

By conducting creep tests at a prescribed constant stress at different temperatures, creep strain versus time data can be obtained as a function of temperature; hence a plot of $\ln(\dot{\epsilon})$ against 1/T should yield a straight line of slope $-Q_A/R$ and an intercept of ln(A). Similarly, creep tests conducted at a given temperature at different constant stress levels gives creep strain versus time data as a function of stress; thus a plot of $\ln(\dot{\epsilon})$ against $\ln(\sigma)$ should be a straight line of slope n and intercept ln(B).

6.2 Compression Creep Testing

Creep data can be obtained by loading specimens in tension, compression, bending or torsion; ideally creep tests should be conducted under constant stress conditions, but unless the data required can only be determined reliably under constant stress conditions (for example, the determination of the physical mechanisms of creep, particularly for the more ductile materials), it is often difficult to justify the additional experimental complexity and expense required to produce constant stress conditions for the small strains usually encountered in creep tests. At present, most creep tests are conducted at constant load using standard dead-load creep machines.

When conducting creep tests on ceramic materials, a choice of loading mode has to be made; to enable fully effective data analysis creep tests should be conducted under uniaxial tension with true axial loading as the stress and strain distribution are uniform across any transverse section within the gauge length. Uniaxial tensile creep tests are, however, just as difficult and expensive to conduct as uniaxial tensile strengths tests, and for the same reasons (see Chapter 4) with the additional requirement of high temperature operation. So most creep studies of ceramic materials have been and are conducted in bending or uniaxial compression.

Creep tests are frequently conducted using three- or four-point bending because they are experimentally easy techniques and are not subject to the problems encountered in uniaxial compression creep tests. Bending techniques, however, produce plastically deformed specimens with both a compressive and a tensile region, and the equations commonly used to calculate the tensile strain and stress from the load-point displacement data of steady-state creep tests assume that the creep behaviour in tension is identical to that in compression (Hollenberg, G.W., et al., 1971); this assumption is not always valid (Morrell, R. and Ashbee, K.H.G., 1973); (Chuang, Tze-Jer, 1986).

The main problems associated with compression tests, including compressive creep tests, are (1) buckling and (2) frictional forces between the specimen ends and the loading platens causing inhomogeneous plastic deformation which is physically manifested as barrelling of the specimen. Buckling of column-shaped specimens due to structural instability may occur during either elastic or plastic deformation, and is the more serious problem. During buckling the specimen is subjected to bending forces of unknown magnitude and distribution, i.e., buckling is a force-deflection phenomenon; hence any attempt at quantitative data analysis may lead to erroneous conclusions.

The buckling of columns is usually analysed using the Euler column theory (Shanley, F.R., 1967), (Ryder, G.H., 1969), which gives the critical load, P above which a perfectly straight column loaded axially in compression will buckle, i.e., the Euler buckling load as

$$P = m.\pi^2 EI/L^2 = m.\pi^2 EA(k/L)^2 \qquad [6.7]$$

where E is the Young's modulus, I the least moment of inertia of the cross-section about the neutral axis, L the length of the column, m a multiplying constant whose value depends on the form of end constraint applied to the column, A the cross-sectional area of the column, and k the least radius of gyration of the cross-section about the neutral axis ($k^2 \equiv I/A$). In the case of a column with pinned, i.e., hinged ends m = 1 while for a column with fixed ends m = 4. Euler's column theory is, however, only applicable to columns which buckle elastically, so this equation is only valid if the average applied stress does not exceed the yield stress. Furthermore, there is a validity condition

$$(L/k)^2 = (m\pi^2 E)/\sigma_Y \qquad [6.8]$$

where L/k is the slenderness ratio, and σ_Y the yield stress in compression. If the slenderness ratio is less than the value given by equation [6.8], the Euler buckling stress will exceed the compressive yield stress, i.e., Euler's theory no longer applies (Ryder, G.H., 1969). For example, an alumina ceramic with E = 330 GPa and using the

compressive strength (= 2 GPa) as σ_Y with m = 1 gives a critical slenderness ratio of about 40, which for a column of circular cross-section gives a critical height to diameter ratio of about 10.

In cases where the average applied stress leads to plastic deformation, i.e., when the yield stress is exceeded, or during plastic creep, it has been shown experimentally that the Euler-Engesser or tangent-modulus formula will accurately predict the critical compressive load beyond which a perfectly straight and aligned solid column will buckle plastically (Shanley, F.R., 1967). The tangent-modulus formula is

$$\sigma_C = \pi^2 E_T/(L_E/k)^2 = \pi^2 E_T/(\alpha L/k)^2 \qquad [6.9]$$

where σ_C is the critical stress above which plastic buckling will occur, E_T the tangent-modulus (defined as $E_T = d\sigma/d\epsilon$ where $d\sigma/d\epsilon$ represents the slope of the compressive stress-strain curve at the stress σ, equal to P/A), and L_E the effective length of the column (defined as αL where L is the actual length of the column). This equation takes account of different end constraints via the effective-length coefficient, α , which equals 1 for a column with pinned ends and a 1/2 for a column with fixed ends; note that in the elastic strain range, $m = 1/\alpha^2$. A similar equation to [6.7] can be written for [6.9]

$$L_E/k = \pi(E_T/\sigma)^{1/2} \qquad [6.10]$$

This equation enables the critical slenderness ratio for a given stress to be calculated. As regards the situation in a compressive test, specimens for which the only constraint to motion in the plane perpendicular to the applied stress axis is the frictional force between the specimen ends and the loading platens would approach the case of $\alpha = 1$, i.e., the case of pinned ends (which means that there is no moment acting at the ends; this case is approximated to in practice when cylindrical or spherical end fittings bear on a flat plate), while specimens with externally constrained ends would approach the case of $\alpha = 1/2$. The buckling load is proportional to $1/L^2$ and, assuming a circular cross-section, to the square of the diameter.

Compression tests, including constant load creep tests, on single and polycrystalline magnesium oxide (MgO) using equation [6.9] to predict the critical buckling loads show that plastic buckling can be prevented by using compression specimens with length, i.e., height to diameter (or thickness) ratios of 2 to 1 or less (Cropper, D.R., and Pask, J.A., 1969).

The effect of frictional forces between the specimen ends and the loading platens during compression tests on specimens with circular or square cross-sections is dependent on the height to diameter or thickness ratio respectively, as can be inferred from a review of the theoretical work on the effect of friction on compression and indentation between flat dies (Bishop, J.F.W., 1958). When there are no frictional forces between the specimen ends and the loading platens (i.e., the coefficient of friction, $\mu = 0$) barrelling cannot occur, and the compressive stress on the specimen equals $2k$ where k is the yield stress in shear and is independent of the height to diameter (or thickness) ratio. Bishop showed that for height to diameter (or thickness) ratios greater than or equal to unity, the compressive stress on the specimen is $2k$ for all values of μ. Thus it can be inferred that barrelling may be minimised if specimen height to diameter (or thickness) ratios of 1 or greater are used. To summarise then, plastic buckling may be prevented and barrelling may be minimised if the specimen height (h) to diameter (d) or thickness (t) ratio is equal to or less than 2 and is equal to or greater than 1 respectively. So the best compromise is h/d or h/t = 1.5; it has been reported that with ratios in the range 1.5 to 2.5 compressive creep rates are apparently independent of h/d (Crosby, A., and Evans, P.E., 1973).

Compression creep tests are usually conducted using right-cylindrical specimens, although right-rectangular specimens with square cross-sections are also used (see Cropper, D.R., and Pask, J. A., 1969; Clarke, D.R., 1985). A finite element analysis of the stress distribution occurring in cylindrical and dumb-bell shaped specimens

during compressive creep tests on polycrystalline magnesia (MgO) and reaction-bonded silicon nitride (Birch, J.M., et al., 1976) suggests that the creep and fracture behaviour shown by cylindrical and dumb-bell shaped specimens under constant stress compressive creep conditions are essentially the same. In general the use of specimens with circular cross-sections rather than square cross-sections is to be preferred because the absence of "sharp" vertical edges implies a less complex stress distribution during compression and the shape of the cross-section causes fewer analytical problems when barrelling occurs, i.e., the cross-section remains effectively circular.

The above discussion leads to the conclusion that the main disadvantages of compressive creep testing can be overcome through careful choice of the specimen height to diameter ratio; hence compressive creep tests have more advantages than disadvantages over creep tests conducted in bending, such as (i) minimizing the inherently non-ductile nature of most ceramics as regards premature failure from either inherent or surface flaws when subject to a tensile stress, (ii) the more uniform stress distribution in right cylindrical specimens in particular, and (iii) no necessity to assume that the creep behaviour in tension is identical to that in compression; however, non-axial loading can cause problems. There are other problems particularly connected with the compressive creep testing of ceramics such as measuring the very small creep strains accurately and producing the high stresses required to produce a given creep rate (See Morrell and Ashbee, 1973; they found that in order to maintain the same secondary creep rate in compression as in tension, a stress $\approx$ 3.5 to 7 times greater than that in tension was required). These problems can normally be solved by using suitable experimental equipment and techniques.

6.3 Compression Creep Rig and Specimen Preparation

The compressive creep tests were conducted using a constant load tensile creep machine with a lever-arm ratio of 10:1 and a lever-arm counterbalance to balance out the mass of the weight-hanger and the load-train (Nicholls, J.R., 1974). The machine had a single lever with a knife-edge fulcrum, and the load-train was connected to the lever and the machine base via a knife-edge joint and a spherical ball/seat joint respectively. To enable compressive loading the machine was fitted with inter-penetrating cages. The temperature control arrangement used was, however, different to that used by Nicholls; the vertical tube furnace had three separate resistance wire windings individually power controlled via type K (NiCr-NiAl) thermocouples by Eurotherm SCR10 P.I.D. temperature controllers. The three thermocouples controlling the furnace were placed alongside the inner wall of the silica furnace tube in a staggered arrangement by suspending their alumina sheaths from two semi-circular insulating plates which also served to significantly reduce heat losses from the top of the furnace. The thermocouple controlling the central furnace zone was placed approximately level with the specimen centre and the centre of the furnace, while the thermocouples controlling the top and bottom furnace zones were placed about 45 mm above and below the central thermocouple respectively. In order to (a) reduce heat losses from the bottom of the furnace, (b) reduce convection currents within the furnace and, (c) prevent excessive heating of the displacement transducers by radiant heating, the bottom of the furnace was plugged with standard duty "Triton" kaowool loose wool insulation.

The creep rig was modified by (1) the addition of a small weight pan above the main weight pan on the weight hanger enabling the easy addition or removal of small masses up to about 3 kg, and (2) a new furnace counterweight to enable the furnace to be moved smoothly up and down about the load-train so as not to affect its alignment.

Two type K thermocouples were used to monitor the apparent specimen temperature; they were placed opposite each other as close to the specimen as possible but without touching it because the specimen height was too low to allow unhindered physical contact. Their alumina sheaths were attached to the lower pull-rod by refractory wire ties. One thermocouple was connected via copper leads to a digital thermometer (with 1°C resolution between 200 and 1200°C and automatic cold-junction compensation), while the other was connected to a chart recorder, or when required to a digital multimeter, using copper leads. The reference or cold junction of this second thermocouple consisted of an ice-water mixture (0°C) in an expanded polystyrene container used for liquid nitrogen. When ice was not conveniently available, water alone remained at a constant temperature of ± 0.5°C (according to an alcohol-in-glass thermometer) for sufficient time to allow the temperature to be checked periodically during a creep test. The temperatures recorded by the two monitoring thermocouples differed by about 2°C. Continuous monitoring of one thermocouple over a 32 hour period at a nominal temperature of 709°C showed a temperature drift of no more than 2°C, although sudden changes in ambient temperature or the presence of draughts produced short-term temperature drifts of 3 to 4°C, but such drifts did not occur very often. In view of the occasional temperature drifts and the errors related to (a) mechanical strains induced by regular use, (b) manufacturer's specification tolerances, (c) the reference junction behaviour, (d) electrical junctions, (e) compensating leads, (f) e.m.f. measurement, and (g) the difference between the apparent and actual specimen temperature and temperature gradients within a specimen, the specimen temperature was considered to be uncertain at any instant to ± 5 to 6°C, but constant to ± 3 to 4°C. The cold-junction compensated e.m.f. of one thermocouple was recorded as a function of time using one channel of the two channel chart recorder used to simultaneously record the displacement transducer meter summed d.c. voltage output.

The weight-hanger and load-train were balanced out using the lever counterweight, but there was still a direct load on any specimen due to the dead-weight of the lower pull-rod and the upper loading cage which was estimated to be 2.581 kgf. This constant load was added to all the loads due to lever loading. An important point to note is that the lever changes its angular position, and hence its effective lever ratio due to the rolling action of the fulcrum in its seat as a specimen is compressed. So in order to keep the lever ratio essentially constant during a creep test the beam should be maintained approximately level throughout the test. Fortunately the compressive creep testing of ceramics generally results in small total axial displacements, for example during the present work the maximum axial displacements were about 1 mm, so any changes in the effective lever ratio during a test would have had a negligible effect on the calculated stresses. The lever-arm was manually levelled at the start of a test after the load-train and specimen had reached thermal equilibrium at the test temperature.

The compressive displacement of a specimen during a creep test was measured using two Mercer displacement transducers placed on directly opposing sides of the load-cage assembly. This enabled non-axial loading, and hence deformation to be accounted for to a certain degree by appropriate treatment of their output signals (a minimum of three transducers placed at 120° intervals would be desirable, but the design of the load-train and furnace system did not allow for this). The output signal of each transducer was fed into a Mercer 155 transducer signal conditioner (analogue displacement meter) which added the two signals and output the summed signal as a d.c. voltage (see Appendix 6A for the control settings). The calibration of the transducers was checked by setting transducer 'A' to its mechanical zero and displacing transducer 'B' from its mechanical zero using a 0.05 mm feeler gauge (previously measured as 0.05 mm thick using a screw micrometer accurate to 0.01 mm) to produce a summed displacement of 50 μm and vice versa, and then repeating

the procedure but with one transducer set to give a displacement of 50 μm, thus giving a summed displacement of 100 μm. The output d.c. voltages were checked for accuracy at 50 μm, 100 μm and 500 μm summed displacements with a digital Thurlby "1905a Intelligent Multimeter". The calibration check was accurate within the accuracy limits imposed by the above calibration checking procedure and was assumed to hold true for all diplacements below 50 μm.

The d.c. voltage output of the transducer meter was also input to the Thurlby multimeter which was used with its data logging and Ax + B scaling programmes running simultaneously. The Ax + B scaling programme continuously converted the input d.c. voltage (equivalent to the summed displacement) to the average diplacement (i.e., summed displacement/2) in μm, which were then automatically logged by the data logging program at any pre-set rate between one reading every 0.3 seconds and one reading every two hours, up to a maximum of 100 readings; the average displacement was continuously displayed directly in μm. Whenever possible the data logged by the multimeter were used for analysis in preference to the data recorded by the chart recorder, although the chart recorder data were examined periodically as a double-check; this was because the multimeter recorded the displacement "accurately" to within 0.01 μm and timed the data logging interval accurately to ± 0.1 second.

Loading platens were prepared by machining blocks of 97.5 % alumina to a dove-tail cross-sectional profile (the sides were at 61° to the base) and nominal dimensions of 50 x 22 x 18 x 6 (mm) using a diamond abrasive grinding wheel fitted to a Jones and Shipman surface grinding machine. The blocks were ground parallel to a thickness of 6 ± 0.025 mm, and the top faces (50 mm x 18 mm) polished to a 0.25 μm finish. Each block was then cut in two, giving two matched loading platens. In the present work, right cylindrical compression creep specimens were used; the SCR25.76 and SCR19.34 specimens were prepared from the same source material as the compressive strength specimens and by the same method (See Chapter 4, Section 4.9.2).

6.4 Determination of Secondary Creep Rates at 709°C

The specimen height and diameter were measured to an accuracy of ± 0.01 mm using a screw micrometer; the specimen ends were found to be parallel to within 0.01 mm with a nominal height of 10 mm, while the nominal diameter was 7 mm. The diameter was measured at both ends and at the centre, and the average of the three measurements taken because the internal diameter of the core drill was slightly smaller towards the top, producing slightly tapered drill cores, i.e., specimens.

In order to obtain as much data as possible from each test run, i.e., specimen, and reduce the experimental scatter due to structural differences between specimens, each specimen tested was subjected to between two and four load or temperature increases at a constant temperature or constant load respectively. The maximum conventional strain was limited to between 7 and 9 % ; at these strains barreling was evident though not yet significant as regards the assumption of homogeneous plastic deformation occurring during creep and a uniform circular cross-section along the specimen length. Following on from these assumptions, is the assumption that the specimen volume remains constant during creep deformation; if this assumption is valid it is easy to show that for right cylindrical specimens

$$d_2 = d_1 (h_1/h_2)^{1/2} \qquad [6.11]$$

where d_1, h_1 and d_2, h_2 are the specimen diameter and height at times t_1 and t_2 respectively. The thermal expansion of the specimens at 709°C was taken into account using the linear thermal expansivity (α) of SCF5 between room temperature and 800°C ($\alpha = 7.5 \times 10^{-6}\ K^{-1}$) because the corresponding values for SCR25.76 and SCR19.34 were not available. The specimen height at 709°C, h_T, is

$$h_T = h_o + \alpha(709 - \theta)h_o \qquad [6.12]$$

where h_o is the specimen height at room temperature, θ. The specimen diameter at 709°C, d_T, is given by

$$d_T = (d_o^2 + 2\alpha(709 - \theta)d_o^2)^{1/2} \qquad [6.13]$$

where d_o is the specimen diameter at room temperature, θ.

For a nominal room temperature (20°C) specimen height of 10.00 ± 0.01 mm, diameter of 7.00 mm, and a temperature of 709 ± 6°C, a possible 50 % error in α will give a maximum error ≈ 0.4 % in h_T and d_T. Since the error in α is unlikely to be as high as 50 %, using $\alpha = 7.5 \times 10^{-6}\ K^{-1}$ to calculate the strains (and hence strain rates) of SCR25.76 and SCR19.34 would not lead to any inaccuracy.

The procedure used to carry out the creep tests for the present work is summarized here:

(a) A specimen was placed centrally between the alumina loading platens and a small mass (< 1 kg) placed on the small weight pan to hold the weight-hanger in contact with the scissor-action screw jack placed beneath it. The screw jack supported the mass on the weight-hanger so that while the load-train and specimen heated up to the test temperature the only load on the specimen was the 2.581 kg dead-weight. When thermal equilibrium obtained the lever-arm was made approximately level by manually adjusting the position of the load train via the lead-screw connecting the load-train to the base of the machine; the spherical ball/seat joint and coupling system ensured that the load-train did not become misaligned.

(b) The required mass was then placed on the weight-hanger and the displacement transducer probes manually displaced to give a zero summed displacement. Once the temperature had stabilized again to ± 3 to 4°C, the test was started by lowering the screw jack as quickly and as smoothly as possible, but without imparting excessive momentum to the loading platens (i.e., to approximate "inertialess" loading and prevent the platens cracking); note that just before the specimen was fully loaded, i.e., before all the "slack" in the load-train was taken up, the transducer meter was re-zeroed so that the mutimeter displayed 000.00 ± ≤ 0.1 μm. To end a test the screw jack was raised to contact the weight-hanger and thus carry the load while either the load or temperature was altered, or the furnace was switched off. To continue testing at a new load the jack was lowered as before once thermal equilibrium had again obtained.

The specimen compressive displacements were recorded at set time intervals; thus the instantaneous true strain at any instant of time, ϵ_j, was calculated using

$$\epsilon_j = \ln(h_j/h_{j-1}) \qquad [6.14]$$

where h_j and h_{j-1} are the instantaneous specimen heights at elapsed times of t_j and t_{j-1} respectively; note h_j is given by

$$h_j = h_T + \delta_j \qquad [6.15]$$

where δ_j is the compressive displacement of the specimen at time t_j; since δ_j is a negative quantity, $h_{j-1} > h_j$. The cumulative true strain, $\Sigma\epsilon_j$, at an elapsed time of t_j was calculated using

$$\Sigma\epsilon_j = \Sigma\epsilon_{j-1} + \epsilon_j \qquad [6.16]$$

where $\Sigma\epsilon_j$ and $\Sigma\epsilon_{j-1}$ are the cumulative true strains at elapsed times of t_j and t_{j-1} respectively. Calculation of the instantaneous specimen heights, instantaneous true strains and cumulative true strains was obviously best carried out using a computer as in the present work. It should be noted that successive true strain increments can be added directly to give the total true strain ($\epsilon_{tot.}$), i.e., $\epsilon_{tot.} = \epsilon_1 + \epsilon_2 + \ldots\ldots + \epsilon_n$, however this is not the case when the strain increments are expressed in terms of conventional strain. The total conventional strain is obtained from $(1 + e_{tot.}) = (1 + e_1)(1 + e_2)\ldots\ldots(1 + e_n)$ where $e_{tot.}$ is the total conventional strain (Lubahn, J.D. and Felgar, R.P., 1961). Note that $\epsilon = \ln(1 + e)$ since the true strain, ϵ is defined as the integral of dl/l from l_o to l, i.e., $\epsilon = \ln(l/l_o)$ and the conventional strain, e is defined as $(l - l_o)/l_o$ where l_o is the initial length.

The force acting on a specimen, F, was calculated in newtons from the equation

$$F = 9.81(2.581 + 10m) \qquad [6.17]$$

where m is the mass on the weight-hanger in kg. Since the creep tests were conducted at constant force, the actual stress on a specimen decreased with time as the cross-sectional area of the specimen increased. So the average of the initial stress at the start of a test and the final stress acting at the end of a test was calculated from

$$\sigma = 2F(1/d_{TI}^2 + 1/d_{TF}^2)/\pi \qquad [6.18]$$

where σ is the average stress on the specimen, F is the force acting on the specimen, and $d_{T,I}$ and $d_{T,F}$ are the calculated initial and final specimen diameters at 709°C respectively.

In order to determine the apparent secondary creep rate from the cumulative true strain versus elapsed time data a customized automatic iterative "least-squares" linear regression programme was written and used; the programme operated on the principle that the most accurate secondary creep rate would be that obtained from the iteration which produced the correlation coefficient (and hence coefficient of determination) nearest to -1 and simultaneously used the most data. This programme was, however, different from that written and used to determine the characteristic temperatures of the Young's modulus versus temperature curves in Chapter 3 because the number of data pairs analysed could be decreased on each iteration in one of three ways; (i) by starting with the initial data pair and going forward through the data, (ii) by starting with the final data pair and working backwards through the data, and (iii) by neglecting data pairs at both "tails" of the data set simultaneously and working towards the centre of the data set. Futhermore, the number of data pairs neglected on each iteration could be preset by user for all three iteration options; in the present work, successive data pairs were neglected.

The iteration option with the most sound physical basis was that starting only with the initial data pair because the experimental creep curves had the form shown in Figure 6.1 for the primary and secondary stages; the tests were stopped before the tertiary stage. This option was always used unless the data obtained towards the end of a test run were badly scattered or showed a marked deviation from the central data group. Once the data limits of the critical iteration were determined, the standard deviation of the "least-squares" estimate of the secondary creep rate was calculated along with the root-mean-square percentage difference between the calculated and experimental cumulative true strain values.

6.5 Experimental Data at 709°C and Data Analysis

The mass placed on the lever weight-hanger, the maximum, minimum and average stress acting on a specimen, the number of data logged, the data logging interval in seconds and the data logging time in hours and minutes are tabulated for each successive test run on every specimen in Table 6B.1 of Appendix 6B. The calculated specimen height and diameter changes during each successive creep test both at room temperature and 709°C on a given specimen are tabulated in Table 6B.2, together with the measured room temperature specimen height and maximum diameter after the last test run on a particular specimen. The measured initial height and mean diameter, the calculated final height and diameter, and the measured final height and maximum diameter of the SCR25.76 and SCR19.34 specimens tested in compression creep are given in Table 6.1, along with the number of creep tests conducted on each specimen.

As the number of data logged and data logging time figures indicate, the amount of creep strain versus time data was too large to be tabulated here, i.e., 1698 data for SCR25.76, equivalent to 1361 hours 45 minutes of data, and 1937 data for SCR19.34, equivalent to 2040 hours 46 minutes of data. So the creep strain versus time data findings are only discussed here in conjunction with the data presented in Appendix 6B; the findings for SCR25.76 are considered first. Specimen SCR25.76 C1 was initially subjected to an average stress of 158 MPa, the mean stress was then reduced to 127 MPa, followed by a further reduction to 101 MPa; in each case the specimen height decreased and the diameter increased with increasing elapsed time as expected, with the secondary strain rate decreasing with decreasing stress. The specimen was then allowed to furnace-cool to room temperature under the load-train dead-weight of 2.581 kgf; the calculated specimen height at room temperature was 9.25 mm, that is 10.01 - (0.25 + 0.25 + 0.26) mm. The measured specimen height was 9.30 mm.

Table 6.1 Initial Measured Specimen Dimensions (I), Final Calculated Specimen Dimensions (F_c), and Final Measured Specimen Dimensions (F_M) at Room Temperature and Number of Compression Creep Tests Per Specimen for SCR25.76 and SCR19.34:

Specimen	Specimen Height (mm)			Specimen Diameter (mm)			Number of Tests
	Data for SCR25.76						
	I	F_c	F_M	I	F_c	F_M	
C1	10.01	9.25	9.30	6.80	7.08	7.13	3
C2	10.01	9.23	9.30	6.79	7.07	7.13	4
C3	10.01	9.08	9.18	6.79	7.13	7.22	5 + 2-R
	Data for SCR19.34						
	I	F_c	F_M	I	F_c	F_M	
D1	10.02	9.26	9.32	6.81	7.09	7.10	4 + 1-R
D2	10.02	9.16	9.18	6.80	7.12	7.18	2 + 1-R
D3	10.01	9.32	9.32	6.79	7.04	7.10	2 + 1-R
D4	10.02	9.54	9.49	6.80	6.97	----	1 + 1-R

Note: 1-R denotes 1 recovery creep test, i.e., creep after a load reduction, and 2-R denotes 2 recovery tests.

The specimen height at room temperature under a stress σ can be estimated from

$$h = h_o(1 - \sigma/E) \qquad [6.19]$$

where h is the height under the stress σ, h_o the original height and E the Young's modulus. Since E = 121.7 GPa for SCR25.76, the specimen height under a stress of 101 MPa is 9.29 mm. So there was a discrepancy of 40 μm not accounted for by elastic strain, i.e., an error of ≈ 0.4 %.

The initial mean stress acting on specimen SCR25.76 C2 was 49 MPa; this was then increased to 73 MPa, followed by a further increase to 100 MPa. The creep behaviour during the test run at each stress level was expected, with a typical primary and secondary stage. The mean stress on the specimen was then reduced from 100 MPa to 25 MPa for test number C2.4; the creep behaviour observed was not expected at that stress level and thus the chart recorder and data logger were not appropriately set to record the data in a suitable manner. The specimen was expected to undergo further compressive creep but with a reduced secondary creep rate; however, the specimen underwent recovery, i.e., the specimen height increased with time at a decreasing rate until a maximum positive displacement of ≈ 2 μm was reached. The specimen then underwent compressive creep at a relatively constant rate; schematic diagram of the apparent strain versus time behavior is shown in Figure 6.2. The test run was allowed to continue until the apparent specimen height was the same as that at the start of the C2.4 test run; the mean stress on the specimen was then increased to 49 MPa for test number C2.5. A typical creep curve was again obtained but as expected, with a lower secondary strain rate than at 100 MPa. The specimen was then unloaded and allowed to cool to room temperature as per specimen C1; the calcuated room temperature specimen height was 10.01 - (0.15 + 0.25 + 0.26 + 0 + 0.12) = 9.23 mm, whereas the measured height was 9.30 mm, i.e., an error of ≈ 0.8 %. Using equation [6.19] at a stress of 49 MPa gives a specimen height of 9.296 mm; so the recovered elastic strain was negligible and cannot account for the calculated height being lower.

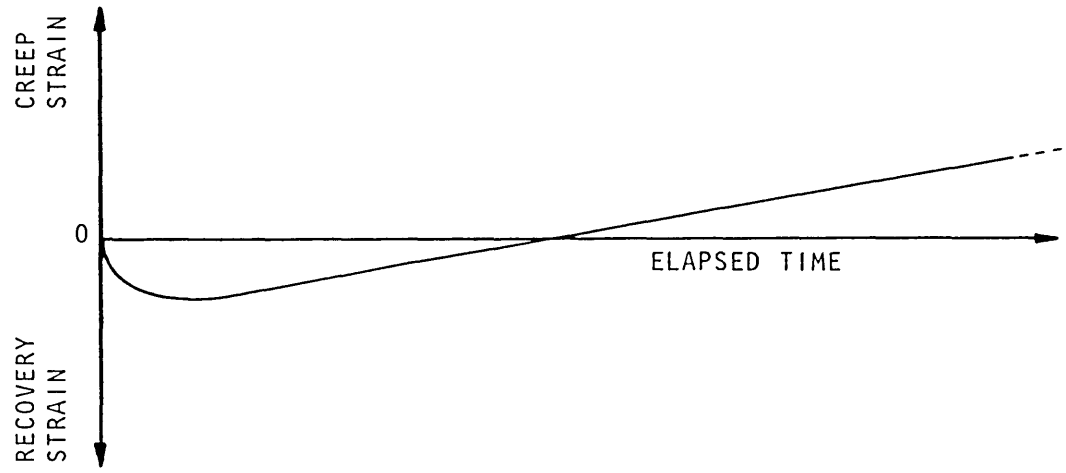


Figure 6.2 Schematic Diagram of the Strain Versus Time Behaviour of SCR25.76 at 709°C After a Reduction of the Imposed Stress From 100 MPa to 25 MPa (Specimen C2) and From 63 MPa to 25 MPa (Specimen C3).

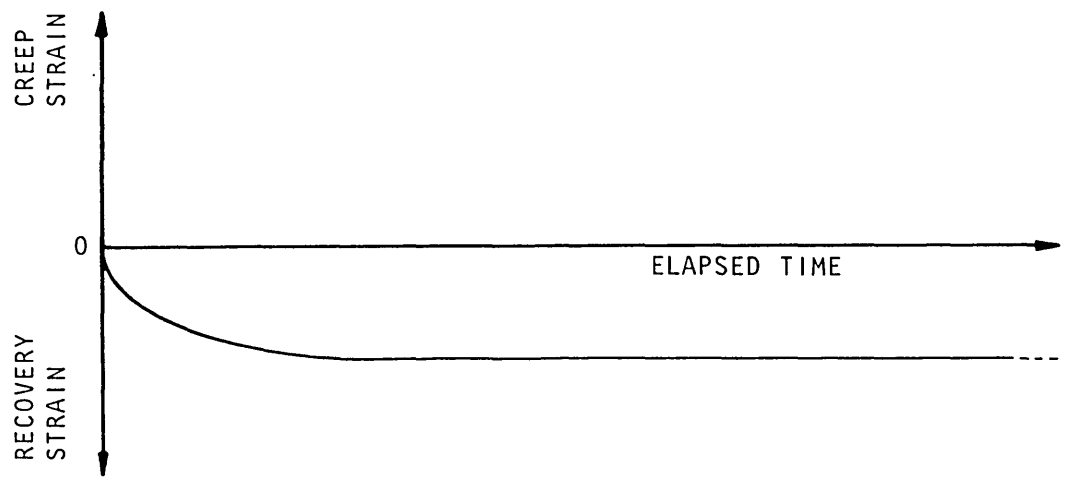


Figure 6.3 Schematic Diagram of the Strain Versus Time Behaviour of SCR25.76 at 709°C After a Reduction of the Imposed Stress From 25 MPa to 3 MPa (Specimen C3).

In order to investigate the possibility of a mean stress of 25 MPa representing some sort of "creep threshold" stress, i.e., a stress level which must be exceeded if normal creep behaviour is to occur, SCR25.76 C3 was initially stressed at 25 MPa, followed by successive imposed mean stresses of 34, 44, 53 and 63 MPa. Typical primary and secondary creep behaviour was observed at each stress level; the stress was then reduced from 63 to 25 MPa. The behaviour observed when the stress on specimen C2 was reduced from 100 to 25 MPa was again observed for this test run. The specimen underwent creep recovery at a decreasing rate, with the specimen height increasing by a maximum of ≈ 0.04 mm after an elapsed time of ≈ 50 hours; this recovery was equivalent to a cumulative strain of ≈ 0.4 % relative to the specimen height at the start of the test. The specimen height then began to decrease slowly with time, decreasing to its original height at the start of the test (= 9.11 mm at 709°C) after an elapsed time of 352 hours; at the end of the test after an elapsed time of 752 hours, the specimen height had decreased to 9.06 mm at 709°C (by calculation, i.e., 10.06 - (0.22 + 0.08 + 0.22 + 0.22 + 0.21 + 0.05)). The stress on specimen C3 was decreased further to 3 MPa, i.e., effectively zero stress; as a consequence the specimen underwent creep recovery right up to the time the test was terminated after 308 hours, with an increase in the specimen height of 0.07 mm, giving a final specimen height of 9.08 mm, equivalent to a strain of ≈ 0.8 % relative to the initial height of 9.01 mm (See the schematic diagram in Figure 6.3). In contrast, the measured final specimen height was 9.18 mm, i.e., a an error of ≈ 1 %.

The average difference between the calculated and measured specimen heights at room temperature after a test was ≈ 70 μm; this difference cannot be explained by the elastic strain recovered on unloading from the prior imposed stress. The probable sources of the error are (i) the accuracy of the displacement transducers at displacements below 50 μm, (ii) transmission of the specimen displacement to the transducers via the alumina platens

and the push-rods attached to the interpenetrating cages, and (iii) the assumption of no barrelling under load.

The fact that normal creep behaviour was observed at an initial imposed stress of 25 MPa indicates that it does not represent a threshold creep stress; the observed recovery on reducing the imposed stress from 100 MPa on specimen C2 and from 63 MPa on specimen C3 to 25 MPa, may occur on reducing the stress to levels below 100 or 63 MPa, i.e., at stress levels other than 25 MPa. Note that no recovery was observed for the stress reduction sequence 158, 127, 101 MPa on specimen C1, so the maximum stress below 100 MPa at which the partial recovery, i.e., viscoelastic recovery, occurs, may represent a "back stress" resisting creep, which must be overcome for normal compression creep to occur.

The secondary creep rates were determined using the method described in Section 6.4; the results are presented in Table 6.2 along with the mean stress imposed, the number of data analysed and the time period covered by the said data, and the coefficient of determination and the root-mean-square percentage difference between the calculated regression estimates of the strain values and the experimental values.

Following the observed creep behaviour of the SCR25.76 specimens, the imposed stress on the SCR19.34 specimens was reduced to 3 MPa, i.e., essentially zero stress, after the last stress increment in order to observe the creep recovery behaviour. An initial stress of 10 MPa was imposed on specimen SCR19.34 D1, i.e., test run D1.1, followed by runs at stresses of 20, 34 and 44 MPa; normal creep behaviour was observed with a primary and a secondary stage. On reducing the stress to 3 MPa, creep recovery occurred and the apparent height of the specimen had increased by 0.18 mm from 9.13 to 9.31 mm after an elapsed time of 429 hours with no significant increase after a further 13 hours and 30 minutes. The recovery was equivalent to a true strain of 0.0195; the calculated specimen height at room temperature was 9.26 mm compared to a measured height of 9.32 mm. The difference (60 μm) is

Table 6.2 Compression True Strain Rate Data for SCR25.76:

Test No.	σ (MPa)	Strain Rate Data ($\times 10^{-8}$ s^{-1}) $\dot{\epsilon}$	s.d.	Coeff. of Det. & Number of Data Analysed C.D.	#.	R.M.S. % Diff. & Time Period Used %	h & m
C1.1	158	83.62	0.27	0.9994	56	0.6	4h 30m
C1.2	127	35.41	0.08	0.9997	72	0.5	11h 55m
C1.3	101	35.21	0.07	0.9999	34	0.1	5h 30m
C2.3	100	41.47	0.20	0.9993	30	0.7	4h 50m
C2.2	73	18.04	0.09	0.9986	56	0.4	9h 10m
C3.5	63	11.64	0.11	0.9975	32	0.3	7h 45m
C3.4b	53	7.41	0.03	0.9990	64	0.3	26h 15m
C2.1	49	16.38	0.07	0.9990	50	0.4	8h 10m
C2.5	49	11.22	0.05	0.9987	63	0.4	10h 20m
C3.3	44	6.98	0.02	0.9991	100	0.5	24h 45m
C3.2	34	5.94	0.04	0.9979	56	0.5	13h 45m
C3.1	24	3.55	0.04	0.9868	120	0.4	19h 50m

Table 6.3 Compression True Strain Rate Data for SCR19.34:

Test No.	σ (MPa)	Strain Rate Data ($\times 10^{-8}$ s^{-1}) $\dot{\epsilon}$	s.d.	Coeff. of Det. & Number of Data Analysed C.D.	#.	R.M.S. % Diff. & Time Period Used %	h & m
D4.1	143	163.65	1.08	0.9993	19	0.4	4h 0m
D3.2	113	48.75	0.12	0.9996	68	0.5	16h 45m
D3.1	97	38.80	0.18	0.9992	42	0.4	10h 15m
D2.2	82	28.16	0.17	0.9993	22	0.1	8h 45m
D2.1	68	24.39	0.07	0.9993	75	0.6	37h 0m
D1.4	44	3.48	0.01	0.9997	54	0.3	79h 30m
D1.3	34	2.30	0.02	0.9986	33	0.3	64h 0m
D1.2b	20	0.71	0.01	0.9897	89	0.6	176h 0m
D1.1	10	0.45	0.01	0.9860	92	0.2	91h 0m

Note: s.d. is the standard deviation of the regression estimate of $\dot{\epsilon}$.
C.D. denotes the coefficient of determination (r^2),
#. is the number of data used in the regression analysis.
% is the root-mean-square percentage difference between the regression strain estimates and the corresponding experimental strain values.
h and m denote the hours and minutes respectively, of the time spanned by the strain data used in the regression analysis.

similar to that observed for the SCR25.76 specimens; the differences were in the range 40 to 100 μm with an average of 70 μm. The range of the observed differences suggests that the error may be random rather than systematic.

Specimen SCR19.34 D2 was subjected to a stress of 68 MPa, and then a stress of 82 MPa, before the stress reduction to 3 MPa; the creep behaviour before the reduction was typical. The creep recovery observed after an elapsed time of 96 hours was equivalent to a true strain of 0.0220. For this specimen the calculated specimen height was 9.16 mm, while the measured height was 9.18; a difference of 20 μm. The initial stress imposed on specimen D3 was 97 MPa, followed by a stress of 113 MPa, before the reduction to 3 MPa. Before the stress reduction, the creep behaviour was normal with the secondary creep rate at 113 MPa being higher than at 97 MPa. The true recovery strain recorded after an elapsed time of 99 hours was 0.0238, and there was no difference between the calculated and measured room temperature specimen height after the test (= 9.32 mm). As the difference between the calculated and measured height was found to range from ≈ 0 to 100 μm, the apparent difference in the calculated and measured specimen height was more likely due to the error in (i) the transference of the specimen displacement to the transducers and (ii) the correlation between true zero compression of the specimen and the apparent zero commpression set via the transducer meter at the start of a test, rather than any inaccuracy in the output of the transducers themselves, which would normally be expected to give rise to a relatively constant, i.e., a systematic error.

For the last specimen tested (D4) the initial stress was 143 MPa which produced a decrease in the specimen height of 0.67 mm after an elapsed time of 11 hours 47 minutes, i.e., a conventional strain of ≈ 7 %. The large strain caused a problem in the measurement of the specimen displacement because after an elapsed time of ≈ 7 hours, the summed transducer displacement was outside the calibrated range of the transducer meter, with the

displacement versus elapsed time slope deviating somewhat from the slope prior to ≈ 7 hours. Hence the calculated specimen height at the end of the test run was not reliable; rather than terminate the test immediately however, the stress was reduced to 3 MPa.

The secondary strain rate at 143 MPa was determined from the data recorded before the transducer meter output went over its calibration limit, and is given in Table 6.3 together with the other secondary creep rate data for SCR19.34 as per Table 6.2. Using the regression parameters for the secondary strain rate at 143 MPa, i.e., a and b in the regression equation $\epsilon = a + bt$, the specimen height at room temperature at the end of the test was estimated as 9.18 mm; the specimen height calculated as for all previous test runs was 9.35 mm. The apparent increase in the specimen height as a consequence of creep recovery was 0.19 mm, giving a final height of 9.18 + 0.19 = 9.37 mm; the normally calculated height at room temperature was 9.54 mm. The creep recovery strain after an elapsed time of 143 hours was ln(9.54/9.35) = 0.0201 or ln(9.37/9.18) = 0.0205. The measured specimen height was 9.49 mm.

After the furnace was turned off and the specimen loading reduced to a dead-weight load of 2.581 kgf as was standard practice, a loud cracking sound was heard from within the furnace. When the furnace and load-train had cooled down to room temperature, the specimen was seen to be cracked off-centre along its length parallel to the "loading axis"; on removal from between the loading platens the specimen was found to be fractured into two sections along its length, thus still allowing its height to be measured.

The creep stress exponents of SCR25.76 and SCR19.34 were determined by conducting a "least-squares" regression analysis on the stress versus strain rate data given in Tables 6.2 and 6.3 respectively in the form of

$$\ln(\dot{\epsilon}) = \ln(B) + n.\ln(\sigma) \qquad [6.20]$$

When all nine data for SCR19.34 were used in the regression analysis, the following regression data were obtained:

Stress exponent n = 2.29

Standard deviation of n = 0.20

Constant B = 2.00×10^{-25}

B + Standard deviation = 67.9×10^{-25}

B - Standard deviation = 0.06×10^{-25}

Correlation Coefficient, r = 0.9748

Coefficient of Determination (= r^2) = 0.9502

Root-Mean-Square % Difference Between the Calculated and Observed Strain Rate Values = 50.

Using n = 2.29 and B = 2.00×10^{-25} in $\dot{\epsilon} = B\sigma^n$ with σ = 10 MPa gave a regression estimate of the strain rate at 10 MPa which was 107 % lower than the experimental value. Thus the datum at 10 MPa was regarded as an "outlier", and not used in the regression analysis of the SCR19.34 data which produced the regression parameter data described below and given in Table 6.4. The regression parameters n and B for SCR25.76 and SCR19.34 are tabulated in Table 6.4, along with their standard deviations, the coefficient of determination and the root-mean-square percentage difference between the calculated and experimental strain rate values. The strain rate data for SCR25.76 and SCR19.34 are plotted against stress as $\ln(\dot{\epsilon})$ versus $\ln(\sigma)$ in Figure 6.4, and the regression lines are drawn through the respective data plots; note that the regression line obtained for SCR19.34 using all nine data is also shown as a dotted line.

The estimated compression creep stress exponent of SCR25.76 over the stress range 24 to 158 MPa was n = 1.6 ± 0.2, compared with n = 2.7 ± 0.2 for SCR19.34 over the stress range 20 to 143 MPa, i.e., n ≈ 2 and ≈ 3 for SCR25.76 and SCR19.34 respectively. The estimated nominal stress dependence of the secondary strain rate at 709°C is $\dot{\epsilon} = 3.6 \times 10^{-20}\ \sigma^{1.4}$ for SCR25.76 between 24 and 158 MPa, and $\dot{\epsilon} = 7.6 \times 10^{-29}\ \sigma^{2.7}$ for SCR19.34 between 20 and 143 MPa, remembering that the B values are subject to a wide variation because of the logarithmic plot. In order to illustrate the resultant uncertainty in the estimated strain rates, it was assumed that a stress of 100 MPa was imposed at 709°C, and that the maximum possible deviation

Table 6.4 Compression Creep Stress Dependence of SCR25.76 and SCR19.34 at 709°C:

Regression Parameters of $\dot{\epsilon} = B\sigma^n$ in the form of $\ln(\dot{\epsilon}) = \ln(B) + n.\ln(\sigma)$	SCR25.76 All 12 data of Table 6.2	SCR19.34 First 8 data of Table 6.3
Stress exponent n	1.62	2.72
Standard deviation of n	0.15	0.17
Constant B	3.62×10^{-20}	7.55×10^{-29}
B + Standard deviation	54.00×10^{-20}	147.00×10^{-29}
B - Standard deviation	0.24×10^{-20}	0.39×10^{-29}
Correlation Coeff. r	0.9595	0.9891
Coefficient of Determination ($= r^2$)	0.9206	0.9784
Root-Mean-Square % Difference Between the Calculated and Observed Strain Rate Values	26	26

Note: The strain rate at 10 MPa (i.e., test SCR19.34 D1.1) was ignored in the "least-squares" linear regression analysis because it was thought that the apparent secondary strain rate was an "outlier"; a regression analysis of all 9 data showed it to be ≈ 107 % higher than the calculated regression estimate (See the text).

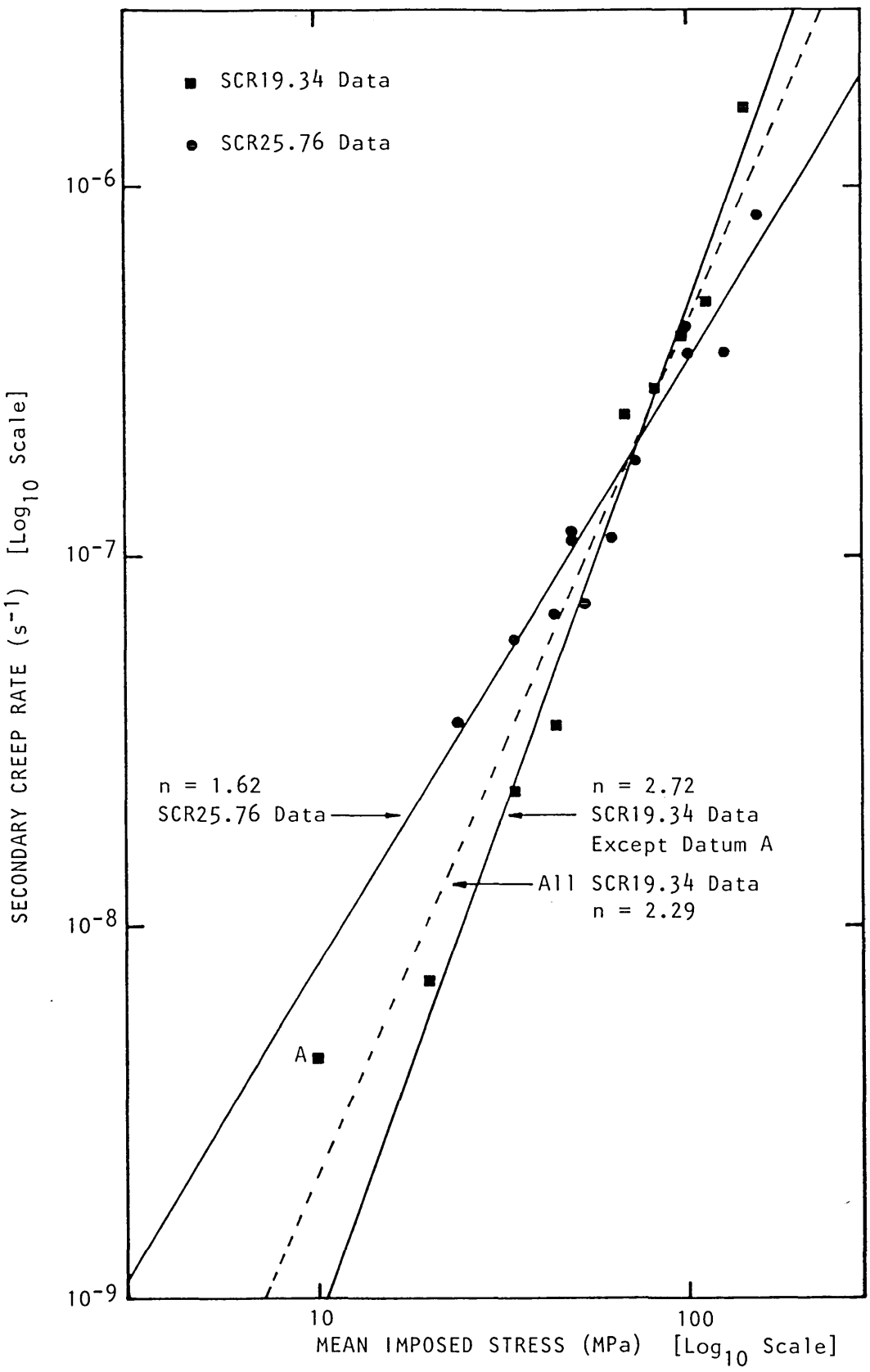


Figure 6.4 Secondary Creep Rate of SCR25.76 and SCR19.34 as a Function of Mean Imposed Stress During Compression Creep Under Constant Load at 709°C.

in B and n was one standard deviation about the regression estimates of B and n; hence B and n lie within the following inclusive limits (See Table 6.4):

SCR25.76: $B = 0.24$ to 54.00 ($\times 10^{-20}$)

$n = 1.5$ to 1.8

SCR19.34: $B = 0.39$ to 147.00 ($\times 10^{-29}$)

$n = 2.6$ to 2.9

Using $\dot{\epsilon} = B\sigma^n$ with $\sigma = 100$ MPa with the above data gives

SCR25.76:

$B = 0.24 \times 10^{-20}$ $n = 1.5$: $\dot{\epsilon} = 2.4 \times 10^{-9}$

$B = 54.00 \times 10^{-20}$ $n = 1.5$: $\dot{\epsilon} = 5.4 \times 10^{-7}$

$B = 0.24 \times 10^{-20}$ $n = 1.8$: $\dot{\epsilon} = 6.0 \times 10^{-7}$

$B = 54.00 \times 10^{-20}$ $n = 1.8$: $\dot{\epsilon} = 1.4 \times 10^{-4}$

SCR19.34:

$B = 0.39 \times 10^{-29}$ $n = 2.6$: $\dot{\epsilon} = 2.5 \times 10^{-9}$

$B = 0.39 \times 10^{-29}$ $n = 2.9$: $\dot{\epsilon} = 6.2 \times 10^{-7}$

$B = 147.00 \times 10^{-29}$ $n = 2.6$: $\dot{\epsilon} = 9.3 \times 10^{-7}$

$B = 147.00 \times 10^{-29}$ $n = 2.9$: $\dot{\epsilon} = 2.3 \times 10^{-4}$

The above results show that the estimated secondary creep strain rates may vary by 5 orders of magnitude, assuming that B and n are uncertain to within one standard deviation.

Finally, no further comment can be made regarding the relationship between the magnitudes of the stress exponents for the two materials and the operative creep deformation mechanisms as time did not allow for further creep tests at other stresses and temperatures, nor for any microstructural examination of the creep specimens as regards the formation of voids within the residual glass, the plastic deformation of crystals (as evidenced by the presence of dislocations), and so on. The study of the high temperature creep of Li_2O - ZnO - SiO_2 glass-ceramics by Morrell and Ashbee (1973) found that the stress exponent was independent of temperature, but a strong function of stress, varying between 1.0 and 6.0 over the stress range $\approx$ 1 to 100 MPa. This behaviour was attributed to creation of voids within the intergranular residual glass even in compression creep, the ease of void creation increasing with increasing stress.

CHAPTER 7

DISCUSSION OF RESULTS, CONCLUSIONS AND SUGGESTIONS FOR FURTHER WORK

7.1 Discussion of Results

The discussion which follows is primarily concerned with the mechanical property data obtained for the four glass--ceramics, SCR25.76, SCR19.34, SCF5 and SCR19.13, in the present work, rather than the techniques used to determine the properties.

The elastic properties will be considered first; the room temperature elastic property data are tabulated in Table 7.1. Note the Young's moduli (E) and shear moduli (G) data were determined directly, while the Poisson's ratio, the bulk moduli (K), longitudinal moduli (L), shear wave velocity (v_s), and the longitudinal wave velocity (v_L) data were calculated. The functional form of the temperature dependence of the Young's modulus and the normalized internal friction at 500°C are presented in Table 7.2.

According to the data in Table 7.1, the magnitudes of the room temperature Young's moduli of the three crystalline materials, i.e., SCF5, SCR19.34 and SCR25.76, are similar; that of SCR19.34 is 5 % and 6 % lower than that of SCF5 and SCR25.76 respectively. The Young's modulus of SCR19.13 is 20 % lower than that of SCF5. The high temperature data, however, shows there are noticeable differences in the temperature dependent behaviour of SCF5, SCR19.34, and SCR25.76; the rates of change of Young's modulus with temperature (dE/dT) are in the ratio 1 : 1.4 : 1.8 Furthermore, at 500°C the normalized internal frictions of SCF5, SCR19.34 and SCR25.76 are in the ratio 1 : 1.7 : 16. These differences in behaviour were attributed to the viscosity of the residual glass in the materials; the estimated viscosities decrease in the order, SCF5 > SCR19.34 > SCR25.76.

Table 7.1 Room Temperature Elastic Property Data:

Material	E (GPa)	G	K	ν	L (GPa)	v_s ms^{-1}	v_L ms^{-1}
SCF5	121	---	---	----	---	----	----
SCR19.34	115	48	65	0.21	129	4000	6600
SCR25.76	122	50	76	0.23	140	4100	6900
SCR19.13	101	---	---	----	---	----	----

Table 7.2 High Temperature Young's Modulus and Internal Friction Data:

Material	Temperature Dependence of Young's Modulus $E = a + bT$	Normalized Internal Friction Q^{-1}/Q_o^{-1} at 500°C
SCF5	a = 121.3 GPa b = - 0.0106 GPa.°C^{-1} for T = 22 to 626°C	3
SCR19.34	a = 114.7 GPa b = - 0.0153 GPa.°C^{-1} for T = 22 to 551°C	5
SCR25.76	a = 122.8 GPa b = - 0.0190 GPa.°C^{-1} for T = 21 to 436°C	48
SCR19.13	----------	--

Table 7.3 Room Temperature Strength Property Data:

Material	Flexural Strength (MPa)	Compressive Strength (MPa)	Weibull Modulus m	Crack Growth Exponent
SCF5	185	----	--	--
SCR19.34	114	726	15	28
SCR25.76	108	1050	11	41
SCR19.13	80	----	--	--

The room temperature strength property data for SCR19.34, SCR25.76, SCF5 and SCR19.13 are tabulated in Table 7.3. It should be noted that the three-point bending flexural strength and the compressive strength data should not be taken as absolute for the reasons discussed previously in Chapter 4; they are only presented for order of magnitude comparisons of the flexural strengths of these materials. Furthermore, the flexural strength data are the 20 S4 data (i.e., fracture away from the mid-span and wedging were accounted for) obtained at a cross-head speed of 1 mm/minute using the room temperature test rig; the discrepancy between the mean flexural strengths determined on the room temperature test rig and those obtained on the high temperature test rig (8 data) is neglected because at present the reason for the difference is not certain; microstructural differences are the most likely cause.

The flexural strengths apparently correlate most closely with the microstructural differences between the materials, as may be expected; the flexural strength decreases as the microstructure becomes more discrete and less dendritic on going from SCF5 to SCR19.13 via SCR19.34 and SCR25.76. The higher compressive strength of SCR25.76 compared to SCR19.34 was tentatively attributed to the lower volume fraction of residual glass in SCR25.76.

The Weibull moduli (m) were obtained using the same S4 flexural strength data and the survival probability estimator, $1 - (j - 0.5)/n$. The sub-critical crack growth exponent was also obtained using S4 flexural strength data obtained at three strain rates using the room temperature test rig; note there is a significant uncertainty in the SCR25.76 value (See Section 4.9.8). Nevertheless, SPT diagrams were constructed for SCR25.76 and SCR19.34 (Figures 4.11 and 4.12); note it follows from the SPT plots that the constant stress which can be endured for a given time and survival probability increases with increasing n and m, as the spacing between the SPT lines decreases with increasing n and the slope of the SPT lines is approximately equal to - m. These observations are consistent with m increasing as the fracture strength

distribution becomes narrower and n increasing with decreasing susceptibility to sub-critical crack growth. Since the mean flexural strength of SCR25.76 is only 5 % lower than that of SCR19.34, the effect of differing m and n values is evident; for a survival probability of 90 % the following conditions were noted from the SPT plots:

Life-time (s)	Stress for SCR25.76 (MPa)	Stress for SCR19.34 (MPa)
1	90	99
100	81	84
10000	72	72
1000000	65	61
100000000	59	52

The data show the effect of the slow crack growth exponent of SCR25.76 being higher than that of SCR19.34.

As regards the high temperature flexural strength data, the flexural strengths of both SCR19.34 and SCR25.76 increase with increasing temperature above 250°C up to 600°C, before decreasing up to 700°C; above 700°C the materials deformed plastically (See Figure 4.14). The very limited data for SCF5 indicate that the fracture behavior is linear elastic up to 800°C; the flexural strength at 800°C was 185 MPa (= room temperature value). The material deformed plastically between 850°C and 900°C.

The room temperature fracture toughness data and the Vickers hardness data for SCR25.76, SCF5, SCR19.34 and SCR19.13 are tabulated below:

Material	K_{Ic} ($MPa.m^{1/2}$)	Av. K_c ($MPa.m^{1/2}$)	Av. γ_E (Jm^{-2})	H (GPa)	E (GPa)
SCR25.76	2.29	2.04	20	7.5	122
SCF5	2.02	1.92	15	7.0	121
SCR19.34	1.83	1.67	13	7.4	115
SCR19.13	1.06	1.03	5	7.0	101

Note the K_c data are the average values of the valid equations which gave values nearest to the K_{Ic} values (equations 3, 8, 9, 10 for SCF5, SCR19.34 and SCR19.13, and equations 11 and 16 for SCR25.76 in Section 5.3.1).

The effective fracture surface energy (γ_e) data are the half-values of the mean values of the experimental and the calculated G_{Ic} values.

These data showed that the K_{Ic} and K_c fracture toughness data correlate with the Young's modulus and the effective fracture surface energies; the former being proportional to the interatomic bonding energy and the latter being the effective energy required to create a virgin surface, i.e., the energy required for fracture.

The high temperature fracture toughness data showed that the apparent toughness of both SCR25.76 and SCR19.34 decreased from room temperature up to 250°C, then increased with increasing temperature above 250°C up to 600°C, but then decreased between 600°C and 700°C. Between room temperature and 700°C the fracture toughness of SCR25.76 was somewhat higher than that of SCR19.34, but above 700°C the toughness of SCR19.34 was markedly higher than that of SCR25.76. This change in behaviour was thought to be due to the higher volume fraction of residual glass in SCR19.34 predominating its higher viscosity (compared to the lower volume fraction and viscosity of the residual glass in SCR25.76), i.e., the larger volume of softening glass made the fracture behaviour more ductile compared to that of SCR25.76.

Further examination of the data showed that the temperature dependence of the toughness was primarily due to the temperature dependence of the effective fracture surface energy rather than the Young's modulus. The limited high temperature data for SCF5 implied that the room temperature fracture toughness may be maintained up to ≈ 800°C, with plastic deformation occurring at 900°C.

The compressive secondary creep data obtained at 709°C under constant load for SCR25.76 and SCR19.34 showed that the nominal stress dependence of the secondary strain rate ($\dot{\epsilon}$) of SCR19.34 was greater than that of SCR25.76; for SCR19.34, $\dot{\epsilon} = 7.6 \times 10^{-29}\sigma^{2.7}$ for σ between 20 and 143 MPa, compared to $\dot{\epsilon} = 3.6 \times 10^{-20}\sigma^{1.6}$ for SCR25.76 between σ = 24 MPa and σ = 158 MPa. So at 709°C, for an imposed stress < 74 MPa the secondary creep rate of SCR25.76 is

greater than that of SCR19.34, while for an imposed stress > 74 MPa the reverse is true. Specimens of both materials exhibited creep recovery when the imposed stress was reduced to 3 MPa; the average recovery of the SCR19.34 specimens was 0.20 mm, i.e., ≈ 2 % of the original specimen height prior to the first creep test. Recovery was also observed in one SCR25.76 specimen when the imposed stress was reduced from 100 MPa to 25 MPa and in another when the imposed stress was reduced from 63 MPa to 25 M a on another SCR25.76 specimen. In both cases the recovery reached a maximum before the specimens apparently underwent secondary compression creep again, reversing the recovered displacement, i.e., the specimen height returned to the initial height which obtained when the stress reduction was made and continued to creep normally.

7.2 Conclusions

A number of conclusions concerning SCF5, SCR19.34 and SCR25.76 can be drawn from the above discussion:

(i) The laboratory SCF5 material which was produced from pure components appears to have the best high temperature mechanical properties, followed by SCR19.34, the pilot-plant material made from pure components.

(ii) As regards the room temperature flexural strength, the two glass-ceramics made from pure components appear to be stronger than SCR25.76, the pilot-plant material produced from iron blast-furnace slag and colliery shale, whereas the compressive strength of SCR25.76 was found to be higher than that of SCR19.34.

(iii) Assuming the room temperature flexural strength S4 data to be reliable, the flexural strength distribution, and by implication the flaw size distribution of SCR19.34 is narrower than that of SCR25.76.

(iv) The SCR25.76 material may be less susceptible to slow crack growth than the SCR19.34 material, although the slow crack growth exponent is subject to wide variation.

(v) The room temperature fracture toughness of SCR25.76 is higher than the toughness of both SCF5 and SCR19.34,

although the values are within 25 % of one another.
(vi) The Young's modulus and Vickers hardness are the least sensitive to microstructural differences, as might be expected given the greater dependence on interatomic bond strengths.

Relating these conclusions to the microstructural differences of the materials indicates that better high temperature behaviour under stress is associated with a lower volume fraction of higher viscosity residual glass, while acceptable flexural strength is favoured by a fine-grained, intermeshing, and effectively continuous dendritic microstructure. The fracture toughness, however, is controlled by the microstructure on a finer, more localized scale and in a more subtle manner which goes beyond the scaling influence of the Young's modulus. Finally, unlike the flexural strength and toughness, the Young's modulus, and particularly the Vickers hardness, are comparatively microstructure-insensitive.

7.3 Suggestions for Further Work

The suggestions for further work are twofold; (i) further detailed investigation of the mechanical properties of the three crystalline materials, and (ii) a new systematic programme of work, starting with a specified initial batch composition, aimed at determining which material and process parameters influence the physical, particularly the mechanical properties, and the microstructures of the resulting glass-ceramic. All the parameters which may affect these properties and the microstructure would be varied systematically, one at a time, leaving the others unchanged; once the determining parameters are identified the properties of the material could be optimized, in particular the mechanical properties.

Further investigation of the mechanical properties of SCF5, SCR19.34, and SCR25.76 would include:
(i) A greater number of flexural strength and fracture toughness tests as a function of temperature, strain-rate, and environment (as well as the surface finish in the case of

flexural strength tests), accompanied by fractographic examination in order to determine which microstructural features are generally responsible for catastrophic failure, and then quantify their morphology and locations.
(ii) A more thorough microstructural analysis of each material as regards the volume fractions of crystal and residual glass, crystal size distribution, crystal morphology distribution and so on.
(iii) Delayed fracture tests to obtain life-time data to correlate with the SPT data obtained in the present work.
(iv) Double-torsion tests to determine the slow crack growth parameters, A and n.
(v) Standard mechanical properties tests (as per the present work) on model glasses with the residual glass compositions, and also on samples of the diopside solid solutions if possible.
(vi) Determination of the thermal shock resistance of the materials, together with further compression creep testing.
Other related work would include viscosity measurements, thermal expansion measurements, and composition analyses.

The second programme of laboratory work, summarized above, would involve choosing, for example, the SCR19.34 parent-glass batch composition, and initially varying the following process parameters in turn:
(a) Melting temperature, (b) Melting time,
(c) Melt homogenization and refining procedure,
(d) The melt environment, (e) Casting procedure,
(f) Heat treatment temperature, and
(d) Heat treatment time.
The resulting changes in microstructure would then be correlated with the change in each of the above parameters in order to find how each parameter influences the resulting microstructure, composition, and properties.

Once the above process parameters are optimized for the given composition, the amounts of Fe_2O_3 and Cr_2O_3 would be varied in turn and the changes correlated with the subsequent changes in microstructure, composition and properties. This would be followed by changes in the base glass composition, particularly the Mg and Ca content.

APPENDIX 3A THEORETICAL UPPER LIMIT FOR POISSON'S RATIO:

Consider an elemental cube of initially unit dimensions within a homogeneous, isotropic, linear elastic solid which is then subject to a triaxial tensile stress state, i.e., there are no shear stresses only normal stresses. The axes of the cube are x, y and z with a corner origin O such that (i) the cube dimensions are unity along x,y,z, (ii) the normal stresses are σ_x, σ_y, σ_z, and (iii) the resultant normal strains are ϵ_x, ϵ_y, ϵ_z. Using equations [3.5] and [3.6] gives the following,

$$\epsilon_x = (\sigma_x - \nu[\sigma_y + \sigma_z])/E$$
$$\epsilon_y = (\sigma_y - \nu[\sigma_x + \sigma_z])/E \qquad [3A.1]$$
$$\epsilon_z = (\sigma_z - \nu[\sigma_x + \sigma_y])/E$$

The volume of the cube is now given by

$$V = (1 + \epsilon_x)(1 + \epsilon_y)(1 + \epsilon_z) \qquad [3A.2]$$

Since the strains are $\ll 1$, the strain product terms in the expansion of [3A.2] are neglected to give

$$V = 1 + \epsilon_x + \epsilon_y + \epsilon_z \qquad [3A.3]$$

The change in volume is thus $\epsilon_x + \epsilon_y + \epsilon_z$. Now the unit volume change, dilatation or volumetric strain, θ is defined as $\theta = \Delta V/V_o$ where ΔV is the change in volume of a body of original volume V_o. Therefore,

$$\theta = \epsilon_x + \epsilon_y + \epsilon_z \qquad [3A.4]$$

Now substituting equations [3A.1] in [3A.4] gives

$$\theta = (1 - 2\nu)(\sigma_x + \sigma_y + \sigma_z)/E \qquad [3A.5]$$

This equation for θ is general since shear stresses cause no change in volume. In the special case of spherical or hydrostatic stress the normal stresses are equal (as are the normal strains therefore), so [3A.5] becomes

$$\theta = 3\sigma_{hyd}(1 - 2\nu)/E \qquad [3A.6]$$

Using equation [3.5], equation [3A.6] can be re-written as

$$K = \sigma_{hyd}/\theta = E/3(1 - 2\nu) \qquad [3A.7]$$

From equation [3A.7] it can be seen that if $\nu = 1/2$ then $K = \infty$ which means the material does not change volume when subject to stress, and if $\nu > 1/2$ a tensile hydrostatic stress produces a decrease in volume and vice versa which is physically improbable. Hence $\nu_{max} = 0.5$.

APPENDIX 3B DERIVATION OF EQUATIONS [3.9] AND [3.10] USING THE ASSUMPTIONS OF UNIFORM STRESS AND UNIFORM STRAIN RESPECTIVELY:

Case 1: Reuss model

With reference to Figure 3B.1, this model considers the situation when each phase is subject to the same stress (σ), but each experiences a different elastic strain (i.e., each phase is subject to the same load) giving

$$\sigma = E_1 \epsilon_1 \text{ and } \sigma = E_2 \epsilon_2 \qquad [3B.1]$$

where E_1 is the Young's modulus of phase 1, E_2 the Young's modulus of phase 2, and ϵ_1 and ϵ_2 are the elastic strains in phases 1 and 2 respectively, assuming they have the same Poisson's ratio. The strains ϵ_1 and ϵ_2 are given by

$$\epsilon_1 = \delta x_1/x_1 \text{ and } \epsilon_2 = \delta x_2/x_2 \qquad [3B.2]$$

The total strain, ϵ is given by

$$\epsilon = (\delta x_1 + \delta x_2)/(x_1 + x_2)$$
$$= \delta x_1/(x_1 + x_2) + \delta x_2/(x_1 + x_2) \qquad [3B.3]$$

If v is the total volume of material, v_1 the volume of phase 1 and v_2 the volume of phase 2 (i.e., $v = v_1 + v_2$), $v_1 = Ax_1$, $v_2 = Ax_2$ and $v = A(x_1 + x_2)$, then

$$V_1 = v_1/v = x_1/(x_1 + x_2)$$
$$V_2 = v_2/v = x_2/(x_1 + x_2) \qquad [3B.4]$$

where V_1 is the volume fraction of phase 1 and V_2 the volume fraction of phase 2, i.e., $V_1 + V_2 = 1$.

Now from [3B.2], $\delta x_1 = \epsilon_1 x_1$ and $\delta x_2 = \epsilon_2 x_2$; thus on substitution in equation [3B.3], ϵ is given by

$$\epsilon = \epsilon_1 x_1/(x_1 + x_2) + \epsilon_2 x_2/(x_1 + x_2) \qquad [3B.5]$$

Using equation [3B.4], equation [3B.5] becomes

$$\epsilon = \epsilon_1 V_1 + \epsilon_2 V_2 \qquad [3B.6]$$

But $\epsilon = \sigma/E$ where E is the effective Young's modulus of the two-phase composite material; thus [3B.6] can be written as $\sigma/E = V_1\sigma/E_1 + V_2\sigma/E_2$, that is,

$$1/E = V_1/E_1 + V_2/E_2 \qquad [3B.7]$$

Making E the subject in equation [3B.7] gives

$$E = \frac{E_1 E_2}{E_1 V_2 + E_2 V_1} \qquad [3B.8]$$

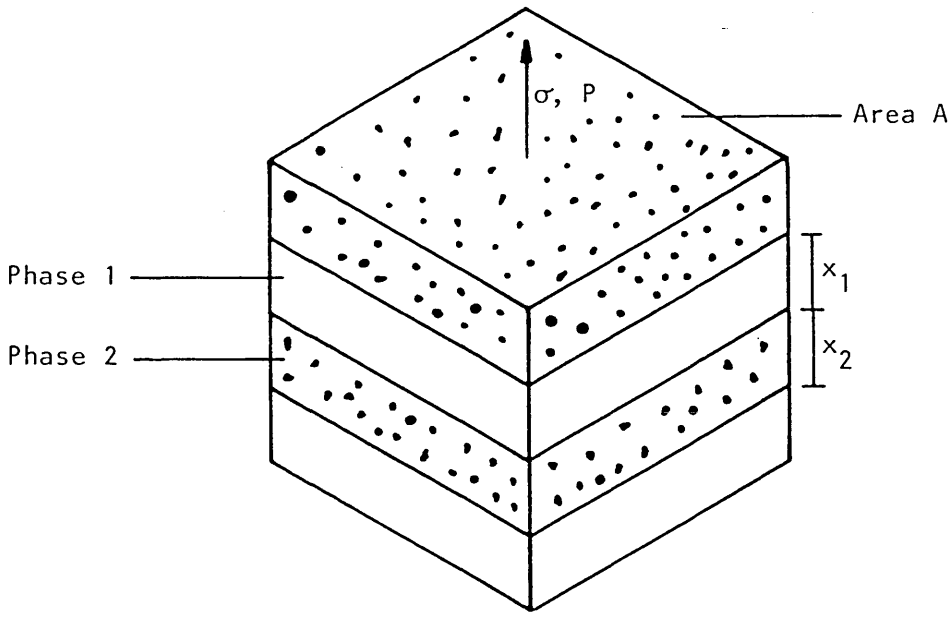
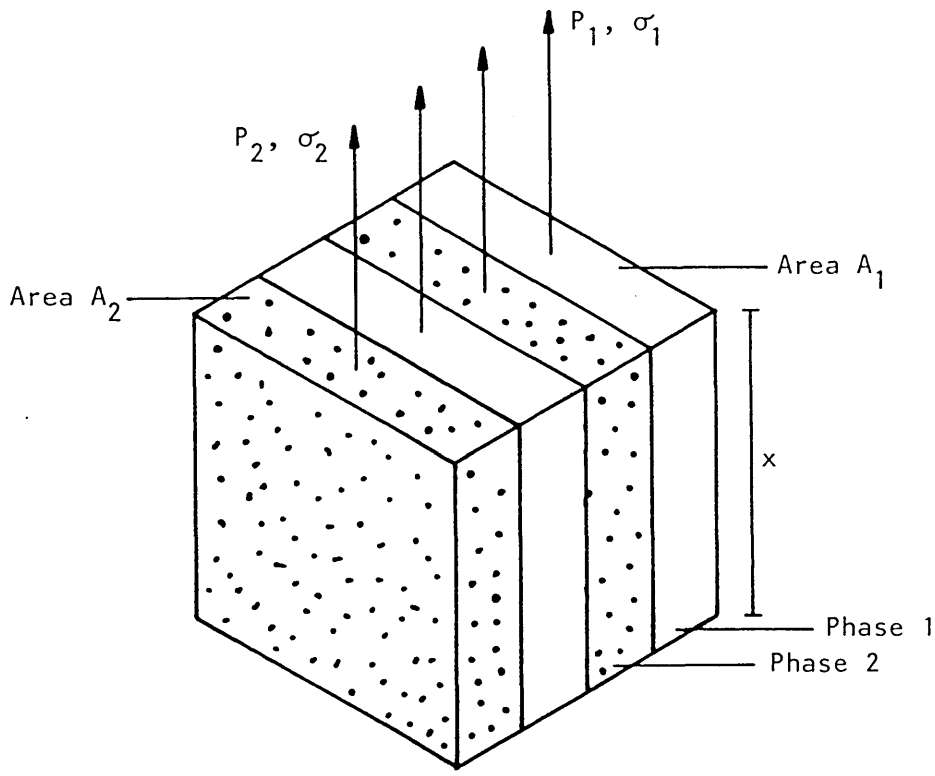


Figure 3B.1 Schematic Diagram of a Simple Layered Two-Phase Composite Material Stressed Perpendicular to the Layers.



Note that area A_1 refers to the total area of phase 1 over which the load P_1 acts, inducing stress σ_1; similarly area A_2 is the total area of phase 2 over which the load P_2 acts, inducing stress σ_2.

Figure 3B.2 Schematic Diagram of a Simple Layered Two-Phase Composite Material Stressed Parallel to the Layers.

APPENDIX 3B CONTINUED:

Case 2: Voigt model

Referring to Figure 3B.2, this model considers the situation when each phase is strained by the same amount (ϵ), but each experiences a different stress such that

$$\sigma_1 = E_1\epsilon \text{ and } \sigma_2 = E_2\epsilon \qquad [3B.9]$$

where σ_1 and σ_2 are the stresses in phase 1 and phase 2 respectively (again assuming the two phases have the same Poisson's ratio). Furthermore,

$$\sigma_1 = P_1/A_1 \text{ and } \sigma_2 = P_2/A_2 \qquad [3B.10]$$

where P_1 and P_2 are the loads borne by phases 1 and 2 respectively, such that

$$P = P_1 + P_2 \qquad [3B.11]$$

where P is the load applied to the two-phase composite material; thus the nominal stress acting on the two-phase composite material, σ is given by

$$\sigma = P/(A_1 + A_2) = E\epsilon \qquad [3B.12]$$

where E is the effective Young's modulus of the composite. Equation [3B.12] can be re-written as

$$P = (A_1 + A_2)E\epsilon \qquad [3B.13]$$

while from equations [3B.9] and [3B.10] it follows that

$$P_1 = A_1E_1\epsilon \text{ and } P_2 = A_2E_2\epsilon \qquad [3B.14]$$

So substituting for P, P_1 and P_2 in equation [3B.11] gives

$$(A_1 + A_2)E\epsilon = A_1E_1\epsilon + A_2E_2\epsilon \qquad [3B.15]$$

Dividing equation [3B.15] by $(A_1 + A_2)\epsilon$ gives

$$E = E_1A_1/(A_1 + A_2) + E_2A_2/(A_1 + A_2) \qquad [3B.16]$$

Using the same nomenclature as in case 1 gives $v_1 = A_1x$, $v_2 = A_2x$, and $v = x(A_1 + A_2)$, and hence

$$V_1 = v_1/v = A_1/(A_1 + A_2)$$
$$V_2 = v_2/v = A_2/(A_1 + A_2) \qquad [3B.17]$$

So equation [3B.16] can be re-written as

$$E = E_1V_1 + E_2V_2 \qquad [3B.18]$$

which is a "law of mixtures"-type equation. Note that in both cases stresses other than those considered here will arise if the two phases have different Poisson's ratios because the elastic Poisson's strains orthogonal to the applied stress will be different in each phase.

APPENDIX 3C DERIVATION OF $\Delta W/W$:

Expressing the stress (σ) and strain (ϵ) as periodic functions of time (t) in the following forms:

$$\sigma = \sigma_o \sin(wt) \qquad [3C.1]$$

$$\epsilon = \epsilon_o \sin(wt - \phi) \qquad [3C.2]$$

where w is the angular frequency ($= 2\pi f$), σ_o the stress amplitude, ϵ_o the strain amplitude, and ϕ the phase angle by which the strain lags behind the stress. Expanding $\sin(wt - \phi)$ gives $\sin(wt)\cos\phi - \cos(wt)\sin\phi$; hence

$$\epsilon = \epsilon_o \sin(wt)\cos\phi - \epsilon_o \cos(wt)\sin\phi \qquad [3C.3]$$

Comparing [3C.1] and [3C.3] shows that $\epsilon_o \cos(wt)\sin\phi$ is the strain component out of phase with the stress. So only considering this component, $\epsilon = \epsilon_o \sin\phi\cos(wt)$ $\therefore$ $d\epsilon/dt = -\epsilon_o w \sin\phi \sin(wt)$ $\therefore$ $d\epsilon = -\epsilon_o w \sin\phi \sin(wt)\, dt$. This gives

$$\Delta W = \int_0^{2\pi/w} \sigma \, d\epsilon = -\int_0^{2\pi/w} \sigma_o \sin(wt).\epsilon_o w \sin\phi \sin(wt)\, dt$$

$$= -\sigma_o \epsilon_o w \sin\phi \int_0^{2\pi/w} \sin^2(wt)\, dt \qquad [3C.4]$$

where ΔW is the energy dissipated per cycle (per unit volume), i.e., from t = 0 to $t = 2\pi/w$. Given that $\sin^2(\theta) = [1 - \cos(2\theta)]/2$, $\sin^2(wt)$ can be integrated as follows

$(1/2)\int 1 - \cos(2wt)\, dt = t/2 - [\sin(2wt)]/4w + c$

Hence [3C.4] becomes

$$\Delta W = -\sigma_o \epsilon_o w \sin\phi \left| t/2 - [\sin(2wt)]/4w \right|_0^{2\pi/w} = \sigma_o \epsilon_o \pi \sin\phi \qquad [3C.5]$$

But $\epsilon_o = \sigma_o/E$ $\therefore$ $\Delta W = [(\sigma_o)^2/E]\pi\sin\phi = E(\epsilon_o)^2\pi\sin\phi$ [3C.6]

Note the maximum energy is dissipated per cycle (per unit volume) when $\phi = \pi/2$, i.e., $\sin\phi = 1$. The maximum energy stored per unit volume, W is stored when $\phi = 0$, $\sigma = \sigma_o$ and thus $\epsilon = \epsilon_o$, giving (since $d\sigma = Ed\epsilon$)

$$W = \int_0^{\sigma_o} \sigma \, d\epsilon = 1/E \int_0^{\sigma_o} \sigma \, d\sigma = 1/2E \left| \sigma^2 \right|_0^{\sigma_o} \qquad [3C.7]$$

Hence $W = (\sigma_o)^2/2E = E(\epsilon_o)^2/2$ for $\phi = 0$, so for $\phi \ll 1$, $W \approx (\sigma_o)^2/2E = E(\epsilon_o)^2$, giving

$$\Delta W/W = 2\pi\sin\phi \approx 2\pi\tan\phi \approx \phi \qquad [3C.8]$$

since for $\phi \ll 1$, $\sin\phi \approx \phi$ and $\tan\phi \approx \phi$.

APPENDIX 3D DIMENSIONS AND MASSES OF THE GLASS-CERAMIC SPECIMENS TESTED:

Specimen	Length ($x10^{-3}$m)	Width ($x10^{-3}$m)	Thickness ($x10^{-3}$m)	Mass ($x10^{-3}$kg)
SCR25.76				
A	79.92	11.87	2.83	8.1133
B	79.94	11.88	2.97	8.5122
C	79.92	11.87	2.97	8.4437
D	79.92	11.88	1.38	3.9333
SCR19.34				
A	79.94	11.89	3.05	8.5187
B	79.92	11.89	3.06	8.5469
C	79.94	11.89	3.00	8.3727
D	79.88	11.88	1.39	3.8913
SCR19.13				
A	68.54	10.09	3.87	7.3819
SCF5				
A	77.10	9.40	5.18	10.8173
B	77.22	9.49	5.08	10.7316
B'	77.22	9.46	2.05	4.3084
C	71.66	9.34	5.04	9.7305
D	70.04	9.36	5.13	9.7042

Specimen SCF5 B' was produced by grinding specimen SCF5 B to a thinner thickness.

APPENDIX 3E HIGH TEMPERATURE YOUNG'S MODULUS AND INTERNAL FRICTION DATA FOR SCR25.76, SCR19.34 AND SCF5:

Table 3E.1 Young's Modulus Data for SCR25.76 A and B:

Temperature (°C)	f_r (Hz)	Young's Modulus, E (GPa)
Specimen SCR25.76 A at 6 mm outside nodes		
24	2895.1	123.18
50	2880.8	121.94
96	2868.2	120.84
157	2856.5	119.80
201	2849.3	119.16
250	2839.5	118.29
24	2894.1	123.09
55	2879.1	121.79
106	2868.7	120.87
156	2857.0	119.84
210	2847.4	118.99
248	2839.7	118.31
291	2831.1	117.56
332	2824.4	116.97
370	2816.0	116.24
405	2808.2	115.57
430	2804.4	115.23
460	2802.6	115.06
491	2803.6	115.11
511	2799.5	114.76
21	2891.8	122.91
Specimen SCR25.76 A at 8 mm outside nodes		
24	2892.2	122.93
53	2876.4	121.57
102	2864.9	120.55
153	2853.6	119.56
207	2844.3	118.73
250	2836.5	118.04
293	2827.7	117.27
333	2819.0	116.52
365	2812.2	115.93
400	2804.5	115.27
423	2799.8	114.86
371	2813.4	116.02
315	2826.9	117.19
234	2843.3	118.62
131	2863.4	120.40
22	2894.3	123.11
22	2893.6	123.05
48	2879.4	121.83
91	2867.5	120.78
147	2855.9	119.76
202	2846.2	118.90
252	2837.7	118.14
301	2828.5	117.33
332	2822.4	116.80
366	2814.0	116.08

APPENDIX 3E CONTINUED:

Table 3E.1 Continued:

Temperature (°C)	f_r (Hz)	Young's Modulus, E (GPa)
Specimen SCR25.76 A at 10 mm outside nodes		
24	3023.5	122.04
54	3007.4	120.72
98	2995.5	119.72
157	2983.0	118.67
201	2975.0	118.00
256	2968.5	117.44
306	2956.3	116.43
337	2949.2	115.84
376	2941.2	115.18
408	2933.7	114.57
436	2926.3	113.97
495	2909.8	112.64
541	2894.1	111.39
585	2845.5	107.64
623	2789	103.4
654	2646	93.0

Table 3E.2 Young's Modulus Data for SCR19.34 A and B:

Temperature (°C)	f_r (Hz)	Young's Modulus, E (GPa)
Specimen SCR19.34 A at 6 mm outside nodes		
28	3055.7	115.14
59	3040.5	113.97
91	3032.2	113.32
132	3023.1	112.61
165	3017.1	112.13
197	3011.8	111.71
235	3005.1	111.19
276	2998.1	110.63
306	2993.2	110.25
337	2987.9	109.83
368	2981.9	109.37
27	3054.1	115.02
395	2977.1	108.99
426	2972.1	108.60
445	2968.3	108.31
473	2963.4	107.93
Specimen SCR19.34 A at 8 mm outside nodes		
29	3054.8	115.07
57	3040.7	113.99
95	3030.2	113.17
154	3019.0	112.28
217	3009.2	111.50
250	3003.1	111.03
300	2995.3	110.41
338	2989.2	109.93
379	2983.1	109.45
416	2976.4	108.92

APPENDIX 3E CONTINUED:

Table 3E.2 Continued:

Temperature (°C)	f_r (Hz)	Young's Modulus, E (GPa)
Specimen SCR19.34 A at 8 mm outside nodes		
443	2971.4	108.54
501	2959.7	107.64
551	2942.3	106.34
596	2910.5	104.01
641	2894.3	102.83
668	2811.8	97.03
674	2732.8	91.65
701	2726.0	91.17
29	3044.8	114.32
Specimen SCR19.34 B at 10 mm outside nodes		
24	3068.2	115.25
49	3052.9	114.08
93	3041.0	113.16
150	3030.2	112.31
200	3022.2	111.67
253	3013.6	110.99
298	3006.4	110.43
333	3001.2	110.02
366	2994.0	109.46
24	3064.5	114.97
50	3051.1	113.95
91	3039.6	113.05
150	3028.6	112.19
200	3021.4	111.61
251	3013.2	110.97
298	3006.2	110.41
335	3000.0	109.93
372	2993.1	109.39
407	2986.9	108.91
432	2982.7	108.58
488	2968.0	107.47
533	2944.7	105.76
576	2920.8	104.01
619	2907.8	103.05
654	2845	98.6
690	2772	93.6
22	3051.5	114.00
53	3036.9	112.89
101	3024.6	111.93
166	3012.7	111.00
219	3003.9	110.31
267	2996.4	109.72
313	2988.9	109.13
348	2982.7	108.65
387	2976.2	108.15
418	2970.0	107.67
445	2965.0	107.29
500	2953.6	106.42
544	2943.3	105.65

APPENDIX 3E CONTINUED:

Table 3E.2 Continued:

Temperature (°C)	f_r (Hz)	Young's Modulus, E (GPa)
Specimen SCR19.34 B at 10 mm outside nodes		
590	2916.4	103.69
626	2838.7	98.21
660	2669.9	86.86
698	2511.3	76.82
728	2218.9	59.96
22	3052.1	114.04

Table 3E.3 Young's Modulus Data for SCF5 B':

Temperature (°C)	f_r (Hz)	Young's Modulus, E (GPa)
Specimen SCF5 B' at 6 mm outside nodes		
23	2290.0	121.4
53	2285.9	120.9
116	2279.3	120.2
172	2274.3	119.6
223	2270.3	119.1
280	2265.9	118.6
328	2262.0	118.2
364	2259.1	117.8
406	2255.5	117.4
439	2252.6	117.1
464	2249.5	116.8
527	2243.1	116.0
571	2238.0	115.5
613	2230.9	114.7
660	2218.6	113.4
696	2204.9	112.0
730	2178.6	109.3
766	2167.0	108.1
24	2286.5	121.0
Specimen SCF 5 B' at 8 mm outside nodes		
22	2286.1	121.0
74	2278.4	120.1
132	2272.5	119.5
194	2267.3	118.9
252	2262.3	118.3
294	2259.3	117.9
341	2255.1	117.4
386	2251.8	117.1
416	2249.1	116.8
451	2245.8	116.4
475	2243.3	116.1
535	2237.4	115.4
585	2232.8	114.9
626	2226.7	114.3
670	2220.2	113.6
700	2214.6	113.0
741	2193.2	110.8

APPENDIX 3E CONTINUED:

Table 3E.3 Continued:

Temperature (°C)	f_r (Hz)	Young's Modulus, E (GPa)
Specimen SCF 5 B' at 8 mm outside nodes		
22	2286.8	121.1

Table 3E.4 Normalized High Temperature Young's Modulus and Internal Friction Data for SCR25.76:

Temperature (°C)	E/E_o	$Q^{-1}/Q^{-1}{}_o$
23	1	1
52	0.990	1.543
95	0.981	1.752
104	0.981	2.941
131	0.979	1.709
147	0.973	2.333
156	0.973	2.868
204	0.967	3.270
234	0.965	2.935
251	0.961	3.371
292	0.955	4.878
304	0.954	0.859
315	0.953	4.682
334	0.949	4.775
370	0.944	6.889
404	0.938	9.348
423	0.934	-----
433	0.935	10.463
436	0.934	4.744
460	0.935	33.706
493	0.929	34.990
511	0.932	68.595
541	0.913	-----
585	0.882	-----
623	0.847	-----
654	0.762	-----

Table 3E.5 Normalized High Temperature Young's Modulus and Internal Friction Data for SCR19.34:

Temperature (°C)	E/E_o	$Q^{-1}/Q^{-1}{}_o$
26	1	1
54	0.991	1.053
94	0.984	1.192
132	0.979	1.597
151	0.976	1.090
165	0.975	1.539
199	0.971	1.158
218	0.969	1.480
235	0.967	1.664
251	0.965	1.184
267	0.963	1.401

APPENDIX 3E CONTINUED:

Table 3E.5 Continued:

Temperature (°C)	E/E_o	Q^{-1}/Q^{-1}_o
276	0.962	2.042
301	0.960	1.464
313	0.958	1.512
336	0.956	1.671
348	0.954	1.717
369	0.951	1.798
383	0.951	2.280
395	0.948	2.302
407	0.948	1.141
420	0.946	2.852
432	0.945	1.114
444	0.943	3.225
473	0.939	6.491
488	0.936	1.326
501	0.935	5.021
533	0.921	1.937
548	0.926	9.220
576	0.905	3.998
590	0.910	-----
596	0.905	8.234
623	0.880	-----
641	0.894	-----
657	0.810	-----
668	0.844	-----
674	0.797	-----
690	0.815	-----
700	0.734	-----
728	0.526	-----

Table 3E.6 Normalized High Temperature Young's Modulus and Internal Friction Data for SCF5:

Temperature (°C)	E/E_o	Q^{-1}/Q^{-1}_o
23	1	1
53	0.997	1.709
74	0.993	1.641
116	0.991	2.039
132	0.988	1.820
172	0.986	2.102
194	0.983	1.693
223	0.982	2.670
252	0.978	1.806
280	0.978	2.467
294	0.975	-----
328	0.974	2.441
341	0.971	-----
364	0.971	2.325
386	0.968	2.257
411	0.967	3.140
439	0.965	3.049

APPENDIX 3E CONTINUED:

Table 3E.6 Continued:

Temperature (°C)	E/E_o	Q^{-1}/Q^{-1}_o
451	0.963	2.818
464	0.963	-----
475	0.960	2.932
531	0.955	3.463
571	0.952	-----
585	0.950	8.324
613	0.945	-----
626	0.945	11.155
660	0.935	-----
670	0.939	-----
696	0.923	-----
700	0.935	-----
730	0.901	-----
741	0.916	-----
766	0.891	-----

APPENDIX 4A DERIVATION OF THE MOMENT OF INERTIA OF A RECTANGULAR SECTION WITH TWO ROUNDED CORNERS OF RADIUS r:

With reference to Figure 4A.1, the moment of inertia with respect to the centroidal axis XX (I_{xx}) is derived using the parallel axis theorem (Gere, J.M., and Timoshenko, S.P., 1984) which is stated mathematically as

$$I_{xx} = \Sigma(I_{xx}(C_j) + A_j(d_j)^2) \qquad [4A.1]$$

where $I_{xx}(C_j)$ is the moment of inertia of section j with respect to the axis through the centroid C_j of section j parallel to axis XX, A_j is the area of section j, d_j is the vertical distance between the centroidal axis XX and the axis through the centroid C_j of section j parallel to axis XX and in the plane of area A_j, and Σ is a summation sign.

Now $W = W/2 + h/2 + y \therefore y = (W - h)/2$

But $h = W - r \therefore y = r/2$. Hence the following obtains $d_1 = r/2$, $d_2 = d_4 = (h - r)/2 + 4r/3\pi$ and $d_3 = h/2$. Now using the quoted moment of inertia formulae for standard plane areas given in the above reference, gives

$I_{xx}(C_1) = Bh^3/12$

$I_{xx}(C_2) = I_{xx}(C_4) = (9\pi^2 - 64)r^4/144\pi$ and

$I_{xx}(C_3) = (B - 2r)r^3/12$

Hence $I_{xx} =$ [4A.2]

$$Bh^3/12 + Bh(r/2)^2 + (B - 2r)r^3/12 + r(B - 2r)(h/2)^2 + 2[(9\pi^2 - 64)r^4/144\pi + (\pi r^2/4)([h - r]/2 + 4r/3\pi)^2]$$

$$= Bh^3/12 + Bhr^2/4 + (B - 2r)(r^3/12 + rh^2/4) + 2[(9\pi^2 - 64)r^4/144\pi + (\pi r^2/4)([h - r]/2 + 4r/3\pi)^2]$$

where $h = W - r$. Assuming $W = 8$ and $B = 4$,

r	h		I_{xx}	$[(I_{xx} - I_o)/I_o] \times 100$ %
0	8	(I_o)	170.667	0
0.05	7.95		170.650	- 0.01
0.10	7.90		170.599	- 0.04
0.30	7.70		170.069	- 0.35
0.50	7.50		169.043	- 0.95
0.70	7.30		167.556	- 1.82
0.90	7.10		165.639	- 2.95
1.00	7.00		164.530	- 6.14

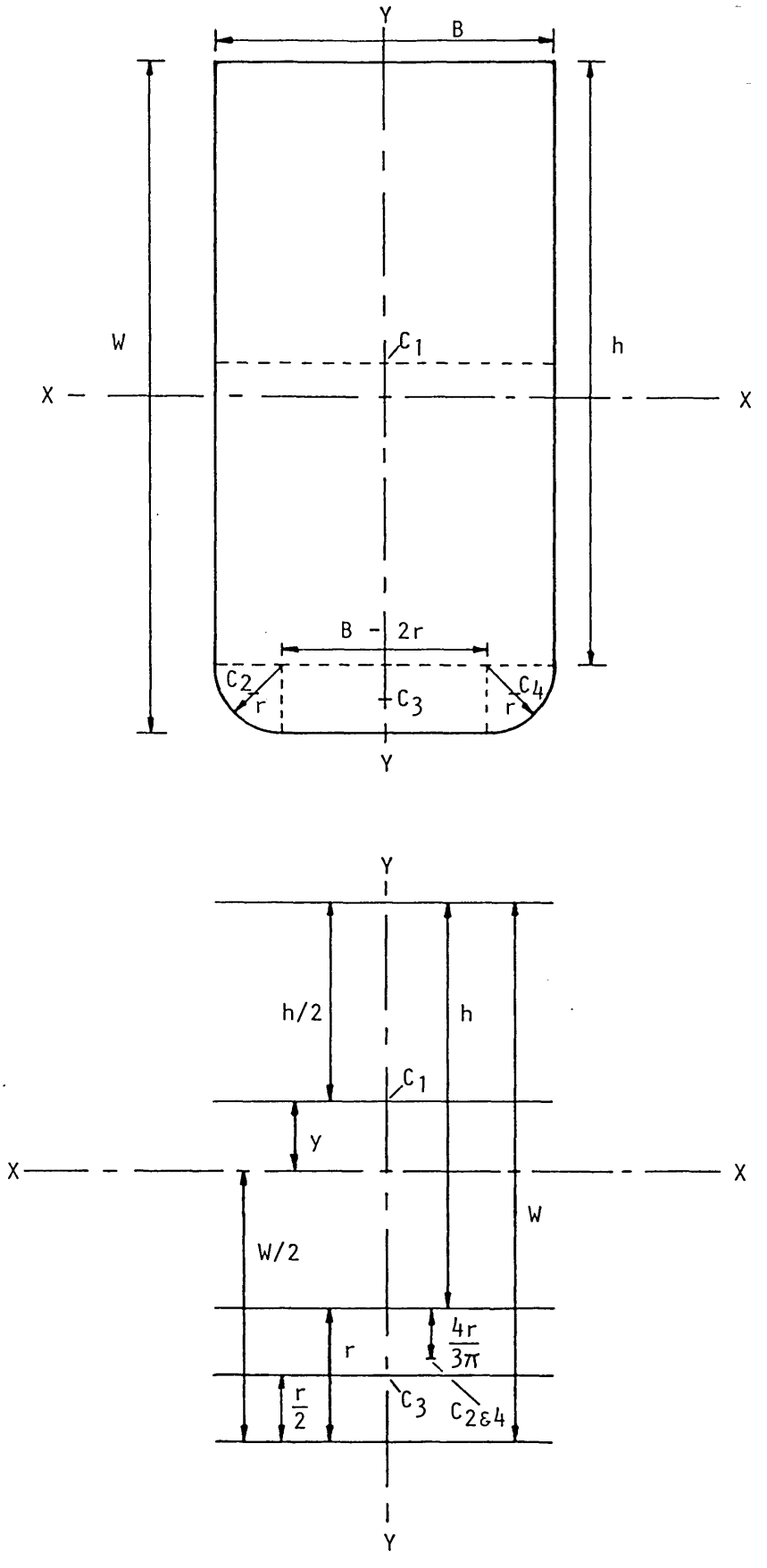


Figure 4A.1 Schematic Cross-Section of Beam With Rounded Bottom Edges Showing the Relevant Dimensions and Centroids (C_j).

APPENDIX 4B DERIVATION OF EQUATION [4.21]:

With reference to Figure 4B.1, and taking moments about section AA,

$M = -Px + (x + s/2)P/2 = -Px + Px/2 + Ps/4 = Ps/4 - Px/2$

$= (s/2 - x)P/2$

Now using $\sigma = My/I$ where $I = BW^3/12$ and $y = W/2 - v$ gives

$\sigma = (P/2)(s/2 - x)(W/2 - v)(12/BW^3)$

$= (6P/BW^3)([s - 2x]/2)([W - 2v]/2)$

$= (6P/4BW^3)(s - 2x)(W - 2v)$

$= (3P/2BW^3)(s - 2x)(W - 2v)$

$= (3P/2BW^3)\frac{(s - 2x)s}{s}.\frac{(W - 2v)W}{W}$

$= (3Ps/2BW^2)\frac{(s - 2x)}{s}.\frac{(W - 2v)}{W}$

$= (3Ps/2BW^2)(1 - 2x/s)(1 - 2v/W)$

This last equation is that given as equation [4.21] in Chapter 4.

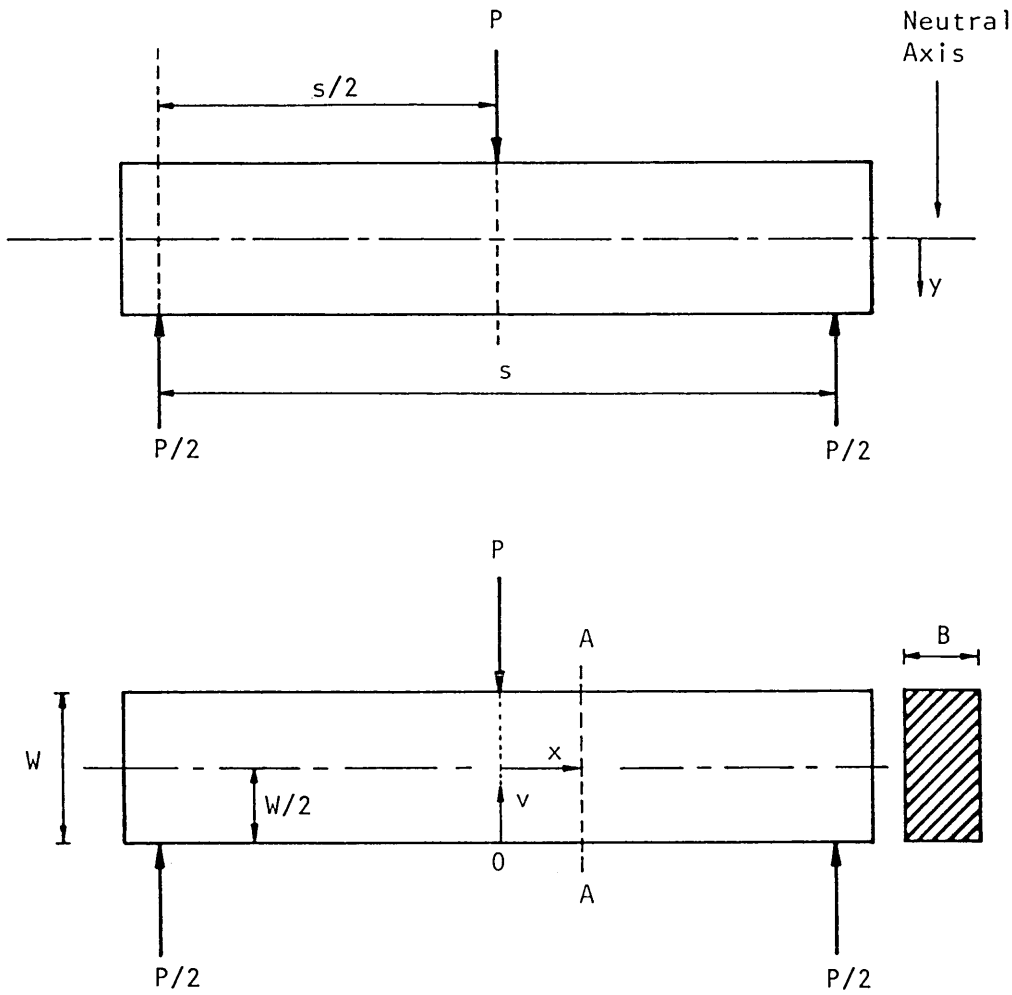


Figure 4B.1 Schematic Diagram of a Beam Subject to Three-Point Loading Showing the Relevant Dimensions and the Transverse Section AA About Which Moments Were Taken.

APPENDIX 4C ROOM TEMPERATURE FLEXURAL STRENGTH DATA FOR SCR25.76 AND SCR19.34 USING THREE-POINT BENDING AND A NOMINAL SPAN-TO-WIDTH RATIO OF 4:

Table 4C.1 Data Obtained on Room Temperature Test Rig at 20°C Using a Nominal Span of 32 mm and a Cross-Head Speed of 1.66. x 10^{-5} ms^{-1} (= 1 mm/minute):

DATA FOR SCR25.76

TEST #.	B (mm)	W (mm)	P (N)	x (mm)	t (s)	x/W	β-Value	S1 (MPa)	S2 (MPa)	S3 (MPa)	S4 (MPa)
MA3	4.013	7.623	461	2.5	11	0.328	+0.0640	94.9	90.9	80.1	82.0
MA18	3.989	7.626	471	2.0	12	0.262	+0.0868	97.5	93.3	85.3	88.0
MA11	3.944	7.638	576	3.5	13	0.458	+0.0421	120.2	115.1	93.9	95.5
MA4	4.006	7.629	558	2.5	14	0.328	+0.0640	114.9	110.0	96.9	99.3
MA6	4.015	7.633	517	1.0	13	0.131	+0.0137	106.1	101.6	99.5	99.9
MA10	3.995	7.636	536	1.5	14	0.196	+0.0868	110.4	105.8	100.1	103.1
MA12	4.025	7.629	546	1.5	13	0.197	+0.0868	111.9	107.1	101.4	104.5
MA5	4.020	7.638	560	1.5	14	0.196	+0.0868	114.6	109.8	103.9	107.0
MA16	3.996	7.638	560	1.5	14	0.196	+0.0868	115.3	110.4	104.5	107.7
MA19	3.998	7.635	633	3.0	14	0.393	+0.0640	130.4	124.8	105.9	108.6
MA13	3.986	7.633	572	1.5	14	0.197	+0.0868	118.2	113.2	107.1	110.4
MA1	4.013	7.637	572	1.0	15	0.131	+0.0137	117.3	112.3	110.0	110.5
MA2	4.017	7.638	580	1.5	15	0.196	+0.0868	118.8	113.8	107.7	110.9
MA17	3.994	7.628	576	1.5	15	0.197	+0.0868	119.0	113.9	107.8	111.1
MA14	4.018	7.625	572	0.5	13	0.066	+0.0137	117.5	112.6	113.9	114.4
MA15	4.063	7.636	609	1.5	15	0.196	+0.0868	123.4	118.2	111.8	115.2
MA7	3.980	7.626	604	1.5	14	0.197	+0.0868	125.3	120.0	113.5	117.0
MA8	3.996	7.637	627	1.5	14	0.196	+0.0868	129.1	123.7	117.0	120.6
MA9	4.030	7.649	647	1.0	14	0.131	+0.0137	131.7	126.1	123.5	124.1
MA20	3.999	7.628	655	1.0	16	0.131	+0.0137	135.1	129.4	126.7	127.3

DATA FOR SCR19.34

TEST #.	B (mm)	W (mm)	P (N)	x (mm)	t (s)	x/W	β-Value	S1 (MPa)	S2 (MPa)	S3 (MPa)	S4 (MPa)
MB5	4.020	7.629	513	1.5	13	0.197	+0.0868	105.2	100.8	95.4	98.3
MB20	4.032	7.629	519	1.5	14	0.197	+0.0868	106.2	101.7	96.2	99.1
MB10	4.010	7.628	519	1.0	13	0.131	+0.0137	106.8	102.2	100.1	100.6
MB4	3.987	7.640	580	2.5	14	0.327	+0.0640	119.6	114.6	100.9	103.4
MB15	3.977	7.629	527	0.0	13	0.000	-0.1332	109.3	104.7	109.3	104.7
MB8	4.006	7.631	550	0.0	14	0.000	-0.1332	113.2	108.4	113.2	108.4
MB18	4.014	7.628	562	0.5	14	0.066	+0.0137	115.5	110.6	111.9	112.4
MB3	4.014	7.651	576	0.5	15	0.065	+0.0137	117.7	112.7	114.0	114.5
MB11	3.987	7.630	590	1.0	15	0.131	+0.0137	122.0	116.8	114.4	114.9
MB12	4.021	7.632	598	1.0	15	0.131	+0.0137	122.6	117.4	114.9	115.4
MB2	3.980	7.638	580	0.5	14	0.065	+0.0137	119.9	114.8	116.2	116.7
MB17	4.026	7.630	633	2.0	15	0.262	+0.0868	129.6	124.1	113.4	117.0
MB13	4.014	7.628	594	0.5	14	0.066	+0.0137	122.1	116.9	118.3	118.8
MB9	4.012	7.629	602	0.5	14	0.066	+0.0137	123.7	118.5	119.9	120.4
MB14	4.015	7.627	604	0.5	15	0.066	+0.0137	124.1	118.9	120.3	120.8
MB6	3.992	7.646	631	1.5	16	0.196	+0.0868	129.8	124.3	117.6	121.2
MB16	3.998	7.632	615	0.0	13	0.000	-0.1332	126.8	121.4	126.8	121.4
MB7	3.992	7.627	617	0.0	15	0.000	-0.1332	127.5	122.1	127.5	122.1
MB19	4.009	7.643	663	1.5	16	0.196	+0.0868	135.9	130.1	123.2	126.9
MB1	4.003	7.634	659	1.0	16	0.131	+0.0137	135.6	129.8	127.1	127.7

APPENDIX 4C CONTINUED:

Table 4C.2 Data Obtained on High Temperature Test Rig at 20°C Using a Cross-Head Speed of 1.66. x 10^{-5} ms^{-1} (= 1 mm/minute):

DATA FOR SCR25.76

TEST #.	B (mm)	W (mm)	P (N)	x (mm)	t (s)	x/W	β-Value	S1 (MPa)	S2 (MPa)	S3 (MPa)	S4 (MPa)
MA88	4.036	7.727	565	4.0	17	0.518	+0.0421	111.7	106.8	83.5	85.1
MA85	4.052	7.721	776	3.5	22	0.453	+0.0421	153.0	146.4	119.3	121.4
MA89a	4.114	7.639	688	2.0	18	0.262	+0.0868	136.5	130.7	119.3	123.1
MA402 *	4.109	7.627	690	1.0	18	0.131	+0.0137	136.5	130.7	127.9	128.5
MA83	3.988	7.732	796	2.5	19	0.323	+0.0640	159.0	152.1	134.0	137.3
MA401 *	4.015	7.632	745	1.5	18	0.197	+0.0868	150.7	144.2	136.3	140.5
MA87	4.030	7.725	855	2.5	19	0.324	+0.0640	169.3	162.0	142.7	146.2
MA90a	4.123	7.641	812	1.0	18	0.131	+0.0137	160.6	153.8	150.5	151.2
MA84	4.074	7.702	867	0.0	18	0.000	-0.1332	170.9	163.5	170.9	163.5
MA86	4.085	7.719	910	0.0	19	0.000	-0.1332	178.1	170.4	178.1	170.4

DATA FOR SCR19.34

TEST #.	B (mm)	W (mm)	P (N)	x (mm)	t (s)	x/W	β-Value	S1 (MPa)	S2 (MPa)	S3 (MPa)	S4 (MPa)
MB402 *	4.010	7.617	617	1.0	16	0.131	+0.0137	125.4	120.0	117.5	118.0
MB401 *	4.009	7.620	737	2.0	20	0.262	+0.0868	149.7	143.3	130.7	134.9
MB83	4.049	7.743	737	1.0	17	0.129	+0.0137	144.6	138.3	135.5	136.1
MB85	4.020	7.695	1004	2.0	20	0.260	+0.0868	200.9	192.2	175.6	181.2
MB84	4.034	7.739	996	1.5	22	0.194	+0.0868	196.3	187.8	177.8	183.3
MB88	4.057	7.741	1145	1.0	23	0.129	+0.0137	224.3	214.6	210.2	211.2
MB89	4.084	7.715	1196	1.0	25	0.130	+0.0137	234.3	224.2	219.6	220.6
MB90	4.004	7.745	1298	0.0	22	0.000	-0.1332	257.4	246.2	257.4	246.2
MB86	4.047	7.738	1341	1.0	23	0.129	+0.0137	263.6	252.1	247.0	248.1
MB87	4.360	7.743	1467	0.5	23	0.065	+0.0137	267.3	255.7	258.9	260.0

All specimens except those denoted by * were tested on a nominal span of 31.75 mm.
The specimens denoted by * were tested on a nominal span of 31.53 mm.

Table 4C.3 Data Obtained on Room Temperature Test Rig at 20°C Using a Nominal Span of 32 mm and a Cross-Head Speed of 1.66. x 10^{-4} ms^{-1} (= 10 mm/minute):

DATA FOR SCR25.76

TEST #.	B (mm)	W (mm)	P (N)	x (mm)	t (s)	x/W	β-Value	S1 (MPa)	S2 (MPa)	S3 (MPa)	S4 (MPa)
MA23	3.991	7.636	615	1.0	1	0.131	+0.0137	126.9	121.5	118.9	119.5
MA26	3.996	7.632	637	1.5	1	0.197	+0.0868	131.4	125.8	119.0	122.7
MA21	3.994	7.638	678	2.0	1	0.262	+0.0868	139.7	133.7	122.2	126.1
MA24	3.988	7.635	665	1.0	1	0.131	+0.0137	137.3	131.5	128.7	129.3
MA22	4.001	7.631	714	2.0	2	0.262	+0.0868	147.1	140.9	128.7	132.8
MA30	3.989	7.637	690	1.5	1	0.196	+0.0868	142.4	136.3	129.0	132.9
MA27	3.993	7.627	714	2.0	2	0.262	+0.0868	147.5	141.3	129.1	133.2
MA25	3.993	7.639	700	0.5	2	0.065	+0.0137	144.2	138.1	139.7	140.3
MA29	3.983	7.630	698	0.5	2	0.066	+0.0137	144.5	138.4	140.0	140.6
MA28	4.007	7.629	714	0.5	2	0.066	+0.0137	147.0	140.7	142.4	143.0

APPENDIX 4C CONTINUED:

Table 4C.3 Continued:

DATA FOR SCR19.34

TEST #.	B (mm)	W (mm)	P (N)	x (mm)	t (s)	x/W	β-Value	S1 (MPa)	S2 (MPa)	S3 (MPa)	S4 (MPa)
MB21	4.015	7.615	675	4.0	1	0.525	+0.0421	139.2	133.3	104.4	106.2
MB29	4.026	7.621	641	3.0	1	0.394	+0.0640	131.6	126.0	106.9	109.6
MB28	4.004	7.615	592	1.0	1	0.131	+0.0137	122.4	117.2	114.7	115.3
MB22	4.037	7.613	600	0.5	1	0.066	+0.0137	123.1	117.9	119.2	119.8
MB30	4.022	7.616	631	1.0	1	0.131	+0.0137	129.8	124.3	121.7	122.3
MB26	4.017	7.619	661	1.0	1	0.131	+0.0137	136.1	130.3	127.6	128.2
MB25	4.021	7.615	665	0.0	1	0.000	-0.1332	136.9	131.1	136.9	131.1
MB23	4.019	7.616	704	1.0	1	0.131	+0.0137	145.0	138.8	135.9	136.5
MB27	4.031	7.608	714	1.0	2	0.131	+0.0137	146.9	140.7	137.7	138.3
MB24	4.059	7.608	787	2.5	2	0.329	+0.0640	160.8	154.0	135.7	138.9

Table 4C.4 Data Obtained on Room Temperature Test Rig at 20°C Using a Nominal Span of 32 mm and a Cross-Head Speed of 1.66. x 10^{-6} ms^{-1} (= 0.1 mm/minute):

DATA FOR SCR25.76

TEST #.	B (mm)	W (mm)	P (N)	x (mm)	t (s)	x/W	β-Value	S1 (MPa)	S2 (MPa)	S3 (MPa)	S4 (MPa)
MA40	3.999	7.630	467	0.0	114	0.000	-0.1332	96.3	92.2	96.3	92.2
MA39	3.980	7.621	481	0.5	117	0.066	+0.0137	99.9	95.7	96.8	97.2
MA35	3.975	7.640	501	1.0	120	0.131	+0.0137	103.6	99.3	97.2	97.6
MA32	4.006	7.626	511	1.0	123	0.131	+0.0137	105.3	100.8	98.7	99.2
MA33	3.996	7.627	527	0.5	123	0.066	+0.0137	108.8	104.2	105.4	105.9
MA34	3.995	7.635	554	1.0	132	0.131	+0.0137	114.2	109.3	107.1	107.5
MA31	4.002	7.631	592	2.0	126	0.262	+0.0868	121.9	116.8	106.7	110.1
MA36	3.997	7.625	550	0.5	129	0.066	+0.0137	113.6	108.8	110.1	110.5
MA38	3.968	7.654	598	1.5	132	0.196	+0.0868	123.5	118.2	111.9	115.3
MA37	3.997	7.631	578	0.5	123	0.066	+0.0137	119.2	114.2	115.5	116.0

DATA FOR SCR19.34

TEST #.	B (mm)	W (mm)	P (N)	x (mm)	t (s)	x/W	β-Value	S1 (MPa)	S2 (MPa)	S3 (MPa)	S4 (MPa)
MB32	4.001	7.614	467	2.0	111	0.263	+0.0868	96.6	92.6	84.6	87.2
MB38	3.996	7.615	540	3.5	135	0.460	+0.0421	111.9	107.1	87.4	88.9
MB32	4.015	7.620	497	1.0	123	0.131	+0.0137	102.3	98.0	95.9	96.4
MB34	4.007	7.616	536	1.5	135	0.197	+0.0868	110.7	106.0	100.3	103.4
MB33	4.008	7.611	570	2.0	138	0.263	+0.0868	117.8	112.9	103.1	106.4
MB39	3.999	7.619	529	0.5	117	0.066	+0.0137	109.4	104.8	106.0	106.4
MB35	4.030	7.611	536	0.5	135	0.066	+0.0137	110.2	105.6	106.8	107.2
MB40	3.993	7.616	536	0.5	132	0.066	+0.0137	111.1	106.4	107.6	108.1
MB37	3.996	7.621	592	2.0	135	0.262	+0.0868	122.4	117.3	107.1	110.5
MB36	4.005	7.616	558	0.5	132	0.066	+0.0137	115.3	110.4	111.7	112.2

APPENDIX 4D ROOM TEMPERATURE FLEXURAL STRENGTH DATA FOR SCF5 AND SCR19.13 USING THREE-POINT BENDING AND A NOMINAL SPAN-TO-WIDTH RATIO OF 4:

Table 4D.1 Data Obtained on High Temperature Test Rig at 20°C Using Alumina Roller Supports With a Nominal Span of 31.75 mm and a Cross-Head Speed of 1.66. x 10^{-5} ms^{-1} (= 1 mm/minute):

DATA FOR SCF5

TEST #.	B (mm)	W (mm)	P (N)	x (mm)	t (s)	x/W	β-Value	S1 (MPa)	S2 (MPa)	S3 (MPa)	S4 (MPa)
MC5	3.759	7.300	678	4.0	23	0.548	+0.0421	161.2	154.6	120.6	122.7
MC6	3.745	7.271	776	1.5	20	0.206	+0.0868	186.7	179.1	169.0	174.0
MD5	3.865	7.929	1200	1.5	26	0.189	+0.0868	235.2	224.8	213.0	219.8
MD6	3.757	7.930	1176	1.5	23	0.189	+0.0868	237.1	226.5	214.7	221.5

The letter D, in MD5 for example, indicates that sodium dichromate ($Na_2Cr_2O_7$) was used as the precursor compound for the Cr_2O_3 nucleating agent, while the C, in MC6 for example, indicates that either sodium chromate (Na_2CrO_4) or sodium dichromate was used as the precursor compound.

Table 4D.2 Data Obtained on Room Temperature Test Rig at 25°C Using a Nominal Span of 32 mm and a Cross-Head Speed of 1.66. x 10^{-5} ms^{-1} (= 1 mm/minute):

DATA FOR SCR19.13

TEST #.	B (mm)	W (mm)	P (N)	x (mm)	t (s)	x/W	β-Value	S1 (MPa)	S2 (MPa)	S3 (MPa)	S4 (MPa)
ME1	3.974	7.837	476	3.0	9	0.385	+0.0640	93.6	89.5	76.1	78.0
ME2	3.994	7.755	444	0.0	7	0.000	-0.1332	88.7	84.9	88.7	84.9
ME3	4.064	7.851	427	0.5	6	0.065	+0.0137	81.8	78.3	79.3	79.6
ME4	3.965	7.867	440	1.0	7	0.125	+0.0137	86.1	82.3	80.7	81.1
ME5	4.148	7.811	497	3.5	8	0.450	+0.0421	94.3	90.2	73.6	74.9

The above data were obtained on a Instron testing machine with a 5000 kg FM Tensile load cell.

APPENDIX 4E LEAST-SQUARES LINEAR REGRESSION DATA FOR THE WEIBULL MODULUS OF SCR25.76 AND SCR19.34 AT ROOM TEMPERATURE ASSUMING A ZERO THRESHOLD STRESS:

Table 4E.1 Data Obtained on Room Temperature Test Rig at 20°C Using a Nominal Span of 32 mm and a Cross-Head Speed of 1.66. x 10^{-3} ms^{-1} (= 1 mm/minute):

DATA FOR SCR25.76 USING 20 S1 DATA

Regression Data	$P_s = 1-j/(n+1)$	$P_s = 1-(j-0.5)/n$	$P_s = 1-(j-0.3)/(n+0.4)$	$P_s = 1-(j-3/8)/(n+1/4)$
Weibull mod. m	11.75	13.43	12.65	12.92
Stand. Dev. of m	0.52	0.57	0.53	0.54
Corr. Coeff. r	0.9830	0.9844	0.9843	0.9845
Coeff. Det. (= r^2)	0.9662	0.9690	0.9689	0.9692
Stand. Error of m	1.86	2.12	2.00	2.04
Intercept I	-218.90	-250.03	-235.54	-240.55
Stand. Dev. of I	9.63	10.52	9.94	10.09

DATA FOR SCR25.76 USING 20 S2 DATA

Regression Data	$P_s = 1-j/(n+1)$	$P_s = 1-(j-0.5)/n$	$P_s = 1-(j-0.3)/(n+0.4)$	$P_s = 1-(j-3/8)/(n+1/4)$
Weibull mod. m	11.75	13.42	12.64	12.91
Stand. Dev. of m	0.52	0.57	0.54	0.55
Corr. Coeff. r	0.9827	0.9841	0.9840	0.9842
Coeff. Det. (= r^2)	0.9657	0.9684	0.9683	0.9686
Stand. Error of m	1.86	2.12	2.00	2.04
Intercept I	-218.23	-249.25	-234.81	-239.80
Stand. Dev. of I	9.67	10.59	9.99	10.14

DATA FOR SCR25.76 USING 20 S3 DATA

Regression Data	$P_s = 1-j/(n+1)$	$P_s = 1-(j-0.5)/n$	$P_s = 1-(j-0.3)/(n+0.4)$	$P_s = 1-(j-3/8)/(n+1/4)$
Weibull mod. m	9.66	11.06	10.41	10.63
Stand. Dev. of m	0.37	0.36	0.36	0.36
Corr. Coeff. r	0.9872	0.9904	0.9894	0.9899
Coeff. Det. (= r^2)	0.9746	0.9809	0.9790	0.9799
Stand. Error of m	1.53	1.75	1.65	1.68
Intercept I	-178.99	-204.80	-192.76	-196.92
Stand. Dev. of I	6.79	6.71	6.64	6.63

DATA FOR SCR25.76 USING 20 S4 DATA

Regression Data	$P_s = 1-j/(n+1)$	$P_s = 1-(j-0.5)/n$	$P_s = 1-(j-0.3)/(n+0.4)$	$P_s = 1-(j-3/8)/(n+1/4)$
Weibull mod. m	9.96	11.40	10.72	10.96
Stand. Dev. of m	0.33	0.30	0.31	0.31
Corr. Coeff. r	0.9900	0.9936	0.9924	0.9930
Coeff. Det. (= r^2)	0.9800	0.9873	0.9849	0.9859
Stand. Error of m	1.57	1.80	1.69	1.73
Intercept I	-184.60	-211.32	-198.85	-203.15
Stand. Dev. of I	6.19	5.64	5.79	5.70

APPENDIX 4E CONTINUED:

Table 4E.1 Continued:

DATA FOR SCR19.34 USING 20 S1 DATA

Regression Data	$P_s = 1-j/(n+1)$	$P_s = 1-(j-0.5)/n$	$P_s = 1-(j-0.3)/(n+0.4)$	$P_s = 1-(j-3/8)/(n+1/4)$
Weibull mod. m	13.96	15.75	14.92	15.21
Stand. Dev. of m	0.63	0.90	0.76	0.80
Corr. Coeff. r	0.9824	0.9720	0.9776	0.9759
Coeff. Det. (= r^2)	0.9651	0.9447	0.9558	0.9523
Stand. Error of m	2.21	2.49	2.36	2.40
Intercept I	-260.17	-293.59	-278.22	-283.57
Stand. Dev. of I	11.64	16.71	14.08	14.93

DATA FOR SCR19.34 USING 20 S2 DATA

Regression Data	$P_s = 1-j/(n+1)$	$P_s = 1-(j-0.5)/n$	$P_s = 1-(j-0.3)/(n+0.4)$	$P_s = 1-(j-3/8)/(n+1/4)$
Weibull mod. m	13.96	15.76	14.93	15.22
Stand. Dev. of m	0.63	0.90	0.76	0.81
Corr. Coeff. r	0.9822	0.9716	0.9774	0.9756
Coeff. Det. (= r^2)	0.9647	0.9441	0.9553	0.9517
Stand. Error of m	2.21	2.49	2.36	2.41
Intercept I	-259.73	-293.07	-277.74	-283.07
Stand. Dev. of I	11.69	16.78	14.14	14.99

DATA FOR SCR19.34 USING 20 S3 DATA

Regression Data	$P_s = 1-j/(n+1)$	$P_s = 1-(j-0.5)/n$	$P_s = 1-(j-0.3)/(n+0.4)$	$P_s = 1-(j-3/8)/(n+1/4)$
Weibull mod. m	12.25	13.90	13.14	13.40
Stand. Dev. of m	0.61	0.77	0.68	0.71
Corr. Coeff. r	0.9785	0.9738	0.9768	0.9759
Coeff. Det. (= r^2)	0.9575	0.9482	0.9541	0.9524
Stand. Error of m	1.94	2.20	2.08	2.12
Intercept I	-227.66	-258.40	-244.19	-249.12
Stand. Dev. of I	11.28	14.21	12.60	13.10

DATA FOR SCR19.34 USING 20 S4 DATA

Regression Data	$P_s = 1-j/(n+1)$	$P_s = 1-(j-0.5)/n$	$P_s = 1-(j-0.3)/(n+0.4)$	$P_s = 1-(j-3/8)/(n+1/4)$
Weibull mod. m	13.28	15.01	14.22	14.49
Stand. Dev. of m	0.63	0.87	0.75	0.79
Corr. Coeff. r	0.9801	0.9711	0.9761	0.9746
Coeff. Det. (= r^2)	0.9606	0.9430	0.9528	0.9498
Stand. Error of m	2.10	2.37	2.22	2.29
Intercept I	-246.96	-279.09	-264.29	-269.44
Stand. Dev. of I	11.76	16.14	13.84	14.57

APPENDIX 4E CONTINUED:

Table 4E.2 Data Obtained on Room Temperature test Rig at 20°C Using a Nominal Span of 32 mm and a Cross-Head Speed of 1.66. x 10^{-4} ms^{-1} (= 10 mm/minute):

DATA FOR SCR25.76 USING 10 S1 DATA

Regression Data	$P_s = 1-j/(n+1)$	$P_s = 1-(j-0.5)/n$	$P_s = 1-(j-0.3)/(n+0.4)$	$P_s = 1-(j-3/8)/(n+1/4)$
Weibull mod. m	19.05	23.30	21.27	21.96
Stand. Dev. of m	1.58	1.79	1.67	1.71
Corr. Coeff. r	0.9737	0.9772	0.9761	0.9766
Coeff. Det. (= r^2)	0.9480	0.9549	0.9527	0.9537
Stand. Error of m	4.26	5.21	4.76	4.91
Intercept I	-357.84	-437.67	-278.22	-412.55
Stand. Dev. of I	29.61	33.57	14.08	32.04

DATA FOR SCR25.76 USING 10 S4 DATA

Regression Data	$P_s = 1-j/(n+1)$	$P_s = 1-(j-0.5)/n$	$P_s = 1-(j-0.3)/(n+0.4)$	$P_s = 1-(j-3/8)/(n+1/4)$
Weibull mod. m	16.51	19.98	18.34	18.90
Stand. Dev. of m	1.06	1.56	1.29	1.38
Corr. Coeff. r	0.9839	0.9765	0.9807	0.9794
Coeff. Det. (= r^2)	0.0.9681	0.9536	0.9618	0.9593
Stand. Error of m	3.69	4.47	4.10	4.23
Intercept I	-309.27	-374.07	-343.36	-353.87
Stand. Dev. of I	19.83	29.14	24.16	25.74

DATA FOR SCR19.34 USING 10 S1 DATA

Regression Data	$P_s = 1-j/(n+1)$	$P_s = 1-(j-0.5)/n$	$P_s = 1-(j-0.3)/(n+0.4)$	$P_s = 1-(j-3/8)/(n+1/4)$
Weibull mod. m	11.44	13.77	12.67	13.05
Stand. Dev. of m	1.28	1.73	1.50	1.58
Corr. Coeff. r	0.9537	0.9421	0.9483	0.9463
Coeff. Det. (= r^2)	0.9095	0.8875	0.8993	0.8955
Stand. Error of m	2.56	3.08	2.83	2.12
Intercept I	-214.78	-258.54	-237.87	-244.96
Stand. Dev. of I	23.90	32.48	28.08	29.51

DATA FOR SCR19.34 USING 10 S4 DATA

Regression Data	$P_s = 1-j/(n+1)$	$P_s = 1-(j-0.5)/n$	$P_s = 1-(j-0.3)/(n+0.4)$	$P_s = 1-(j-3/8)/(n+1/4)$
Weibull mod. m	10.22	12.32	11.33	11.67
Stand. Dev. of m	0.60	0.96	0.77	0.83
Corr. Coeff. r	0.9867	0.9766	0.9821	0.9804
Coeff. Det. (= r^2)	0.9735	0.9538	0.9646	0.9612
Stand. Error of m	2.29	2.75	2.53	2.61
Intercept I	-190.87	-230.22	-211.62	-217.99
Stand. Dev. of I	11.10	17.87	14.29	15.44

APPENDIX 4E CONTINUED:

Table 4E.3 Data Obtained on Room Temperature test Rig at 20°C Using a Nominal Span of 32 mm and a Cross-Head Speed of 1.66. x 10^{-6} ms^{-1} (= 0.1 mm/minute):

DATA FOR SCR25.76 USING 10 S1 DATA

Regression Data	$P_s = 1-j/(n+1)$	$P_s = 1-(j-0.5)/n$	$P_s = 1-(j-0.3)/(n+0.4)$	$P_s = 1-(j-3/8)/(n+1/4)$
Weibull mod. m	11.60	13.99	12.86	13.24
Stand. Dev. of m	0.66	1.08	0.86	0.93
Corr. Coeff. r	0.9874	0.9770	0.9826	0.9808
Coeff. Det. (= r^2)	0.9749	0.9545	0.9655	0.9621
Stand. Error of m	2.59	3.13	2.88	2.96
Intercept I	-215.24	-259.54	-238.59	-245.76
Stand. Dev. of I	12.19	19.99	15.89	17.22

DATA FOR SCR25.76 USING 10 S4 DATA

Regression Data	$P_s = 1-j/(n+1)$	$P_s = 1-(j-0.5)/n$	$P_s = 1-(j-0.3)/(n+0.4)$	$P_s = 1-(j-3/8)/(n+1/4)$
Weibull mod. m	12.47	15.05	13.83	14.25
Stand. Dev. of m	0.93	1.35	1.13	1.20
Corr. Coeff. r	0.9786	0.9695	0.9744	0.9729
Coeff. Det. (= r^2)	0.9577	0.9399	0.9495	0.9465
Stand. Error of m	2.79	3.37	3.09	3.19
Intercept I	-230.72	-278.52	-255.88	-263.63
Stand. Dev. of I	17.12	24.87	20.82	22.12

DATA FOR SCR19.34 USING 10 S1 DATA

Regression Data	$P_s = 1-j/(n+1)$	$P_s = 1-(j-0.5)/n$	$P_s = 1-(j-0.3)/(n+0.4)$	$P_s = 1-(j-3/8)/(n+1/4)$
Weibull mod. m	14.46	17.75	16.18	16.71
Stand. Dev. of m	1.25	1.33	1.30	1.31
Corr. Coeff. r	0.9713	0.9782	0.9753	0.9764
Coeff. Det. (= r^2)	0.9434	0.9569	0.9513	0.9534
Stand. Error of m	3.23	3.97	3.62	3.74
Intercept I	-268.35	-329.33	-300.14	-310.07
Stand. Dev. of I	23.20	24.69	23.99	24.20

DATA FOR SCR19.34 USING 10 S4 DATA

Regression Data	$P_s = 1-j/(n+1)$	$P_s = 1-(j-0.5)/n$	$P_s = 1-(j-0.3)/(n+0.4)$	$P_s = 1-(j-3/8)/(n+1/4)$
Weibull mod. m	10.73	13.08	11.96	12.34
Stand. Dev. of m	1.16	1.41	1.28	1.32
Corr. Coeff. r	0.9564	0.9564	0.9572	0.9571
Coeff. Det. (= r^2)	0.9148	0.9147	0.9162	0.9160
Stand. Error of m	2.40	2.92	2.67	2.76
Intercept I	-198.38	-241.73	-221.13	-228.16
Stand. Dev. of I	21.36	26.03	23.59	24.37

APPENDIX 4F DERIVATION OF THE REDUCTION FORMULA FOR THE INTEGRAL AFTER M. LEON AND P. KITTL (1985):

To begin with the rule for integration by parts used in the derivation is obtained as follows:

Given $\int_a^b (u.v)\,dx$ where $u = f(x)$ and $v = h(x)$, and $\frac{d}{dx}(u.w) \equiv u\frac{dw}{dx} + w\frac{du}{dx}$ where $w = g(x)$

Hence, $\int_a^b \left(\frac{d}{dx}(u.w)\right)dx \equiv \int_a^b \left(u\frac{dw}{dx}\right)dx + \int_a^b \left(w\frac{du}{dx}\right)dx \quad \therefore \left|u.w\right|_a^b = \int_a^b \left(u\frac{dw}{dx}\right)dx + \int_a^b \left(w\frac{du}{dx}\right)dx$

$\therefore \int_a^b \left(u\frac{dw}{dx}\right)dx \equiv \left|u.v\right|_a^b - \int_a^b \left(w\frac{du}{dx}\right)dx$ Now let $\frac{dw}{dx} = v \quad \therefore w = \int_a^b v\,dx$

This gives the rule $\int_a^b (u.v)\,dx \equiv \left|u\int v\,dx\right|_a^b - \int_a^b \left[\left(\int v\,dx\right)\frac{du}{dx}\right]dx$ [4D.1]

Equation [4D.1] is now used with the substitutions $m + 1 = n$ and $\emptyset - 1 = x$, to integrate

$I = \int_a^b \frac{(\emptyset - 1)^{m+1}}{\emptyset}\,d\emptyset$ where $b = \sigma/\sigma_L$ and $a = 1$ [4D.2]

Since $\emptyset = x + 1$, $d\emptyset = dx$ and the integration limits $\emptyset = b$ and $\emptyset = a$ become $x = b - 1$ and $x = 0$ respectively. Ignoring the integration limits for the present, equation [4D.2] becomes

$$I_n = \int \frac{x^n}{x+1}\,dx = \int x^{n-1}.\frac{x}{x+1}\,dx = x^{n-1}\int \frac{x}{x+1}\,dx - \int\left[\left(\int \frac{x}{x+1}\,dx\right).\frac{d}{dx}(x^{n-1})\right]dx$$

$$= x^{n-1}[x - \ln(x+1)] - \int([x - \ln(x+1)][n-1]x^{n-2})\,dx$$

$$= x^n - (x^{n-1})\ln(x+1) - (n-1)\int x^{n-2}[x - \ln(x+1)]\,dx$$

$$= x^n - (x^{n-1})\ln(x+1) - (n-1)I^* \quad \text{Now } I^* = \int x^{n-1} - (x^{n-2})\ln(x+1)\,dx$$

$$\therefore I^* = \int x^{n-1}\,dx - \int (x^{n-2})\ln(x+1)\,dx = \frac{x^n}{n} - \int (x^{n-2})\ln(x+1)\,dx = \frac{x^n}{n} - I^{**}$$

$$\text{Now } I^{**} = \ln(x+1)\int x^{n-2}\,dx - \int\left[\left(\int x^{n-2}\,dx\right)\frac{d}{dx}(\ln[x+1])\right]dx$$

$$= \ln(x+1)\left[\frac{x^{n-1}}{n-1}\right] - \int\left(\frac{x^{n-1}}{n-1}\right)\frac{1}{x+1}\,dx = \frac{x^{n-1}}{n-1}\ln(x+1) - \frac{1}{n-1}\int \frac{x^{n-1}}{x+1}\,dx$$

$$\text{So } I_n = x^n - (x^{n-1})\ln(x+1) - (n-1)\left(\frac{x^n}{n} - \left[\frac{x^{n-1}}{n-1}\ln(x+1) - \frac{1}{n-1}\int \frac{x^{n-1}}{x+1}\,dx\right]\right)$$

$$\therefore I_n = x^n - (x^{n-1})\ln(x+1) - \frac{(n-1)x^n}{n} + (x^{n-1})\ln(x+1) - \int \frac{x^{n-1}}{x+1}\,dx$$

$$= x^n - \frac{(n-1)x^n}{n} - \int \frac{x^{n-1}}{x+1}\,dx = x^n\left[1 - \frac{(n-1)}{n}\right] - \int \frac{x^{n-1}}{x+1}\,dx = \frac{x^n}{n} - \int \frac{x^{n-1}}{x+1}\,dx \quad [4D.3]$$

APPENDIX 4F CONTINUED:

Comparing equation [4D.3] with $I_n = \int \frac{x^n}{x+1}\,dx$ shows that $\int \frac{x^{n-1}}{x+1}\,dx = I_{n-1}$; hence the reduction formula is

$$I_n = \frac{x^n}{n} - I_{n-1} \qquad [4D.4]$$

For example, $I_1 = x - I_0 = x - \int \frac{1}{x+1}\,dx = x - \ln(x+1)$; $I_2 = \frac{x^2}{2} - I_1 = \frac{x^2}{2} - x + \ln(x+1)$

$I_3 = \frac{x^3}{3} - I_2 = \frac{x^3}{3} + \frac{x^2}{2} + x - \ln(x+1)$ and so on. The constant of integration implicitly carried through the derivation cancels out when the integral is integrated between limits.

Inserting the integration limits gives $I_n = \int_0^{b-1} \frac{x^n}{x+1}\,dx = \frac{x^n}{n}\Big|_0^{b-1} - \int_0^{b-1} \frac{x^{n-1}}{x+1}\,dx$

where $b = \sigma/\sigma_L$ and $n = m + 1$. Note the integral is not defined for $x = -1$ as $\ln(0) = -\infty$

The computing algorithm to determine I_n for different m values and then evaluate $\ln\xi^*$ is

```
10    for m = m1 to m2 step dm
20    for b = b1 to b2 step db
30    In = lnb : n = m + 1 : gosub 100
40    lnξ* = mlnb + ln(In[n/(b)^n])
50    next b : next m : end
100   for i = 1 to n
110   In = -In + ([b - 1]^i)/i
120   next i : return
```

The following computer programme is written in AMSTRAD LOCOMOTIVE BASIC:

```
10    REM This program evaluates the non-dimensional variables for the
20    REM Weibull function nomogram for a variable stress field in the
30    REM case of a rectangular beam subjected to 3-point flexure after
40    REM Leon, M. and Kittl,P., J. Mater. Sci., Vol.29, (1985), pp. 3778-3782.
50    PRINT#8, CHR$(27);CHR$(108);CHR$(9)
60    CLEAR : MODE 2
70    REM List of variables : m = Weibull modulus : n = m + 1
80    REM s = sigma/sigmaL : z = ln(zi)
90    PRINT "Please enter the Weibull modulus (m) range and the increment (dm) "
100   PRINT "as m(min), m(max), dm [CR] : (Note m must be >= 0)"
110   PRINT : INPUT m1,m2,dm
120   WHILE m1 < 0 OR m2 < 0 : PRINT : PRINT "Both m(min) and m(max) must be >= 0." : INPUT "Please
      re-enter m(min),m(max),dm : ",m1,m2,dm : WEND
130   WHILE m2 - m1 < 0 OR dm < 0 : PRINT : PRINT "m(min) must be less than m(max) and/or dm must
      be a positive number > 0." : INPUT "Please re-enter m(min),m(max),dm : ",m1,m2, dm : WEND
140   PRINT : PRINT "Now enter the sigma/sigmaL ratio (s) range and increment (ds) "
150   PRINT "as s(min),s(max),ds [CR] : (Note s cannot = 1)
160   PRINT : INPUT s1,s2,ds
170   WHILE s1 = 1 or s2 = 1 : PRINT : PRINT "Both s(min) and s(max) must be positive numbers other
      than 1." : INPUT "Please re-enter s(min),s(max),ds : ",s1,s2,ds : WEND
180   WHILE s2 - s1 < 0 OR ds < 0 : PRINT : PRINT "s(min) must be less than s(max) and/or ds must
      be a positive number > 0." : INPUT "Please re-enter s(min),s(max),ds : ",s1,s2,ds : WEND
190   REM Calculation of ln(zi) as a function of ln(sigma/sigmaL)
200   CLS
210   FOR j = m1 TO m2 STEP dm
220   CLS : x = 0 : GOSUB 290 : x = 8 : GOSUB 290
230   FOR i = s1 TO s2 STEP ds
```

APPENDIX 4F CONTINUED:

```
240    rfi = LOG(i) : n = j + 1 : GOSUB 330
250    z = j * LOG(i) + LOG(rfi * n/(i^n))
260    x = 0 : GOSUB 380 : x = 8 : GOSUB 380
270    NEXT i : NEXT j
280    END
290    REM Print subroutine 1
300    PRINT#x : PRINT#x, "Weibull modulus (m) = ";j : PRINT#x
310    PRINT#x : "sigma/sigmaL"SPC(3)"ln(sigma/sigmaL)"SPC(3)"def. integral"SCPC(3)"ln(zi function)"
       : PRINT#x
320    RETURN
330    REM subroutine to evaluate definite integral using reduction formula
340    FOR k = 1 TO n
350    rfi = -1 * rfi + ((i - 1)^k)/k
360    NEXT k
370    RETURN
380    REM Print subroutine 2
390    PRINT#x, USING"######.####";i;
400    PRINT#x, TAB(17) USING"###.####";LOG(i);
410    PRINT#x, TAB(36) USING"##.####^^^^";rfi;
420    PRINT#x, TAB(52) USING"##.####^^^^";z
430    RETURN
```

APPENDIX 4G ELEVATED TEMPERATURE FLEXURAL STRENGTH DATA FOR SCR25.76, SCR19.34 AND SCF5 USING THREE-POINT BENDING, A NOMINAL SPAN-TO-WIDTH RATIO OF 4 AND A CROSS-HEAD SPEED OF 1.66×10^{-5} ms^{-1} (= 1 mm/minute):

Table 4G.1 Data Obtained on High Temperature Test Rig at 250°C

DATA FOR SCR25.76

TEST #.	B (mm)	W (mm)	P (N)	x (mm)	t (s)	x/W	β-Value	S1 (MPa)	S2 (MPa)	S3 (MPa)	S4 (MPa)
MA601	4.047	7.719	528	2.0	17	0.259	+0.0868	104.3	99.8	91.1	94.1
MA602	4.070	7.699	438	1.0	15	0.130	+0.0137	86.5	82.7	81.0	81.4
MA603	4.151	7.734	652	3.0	20	0.388	+0.0640	125.1	119.7	101.4	104.0
MA604	4.057	7.689	540	0.5	16	0.065	+0.0137	107.2	102.6	103.8	104.3
MA605	4.093	7.695	750	3.0	18	0.390	+0.0640	147.4	141.0	119.5	122.6
MA606	4.128	7.676	723	0.0	18	0.000	-0.1332	141.6	135.5	141.6	135.5
MA607	4.018	7.716	493	1.5	16	0.194	+0.0868	98.1	93.9	88.9	91.6
MA608	4.082	7.719	729	0.0	18	0.000	-0.1332	142.7	136.6	142.7	136.6

DATA FOR SCR19.34

TEST #.	B (mm)	W (mm)	P (N)	x (mm)	t (s)	x/W	β-Value	S1 (MPa)	S2 (MPa)	S3 (MPa)	S4 (MPa)
MB601	4.081	7.715	739	1.0	19	0.130	+0.0137	144.9	138.6	135.8	136.4
MB602	4.053	7.714	731	1.5	18	0.194	+0.0868	144.3	138.1	130.7	134.8
MB603	4.051	7.736	967	0.5	20	0.065	+0.0137	190.0	181.7	184.0	184.8
MB604	4.052	7.752	943	1.0	19	0.129	+0.0137	184.4	176.4	172.8	173.6
MB605	3.996	7.701	766	0.5	18	0.065	+0.0137	153.9	147.3	149.1	149.8
MB606	4.089	7.731	786	2.0	19	0.259	+0.0868	153.2	146.5	133.9	138.2
MB607	4.032	7.725	872	2.0	18	0.259	+0.0868	172.6	165.1	150.9	155.7
MB608	4.069	7.721	841	1.5	19	0.194	+0.0868	165.1	158.0	149.5	154.2

The above data were obtained using alumina support rollers with a 31.75 mm span.

Table 4G.2 Data Obtained on High Temperature Test Rig at 500°C

DATA FOR SCR25.76

TEST #.	B (mm)	W (mm)	P (N)	x (mm)	t (s)	x/W	β-Value	S1 (MPa)	S2 (MPa)	S3 (MPa)	S4 (MPa)
MA41 a	4.154	7.624	674	1.5	23	0.197	+0.0868	132.9	136.6	120.3	124.0
MA42 a	4.144	7.634	748	1.5	23	0.196	+0.0868	147.5	151.6	133.5	137.6
MA43 a	4.130	7.625	580	0.5	16	0.066	+0.0137	115.0	115.5	111.4	111.9
MA301 b	4.002	7.627	491	0.5	14	0.066	+0.0137	99.7	95.5	96.6	97.0
MA44 c	4.052	7.713	721	0.0	24	0.000	-0.1332	142.2	136.0	142.2	136.0
MA45 c	4.042	7.734	507	1.0	22	0.129	+0.0137	99.7	95.4	93.4	93.8
MA46 c	4.065	7.740	782	3.5	24	0.452	+0.0421	152.6	146.0	118.9	121.0
MA47 d	4.070	7.694	841	1.0	22	0.130	+0.0137	166.2	159.1	155.8	156.5

APPENDIX 4G CONTINUED:

Table 4G.2 Continued:

DATA FOR SCR19.34

TEST #.		B (mm)	W (mm)	P (N)	x (mm)	t (s)	x/W	β-Value	S1 (MPa)	S2 (MPa)	S3 (MPa)	S4 (MPa)
MB41	b	4.136	7.637	703	0.5	18	0.065	+0.0137	137.8	131.9	133.5	134.1
MB42	b	4.190	7.653	707	0.5	18	0.065	+0.0137	136.3	130.4	131.9	132.5
MB43	b	4.145	7.640	735	0.5	18	0.065	+0.0137	143.7	137.5	139.1	139.8
MB301	b	3.984	7.649	505	2.0	14	0.261	+0.0868	102.5	98.1	89.5	92.3
MB44	c	4.050	7.747	978	1.5	26	0.194	+0.0868	191.3	183.0	173.2	178.6
MB45	c	3.993	7.713	1179	1.0	29	0.130	+0.0137	235.9	225.7	221.0	222.1
MB46	d	4.331	7.733	1143	0.5	23	0.065	+0.0137	210.2	201.1	203.6	204.5
MB47	d	4.049	7.730	912	1.0	21	0.129	+0.0137	179.5	171.8	168.2	169.0

a Silicon nitride knife-edge supports with 31.74 mm span
b Silicon nitride knife-edge supports with 31.53 mm span
c Silicon nitride knife-edge supports with 31.69 mm span
d Alumina roller supports with 31.75 mm span

Table 4G.3 Data Obtained on High Temperature Test Rig at 600°C

DATA FOR SCR25.76

TEST #.		B (mm)	W (mm)	P (N)	x (mm)	t (s)	x/W	β-Value	S1 (MPa)	S2 (MPa)	S3 (MPa)	S4 (MPa)
MA51	a	4.129	7.645	806	0.5	19	0.065	+0.0137	158.0	151.2	153.0	153.7
MA52	a	4.148	7.620	853	0.0	19	0.000	-0.1332	167.5	160.3	167.5	160.3
MA53	a	4.132	7.647	817	0.5	19	0.065	+0.0137	159.9	153.0	154.8	155.6
MA201	a	4.016	7.635	503	0.0	15	0.000	-0.1332	101.6	97.2	101.6	97.2
MA54	b	4.028	7.737	644	2.0	21	0.258	+0.0868	127.2	121.7	111.2	114.8
MA55	b	4.095	7.708	762	1.0	20	0.130	+0.0137	149.2	142.7	139.8	140.4
MA56	b	4.031	7.713	802	0.0	20	0.000	-0.1332	159.3	152.4	159.3	152.4
MA57	b	4.044	7.734	530	4.5	18	0.582	+0.0421	104.3	99.8	74.8	76.2

DATA FOR SCR19.34

TEST #.		B (mm)	W (mm)	P (N)	x (mm)	t (s)	x/W	β-Value	S1 (MPa)	S2 (MPa)	S3 (MPa)	S4 (MPa)
MB51	a	4.141	7.602	908	1.0	20	0.131	+0.0137	179.4	171.8	168.1	168.9
MB52	a	4.161	7.640	874	0.5	17	0.065	+0.0137	170.2	162.9	164.8	165.5
MB53	a	4.129	7.653	880	1.0	19	0.131	+0.0137	172.1	164.7	161.2	161.9
MB201	a	3.938	7.628	562	2.5	17	0.328	+0.0640	116.0	111.0	97.6	100.0
MB54	b	4.009	7.704	1045	2.0	25	0.260	+0.0868	209.2	200.1	182.8	188.7
MB55	b	4.079	7.738	825	1.5	20	0.194	+0.0868	160.9	153.9	145.7	150.2
MB56	b	4.078	7.739	868	1.0	20	0.129	+0.0137	169.3	161.9	158.6	159.3
MB57	b	4.079	7.748	1018	1.5	23	0.194	+0.0868	198.0	189.4	179.3	184.9

a Silicon nitride knife-edge supports with 31.53 mm span
b Alumina roller supports with 31.75 mm span

APPENDIX 4G CONTINUED:

Table 4G.4 Data Obtained on High Temperature Rig at 700°C

DATA FOR SCR25.76

TEST #.		B (mm)	W (mm)	P (N)	x (mm)	t (s)	x/W	β-Value	S1 (MPa)	S2 (MPa)	S3 (MPa)	S4 (MPa)
MA61	a	4.083	7.630	507	1.0	15	0.131	+0.0137	100.9	96.5	94.5	94.9
MA62	a	4.073	7.633	464	1.0	13	0.131	+0.0137	92.5	88.5	86.6	87.0
MA63	a	4.105	7.622	566	0.0	15	0.000	-0.1332	112.2	107.4	112.2	107.4
MA101	a	3.784	7.633	536	3.0	15	0.393	+0.0640	115.0	110.0	93.1	95.5
MA64	b	4.078	7.715	770	2.5	24	0.324	+0.0640	151.1	144.6	127.3	130.4
MA65	b	4.005	7.693	778	2.5	23	0.325	+0.0640	156.3	149.6	131.7	134.9
MA66	b	4.020	7.721	554	1.0	20	0.130	+0.0137	110.1	105.3	103.2	103.6
MA67	b	4.003	7.716	743	2.5	23	0.324	+0.0640	148.5	142.1	125.1	128.2

DATA FOR SCR19.34

TEST #.		B (mm)	W (mm)	P (N)	x (mm)	t (s)	x/W	β-Value	S1 (MPa)	S2 (MPa)	S3 (MPa)	S4 (MPa)
MB61	a	4.096	7.649	886	2.0	19	0.261	+0.0868	174.9	167.3	152.7	157.6
MB62	a	4.112	7.603	874	0.0	19	0.000	-0.1332	173.9	166.5	173.9	166.5
MB63	a	4.102	7.604	921	0.0	20	0.000	-0.1332	183.7	175.8	183.7	175.8
MB101	a	3.770	7.613	472	0.5	14	0.066	+0.0137	102.2	97.8	98.9	99.4
MB64	b	4.025	7.728	1108	1.5	29	0.194	+0.0868	219.5	210.0	198.8	205.0
MB65	b	3.999	7.757	1069	0.0	28	0.000	-0.1332	211.6	202.4	211.6	202.4
MB66	b	4.063	7.733	699	4.5	23	0.582	+0.0421	137.0	131.1	98.2	100.0
MB67	b	4.022	7.721	841	2.0	26	0.259	+0.0868	167.0	159.8	146.0	150.7

a Silicon nitride knife-edge supports with 31.53 mm span
b Alumina roller supports with 31.75 mm span

Table 4G.5 Data Obtained on High Temperature Rig at 750°C and 800°C

DATA FOR SCR25.76

TEST #.		B (mm)	W (mm)	θ (°C)	
MA701	a	4.048	7.681	750	Plastic flow occurred when the linear response limit was reached at a load of ≈ 255 N and a cross-head displacement of ≈ 0.43 mm.
MA71	b	3.935	7.629	800	Plastic flow occurred when the linear response limit was reached at a load of ≈ 165 N and a cross-head displacement of ≈ 0.33 mm.
MA501	b	4.144	7.624	800	Plastic flow occurred when the linear response limit was reached at a load of ≈ 143 N and a cross-head displacement of ≈ 0.31 mm

DATA FOR SCR19.34

TEST #.		B (mm)	W (mm)	θ (°C)	
MB701	a	4.006	7.742	750	Plastic flow occurred when the linear response limit was reached at a load of ≈ 243 N and a cross-head displacement of ≈ 0.43 mm.
MB71	b	3.739	7.613	800	Plastic flow occurred when the linear response limit was reached at a load of ≈ 153 N and a cross-head displacement of ≈ 0.38 mm.
MB501	b	3.933	7.617	800	Plastic flow occurred when the linear response limit was reached at a load of ≈ 161 N and a cross-head displacement of ≈ 0.38 mm

a Silicon nitride knife-edge supports with 31.53 mm span
b Alumina roller supports with 31.75 mm span

APPENDIX 4G CONTINUED:

Table 4G.6 Data Obtained on High Temperature Test Rig for SCF5

DATA AT 600°C

TEST #.	B (mm)	W (mm)	P (N)	x (mm)	t (s)	x/W	β-Value	S1 (MPa)	S2 (MPa)	S3 (MPa)	S4 (MPa)
MC4	3.724	7.494	624	1.0	24	0.133	+0.0137	142.1	136.1	133.1	133.8
MD4	3.662	7.791	447	1.5	21	0.193	+0.0868	95.8	91.6	86.7	89.4

DATA AT 745°C

TEST #.	B (mm)	W (mm)	P (N)	x (mm)	t (s)	x/W	β-Value	S1 (MPa)	S2 (MPa)	S3 (MPa)	S4 (MPa)
MC2	3.884	7.299	667	2.0	22	0.274	+0.0868	155.1	148.8	135.6	139.7

DATA AT 800°C

TEST #.	B (mm)	W (mm)	P (N)	x (mm)	t (s)	x/W	β-Value	S1 (MPa)	S2 (MPa)	S3 (MPa)	S4 (MPa)
MC1	3.975	7.262	1071	1.5	34	0.207	+0.0868	243.3	233.4	220.3	226.8
MD1	3.665	7.906	1220	7.0	30	0.885	+0.0095	253.6	242.4	141.8	142.6

DATA AT 850°C

MD2	4.182	7.909	902	0.0	43	0.000	-0.1332	155.1	148.8	135.6	139.7

MC3 4.132 7.647 Plastic flow occurred when the linear response limit was reached at a load of ≈ 502 N and a cross-head displacement of ≈ 0.72 mm.

DATA AT 900°C

MD3 4.079 7.879 Plastic flow occurred when the linear response limit was reached at a load of ≈ 86 N and a cross-head displacement of ≈ 0.15 mm.

All the above data were obtained using alumina roller supports with a span of 31.75 mm.
D denotes that the Cr_2O_3 precursor compound was sodium dichromate ($Na_2Cr_2O_7$).
C denotes that the Cr_2O_3 precursor compound was either sodium dichromate or chromate (Na_2CrO_4).

APPENDIX 5A DERIVATION OF ELASTIC STRAIN ENERGY RELEASE RATE EQUATIONS

A cracked plate of thickness B with a through-thickness semi-crack of length c will be considered in terms of the energy released as the end of the crack extends a distance δc when the crack is subject to a uniaxial tensile load P applied perpendicular to the crack plane at the ends of the plate. To begin with a result from linear elasticity theory will be confirmed by a geometrical construction. According to linear elasticity theory the work done by the external load on the plate during an infinitesimal crack extension δc, U_w is equal to twice the increase in the elastic strain energy of the system due to the presence of the crack, $-2U_c$, i.e., the negative potential energy of the load. Figure 5A.1 shows the load versus crack length curves (i) before the crack extension δC (OA) and afterwards (OB) under constant load (dead-weight loading) and (ii) before the crack extension δC (OA) and afterwards (OD) at constant load application-surface displacement (infinitely stiff testing machine). Consider the following:

Case 1 : Constant Displacement

When crack extension occurs at constant displacement the applied load does no work on the plate and $\delta U_w = 0$, and the load decreases from P_o to P_1 since the stiffness of the plate has decreased due to the crack extension, and the elastic strain energy of the plate due to the presence of the crack decreases because energy has been used to create new crack surfaces, i.e., to extend the crack. The elastic strain energy released is represented by area OAD, being the difference in the elastic strain energy of the plate before crack extension (area OAE) and that after crack extension (area ODE), i.e., $x_o(P_1 - P_o)/2$.

Case 2 : Constant Load

When crack extension occurs at constant load, the load-application surface is displaced from x_o to x_1, i.e., the applied load moves a distance $x_1 - x_o = x$ and does work on the plate equal to $P_o x$ which is represented by area ABFE. Simultaneously, the elastic strain energy of the plate due to the presence of the crack is increased by an amount represented by the difference in the strain energy of the plate before crack extension (area OAE) and after crack extension (area OBF), i.e., $P_o x/2$. So of the work done on the plate by the applied load only $P_o x - P_o x/2 = P_o x/2$ is available to extend the crack; thus $U_w = -2U_c$.

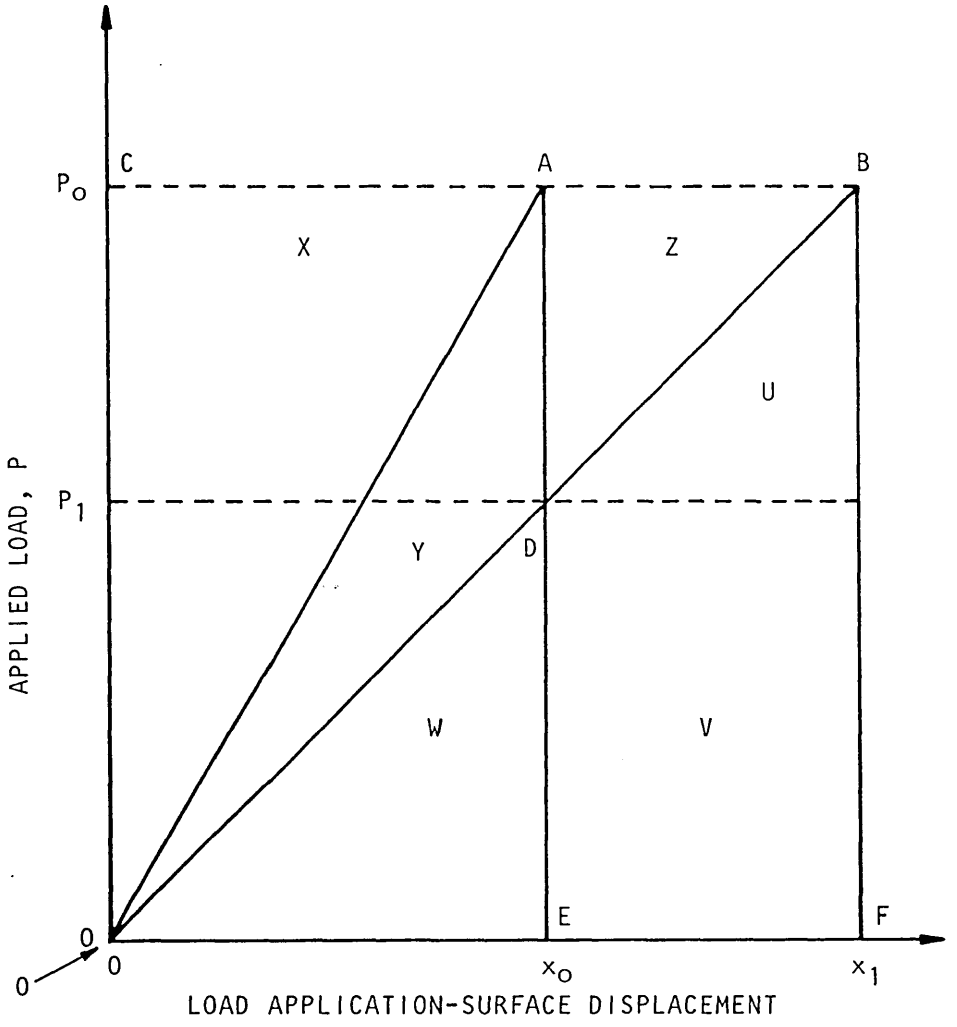
In Figure 5A.1 it can be seen that area Z ≡ area U, and that area OBF ≡ area U + V + W, area OAE ≡ area W + Y and area OAB ≡ Y + Z. Therefore, area OBF - area OAE = area U + V - Y. Furthermore, area X + Y + Z ≡ U + V + W, i.e., area X + Y ≡ area V + W and area X ≡ area W + Y. Using these last two identities shows that area W + 2Y ≡ area V + W, i.e., area 2Y ≡ area V; thus area OBF - area OAE = area U + V - Y ≡ area Y + U ≡ area Y + Z ≡ area OAB. Now in the limit of δc tending to zero, area Z tends to zero, so area OAB tends to area OAD and the decrease in the elastic strain energy of the plate under constant displacement conditions is equal in magnitude to the increase in the elastic strain energy under constant load conditions.

The strain energy release rate, G, per unit thickness is defined as

$$G = -\frac{d}{dc}(U_w + U_c) \qquad [5A.1]$$

See Chapter 5 section 5.1 and Chapter 4 section 4.3.1. The equality of the magnitudes of the changes in the elastic strain energy due to the presence of the crack under constant displacement and constant load conditions means that under fixed displacement conditions ($U_w = 0$), $G = -dU_c/dc$ while under constant load conditions ($U_w = -2U_c$), $G = dU_c/dc$, i.e., the strain energy release rate is equal in magnitude to dU_c/dc under both constant displacement and constant load conditions; under the latter conditions the work done by the applied load increases the elastic strain energy of the plate and provides the energy for crack extension, while under the former conditions the applied load does no work on the plate and the elastic strain energy decreases as the crack extends. Since $U_c = (\beta\pi c^2\sigma^2)/E$ where $\beta = 1$ for plane stress and $(1 - \nu^2)$ for plane strain conditions, the magnitude of G is given by

$$\frac{dU_c}{dc} = G = \frac{\beta\pi\sigma^2 c}{E} \qquad [5A.2]$$



Note: U, V, W, X, Y and Z denote areas
A, B, C, D, E and F denote points

Figure 5A.1 Schematic Applied Load Versus Load Application-Surface Displacement Diagrams for Constant Displacement and Constant Load Conditions.

APPENDIX 5A CONTINUED:

The derivation which follows is modelled on the derivation given by H.L. Ewalds and R.J.H. Wanhill (1984) after Irwin:

Since the plate thickness is B, and $U_w = -Px$ and $U_c = Px/2$, equation [5A.1] can be written as

$$G = -\frac{1}{B}\left(-P.\frac{dx}{dc} + \frac{1}{2}.\frac{J}{dc}(Px)\right) \qquad [5A.3]$$

where P is the applied tensile load and x the total load application-surface displacement. Now the compliance of the plate, ξ, is defined as the load application-surface displacement divided by the load, i.e., the reciprocal of stiffness. So $\xi = x/P$ and has units of mN^{-1}; thus [5A.3] becomes

$$G = -\frac{1}{B}\left(-P.\frac{d}{dc}(\xi P) + \frac{1}{2}.\frac{d}{dc}(\xi P^2)\right) = -\frac{1}{B}\left(-P\xi.\frac{dP}{dc} - P^2.\frac{d\xi}{dc} + \frac{1}{2}P^2.\frac{d\xi}{dc} + P\xi.\frac{dP}{dc}\right) = -\frac{1}{B}\left(-\frac{1}{2}.P^2.\frac{d\xi}{dc}\right)$$

Therefore,

$$G = \frac{P^2}{2B}.\frac{d\xi}{dc} \qquad [5A.4]$$

Now consider the magnitude of the change dU_c/dc

$$(1/B)(dU_c/dc) = (1/2B)(dPx/dc) = (1/2B)\left(P.\frac{dx}{dc} + x.\frac{dP}{dc}\right) = (1/2B)\left(P.\frac{d}{dc}(\xi P) + P\xi.\frac{dP}{dc}\right)$$

$$= (1/2B)\left(P^2.\frac{d\xi}{dc} + 2P\xi.\frac{dP}{dc}\right) = \frac{P^2}{2B}.\frac{d\xi}{dc} + \frac{x}{B}.\frac{dP}{dc} \qquad [5A.5]$$

For constant load conditions, P is constant and hence $dP/dc = 0$; so equation [5A.5] becomes

$$(1/B)(dU_c/dc)P = \frac{P2}{2B}.\frac{d\xi}{dc} \qquad [5A.6]$$

For constant displacement conditions, x is constant and hence $dx/dc = 0$; so equation [5A.5] becomes

$$(1/B)(dU_c/dc)_x = \frac{P^2}{2B}.\frac{d\xi}{dc} + \frac{x}{B}.\frac{d}{dc}(x/\xi)$$

$$= \frac{P^2}{2B}.\frac{d\xi}{dc} + \frac{x}{B}\left(x.\frac{d\xi^{-1}}{dc} + \xi^{-1}.\frac{dx}{dc}\right)_x$$

$$= \frac{P^2}{2B}.\frac{d\xi}{dc} + \frac{x^2}{B}.\frac{d\xi^{-1}}{d\xi}.\frac{d\xi}{da}$$

$$= \frac{P^2}{2B}.\frac{d\xi}{dc} - \frac{P^2}{B}.\frac{d\xi}{dc}$$

$$= -\frac{P^2}{2B}.\frac{d\xi}{dc} \qquad [5A.7]$$

Hence for both constant displacement and constant load conditions, the magnitude of G is equal to (1/B)(dUC/dc) and is independent of the loading configuration for an infinitesimal crack extension, and G is given by

$$G = \frac{P^2}{2B}.\frac{d\xi}{dc} = (1/B)(dU_c/dc)_P = -(1/B)(dU_c/dc)_x \qquad [5A.8]$$

Note that for a crack of length 2c which extends by δc at each end, i.e., a total of $2\delta c$, G must be multiplied by a factor of 1/2.

APPENDIX 5B INDENTATION FRACTURE TOUGHNESS DATA AFTER M.T. LAUGIER (1985) AS DERIVED FROM ANTIS ET AL. (1981):

Table 5B.1 Data after Laugier:

MATERIAL	$P/c^{3/2}$ (MPa.m$^{1/2}$)	E/H	k_A	k_L	k_{EC}	K_cA		K_cL (MPa.m$^{1/2}$)		K_cEC		K_{1c}
							*		*		*	$
WC-Co	210	43.6	0.00865	0.00456	0.0126	22		26		20		12
Si_3N_4 (NC132) #	60	16.2	0.0166	0.0103	0.0219	3.9	4.1	3.8	3.9	3.8	4.0	4.0
SiC	50	18.2	0.0188	0.0114	0.0251	3.4	3.6	3.4	3.5	3.4	3.5	4.0
Al_2O_3 (AD999) #	36	20.2	0.0241	0.0145	0.0326	2.6	2.8	2.6	2.7	2.5	2.6	3.9
Al_2O_3 (AD90) #	31	29.8	0.0171	0.0096	0.0241	2.7	2.9	3.0	3.0	2.5	2.6	2.9
Glass ceramic #	43	12.8	0.0162	0.0105	0.0210	2.5	2.6	2.3	2.4	2.5	2.6	2.5
Si_3N_4 (NC350)	33	17.7	0.0144	0.0088	0.0192	2.2	2.4	2.2	2.3	2.2	2.3	2.0
Sapphire	22	19.5	0.0216	0.0130	0.0291	1.6	1.6	1.6	1.6	1.5	1.6	2.11
Glass (AS) #	19	13.5	0.0130	0.0084	0.0169	1.1	1.2	1.1	1.1	1.1	1.2	0.91
Glass (SLI) #	14	12.7	0.0148	0.0096	0.0192	0.80	0.85	0.76	0.77	0.82	0.86	0.74
Glass (SLII) #	14	13.0	0.0148	0.0096	0.0192	0.80	0.85	0.76	0.77	0.82	0.86	0.75
Glass LA #	14	13.3	0.0133	0.0086	0.0172	0.82	0.87	0.78	0.79	0.83	0.87	0.68
Si	13	15.8	0.0135	0.0085	0.0178	0.83	0.88	0.81	0.83	0.82	0.86	0.70

$ Experimental results
* Predicted toughness data when WC-Co is excluded
Materials designated as "reference materials" by Ponton after Antis et al.(1981)

Mean k_A = 0.016, S.D. = 0.004; v = 25% Mean k_A' = 0.017, S.D. = 0.004, v = 21%
Mean k_L = 0.0098, S.D. = 0.0025; v = 25.5% Mean k_L' = 0.010, S.D. = 0.002, v = 19%
Mean k_{EC} = 0.021, S.D. = 0.006; v = 26% Mean k_{EC}' = 0.022, S.D. = 0.005, v = 23%

' prime indicates WC-Co has been excluded and v denotes coefficient of variation

Table 5B.2 Mean k_A, k_L and k_{EC} values calculated using k_A, k_L and k_{EC} data above:

(a) Using all data above (12 data):

Mean k_A = 0.0160 s.d. = 0.0041 CV = 26%
Mean k_L = 0.00981 s.d. = 0.00251 CV = 25.6%
Mean k_{EC} = 0.0214 s.d. = 0.0056 CV = 26%

(b) Using all data except WC-Co data (11 data):

Mean k_A = 0.0167 s.d. = 0.0036 CV = 21%
Mean k_L = 0.0103 s.d. = 0.0020 CV = 19%
Mean k_{EC} = 0.0222 s.d. = 0.0051 CV = 23%

(c) Using the data denoted by # (indicating the designated well-behaved, "reference" materials used by Antis et al. to obtain their "calibration" constant of 0.016 ± 0.004 (8 data):

Mean k_A = 0.0164 s.d. = 0.0037 CV = 23%
Mean k_L = 0.0102 s.d. = 0.0020 CV = 20%
Mean k_{EC} = 0.0218 s.d. = 0.0054 CV = 25%

s.d. is the sample standard deviation and CV is the coefficient of variation
k_A, k_L and k_{EC} refer to the calibration constants for the Antis et al., Laugier, and Evans and Charles fracture toughness equations.

APPENDIX 5C PLANE STRAIN FRACTURE TOUGHNESS DATA FOR SCR25.76, SCR19.34, SCF5 AND SCR19.13 AS DETERMINED USING SINGLE-EDGE NOTCHED BEAM (SENB) SPECIMENS (ASTM E399-81) LOADED IN THREE-POINT BENDING (NOMINALLY S/W = 4) AT A CROSS-HEAD SPEED OF 1 MM/MINUTE IN AIR

Table 5C.1 Room Temperature Data

Data for SCR25.76 at 19°C using a nominal span and notch width of 31.53 mm and 0.152 mm respectively

TEST #.	a (mm)	B (mm)	W (mm)	a/W	P (N)	t_F (s)	Comp. Fac. (Y)	K_{1C} (MPa.m$^{1/2}$)
AK12	1.200	4.019	7.894	0.153	211	12	1.7496	2.44
AK14	1.194	4.040	7.850	0.152	217	12	1.7498	2.49
AK17	1.194	4.019	7.856	0.152	202	13	1.7498	2.33
AK20	1.219	4.027	7.867	0.155	160	10	1.7490	1.85
AK32	1.192	4.026	7.865	0.152	202	8	1.7499	2.32
AK37 *	1.238	4.101	7.871	0.157	199	14	1.7484	2.29
AK38 *	1.226	4.096	7.870	0.156	202	8	1.7488	2.32

Data for SCR19.34 at 19°C using a nominal span and notch width of 31.53 mm and 0.152 mm respectively

TEST #.	a (mm)	B (mm)	W (mm)	a/W	P (N)	t_F (s)	Comp. Fac. (Y)	K_{1C} (MPa.m$^{1/2}$)
BK9	1.219	4.019	7.837	0.156	157	11	1.7489	1.84
BK17	1.219	4.003	7.852	0.156	150	10	1.7488	1.77
BK30	1.219	4.049	7.835	0.156	164	11	1.7488	1.91
BK32	1.219	4.038	7.834	0.156	151	10	1.7488	1.76
BK26	1.219	4.016	7.830	0.156	156	6	1.7488	1.83
BK16 *	1.238	3.999	7.829	0.158	153	10	1.7483	1.83
BK24 *	1.251	4.023	7.827	0.160	158	10	1.7479	1.89

* span of 31.75 mm using alumina roller supports instead of silicon nitride knife-edge supports

Data for SCF5 at 20°C using a nominal span and notch width of 31.75 mm and 0.152 mm respectively

TEST #.	a (mm)	B (mm)	W (mm)	a/W	P (N)	t_F (s)	Comp. Fac. (Y)	K_{1C} (MPa.m$^{1/2}$)
DK5	1.283	3.614	8.124	0.158	172	17	1.7483	2.15
CK5	1.187	3.699	7.632	0.161	145	9	1.7477	2.07
DK6	1.207	4.046	8.055	0.150	175	8	1.7505	1.93
CK6	1.232	4.920	7.297	0.169	174	7	1.7468	1.94

These data and all subsequent data for SCF5 were obtained using alumina roller supports.

Data for SCR19.13 at 24°C using a nominal span and notch width of 32 mm and 0.27 mm respectively

TEST #.	a (mm)	B (mm)	W (mm)	a/W	P (N)	t_F (s)	Comp. Fac. (Y)	K_{1C} (MPa.m$^{1/2}$)
BK1	0.90	4.02	7.88	0.11	90	--	1.772	0.9
BK2	1.33	3.97	7.87	0.17	85	--	1.747	1.1
BK3	0.87	4.01	7.88	0.11	102	--	1.775	1.0
BK4	1.28	4.01	7.85	0.16	98	--	1.747	1.2
BK5	0.86	4.02	7.87	0.11	110	--	1.776	1.1

Note the notch depth (a), the specimen breadth (B) and width (W) data for SCR19.13 are only quoted to within ± 0.01 mm because the dimensional uniformity was not as good as for the other materials, especially SCR25.76 and SCR19.34 (having been prepared using different equipment). Also the SCR19.13 specimens were tested on the room temperature testing rig.

APPENDIX 5C CONTINUED:

Table 5C.2 Data at 250°C

Data for SCR25.76 using a nominal span and notch width of 31.75 mm and 0.152 mm respectively

TEST #.	a (mm)	B (mm)	W (mm)	a/W	P (N)	t_F (s)	Comp. Fac. (Y)	K_{1C} (MPa.$m^{1/2}$)
AK5	1.251	3.977	7.854	0.159	124	8	1.7480	1.49
AK22	1.251	4.023	7.862	0.159	111	9	1.7481	1.31
AK23	1.251	3.983	7.862	0.159	122	8	1.7481	1.46
AK34	1.245	3.984	7.866	0.158	133	8	1.7482	1.59
AK35	1.245	4.012	7.865	0.158	123	11	1.7482	1.46

Data for SCR19.34 using a nominal span and notch width of 31.75 mm and 0.152 mm respectively

TEST #.	a (mm)	B (mm)	W (mm)	a/W	P (N)	t_F (s)	Comp. Fac. (Y)	K_{1C} (MPa.$m^{1/2}$)
BK2	1.270	4.030	7.816	0.162	108	8	1.7475	1.30
BK11	1.264	4.005	7.836	0.161	116	8	1.7477	1.40
BK25	1.270	3.964	7.827	0.162	107	8	1.7475	1.31
BK36	1.257	4.032	7.826	0.161	115	8	1.7478	1.37
BK38	1.245	4.054	7.814	0.159	116	8	1.7480	1.38

The above data for SCR25.76 and SCR19.34 were obtained using alumina roller supports.

Table 5C.3 Data at 500°C

Data for SCR25.76 using a nominal span and notch width of 31.53 mm and 0.152 mm respectively

TEST #.	a (mm)	B (mm)	W (mm)	a/W	P (N)	t_F (s)	Comp. Fac. (Y)	K_{1C} (MPa.$m^{1/2}$)
AK8	1.194	4.043	7.850	0.152	151	14	1.7498	1.73
AK10	1.194	3.903	7.847	0.152	147	14	1.7498	1.75
AK19	1.219	3.886	7.868	0.155	132	13	1.7490	1.58
AK27	1.194	4.007	7.855	0.152	145	13	1.7498	1.68
AK21	1.207	4.010	7.870	0.153	100	6	1.7494	1.16

Data for SCR19.34 using a nominal span and notch width of 31.53 mm and 0.152 mm respectively

TEST #.	a (mm)	B (mm)	W (mm)	a/W	P (N)	t_F (s)	Comp. Fac. (Y)	K_{1C} (MPa.$m^{1/2}$)
BK8	1.219	4.051	7.833	0.156	130	14	1.7488	1.51
BK10	1.219	4.041	7.837	0.156	152	13	1.7489	1.77
BK21	1.219	4.012	7.811	0.156	128	11	1.7487	1.51
BK29	1.219	4.005	7.835	0.156	127	11	1.7488	1.49
BK15	1.207	4.047	7.836	0.154	105	6	1.7492	1.21

The above data for SCR25.76 and SCR19.34 were obtained using silicon nitride knife-edge supports

APPENDIX 5C CONTINUED:

Table 5C.4 Data at 600°C

Data for SCR25.76 using a nominal span and notch width of 31.53 mm and 0.152 mm respectively

TEST #.	a (mm)	B (mm)	W (mm)	a/W	P (N)	t_F (s)	Comp. Fac. (Y)	K_{1C} (MPa.$m^{1/2}$)
AK1	1.219	3.895	7.865	0.155	163	13	1.7490	1.95
AK6	1.194	4.038	7.852	0.152	167	13	1.7498	1.92
AK11	1.194	4.017	7.853	0.152	189	14	1.7498	2.18
AK24	1.194	4.035	7.860	0.152	144	12	1.7499	1.65
AK30	1.194	3.993	7.858	0.152	125	8	1.7498	1.45

Data for SCR19.34 using a nominal span and notch width of 31.53 mm and 0.152 mm respectively

TEST #.	a (mm)	B (mm)	W (mm)	a/W	P (N)	t_F (s)	Comp. Fac. (Y)	K_{1C} (MPa.$m^{1/2}$)
BK6	1.219	4.032	7.831	0.156	137	12	1.7488	1.60
BK7	1.219	3.988	7.832	0.156	142	12	1.7488	1.68
BK20	1.219	4.027	7.804	0.156	140	12	1.7487	1.65
BK33	1.207	3.999	7.833	0.154	134	14	1.7492	1.57
BK19	1.200	4.081	7.815	0.154	126	7	1.7494	1.45

Data for SCF5 using a nominal span and notch width of 31.75 mm and 0.152 mm respectively

TEST #.	a (mm)	B (mm)	W (mm)	a/W	P (N)	t_F (s)	Comp. Fac. (Y)	K_{1C} (MPa.$m^{1/2}$)
DK4	1.251	3.769	8.088	0.155	120	17	1.7491	1.43
CK4	1.168	3.918	7.208	0.162	101	13	1.7475	1.41

Table 5C.5 Data at 700°C

Data for SCR25.76 using a nominal span and notch width of 31.53 mm and 0.152 mm respectively

TEST #.	a (mm)	B (mm)	W (mm)	a/W	P (N)	t_F (s)	Comp. Fac. (Y)	K_{1C} (MPa.$m^{1/2}$)
AK16	1.194	4.017	7.855	0.152	123	11	1.7498	1.42
AK29	1.194	4.021	7.858	0.152	146	10	1.7498	1.68
AK33	1.194	4.024	7.864	0.152	177	10	1.7499	2.03
AK36	1.194	4.029	7.870	0.152	143	10	1.7499	1.64
AK3	1.207	4.012	7.859	0.154	115	8	1.7494	1.33

Data for SCR19.34 using a nominal span and notch width of 31.53 mm and 0.152 mm respectively

TEST #.	a (mm)	B (mm)	W (mm)	a/W	P (N)	t_F (s)	Comp. Fac. (Y)	K_{1C} (MPa.$m^{1/2}$)
BK4	1.219	4.009	7.825	0.156	121	9	1.7488	1.42
BK12	1.219	4.016	7.839	0.156	125	9	1.7489	1.46
BK22	1.219	4.045	7.816	0.156	113	8	1.7488	1.32
BK34	1.207	4.083	7.832	0.154	114	8	1.7492	1.31
BK5	1.219	3.979	7.828	0.156	101	6	1.7488	1.20

All the above data for SCR25.76 and SCR19.34 were obtained using silicon nitride knife-edge supports

APPENDIX 5C CONTINUED:

Table 5C.6 Data at 750°C

Data for SCR25.76 using a nominal span and notch width of 31.53 mm and 0.152 mm respectively

TEST #.	a (mm)	B (mm)	W (mm)	a/W	P (N)	t_F (s)	Comp. Fac. (Y)	K_{1C} (MPa.$m^{1/2}$)
AK4	1.219	4.035	7.860	0.155	155	11	1.7490	1.80
AK7	1.207	4.018	7.857	0.154	150	12	1.7494	1.74
AK15	1.194	4.009	7.853	0.152	158	12	1.7498	1.83
AK25	1.207	4.015	7.858	0.154	177	11	1.7494	2.05
AK26	1.207	4.041	7.860	0.154	134	9	1.7494	1.58

Data for SCR19.34 using a nominal span and notch width of 31.53 mm and 0.152 mm respectively

TEST #.	a (mm)	B (mm)	W (mm)	a/W	P (N)	t_F (s)	Comp. Fac. (Y)	K_{1C} (MPa.$m^{1/2}$)
BK14	1.219	4.035	7.836	0.156	244	15	1.7489	2.84
BK18	1.219	4.048	7.822	0.156	157	13	1.7488	1.83
BK23	1.219	3.960	7.822	0.156	296	17	1.7488	3.53
BK28	1.219	4.045	7.841	0.155	303	18	1.7489	3.52
BK27	1.219	4.031	7.835	0.156	222	13	1.7488	2.59

Table 5C.7 Data at 775°C

Data for SCR25.76 using a nominal span and notch width of 31.53 mm and 0.152 mm respectively

TEST #.	a (mm)	B (mm)	W (mm)	a/W	P (N)	t_F (s)	Comp. Fac. (Y)	K_{1C} (MPa.$m^{1/2}$)
AK2	1.219	4.003	7.861	0.155	159	14	1.7490	1.86
AK13	1.194	3.982	7.851	0.152	220	24	1.7498	2.56
AK18	1.207	4.013	7.859	0.154	161	15	1.7494	1.87
AK31	1.194	4.009	7.859	0.152	197	17	1.7498	2.28
AK28	1.207	3.893	7.856	0.154	159	11	1.7494	1.90

Data for SCR19.34 using a nominal span and notch width of 31.53 mm and 0.152 mm respectively

TEST #.	a (mm)	B (mm)	W (mm)	a/W	P (N)	t_F (s)	Comp. Fac. (Y)	K_{1C} (MPa.$m^{1/2}$)
BK1	1.232	3.971	7.809	0.158	316	28	1.7483	3.79
BK13	1.219	4.015	7.835	0.156	230	20	1.7488	2.69
BK31	1.207	3.989	7.834	0.154	479	39	1.7492	5.62
BK37	1.219	4.016	7.822	0.156	450	39	1.7488	5.29
BK35	1.219	3.947	7.829	0.156	301	25	1.7488	3.59

Note: The SCR19.34 specimens tested at 775°C were found to have a slight curvature in the plane of loading, i.e., the tensile face was slightly convex, when the specimen halves were matched up; however the load - cross-head displacement charts showed that the response was nevertheless "linear-elastic" up to fracture.

Note: All the above data were obtained using silicon nitride knife-edge supports.
P denotes the fracture load.
t_F denotes the time to failure.
Comp. Fac. denotes the compliance factor, Y.

APPENDIX 5C CONTINUED:

Table 5C.8 Data at 792°C

Data for SCR25.76 using a nominal span and notch width of 31.53 mm and 0.152 mm respectively

TEST #.	a (mm)	B (mm)	W (mm)	a/W	
AK9	1.232	4.008	7.850	0.157	In the region of linear load - cross-head displacement response, a load of 236 N was sustained at a cross-head displacement of 0.455 mm

Data for SCR19.34 using a nominal span and notch width of 31.53 mm and 0.152 mm respectively

BK3	1.219	4.006	7.838	0.156	In the region of linear load - cross-head displacement response, a load of 181 N was sustained at a cross-head displacement of 0.455 mm

Note: The above data were obtained using silicon nitride knife-edge supports.

Table 5C.9 Data for SCF5 using a nominal span and notch width of 31.75 mm and 0.152 mm respectively

Data at 800°C

TEST #.	a (mm)	B (mm)	W (mm)	a/W	P (N)	t_F (s)	Comp. Fac. (Y)	K_{1C} (MPa.$m^{1/2}$)
DK1	1.213	3.811	8.032	0.151	150	14	1.7501	1.77
CK1	1.245	3.657	7.818	0.159	162	13	1.7480	2.13

Data at 850°C

TEST #.	a (mm)	B (mm)	W (mm)	a/W	P (N)	t_F (s)	Comp. Fac. (Y)	K_{1C} (MPa.$m^{1/2}$)
DK2	1.276	3.788	8.116	0.157	200	16	1.7485	2.38
CK2	1.257	3.702	7.308	0.172	212	23	1.7467	3.16

Data at 900°C

TEST #.	a (mm)	B (mm)	W (mm)	a/W	
DK3	1.219	3.694	8.066	0.151	Plastic deformation occurred almost immediately
CK3	1.130	3.974	7.641	0.151	Plastic deformation occurred almost immediately

Note concerning SCF5: Test numbers prefixed by D indicate that the precursor compound for Cr_2O_3 was sodium dichromate ($Na_2Cr_2O_7$), while those prefixed by C indicate that the precursor compound was either sodium dichromate or sodium chromate (Na_2CrO_4).

The specimen coded as DK were not polished on their tensile faces, while the tensile faces of those specimens coded as CK had been polished on a 14μm diamond lap (as they were originally intended as flexural strength specimens).

Table 5D.1 Applied Load and Cross-Head Displacement Data:

TEST #.	a (mm)	B (mm)	W (mm)	a/W	APPLIED LOAD (N)								
					0	9.82	19.65	29.47	39.29	49.12	58.94	68.76	78.59
					CROSS-HEAD DISPLACEMENT (x 10^{-3} M)								
1	0.978	3.979	8.136	0.12	0	0.030	0.065	0.090	0.120	0.150	0.180	0.205	0.225
2	1.099	3.986	8.092	0.14	0	0.035	0.070	0.095	0.125	0.160	0.190	0.215	0.235
3	1.194	4.278	8.130	0.15	0	0.030	0.065	0.095	0.125	0.155	0.185	0.210	0.235
4	1.162	4.028	8.103	0.14	0	0.040	0.070	0.095	0.125	0.155	0.185	0.210	0.235
5	1.308	4.023	8.123	0.16	0	0.035	0.065	0.095	0.120	0.155	0.185	0.210	0.230
6	1.365	4.015	8.135	0.17	0	0.040	0.070	0.100	0.125	0.165	0.195	0.215	0.240
7	1.448	3.983	8.073	0.18	0	0.040	0.070	0.100	0.130	0.165	0.195	0.220	0.245
8	2.426	3.990	8.059	0.30	0	0.040	0.080	0.110	0.145	0.190	0.225	0.260	0.285

Note: Specimen number 8 fractured at a load of 82 N, which produced a K_{1c} value of 1.37 MPa.$m^{1/2}$.

Table 5D.2 Compliance Data as Obtained From Regression Analysis of Nine Data Per Test:

TEST #.	a (x 10^{-3} m)	Compliance, $\bar{Q}$ (x 10^{-6} mN^{-1})	Coefficient of Determination (r^2)
1	0.978	2.90969 ± 0.05655	0.9974
2	1.099	3.02845 ± 0.06958	0.9963
3	1.194	3.02145 ± 0.04991	0.9981
4	1.162	2.95210 ± 0.05640	0.9975
5	1.308	2.96059 ± 0.06076	0.9971
6	1.365	3.05390 ± 0.07939	0.9953
7	1.448	3.11328 ± 0.06121	0.9973
8	2.426	3.68165 ± 0.06444	0.9979

Regression analyses of the ($\bar{Q}$,a) data for tests 1 to 7 assuming equations of the form (i) $\bar{Q} = A + Ba$ (ii) $\bar{Q} = Aexp(Ba)$; (iii) $\bar{Q} = Aa^B$; (iv) $\bar{Q} = Aexp(B/a)$; (v) $\bar{Q} = A(1/a)^B$ showed that the equation $\bar{Q} = A + Ba$ best fitted the data, giving B (i.e., $d\bar{Q}/da$) as (3.21 ± 1.26) x 10^{-4} N^{-1} and A as (2.613 ± 0.155) x 10^{-6} mN^{-1}, with a Pearson correlation coefficient (r) of 0.7523 and hence a coefficient of determination (r^2) of 0.5659. The r.m.s. difference between the calculated and observed $\bar{Q}$ values was 1 %.

APPENDIX 5E ROOM TEMPERATURE VICKERS AND KNOOP INDENTATION DATA FOR SCF5 AND VICKERS INDENTATION DATA FOR SCR25.76, SCR19.34 AND SCR19.13

Table 5E.1 Knoop indentation data for SCF5 in air:

Indent #.	Peak Applied Load, P (N)	Minor Diagonal Length, b* (μm)	Major Diagonal Length, a* (μm)	b*/a*	Knoop Hardness (GPa)
1.2	149	65.0	598.0	0.1087	5.9
1.1	147	65.0	598.0	0.1087	5.8
1.3	146	65.0	598.0	0.1087	5.8
1.4	98	52.0	481.0	0.1081	6.0
1.5	98	52.0	481.0	0.1081	6.0
1.6	96	52.0	474.5	0.1096	6.1
1.8	49	39.0	338.0	0.1154	6.1
1.9	49	39.0	338.0	0.1154	6.1
1.7	47	39.0	331.5	0.1176	6.1
2.1	149	65.0	611.0	0.1064	5.7
2.3	149	65.0	611.0	0.1064	5.7
2.2	148	65.0	604.5	0.1075	5.8
2.10	148	65.0	611.0	0.1064	5.6
2.5	101	52.0	494.0	0.1053	5.9
2.4	100	52.0	481.0	0.1081	6.2
2.6	100	52.0	481.0	0.1081	6.2
2.7	51	39.0	338.0	0.1154	6.4
2.8	49	39.0	338.0	0.1154	6.1
2.9	49	39.0	331.5	0.1176	6.3

Note: a* and b* refer to the recovered indent dimensions.
The digit before . in the indent #. refers to the specimen number in this table and subsequent tables.

Table 5E.2 Vickers indentation data for SCF5 in air:

Indent #.	Peak Applied Load, P (N)	Half-Diagonal Length, a (μm)	Radial Crack Length, c (μm)	Palmqvist Crack Length, l (μm)	Vickers Hardness (GPa)
1.3	149	101.565 (4)	401.27 (2)	299.71 (4)	6.7
1.1	148	99.070 (4)	375.46 (4)	276.39 (4)	7.0
1.2	147	100.735 (4)	399.60 (4)	298.87 (4)	6.7
1.4	98	79.920 (4)	------	------	7.1
1.5	97	79.920 (4)	298.04 (4)	218.12 (4)	7.0
1.6	97	80.755 (4)	297.20 (4)	216.45 (4)	6.9
1.8	50	57.445 (4)	203.96 (4)	146.52 (4)	7.0
1.9	50	56.610 (4)	207.29 (4)	150.68 (4)	7.2
1.7	47	54.945 (4)	198.81 (4)	143.87 (4)	7.2
2.2	151	101.565 (4)	------	------	6.8
2.10	147	100.735 (4)	------	------	6.7
2.3	146	99.070 (4)	377.96 (2)	278.89 (2)	6.9
2.6	102	82.420 (4)	318.02 (4)	235.60 (4)	7.0
2.5	100	79.920 (4)	288.88 (4)	208.96 (4)	7.3
2.4	97	79.920 (4)	293.04 (4)	213.12 (4)	7.0
2.7	53	57.445 (4)	173.99 (4)	116.55 (4)	7.4
2.9	51	59.111 (4)	193.97 (4)	134.86 (4)	6.8
2.8	50	56.610 (4)	199.80 (4)	143.19 (4)	7.2

APPENDIX 5E CONTINUED:
Table 5E.2 Continued:

Indent #.	Peak Applied Load, P (N)	Half-Diagonal Length, a (μm)	Radial Crack Length, c (μm)	Palmqvist Crack Length, l (μm)	Vickers Hardness (GPa)
3.1	152	101.565 (4)	374.63 (2)	273.07 (2)	6.8
3.2	150	99.070 (4)	339.60 (2)	240.53 (2)	7.1
3.3	148	100.735 (4)	378.79 (4)	278.06 (4)	6.8
3.5	103	83.250 (4)	326.34 (4)	243.09 (4)	6.9
3.4	100	79.920 (2)	------	------	7.2
3.6	99	81.585 (4)	301.37 (4)	219.79 (4)	6.9
3.9	51	55.780 (4)	208.96 (4)	153.18 (4)	7.6
3.8	49	56.610 (4)	180.65 (4)	124.04 (4)	7.1
3.7	48	56.610 (4)	161.51 (4)	104.90 (4)	7.1

Table 5E.3 Vickers indentation data for SCR19.13 in air:

Indent #.	Peak Applied Load, P (N)	Half-Diagonal Length, a (μm)	Radial Crack Length, c (μm)	Palmqvist Crack Length, l (μm)	Vickers Hardness (GPa)
4	66	65.20 (4)	324.2 (4)	259.0 (4)	7.2
3	65	66.00 (2)	297.4 (4)	231.4 (4)	6.9
19	63	64.75 (4)	317.6 (4)	252.9 (4)	7.0
8	62	63.50 (4)	290.4 (4)	226.9 (4)	7.1
5	60	61.05 (4)	340.7 (4)	279.7 (4)	7.5
10	53	61.05 (4)	270.6 (4)	209.6 (4)	6.6
7	50	56.95 (4)	314.3 (4)	257.4 (4)	7.1
16	49	56.95 (4)	252.5 (4)	195.6 (4)	7.0
18	49	60.25 (4)	287.9 (4)	227.7 (4)	6.3

Table 5E.4 Vickers indentation data for SCR25.76 and SCR19.34 at a nominal load of 49 N in air:

Indent #.	Half-Diagonal Length, a (μm)	Radial Crack Length, c (μm)	Palmqvist Crack Length, l (μm)	Vickers Hardness (GPa)
		Data for SCR25.76		
1	54.75 (4)	201.1 (4)	146.4 (4)	7.6
2	55.00 (4)	207.3 (4)	152.3 (4)	7.5
3	55.50 (4)	208.1 (4)	152.6 (4)	7.4
4	55.80 (4)	215.4 (4)	159.6 (4)	7.3
5	56.00 (4)	213.2 (4)	157.2 (4)	7.3
6	54.70 (4)	210.2 (4)	155.5 (4)	7.6
7	54.90 (4)	216.2 (4)	161.3 (4)	7.5
8	54.70 (4)	208.9 (4)	154.2 (4)	7.6
9	55.10 (4)	199.0 (4)	143.9 (4)	7.5
		Data for SCR19.34		
1	55.75 (4)	205.0 (4)	149.3 (4)	7.3
2	55.45 (4)	199.2 (4)	143.8 (4)	7.4
3	55.25 (4)	200.9 (4)	145.7 (4)	7.5
4	55.65 (4)	206.7 (4)	151.1 (4)	7.3
5	56.00 (4)	194.3 (4)	138.3 (4)	7.3
6	55.40 (4)	192.0 (4)	136.6 (4)	7.4
7	55.60 (4)	192.1 (4)	136.5 (4)	7.4
8	56.25 (4)	199.6 (4)	143.4 (4)	7.2
9	55.40 (4)	201.1 (4)	145.7 (4)	7.4

APPENDIX 5F VICKERS HARDNESS, H, CONTACT PRESSURE, H*, C/A, $P/C^{3/2}$, AND P/L DATA FOR SCR25.76, SCR19.34, SCF5 AND SCR19.13:

Table 5F.1 Room temperature data for SCF5 in air:

I #.	P (N)	H (GPa)	c/a	H* (GPa)	$P/c^{3/2}$ (x 10^7 $Nm^{-3/2}$)	P/l (x 10^5 Nm^{-1})
1.3	149	6.7	3.95	7.2	1.8537	4.9715
1.1	148	7.0	3.79	7.5	2.0343	5.3548
1.2	147	6.7	3.97	7.2	1.8403	4.9185
1.4	98	7.1	----	7.7	------	------
1.5	97	7.0	3.73	7.6	1.8852	4.4471
1.6	97	6.9	3.68	7.4	1.8932	4.4814
1.8	50	7.0	3.55	7.6	1.7165	3.4125
1.9	50	7.2	3.66	7.8	1.6753	3.3183
1.7	47	7.2	3.62	7.8	1.6766	3.2668
2.2	151	6.8	----	7.3	------	------
2.10	147	6.7	----	7.2	------	------
2.3	146	6.9	3.82	7.4	1.9869	5.2350
2.6	102	7.0	3.86	7.5	1.7985	4.3294
2.5	100	7.3	3.61	7.8	2.0367	4.7856
2.4	97	7.0	3.67	7.6	1.9337	4.5514
2.7	53	7.4	3.03	8.0	2.3093	4.5474
2.9	51	6.8	3.28	7.3	1.8879	3.7817
2.8	50	7.2	3.53	7.8	1.7704	3.4919
3.1	152	6.8	3.69	7.4	2.0962	5.5663
3.2	150	7.1	3.43	7.6	2.3968	6.2362
3.3	148	6.8	3.76	7.3	2.0075	5.3226
3.5	103	6.9	3.82	7.4	1.7472	4.2371
3.4	100	7.2	----	7.8	------	------
3.6	99	6.9	3.69	7.4	1.8923	4.5043
3.9	51	7.6	3.75	8.2	1.6884	3.3294
3.8	49	7.1	3.19	7.7	2.0181	3.9503
3.7	48	7.1	2.85	7.5	2.3385	4.5758

Table 5F.2 Room temperature data for SCR19.13 in air:

I #.	P (N)	H (GPa)	c/a	H* (GPa)	$P/c^{3/2}$ (x 10^7 $Nm^{-3/2}$)	P/l (x 10^5 Nm^{-1})
4	66	7.2	4.97	7.8	1.1306	2.5483
3	65	6.9	4.51	7.5	1.2674	2.8090
9	63	7.0	4.91	7.5	1.1131	2.4911
8	62	7.1	4.57	7.7	1.2528	2.7325
5	60	7.5	5.58	8.1	0.0954	2.1452
10	53	6.6	4.43	7.1	1.1907	2.5286
7	50	7.1	5.52	7.7	0.8973	1.9654
6	49	7.0	4.43	7.6	1.2212	2.5051
8	49	6.3	4.78	6.8	1.0031	2.1520

Note: I #. is the indent number, $H = 1.8544P/(4a^2)$, $H^* = P/(2a^2)$

APPENDIX 5F CONTINUED:

Table 5F.3 Room temperature data for SCR25.76 in air:

I #.	H (GPa)	c/a	H* (GPa)	$P/c^{3/2}$ (x 10^7 $Nm^{-3/2}$)	P/l (x 10^5 Nm^{-1})
1	7.6	3.67	8.2	1.7182	3.3470
2	7.5	3.77	8.1	1.6417	3.2173
3	7.4	3.78	8.1	1.6323	3.2110
4	7.3	3.86	7.9	1.5500	3.0702
5	7.3	3.81	7.8	1.5740	3.1170
6	7.6	3.84	8.2	1.6079	3.1511
7	7.5	3.94	8.1	1.5414	3.0378
8	7.6	3.82	8.2	1.6229	3.1777
9	7.5	3.61	8.1	1.7455	3.4051

Table 5F.4 Room temperature data for SCR19.34 in air:

I #.	H (GPa)	c/a	H* (GPa)	$P/c^{3/2}$ (x 10^7 $Nm^{-3/2}$)	P/l (x 10^5 Nm^{-1})
1	7.3	3.68	7.9	1.6694	3.2820
2	7.4	3.59	8.0	1.7429	3.4075
3	7.5	3.64	8.0	1.7208	3.3631
4	7.3	3.71	7.9	1.6489	3.2429
5	7.3	3.47	7.8	1.8092	3.5430
6	7.4	3.47	8.0	1.8418	3.5871
7	7.4	3.46	7.9	1.8404	3.5897
8	7.2	3.55	7.7	1.7376	3.4170
9	7.4	3.63	8.0	1.7182	3.3631

Note: I #. is the indent number, $H = 1.8544P/(4a^2)$, $H^* = P/(2a^2)$

APPENDIX 5G ROOM TEMPERATURE VICKERS INDENTATION FRACTURE TOUGHNESS DATA FOR SCR25.76, SCR19.34, SCF5 AND SCR19.13:

Table 5G.1 Data for SCF5 in air:

I #.	K_c (MPa.m$^{1/2}$)															
	Eq.1	Eq.2	Eq.3	Eq.4	Eq.5	Eq.6	Eq.7	Eq.8	Eq.9	Eq.10	Eq.11	Eq.12	Eq.13	Eq.14	Eq.15	Eq.16
1.3	0.95	1.37	1.88	1.06	1.21	1.21	1.30	1.83	1.84	1.97	2.73	3.37	2.25	3.12	0.98	2.41
1.1	1.05	1.51	2.04	1.14	1.30	1.29	1.40	1.97	1.99	2.10	2.84	3.42	2.34	3.25	1.04	2.56
1.2	0.95	1.37	1.86	1.05	1.20	1.20	1.29	1.81	1.82	1.95	2.71	3.35	2.24	3.11	0.98	2.40
1.4	----	----	----	----	----	----	----	----	----	----	----	----	----	----	----	----
1.5	0.97	1.40	1.89	1.05	1.20	1.19	1.29	1.82	1.84	1.94	2.60	3.10	2.14	2.97	0.95	2.34
1.6	0.98	1.40	1.91	1.07	1.22	1.21	1.31	1.85	1.86	1.95	2.64	3.12	2.14	2.97	0.95	2.32
1.8	0.88	1.27	1.72	0.96	1.10	1.09	1.18	1.66	1.68	1.74	2.32	2.69	1.87	2.60	0.83	2.05
1.9	0.86	1.24	1.66	0.92	1.05	1.04	1.14	1.60	1.62	1.69	2.24	2.64	1.85	2.57	0.83	2.05
1.7	0.86	1.24	1.66	0.92	1.06	1.04	1.14	1.61	1.62	1.69	2.23	2.61	1.84	2.55	0.83	2.03
2.2	----	----	----	----	----	----	----	----	----	----	----	----	----	----	----	----
2.10	----	----	----	----	----	----	----	----	----	----	----	----	----	----	----	----
2.3	1.02	1.47	2.00	1.12	1.28	1.27	1.37	1.94	1.95	2.07	2.81	3.40	2.31	3.21	1.02	2.51
2.6	0.93	1.33	1.80	1.01	1.15	1.15	1.24	1.75	1.76	1.87	2.54	3.09	2.11	2.92	0.93	2.29
2.5	1.05	1.51	2.02	1.12	1.28	1.26	1.38	1.95	1.96	2.05	2.70	3.16	2.22	3.09	1.00	2.46
2.4	1.00	1.43	1.94	1.08	1.23	1.22	1.33	1.87	1.89	1.98	2.65	3.12	2.16	3.00	0.96	2.37
2.7	1.19	1.71	2.23	1.25	1.43	1.41	1.55	2.19	2.23	2.13	2.78	2.93	2.17	3.02	0.99	2.43
2.9	0.97	1.40	1.92	1.07	1.23	1.22	1.31	1.86	1.88	1.88	2.55	2.82	1.96	2.73	0.86	2.11
2.8	0.91	1.31	1.76	0.97	1.11	1.10	1.20	1.69	1.71	1.77	2.33	2.69	1.90	2.64	0.85	2.10
3.1	1.08	1.55	2.12	1.19	1.36	1.35	1.45	2.05	2.07	2.17	2.95	3.50	2.38	3.31	1.05	2.58
3.2	1.23	1.78	2.40	1.33	1.52	1.51	1.64	2.31	2.34	2.39	3.17	3.60	2.53	3.52	1.13	2.78
3.3	1.03	1.49	2.04	1.14	1.31	1.30	1.40	1.97	1.99	2.10	2.87	3.44	2.33	3.23	1.02	2.51
3.5	0.90	1.30	1.75	0.99	1.13	1.12	1.21	1.71	1.71	1.83	2.50	3.07	2.08	2.89	0.92	2.26
3.4	----	----	----	----	----	----	----	----	----	----	----	----	----	----	----	----
3.6	0.97	1.40	1.91	1.07	1.22	1.21	1.31	1.85	1.86	1.95	2.64	3.13	2.15	2.98	0.95	2.33
3.9	0.87	1.25	1.64	0.91	1.04	1.01	1.12	1.58	1.60	1.68	2.18	2.60	1.86	2.59	0.86	2.10
3.8	1.04	1.50	2.01	1.12	1.28	1.27	1.38	1.95	1.98	1.95	2.59	2.82	2.01	2.80	0.90	2.21
3.7	1.20	1.73	2.27	1.31	1.50	1.49	1.61	2.28	2.33	2.15	2.91	2.97	2.16	3.01	0.96	2.36

Table 5G.2 Data for SCR19.13 in air:

I #.	K_c (MPa.m$^{1/2}$)															
	Eq.1	Eq.2	Eq.3	Eq.4	Eq.5	Eq.6	Eq.7	Eq.8	Eq.9	Eq.10	Eq.11	Eq.12	Eq.13	Eq.14	Eq.15	Eq.16
4	0.58	0.84	1.02	0.57	0.65	0.62	0.71	1.01	1.00	1.06	1.46	2.06	1.51	2.09	0.73	1.79
3	0.65	0.94	1.16	0.65	0.74	0.72	0.81	1.15	1.14	1.24	1.63	2.17	1.58	2.19	0.75	1.84
9	0.57	0.83	1.02	0.57	0.65	0.63	0.71	1.01	1.00	1.07	1.48	2.06	1.49	2.06	0.71	1.74
8	0.65	0.93	1.13	0.63	0.73	0.70	0.79	1.12	1.12	1.21	1.58	2.12	1.56	2.17	0.75	1.84
5	0.49	0.71	0.89	0.47	0.54	0.51	0.59	0.84	0.82	0.82	1.25	1.89	1.39	1.93	0.68	1.67
10	0.61	0.88	1.11	0.63	0.72	0.70	0.78	1.10	1.10	1.19	1.59	2.10	1.49	2.07	0.69	1.71
7	0.46	0.67	0.84	0.45	0.52	0.50	0.57	0.80	0.79	0.79	1.22	1.83	1.32	1.84	0.64	1.57
16	0.63	0.91	1.11	0.62	0.71	0.69	0.78	1.10	1.10	1.19	1.54	2.04	1.49	2.07	0.71	1.75
18	0.52	0.74	0.95	0.54	0.62	0.61	0.67	0.95	0.94	1.01	1.45	2.00	1.37	1.90	0.62	1.53

Note: I #. is the indent number and the equations numbered 1 to 16 are given in Section 5.3.1

APPENDIX 5G CONTINUED:

Table 5G.3 Data for SCR25.76 in air:

I #.	K_c (MPa.m$^{1/2}$)															
	Eq.1	Eq.2	Eq.3	Eq.4	Eq.5	Eq.6	Eq.7	Eq.8	Eq.9	Eq.10	Eq.11	Eq.12	Eq.13	Eq.14	Eq.15	Eq.16
1	0.88	1.27	1.68	0.93	1.02	1.00	1.11	1.56	1.57	1.65	1.92	2.27	1.81	2.51	0.83	2.01
2	0.85	1.22	1.61	0.89	1.06	1.03	1.15	1.62	1.64	1.70	1.97	2.29	1.84	2.56	0.85	2.06
3	0.84	1.21	1.60	0.89	1.04	1.02	1.13	1.60	1.61	1.68	1.94	2.28	1.83	2.55	0.85	2.05
4	0.80	1.15	1.53	0.85	1.01	0.98	1.09	1.54	1.55	1.63	1.90	2.26	1.80	2.50	0.83	2.00
5	0.81	1.17	1.56	0.87	1.11	1.09	1.20	1.70	1.72	1.76	2.05	2.34	1.88	2.61	0.86	2.08
6	0.83	1.19	1.56	0.87	1.12	1.09	1.21	1.71	1.73	1.78	2.04	2.34	1.89	2.63	0.88	2.11
7	0.79	1.14	1.50	0.83	1.12	1.09	1.22	1.72	1.74	1.78	2.05	2.34	1.89	2.63	0.87	2.10
8	0.84	1.20	1.58	0.88	1.07	1.05	1.16	1.64	1.65	1.71	2.00	2.32	1.84	2.56	0.84	2.03
9	0.90	1.29	1.71	0.95	1.04	1.02	1.13	1.60	1.61	1.68	1.94	2.28	1.83	2.54	0.85	2.04

Table 5G.4 Data for SCR19.34 in air:

I #.	K_c (MPa.m$^{1/2}$)															
	Eq.1	Eq.2	Eq.3	Eq.4	Eq.5	Eq.6	Eq.7	Eq.8	Eq.9	Eq.10	Eq.11	Eq.12	Eq.13	Eq.14	Eq.15	Eq.16
1	0.86	1.24	1.62	0.89	1.02	1.00	1.11	1.56	1.57	1.65	1.92	2.27	1.81	2.51	0.83	2.01
2	0.90	1.29	1.68	0.93	1.06	1.03	1.15	1.62	1.64	1.70	1.97	2.29	1.84	2.56	0.85	2.06
3	0.89	1.28	1.66	0.91	1.04	1.02	1.13	1.60	1.61	1.68	1.94	2.28	1.83	2.55	0.85	2.05
4	0.85	1.22	1.59	0.88	1.01	0.98	1.09	1.54	1.55	1.63	1.90	2.26	1.80	2.50	0.83	2.00
5	0.93	1.34	1.76	0.97	1.11	1.09	1.20	1.70	1.72	1.76	2.05	2.34	1.88	2.61	0.86	2.08
6	0.95	1.37	1.78	0.98	1.12	1.09	1.21	1.71	1.73	1.78	2.04	2.34	1.89	2.63	0.88	2.11
7	0.95	1.37	1.78	0.98	1.12	1.09	1.22	1.72	1.74	1.78	2.05	2.34	1.89	2.63	0.87	2.10
8	0.89	1.29	1.70	0.94	1.07	1.05	1.16	1.64	1.65	1.71	2.00	2.32	1.84	2.56	0.84	2.03
9	0.88	1.27	1.66	0.91	1.04	1.02	1.13	1.60	1.61	1.68	1.94	2.28	1.83	2.54	0.85	2.04

Note: I #. is the indent number and the equations numbered 1 to 16 are given in Section 5.3.1

APPENDIX 6A TRANSDUCER METER, DIGITAL MULTIMETER AND CHART RECORDER CONTROL SETTINGS:

(1) Mercer 155 Transducer Meter Settings:

(a) Back Panel: One transducer plugged into the 'A+' socket and the other into the 'B+' socket with both switches set to the 'NORMAL' position.

(b) Front Panel: The 'A/A,B' switch set to the 'A,B' position in order to sum the input signals at 'A+' and 'B+'; the range switch was set to the ± 500μm range (on the 'electric' scale).

On the ± 500 μm range the output d.c. voltage was ± 1000 mV at full scale deflection of the meter, i.e., ± 500μm displacement (in this instance the summed displacement).

(2) 'Thurlby' Multimeter Settings:

The display was set to 5.5 digits on the 2000 mV d.c. range (i.e., 000.00) with the data logger and Ax + B programmes running simultaneously (A = 0.25 and B = 0). The running average, minimum and maximum, i.e., AvLoHi programme, was also run towards the end of each test to log the maximum specimen displacement.

(3) 'Omniscribe Series 5000' Chart Recorder Settings:

A chart speed of 25 mm/hour was used, with a full scale voltage of 1 V and resolution of 0.01 V (i.e., 5μm) for the transducer meter output. Note a passive low-pass RC filter was connected across the chart recorder terminals to attenuate any a.c. noise. The thermocouple e.m.f. was simultaneously recorded using a full scale voltage of 100 mV with a resolution of 25°C. The furnace temperature stability was checked using a 'Servoscribe 1S' single pen chart recorder with 2.5°C resolution.

APPENDIX 6B COMPRESSION CREEP TEST DATA FOR SCR25.76 AND SCR19.34 AT 709°C:

Table 6B.1 Compression Creep Load, Stress and Data Acquisition Parameter Data for Each Test Run:

Data for SCR25.76 Specimens

TEST #.	Hanger Load (kg)	Intial Stress (MPa)	Final Stress (MPa)	Mean Stress (MPa)	No. of Data Logged	Data Logging Interval (s)	Data Logging Time
C1.1	59.674	160	156	158	63	300	5 h 10 m
C1.2	49.134	128	125	127	87	600	14 h 20 m
C1.3	40.056	102	100	101	79	600	13 h 0 m
C2.1	18.198	50	49	49	100	600	16 h 30 m
C2.2	27.847	74	72	73	99	600	16 h 20 m
C2.3	39.287	102	99	100	81	600	13 h 20 m
C2.5	19.522	49	49	49	100	600	16 h 30 m
C3.1	8.970	25	24	24	160	600	26 h 30 m
C3.2	12.956	35	34	34	97	900	24 h 0 m
C3.3	16.865	44	44	44	189	900	47 h 0 m
C3.4a	20.977	54	53	53	98	900	24 h 15 m
C3.4b	20.977	54	53	53	96	1500	39 h 35 m
C3.5	25.428	64	62	63	182	900	45 h 15 m
C3.6	9.924	25	25	25	189	14400	752 h 0 m
C3.7	1.115	3	3	3	78	14400	308 h 0 m

Data for SCR19.34 Specimens

TEST #.	Hanger Load (kg)	Intial Stress (MPa)	Final Stress (MPa)	Mean Stress (MPa)	No. of Data Logged	Data Logging Interval (s)	Data Logging Time
D1.1	3.455	10	10	10	367	3600	366 h 0 m
D1.2a	7.342	20	19	20	100	7200	198 h 0 m
D1.2b	7.342	20	19	20	89	7200	176 h 0 m
D1.3	13.310	34	34	34	91	7200	180 h 0 m
D1.4	17.723	44	43	44	99	5400	147 h 0 m
D1.5	0.689	2	2	2	296	5400	442 h 30 m
D2.1	25.851	70	66	68	100	1800	49 h 30 m
D2.2	33.366	84	80	82	100	1500	41 h 15 m
D2.3a	1.000	3	3	3	100	1500	41 h 15 m
D2.3b	1.000	3	3	3	97	3600	96 h 0 m
D3.1	36.605	99	95	97	100	900	24 h 45 m
D3.2	45.109	116	111	113	100	900	24 h 45 m
D3.3	1.000	3	3	3	100	3600	99 h 0 m
D4.1	55.201	148	138	143	54	800	11 h 47 m
D4.2	1.000	3	3	3	144	3600	143 h 0 m

Note: (a) The hanger load was the mass placed on the weight-hanger.
(b) h and m under the table heading 'Data Logging Time' denote hours and minutes respectively.
(c) The data for the stress acting on a specimen are quoted to the nearest MPa.
(d) a and b under the table heading 'TEST #.' denote successive data sets obtained from the same test run.

APPENDIX 6B CONTINUED:
Table 6B.2 Calculated Specimen Dimensional Change Data for Each Test Run:

Data for SCR25.76

TEST #.	hI at RT (mm)	hF at RT (mm)	hI at 709°C (mm)	hF at 709°C (mm)	dI at RT (mm)	dF at RT (mm)	dI at 709°C (mm)	dF at 709°C (mm)
C1.1	10.01 *	9.76	10.06	9.81	6.80 *	6.89	6.83	6.92
C1.2	9.76	9.51	9.81	9.56	6.89	6.98	6.93	7.02
C1.3	9.51	9.25	9.56	9.30	6.98	7.08	7.02	7.11
		9.30 *				7.13 $		
C2.1	10.01 *	9.86	10.06	9.91	6.79 *	6.84	6.82	6.88
C2.2	9.86	9.61	9.91	9.66	6.84	6.93	6.88	6.96
C2.3	9.61	9.35	9.66	9.40	6.93	7.03	6.97	7.06
C2.5	9.35	9.23	9.40	9.28	7.03	7.07	7.07	7.11
		9.30 *				7.13 $		
C3.1	10.01 *	9.79	10.06	9.84	6.79 *	6.87	6.82	6.90
C3.2	9.79	9.71	9.84	9.76	6.87	6.90	6.91	6.94
C3.3	9.71	9.49	9.76	9.54	6.90	6.98	6.94	7.01
C3.4a,b	9.49	9.27	9.54	9.32	6.98	7.06	7.02	7.10
C3.5	9.27	9.06	9.32	9.11	7.06	7.14	7.10	7.18
C3.6	9.06	9.01	9.11	9.06	7.14	7.16	7.18	7.20
C3.7	9.01	9.08	9.06	9.13	7.16	7.13	7.20	7.17
		9.18 *				7.22 $		

Data for SCR19.34

TEST #.	hI at RT (mm)	hF at RT (mm)	hI at 709°C (mm)	hF at 709°C (mm)	dI at RT (mm)	dF at RT (mm)	dI at 709°C (mm)	dF at 709°C (mm)
D1.1	10.02 *	9.79	10.07	9.84	6.81 *	6.89	6.84	6.92
D1.2a,b	9.79	9.55	9.84	9.60	6.89	6.98	6.93	7.01
D1.3	9.55	9.30	9.60	9.35	6.98	7.07	7.02	7.11
D1.4	9.30	9.08	9.35	9.13	7.07	7.16	7.11	7.19
D1.5	9.08	9.26	9.13	9.31	7.16	7.09	7.20	7.13
		9.32 *				7.10 $		
D2.1	10.02 *	9.44	10.07	9.49	6.80 *	7.01	6.83	7.04
D2.2	9.44	8.95	9.49	9.00	7.01	7.20	7.05	7.24
D2.3a,b	8.95	9.16	9.00	9.20	7.20	7.12	7.24	7.16
		9.18 *				7.18 $		
D3.1	10.01 *	9.56	10.06	9.62	6.79 *	6.95	6.82	6.98
D3.2	9.56	9.09	9.61	9.14	6.95	7.13	6.99	7.16
D3.3	9.09	9.32	9.14	9.36	7.13	7.04	7.17	7.08
		9.32 *				7.10 $		
D4.1	10.02 *	9.35	10.07	9.40	6.80 *	7.04	6.83	7.08
D4.2	9.35	9.54	9.40	9.58	7.04	6.97	7.08	7.01
		9.49 *						

Note: hI and dI denote the specimen height and diameter before a test run respectively.
hF and dF denote the specimen height and diameter after a test run respectively.
* denotes a physically measured dimension and $ denotes the maximum diameter measured.

REFERENCES

ANSI/ASTM C623-71, (Reapproved 1977),
"Standard Test Method for Young's Modulus, Shear Modulus, and Poisson's Ratio for Glass and Glass-Ceramics by Resonance",
ASTM Standards Annual Year Book - 1978
pub. American Society for Testing and Materials.

ANSI/ASTM C848-78,
"Standard Test Method for Young's Modulus, Shear Modulus, and Poisson's Ratio for Ceramic Whitewares by Resonance",
ASTM Standards Annual Year Book - 1978
pub. American Society for Testing and Materials.

Antis, G.R., Chantikul, P., Lawn, B.R., and Marshall, D.B., (1981),
"A Critical Evaluation of Indentation Techniques for Measuring Fracture Toughness: 1, Direct Crack Measurements",
J. Am. Ceram. Soc., 64, [9], pp. 533-538.

Ault, N.N. and Ueltz, H.F.G., (1953),
"Sonic Analysis for Solid Bodies",
J. Am. Ceram. Soc., 36, [6], pp. 199-203.

Bailey, J.E., and Hill, N.A., (1970),
"The Effect of Porosity and Microstructure on the Mechanical Properties of Ceramics",
Proc. Brit. Ceram. Soc., 15, pp. 15-35.

Bansal, G.K., (1976),
"Effect of Flaw Shape on Strength of Ceramics",
J. Am. Ceram. Soc., 59, [1-2], pp. 87-88.

Beall, G.H,., and Duke, D.A., (1983),
"Glass-Ceramic Technology",
in Glass: Science and Technology,
Volume 1 (Glass-Forming Systems),
edited by D.R. Uhlmann and N.J. Kreidl,
pub. Academic Press Inc., pp. 403-445.

Bell, J.F., (1982),
"Erosion Resistance and Development of Glass-Ceramics Made by Controlled Cooling",
Ph.D. Thesis (University of London),
Department of Materials, Imperial College of Science and Technology, London.

Bennett, A., (1986),
"Requirements for Engineering Ceramics in Gas Turbine Engines",
Mat. Sci. and Tech., 2, pp. 895-899.

Berezhnoi, A.I., (1970),
Glass-Ceramics and Photo-Sitalls,
translated by S.A. Mersol and edited by A.G. Pincus,
pub. Plenum Press (New York).

Bergman, B., (1984),
"On the Estimation of the Weibull Modulus",
J. Mater. Sci. Lett., 3, pp. 689-692.

Bergman, B., (1986),
"Estimation of Weibull Parameters Using a Weight Function",
J. Mater. Sci. Lett., 5, pp. 611-614.

Bhat, D.G., (1981),
"Comment on "Elastic/Plastic Indentation Damage in Ceramics: The Median/radial Crack System"",
J. Am. Ceram. Soc., 64, [11], pp. C165-C166.

Birch, J.M., Wilshire, B., Owen, D.J.R., and Shantaram, D., (1976),
"The Influence of Stress Distribution on the Deformation and Fracture Behaviour of Ceramic Materials Under Compression Creep Conditions",
J. Mater. Sci., 11, pp. 1817-1825.

Bishop, J.F.W., (1958),
"On the Effect of Friction on Compression and Indentation Between Flat Dies",
J. Mech. Phys. Solids., 6, pp. 132-144.

Broek, D., (1983),
Elementary Engineering Fracture Mechanics,
3rd Revised Edition,
pub. Martinus Nijhoff Publishers, Chap. 4.

Brown, W.F. (Jr.), and Srawley, J.E., (1966),
"Plane Strain Crack Toughness Testing of High Strength Metallic Materials",
ASTM Special Technical Publication No. 410,
pub. American Society for Testing and Materials.

Cannon, W.R., and Langdon, T.G., (1983),
"Review: Creep of Ceramics",
J. Mater. Sci., 18, pp. 1-50.

Carter, S., (1986),
Private Communication,
Department of Materials, Imperial College of Science and Technology, London.

Carter, S., and Rogers, P.S., (1986),
Private Communication,
Department of Materials, Imperial College of Science and Technology, London.

Chatfield, C., (1983),
Statistics for Technology - A Course in Applied Statistics,
3rd Edition, pub. Chapman and Hall.

Chuang, Tze-Jer, (1986),
"Estimation of Power-Law Creep Parameters from Bend Test Data",
J. Mater. Sci., 21, pp. 165-175.

Clarke, D.R., (1985),
"High-Temperature Deformation of a Polycrystalline Alumina Containing an Intergranular Glass Phase",
J. Mater. Sci., 20, pp. 1321-1332.

Creyke, W.E.C., (1979),
in Materials in Engineering Applications,
Volume 1, pp. 134-142,
pub. Scientific and Technical Press.
[as cited by A. Bennett (1986)].

Cropper, D.R., and Pask, J.A., (1969),
"Effect of Plastic Instability on Compressive Deformation",
Am. Ceram. Soc. Bull., 48, [5], pp. 555-558.

Crosby, A., and Evans, P.E., (1973),
"Creep in Pure and Two Phase Nickel-Doped Alumina",
J. Mater. Sci., 8, pp. 1573-1580.

Dalgleish, B.J., Pratt, P.L., Rawlings, R.D., and Fakhr, A., (1980),
"The Fracture Toughness Testing of Ceramics and Acoustic Emission",
Mater. Sci. and Eng., 45, pp. 9-20.

Davidge, R.W., (1979),
Mechanical Behaviour of Ceramics,
pub. Cambridge University Press.

Davidge, R.W., McLaren, J.R., and Tappin, G., (1973),
"Strength-Probability-Time (SPT) Relationships in Ceramics,
J. Mater. Sci., 8, pp. 1699-1705.

Davis, W.R., (1968),
"Measurement of the Elastic Constants of Ceramics by Resonant Frequency Methods",
Trans. Brit. Ceram. Soc., 67, pp. 515-541.

Doyle, P.J., (1979),
Glass-Making Today,
edited and compiled by P.J. Doyle,
pub. Portcullis Press Ltd.

Eisenstadt, M.M., (1971),
Introduction to Mechanical Properties of Materials,
pub. Macmillan Publishing Company, Chapter 6, p. 173.

Evans, A.G., (1974a),
"Slow Crack Growth in Brittle Materials Under Dynamic Loading Conditions",
Int. J. Fract., 10, pp. 251-259.

Evans, A.G., (1974b),
"Fracture Mechanics Determinations",
in Fracture Mechanics of Ceramics,
Volume 1 (Concepts, Flaws, and Fractography),
edited by R.C. Bradt, D.P.H. Hasselman and F.F. Lange,
pub. Plenum Press, pp. 17-48.

Evans, A.G., (1979),
"Fracture Toughness: The Role of Indentation Techniques",
in Fracture Mechanics Applied to Brittle Materials,
ASTM Special Technical Publication No. 678,
pub. American Society for Testing and Materials,
pp. 112-135.

Evans, A.G., and Charles, E.A., (1976),
"Fracture Toughness Determinations by Indentation",
J. Am. Ceram. Soc., 59, [7-8], pp. 371-372.

Evans, A.G., and Langdon, T.G., (1976),
"Structural Ceramics",
Prog. Mater. Sci., 21, pp. 171-441.

Evans, A.G., and Wilshaw, T.R., (1976),
"Quasi-Static Solid Particle Damage in Brittle Solids - 1. Observations, Analysis and Implications",
Acta. Met., 24, pp. 939-956.

Evans, D., (1986),
Private Communication,
Department of Materials, Imperial College of Science and Technology, London.

Ewalds, H.L., and Wanhill, R.J.H., (1984),
Fracture Mechanics,
pub. Edward Arnold (Publishers) Ltd.

Exner, H.E., (1969),
Trans. AIME, 245, p. 677.
[as cited by D.K. Shetty, I.G. Wright, Mincer, P.N., and A.H.. Clauer (1985)].

Fessler, H., Fricker, D.C., and Godfrey, D.J., (1983),
"A Comparative Study of the Mechanical Strength of Reaction-Bonded Silicon Nitride",
in Ceramics for High-Performance Applications,
Volume 3 (Reliability), edited by E.M. Lenoe, et al.,
pub. Plenum Publishing Corp., pp. 705-736.

Field, M.B. and Tucker, R.W., (1971),
"Elastic Properties of
$0.98Li_2O - 1.0Al_2O_3 - nSiO_2$ Glasses and
Keatite-Phase Glass-Ceramics",
J. Am. Ceram. Soc., 54, [6], pp. 309-314.

Fine, M.E., (1952),
"Dynamic Methods for Determining the Elastic
Constants and Their Temperature Variation in
Metals",
in Symposium on Determination of Elastic Constants,
ASTM Special Technical Publication No. 129,
pub. American Society for Testing and Materials,
pp. 43-70.

Förster, Fritz, (1937),
"Ein neues Meßverfarhen zur Bestimmung des
Elastizitätsmoduls und der Dämpfung",
(A new method of measurement for the determination
of the modulus of elasticity and the damping),
Zeitschrift für Metallkunde, 29, [4], pp. 109-115.

Förster, F. and Köster, W., (1938),
"Elasticity and Damping in Relation to the State of
the Material",
The Engineer, 166, [12], pp. 626-628.

Francois, J-P., and McLaren, J.R., (1982),
"Measurement of K_{Ic} for Cobalt Bonded Tungsten
Carbide by Bend and Indentation Techniques",
Proc. Brit. Ceram. Soc., 32, pp. 227-236.

Freiman, S.W., (1983),
"A Critical Evaluation of Fracture Mechanics
Techniques for Brittle Materials",
in Fracture Mechanics of Ceramics,
Volume 6 (Measurements, Transformations, and
High-Temperature Fracture),
edited by R.C. Bradt, A.G. Evans, D.P.H. Hasselman,
and F.F. Lange,
pub. Plenum Press, pp. 27-45.

Freiman, S.W. and Hench, L.L., (1972),
"Effect of Crystallization on the Mechanical
Properties of $Li_2O - SiO_2$ Glass-Ceramics",
J. Am. Ceram. Soc., 55, [2], pp. 86-90.

Garofalo, F., (1965),
Fundamentals of Creep and Creep-Rupture in Metals,
pub. The Macmillan Co.

Garofalo, F., Malenock, P.R., and Smith, G.V., (1952),
"The Influence of Temperature on the Elastic
Constants of Some Commercial Steels",
in Symposium on Determination of Elastic Constants,
ASTM Special Technical Publication No.129,
pub. Am. Soc. for Testing and Materials, pp. 10-30.

Gere, J.M., and Timoshenko, S.P., (1984),
Mechanics of Materials,
2nd Edition,
pub. PWS Publishers (Wadsworth Inc.).

Glandus, J.C., and Boch, P., (1984),
"Uncertainty on the Mean Strength and Weibull's Modulus of an Alumina Batch as a Function of the Number of Samples",
J. Mater. Sci. Lett., 3, pp. 74-76.

Griffith, A.A., (1920),
"The Phenomena of Rupture and Flow in Solids",
Philos. Trans. Roy. Soc. Lond., A221, pp. 163-198.

Hench, L.L., and Freiman, S.W., (1971), [Editors],
Advances in Nucleation and Crystallization in Glasses, (Symposium Proceedings of the Glass Division of the American Ceramic Society),
pub. The American Ceramic Society Inc.

Hlaváč, J., (1983),
The Technology of Glass and Ceramics - An Introduction,
pub. Elsevier Scientific Pub. Co., Chap 3.

Hoagland, R.G., Marschall, C.W., and Duckworth, W.H., (1976),
"Reduction of Errors in Ceramic Bend Tests",
J. Am. Ceram. Soc., 59, [5-6], pp. 189-192.

Hollenberg, G.W., Terwilliger, G.R., and Gordon, R.S., (1971),
"Calculation of Stresses and Strains in Four-Point Bending Creep Tests",
J. Am. Ceram. Soc., 54, [4], pp. 196-199.

Inglis, C.E., (1913),
"Stresses in a Plate Due to the Presence of Cracks and Sharp Corners",
Trans. Inst. Naval Archit., 55, p. 219.
[as cited by B.R. Lawn and T.R. Wilshaw (1975)].

Irwin, G.R., (1957),
"Analysis of Stresses and Strains Near the End of a Crack Traversing a Plate",
J. Appl. Mech. (Trans. ASME), 24, [9], pp. 361-364.

Jayatilaka, Ayal De S., (1979),
Fracture of Engineering Brittle Materials,
pub. Elsevier Applied Science Publishers.

Jayatilaka, Ayal De. S., and Trustrum, K., (1977),
"Statistical Approach to Brittle Fracture",
J. Mater. Sci., 12, pp. 1426-1430.

Kamiya, N., and Kamigaito, O., (1984),
"Estimation of Weibull Parameters by Omission of Some Data in a Sample",
J. Mater. Sci., 19, pp. 4021-4025.

Kapur, K.C., and Lamberson, L.R., (1977),
Reliability in Engineering Design,
pub. John Wiley and Sons.

Käse, H.R., Tesk, J.A., and Case, E.D., (1985),
"Elastic Constants of Two Dental Porcelains",
J. Mater. Sci., 20, pp. 524-531.

Kittl, P., (1980),
"Transformation of a Flexural Stress Weibull's Diagram into a Tractional One",
Res Mechanica, 1, pp. 161-165.

Kolsky, H., (1963),
Stress Waves in Solids,
pub. Dover Publications Inc.

Lankford, J., (1982),
"Indentation Microfracture in the Palmqvist Crack Regime: Implications for Fracture Toughness Evaluation by the Indentation Method",
J. Mater. Sci. Lett., 1, pp. 493-495.

Laugier, M.T., (1985),
"The Elastic/Plastic Indentation of Ceramics",
J. Mater. Sci. Lett., 4, pp. 1539-1541.

Lawn, B.R., Evans, A.G., and Marshall, D.B., (1980),
"Elastic/Plastic Indentation Damage in Ceramics: The Median/Radial Crack System",
J. Am. Ceram. Soc., 63, [9-10], pp. 574-581.

Lawn, B.R., and Fuller, E.R., (1975),
"Equilibrium Penny-Like Cracks in Indentation Fracture",
J. Mater. Sci., 10, pp. 2016-2024.

Lawn, B.R., and Swain, M.V., (1975),
"Microfracture Beneath Point Indentations in Brittle Solids",
J. Mater. Sci., 10, pp. 113-122.

Lawn, B.R., and Wilshaw, T.R., (1975),
Fracture of Brittle Solids,
pub. Cambridge University Press.

Lee, S.H., and Kim, H.C., (1984),
"Acoustic Emission During Indentation Fracture of Soda-Lime Glass",
J. Mater. Sci. Lett., 3, pp. 907-910.

Leon, M., and Kittl, P., (1985),
"On the Estimation of Weibull's Parameters in Brittle Materials",
J. Mater. Sci., 20, pp. 3778-3782.

Lubahn, J.D., and Felgar, R.P., (1961),
Plasticity and Creep of Metals,
pub. John Wiley and Sons Inc., p. 23-25.

Lytton, J.L., Hren, J.A., Kamber, K.T., and Sherby, O.D., (1964),
"Apparatus for the Determination of Dynamic Young's Modulus and Internal Friction in Vacuum at Temperatures From 25°C to 1200°C",
Brit. J. App. Phys., 15, pp. 1573-1583.

Marion, R.H., (1979),
"Use of Indentation Fracture to Determine Fracture Toughness",
in Fracture Mechanics Applied to Brittle Materials,
ASTM Special Technical Publication No. 678,
pub. American Society for Testing and Materials,
pp. 103-111.

Marlowe, M.O. and Wilder, D.R., (1965),
"Elasticity and Internal Friction of Polycrystalline Yttrium Oxide",
J. Am. Ceram. Soc., 48, [5], pp. 227-233.

Marschall, C.W. and Rudnick, A., (1974),
"Conventional Strength Testing of Ceramics",
in Fracture Mechanics of Ceramics,
Volume 1 (Concepts, Flaws and Fractography),
edited by R.C. Bradt, D.P.H. Hasselman and F.F. Lange,
pub. Plenum Press, pp. 69-92.

Marshall, D.B., (1983),
"Controlled Flaws in Ceramics: A Comparison of Knoop and Vickers Indentation",
J. Am. Ceram. Soc., 66, [2], pp. 127-131.

Marshall, D.B., and Evans, A.G., (1981),
"Reply to "Comment on 'Elastic/Plastic Indentation Damage in Ceramics: The Median/Radial Crack System'"",
J. Am. Ceram. Soc., 64, [12], pp. C182-C183.

Marshall, D.B., and Lawn, B.R., (1979),
"Residual Stress Effects in Sharp Contact Cracking - Part 1. Indentation Fracture Mechanics",
J. Mater. Sci., 14, pp. 2001-2012.

Marshall, D.B., Tatsuo Noma, and Evans, A.G., (1982),
"A Simple Method for Determining Elastic-Modulus-to-Hardness Ratios using Knoop Indentation Measurements",
J. Am. Ceram. Soc., 65, [10], C175-C176.

Masahiko Shimada, Ken'chi Matsushita, et al., (1984),
"Temperature Dependence of Young's Modulus and Internal Friction in Alumina, Silicon Nitride, and Partially Stabilized Zirconia Ceramics",
J. Am. Ceram. Soc., 67 , [2], pp. C23-C24.

McMillan, P.W., (1979),
Glass-Ceramics, 2nd Edition,
pub. Academic Press Inc. (London) Ltd.

Miranzo, P., and Moya, J.S., (1984),
"Elastic/Plastic Indentation in Ceramics: a Fracture Toughness Determination Method",
Ceram. Int., 10, [4], pp. 147-152.

Morrell, R., (1985),
Handbook of Properties of Technical & Engineering Ceramics - Part 1: An Introduction for the Engineer and Designer,
pub. Her Majesty's Stationery Office, pp. 95-96.

Morrell, R., and Ashbee, K.H.G., (1973),
"High Temperature Creep of Lithium Zinc Silicate Glass-Ceramics - Part 1. General Behaviour and Creep Mechanisms",
J. Mater. Sci., 8, pp. 1253-1270.

Newnham, R.C., (1975),
"Strength Tests for Brittle Materials",
Proc. Brit. Ceram. Soc., 25, pp. 281-293.

Nicholls, J.R., (1974),
"Structure and Mechanical Properties of Ni_3Al, With Iron Additions",
Ph.D. Thesis (University of London),
Department of Materials, Imperial College of Science and Technology, London.

Niihara, K., (1983),
"A Fracture Mechanics Analysis of Indentation-Induced Palmqvist Crack in Ceramics",
J. Mater. Sci. Lett., 2, pp. 221-223.

Niihara, K., Morena, R., and Hasselman, D.P.H., (1982),
"Evaluation of K_{Ic} of Brittle Solids by the Indentation Method with Low Crack-to-Indent Ratios",
J. Mater. Sci. Lett., 1, (1982), pp. 13-16.

Niihara, K., Morena, R., and Hasselman, D.P.H., (1983),
"Indentation Fracture Toughness of Brittle Materials for Palmqvist Cracks",
in Fracture Mechanics of Ceramics,
Volume 5 (Surface Flaws, Statistics, and Microcracking),
edited by R.C. Bradt, A.G. Evans, D.P.H. Hasselman, and F.F. Lange,
pub. Plenum Press, pp. 97-105.

Nowick, A.S., (1953),
"Internal Friction in Metals",
Progress in Metal Physics, 4, (1953), pp. 1-70.

Nowick, A.S. and Berry, B.S., (1972),
Anelastic Relaxation in Crystalline Solids,
pub. Academic Press Inc.

Nye, J.F., (1969),
Physical Properties of Crystals - Their representation by tensors and matrices,
pub. Oxford University Press, Chap. 8.

Orowan, E., (1948-49),
"Fracture and Strength of Solids",
Rep. Prog. Phys., 12, pp. 185-232.

Orowan, E., (1955),
"Energy Criteria of Fracture",
The Welding Journal, 34, [3],
Welding Research Supplement, pp. 157s-160s.

Pabst, R.F., (1974),
"Determination of K_{1c} - Factors with Diamond-Saw-Cuts in Ceramic Materials",
in Fracture Mechanics of Ceramics,
Volume 2 (Microstructure, Materials, and Applications),
edited by R.C. Bradt, D.P.H. Hasselman and F.F. Lange,
pub. Plenum Press, pp. 555-565.

Pabst, R.F., Kromp, K., and Popp, G., (1982),
"Fracture Toughness - Measurement and Interpretation",
Proc. Brit. Ceram. Soc., 32, pp. 89-105.

Paris, P.C., and Sih, G.C., (1965),
"Stress Analysis of Cracks",
Symposium on Fracture Toughness Testing and Its Applications,
ASTM Special Technical Publication No. 381,
pub. American Society for Testing and Materials
pp. 30-83.

Parker, A.P., (1981),
The Mechanics of Fracture and Fatigue - (An Introduction),
pub. E. & F.N. Spon Ltd.

Parker, B.A., (1967),
"The Ageing Behaviour of Certain Nickel Alloys Containing Aluminium and Titanium",
DIC Thesis,
Department of Materials, Imperial College of Science and Technology, London.

Patel, H., (1985),
Private Communication,
Department of Materials, Imperial College of Science and Technology, London.

Picket, G., (1945),
"Equations for Computing Elastic Constants From Flexural and Torsional Resonant Frequencies of Vibration of Prisms and Cylinders",
ASTM Proceedings, 45, pp. 846-865.

Pollard, H.F., (1977),
Sound Waves in Solids,
pub. Pion Ltd.

Rawlings, R.D., (1983),
"Hardness Testing of Aluminas in Air and a Simulated Body Environment",
Mater. Sci. and Eng., 61, pp. L1-L5.

Richards, J.T., (1952),
"An Evaluation of Several Static and Dynamic Methods for Determining Elastic Moduli",
Symposium on Determination of Elastic Constants,
ASTM Special Technical Publication No. 129,
pub. American Society for Testing and Materials
pp. 71-100.

Roberts, M.H., and Nortcliffe, J., (1947),
"Measurement of Young's Modulus at High Temperatures",
J. Iron and Steel Inst. Lond., 157, [11],
pp. 345-348.

Rogers, P.S., Williamson, J., and Johnson, P.E., (1974),
United Kingdom Patent 1 462 035.

Rogers, P.S., Williamson, J., and Johnson, P.E., (1975),
United States Patent 3 901 716.

Rogers, P.S., Williamson, J., Bell, J.F., and Campbell, M., (1984),
"Erosion-Resistant Glass-Ceramics Made by Direct Controlled Cooling From the Melt",
Proceedings of the International Seminar on Energy Conservation in Industry (DUsseldorf, February 1984),
Volume 3 (Applications and Technologies),
pub. Commission of the European Communities.

Rogers, P.S., Williamson, J., Bell, J.F., and Campbell, M., (1986),
"Ceramic Materials from Molten Blast-Furnace Slag by Direct Controlled Cooling",
Commission of the European Communities Energy R & D Programme - Energy Conservation, Final Report EUR 10389 EN,
pub. Commission of the European Communities.

Ryder, G.H., (1969),
Strength of Materials,
3rd. Edition (SI Units),
pub. The Macmillan Press ltd., Chap. 9.

Sack, R.A., (1946),
"Extension of Griffith's Theory of Rupture to Three Dimensions",
Proc. Physical. Soc. Lond., 58, pp. 729-736.

Seddon, I.N., (1946),
"The Distribution of Stress in the Neighbourhood of a Crack in an Elastic Solid",
Proc. Roy. Soc. Lond., 187A, pp. 229-260.

Schreiber, E., Anderson, O.L. and Naohiro Soga, (1973),
Elastic Constants and Their Measurement,
pub. McGraw-Hill Inc.

Shanley, F.R., (1967),
Mechanics of Materials,
pub. McGraw-Hill Inc., Chap. 11.

Shetty, D.K., Rosenfield, A.R., and
Duckworth, W.H., (1985),
"Indenter Flaw Geometry and Fracture Toughness Estimates for a Glass-Ceramic",
J. Am. Ceram. Soc., 68, [10], pp. C284-C284.

Shetty, D.K., and Wright, I.G., (1986),
"On Estimating Fracture Toughness of Cemented Carbides from Palmqvist Crack Sizes",
J. Mater. Sci. Lett., 5, (1986), pp. 365-368.

Shetty, D.K., Wright, I.G., Mincer, P.N., and
Clauer, A.H., (1985),
"Indentation Fracture of WC-Co Cermets",
J. Mater. Sci., 20, pp. 1873-1882.

Simmons, J.H., Uhlmann, D.R., and Beall, G.H.,
(1982), [Editors],
"Nucleation and Crystallization in Glasses",
Volume 4 in Advances in Ceramics,
pub. The American Ceramic Society Inc.

Spinner, S., (1956),
"Elastic Moduli of Glasses at Elevated Temperatures by a Dynamic Method",
J. Am. Ceram. Soc., 39, [3], pp. 113-118.

Spinner, S., (1961),
"Temperature Dependence of Elastic Constants of Some Cermet Specimens",
J. Res. Nat. Bur. Stand., 65C, [2], pp. 89-96.

Spinner, S., and Cleek, G.W., (1960),
"Temperature Dependence of Young's Modulus of Vitreous Germania and Silica",
J. App. Phys., 31, [8], pp. 1407-1410.

Spinner, S., and Tefft, W.E., (1961),
"A Method for Determining Mechanical Resonance Frequencies and for Calculating Elastic Moduli from These Frequencies",
ASTM Proceedings, 61, pp. 1221-1238.

Spinner, S., and Valore, R.C. (Jr.), (1958),
"Comparison of Theoretical and Empirical Relations Between the Shear Modulus and Torsional Resonance Frequencies for Bars of Rectangular Cross Section",
J. Res. Nat. Bur. Stand., 60, [5], pp. 459-464.

Srawley, J.E., (1976),
"Wide Range Stress Intensity Factor Expressions for ASTM E399 Standard Fracture Toughness Specimens",
Int. J. Fract., 12, pp. 475-476.

Stewart, D.R., (1972),
"Concepts of Glass-Ceramics",
in Introduction to Glass-Science,
edited by L.D. Pye, H.J. Stevens and W.C. LaCourse,
pub. Plenum Press.

Stewart, D.R., (1985),
"Glass-Ceramics"
in Encyclopedia of Glass, Ceramics and Cement,
edited by M. Grayson,
pub. John Wiley and Sons Inc., pp. 538-549.

Stookey, S.D., and Maurer, R.D., (1962),
"Catalyzed Crystallization of Glass - Theory and Practice",
Prog. Ceram. Sci., 2, pp. 78-101.

Sullivan, J.D., and Lauzon, P.H., (1986a),
"Experimental Probability Estimators for Weibull Plots",
J. Mater. Sci. Lett., 5, pp. 1245-1247.

Sullivan, J.D., and Lauzon, P.H., (1986b),
"Shape Profiles of Cracks Formed Under a Vickers Pyramid Indenter",
J. Mater. Sci. Lett., 5, pp. 247-248.

Tabor, D., (1951),
The Hardness of Metals,
pub. Oxford University Press.

Timoshenko, S., (1955),
Strength of Materials - Part 1 Elementary,
3rd Edition (International Student Edition),
pub. Van Nostrand Reinhold, Chap. 12, pp. 368-370.

Timoshenko, S.P., and Goodier, J.N., (1970),
Theory of Elasticity,
3rd Edition, pub. McGraw-Hill Inc., Chap. 4, Art. 40,
pp. 113-122.

Trustrum, K., and Jayatilaka, Ayal De S., (1979),
"On Estimating the Weibull Modulus for a Brittle Material",
J. Mater. Sci., 14, pp. 1080-1084.

Urbain, G., Cambier, F., Deletter, and
Anseau, M.R., (1981),
"Viscosity of Silicate Melts",
Trans. J. Br. Ceram. Soc., 80, pp. 139-141.
[cited by S. Carter (1986)].

von Kármán, T., and Seewald, F., (1927),
Abhandl. Aerodynam. Inst., Tech. Hochschule,
Aachen, 7.
[as cited by S.P. Timoshenko and J.N. Goodier, 1970].

von Mises, R., (1928),
Z. Angew. Math. Mech., 8, p. 161.
[as cited by R.W. Davidge (1979)].

Wachtman, J.B. (Jr.), and Lam, D.G. (Jr.), (1959),
"Young's Modulus of Various Refractory Materials as a Function of Temperature",
J. Am. Ceram. Soc., 42, [5], pp. 254-260.

Wachtman, J.B. (Jr.), and Tefft, W.E., (1958),
"Effect of Suspension Position on Apparent Values of Internal Friction Determined by Forster's Method",
Rev. Sci. Instr., 29, [6], pp. 517-520.

Weibull, W., (1951),
"A Statistical Distribution Function of Wide Applicability",
J. Appl. Mech., 18, pp. 293-297.

Weil, N.A., and Daniel, I.M., (1964),
"Analysis of Fracture Probabilities in Nonuniformly Stressed Brittle Materials",
J. Am. Ceram. Soc., 47, [6], pp.268-274.

Whittemore, O.J., and Ault, N.N., (1956),
"Thermal Expansion of Various Ceramic Materials to 1500°C",
J. am. Ceram. Soc., 39, [12], pp. 443-444.

Wiederhorn, S.M., (1974),
"Subcritical Crack Growth in Ceramics",
in Fracture Mechanics of Ceramics,
Volume 2 (Microstructure, Materials, and Applications),
edited by R.C. Bradt, D.P.H. Hasselman and F.F. Lange,
pub. Plenum Press, pp. 613-646.

Wyatt, O.H., and Dew-Hughes, D., (1974),
Metals, Ceramics and Polymers - An introduction to the structure and properties of engineering materials,
pub. Cambridge University Press, Chap. 3.

Zener, C., (1948),
Elasticity and Anelasticity of Metals,
pub. University of Chicago Press, Chap. 6.